Parametric analysis of groundshock loading on steel plates and reinforced concrete slabs

by

Leon Robert Beer

MEng(Hons) Sheffield

Thesis submitted to the University of Sheffield
for the degree of Doctor of Philosophy

University of Sheffield
Department of Civil and Structural
Engineering

January 2006

The value of an ambitious goal is not measured by what it will bring to you. The worth of a goal is measured by what it will make of you in the process of following and attaining it.

An outrageous and impractical goal can be just as valuable as a prudent and pragmatic one. What matters is not how realistic or practical your objective may be, but how much it compels you to push beyond your limitations.

There are stunningly brilliant possibilities for your life that you've never even imagined. Set yourself on a meaningful and ambitious course and the best of those possibilities will begin snapping into focus.

It pays to dream big dreams. And it certainly pays to follow the biggest and most ambitious of them. For the biggest dreams will put you face to face with the biggest challenges. Those challenges, difficult as they may be, will nourish you in ways that nothing else can.

Declaration

I declare that the work in this thesis has been composed by myself and no portion of the work has been submitted in support of an application for another degree or qualification of this or any other University or other institute of learning. The work has been my own except where indicated by references.

Dedication

The thesis is dedicated to my parents Robert and Carole Beer who have encouraged, motivated and have been a pillar of strength during an immensely challenging period of my life.

Acknowledgments

I would like to show my gratitude in thanking my two supervisors. Dr Alan Watson for giving me the privileged opportunity to read for a PhD degree.
I am forever grateful to Dr Andy Tyas who has willingly help shaped my research abilities and given me direction. His guidance and positive suggestions have been crucial in my understanding of the subject. My appreciation also extends to Dr Jim Warren who has also been of assistance.
I also thank my Industrial Supervisor, Dr Jim Sheridan from [dstl], for providing the funding for this proposed research project as well as giving me the opportunity in gaining invaluable industrial experience whilst working at [dstl] in Farnborough. My gratitude also goes out to Cathy O'Carroll for giving me the opportunity to work in QinetiQ with Paul Morrissy whom I am grateful to in helping me with the numerical work during the last few months of the research.
I am forever thankful and grateful to my two committed technicians, Mr Alan Hindle and Mr Roy Mellor, for their technical and practical help during the intense experimental programme. I value their knowledge and encouragement, as well as the jovial conversions we had.
My brother Alex, who I am forever indebted to, in helping me achieve a healthy balance between 'work and play' teaching me the importance of having 'fun' and my youngest brother Nicky, who has continuously looked up to me as a role model.
Most importantly, I am forever grateful to my parents, Robert and Carole Beer who have given me the emotional support throughout such a challenging task.

Words of Warning

The methodology describing the implementation of the explosive charge should not be carried out without the use of personnel trained in the required Health & Safety procedure.

Summary

Hardened underground structures are purposely constructed beneath the ground surface for additional protection. The protection and sustainability of such a structure is provided by the soil overburden, supported by the structure's roof slab, also called a primary slab. The soil overburden usually contains one or more layers of protective reinforced concrete slabs, defined as secondary slabs. Hardened sub-surface structures can experience a degree of damage from sub-surface explosions, caused by the detonation of airborne weapons at variable depths within the soil overburden layer. The research objective was to evaluate the degree to which material and geometric parameters influenced the magnitude of groundshock loading and hence the severity of damage to sub-surface positioned reinforced concrete slabs.

The work was of an experimental nature, performed within a purposely built test cell. The experimental set-up involved positioning cylindrical charges within the soil overburden at variable standoffs from an initially positioned steel plate, then from a primary slab, which was subjected to a series of cumulative loadings. The structural response of both the steel plate and a reinforced concrete slab were evaluated using an energy balance procedure.

A parametric study was performed, determining the influence each geometric parameter had to the magnitude of groundshock loading. The variability of data associated with the material parameters was analysed and compared to the published literature.

Numerical simulations were performed at the end of the experimental stage (using the non-linear finite element programme AUTODYN2D) to investigate phenomena that could not be investigated experimentally.

A visual damage assessment in the form of a crack pattern analysis and chronological order of occurring mechanisms upon reinforced concrete slabs was performed. The severity of damage to the primary slabs was then associated with the cumulative load impulse history.

The research yielded the following conclusions:

1. An idealised half sine-wave load distribution approximated the pressure-time history profiles recorded by pressure gauges.
2. The steel plate and one concrete slab (for which conclusive data was obtained) responded impulsively to groundshock loading.
3. The magnitude of groundshock loading was most sensitive to a change in the charge standoff.
4. The reduction in the soil overburden above the top face of a secondary slab did not influence the groundshock loading induced into a primary slab.
5. The effect of the propagating groundshock wave overrode any initial form of soil compaction between the charge and target. This was due to the significantly high stresses induced into the soil, which were well above the initial insitu stresses.
6. Internal weakening of a primary slab, which was unidentifiable from the external damage, caused significant loss in structural strength and stiffness.

Glossary of terms

Bandwidth	Range of frequencies a pressure gauge will respond to
CEDUS laboratories	Civil Engineering Department of the University of Sheffield: Experimental testing laboratories
GREAC cell	Gauged reactive confinement cell used un determining equation of state properties for materials
Diaphragm pressure gauges (DPGs)	Steel hollow circular bodies on plan with a circular lid bolted to the body. A strain gauge is attached to the underside of the lid, which stretches as load is applied to the gauge. They react under pressure loading, by outputting a strain time response, which is converted into an equivalent dynamic pressure
Impulse	Area under a pressure-time history plot, causing the structure to response to the total duration of load rather than just the peak.
LVDT	Linear variable displacement transducers provide a simple and reliable means of converting mechanical displacement into an electrical signal. They do not suffer from electrical hysteresis and can be adapted to harsh environments
Nyquist criteria	Frequency limit used to ensure that if frequencies associated with the response of a structure are smaller than the limit, the true response is captured
Pendine blocks	Reinforced concrete blocks used to construct the test cell
PE4	Military plastic explosive
Primary slab	Reinforced concrete slab that has been clamped to a steel support structure, mimicking that of a roof slab, carrying an overburden of soil.
Secondary slab	Reinforced concrete slab acting as a protective layer, freely supported by the dead weight of soil below it, whilst supporting the overburden of soil above it. Its purpose is to reduce the magnitude of damage caused to the primary slab upon attack
Small-scale test cell	Configuration of reinforced concrete pendine blocks, arranged in a geometric fashion leaving an internal plan area in which an explosive test occurs. The internal volume of the test cell dictates the volume of soil overburden and surface areas of the primary and secondary slabs.
Slab weakening	Loss of structural strength and stiffness due to pre-damage

List of symbols and abbreviations

A_{ct}	Area of cratering on the top face that does not include perforation
A_{cb}	Area of cratering on the bottom face that does not include perforation
A_p	Area of perforation that
A_c	Loaded area of concrete cube
A_{steel}	Cross-sectional area of steel rebar
A_{bar}	Cross-sectional area of rebar
A_l	Cross-sectional area of the steel rebar at maximum load
A_s	Minimal area of steel
b	Breath of a reinforced concrete slab
c	Seismic velocity
C_v	Intercept voltage
C_l	Constant parameter
C	Loading wave velocity
C_g	Longitudinal wave velocity
C_p	Charge position
d	Depth of the section
dt	Increment of time
DSO	Digital storage oscilloscope
D	Diameter of a concrete cylinder
DPG	Diaphragm pressure gauge
d_{max}	Maximum peak deflection
d_{cr}	Cumulative residual deflection
d_c	Crater depth
E_l	Energy released per unit mass of disturbed air
E	Modulus of elasticity
f_t	Total coupling factor
f_i	Coupling factor for each component material, i.e. air, soil, concrete.
f	Nyquist frequency
FFT	Fast Fourier Transform
F_c	Compressive force
F_t	Tensile force
g	Percentage reduction in soil overburden.
G_n	Group number
I	Impulse
i_s	Specific impulse per unit area
I_D	Density index
k	Constant of proportionality
K_s	Strain gauge factor
f_n	Natural frequency
L_p	Span of a panel
Le	Effective length of the primary slab that is not restraint
L	Length of a concrete cylinder
L_i	Length of charge in contact with each material

L_t	Total charge length
LVDT	Linear variable displacement transducer
M_1	Gradient
M	Stiffness or modulus of the soil
m	Mass of the steel plate
m_{cw}	Mass of container and wet soil
m_{cd}	Mass of container and dry soil
m_c	Mass of container
n	Soil attenuation coefficient
N_{bars}	Number of rebars within a concrete slabs cross-section
P_{t1}	Magnitude of pressure at a duration of time
P_c	Maximum load applied at the point of failure to a concrete cube
P_s	Maximum tensile load applied to a steel rebar at the point of failure
P_{ff} (t)	Reflected pressure
P_i (t)	Interaction pressure
P_o	Pressure
$P_{s\,max}$	Maximum peak pressure
r_b	Radius of a bar
R_n	Response number
S_{bb}	Charge standoff to the bottom face of the secondary slab
SG	Strain gauge
S_{tb}	Charge standoff to the top face of the secondary slab
S_r	Charge standoff
Sr/Le	Charge standoff to effective span ratio defining the loading environment as near or far field
$S_{\%}$	Percentage of steel reinforcement within the cross-sectional area of the concrete slab
t_p	Thickness of a panel
t	Strain due to tension
t_1	Loading phase
t_a	Duration of the blast wave to travel from source to point of application
T_B	Strain due to bending
t_{bs}	Thickness of the secondary slab
t_d (P)	Duration of the load
t_d	Duration of the transient load
t_{end} (P)	Time when the load has fully dissipated
t_{end} (δ)	Time when the response ends
t_d (δ)	Duration of the response
$t_{maxpeak}$ (P)	Time at maximum peak pressure associated with the central response of DPG1
T_n	Test number
t_{rp}	Thickness of the primary steel plate
t_{bs}	Thickness of the secondary reinforced concrete slab
t_{rs}	Thickness of the primary reinforced concrete slab
t_r (P)	First response time of DPG1
t_r(δ)	First response time of the central LVDT
$t_{maxpeak}$ (δ)	Time at maximum peak deflection associate with the response of the central LVDT
$t_{second\ peak}$(δ)	Time at the second peak associate with the response of the central LVDT
T	Natural period of vibration of a structure
T_1	First natural period of oscillation

T_2	Second natural period of oscillation of a structure
$T_1(\delta)$	First natural period of oscillation associated with the response of the central LVDT
$T_2(\delta)$	Second natural period of oscillation associated with the response of the central LVDT
T_c	Strain in the compression face of the rebar
T_t	Strain in the tensile face of the rebar
u	particle velocity
u_g	Soil particle velocity
u_k	Transducer velocity
v_{lvdt}	Voltage output from an LVDT
v_{max}	Maximum downwards velocity of the steel plate
V	Variable parameter
V_1	Maximum downwards velocity of the primary slab
V_2	Maximum upwards velocity of the primary slab which is $< V_1$
w	Water content
W_i	Weight of the charge in contact with each component material
W	Charge mass
X_{cv}	Horizontal distance between the centre of mass of the charge and the secondary slab
x	Particle displacement
x_1	Voltages recorded on the horizontal axis
Y_{cc}	Vertical distance between the centre of masses of the charge and the secondary slab
z	Scaled distance
Z_1	Soil overburden confined between the primary and secondary slab
Z_2	Soil overburden above the secondary slab
Z_3	Total depth of soil overburden above a primary steel plate or a reinforced concrete slab
δ	Deflection
Δt	Sampling rate
e_0	Output voltage
ε_0	Strain
ε_1	Strain measurement on the top face of the rebar
ε_2	Strain measurement on the bottom face of the rebar
$(^{\varepsilon_0})$	Residual strain or deformation achieved within the material once the applied stress has been removed.
e_i	Input voltage
θ	Charge orientation to the horizontal
ρ	Soil bulk density
ρ_D	Soil bulk density associated with insitu samples taken from soil overburden within the test cell
$\rho_{D,min}$	Minimum dry density taken from the compaction tests
$\rho_{D,max}$	Maximum dry density taken from the compaction tests
$\rho_1 C_1$	Acoustic impedance of the material that contains the incident and reflected wave
$\rho_2 C_2$	Acoustic impedance of the material that contains the transmitted wave
ρ_D	Dry bulk density
$\rho_{D,min}$	Minimum dry density

$\rho_{D,\max}$	Maximum dry density
σ	Yield stress
σ_c	Compressive strength of a concrete cube
σ_R	Reflective stress
σ_I	Incident stress
σ_h	Horizontal tensile strength of a concrete cylinder
σ_u	Ultimate tensile stress of high yield steel
rh_o	Mass density
ϖ	Natural period of oscillation

List of figures

List of plates

List of tables

Chapter One

Introduction

1.1 Scope of the thesis

A series of simple preliminary steel plate tests was initially performed, providing quantitative data for response characterisation of a primary steel plate subjected to groundshock loading. Previous publications by **Pope (2002)** and **Tyas & Pope (2004)** indicated an impulsive panel response during airblast testing using an energy balance procedure. The procedure was applied to the steel test results yielding a linear relationship that existed between deflection and impulse, determining the plate's response as impulsive.
The concrete tests performed after the steel tests, were of a complex nature and involved a greater number of parameters that were investigated. Incomplete data from a number of the concrete tests prevented the energy balance procedure from being performed. Results from the steel tests and available data from the concrete tests were used to determine load duration and natural period of response ratio values to hypothesise the response of a primary slab.
A parametric influence on groundshock was then investigated, followed by a qualitative assessment of damage subjected to reinforced concrete slabs.
The structure of the thesis has been separated into seven chapters followed by a Reference and an Appendix section.

Chapter 1 Introduction – A summary of each chapter has been presented, followed by an overall aim of the work that initially involved characterising the response of a primary slab to groundshock loading, identifying the parameters that influenced the loading and commenting on reasons for a reduction in the test matrix

Chapter 2 Literature review – Background reading from books, PhD theses and journal papers has been used to gather an understanding into the area surrounding sub-surface explosions, techniques implemented and software packages used to both model and simulate explosive loading events. The literature review found considerable information on airblast loadings of structures, but relatively little on groundshock loading. An energy balance procedure involving an impulse-deflection analysis has been identified and used as a basis for an analysis of the experimental results from the current work.

Chapter 3 Experimental Methodology - The experimental objectives have been discussed in detail focusing on the stages of testing, defined as I, II and III which formed the test matrix. The test cell used to perform the explosive tests has been described from a functional perspective, focusing on its geometry and the steel support structure used to support the primary slab. The design and casting procedures of the reinforced concrete slabs have been discussed followed by a detailed account of the calibration procedure involving the linear variable differential transformers LVDTs and the diaphragm pressure gauges DPGs. The activities involved in a typical test

setup have been described in chronological order concluding with a discussion on test repeatability.

Chapter 4 Results – Qualitative analyses of the damage to the secondary and primary slabs based upon photographic evidence and cross-sectional elevations have been presented and discussed. This is followed by an interpretation of graphical plots containing that of deflection, pressure and strain responses.
The characterisation of a primary steel plate and reinforced concrete slab's response to groundshock loading was performed. This was followed by a damage analysis of the primary and secondary slabs, concluding with the variability of the material properties, influence of soil compaction on stress wave propagation and a chapter summary.

Chapter 5 Discussion – Confidence in the results have been discussed in terms of the Nyquist criteria, followed by procedures used to characterise the response of a primary slab. Geometric parameter assessment in influencing groundshock followed by an investigation into the justification of material parameter variation has been documented. Damage classification of primary reinforced concrete slabs has also been discussed followed by an overall summary.

Chapter 6 Conclusion – This chapter has been split into four sections. Structural response of the steel plate and reinforced concrete slabs, variability of both the material and geometric parameters in influencing groundshock loading, soil compaction and severity of damage subjected to the primary and secondary slabs.

Chapter 7 Future work - Improvements to the experimental work have been discussed that could have been performed if there was a greater awareness at the time, followed by activities that would further the research.

Appendix – The peripheral test data in the form of deflection-time, pressure-time and strain-time histories have been presented. The results from the numerical simulations performed using AUTODYN2D are also presented, concluding with information relating to material and instrumentation suppliers.

1.2 Overall aim of the thesis

The research was separated into two main objectives:
1. Response characterisation of a primary slab whilst subjected to near field groundshock loading.
2. Identification of parameters that influenced the magnitude of groundshock loading and hence damage to reinforced concrete slabs within a complex subsurface arrangement. The parameters that were investigated are stated as follow:

1. Presence of a secondary slab and charge positioned relative to it.
2. Charge standoff to the primary slab.
3. Cumulative loading upon a primary slab.
4. Soil depth between the top face of the primary slab and bottom face of the secondary slab.
5. Soil depth above the secondary slab.
6. Soil compaction prior to charge detonation.

The tests were of an explosive nature and were performed within a reinforced concrete test cell, constructed from concrete pendine blocks, as illustrated in detail in Chapter 3. A simple diagrammatic representation of a test setup is illustrated in figure 1.2.1. The experimental arrangement involved detonating an inclined cylindrical charge relative to a secondary slab when positioned, at varying standoffs above a primary slab.

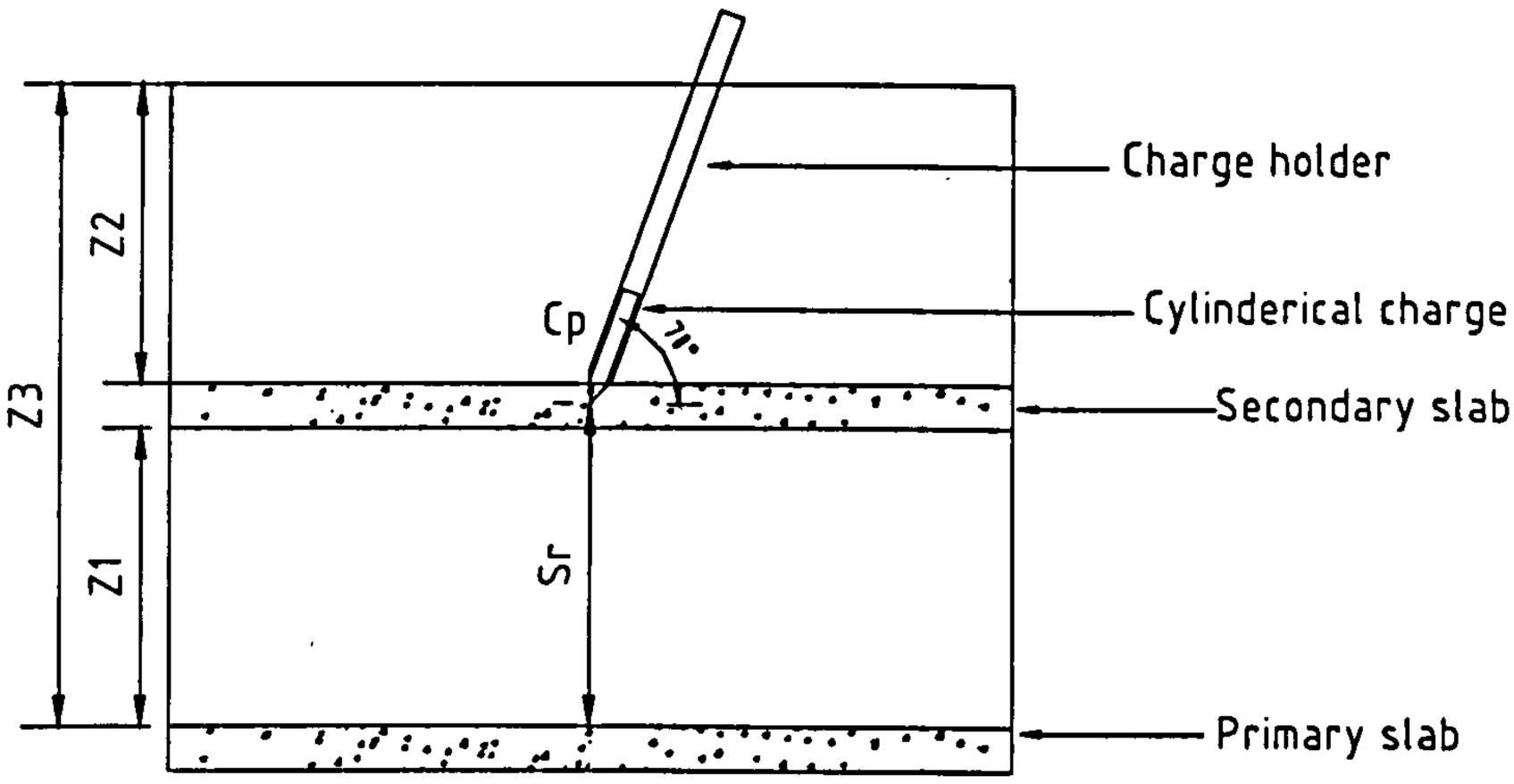

C_p = Charge position relative to the secondary slab
S_r= Charge standoff (vertical distance between the tip of the charge and the top face of the primary slab)
Z_1 = Soil overburden confined between the primary and secondary slab
Z_2 = Soil overburden above the secondary slab
Z_3 =Total soil overburden and secondary slab if present, above the primary slab

Figure 1.2.1 Cross-sectional elevation of a concrete test set up within the test cell

Positioned reinforced concrete slabs dictated the main theme of the research as their damage mechanisms were of particular interest, as well as evaluating the parameters that influenced groundshock loading within the geometry of a test setup.
Steel plate tests were initially performed within the test cell, involving a primary steel plate only, carrying a fixed volume of soil overburden, to assess the performance of the instrumentation but more importantly to characterise the response of the steel plate whilst subjected to groundshock loading.
Concrete tests were then performed to determine a primary slab response from the determination of load duration and natural frequency of response ratio values. The ratio values were compared to those achieved from the steel plate tests, concluding that impulsive behaviour was observed.
The damaged primary slabs were closely analysed and damage mechanisms identified. Four primary slabs in total were subjected to cumulative loading that involved secondary slabs positioned within the soil environment and the final damage observed was associated with a magnitude of groundshock loading.
Time and resource constraints necessitated rationalisation of the parametric study. A test matrix was developed and consequently 19 tests were conducted with some tests involving variation of more than one parameter.

Chapter Two

Literature review

2.1 Introduction

The literature has been used to characterise structural response, validate experimental procedures, interpret time history data, determine data variability, identify parameters that influence groundshock and damage mechanisms on reinforced concrete slabs.
A general interest in groundshock commenced before 1939 with quarry blasts, which had been organised by the U.S Bureau of Mines. In 1940 the British showed an interest in underground explosions. By 1941 a report was published detailing average curves for earth movement and wall damage as functions of distance and size of charge. The British then carried out damage analyses to foundation walls, caused from actual bombing incidents. Proposals for protection against such incidents by means of using secondary slabs and spaced walls were implemented, as described in **National Defence Research Committee (1946).** The results led to the conclusion that a systematic study of the phenomena occurring underground subsequent to the explosion of the buried bomb was necessary. Authors since then have investigated the affects of groundshock, adding to a progression of knowledge within the area.

2.2 Reinforced concrete slabs

The design code **TM5-1300 (1991)** has been used to design structures against blast loading. For the design of reinforced concrete slabs, it suggests a minimal area of flexural reinforcement governed by equation (2.2.1).

$$A_s \geq 0.0015bd$$

Equation (2.2.1)

A_s = Minimal area of steel
b = Breath of the section
d = Depth of the section

The design code **BS8110 (1997)** is used to design reinforced concrete slabs that are subjected to static loading, throughout their life span. Clause (3.3.1.3) states that '*the nominal cover should not be less than the nominal maximum size of the aggregate' which had a maximum size of 5mm*'. Clause (3.12.11.1) also states that *'the minimal horizontal distance between the bars should not be less than maximum size of the aggregate + 5mm'.*
For the purposes of design, the compressive strength of a slab is assessed by uniaxial crushing of a standard cube as described in **BS 1881(1983)** part 116. The tensile strength of concrete can be indirectly determined by crushing a cylinder orientated with its major axis perpendicular to the load and is also described in **BS 1881 (1983)** part 117. The vertical load will induce compressive stresses, fracturing the specimen due to the complimentary horizontal expansion.

Pope (2002) carried out experimental work on plate-reinforced panels, subjected to airblast explosions. He did not use reinforced concrete slabs, whereas **Duranovic (1994)** did within the airblast environment. The concrete mix design used by **Duranovic (1994)** was associated with strength of 40N/mm^2. The consistent proportions are illustrated in table 2.2.1. He varied the percentage of reinforcement within a slab as well as only placing rebars in the bottom face in a number of slabs. This was done to compare to the difference in damage magnitudes to slabs with a different geometry and amount of reinforcement.
A slab that is fixed around its perimeter would normally contain additional top face reinforcement to sustain the tensile stresses induced by the hogging moments at the supports. In the absence of top face bars, cracks develop quickly and the average bending stiffness is similar to that of a simply supported slab. The reinforcement parameter was not varied during this research as other parameters were varied instead. The material properties of concrete depend upon its water/cement ratio and the manner in which it is prepared. **Neville (1981)** has discussed many influential factors such as preparation of moulds prior to the concrete being poured and the curing procedure, which were taken into account during the experimental stage of this research.

Table 2.2.1 Mix design (Duranovic N, 1994)

Materials	Cement	Sand	Water
Parts	1	3	0.6

The workability of fresh concrete during the casting procedure is an important part of its characterisation. **British Cement Association (2000)** describes the activities involved in a slump test procedure and segregates the heights of a slump into classes that are satisfactory for normal concrete.

2.3 Transient loading

2.3.1 Characterising the response to transient loading

2.3.1.1 Response regimes

Three different responses have been discussed by **Khan & Keller (1997)** differentiating between impulsive, quasi-static and dynamic loading.
Impulsive response - In the case where the duration of the induced load is significantly less than the natural frequency of the structure, $t_d << T$, the load has finished acting before the structure has had time to respond significantly and the deformations to the structure occur after t_d. The maximum deflection is a function of impulse, stiffness and mass of the structure. When an impulse is delivered to a structure, it produces an instantaneous velocity change, where momentum is acquired and the structure gains kinetic energy that is converted to strain energy.
Quasi-static response - In the case where the duration of the induced load is greater than the natural frequency of the structure, $t_d >> T$, the load may be considered as remaining constant, whilst the structure attains its maximum deflection. The maximum deflection is solely a function of the peak load and stiffness of the structure. The

structure reaches its maximum deflection before the peak load has undergone any significant decay, as also discussed by **Smith and Mays (1995).**
Dynamic response - This case of loading lies within a range dictated by the boundaries defined by impulsive and quasi-static loading. The response is more difficult to determined, requiring a harmonic analysis for simple loads and boundary conditions or a numerical time stepping solution for more complex cases.

2.3.1.2 Impulse load variation with time

Damping has much less importance in controlling the maximum response of a structure to impulsive loads than for periodic or harmonic loads because the maximum response to a particular impulsive load will be reached in a short duration, before the damping forces can absorb much energy from the structure.
Idealised load-time histories may be considered which essentially capture the main features of real load-time histories. Three such idealisations are:

1. half sine-wave impulse,
2. rectangular impulse,
3. triangular impulse.

The temporal profiles associated with three idealisations are illustrated in figure 2.3.1. The response to such a load is divided into two phases:

1. Loading phase – Structure is subjected to an impulse within the duration of loading.
2. Free vibration motion phase – Load has been removed.

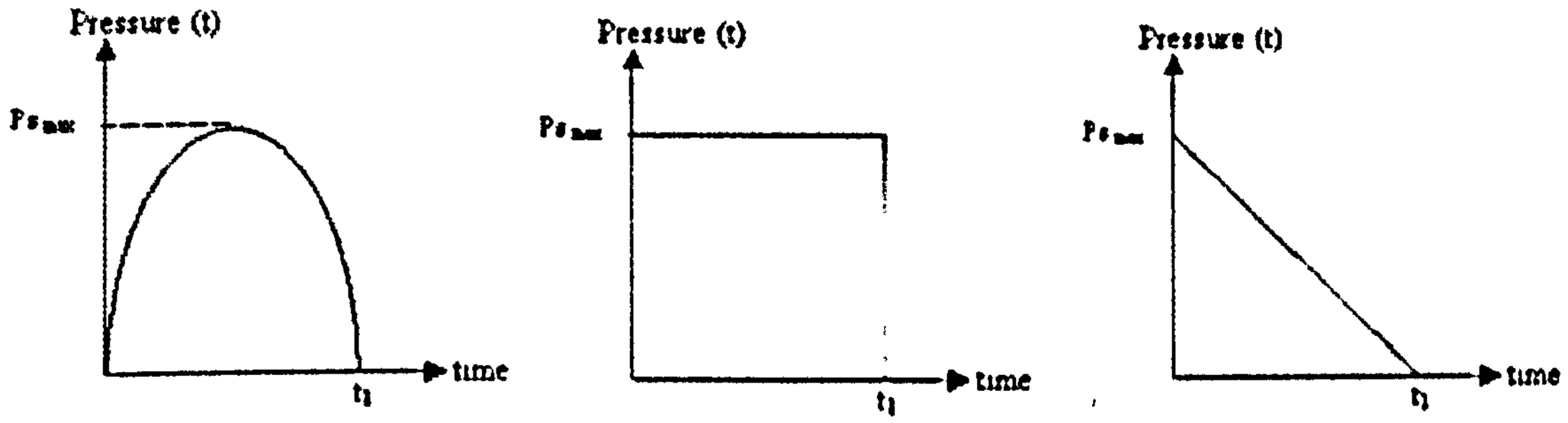

Half sine wave Rectangular Triangular

Ps_{max} = Maximum peak pressure
t_1 = Loading phase

Figure 2.3.1 Idealised impulse load distributions (Clough & Penzien, 1993).

A triangular load distribution would represent the pressure-time history in figure 2.3.3, which is indicative of an airblast event. The impulsive response would be defined by equation (2.3.1). In the case of a half sine-wave or a rectangular idealised load distribution the impulsive response would be defined by equation (2.3.1), according to **Clough & Penzien (1993).**

$$\frac{t_d}{T} < 0.37$$

Equation (2.3.1)

$$\frac{t_d}{T} < 0.5$$

Equation (2.3.2)

t_d = Duration of the transient load.

T = Natural period of vibration for a structure.

The different values in equations (2.3.1) and (2.3.2) may be explained by the differences in the frequency spectra of the different shape idealised load-time histories **Smith & Mays (1995)** stated that '*the natural period of the structure is to be evaluated in order to determine the type of loading that the structure is required to resist'*. For idealized triangular load distribution, three different responses are achievable and indicated in figure 2.3.2. The two points at which the analytical solution curve intersects the quasi-static and the impulsive asymptotes are associated with values 0.4 and 40. This defines the impulsive, quasi-static and dynamic regions of structural response.

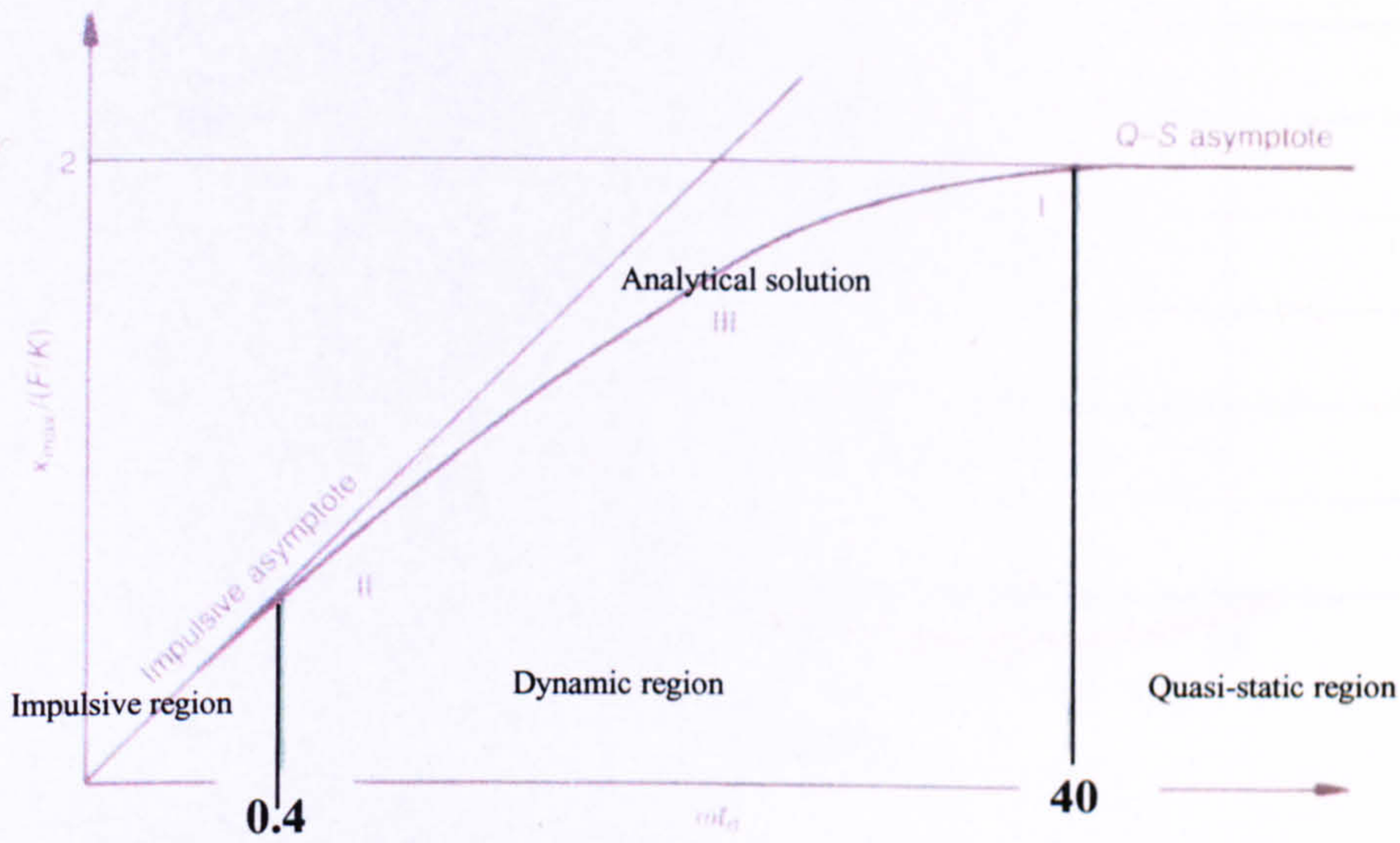

x_{max} /(F/k)= Ratio of maximum peak deflection to the force applied and stiffness of the structure

F=Force applied

K=Stiffness

ωt_d = Ratio of load induced duration to response duration

Figure 2.3.2 Graphical representation of quasi-static (I), impulsive (II) and dynamic (III) response associated with a triangular load distribution (Smith & Mays, 1995)

2.3.2 Impulsive loading and energy balance method

Conventional parameters that characterise transient loads are:

1. peak pressure
2. impulse

Peak pressure is difficult to measure experimentally, with a confidence of accuracy, as the gauge's band-width frequency can be less than the frequency associated with the

peak pressure. Impulse measurement can be done with accuracy, as an inaccurate peak pressure reading does not significantly change the impulse value
The recorded rise to peak pressure at a location from the source followed by a decay that is relatively smooth is an example of a measurement of airblast, as illustrated in figure 2.3.3. The total impulse contained in such a load distribution is indicative of a triangular distribution and stated as follow:

$$\Sigma(P_s t_d)dt$$

Equation (2.3.3)

P_s= Maximum peak pressure
t_d= Duration of the positive decaying pressure
dt= Increment of time

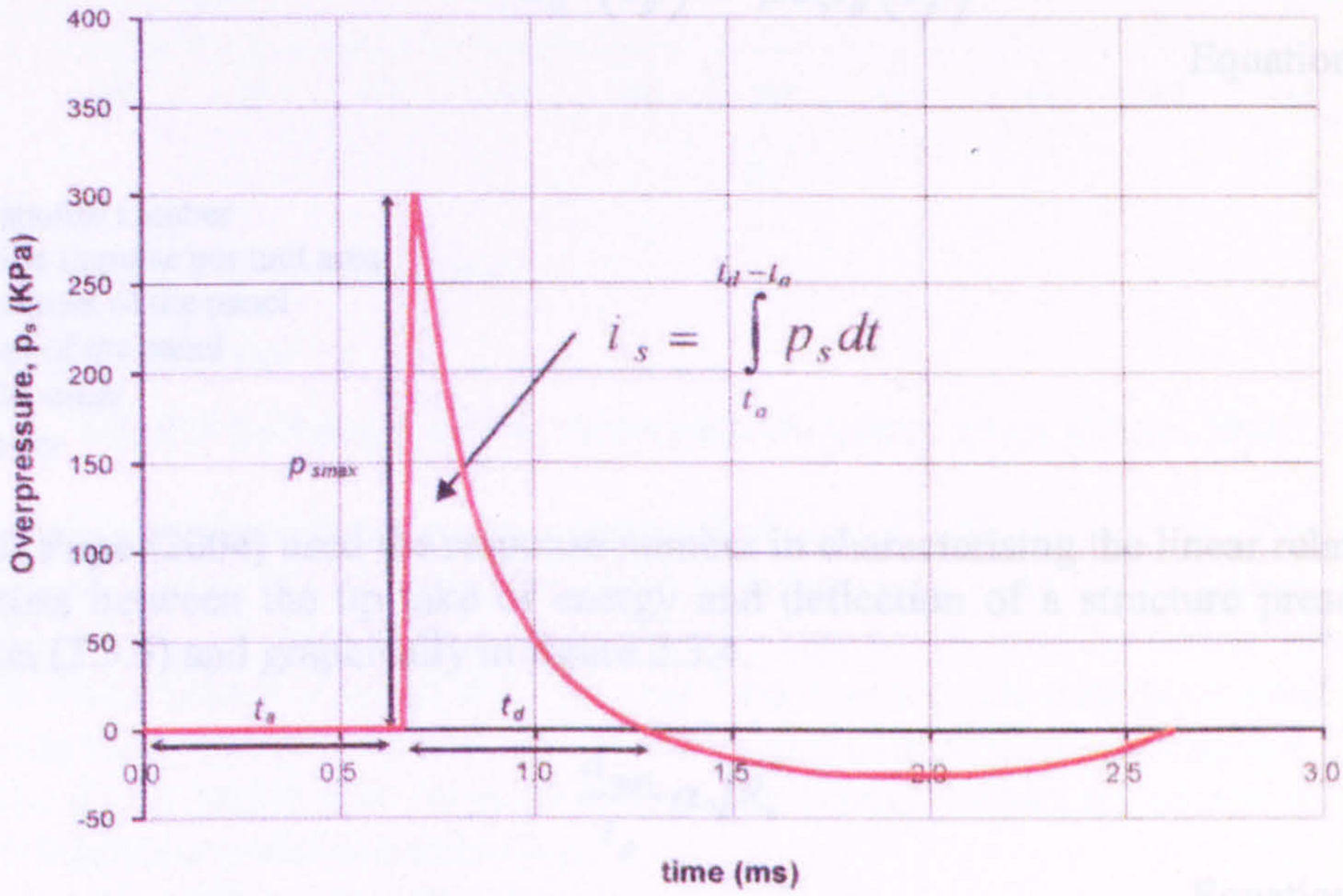

$P_{s\,max}$ = Maximum peak pressure
t_a = Duration of the blast wave to travel from source to point of application
t_d=Duration of the positive decaying pressure
i_s =Specific impulse

Figure 2.3.3 Overpressure-time history

A great deal of research has been conducted on the phenomena associated with air blast as discussed by **Smith & Mays (1995)** and **Smith & Hetherington (1994).** In air, the shock wave resulting from an explosive detonation is defined as a blast wave. As the blast wave moves away from the explosion, caused by converting a mass of explosive into a volume of expanding gas, the flow of the mass of air behind the blast front produces a strong wind. The response of panels subjected to airblast tests was researched from **Tyas & Pope (2004)**. The energy balance procedure described by the authors involved equating the kinetic energy induced into a panel with the maximum strain energy.
The authors stated that '*for the energy balance to be valid, the loading is assumed impulsive'*. This implies that the panel does not deform as the pressure is applied and is only mobilised when the pressures have dissipated. The authors demonstrated that a

linear relationship exists between the energy uptake of a panel and its maximum response.
Representing the linear relationship generically, taking into account the loaded structure's material and geometric properties, a dimensionless number, defined as the 'response number' is generally used. The response number is used for analysing a fully rigid plastic structure, subjected to loading that causes an impulsive response. **Zhao (1998)** presented the response number that takes into account the geometry of the structure (l_p/t_p) the inertia of the load, ρV_0^2 and the plastic limit of the slab, including the resistance ability of the material to plastic deformation, σ_0.

$$R_n = \frac{\rho V_0^2}{\sigma_0}\left(\frac{l_p}{t_p}\right)^2 = \frac{I_\bullet^2}{\rho\sigma_\bullet t_p^2}\left(\frac{l_p}{t_p}\right)^2$$

Equation (2.3.4)

R_n = Response number
I =Specific impulse per unit area
t_p = Thickness of the panel
L_p = Span of the panel
σ = Yield stress
ρ = Density

Tyas & Pope (2004) used the response number in characterising the linear relationship that exists between the up take of energy and deflection of a structure presented in equation (2.3.5) and graphically in figure 2.3.4.

$$\frac{d_{max}}{t_p}\alpha\sqrt{R_n}$$

Equation (2.3.5)

d_{max} = Central maximum peak deflection
R_n = Response number
t_p = Thickness of the panel

A structure that responds impulsively to the load, responds to the total energy contained within the load, rather than the peak pressure that is associated with a quasi-static response.

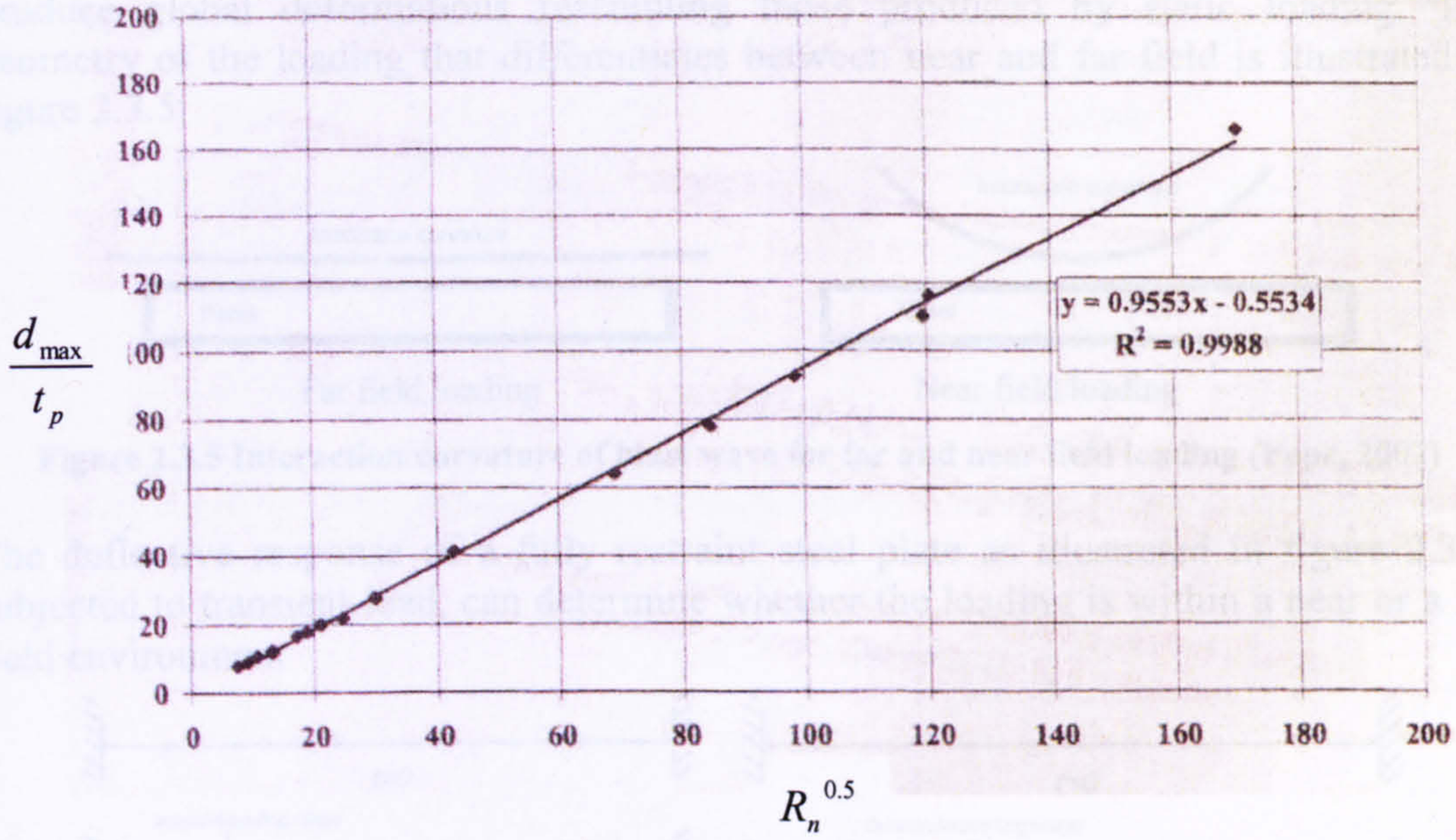

d_{max} = Central maximum peak deflection
R_n = Response number
t_p = Thickness of the panel

Figure 2.3.4 Panel deflection versus response number (Tyas & Pope, 2004)

Although the response number was initially derived for uniform loading, **Tyas & Pope (2004)** have shown that it also gives good correlation for near field loading, which is characterised by its non-uniformity of specific impulse across the beam. Essentially, **Tyas & Pope (2004)** showed that for near-field loading, the central or peak impulse dominates the response. The authors proved that during airblast the impulse delivered centrally into a panel was proportional to the central deflection of the panel. The authors did not consider the following:

1. Loading affect caused by the geometry of a charge
2. Consistency of the linear relationship in figure 2.3.4 caused by loading within different environments (soil, air, etc).

They characterised the loading environment geometrically, by relating the charge standoff distance to the effective span of the slab. This is discussed in section 2.3.3.

2.3.3 Near and far field loading

The charge standoff relative to a primary slab influences the distribution of load into a primary slab, thus defining the load environment as near or far field. **Pope (2002)** makes a clear distinction between near and far field loading which affects the area of deformation occurring over a slab. When a localised load within a near field environment is applied to the centre of a slab, the transfer of stress to the outer supported regions is rapid relative to the slab movement. The localised momentum can be applied at such a rate that there is insufficient time for significant momentum to be transferred to the slab periphery. Therefore deformations are confined to the explosion epicentre. Momentum imparted by far field loadings is evenly distributed across the slab's span and the associated transient bending moment and shear force distributions

produce global deformations resembling those produced by static loading. The geometry of the loading that differentiates between near and far field is illustrated in figure 2.3.5.

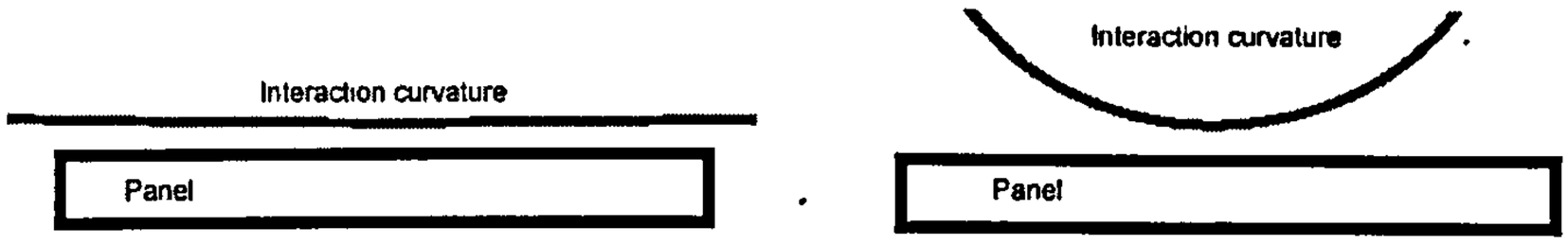

Far field loading Near field loading

Figure 2.3.5 Interaction curvature of blast wave for far and near field loading (Pope, 2002)

The deflective response of a fully restraint steel plate as illustrated in figure 2.3.6, subjected to transient load, can determine whether the loading is within a near or a far field environment

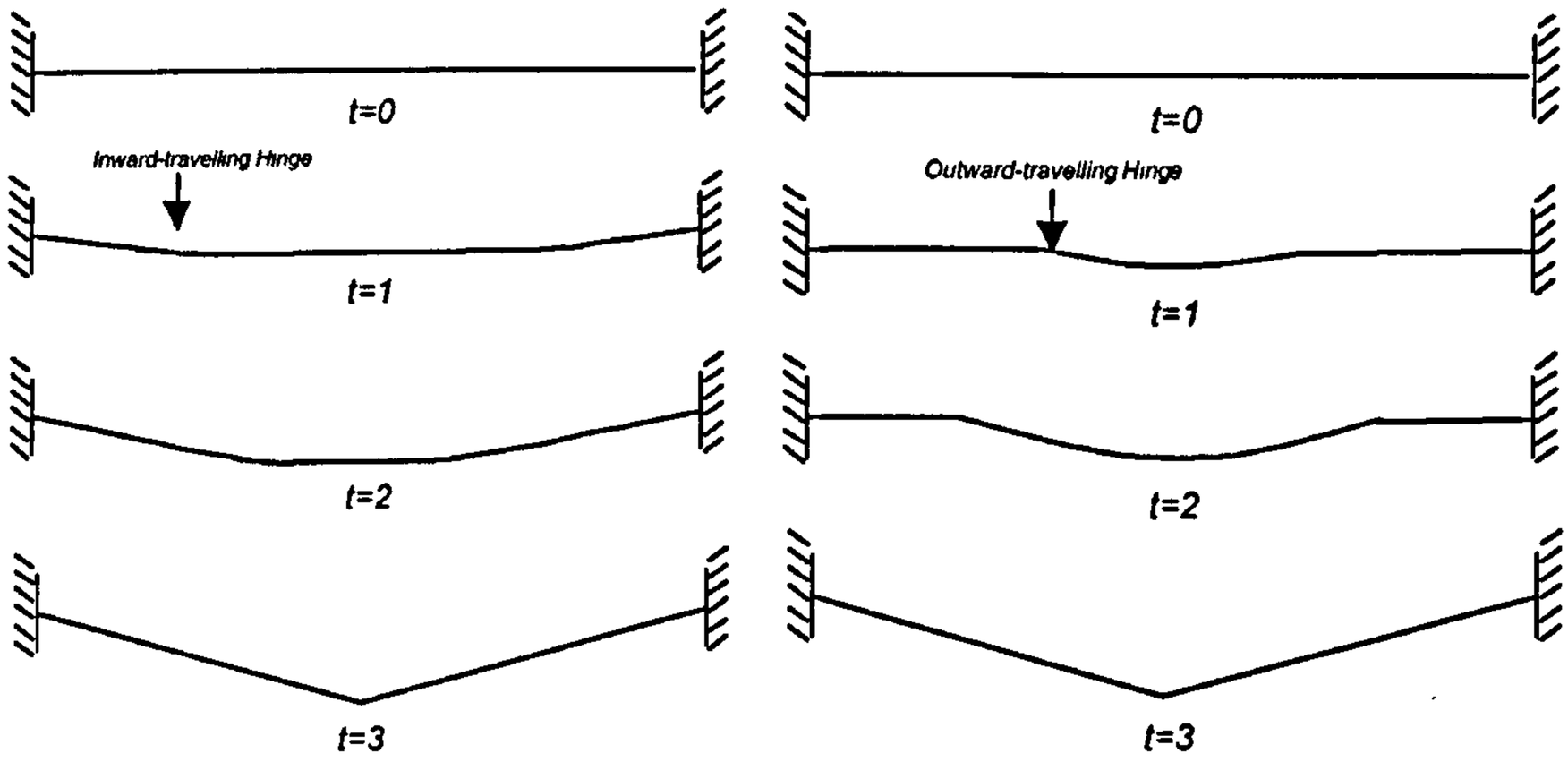

Far field loading response of panel Near field loading response of a panel

Figure 2.3.6 Evolving deformation of a steel plate exposed the far and near field loading (Pope, 2002)

Near field loading dominates when the charge standoff is small relative to the panel span so that the curvature of the shock front induces greater pressures and impulses around the epicentral panel regions. Far field loading dominates when the charge standoff is greater than the span of the panel causing the load to have a uniform spatial distribution across the top face of the panel.

Pope (2002) stated that '*within the near field, the loading decays rapidly from an epicentral peak to much lower values at the panel perimeter'*. This will be evaluated from the experimental results. **Lam *et al* (2004)** stated that '*if the scaled distance parameter is much less than 1 (Z << 1), the loading can be classified as near-field'*.

The damage mechanisms in figures 2.3.7 and 2.3.8, identified by **Krauthammer (1999)** associated with airblast, relate to those sustained from within near and far field environments. The author did not comment whether the same mechanisms would occur in groundshock. There was also no verification that discussed whether the damage mechanisms sustained in both the near and the far field environments are dependent upon the medium through which the transient wave propagated.

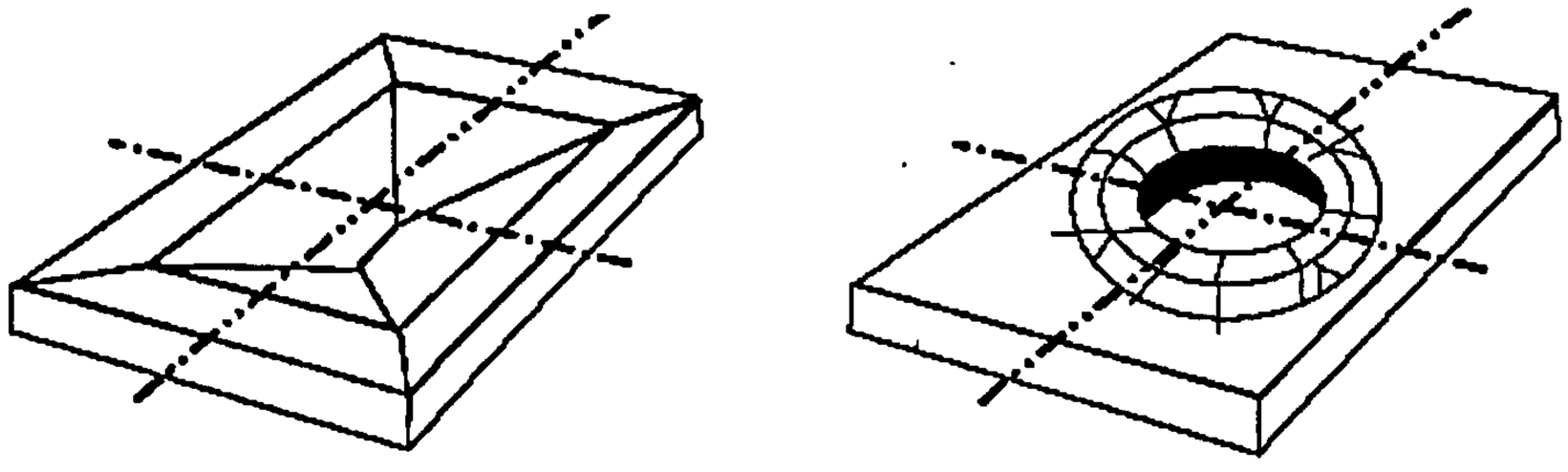

Local bending

Local shear and spall

Figure 2.3.7 Typical modes of panel deformation produced by near-field charges (Krauthammer, 1999)

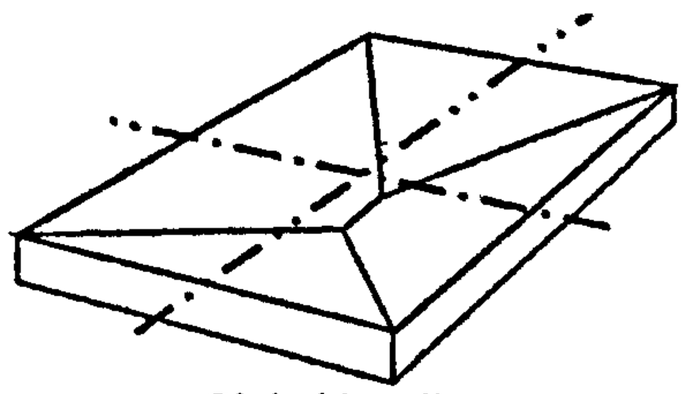

Global bending

Figure 2.3.8 Typical modes of panel deformation produced by far-field charges (Krauthammer, 1999)

The free field stress and impulse parameters both take into account the loading wave velocity. The free field stress that would exist within a soil environment is defined by equation (2.4.6).

$$P_s = \rho C u$$

Equation (2.3.6)

P_s = Pressure
ρ = Density of the soil
C = Loading wave velocity
u = Particle velocity

The free field impulse is defined by equation (2.3.7).

$$i_s = \rho C x$$

Equation (2.3.7)

i_s= Impulse
ρ = Density of the soil
C = Loading wave velocity
x = Peak particle displacement

The seismic velocity provides a measure of stiffness and the density of the soil, defined by equation (2.3.8).

$$c = \left(\frac{M}{rh_o}\right)^{1/2} = \sqrt{\frac{E}{\rho}}$$

Equation (2.3.8)

c = Seismic velocity
M = Stiffness or modulus of the soil
rh_o = Mass density.
E = Modulus of elasticity
ρ = Density.

Cementation in granular soils, such as dry desert alluvium, would transfer high seismic velocities, due to the strong bonds created by cementation. These materials may also exhibit a high content of air filled voids as described by **Hyde (1991)**. Low seismic velocities indicate poor ground shock transmission within a soil, which is good if an underground structure is to be embedded within it. The loading wave velocity is related to the seismic velocity and the particle velocity, as presented by **Smith & Hetherington (1994)** in equation (2.3.9).

$$C = c + \left(\frac{n+1}{n-2}\right)u \quad \text{for sand}$$

Equation (2.3.9)

C= Loading wave velocity
c = Seismic velocity of a particular soil
n = Attenuation coefficient
u = Particle velocity

Equation (2.3.9) implies that when the soil particle velocity parameter significantly decreases, the loading wave velocity equates to the seismic velocity at a range away from the source. It is interesting to note that the semi-empirical code CONWEP, based upon the experimental data from **TM 5-855-1 (1985)** does not take into account the attenuating loading wave velocity. Instead, it uses a value for the seismic velocity, which is related to a significantly attenuated loading wave velocity, occurring at an initial distance away from the source.

2.3.4 Scaling of parameters

In general, the scaling of parameters at a given scale, as illustrated in figure 2.3.9 is performed in order to evaluate the influence of parameters at a different scale, for a given load distribution. Hopkinson-Crantz scaling, also called 'cube root scaling', provides simple and approximate method for relating the parameters of blast waves (e.g peak pressure, impulse and duration) produced by geometrically similar charges of different masses at different standoffs.

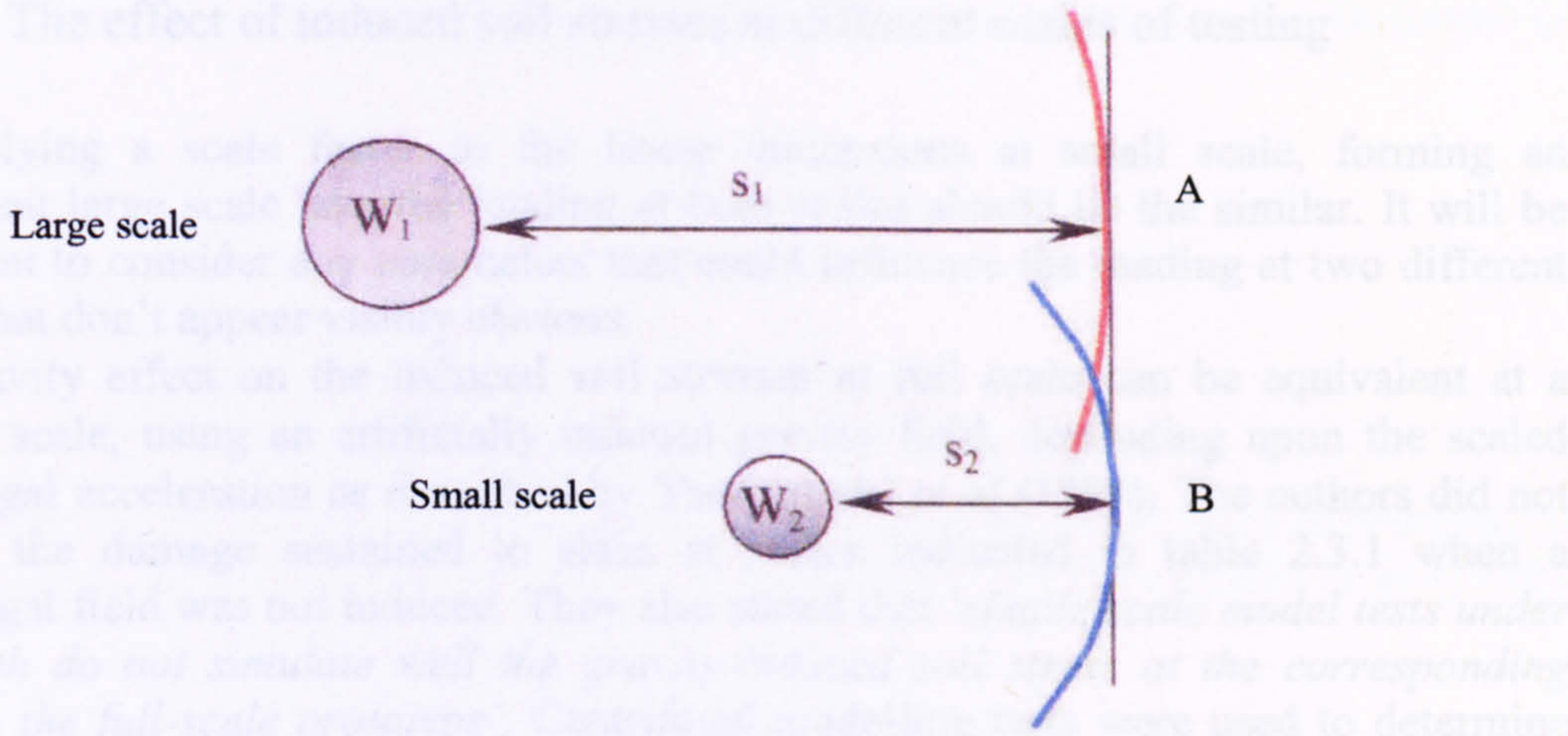

W = Mass of charge
S = Charge standoff

Figure 2.3.9 Scaling relationship between two explosive charges (Pope, 2002)

The basic cube root relationships governing are:

$$W_1 \propto d_1^3$$

Equation (2.3.10)

$$W_2 \propto d_2^3$$

Equation (2.3.11)

W = Mass of charge (kg)
d = Diameter of the charge (m)

$$\frac{d_1}{d_2} = \left(\frac{W_1}{W_2}\right)^{1/3}$$

Equation (2.3.12)

$$Z = \frac{S}{\sqrt[3]{W}}$$

Equation (2.3.13)

Z = Scaled distance ($mkg^{-1/3}$)
S = Charge standoff (m)
W = Mass of charge in (kg)

The scaled distance of a charge from a target can be used as a reference quantity for determining the same parameter for a charge at the same scaled distance, but with a different combination of mass and charge standoff. In both situations the value of the chosen scaled parameter is the same.
Parameters associated with transient load distribution can be measured or calculated at different scales with the use of a scale factor. A number of these parameters are stated as:

1. peak pressure,
2. velocity,
3. impulse,
4. arrival time of the transient wave,
5. load duration of the transient wave.

2.3.4.1 The effect of induced soil stresses at different scales of testing

By applying a scale factor to the linear dimensions at small scale, forming an equivalent large scale test, the loading at both scales should be the similar. It will be important to consider any parameters that could influence the loading at two different scales that don't appear visibly obvious.

The gravity effect on the induced soil stresses at full scale can be equivalent at a smaller scale, using an artificially induced gravity field, depending upon the scaled centrifugal acceleration as described by **Yamaguchi *et al* (1999).** The authors did not discuss the damage sustained to slabs at scales indicated in table 2.3.1 when a centrifugal field was not induced. They also stated that '*simple scale model tests under the earth do not simulate well the gravity-induced soil stress at the corresponding point to the full-scale prototype*'. Centrifugal modelling tests were used to determine the response and damage evaluation of reinforced concrete beams subjected to explosive loading in sand. The centrifuge modelling technique was verified by conducting tests on beams, at scales of 1/20, 1/40 and 1/60. The centrifuge apparatus is illustrated in figure 2.3.10.

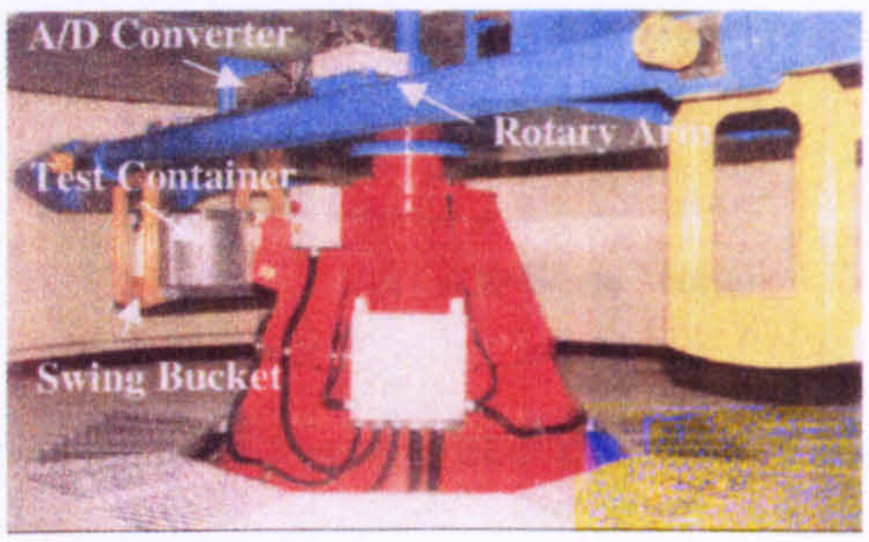

Figure 2.3.10 Centrifuge machine (Yamaguchi *et al*, 1999)

The full scale beam was subjected to two explosive tests to cause more damage. A bare cylindrical charge of mass 69kg was used on the full-scale beam. The charge mass used in a 1/N scale test was $69/N^3$. The scale structures were in turn buried in a test container filled with soil, as illustrated in figure 2.3.11.

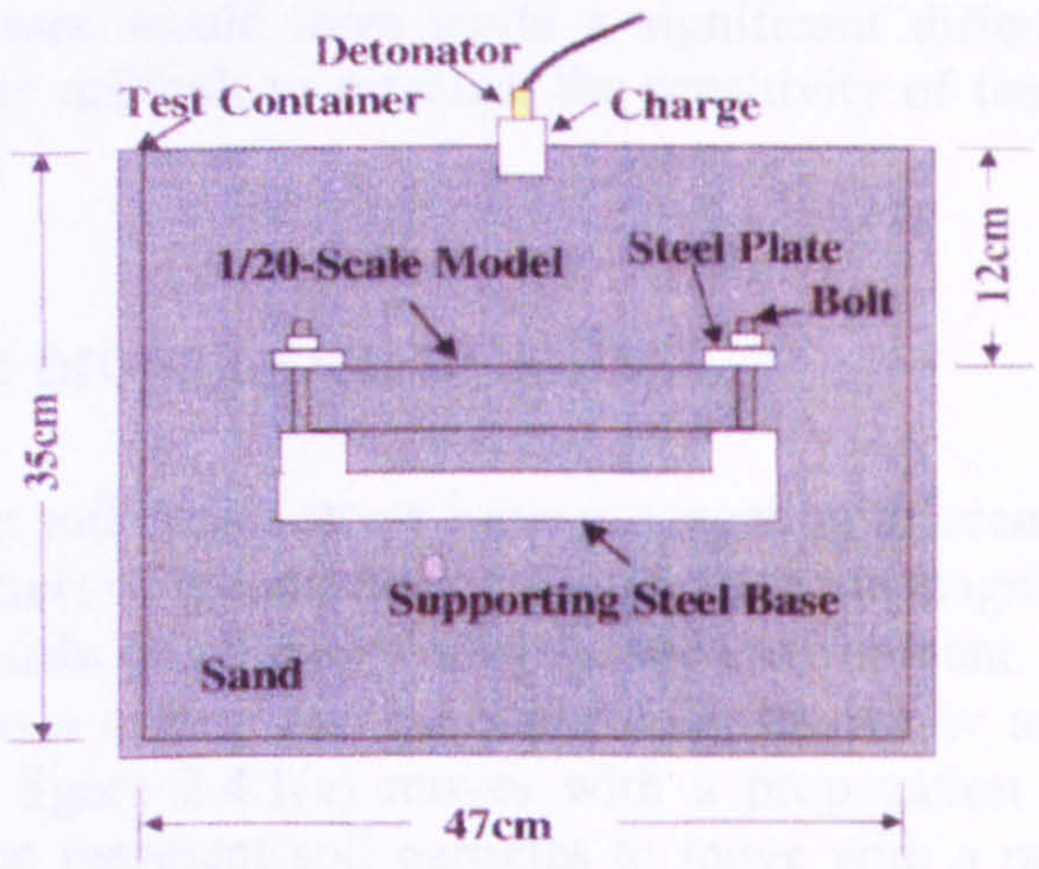

Figure 2.3.11 Test setup in the test container at 1/20-scale model (Yamaguchi et al, 1999)

The charge masses and centrifugal accelerations applied to the beams are illustrated in table 2.3.1.

Table 2.3.1 Test conditions (Yamaguchi et al, 1999)

Scale model	Charge mass	Centrifugal acceleration
1/20	8.64g	20G
1/40	1.08g	40G
1/60	0.32g	60G

Each scaled beam suffered two detonations. The damage failure patterns as observed in figure 2.3.12, '*are similar on the whole*' as commented by **Yamaguchi *et al* (1999).**

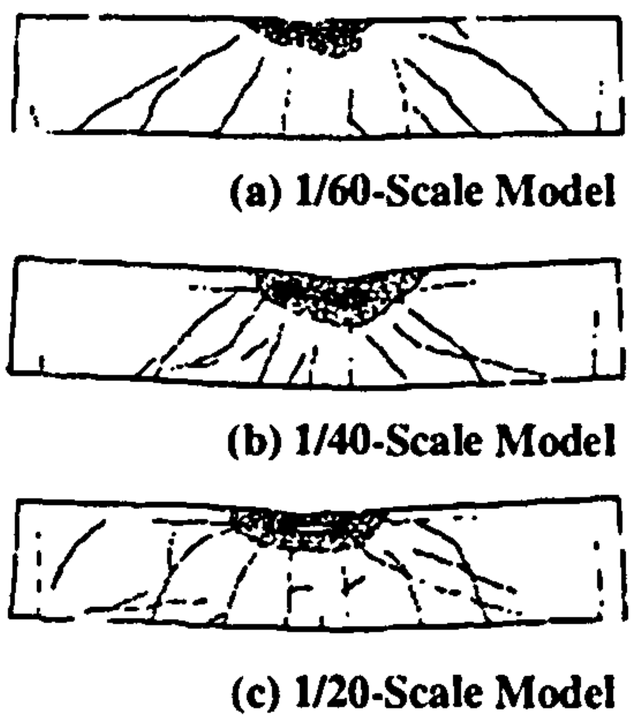

(a) 1/60-Scale Model

(b) 1/40-Scale Model

(c) 1/20-Scale Model

Figure 2.3.12 Failure patterns due to dynamic loading (Yamaguchi *et al*, 1999)

The authors concluded that '*centrifuge modelling tests are useful to roughly evaluate the damage of underground reinforced concrete beams in sand subjected to explosive loading*'.

Renick (2000) stated that '*gravity has little direct effect on the damage modes, but does affect the final rest position of the loose rubble*', contradicting the work performed by the authors.

Yamaguchi *et al* (1999) did not state whether the damaged slabs in figure 2.3.12 correlate to a full scale slab. There appears to be insignificant evidence that suggests the scaled soil stresses would have made a significant difference to the damaged beams. It is therefore difficult to establish the sensitivity of the parameter associated with induced gravity.

2.4 Stress wave propagation in soils

Charge detonation in soil causes stress wave propagation to occur. The parameters that influence the magnitude of groundshock also influence the magnitude of damage to the reinforced concrete slabs positioned within the soil environment.

The force applied to a system can be either compressive or tensile. A compressive wave illustrated in figure 2.4.1(a) moves with a propagation velocity, causing the individual trucks that represent soil particles to move with a particle velocity that is less than the propagation velocity. The energy applied to the particles directly by the stress wave is used to reduce the bond between the particles hence allowing movement

against friction. A tensile wave as illustrated in figure 2.4.1(b) moves with a propagation velocity in the right direction, causing the trucks to move to the left.

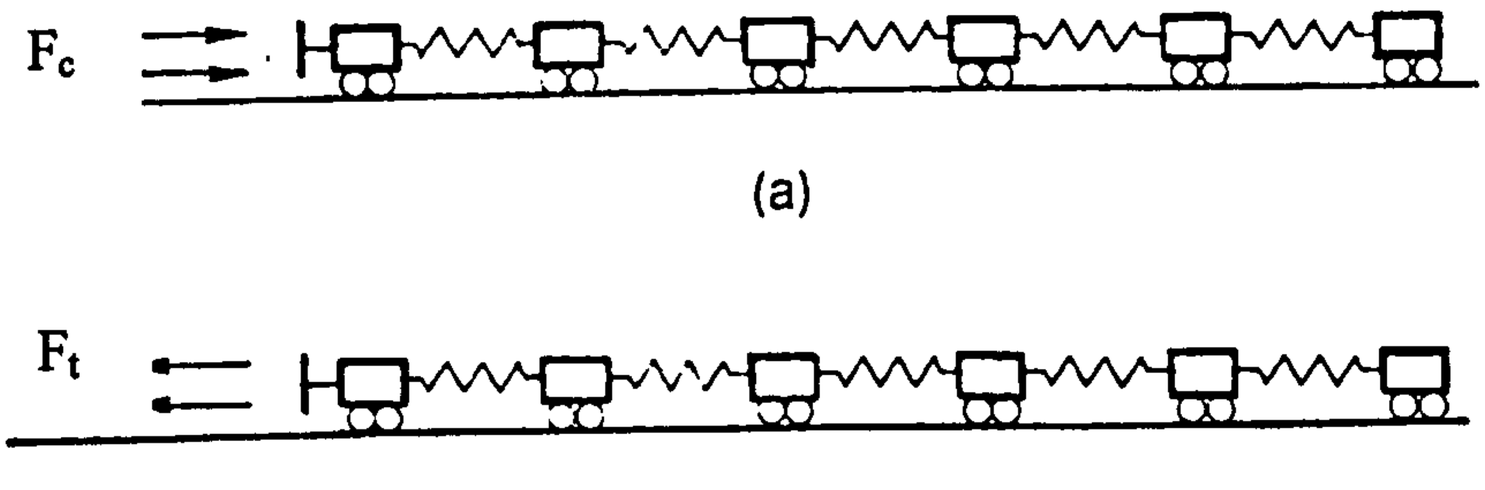

(a)

(b)

F_c = Compressive force
F_t= Tensile force

Figure 2.4.1 (a) Transmission of a compressive stress wave (b) Transmission of a tensile stress wave (Smith & Hetherington, 1998)

Zhongqi & Yong (2003) performed numerical simulations that modelled groundshock as illustrated in figure 2.4.2.

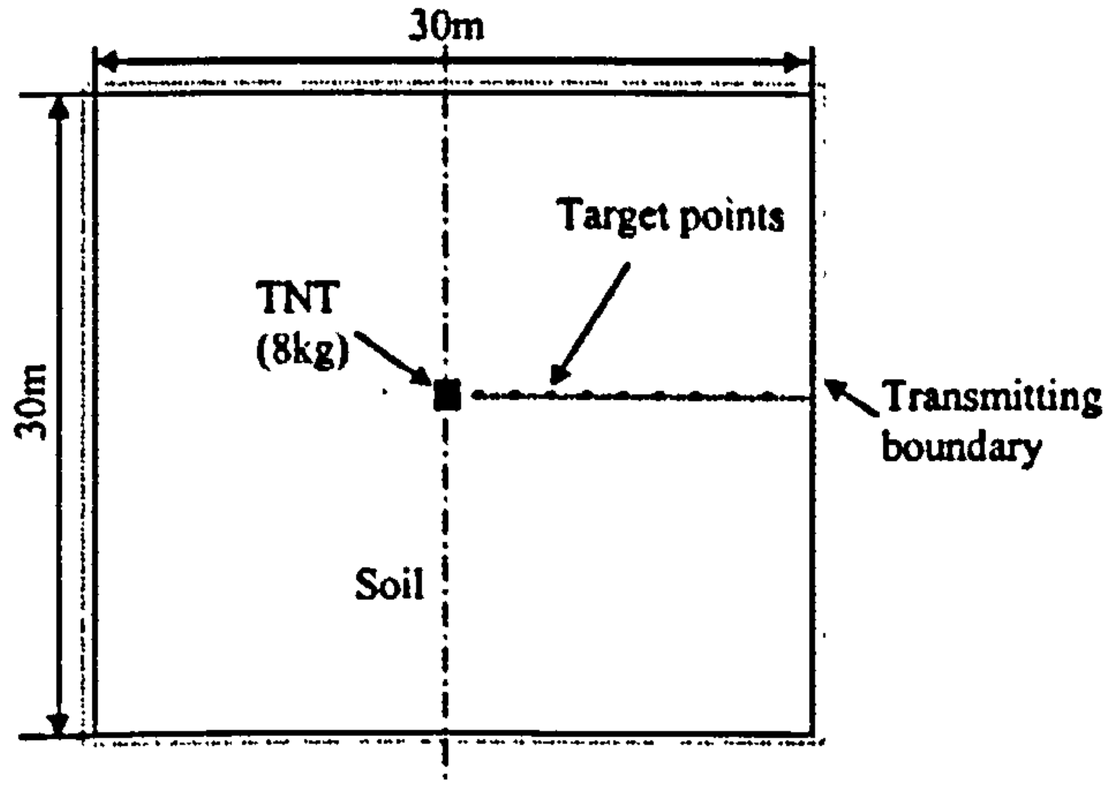

Figure 2.4.2 Configuration of the numerical model (Zhongqi & Yong, 2003)

The target points recorded pressure-time histories containing multiple peaks as illustrated in figure 2.4.3. The authors stated that '*the secondary peak is essentially borne primarily by the solid skeleton. Its peak pressure is much lower than the primary, at which level the strength of the skeleton plays an effective role'*. The initial peak associated with maximum peak pressure appears to influence the soil phases, compressing the soil and decreasing the void spaces. The secondary peak indicates that the soil deformation mechanism has changed, due to a reduction of load. The deformation now affects the soil skeleton. The contact movement between the solid particles and breaking of bond linkages governs this.

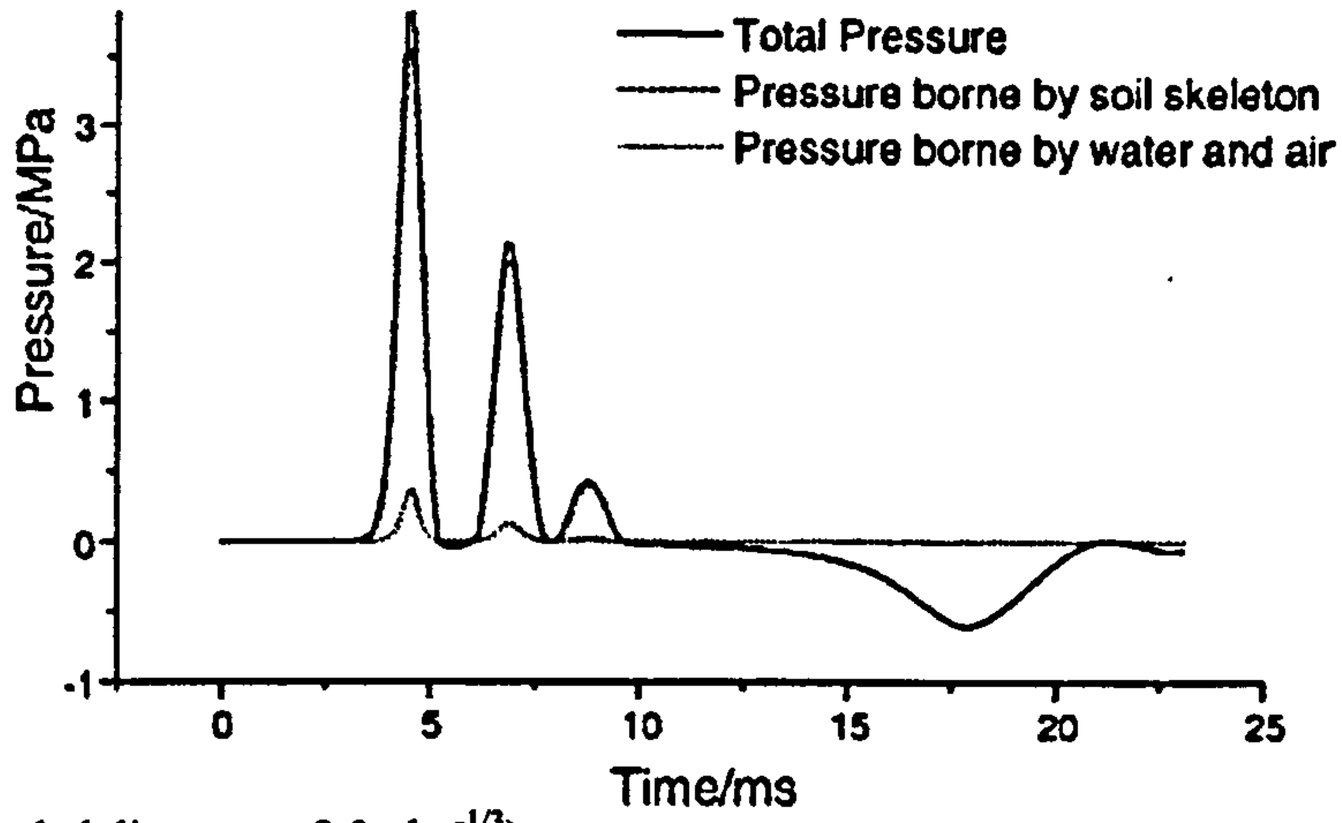

Target point 4 (scaled distance = 2.0mkg$^{-1/3}$)

Figure 2.4.3 Pressure time histories in soil containing multiple peaks (Zhongqi & Yong, 2003)

There appears to be a phenomenon in groundshock measurements with the observation of multiple peaks. The authors have not commented on the possible effect of particle impact or reflection from the target points that might have caused the multiple peaks. **Buell (1985)** commented on the effect caused when a stress wave hits an inclusion such as an air void or a reinforcement bar in concrete, causing it to partially scatter around it.

2.4.1 Stress wave attenuation

Attenuation is associated with the loss of energy. A stress wave propagating through a medium will attenuate with range. This will occur at different degrees depending upon the particle velocity of the medium.

Ahmed (1994) stated that '*attenuation is the weakening of a stress wave as it propagates through a material. Stress waves with stresses below the dynamic elastic limit of concrete will attenuate at very small rates, but stress waves with peak stresses above the dynamic elastic limit will attenuate rapidly by using energy to plastically deform the material*'.

The attenuation rate can be calculated for different materials using two different procedures.

1. Particle velocities are recorded within a medium at scaled distances. The gradient of such a plot is defined as the attenuation rate and is illustrated in figure 2.4.4.

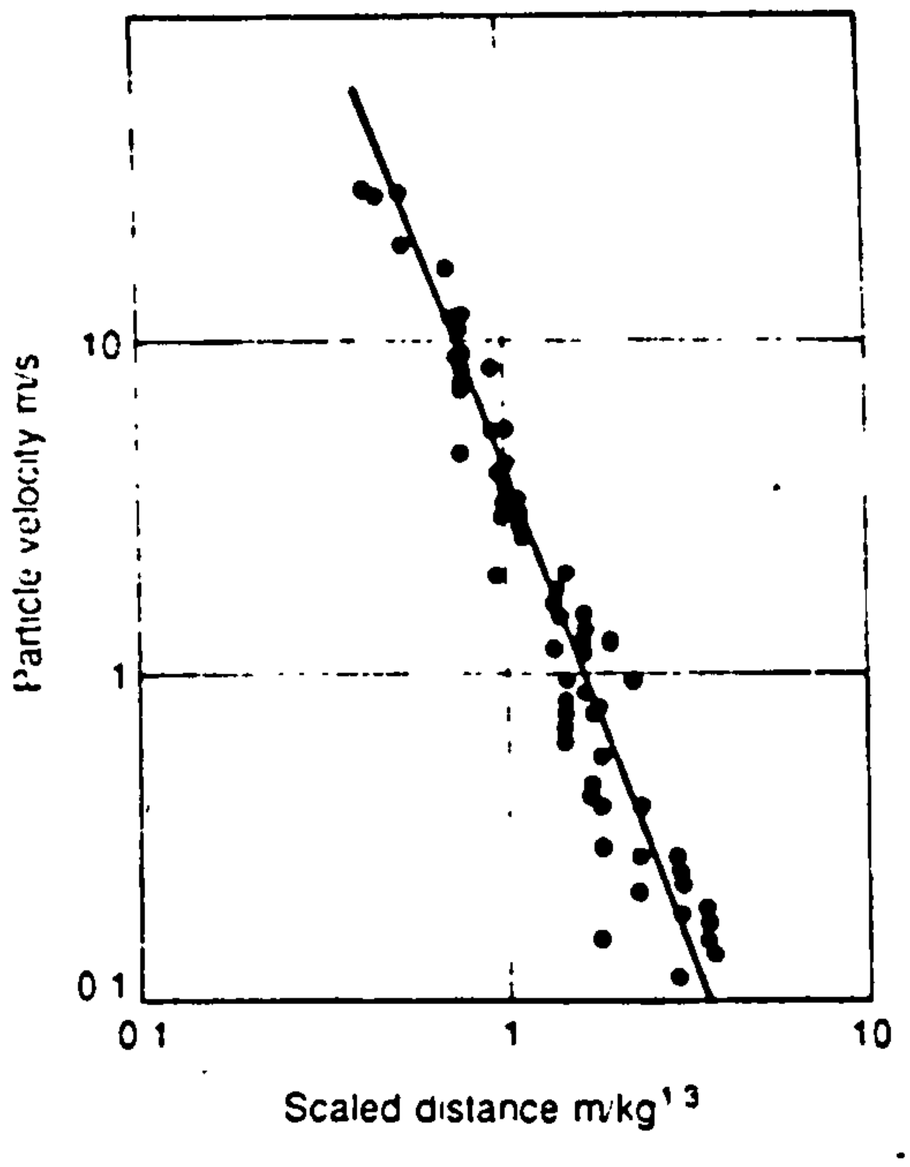

Figure 2.4.4 Calculating the attenuation rate for a material (Smith & Hetherington, 1994)

2. An estimate of the attenuation coefficient can also be made from an unconfined uniaxial compression test, which involves an incremental increase in stress applied to a sample over a given time. The stress is then removed at a peak value and the corresponding maximum strain value decreases to the residual strain as the sample relaxes. This is illustrated in figure 2.4.5.

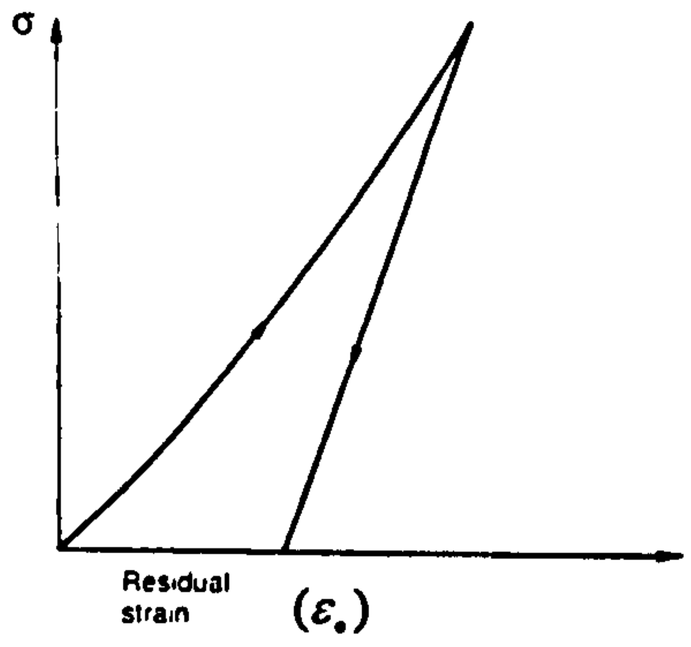

Figure 2.4.5 A plot of the compressive stress versus strain for a particular soil within an unconfined uniaxial compression test (Smith & Hetherington, 1994)

The attenuation coefficient is calculated by using the residual strain value.

$$n = \frac{2+(\varepsilon_{\circ})}{1-(\varepsilon_{\circ})}$$

Equation (2.4.1)

n = Attenuation coefficient

$(\varepsilon_{\circ})$ = Residual strain or deformation achieved within the material once the applied stress has been removed.

Hyde (1991) stated that *'The attenuation rate with range of the ground shock magnitude is controlled by the irreversible crushing of the void volume within a soil matrix'*. Soils with high relative density or a low volume of air voids will attenuate the ground shock more slowly than low relative density, or high air void, materials. Various types of soil with their associated attenuation values are illustrated in table 2.4.1.

Table 2.4.1 Attenuation values associated with the soil type (Smith & Hetherington, 1994)

Soil type	Attenuation coefficient (n)
Saturated clay	1.5
Partially saturated clay and silt	2.5
Very dense sand	2.5
Dense sand, dry or wet	2.75
Loose sand, dry or wet	3.0
Very loose	3.25

The soil that will be used during the explosive testing will have an attenuation coefficient between 2.5 - 3.0.

2.4.2 Soil compaction

A thorough literature review has revealed the following:

1. Techniques used to compact a soil.
2. Less development investigating whether the passage and magnitude of the groundshock wave is independent upon the initial mode of soil compaction.

Bement & Selby (1997) performed experiments to identify the volume reduction of a range of granular soils in response to uniform vibration. When consolidated at stresses in the range of 10 to 100kPa they concluded that the compaction of soils is strongly dependent upon vertical induced stress and that compaction reduces to small values when the stress exceeds 100kPa.

Horvath *et al* (1996) devised a procedure for researching the density dependence of static friction in sand. The experimental procedure involved inserting a glass rod into the soil sample, compacting the soil, and then pulling the rod out from the soil by a calibrated steel spring. The elongation of the spring would be adjusted and measured by a computer controlled stepping motor.

An in depth account of the procedure and the theory behind it is described in the paper written by the authors. Essentially, larger pull out forces of the glass rod are associated with larger packing densities of the soil particles and hence a greater compaction. The authors stated the following:

1. Pullout force does not depend on the grain sizes in the soil sample.
2. Longer vibration time applied to a soil sample results in a larger soil bulk density, with increased closeness of packing.

A three phase soil model, based upon the deformation of soils at high stresses was used but not developed by **Zhongqi & Yong (2003)** to compare the numerical results with a series of field tests concerning explosions in soil. In analysing the deformation of soils, two deformation mechanisms exists:

1. Deformation of the soil skeleton – reduction in water and air content.
2. Deformation of all the soil phases – stages of soil compaction.

Mechanism 1 would occur at lower levels of induced stress, perhaps within the far-field environment as discussed by **Tyas & Pope (2004).** Water bearing soils contain less air than dry soils and the bonds between the solid particles are weaker. When these soils are subjected to static loading or significantly reduced transient loading, the water and air are pressed out of the voids and the compressibility controls the soil skeleton as dictated by mechanism 1. In the far field environment where the transient stress has significantly depreciated, at a greater distance away from the source, mechanism 1 is also predominant in squeezing the air and water out of the voids rather than intensely compacting the soil, due to the attenuation in stress.

Mechanism 2 is associated with rapid loading of the soil involving significantly high stresses that have just been induced into the soil environment once the charge is detonated. Due to such initial high stresses induced, compaction occurs at a fast rate that is independent of the soil's initial compaction, followed by an increase in soil bulk density.

The void ratio at the time of peak pressure, at varying distances from the charge has been calculated using a numerical model as illustrated in figure 2.4.6. Within the scaled range of $0-1.5mkg^{-1/3}$ the void ratio is reduced as well as the degree of saturation as illustrated in figure 2.4.7. At scaled distances $>1.5mkg^{-1/3}$ there is negligible change in both parameters. This could suggest that for this test set up, the near field environment lies within the range $0-1.5mkg^{-1/3}$ where the magnitude of the propagating stress wave remains significantly high, locally, significantly increasing the soil density by compaction.

The determination of a near and a far field environment has already been described by **Pope (2002).** The soil deformation mechanisms described by **Zhongqi & Yong (2003)** could also be used to determine a boundary between both environments, as illustrated in equation (2.4.2).

$$\text{Near field} < 1.5mkg^{-1/3} < \text{far field}$$

Equation (2.4.2)

Near field environment - Deformation of all the soil phases
Far field environment - Deformation of the soil skeleton

In the far field environment, the stress wave has significantly attenuated such that the stress wave has less of an effect on both the void ratio and degree of saturation. When the magnitude of stress is low, the strength of the soil skeleton takes effect, resulting in the pressure on the air being much less.

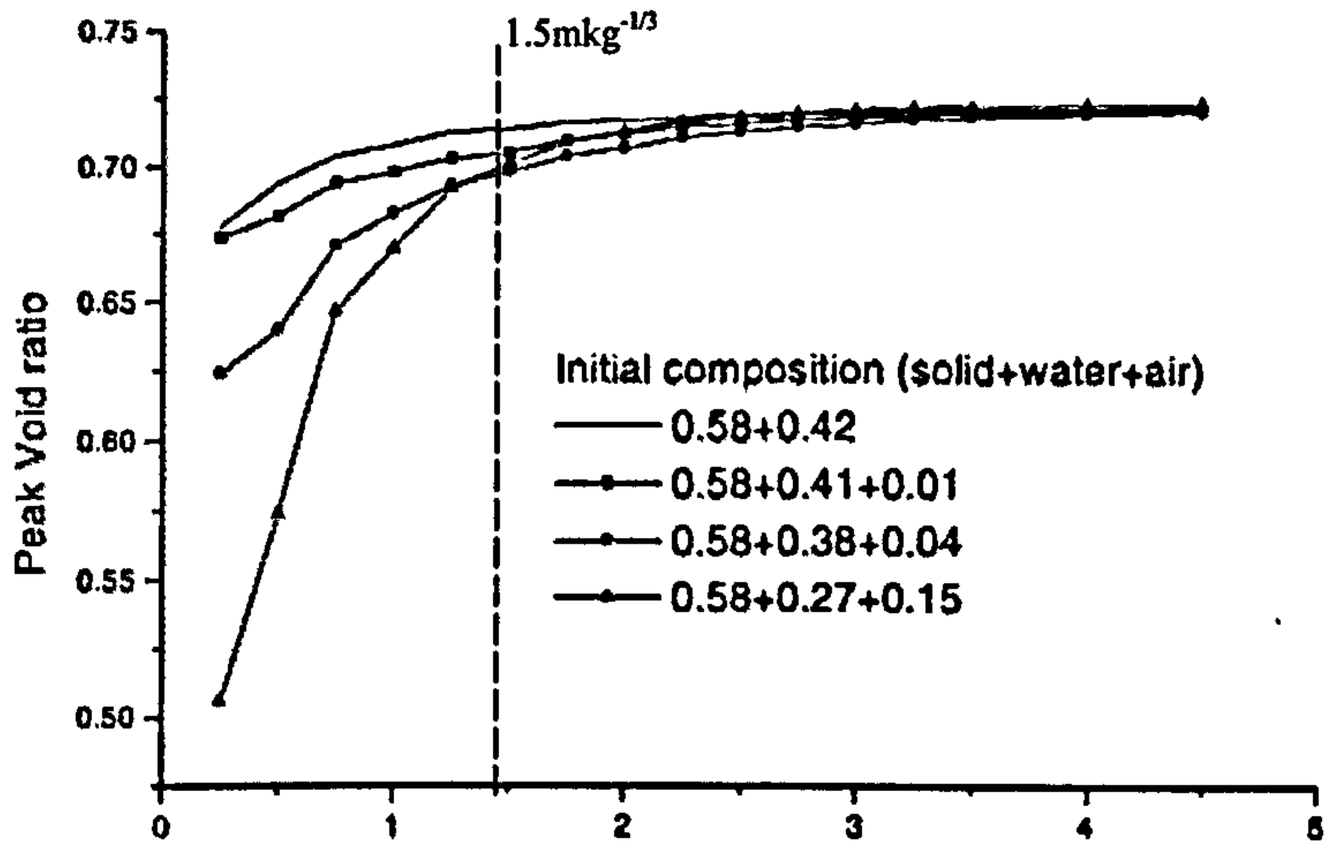

Void ratio corresponding to peak pressure at different locations

Figure 2.4.6 Change in characteristic soil properties as a function of scaled range under loading (Zhongqi & Yong, 2003)

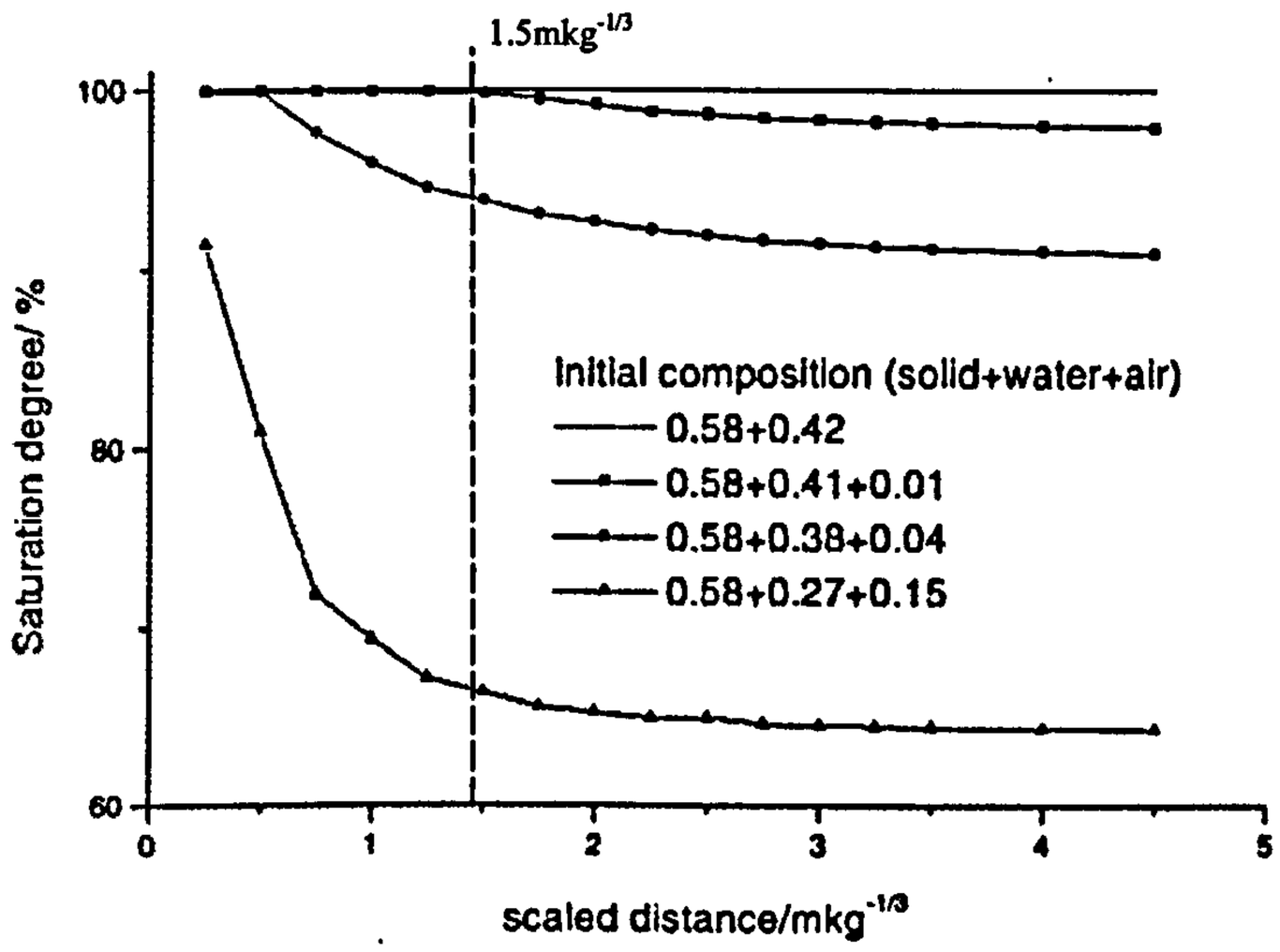

Saturation degree corresponding to peak pressure at different locations

Figure 2.4.7 Change in characteristic soil properties as a function of scaled range under loading (Zhongqi & Yong, 2003)

Zhongqi & Yong (2003) stated that '*the greater the air content within the soil, the larger the reduction of the void ratio when the soil is subjected to transient pressures*'. This suggests that if the soil in a near field environment had not been compacted prior to the detonation of a charge, the induced stress wave would compact the soil to a density associated with the level of induced stress at that interval of time.

2.4.2.1 Equation of state for a soil

The equation of state describes how a material's bulk density increases as the material is subjected to greater magnitudes of induced stress, causing compaction above its

initial insitu value. A typical equation of state for a soil is illustrated in figure 2.4.8 indicating an increase in bulk density over three stages.

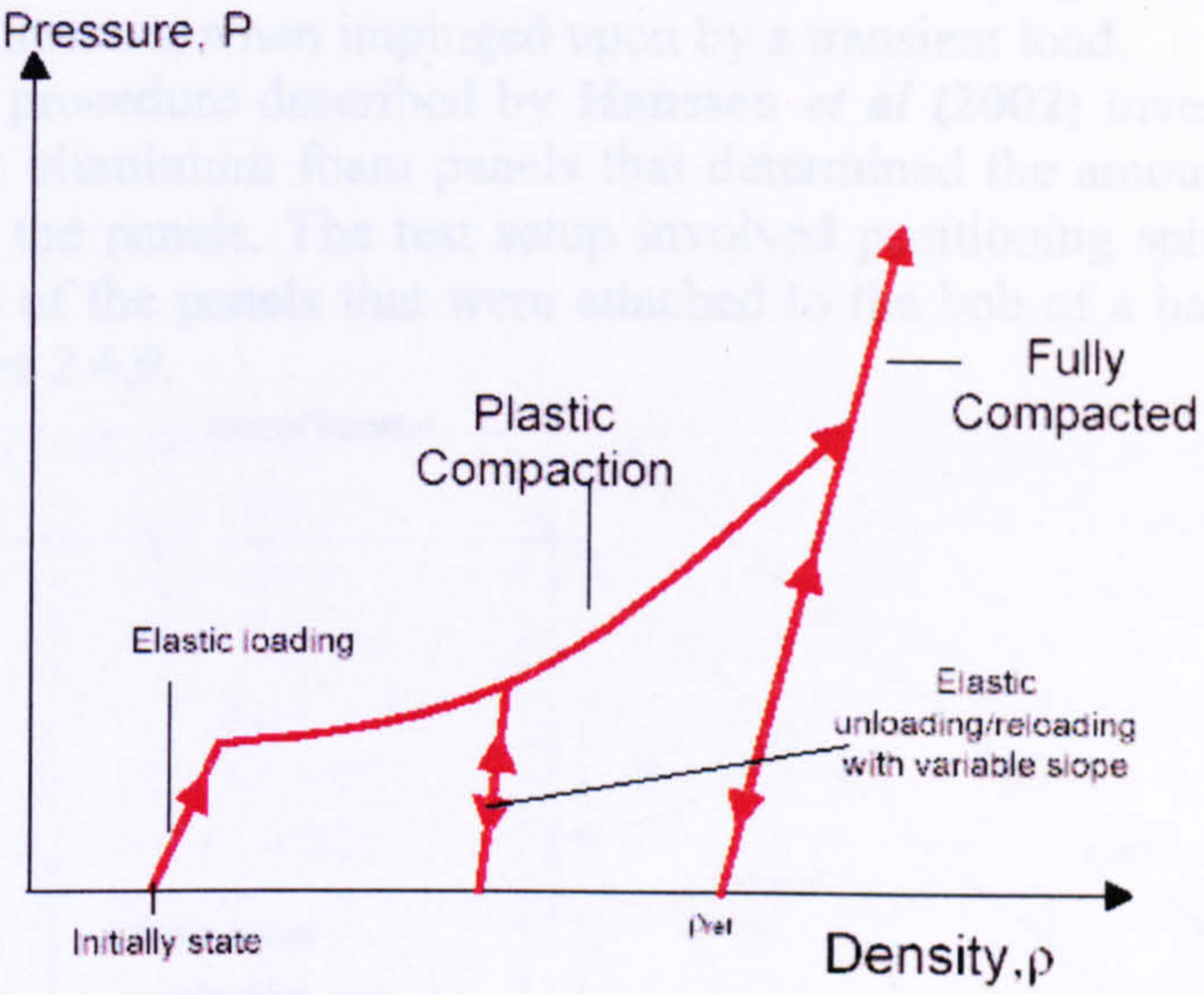

Figure 2.4.8 Equation of state curve (Pullen & Newman, 1995)

Equations of state curves are generally used in hydrocode simulations where a material's deformation behaviour at high loads is of interest.

A material's equation of state is obtained from the use of a Gauged Reactive Confinement cell. The material is statically positioned into the device and induced with stresses. A theoretical understanding of such a test is described in greater detail in **Pullen & Newman (1995).** The work performed and documented by the authors discuss the results of a three-year project that investigated the dynamic properties of shocked geological materials

The overall objective was to produce static and dynamic material data for concrete, rock and soils. The data would then be implemented in appropriate FORTRAN subroutines for use in hydrocodes. The purpose was to improve the accuracy of hydrocode predictions that involved the response of geologic materials to conventional weapons effects. The three phases of compaction caused by induced stress involve:

1. the elastic phase,
2. the plastic phase,
3. the hydrodynamic phase – curve shows an increase in stiffness.

Porous materials such as soil and concrete undergo non-linear volumetric changes as illustrated in figure 2.4.8 at relatively low loadings due to increased compaction and closure of the voids. These effects are introduced into a material model in the form of a standard porous equation of state to relate pressure to density.

The equation of state is currently the most useful way in characterising a soil's response to an increase in transient loading. A soil subjected to such a procedure will indicate two distinct characteristics:

1. maximum soil bulk density associated with compaction at a maximum stress,
2. maximum residual soil bulk density associated with the maximum stress.

2.4.3 Reducing stress wave reflection

Work has been performed on different materials in identifying the degree of energy absorption and reflection, when impinged upon by a transient load.
An experimental procedure described by **Hanssen *et al* (2002)** investigated the blast loading effects to aluminium foam panels that determined the amount of energy that was absorbed by the panels. The test setup involved positioning spherical charges at standoffs in front of the panels that were attached to the bob of a ballistic pendulum, illustrated in figure 2.4.9.

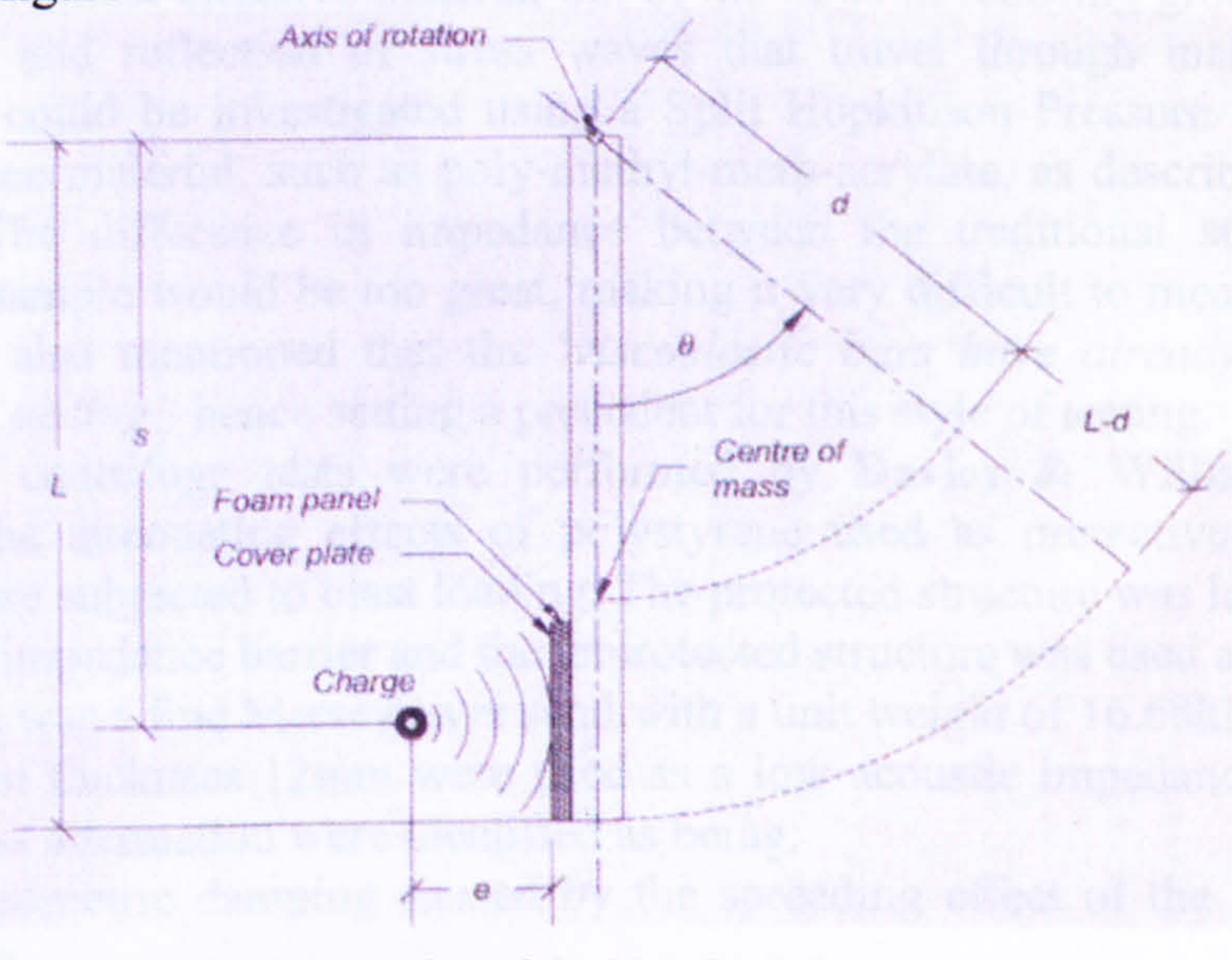

Figure 2.4.9 Simplified illustration of the blast loaded pendulum (Hanssen *et al*, 2002)

The propagating shock wave caused the foam panel to move in the direction dictated by the pendulum setup. '*The maximum swing of the pendulum was used to calculate the energy and impulse transferred from the blast loading*'. An analytical solution based on shock-wave theory was demonstrated in understanding the deformation behaviour of the foam panels whist subjected to a linearly decaying blast load.
The paper described aluminium foam as a '*new light weight material with excellent plastic energy absorbing characteristics*'. The findings from **Hanssen *et al* (2002)** suggested that foam panels were a possible cheap material, reducing reflective stress waves back into the soil as a result of charge detonation.
Bull & Woodford (2000) investigated the effects of polystyrene in reducing groundshock effects when positioned as a subsurface barrier layer beneath a concrete runway. A chemical explosion in a subgrade causes a steep rise in gas pressure and momentum. Materials such as polystyrene and concrete are used to screen out and attenuate the loading effects. The paper states that '*polystyrene does not deform under normal traffic loads. Laying it in sections up to 900mm thick has been considered'*. The experimental work performed by the authors involved positioning three different types of material between the runway and the subgrade. The depth of the material layer was 300mm. The materials tested within the setup included polystyrene, concrete and a combination of the two materials. The situations were also modelled numerically. The results were based upon the percentage reduction in peak pressure behind the subsurface barriers. A comparison between numerical and experimental results is illustrated in table 2.4.2.

Table 2.4.2 Percentage reduction in peak pressure (Bull & Woodford, 2000)

Barrier type	Numerical model	Experimental model
Polystyrene	75%	92%
Concrete	30%	78%
Composite	69%	93%

The numerical model under predicted the percentage decreases in recorded pressures. The authors did not directly state why this occurred but concluded that the polystyrene barrier was the most effective material out of the three in reducing ground shock. The transmission and reflection of stress waves that travel through materials such as polystyrene, could be investigated using a Split Hopkinson Pressure Bar made of a low-impedance material, such as poly-methyl-meth-acrylate, as described by **Gary *et al* (1995).** The difference in impedance between the traditional steel bar and a polystyrene sample would be too great, making it very difficult to measure reflection. The authors also mentioned that the '*viscoelastic bars have already been used in experimental testing*', hence setting a precedent for this style of testing.

A series of centrifuge tests were performed by **Davies & Williams (1992)** to investigate the attenuating effects of polystyrene used as protective barriers. Two structures were subjected to blast loading. The protected structure was located behind a low acoustic impedance barrier and the unprotected structure was used as a control.

The soil used was a fine Mersey river sand with a unit weight of 16.68kN/m^3. Sheets of polystyrene of thickness 12mm were used as a low acoustic impedance barrier. Two forms of stress attenuation were identified as being:

1. the geometric damping caused by the spreading effect of the wave from the source.
2. the energy absorbing ability of the polystyrene.

The low acoustic impedance of the polystyrene barrier reduced the measured '*peak free field stress from 1.17MPa to 0.08MPa*'. The polystyrene also reduced the peak acceleration by '*approximately 70%*', concluding that polystyrene is an effective barrier in reducing shock loading into buried structures.

Perry *et al* (1992) performed impact tests on different thicknesses of concrete, made with various lightweight aggregates such as expanded shale and polystyrene beads. The authors concluded that *'polystyrene concrete exhibited the most beneficial properties required for an ideal energy absorbing material'*.

Tedesco *et al* (1987) defined three theoretical cases that dictated the magnitude of the reflective wave. The conditions relate to the difference in acoustic impedance of two materials between a boundary interface.

1. $\rho_1 C_1 = \rho_2 C_2$, $\frac{\sigma_R}{\sigma_1} = 0$, therefore $\sigma_R = 0$.
2. $\rho_1 C_1 < \rho_2 C_2$, $\frac{\sigma_R}{\sigma_1}$ is positive. If σ_1 is a compressive wave, the reflective wave will be compressive.
3. $\rho_1 C_1 > \rho_2 C_2$, $\frac{\sigma_R}{\sigma_1}$ is negative. If σ_1 is a compressive wave, the reflective wave will be tensile.

σ_R =Reflective stress

σ_I =Incident stress

$\rho_1 C_1$ = Acoustic impedance of the material that contains the incident and reflected wave

$\rho_2 C_2$ = Acoustic impedance of the material that contains the transmitted wave

2.5 Soil characteristics

Maximum and minimum density tests for a gravely soil are performed according to **BS1377 (1990)**. The maximum density represents the densest packing of particles and corresponds to minimum porosity. The minimum density represents the loosest packing of particles and corresponds to maximum porosity. The porosity gives an indication as a percentage of the volume of voids including water and air, within a soil sample. The determination of the density index also refers to the relative density. This characterises the soil into one of the groups presented in table 2.5.1. It defines the soil in terms of the state of particle packing as a means of quantifying compaction as expressed by **Head (1992)**.

Table 2.5.1 Density index description (Head, 1992)

Material state	Density index range I_D (%)
Very loose	0-15
Loose	15-35
Medium	35-65
Dense	65-85
Very dense	85-100

The density index is defined by equation (2.5.1).

$$I_D = \frac{\rho_D - \rho_{D,\min}}{\rho_{D,\max} - \rho_{D,\min}} \frac{\rho_{D,\max}}{\rho_D}$$

Equation (2.5.1)

I_D = Density index (%)

ρ_D = Dry density

$\rho_{D,\min}$ = Minimum dry density

$\rho_{D,\max}$ = Maximum dry density

The dry density defined by equation (2.5.2) will vary depending upon the soil moisture content, indicating a variation in the relative density.

$$\rho_D = \frac{100}{100 + w} \rho$$

Equation (2.5.2)

ρ = Soil bulk density

w = Water content as a percentage

2.6 Parameters that influence groundshock loading

Groundshock is associated with stress waves propagation through a soil medium. An explosion caused by a charge detonation induces stress waves in the medium. Structures of any description within the area surrounding groundshock will experience an induced shock front. Depending on the severity of the explosion and the structure's resistance to the loading, the following can occur:

1. The structure will crack under loading and lose all degrees of redundancy.
2. The structure will transfer the load safely.

Protective layers of reinforced concrete slabs called secondary slabs help reduce stress wave propagation within the soil. They absorb the energy of the propagating stress wave and increase attenuation. When an explosive charge is detonated within a soil, its mass as a solid, instantaneously converts into an equivalent amount of gas. The expansion of the gas occurs at high radial velocities, causing high transient pressures to attenuate with range from the source.

2.6.1 Charge orientation

Findings from **National Defence Research Committee (1946)** suggested that weapons are dropped from the air into the ground at an average angle from the vertical of 15°. With low flying planes the inclination to the vertical is much greater, usually 45° or more. It would be sensible to adopt an angle of charge inclination during the experimental testing that lies within the range, $15° < \theta < 45°$ to the vertical. The maximum peak pressure recorded at a fixed location a distance away from a detonated charge was investigated by **Zimmerman *et al* (1999).** The authors considered the effect of varying the following parameters:

1. charge shape,
2. length to diameter ratio of the charge,
3. circumference angle.

If a cylindrical charge is detonated so that its longer side is parallel to the surface of a boundary, a smaller force will be directed towards it, but exerted over a large area. This causes larger pressures to be present on the surface. If the cylindrical charge is detonated so that its shorter side is parallel to the surface, with the head pointing down towards the surface, the force exerted will be greater, but acting over a smaller area. This causes smaller pressures to be present on the surface.
Watson *et al* (1989) investigated the damage caused to reinforced concrete beams as a result of varying the angle of inclination and the standoff distance between the charge and the top face of a beam. They found that the damage to the beams increased as the inclination of the charge decreased from 90° to 0°, relative to the horizontal. **Renick (2000)** stated that '*Oblique orientations of the charge rather than normal to a horizontal surface does not substantially change the mechanisms of damage, but may strongly affect the magnitude and distribution of damage*'.
Renick (2000) and **Watson *et al* (1989)** did not investigate whether a change in the charge orientation affected the loading geometry across a rigid boundary.

2.6.2 Moisture content and grain size

Hyde (1991) discussed the effect of water content within the soil and the effect it has on cohesive and granular soils. Water is bound within the skeletal structure of the soil, providing a contribution to the overall stiffness and strength of the soil structure.
The authors stated that '*soil water content can have a profound influence on groundshock propagation in cohesive soil, particularly if moisture content is 25% or greater*'. The author also stated that '*effects of water in sands with low relative densities can produce effects similar to those seen in cohesive soils*'. The stiffness of granular soils is provided by the grain-to-grain contacts in the soil skeleton, with only a small contribution coming from the water. Moisture in the soil changes rapidly with depth, particularly at the boundary of the water table. The velocity of a stress wave through a water soaked soil is appreciably higher than the velocity through water itself. Water in sands with a high relative density does not show a large influence on the pore water pressures within the shock wave propagation. Water in sands with a low relative density can produce effects similar to those in cohesive soils. The soil skeleton can collapse and the loss of grain-to-grain contact would result in high pore water pressures.

2.6.3 Charge position relative to different media

The transfer of transient energy into sub-surface structures is never 100% efficient. This can be quantified by the incorporation of a coupling factor. The magnitude of the stress would be enhanced if detonation occurs at a greater depth in the ground, where compaction is greater with increasing depth. The coupling factor is defined as '*the ratio of the ground shock magnitude from a partially buried or shallow-buried weapon, a near surface burst, to that from a fully buried weapon, contained burst, within the same medium*' stated in **Hyde (1991).**
Coupling factors are different depending upon the material that the charge is embedded in and its depth beneath the soil surface. The coupling factor in air remains constant, as air particles do not compact further with height above the ground. In soil and concrete, the coupling factor increases with scaled depth of burst. The variation in the coupling factor, associated with three different materials, is illustrated in figure 2.6.1.

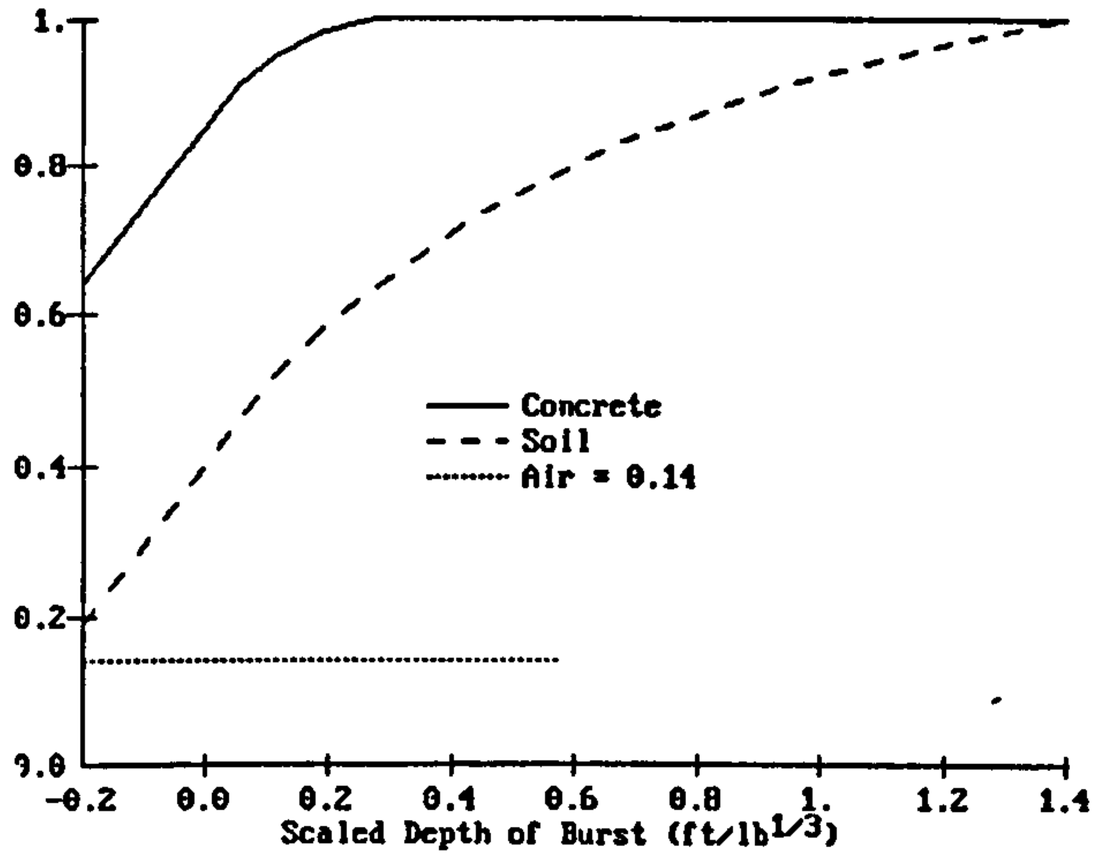

Figure 2.6.1 Ground shock coupling factors versus scaled depth of burst in three different materials (Hyde, 1991)

Hyde (1991) stated that the coupling factor is expressed in two ways defined by equations (2.6.1) and (2.6.2).

$$f_t = \sum f_i \left(\frac{W_i}{W} \right)$$

Equation (2.6.1)

f_t = Total coupling factor

f_i = Coupling factor for each component material, i.e. air, soil, concrete.

W_i = Weight of the charge in contact with each component material

W = Total charge weight.

The coupling factor can also be expressed in terms of length of charge embedded within a given medium.

$$f_t = \sum f_i \left(\frac{L_i}{L_t} \right)$$

Equation (2.6.2)

L_i = Length of charge in contact with each material

L_t = Total charge length

2.7 Measuring ground shock

2.7.1 Face-on and side-on loading

The orientation of pressure gauges to the direction of the propagating wave in any medium depends upon the parameter that is being measured. Two geometric ways of measuring the loading, known as side-on and face-on are illustrated in figure 2.7.1.

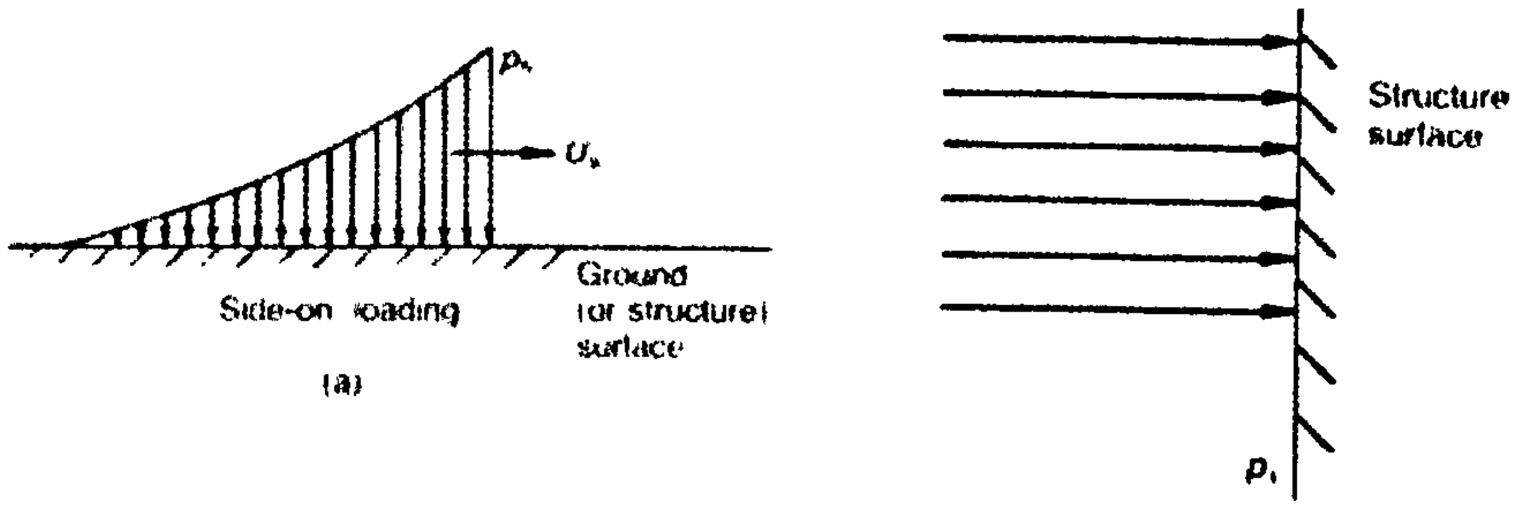

Figure 2.7.1 Orientations of loading (Smith & Mays, 1995)

Dongen & Weerheijm (1992) have outlined an analytical procedure for calculating the free field pressure with the use of an accelerometer built into a pressure gauge. The calculations that follow demonstrate how free field pressures within a soil environment are established. When a pressure transducer faces a plane ground shock it experiences a reflected and an interactive pressure defined by equation (2.7.1).

$$P_i(t) = P_{ff}(t) + P_r(t)$$

Equation (2.7.1)

P_{ff} (t)= Incident free field pressure

P_r (t)= Reflected pressure

P_i (t)= Interaction pressure

The wave pressure is associated with the incident free field pressure defined by equation (2.7.2).

$$P_{ff}(t) = \rho C_g u_g(t)$$

Equation (2.7.2)

ρ = Soil density

C_g = Longitudinal wave velocity

u_g = Soil particle velocity

$$P_r(t) = \rho C_g \left(u_g(t) - u_k(t)\right)$$

Equation (2.7.3)

u_k = Transducer velocity

The velocity of the transducer was calculated by integrating the measured acceleration and the ground shock velocity was calculated based on recorded times of arrival. Re-arranging equation (2.7.1), then substituting equation (2.7.3) into equation (2.7.2) to calculate the incident free field pressure:

$$P_{ff}(t) = P_i(t) - P_r(t)$$

Equation (2.7.4)

$$P_{ff}(t) = P_i(t) - \rho C_g u_g + \rho C_g u_k$$

Equation (2.7.5)

$$P_{ff}(t) = P_i(t) - P_{ff}(t) + \rho C_g u_k$$

Equation (2.7.6)

$$2P_{ff}(t) = P_i(t) + \rho C_g u_k$$

Equation (2.7.7)

$$P_{ff}(t) = \frac{P_i(t) + \rho C_g u_k(t)}{2}$$

Equation (2.7.8)

It was concluded that the velocity of the pressure transducer has a significant effect on the recorded pressures. Four conditions were then presented:

1. The transducer does not move during impact, therefore maximum reflection of the free field pressure occurs.
2. The transducer moves slower than the soil particles.
3. The velocity of the soil particles is the same as that of the transducer, so the response of the transducer is the same as the moving soil.
4. The transducer moves faster than the soil particles, resulting in a cavity forming in front of the transducer and the surrounding soil.

The cost and repairability of a pressure transducer with a built in accelerometer was not discussed by **Dongen & Weerheijm (1992)**.

2.7.2 Pressure gauges

Archer (1985) used a number of gauges called diaphragm pressure gauges, DPGs, consisting of a hollow steel cylindrical body, with a circular diaphragm lid, fixed to the body. The bottom face of the lid contained a strain gauge, positioned centrally, which was attached to a resistor positioned within the hollow cavity of the gauge. A number of these gauges were used to estimate the response time of a stress wave at various standoff distances from a charge. **Archer (1985)** used a static procedure for calibrating the gauges. Each gauge was calibrated as a beam subjected to a central knife-edge loading in a compression machine. The point load applied was converted to an equivalent stress over the area of the gauge subjected to strain. A stress-strain relationship for the central knife-edge load bending moment was calculated, then re-calculated to take into account an equivalent uniformly distributed pressure.
Warren (2002) used a gas gun as illustrated in plate 2.7.1 for exerting known transient air pressures into fluids that varied in viscosity.

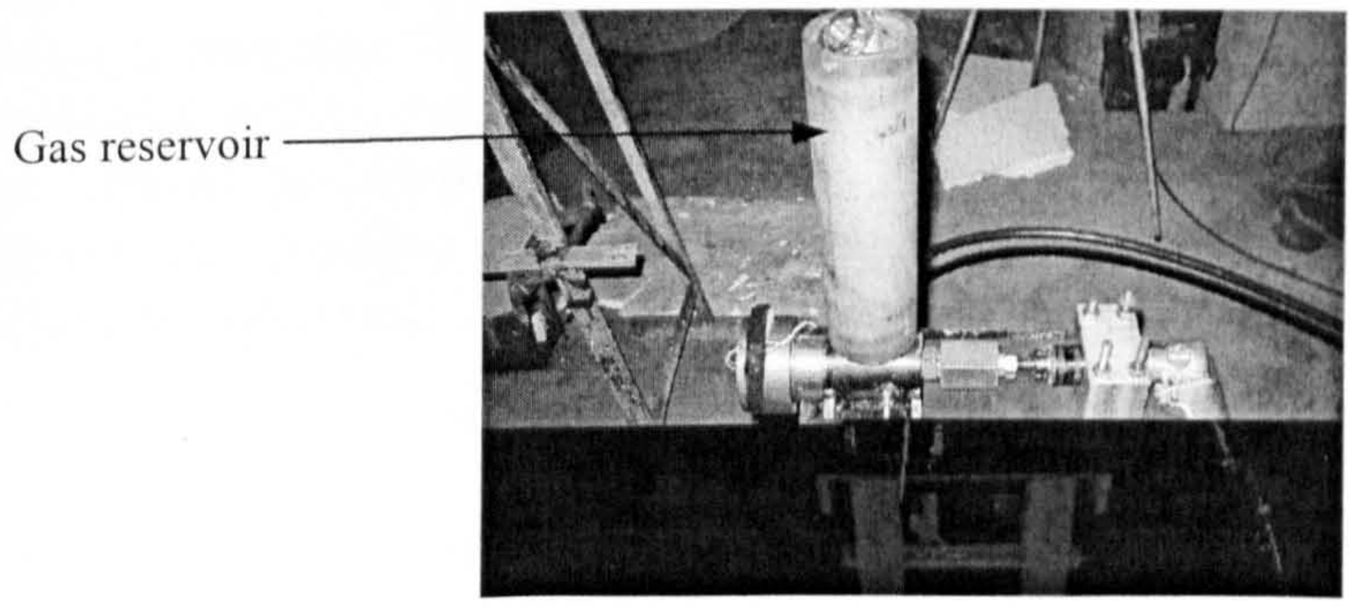

Plate 2.7.1 Gas gun (Warren, 2002)

Air blast tests were performed by **Duranovic (1994)** and **Pope (2002)**. They both used kulite pressure transducers to measure pressure-time histories. A kulite gauge is a pressure transducer that measures transient air pressures during airblast. It is a reputable instrument designed, constructed and calibrated by kulite Ltd.
Although the authors commented on the expense of such gauges, they did not comment on their ability in measuring groundshock.
Pope (2002) performed a number of tests using hemispherical charges of PE4 to load plate-reinforced panels. Estimates from analytical prediction methods indicated that the pressures associated with near field loading caused significant panel damage and were well in excess of the measurement capacity of the conventional pressure transducers. This led to the suggestion that '*blast measurements should be conducted at ranges within the capacity of the transducers'*. **Pope (2002)** also identified the importance of using pressure gauges that can respond to the frequencies of the propagating wave, characterising the true pressure-time history at a designated location. He used three pressure transducers positioned flush to the top face of a steel plate, along one of the diagonal axes, as illustrated in figure 2.7.2.

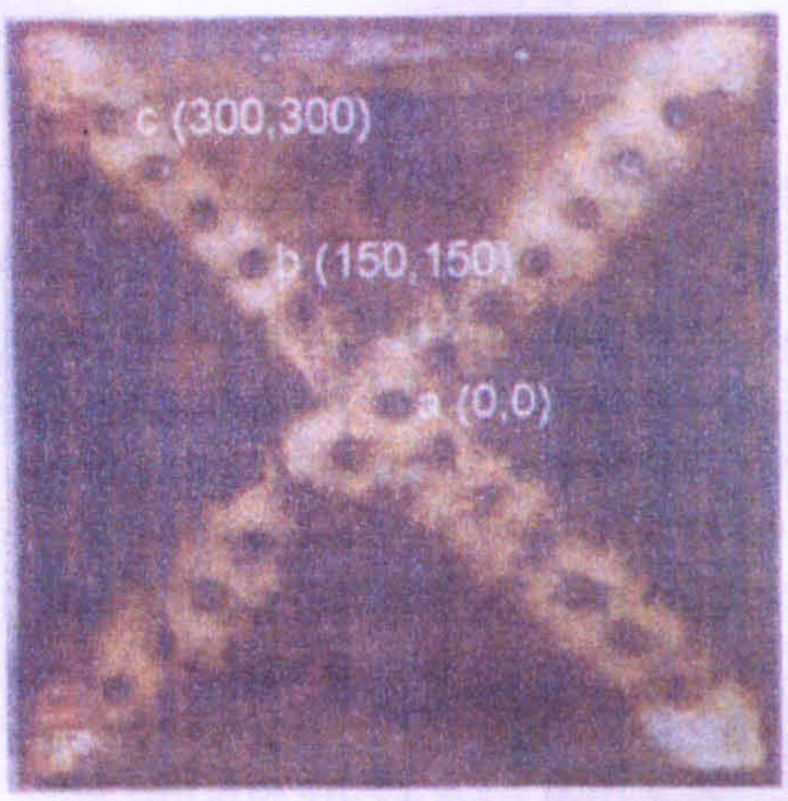

Pressure plate with three pressure transducers

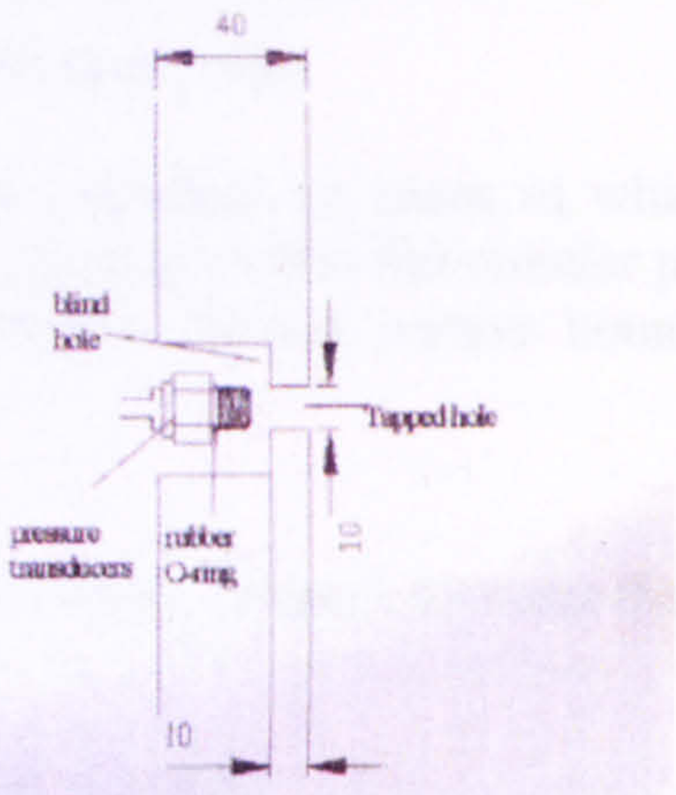

Pressure transducer positioned flush to the top face

Figure 2.7.2 Positioning and cross-sectional elevation of a pressure transducer (Pope, 2002)

MacPherson *et al* (2000) performed airblast tests using fibre optic pressure sensors. The attraction of such devices is due to their low cost of production, size and high-band width. The authors described the construction of such a device, relating it to diaphragm theory as well as describing the calibration procedure. However, their range of pressures is initially unknown and the ability to sustain impact loading from soil particles is uncertain. With greater development the ability of these gauges to measure groundshock will be evaluated.
Heap (1964) performed a theoretical analysis to determine equations for load, deflection and bending moments relating to the response of thin, flat circular plates subjected to static load. A pictorial view of a loaded plate is illustrated in figure 2.7.3.

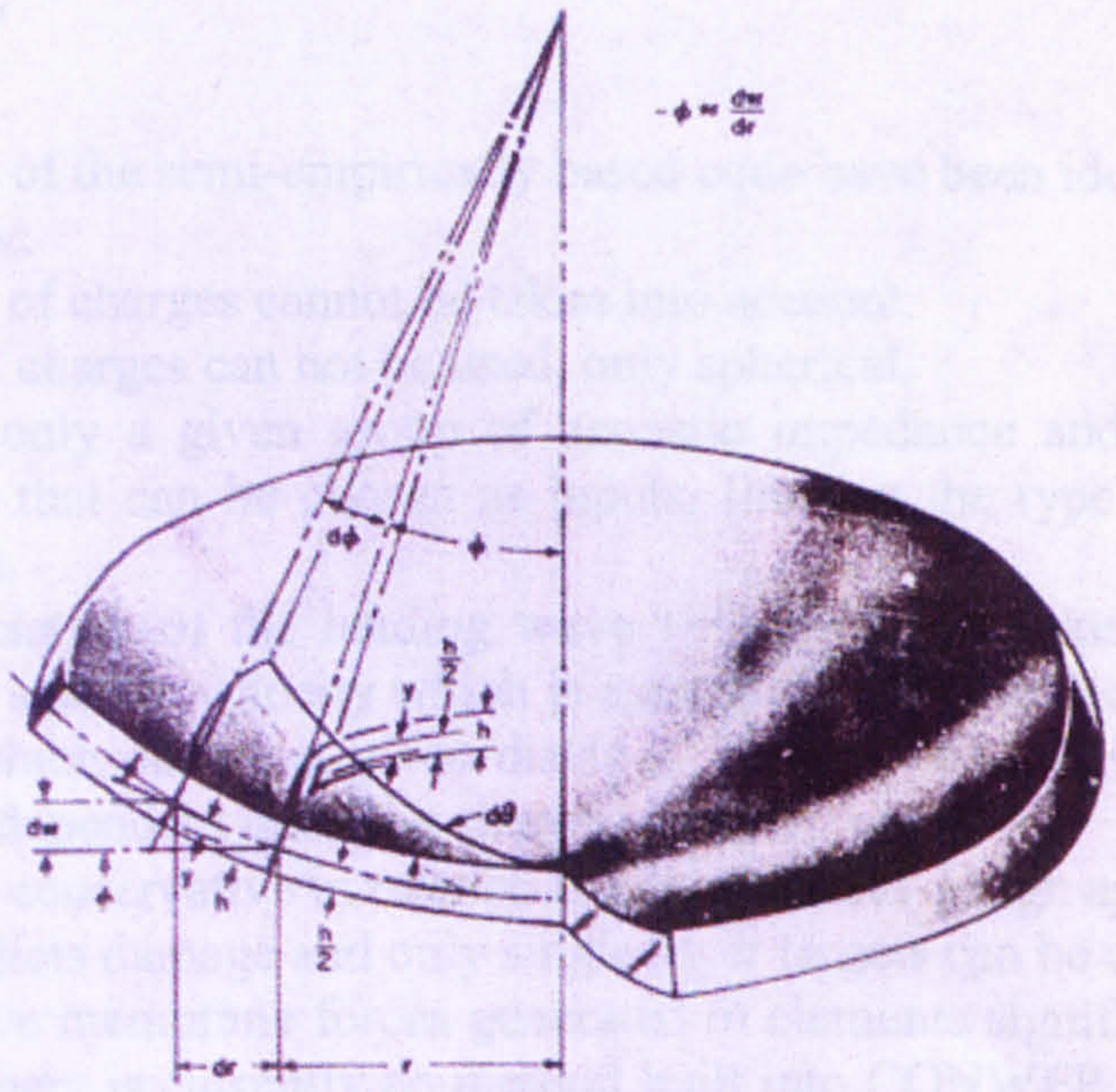

Figure 2.7.3 Bending of circular plates (Heap, 1964)

For a variable load subjected to a plate, the author described six cases in which a '*constant force divided by the radial distance squared*' acts on a thin flat circular plate. Equations associated with the response of a diaphragm having certain boundary conditions are bound by the following assumptions:

1. plate is assumed to be perfectly elastic,
2. plate is initially flat with a uniform thickness,
3. maximum deflection in comparison with the thickness is small, no more than half the thickness,
4. deformation of the plate is symmetrical,
5. the middle surface of the plate is not strained by bending.

2.8 Assessing groundshock numerically

Experimental work is expensive and time consuming. Simulating groundshock numerically is less expensive but a greater degree of theoretical understanding is required. Semi-empirical models have been constructed from experimental data and contain fundamental material properties. **Hyde (1991)** produced a programme that was built using equations and curves from **TM5-855-1 (1985)** called CONWEP. The equations used were semi-empirically based, using data extrapolated from experimental work. **Hyde (1991)** stated that '*data has been collected using charge weights less than 1kg to over 400,000kg*'. Curve fitting procedures were used to present the data with polynomial equations. Numerical models such as AUTODYN2D include a non-linear solution method, analysing the problem at time steps. Groundshock tests at any scale are expensive. Numerical methods, validated against proven prediction techniques and experimental data, can provide a cost effective means of examining the highly dynamic process involved in stress wave propagation.

2.8.1 CONWEP

The disadvantages of the semi-empirically based code have been identified and are described as follow:

1. Inclination of charges cannot be taken into account.
2. Cylindrical charges can not be used, only spherical.
3. There are only a given group of acoustic impedance and attenuation factor parameters that can be chosen as inputs, limiting the type of soil used as an overburden.
4. The depreciation of the loading wave velocity is not taken into account and instead the seismic velocity which is associated with the decayed loading wave velocity, which occurs at given distance from the source is always taken into account, independent upon the charge standoff.
5. Results are conservative in relation to the structural design application.
6. It over predicts damage and only single layer targets can be considered.
7. Compressive membrane forces generated in elements significantly enhance the strength. There is currently no method built into CONWEP that determines the magnitude of this effect, therefore it is neglected.

2.8.2 AUTODYN2D

The use of a commercially available code, validated against proven techniques and experimental data, provides a cost effective means of examining dynamic processes involved in stress wave propagation. AUTODYN2D is a general-purpose engineering software package that is based upon finite element calculations. It runs hydrocode simulations to solve non-linear dynamic problems in two-dimensional and three-dimensional formats.

A simulation uses axial symmetry; therefore physical problems of a symmetrical nature are suitable for modelling. The simulation consists of a number of sub grid arrangements, each filled with a particular material. These sub grids are connected together forming an inter-connective moving global grid. All the AUTODYN2D processors use explicit time integration, which implies that the variables are integrated within time intervals, based upon previous time step values. The mechanics behind AUTODYN2D are explained within the **AUTODYN theory manual (1998).**

Ma *et al* (1999) performed finite element calculations using AUTODYN2D to calculate stress wave propagation in rock mass. The numerical results agreed well with the field data, as illustrated in figures 2.8.1 and 2.8.2, for both peak particle velocity and peak particle acceleration. This indicated that AUTODYN2D '*can predict stress wave attenuation well*'.

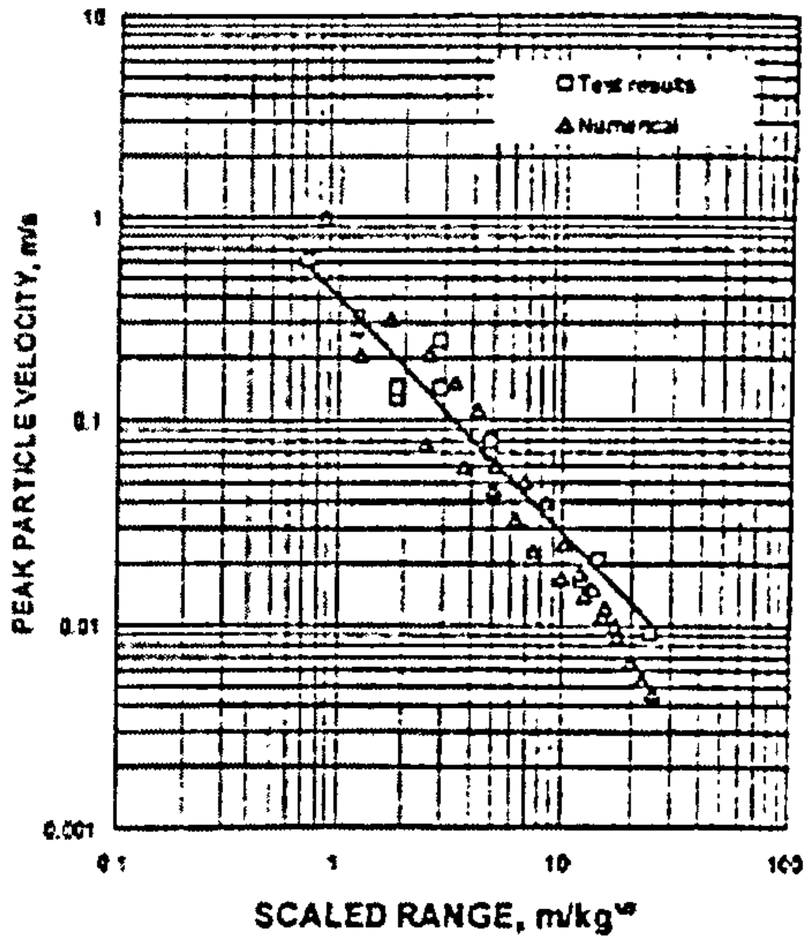

Figure 2.8.1 Attenuation of the peak particle velocity (Ma *et al*, 1999)

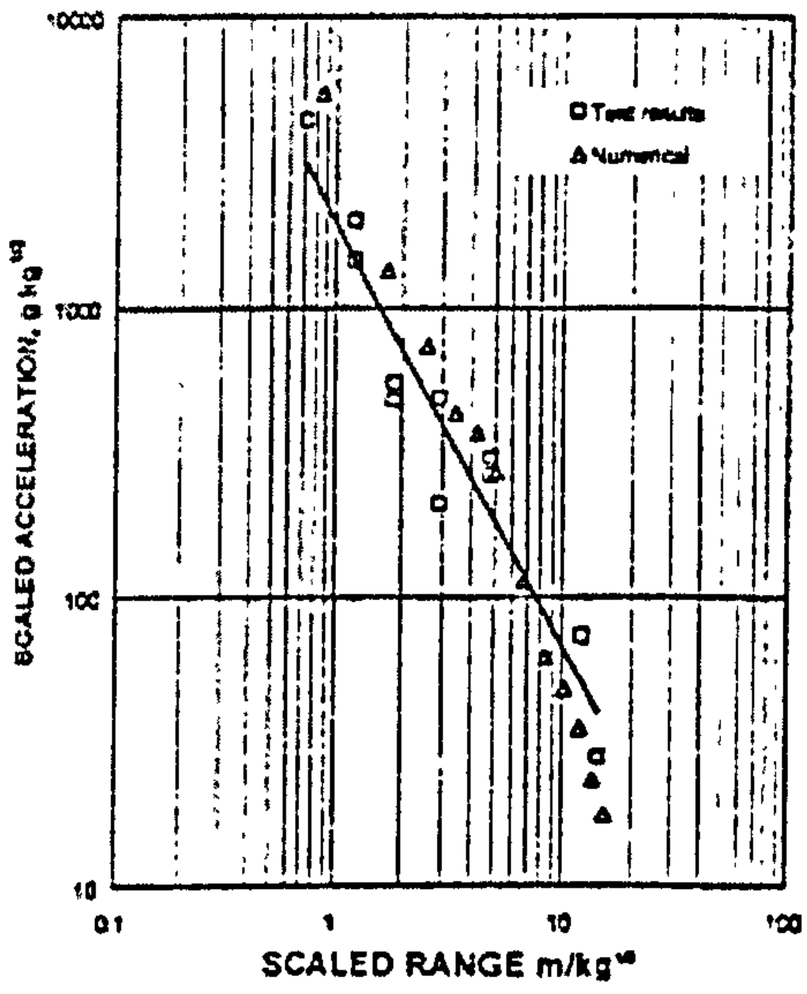

Figure 2.8.2 Attenuation of the peak particle acceleration (Ma et *al*, 1999)

Chapman *et al* (1994) used AUTODYN2D to simulate a '*free air blast from a condensed high explosive*'. The objectives of the work involved investigating the following:

1. parametric study on airblast,
2. parameter output values associated with a variation in a simulation grid size.

The problem was represented using an Euler grid in which material is transported from one cell of the grid to another. The grid remained fixed in space and without deformation, in contrast to a Lagrangian grid that does deform.
The authors found that the coarser the overall grid size, the slower the rate of rise of the pressure front, as is illustrated in figure 2.8.3. A global grid is defined by a geometric boundary containing interlinking grids of a given size. The variation in pressure output from target points was associated with a variation in the grid geometry.

Square grids of sizes of 1x1mm, 3x3mm and 10x10mm were set up and the overpressure recorded at a fixed designated position.

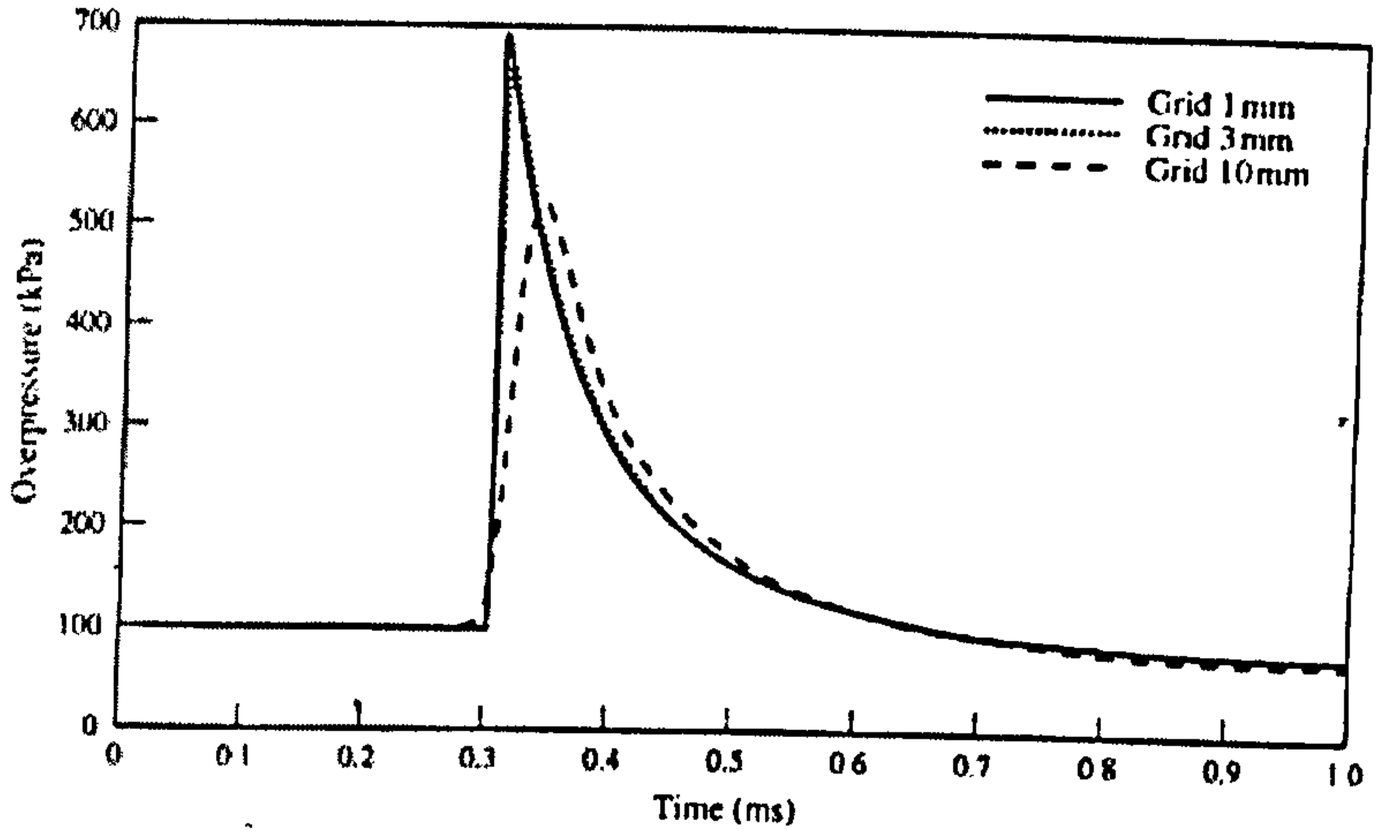

Figure 2.8.3 Pressure front at Z=1.19m/kg$^{1/3}$ for grid sizes 1,3 and 10mm (Chapman *et al*, 1994)

The authors found that the smaller the grid sizes, the longer the duration of the simulation. This was due to a greater number of calculations that were performed within the global grid. It was concluded that a grid size of 3mmx3mm provided a good blast wave shape while minimizing computer time. **Chapman *et al* (1994)** concluded that *'the variation of the grid size affects the final loads'*.
Tyas & Pope (2004) performed airblast simulations using AUTODYN2D. A series of models were developed in which the grid resolution was continually decreased until the predicted loading magnitudes on the surface of the panel converged to within 4%.

.

2.9 Damage to reinforced concrete slabs

Reinforced concrete slabs subjected to high transient loads suffer a loss in strength and stiffness. This is indicated by slab deformations, which exhibit yield line patterns.
Three possible outcomes from a damage assessment on a reinforced concrete slab would be:

1. identification of crack patterns,(e.g yield lines),
2. quantification of the degree of damage,
3. graphical representation of damage (e.g perforation, spalling and scabbing).

2.9.1 Crack propagation

Archer (1985) evaluated the damage to reinforced concrete slabs using different procedures. Fine cracks were detected in the damaged slabs by initially sponging a dark watercolour paint over the surface of the concrete, allowing it to soak, prior to testing. This allowed the smallest of cracks to be identified during the post-test analysis. Electrically conductive silver paint was applied in 2mm wide lines on the surface of the concrete and perpendicular to the expected cracks. The crack velocity and direction of propagation was determined as a result of this detailed procedure. An

attempt was made to determine the time at which pieces of concrete were ejected from the surface of the slab during a test.
Although **Archer (1985)** commented on the time and velocity of cracks during damage, he did not discuss the following:

1. removal of damaged slabs from the test site,
2. cleaning damaged slabs ready for visual inspection,
3. crack patterns.

Duranovic (1994) segregated the cracks produced on fully restraint reinforced concrete slabs, subjected to airblast into the following:

1. radial cracks,
2. circumferential cracks,
3. corner cracks,
4. reinforcement cracks.

Pope (2002) performed airblast tests on plate reinforced concrete slabs. Two cracks in particular were identified, radial and circumferential cracks as illustrated in figure 2.9.1. These appeared to be visible on reinforced concrete slabs, associated with the work performed by **Duranovic (1994)**.

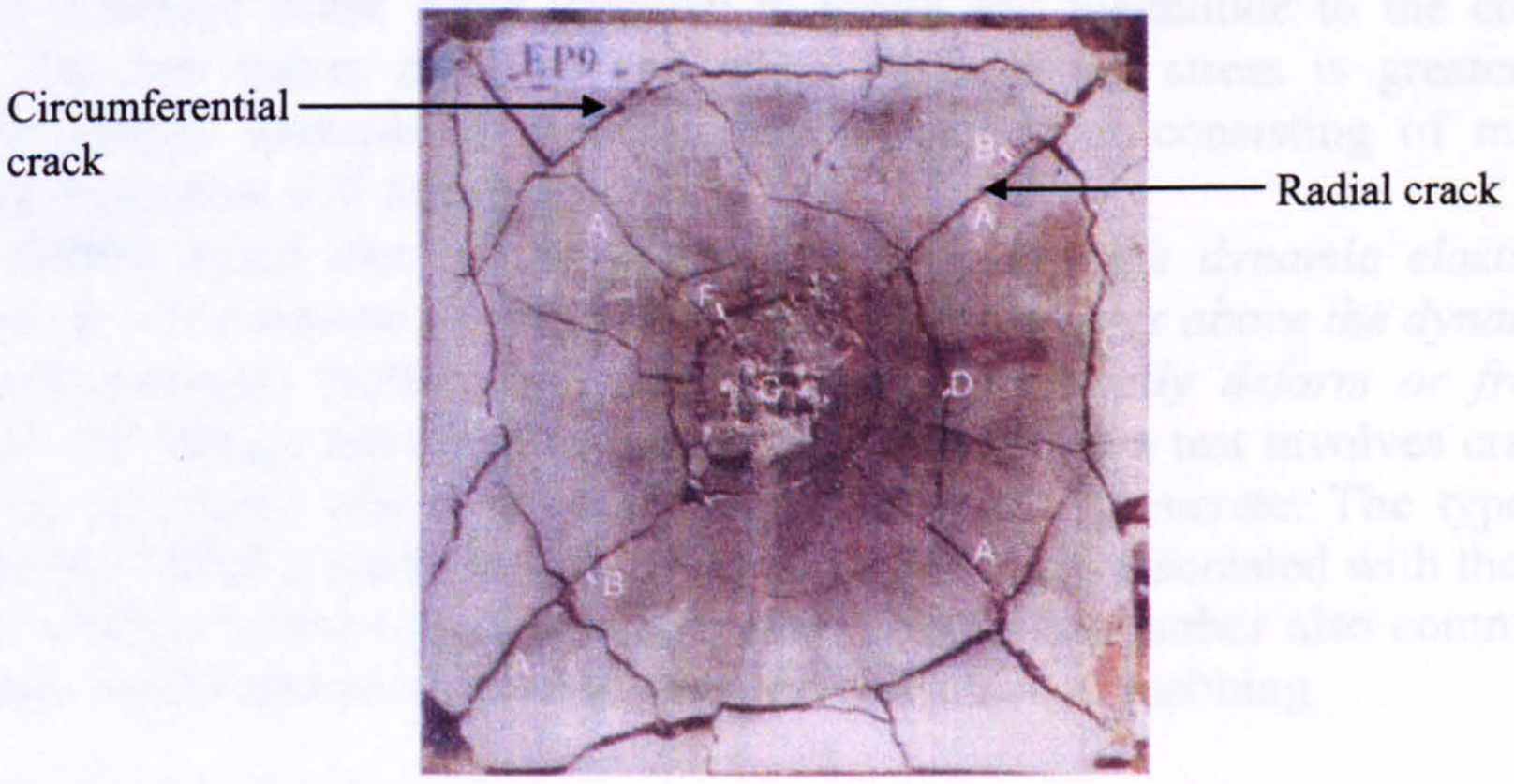

Figure 2.9.1Crack patterns on the top face of a steel plate reinforced concrete slab subjected to airblast (Pope, 2002)

The procedure of cracking has been described by **Park (2000),** commenting on the importance of yield line patterns produced to reinforced concrete slabs. At low static loads before cracking, the distributions of bending moments are in accordance with elastic plate theory. After cracking, further loading causes yielding of the steel at the section of maximum bending moment.
As the load applied to the slab increases, so does the number of cracks. When the concrete fails, the load is carried purely by the steel reinforcement, which in turn will yield, if the load increases. A system of yield lines forming a collapse mechanism is known as a yield line pattern. A yield line is an idealisation for a band of intense cracking across which the steel has yielded. Yielding of the steel begins at the section of maximum bending moment given by elastic theory. The positions of the yield lines developed by further loading are governed by the arrangement of reinforcement, boundary conditions and type of loading.

Park (2000) has made reference to a slab's ability to distribute a static load whilst producing yield line. These lines are also evident upon slabs subjected to transient loading from airblast, discussed by **Duranovic (1994)** and **Pope (2002).**
Wood (1961) commented on the nature of cracks that form on reinforced concrete slabs when they are subjected to explosive loading. He described the face of the slab that is in contact with the greatest proportion of the charge, being forced into compression and yield lines in the form of circumferential cracks occurring on the surface as a result of radial forces. The opposite face then goes into tension, exhibiting radial cracks, caused by circumferential forces.

2.9.2 Scabbing of reinforced concrete slabs

Concrete is a composite material composed of cement, water and aggregate. When subject to increasing dynamic load, concrete will eventually fail in a sudden brittle manner. The failure can be either partial or total, but is associated with a release of fragmentation.
Scabbing occurs on the bottom face of a slab, subjected to loading via the top face and occurs due to tensile failure in the concrete, normal to its free surface. It is caused by the propagation of a compressive stress wave, which is reflected back from the bottom face, as a tensile stress wave identical in shape and magnitude to the compressive wave. The two waves combine and when the resultant stress is greater than the dynamic tensile strength of the concrete, a scab layer consisting of many small concrete fragments will form.
Buell (1985) stated that '*if the stress wave is below the dynamic elastic limit of concrete, it will attenuate at very small rates, whilst stresses above the dynamic elastic limit will attenuate rapidly by using energy to plastically deform or fracture the material*'. If damage sustained to the concrete slabs from a test involves cracking and cratering, the stress will be within the plastic limit of concrete. The type of stress propagation within a concrete slab could be qualitatively associated with the degree of damage relative to the region on a stress-strain plot. The author also commented that steel fibre reinforcement showed the greatest resistance to scabbing.

2.9.3 Recording damage

Hader (1983) produced experimental test data, as illustrated graphically in figure 2.9.2 relating slab thickness to charge standoff distance and the cube root of the TNT equivalent of an explosive weight for bare explosive charges, causing damage in terms of perforation and spalling. The author did not consider an evaluation of damage associated with cumulative loading.

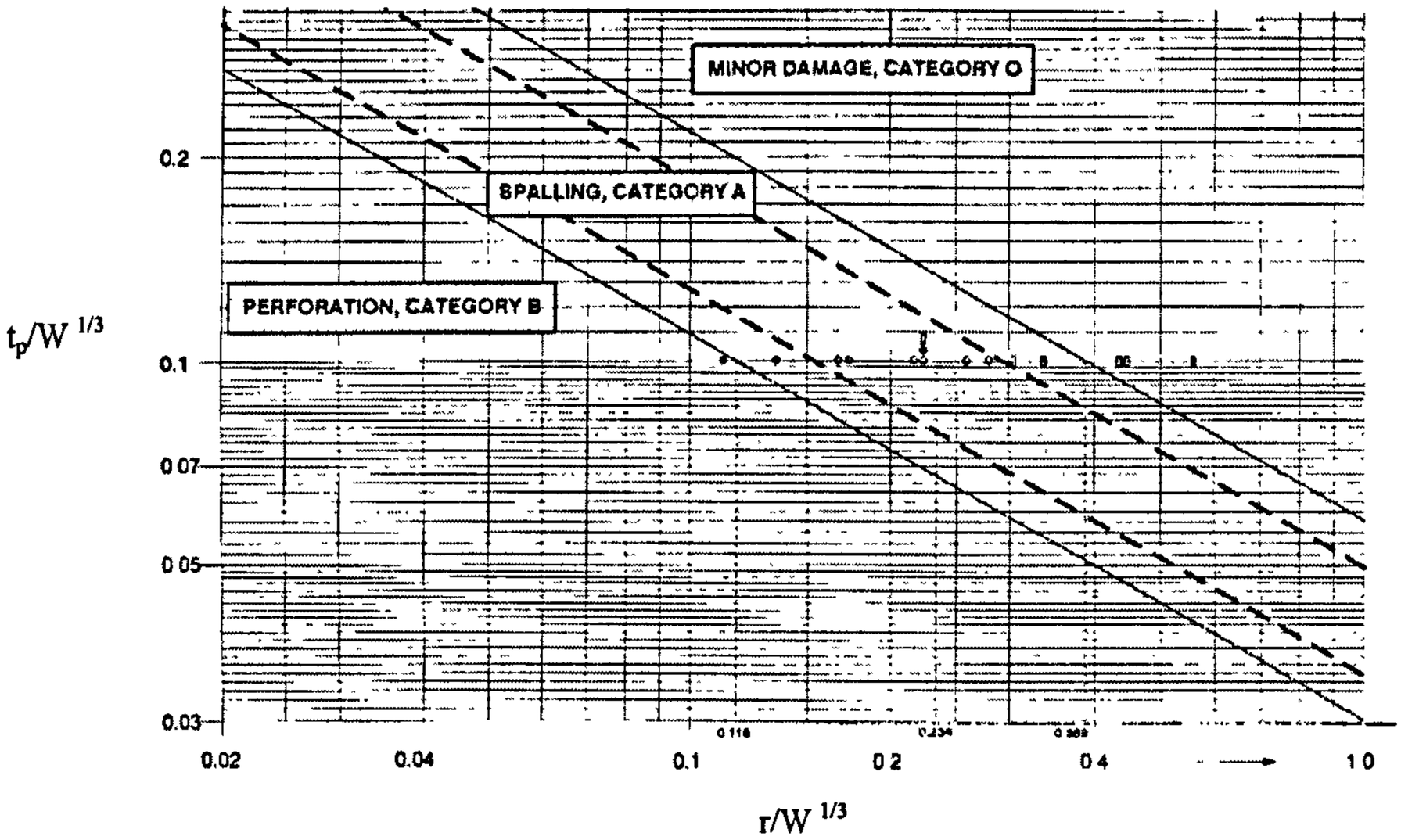

$t_p/kg^{1/3}$ = Scaled distance
$r/kg^{1/3}$ = Scaled wall thickness

Figure 2.9.2 Estimate of slab damage (Hader, 1983)

McVay (1988) performed tests and recorded the results in a similar fashion to **Hader (1983)**. **McVay (1988)** conducted experiments to differentiate between spall, breach and no damage associated with varying thicknesses of slab and standoff distances of close-in spherical charges. **Duranovic (1994)** represented damage in terms of:

1. substantial – damage was done to over one-half of the target,
2. moderate – damage done to one-fourth of the target,
3. little/small – damage done to less than one-fourth of the target,
4. major cracks – cracks were greater than one-eighth inches in diameter,
5. hairline cracks – cracks were less than one-eighth inches in diameter.

The author did not associate damage with a magnitude of load.

2.9.4 Damage mechanism

Renick (2000) considered the damage mechanisms that were employed when a charge was detonated within an air/concrete/soil experimental set-up. The position of the charge relative to two different layers described in figure 2.9.3 is similar to a setup that will be implemented during the experimental stage of the research. The author stated that '*gravity has little direct effect on the damage modes, but does affect the final rest position of the loose rubble*'.
Mechanisms of failure are illustrated in figure 2.9.3. These are segregated into seven situations, illustrating mechanisms of failure, associated with the detonation of a charge.

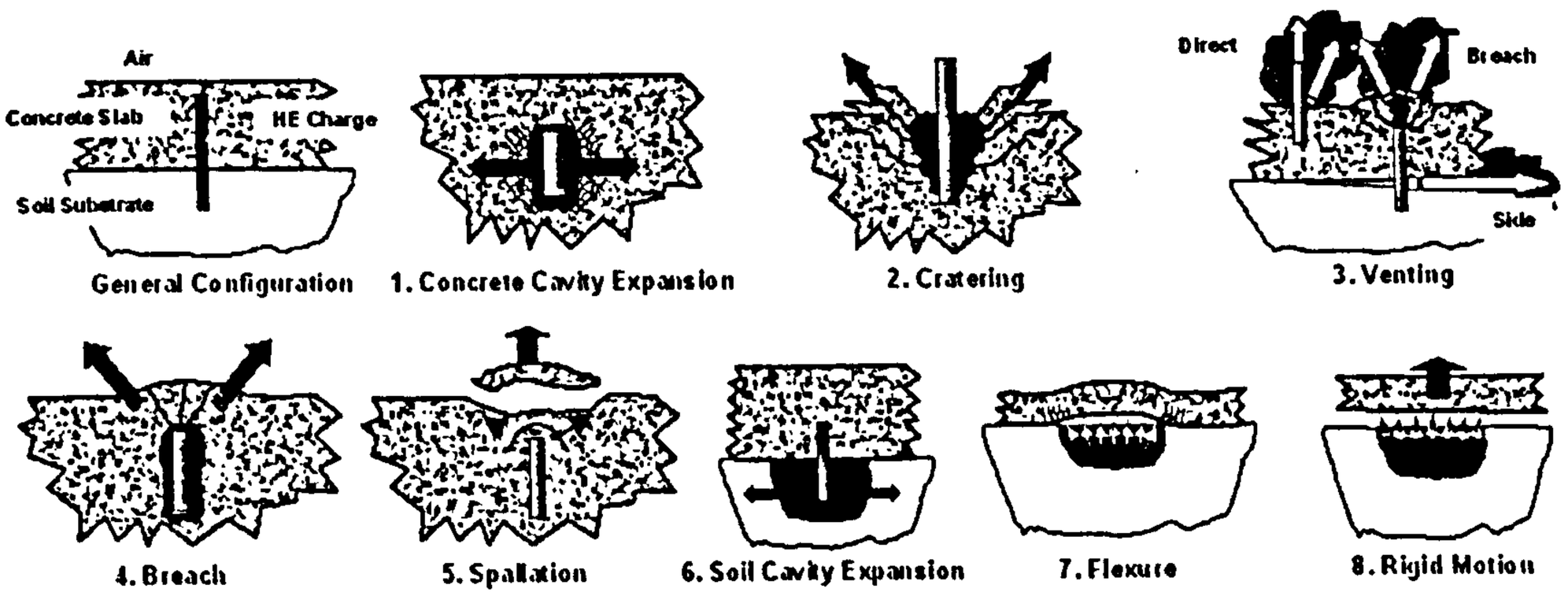

Figure 2.9.3 Schematic of air/concrete/soil configuration and high explosive response mechanisms (Renick, 2000)

The author stated that '*Flexural damage and breach were determined to be the most effective damage modes in the cumulative damage process for most hardened targets*'. These damage mechanisms will relate to a charge positioned relative to a secondary slab during the experimental stage of the research.

Cameron *et al* (2000) performed a number of tests on reinforced concrete slabs. The tests were segregated into two phases of multiple hit attacks, which are also known as cumulative attacks. The authors concluded that if enough explosive is coupled with the soil underneath a concrete slab, a larger flexural type crater is formed with regions of enhanced penetrability. **Hu *et al* (2004)** performed tests that determined the effect a burster layer or secondary slab would have in reducing the load into the soil overburden below the slab. The authors performed experimental contact charge explosions on four different types of slabs:

1. steel reinforced concrete,
2. concrete,
3. steel fiber reinforced concrete,
4. polypropylene fiber reinforced concrete.

The test setup involved positioning a slab on the surface of a soil layer, which contained pressure sensors. Pressure gauges of some description were used to determine which slab absorbed the greatest amount of energy. However, the authors did not discuss four possible characteristics of the gauges:

1. type,
2. sustainability,
3. damaged or undamaged,
4. loading response.

Although the magnitude of damage subjected to all four types of slabs varied, there were fundamental geometric similarities as stated as follow:

1. Top face – Circumferential quadrant cracks and cross-shaped radial cracks dominated the surface.
2. Bottom face – Radial cracks that propagated from the perimeter to the centre dominated the surface.

Similarities on both faces of a slab have also been observed by authors **Duranovic (1994)** and **Pope (2002).**
It was concluded that steel fiber reinforced concrete specimens had the best capacity in resisting the explosion. **Deng *et al* (2004)** stated that damage reinforced concrete slabs subjected to transient loading can experience either one or a multiple of the following:

1. explosive cratering,
2. explosive spalling,
3. explosive perforation,
4. explosive punching.

There has been no evidence that these classifications are universal. Pictorial elevations of these damage modes are illustrated in figure 2.9.4. The authors did not comment on the geometric size, mass and inclination of the charge that caused these four damage modes.

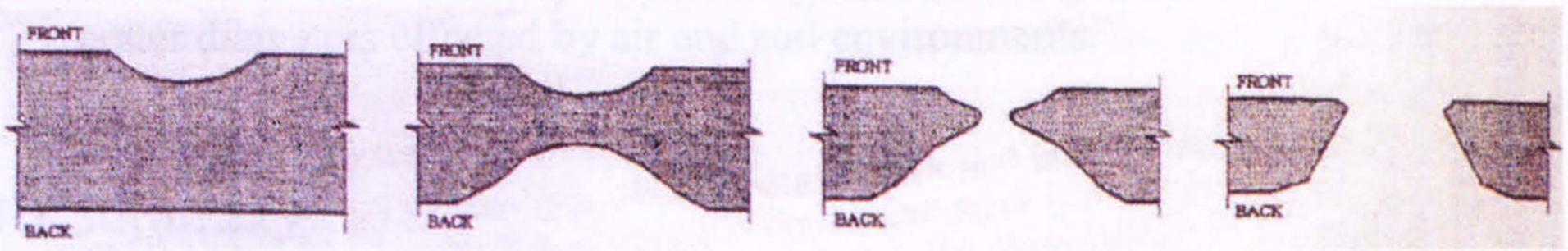

Explosive cratering Explosive spalling Explosive perforation Explosive punching

Figure 2.9.4 Damaged shapes (Deng *et al*, 2004)

Duranovic (1994) conducted tests to observe the damage sustained by two-way spanning reinforced concrete slabs, exposed to near field explosive loading from a spherical charge. The top and bottom face of the damaged slab, illustrated in figure 2.9.5 indicates square cracks on both faces. This demonstrates an efficient load transfer from the concrete to the steel. This phenomenon of load transfer should occur irrespective of the charge inclination. If the mass of the charge is not large enough, the stresses induced into the slab might be '*below the dynamic elastic limit of concrete'* as stated by **Buell (1985).** This would imply that fracturing of the concrete might not occur and that the load path would be difficult to identify. The arrangement of rebars above the perforation was still intact after the test. This implies that although the concrete failed, the load was not large enough de-member the individual steel rebars within the square grid arrangement.

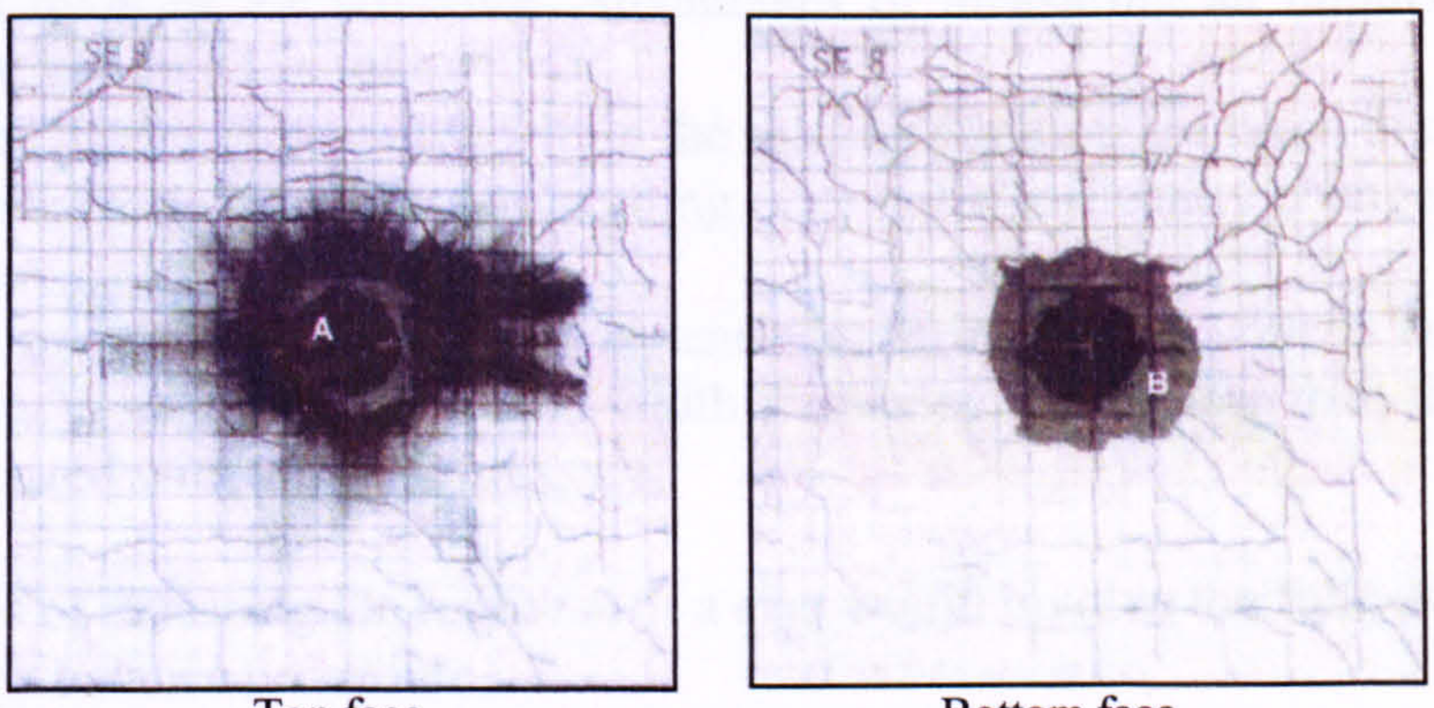

Top face Bottom face

Figure 2.9.5 Damaged mechanisms on a slab that has been subjected to airblast (Duranovic, 1994)

Cratering on concrete slabs occurs as a result of the stress wave propagation that exceeds the elastic compressive strength of the concrete. The size of the crater is limited by the degree of energy dissipation due to plastic work, which may rapidly attenuate the magnitude of the stress wave. **Wright (1991)** concluded that the crater depth produced by a charge was proportional to the charge diameter.

$$d_c = kW^{0.33}$$

Equation (2.9.1)

k=Constant of proportionality
W =Mass of the charge
d_c = Crater depth

Equation (2.9.1) would only be valid if the charge was spherical and in contact with the slab. **Wright (1991)** did not pursue any further in predicting the following:

1. crater diameters caused by a contact cylindrical charge,
2. crater diameters effected by air and soil environments.

2.10 Summary

Three types of responses associated with transient loading have been identified:

1. Impulsive – load has finished acting before the structure has had time to respond significantly.
2. Quasi-static – load may be considered as remaining constant, whilst the structure attains its maximum deflection.
3. Dynamic – dictated by the boundaries defined by impulsive and quasi-static loading.

Idealised load-time histories may be considered which essentially capture the main features of real load-time histories. Three such idealisations are:

1. half sine-wave load distribution,
2. rectangular load distribution,
3. triangular load distribution.

An impulsive response indicates that its maximum deflection is a function of impulse, stiffness and mass of the structure. Advantages of measuring an impulse instead of peak pressure are stated as follow:

1. All the pressures recorded within the loading duration are taken into account.
2. An inaccurate peak pressure reading does not significantly change the impulse value.
3. Peak pressure is difficult to measure experimentally, with a confidence of accuracy, as the gauge's band-width frequency can be less than the frequency associated with the peak pressure.

Two methods of assessing the response of a slab would involve the following:

1. energy balance procedure,
2. ratio values calculations of load duration and natural period of response.

The energy balance relationship is associated with the strain and kinetic energy. It can also be represented using the 'Response number' parameter, which takes into account the geometry and material properties of a panel. The parameter is effective when slabs of varying geometry are used. The environment in which a charge is detonated influences the spatial distribution of loading across a slab. The two generic environments are stated as follow:

1. Near field – Charge standoff is less than effective span of the slab.
2. Far field - Charge standoff is greater than effective span of the slab.

The damage mechanisms associated with near and far field loading are stated as follow:

1. Near field - Local bending, shear and spalling.
2. Far field – Global bending.

Explosive tests at varying scales are performed with the objective of validating the scaling law, so results at full scale can be predicted. Explosive tests at full scale are incredibly expensive, so smaller scaled tests are performed instead. The scaling law states that a varying parameter such as impulse should remain constant in two different scale tests, when there is a variation in charge mass and standoff distance. Establishing a linear scale factor, allows the scaled distance associated with charge mass and standoff to be calculated.

The inclination of a weapon dropped from the air can lie within the range $15^\circ < \theta < 45^\circ$ to the vertical. The inclination of a detonated charge influences the loading upon a slab positioned below it:

1. Vertical charge – a larger force will be directed towards it, acting over a smaller area. This causes smaller pressures to be present on the slab.
2. Horizontal charge - a smaller force will be directed towards it, acting over a larger area. This causes larger pressures to be present on the slab.

A stress wave propagates with a depreciating loading wave velocity that is dependent upon the following:

1. soil attenuation coefficient,
2. size of the charge,
3. range from the source.

A stress wave will decay with range from the source and finally equilibrate into the seismic velocity, which is constant for a particular medium. It has been indicated that the semi-empirical code CONWEP does not take into account the attenuating loading wave velocity. Instead, it assumes a seismic velocity for the material, for pressure and impulse calculations. This leads to underpredicted pressure and impulse results.

As a stress wave propagates through a medium, it attenuates. Attenuation is a process where the wave loses energy, due to overcoming large frictional forces within the medium. This causes a reduction in magnitude, collaterally influencing the loading wave and soil particle velocities.

The literature based upon experimental and numerical results suggest that polystyrene is a cost effective, efficient energy absorbing material.

The most effective way of measuring groundshock is with pressure transducers. They can either be positioned face-on or side-on to the incoming stress wave. Each orientation records a different characteristic of groundshock loading as indicated:

1. Face-on measures reflective pressure.
2. Side-on measures the free field pressure in the propagating medium.

DPGs were used to determine response times of a stress wave. The gauges were subjected to a static calibration procedure. They were associated with being robust, easily replaceable and cost effective. However, a band-width was not given.
Kulite pressure gauges are useful at measuring airblast, due to their high bandwidth. They are not physically suitable for measuring groundshock, as soil particle impact could damage them.
It has been found that pressure-time histories recorded from groundshock loading can contain multiple peaks. A plausible reason for this considers both the initial and a secondary peak:

1. Initial peak is associated with maximum peak pressure appears to affect the soil phases, compressing the soil and decreasing the void spaces.
2. Secondary peak indicates that the soil deformation mechanism has changed, due to a reduction of load. The deformation now affects the soil skeleton. The contact movement between the solid particles and breaking of bond linkages governs this.

The degree and variability of soil compaction is related to the density index. The equation of state for a soil illustrates the increase in soil bulk density associated with an increase in stress. It describes soil behaviour under high transient stresses.
The variation in insitu soil stress with gravity was investigated. A lack of evidence in the literature indicates that the parameter is less sensitive to the effects of gravity.
The usability of two numerical tools, CONWEP and AUTODYN2D, has been investigated. CONWEP contains the following characteristics:

1. semi-empirical code – based upon experimental data,
2. easy to use,
3. does not take into account cylindrical charges,
4. does not take into account the depreciation of the loading wave velocity and instead assumes a constant value of seismic velocity,
5. limited materials library preventing soil characteristics that are not on the database from being implemented.

AUTODYN2D contains the following characteristics

1. capable of outputting results that are similar to those achieved experimentally,
2. axial symmetry setup.

It was established that the material grid mesh resolution was a sensitive parameter in determining the output of measured parameters, i.e. impulse, pressure, and deflection. Before running a simulation this parameter should be investigated. Damage mechanisms expected to form on reinforced concrete slabs consist of:

1. cratering,
2. perforation,
3. punching shear,
4. spalling,
5. scabbing.

There appears to be a similarity with the crack patterns observed on slabs subjected to airblast and groundshock. Such patterns contain the following:

1. circumferential cracks – irregular concentric circles that can be discontinuous,
2. radial cracks – perpendicular to circumferential cracks and can be discontinuous,
3. corner cracks- diagonal cracks that propagate at the corners of the slab,
4. reinforcement cracks – indicate load transfer from the failed concrete into the steel.

If enough explosive is coupled with the soil underneath a concrete slab, a larger flexural type crater is formed with regions of enhanced penetrability. Flexural damage and breach were considered as being effective damage modes within a cumulative damage process for most hardened targets.

Chapter Three

Experimental methodology

3.1 Overview of the experimental programme

The experimental work was performed in a test cell constructed from reinforced concrete pendine blocks, as illustrated in plate 3.1.1.

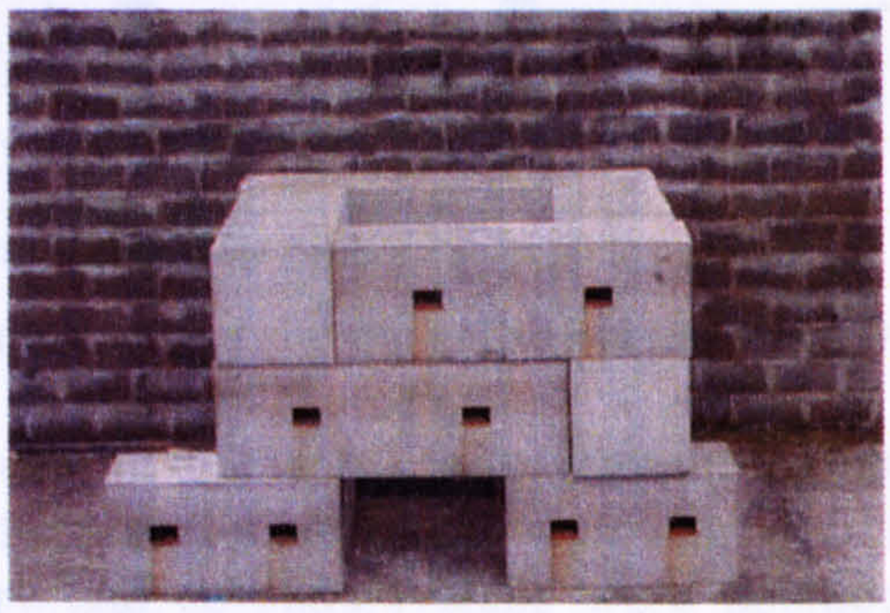

Plate 3.1.1 Test cell

The experimental work involved the implementation of a steel plate during the steel tests and reinforced concrete slabs during the concrete tests, upon a steel support structure, positioned within the internal space of the test cell. The dimensions of the plate and slabs were of 1000x1000x10mm and 1000x1000x73mm.

The steel test frame illustrated in figure 3.1.1 represented an underground structure. It supported a steel plate then a reinforced concrete slab as well as soil overburden. A typical steel test involved a vertically positioned cylindrical charge within the soil overburden depth. A hollow tube made of acetate was positioned vertically in the soil during compaction as illustrated in figure 3.1.1. It served as two functions:

1. secure lowering of the charge,
2. dictated the charge standoff distance from the steel plate.

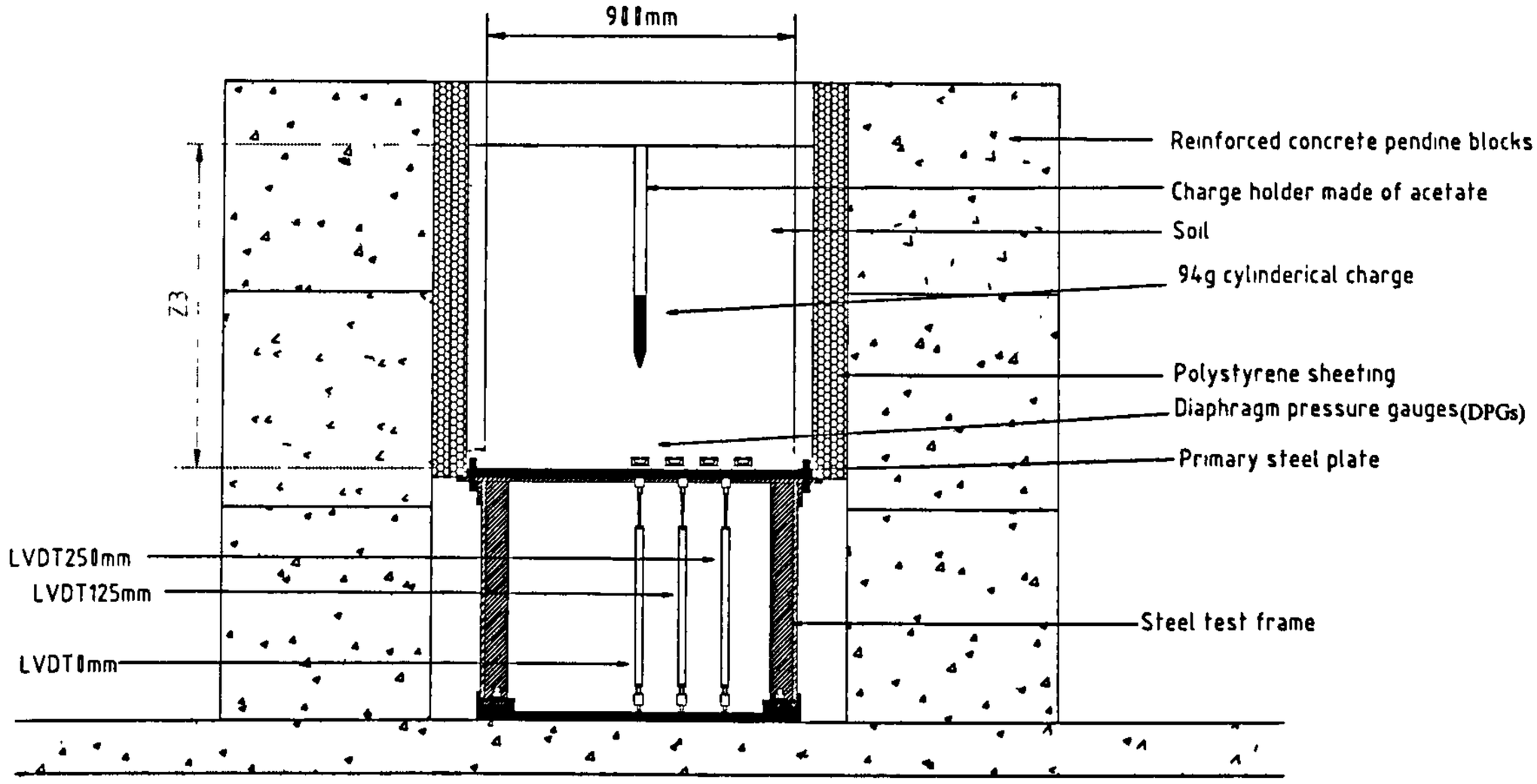

Z_3 = Total soil overburden depth above the primary steel plate

Figure 3.1.1 Cross-sectional elevation of a steel test set up within the test cell

The total soil overburden in the steel tests remained constant, whilst the charge standoff varied. The reinforced concrete tests were split into three stages of testing. In Stages I and II primary and secondary slabs were positioned. Their function and boundary conditions are described as follow:

1. The primary slab, also defined as a roof slab, was clamped around its perimeter and secured to the steel test frame.
2. The secondary slab, also defined as a burster slab, served as an energy absorbing layer, supported by the soil above and beneath its faces.

Positioning of a secondary slab segregated the total soil overburden into two distinct depths, as illustrated in figure 3.1.2.

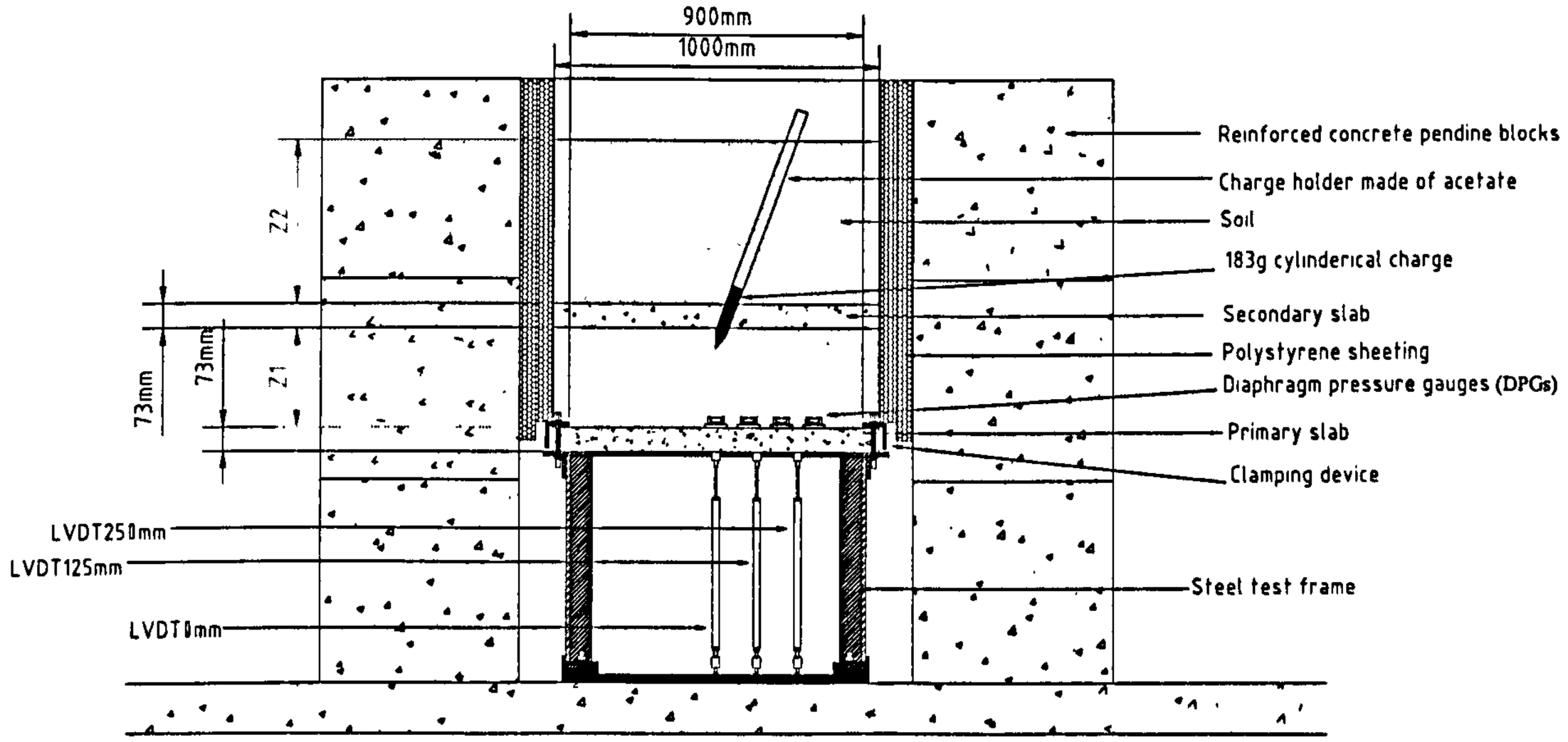

Z_1 = Soil overburden depth between the primary and the secondary slab
Z_2 = Soil overburden depth above the secondary slab

Figure 3.1.2 Cross-sectional elevation of a concrete test set up within the test cell

The soil compaction procedure applied during the steel and a concrete tests was identical. The negligible effect it had to stress wave propagation has been discussed in detail in section 4.6. The soil was poured manually into the test cell in layers using a shovel, compacting each layer in turn by impacting the soil surface with the flat face of the shovel. The surface of each layer was flat prior to the next layer of soil being applied. The effect of soil settlement was ignored as the explosive test was performed an hour after soil compaction.

A cylindrical charge of PE4 was statically positioned at an inclination of 70° to the horizontal, and used throughout the concrete tests. This introduced non-symmetrical loading, which was greatest along plane D1-B1 illustrated in figure 3.1.3.

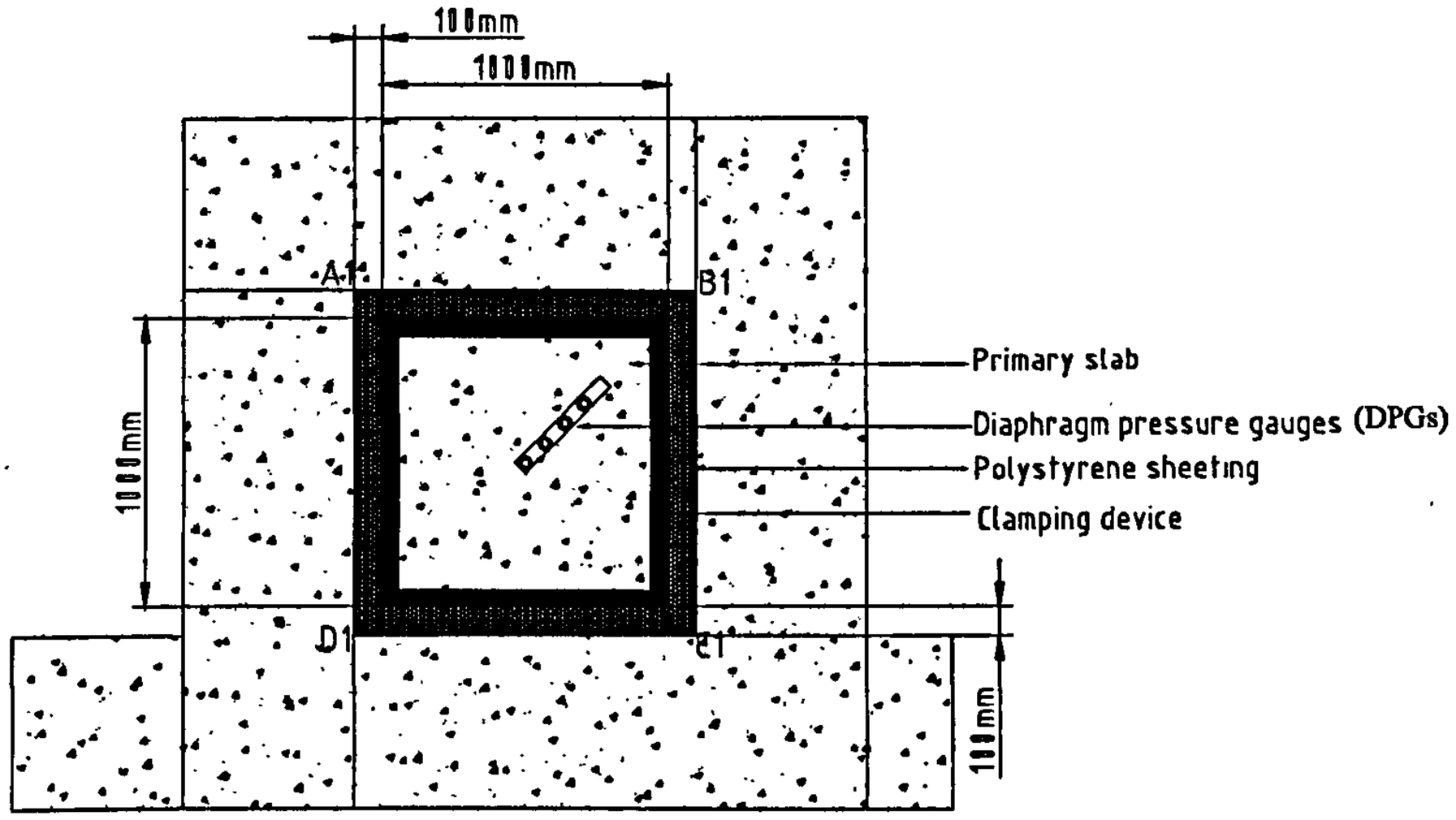

Figure 3.1.3 Plan elevation of a concrete test set up within the test cell with the DPGs positioned along the plane of greatest load

During the steel and concrete tests, LVDTs and DPGs served the purpose of measuring the following:

1. Linear variable differential transducers (LVDTs) – three in total were used, $LVDT_{0mm}$, $LVDT_{125mm}$ and $LVDT_{250mm}$ that measured deflection-time histories at locations 0, 125mm and 250mm radially from the centre of the slab.
2. Diaphragm pressure gauges (DPGs) – four in total were used. The central DPG and $LVDT_{0mm}$, were positioned within the same vertical plane during most tests. The other DPGs were positioned at eccentricities from the centre.
3. Strain gauges (SGs) – These were used during the concrete tests. Four in total were used. Two were attached to the central rebar in the top and two in the bottom reinforcement mesh. Two strain gauges connected in series would output a strain-time response that would neglect bending.

3.1.1 Reasons for performing small-scale tests

The experimental work described in this chapter involved small-scale testing. It was intended to reproduce small-scale tests of full size tests, which was of interest to the project sponsor. Whilst no full-scale tests have yet been conducted, and hence no data

at that scale available, care was taken to ensure that the experimental work conducted in this project was at a specific scale factor of the full-scale arrangement.
It is very expensive and in most cases impractical to carry out explosive testing at full scale. At smaller scales, more tests can be performed at a faster rate with fewer health and safety problems.

3.2 Design and construction of the test cell

The explosive tests were all performed within a test cell, built from reinforced concrete pendine blocks. The test cell sustained the following characteristics:

1. Sufficient integrity and strength to cope with the large transient loads that would occur within the internal space of the test cell.
2. Rapid construction and dismantling of the cell.

3.2.1 Geometric arrangement of the test cell

The test cell had to be modular as illustrated in figure 3.2.1, so that it could be assembled and disassembled quickly, and strong enough to cope with the large transient loads. The walls were built up using the pendine blocks, forming an internal space, with enough room to contain the steel test frame. Sand was then poured into the internal space of the test cell, initially carried by a steel plate but then by a primary reinforced concrete slab during the concrete tests.

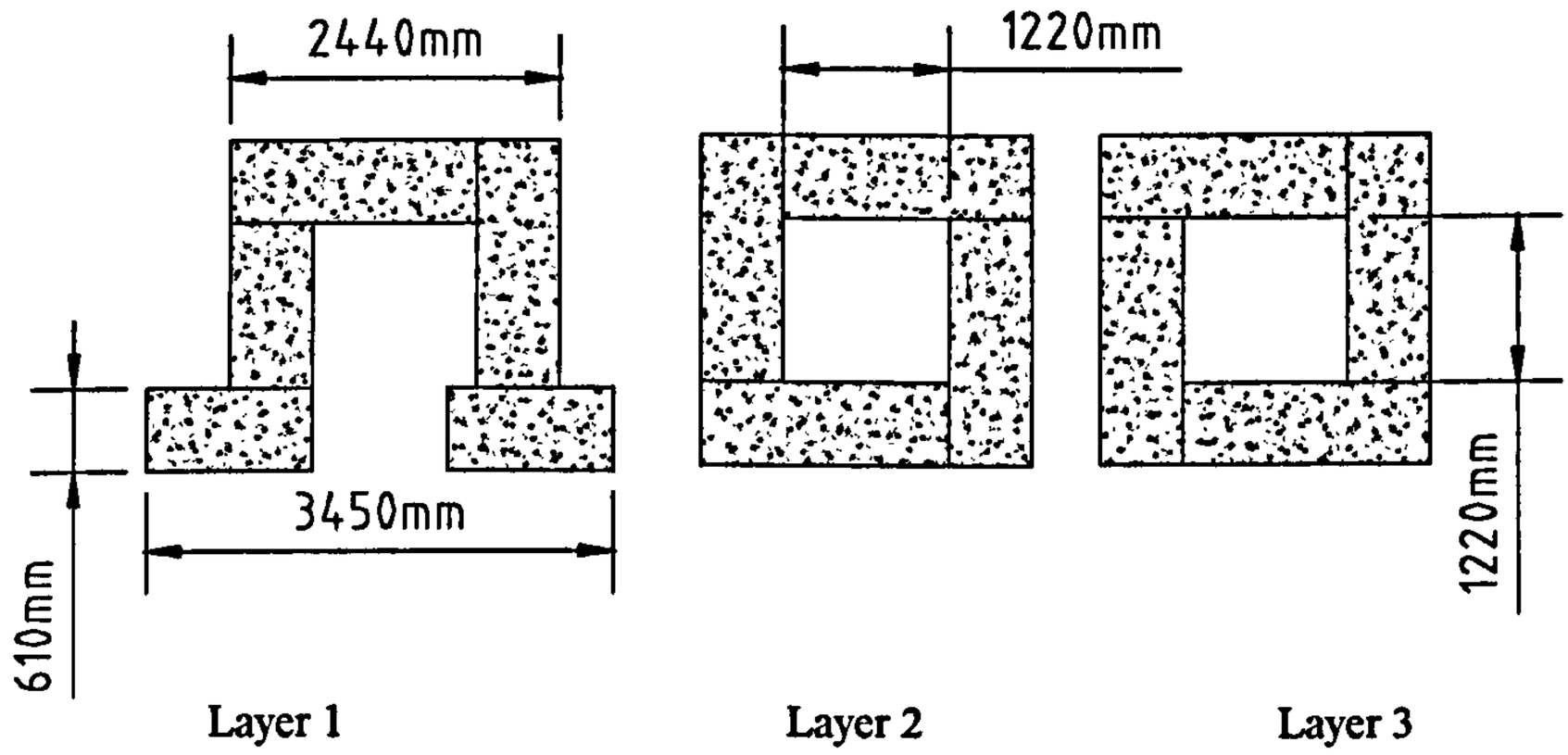

Figure 3.2.1 Plan view of the three layers used to form the small-scale test cell

Rectangular hollow sections were cast into the blocks, as illustrated in plate 3.2.1, so they could be transported to site using a forklift truck. This allowed the test cell to be dismantled and constructed promptly.

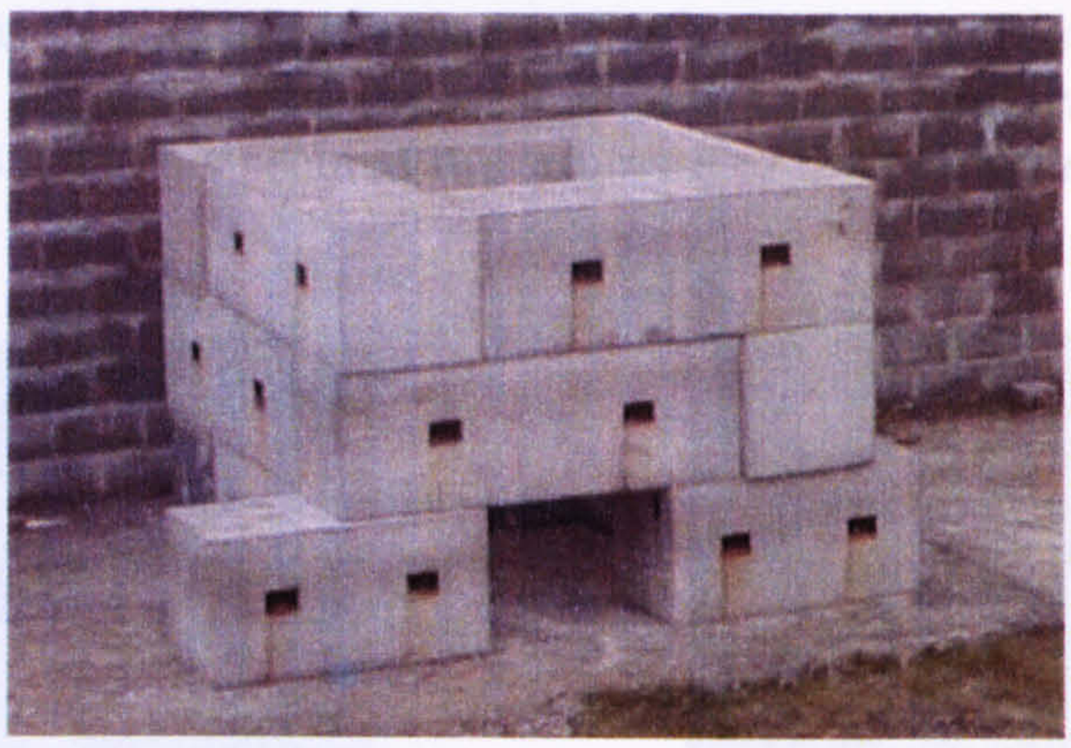

Plate 3.2.1 Assembled test cell

3.2.2 Polystyrene lining

Findings from **Hanssen *et al* (2002), Bull & Woodford (2000)** and **Davies & Williams (1992)** suggested that polystyrene is an effective energy-absorbing medium. The literature suggested that polystyrene would reduce reflection from the internal sides of the test cell, which could have influenced the final damage to the slabs.
Due to project time restraints, the energy absorbing capabilities of the polystyrene were not researched, leaving scope for further work in assessing materials that either eradicate or reduce the reflective stress waves.
Polystyrene sheeting also served in filling the gap between the internal perimeter of the test cell and the perimeter of the primary slab. This ensured that the soil overburden was supported over the entire plan area of the primary slab.

3.2.3 Design of the steel support structure

A steel test frame illustrated in plate 3.2.2 supported the primary reinforced concrete slab. The structure was constructed from angle sections, which were welded together. It was then painted white to prevent the steel from rusting, whilst remaining stationary in the harsh outdoor environment.

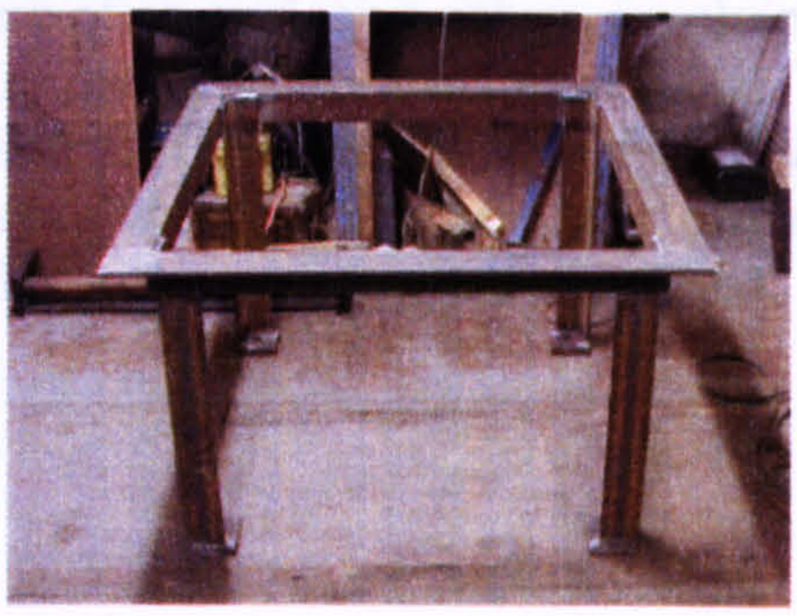

Plate 3.2.2 Steel support frame

The top frame section consisted of four welded angle sections of size 80x80x12mm and four leg sections of size 80x80x10mm. The legs were positioned on welded base plates, individually clamped into the ground, by a lever-arm clamping system, as illustrated in plate 3.2.3. This secured the structure to the ground during the explosive tests.

Base plate Clamping system

Plate 3.2.3 Securing the legs of the support structure to the ground

3.3 Experimental test matrix

The test matrix was segregated into steel and concrete tests. The steel tests were considered as preliminary tests, prior to the concrete tests. They were performed for two reasons:

1. Understanding the response of the instrumentation prior to the concrete tests.
2. Characterising the response of a primary steel plate subjected to groundshock loading.

The concrete tests dominated the test matrix. They were performed for two reasons:

1. Characterising the response of a primary reinforced concrete slab subjected to groundshock.
2. Identifying the parameters that influenced the magnitude of groundshock loading within a complex subsurface arrangement and hence the damage mechanisms upon the slabs.

All the tests performed were of an explosive nature, involving a mass of PE4, moulded into a cylindrical geometry as illustrated in figure 3.3.1. The mass of charge used during the steel tests was 94g as it was important that the response of the primary plate remained elastic. The mass of charge used during the concrete tests was 183g, as the damage to the primary and secondary slabs were of interest.

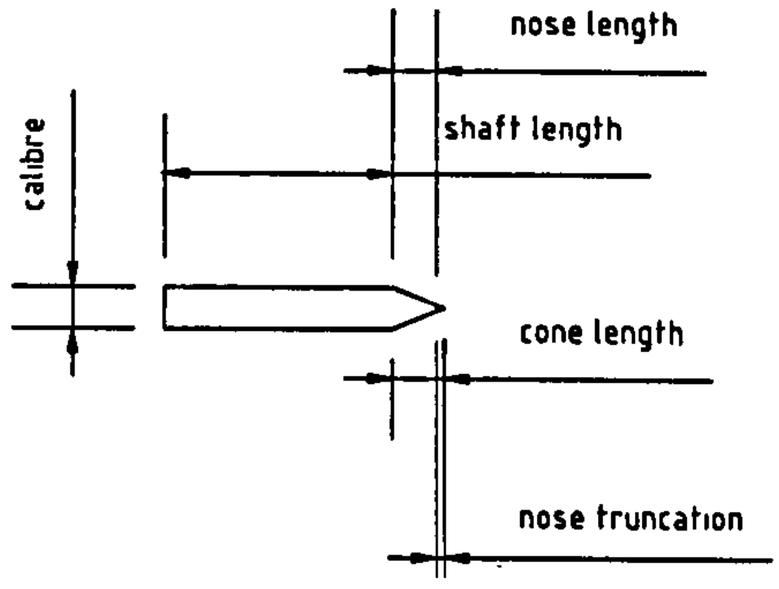

Figure 3.3.1Cylindrical charge

3.3.1 Steel tests

Only four explosive tests were performed on the same primary steel plate using a cylindrically shaped charge.

3.3.2 Test matrix for the steel tests

The characteristics of the four steel tests performed are illustrated in table 3.3.1.

Table 3.3.1 Steel test matrix

T_n	S_r (mm)	Z_3 (mm)	W (g)	θ	t_{rp} (mm)
ST1	600	1000	94	90°	10
ST2	500	1000	94	90°	10
ST3	300	1000	94	90°	10
ST4	150	1000	94	90°	10

T_n = Test number
S_r = Charge standoff to the primary steel plate
Z_3 = Total soil overburden above the primary plate
W = Charge mass
t_{rp} = Thickness of the primary plate
θ = Charge orientation to the horizontal

3.3.3 Concrete tests - Stage I

Stage I consisted of 13 tests, RCIT1-13, that were segregated into four groups of tests. Each group of tests involved a single primary slab that was subjected to cumulative loading, whilst a fresh secondary slab was implemented in every test. Within each group of tests, the following was considered:

1. The charge position relative to the secondary slab varied.
2. The soil overburden contained between the primary and secondary slab remained constant.

The soil overburden above the secondary slab remained constant during Stage I, whilst the following were investigated:

1. The response of a primary slab subjected to groundshock.
2. The relationship between cumulative loading and magnitude of damage encountered by the primary slabs.
3. Identification of failure mechanisms on both the primary and secondary slabs.

3.3.4 Charge positioning

The plan of a secondary slab is illustrated in figure 3.3.2 with reference points around its perimeter that differentiated the top from the bottom face of a slab.

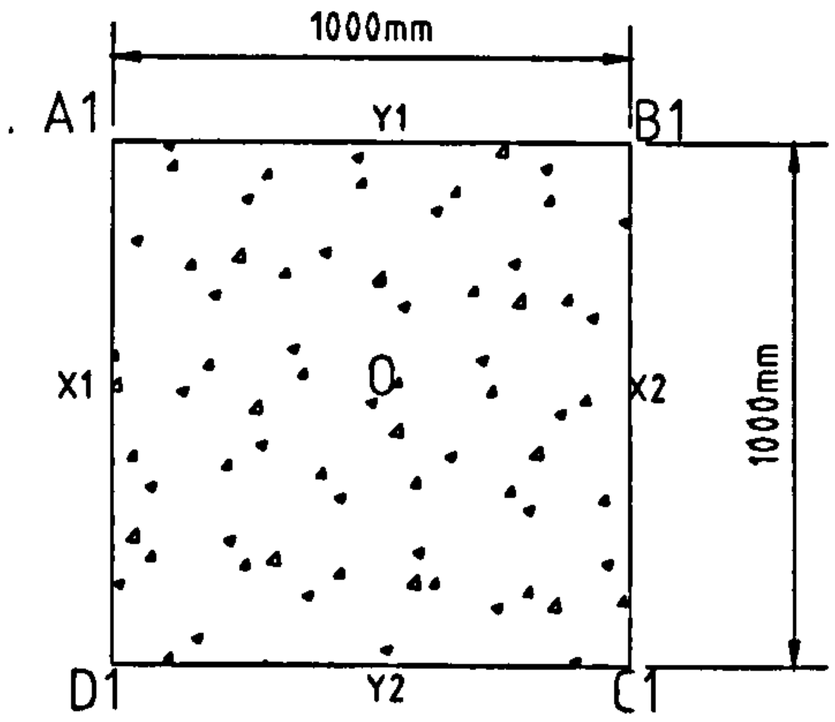

Figure 3.3.2 Plan of the top face of a secondary slab

The cylindrical charges were positioned at an inclination of 70° to the horizontal, at point O in figure 3.3.2 along the diagonal plane D1-B1. The geometry of the four charge positions relative to a secondary slab, are illustrated in figure 3.3.3. **Renick (2000)** considered the damage mechanisms that were employed when a charge was detonated within an air/concrete/soil experimental set-up. The position of the charge relative to two different layers described in figure 2.9.3 was similar to the configuration identified by charge position C in figure 3.3.3 where it was positioned in the soil and concrete mediums. The only variation was that there was a significant amount of soil overburden above the secondary slab that was not present in the experimental setup described by **Renick (2000).** The damage mechanisms associated with charge position C have been equated to a number of those observed by **Renick (2000),** discussed in section 4.5.2.

The coupling factor discussed in section 2.6.3 was not calculated for each of the four charge positions. However, the varying charge positions were associated with damage mechanisms observed on the top and bottom faces of the secondary slabs.

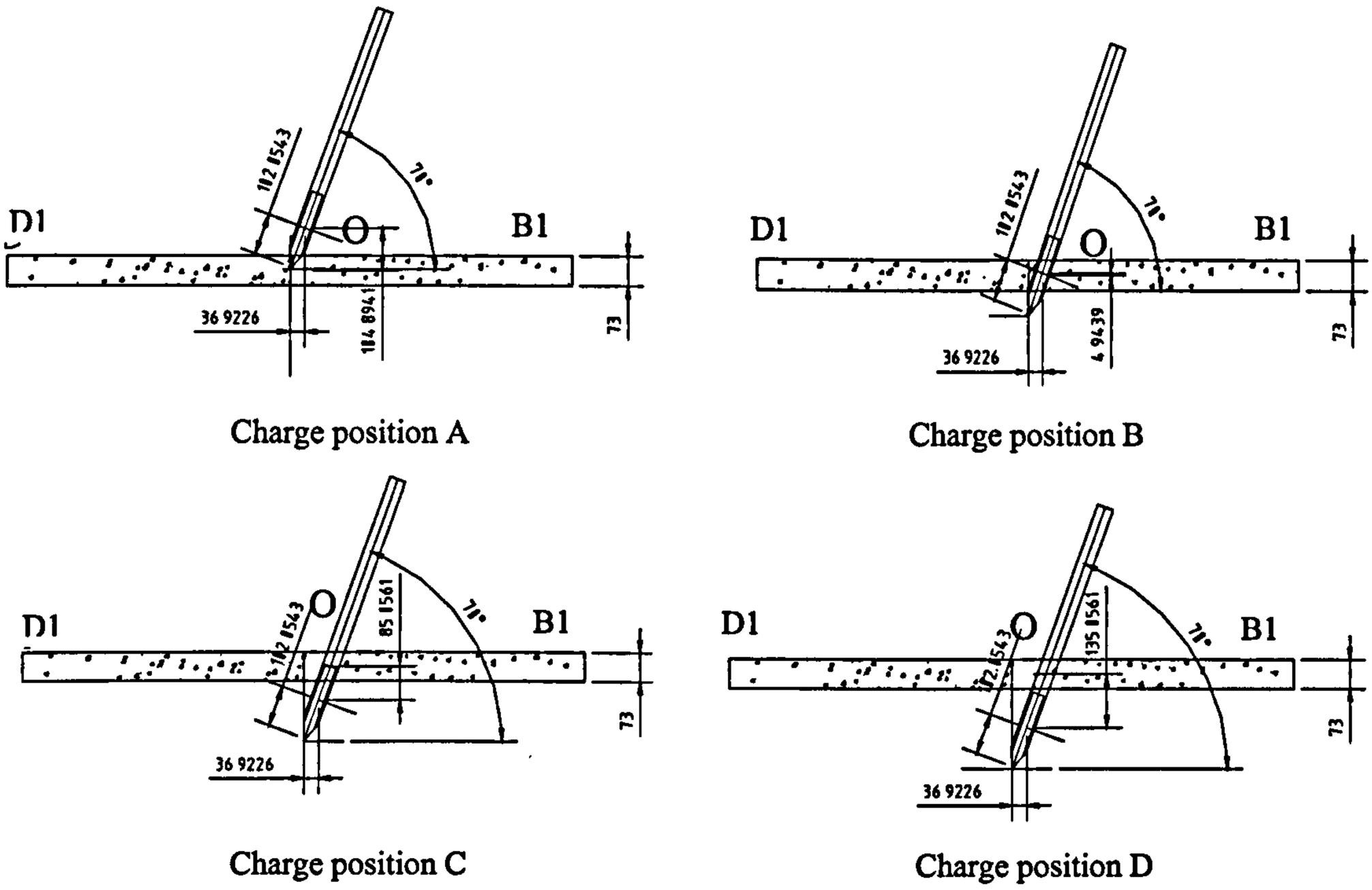

Figure 3.3.3 four charge positions used relative to the secondary slab along diagonal D1-B1

The charge standoff was defined as the vertical distance between the virtual tip of the charge and the top face of the primary slab that varied through out the tests. Its vertical plane remained constant, as it passed through the centre of mass of the primary slab, as illustrated by figure 3.3.4.

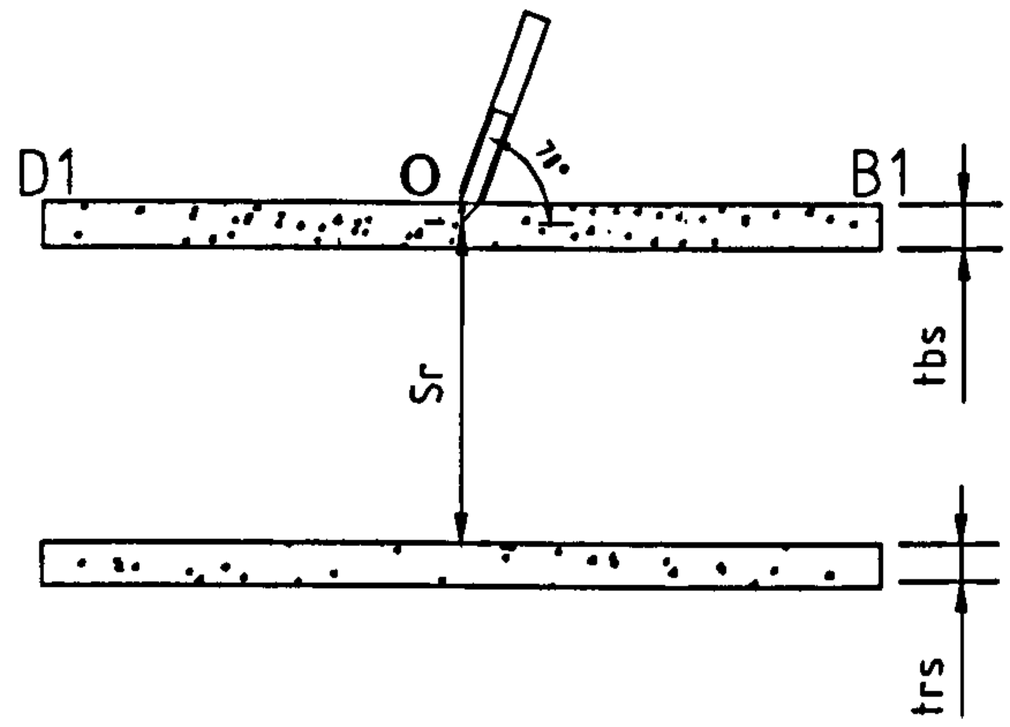

Figure 3.3.4 Charge standoff

Sr=Charge standoff
D1-B1 = Diagonal plane in which the charge was positioned.
t_{rs} = Thickness of the primary reinforced concrete slab.
t_{bs} =Thickness of the secondary reinforced concrete slab.

The four charge positions implemented varied according to the proportion of their mass within the thickness of the secondary slab. A hole was artificially drilled through the secondary slab at an inclination of 70° to the horizontal, at an eccentricity from the centre of the slab along plane O-B1. The horizontal distance X_{cv} between the centre of

mass of the charge and the vertical plane that passed through the centre of mass of the secondary slab remained constant for every charge position. However, the vertical distance between the centre of masses of the charge and the secondary slab varied, defining a charge position, as illustrated in table 3.3.2.

Table 3.3.2 Charge positions relative to the secondary slab

Tests	C_p	Y_{cc} (mm)	X_{cv} (mm)
1	A	105	37
2	B	5	37
3	C	-85	37
4	D	-135	37

C_p = Charge position
Y_{cc} = Vertical distance between the centre of mass of the charge and the secondary slab
X_{cv} = Horizontal distance between the centre of mass of the charge and the secondary slab

Positive values of Y_{cc} implied that the centre of mass of charge was above the centre of mass of the secondary slab and negative values implied the opposite.

3.3.5 Concrete tests - Stage II

Stage II consisted of 3 tests RCIT14-16. The depth of soil overburden above the secondary slab varied, whilst the soil overburden between the primary and secondary slab remained constant as well as the charge position. The objective was to establish whether a reduction in the soil overburden above the secondary slab influenced the damage as well as the loading across the primary slab.

3.3.6 Concrete tests - Stage III

Stage III consisted of 3 tests, RCIT17-19. Secondary slabs were omitted from the soil environment. The objective was to establish the degree of weakening subjected to a primary slab from cumulative loading. The results from tests RCIT9-11 involving positioned secondary slabs were used in collaboration with the results from tests RCIT17-19.

3.3.7 Test matrix for the concrete tests

The test matrix described the tests that were performed within each of the three stages, as illustrated in tables 3.3.3, 3.3.4 and 3.3.5. It is evident from the experimental stages in tables 3.3.3 and 3.3.5 that the ratio of standoff to effective span of the primary slab was always less than 1.0, defining the loading environment as near field in accordance with **Tyas & Pope (2004)**.

Table 3.3.3 Stage I

T_n	G_n	S_{bb} (mm)	S_{tb} (mm)	S_r (mm)	Z_1 (mm)	Z_2 (mm)	W (g)	θ	t_{bs} (mm)	t_{rs} (mm)	Sr/Le	C_p
1	1	-40	33	540	500	500	183	70°	73	73	0.6	A
2	1	60	133	440	500	500	183	70°	73	73	0.5	B
3	1	150	223	350	500	500	183	70°	73	73	0.4	C
4	1	200	273	300	500	500	183	70°	73	73	0.3	D
5	2	-40	33	340	300	500	183	70°	73	73	0.4	A
6	2	60	133	240	300	500	183	70°	73	73	0.3	B
7	2	150	223	150	300	500	183	70°	73	73	0.2	C
8	2	200	273	100	300	500	183	70°	73	73	0.1	D
9	3	-40	33	190	150	500	183	70°	73	73	0.2	A
10	3	60	133	90	150	500	183	70°	73	73	0.1	B
11	3	150	223	0	150	500	183	70°	73	73	0	C
12	4	-40	33	113	75	500	183	70°	73	73	0.1	A
13	4	60	133	13	75	500	183	70°	73	73	0.01	B

T_n = Test number
G_n = Group number
S_{bb} = Charge standoff to the bottom face of the secondary slab
S_{tb} = Charge standoff to the top face of the secondary slab
S_r = Charge standoff to the primary slab
Z_1 = Soil overburden between the primary and secondary slab
Z_2 = Soil overburden above the secondary slab
W = Charge mass
t_{bs} = Thickness of the secondary slab
t_{rs} = Thickness of the primary slab
C_p = Charge position
θ = Charge orientation to the horizontal
L_e = Effective span of the slab
Sr/Le = Charge standoff to effective span ratio

Table 3.3.4 Stage II

T_n	G_n	S_{bb} (mm)	S_{tb} (mm)	S_r (mm)	Z_1 (mm)	Z_2 (mm)	W (g)	θ	t_{bs} (mm)	t_{rs} (mm)	Sr/Le	C_p
14	5	60	133	90	150	300	183	183	70°	73	0.1	B
15	5	60	133	90	150	150	183	183	70°	73	0.1	B
16	5	60	133	90	150	73	183	183	70°	73	0.1	B

Table 3.3.5 Stage III

T_n	G_n	S_r (mm)	Z_3 (mm)	W (g)	θ	Sr/Le	t_{rs} (mm)
17	6	190	723	183	70°	0.2	73
18	6	90	723	183	70°	0.1	73
19	6	0	723	183	70°	0	73

Z_3 = Total soil overburden above the primary slab without a positioned secondary slab

The objectives associated with the three stages of testing involved parameters that remained constant and varied, as illustrated in table 3.3.6.

Table 3.3.6 Constants and variables

Stages	Z_1	Z_2	Z_3	θ	t_{bs}	t_{rs}	S_r	C_p	W
1	V	C_1	-	C_1	C_1	C_1	V	V	C_1
2	C_1	V	-	C_1	C_1	C_1	C_1	C_1	C_1
3	-	-	C_1	C_1	-	C_1	V	-	C_1

C_p = Charge position
C_1= Constant parameter
V= Variable parameter
t_{bs} = Thickness of the secondary slab
t_{rs} = Thickness of the primary slab
W = Charge mass
Z_1 = Soil overburden between the primary and secondary slab
Z_2 = Soil overburden above the secondary slab
Z_3 = Total soil overburden above the primary slab without a positioned secondary slab
θ = Charge orientation to the horizontal

In each test primary and secondary slabs were given a description as indicated below:

Group description:
RCIT1-4
RC: reinforced concrete slab.
I: inclined charge.
T1-4 four tests performed.

Test description:
RCIT1
T1: test number one

Primary slab description:
RCR73IT1-4
R73: primary slab of thickness 73mm.
T1-4: primary slab subjected to four cumulative tests.

Secondary slab description:
RCB73IT1
B73: secondary slab of thickness 73mm

Both the primary and secondary slabs were identical in geometry for ease of fabrication. This allowed all the meshes to be constructed to one size. The only physical difference was that the primary slabs were cast with LVDT steel connectors, attached to a central bottom rebar. Both slabs were 73mm thick, reduced from a full-scale thickness. The implementation of fresh primary and secondary slabs used throughout the testing is illustrated in table 3.3.7.

Table 3.3.7 Group and test description

Test	Stage	Group number	Group	Test	Primary slab	Secondary slab
1	I	1	RCIT1-4	RCIT1	RCR73IT1-4	RCB73IT1
2	I	1		RCIT2		RCB73IT2
3	I	1		RCIT3		RCB73IT3
4	I	1		RCIT4		RCB73IT4
5	I	2	RCIT5-8	RCIT5	RCR73IT5-8	RCB73IT5
6	I	2		RCIT6		RCB73IT6
7	I	2		RCIT7		RCB73IT7
8	I	2		RCIT8		RCB73IT8
9	I	3	RCIT9-11	RCIT9	RCR73IT9-11	RCB73IT9
10	I	3		RCIT10		RCB73IT10
11	I	3		RCIT11		RCB73IT11
12	I	4	RCIT12-13	RCIT12	RCR73IT12-13	RCB73IT12
13	I	4		RCIT13		RCB73IT13
14	II		RCIT14-16	RCIT14	RCR73IT14-16	RCB73IT14
15	II			RCIT15		RCB73IT15
16	II			RCIT16		RCB73IT16
17	III		RCIT17-19	RCIT17	RCR73IT17-19	RCB73IT17
18	III			RCIT18		RCB73IT18
19	III			RCIT19		RCB73IT19

3.3.8 Severity of damage associated with cumulative loading

Cumulative loading, defined within the context of the experimental work, was associated with loading induced into the primary slab, caused by a series of detonated charges at variable charge standoff distances.

The final damage subjected to the primary slabs as illustrated in table 4.5.1 was considered as minimal, as a fresh secondary slab was positioned every time, a charge was detonated during the cumulative loading procedure. A fresh secondary slab would absorb a significant amount of the load prior to it being induced into an already damaged primary slab

The maximum damage would have been achieved if a single secondary slab remained in position as long as the primary slab did. This altered approach ensured the completeness of the test matrix, as well as the variability of the parameters considered.

In reality an underground structure would experience an attack from a number of airborne missiles. The secondary slab within the soil environment would also experience cumulative loading and be subjected to cumulative damage.

There was not enough time to assess the cumulative damage to a secondary slab, which would have caused a maximum damage to a primary slab. Instead, the failure mechanisms of a secondary slab were associated with the variation in charge position.

3.4 Design of the reinforced concrete slabs

Reinforced concrete slabs were used throughout the experimental programme. The slabs were defined as primary and secondary, each with different support conditions and subjected to different magnitudes of loading. They both acquired a plan area of 1000x1000mm and a depth of thickness of 73mm. The primary slabs were positioned on the top frame of the steel support structure, over a bearing support of 50mm with fully fixed boundary conditions and an effective length of 900mm. The secondary slabs were embedded within the soil overburden.

Design checks in accordance with **BS8110 (1997)** were made and stated as follow:

1. minimal percentage of steel reinforcement,
2. concrete cover.

3.4.1 Percentage and geometric arrangement of the reinforcement

The geometry of a slab, nominal amount of reinforcement and strength of the concrete was decided prior to the formulation of the test matrix. The slabs were not being designed to dissipate the loading. Instead, they were expected to receive degrees of damage according to **Duranovic (1994), Park (2000), Renick (2000)** and **Wood (1961)** in the form of the following:

1. cracking,
2. perforation,
3. cratering,
4. flexure.

It was decided to choose a nominal amount of reinforcement based on the design guidelines from **TM5-1300 (1991)** table 4.3 - Minimal area of flexural reinforcement for two way spanning slabs.
The aggregate of the steel area in the x and y-direction in the mesh equated to the minimal area, defined by equation (3.4.1)

$$A_s \geq 0.0015bd$$

Equation (3.4.1)

A_s = Minimal area of steel contained within the concrete filled slab
b = Breath of the section 1000mm
d = Depth of the section 73mm

Using equation (3.4.1), the area of reinforcement in the tension zone yielded $A_s \geq 0.0015.1000.73 = 109.5mm^2$. The minimal area of steel reinforcement associated with the cross-sectional area of a rebar could not be less than 109.5mm^2.

$$A_{bar} = \pi r_b^{\,2}$$

Equation (3.4.2)

A_{bar} = Cross-sectional area of bar
r_b = Radius of a bar

Using equation (3.4.2), $A_{bar} = \pi.(3)^2 = 28.279mm^2$. It was decided to construct a mesh size of 100x100x6mm, which could be scaled up linearly to 200x200x12mm if larger scale slabs were to be tested in the future. Based upon a mesh geometry of 100x100x6mm, the cross-sectional area of steel was calculated using equation (3.4.3).

$$A_{steel} = A_{bar} N_{bars}$$

Equation (3.4.3)

A_{steel} = Cross-sectional area of steel ($28.279mm^2$)

N_{bars} = Total number of bars used within the x and y-directions of the mesh (18), 9 bars in each direction.

Therefore,

$$A_{steel} = 509mm^2$$

Equation (3.4.4)

As $A_{steel} > A_s$ the minimal amount of steel requirement was satisfied.

$$S_{\%} = \frac{A_{steel}}{A_{slab}} x100\%$$

Equation (3.4.5)

$S_{\%}$ = Percentage of steel within a cross-sectional area of the slab

Therefore using equation (3.4.5), the percentage of steel reinforcement in a slab was 0.70%, with 0.35% of steel in both the x and y-direction. **BS8110 (1997)** presented a minimal and maximum percentage of steel as a percentage of the gross cross-sectional area of a section.

$$0.13\%bh \leq A_s \leq 4\%bh \text{ when } f_y = 460N/mm^2$$

Equation (3.4.6)

The percentage of steel within the reinforced concrete slab was 0.7%, satisfying the requirements of **BS8110 (1997).** As all the slabs were geometrically identical, their plan and cross-sectional elevations illustrated in figure 3.4.1 were similar. The nominal concrete cover was taken as 10mm, as suggested by **BS8110 (1997)** clause 3.3.1.3 stating that '*the nominal cover should not be less than the nominal maximum size of the aggregate*' which had a maximum size of 5mm. Clause 3.12.11.1 also stated that '*the minimal horizontal distance between the bars should not be less than maximum size of the aggregate + 5mm*'.

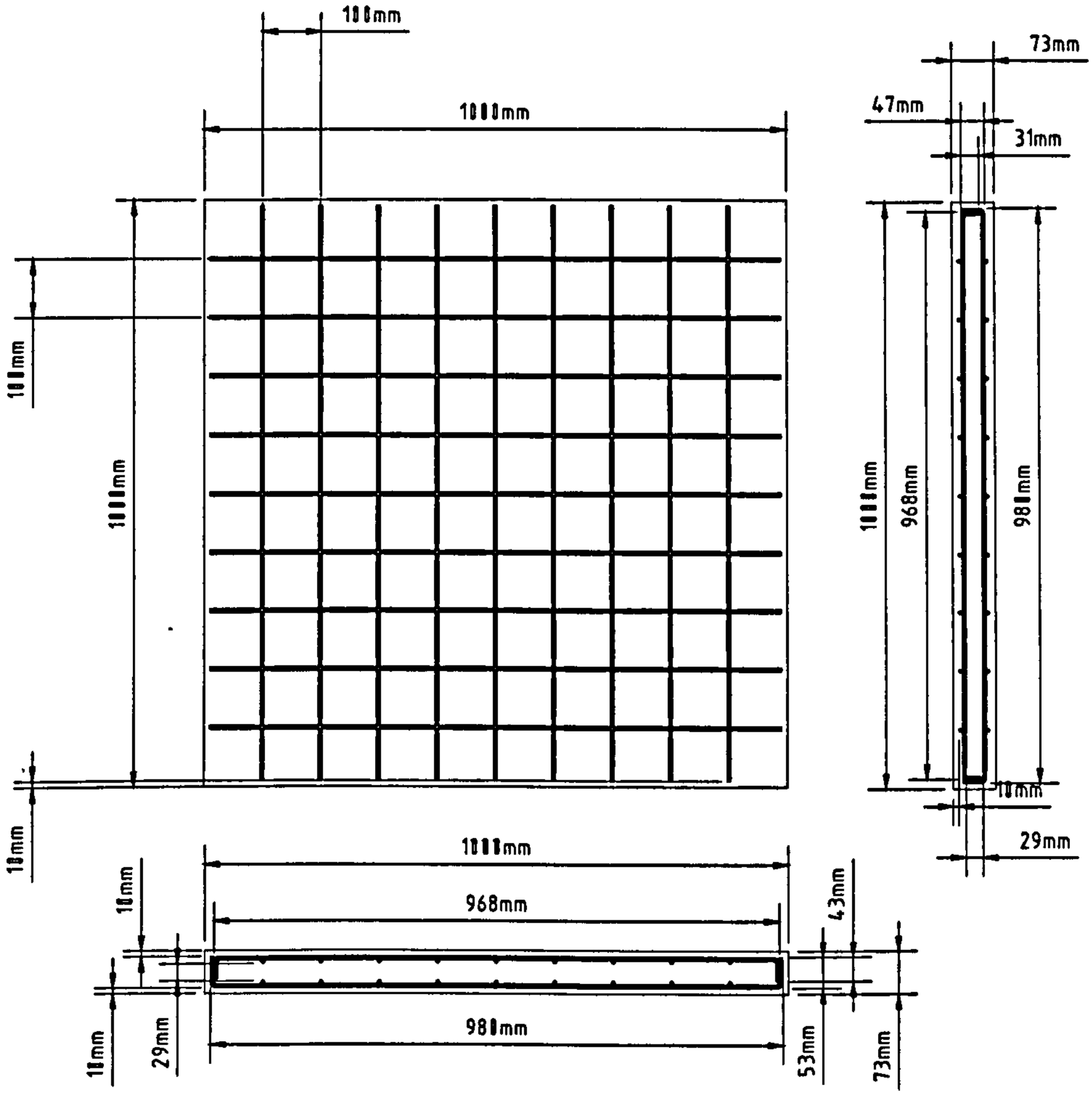

Figure 3.4.1 Plan and cross-sectional elevation of the reinforced concrete slab design

3.4.2 Construction of the steel reinforcement meshes

It was difficult to order pre-fabricated meshes already made, with dimensions of 100x100x6mm. High yield steel ribbed bars were bought in 6m lengths. The bars were cut into much smaller lengths, which were bent to 90° at either end, as illustrated in plate 3.4.1.

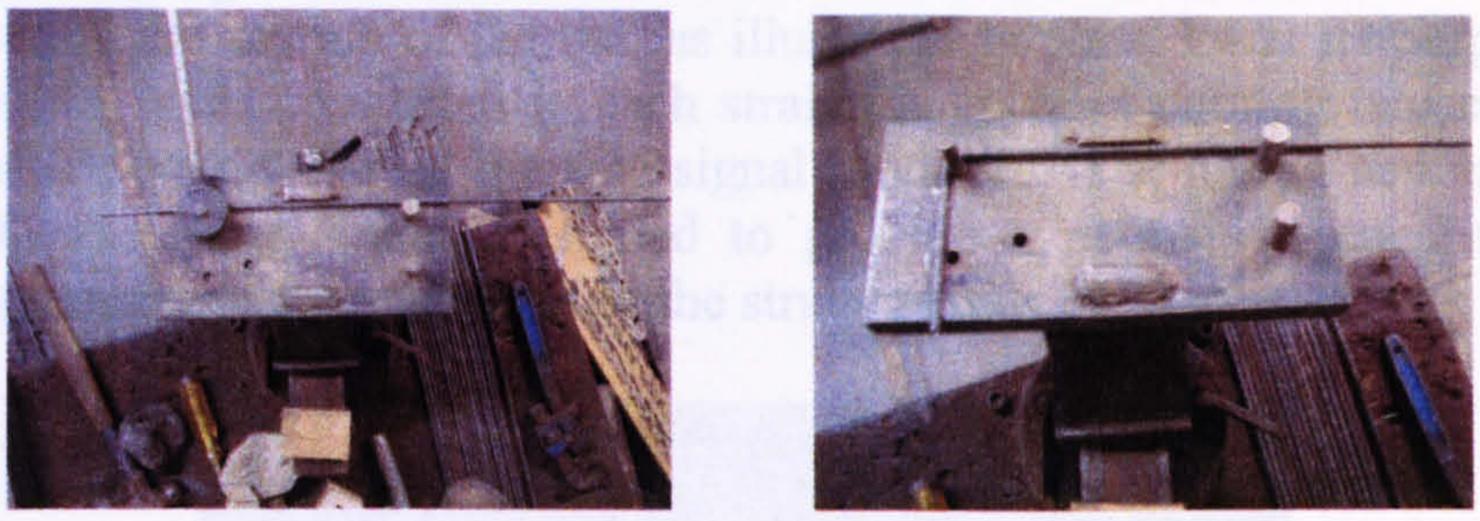

Plate 3.4.1 Bending the steel rebars

Four specific lengths of bar were cut. Two sizes were used to form the top and bottom mesh. Each mesh was independently constructed, by tying the orthogonal positioned bars with wire. The mesh was constructed on a wooden jig, illustrated in plate 3.4.2. It served as a template for the mesh, allowing the bars to fit into the wooden carved wedges during the wiring of all the single bars.

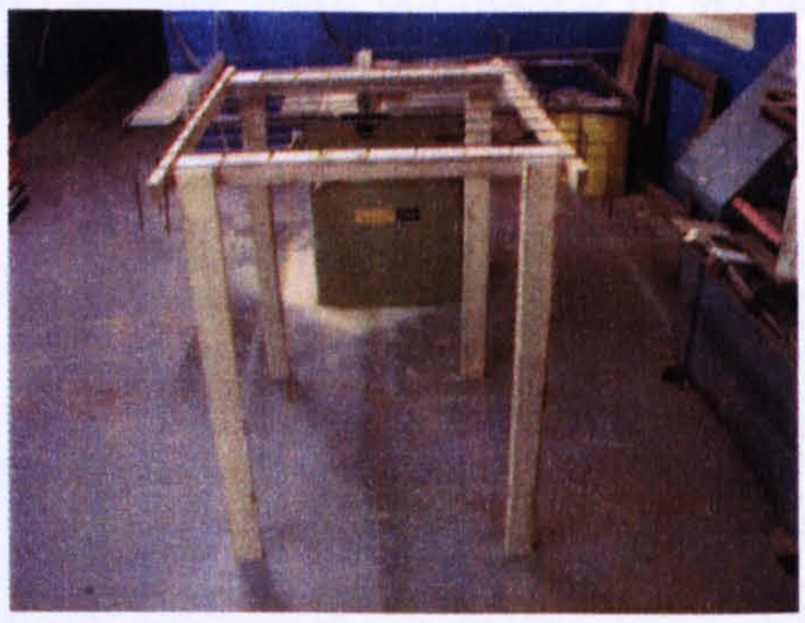

Plate 3.4.2 Positioning the steel bars onto the wooden jig

Complete top and bottom meshes were then wired together to form a mesh cage. Each cage was then positioned into a concrete slab mould, ready for casting.

3.4.3 Positioning the strain gauges on the rebars

Two strain gauges were attached to a single central rebar in either the top or the bottom mesh. Top and bottom face strain gauge readings associated with the response of a central rebar, indicated the variation in tension rather then bending as indicated analytically in section 3.4.3.1.

Prior to attaching the strain gauges onto the bars, the following procedures were performed:

1. Section of the rebar designated for the strain gauge attachment was smoothed over.
2. Acetone was applied to the section of rebar allowing the strain gauges to adhere to it more effectively.
3. Cyano-Acrylate cement was then applied to the section of bar. It served as adhesive glue, attaching the strain gauges to the steel.

After the strain gauges were attached, semi-flexible heat shrinkable tubing was then wrapped around the section of the bar, as illustrated in plate 3.4.3. Its purpose was to prevent the two wires connected to each strain gauge from coming into contact with the steel, which would disrupt the true signal produced. The tubing had an integrally bonded adhesive inner lining, designed to provide a permanent encapsulation for protection against moisture getting into the strain gauges.

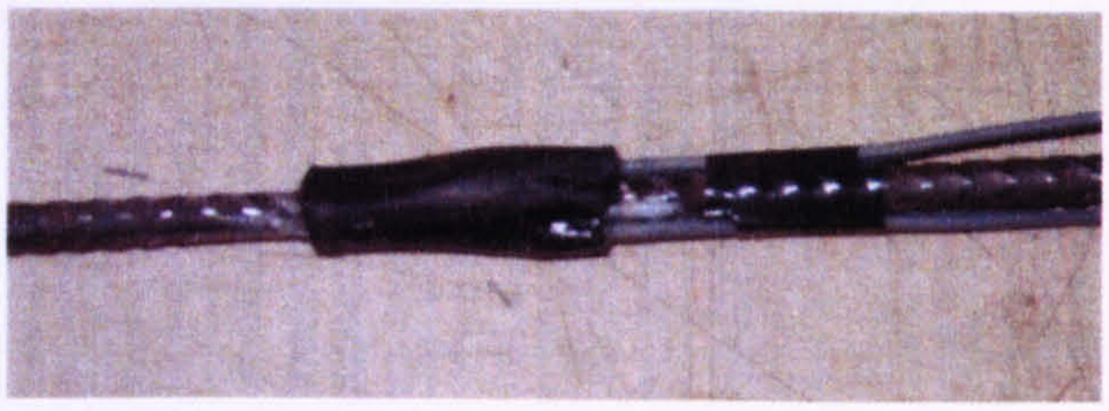

Plate 3.4.3 Connecting two strain gauges to a central rebar

A soldering iron was then used to attach the strain gauge wires to the wires within the flying cable. The two strain gauges were connected in series. Each strain gauge had a resistance of 120Ω, resulting in an overall resistance of 240Ω. The top and bottom rebars containing the strain gauges were then wired into the mesh design, as illustrated in plate 3.4.4.

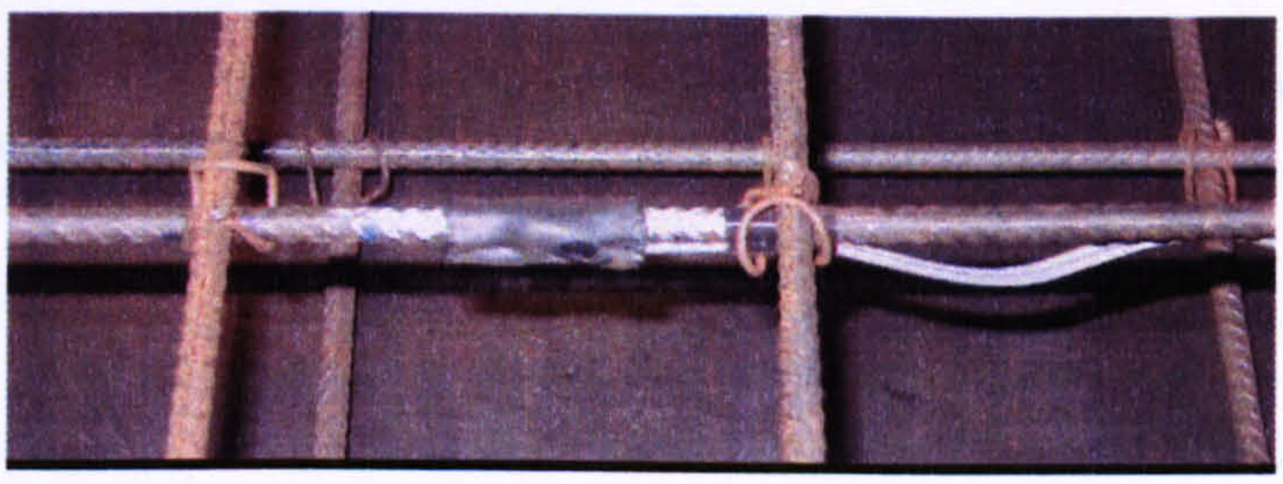

Plate 3.4.4 Strain gauges attached to the central bars in the lower and upper mesh

3.4.3.1 Analytical approach for eradicating bending

Two strain gauges on either side of a central steel rebar outputted strain-time histories that were associated with either compression or tension depending on the flexure response of the mesh cage. The circuit setup ensured that values of bending were eradicated. The analytical procedure that follows illustrates the removal of bending.

$$T_c = t + T_B \qquad \text{Equation (3.4.7)}$$

$$T_t = t - T_B \qquad \text{Equation (3.4.8)}$$

T_c= Strain in the compression face of the rebar
T_t= Strain in the tensile face of the rebar
t = Strain due to tension
T_B = Strain due to bending

Equating equation (3.4.7) and (3.4.8),

$$T_c + T_t = (t + T_B) + (t - T_B)$$

Equation (3.4.9)

$$T_c + T_t = 2t$$

Equation (3.4.10)

Re-arranged for t,

$$t = \frac{T_c + T_t}{2}$$

Equation (3.4.11)

$$t = \frac{\varepsilon_1 + \varepsilon_2}{2} = \frac{\varepsilon_0}{2}$$

Equation (3.4.12)

ε_0 = Single output strain from two strain gauges.

ε_1 = Strain measurement on the top face

ε_2 = Strain measurement on the bottom face

Each strain gauge outputted a voltage-time history, which was converted to an equivalent strain-time history with the use of a conversion factor.

$$\varepsilon_0 = \frac{e_0}{0.5K_s e_i} = 2\frac{e_0}{K_s e_i}$$

Equation (3.4.13)

e_0 = Output voltage

K_s = Strain gauge factor

ε_0 = Strain

e_i = Input voltage

3.4.4 Attaching the LVDTs

The LVDTs were attached to steel connectors, which in turn were attached to the central rebar in the bottom steel mesh of a slab, as illustrated in plate 3.4.5.
Connecting the LVDTs to the concrete would have weakened the area and increased the chance of scabbing during a test, causing instantaneous detachment of the LVDTs.

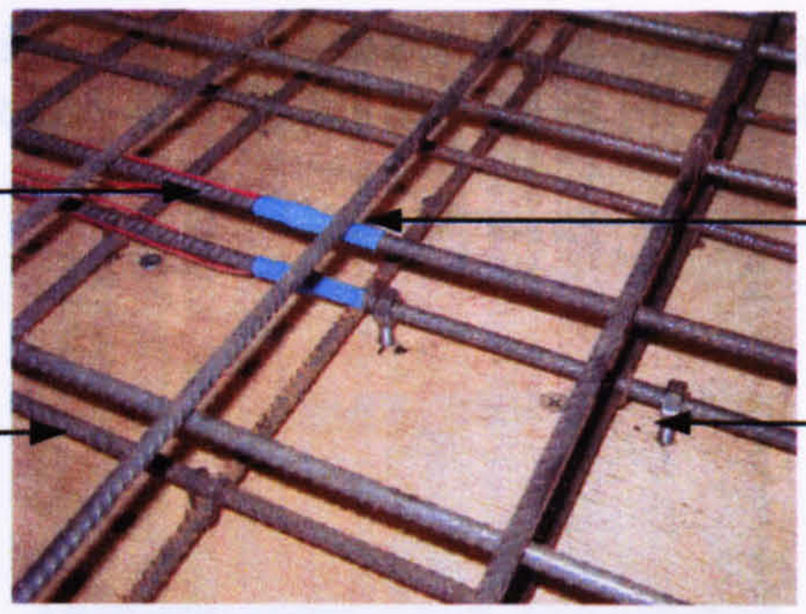

Plate 3.4.5 LVDT connectors

3.4.5 Casting of the slabs

3.4.5.1 Concrete mix design

The concrete mix design was based upon a mix used by **Duranovic (1994)**, who obtained final compressive strengths of 40N/mm^2. Rapid hardening Portland cement was used in order to gain an early compressive strength, reducing the curing time of the slabs. The mix design was based upon the mass of the constituents, rather than the volume, as illustrated in table 3.4.1.

Table 3.4.1 Mix design (Duranovic, 1994)

	Cement	Sand	Water
Mix design	1	3	0.6

3.4.5.2 Preparation of the moulds

Six moulds were used to cast the slabs. All the moulds were geometrically identical, with internal dimensions of 1000x1000x73mm. Prior to the casting, the moulds were all positioned on a horizontal floor and in some cases on brick supports, to achieve a flat base, as illustrated in plate 3.4.6. Each mould was internally and externally coated in brick oil. This prevented the concrete from forming a strong bond with the sides of the moulds and making the de-moulding operation an easier task.

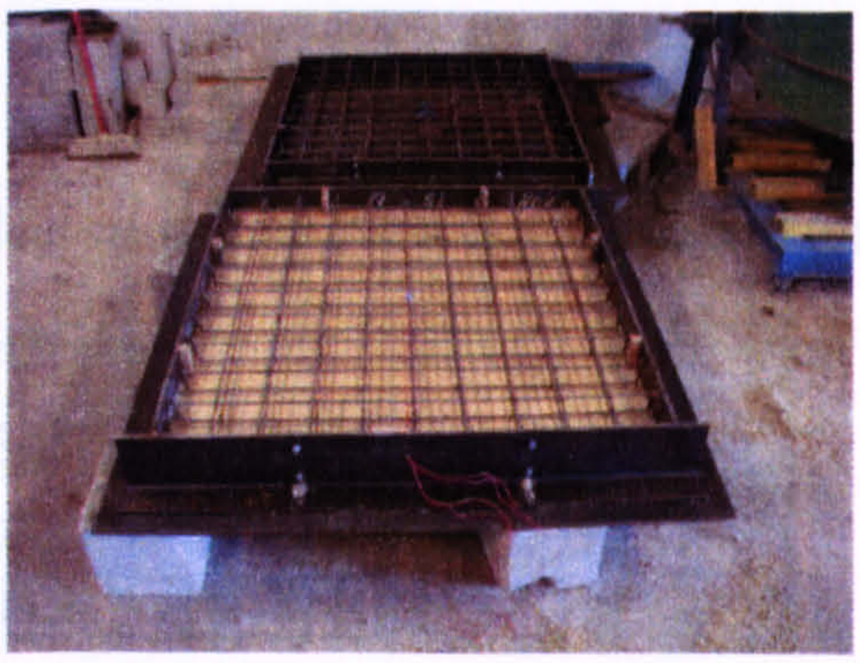

Plate 3.4.6 Mesh cage positioned within a mould

Prior to the casting operation, sufficient cover was achieved around the perimeter of the slabs by the use of wooden spacers, illustrated in plate 3.4.7.

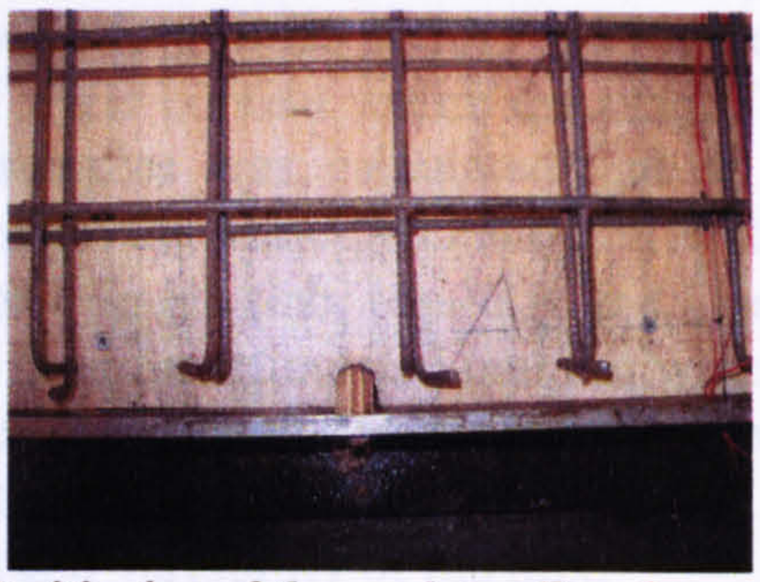

Plate 3.4.7 Positioning of the mesh to allow for concrete cover

Each of the moulds had holes drilled into their sides as illustrated in plate 3.4.8 so the flyer cables attached to the strain gauge wires could pass through them.

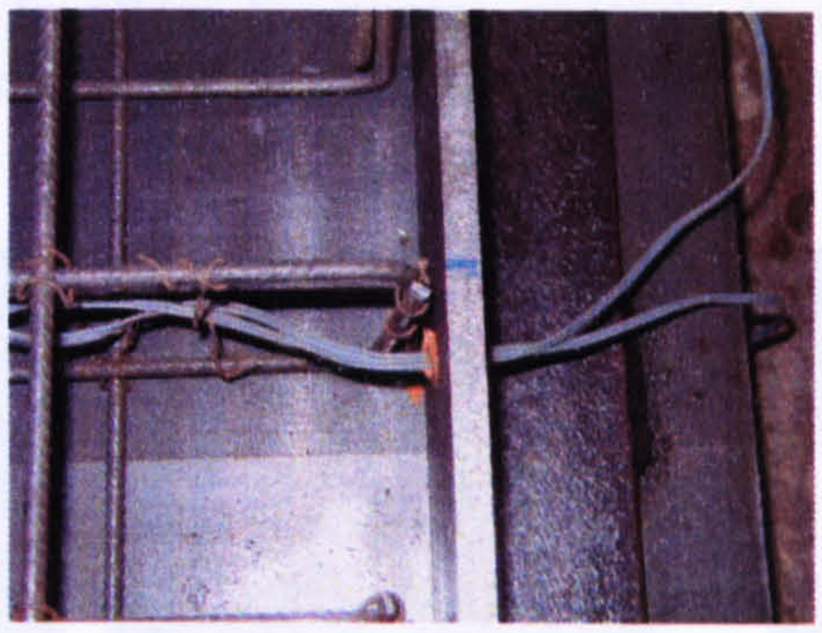

Plate 3.4.8 Flyer cables

3.4.5.3 Materials used in the casting operation

Prior to mixing the materials together to form the concrete, a number of calculations were made, as illustrated in table 3.4.2.

Table 3.4.2 Properties of the slab

Area	$1m^2$
Thickness	0.073mm
Volume	$0.073m^3$
Density	$2400kg/m^3$
Mass	175.2kg

The mass of each individual constituent was calculated and illustrated in table 3.4.3.

Table 3.4.3 Mass of the constituents

	Cement	Sand	Water
Parts	1	3	0.6
Ratio	1/4.6	3/4.6	0.6/4.6
Mass (kg)	38.1	114.26	22.85

The sand already contained a percentage of water that needed to be taken into account when calculating the amount of water needed to cast a single slab.

Two days prior to the casting operation, sand used for a casting was shovelled into large industrial buckets. Soil samples were taken from the buckets at various depths using containers. The masses of the containers were known, prior to sampling. The soil samples were oven dried according to **BS 1377-9 (1990)** Test 1(A), for the purpose of calculating a percentage of water content within the sand. The estimated water content within each of the four samples was calculated and an average value expressed. Assuming a linear relationship, the same percentage of water was applied to the mass of sand that was used to cast a single slab, resulting in an insitu mass of retained water. This amount was deducted from the calculated mass of water added to the mix.
Cubes and cylinders associated with the primary and secondary slabs were cast and crushed for a number of reasons:

1. to evaluate strength and variability of the mix,
2. to establish an average compressive and tensile strength for the primary and secondary slabs on the day of a test.

The total mass of the slab's constituents was increased by 15% as recommended by **Kong & Evans (1987)** to allow for excess concrete to be made into cubes and cylinders. The apparatuses illustrated in plate 3.4.9 were used to weigh and mix the constituents.

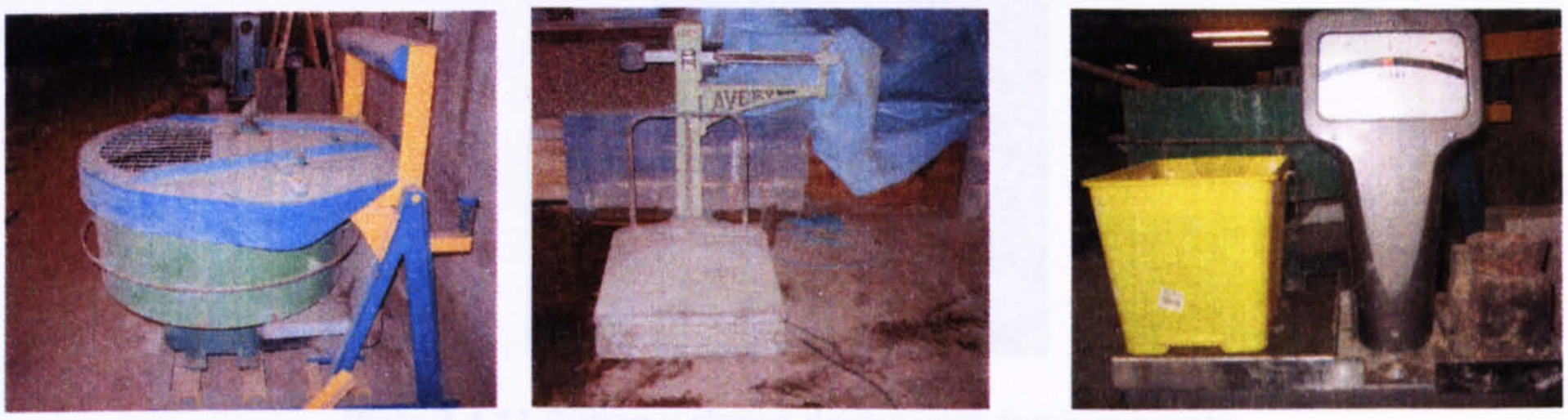

Pan mixer | Aggregate weighing scales | Water weighing scales

Plate 3.4.9 Mixing and measuring apparatuses used in casting

When all the constituents were considered as being fully mixed together, the concrete was cast into the moulds in two layers. Each layer was vibrated with the use of a vibrating poker, as illustrated in plate 3.4.10, until no air bubbles appeared on the concrete surface. Once a mould was filled with concrete that had been vibrated, a surface finish was applied by hand. The slabs, cylinders and cubes were then covered with polystyrene sheets and left for 24 hours, before being checked. During the next six days they were left under damp sacking and polystyrene sheeting in an attempt to prevent dehydration.

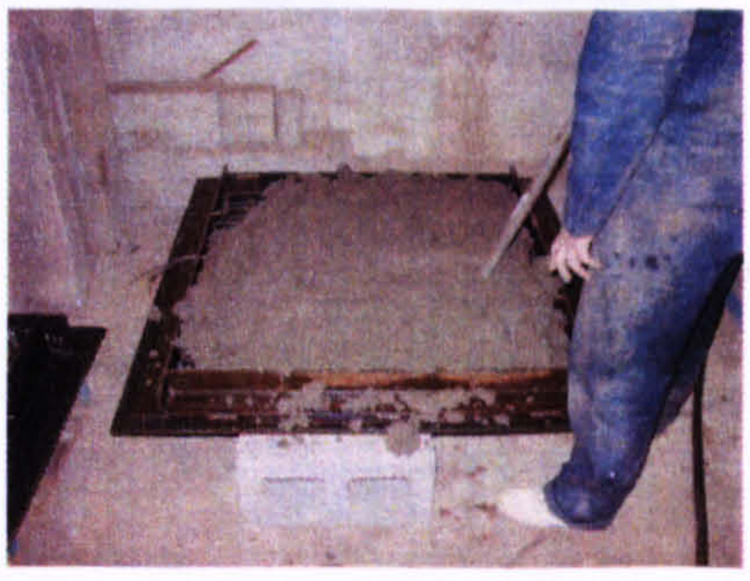

Plate 3.4.10 Vibrating the concrete

3.4.5.4 Slump test

During the casting process slump tests were performed in accordance with **British Cement Association (2000),** stating that the workability classes, S1–S3 are satisfactory for normal concrete. The experimental tests yielded an average slump of 70mm within a range of 52-81mm classing the concrete as S2 and having good workability.

Concrete was poured into the mould in three layers. Each stage occupied a 1/3 of the mould's volume. Within each stage, the volume of concrete was rodded 25 times, within its layer. The top surface of the concrete within the mould was then levelled off, leaving a horizontal surface of concrete, ready for the mould removal, as illustrated in plate 3.4.11.

Plate 3.4.11 Filling a slump devise with fresh concrete

The mould was then removed carefully and placed beside the slumped concrete and the rod positioned horizontally across the mould. The vertical distance between the slumped concrete and the horizontal rod was measured, as illustrated in plate 3.4.12.

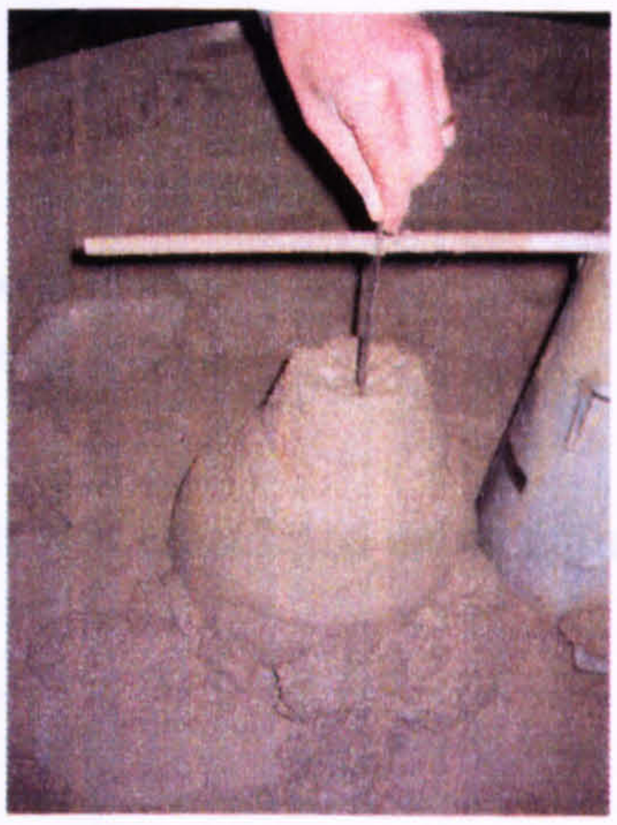

Plate 3.4.12 Slump test

3.4.6 Static testing

3.4.6.1 Crushing of concrete cubes and cylinders

Cubes of dimensions 100x100x100mm and 50x50x50mm were crushed as illustrated in plate 3.4.13, in accordance with **BS 1881 part 116 (1983).** Cylinders of dimensions 100x50mm were also crushed in accordance with **BS 1881 part 117 (1983).**

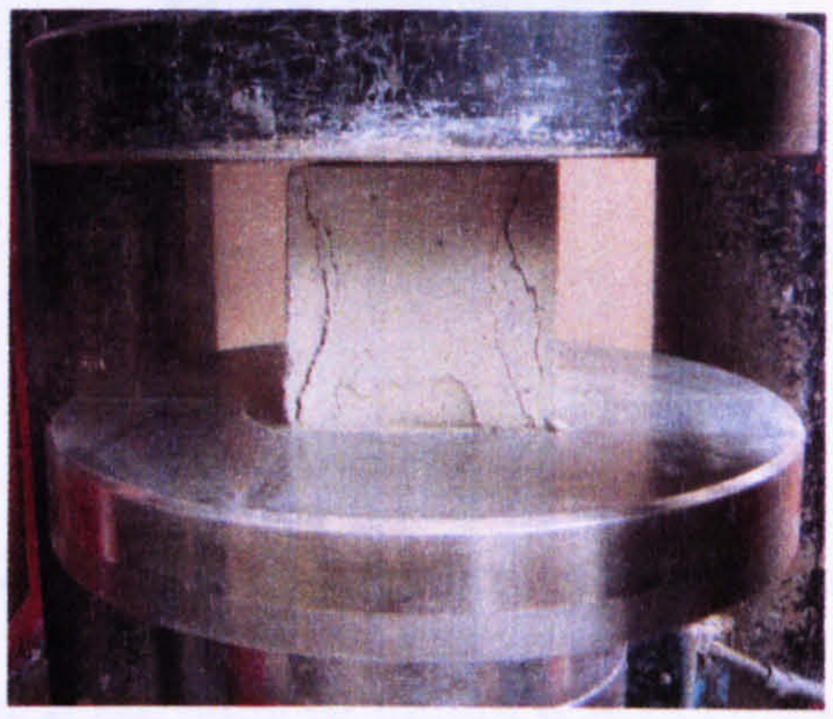

Plate 3.4.13 Crushing of concrete cubes

The rates of loading used on the samples are illustrated in table 3.4.4.

Table 3.4.4 Loading rates

Dimensions (mm)	Type of loading	Rate of loading (kN/mm/min)
100x100x100	Direct compressive test	150
50x50x50	Direct compressive test	37.5
100x50	Indirect tensile test	11.8

The cube compressive strength was calculated using equation (3.4.14):

$$\sigma_c = \frac{P}{A}$$

Equation (3.4.14)

σ_c = Compressive strength of a concrete cubes

P_c = Maximum load applied at the point of failure

A_c =Loaded area of a concrete cube

The cylindrical tensile strength was calculated using equation (3.4.15)

$$\sigma_h = \frac{2P}{\pi LD}$$

Equation (3.4.15)

σ_h = Horizontal tensile strength of a concrete cylinder

D = Diameter of a concrete cylinder

L = Length of a concrete cylinder

3.4.6.2 Tensile testing of a section of steel rebar

The ultimate tensile strength of the steel rebar was estimated from a static tensile test, illustrated in plate 3.4.14, in accordance with **BS 4449 (1997).**

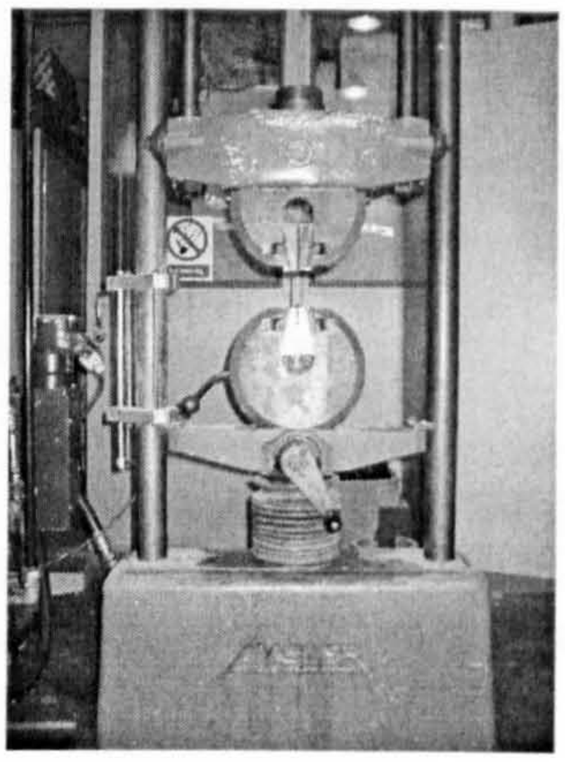

Plate 3.4.14 Static tensile test on a 6mm steel rebar

The ultimate tensile stress at the point of failure was calculated using equation (3.4.16).

$$\sigma_u = \frac{P_s}{A_l}$$

Equation (3.4.16)

σ_u =Ultimate tensile stress of high yield steel
P_s = Maximum tensile load of the steel rebar; (Failure occurred at = 7.1kN)
A_l = Cross-sectional area of the steel rebar at maximum load (Area under load = 12.56mm^2)

The ultimate tensile stress of a high yield steel bar used to form the reinforcement mesh was 565N/mm^2.

3.5 Calibration of the instrumentation

The LVDTs and DPGs were both initially calibrated prior to testing and then during the experimental program. The LVDTs were calibrated with relative ease. The DPGs were calibrated using a gas gun that was initially used by **Warren (2002).**

3.5.1 Calibration of the linear variable differential transducers

Each LVDT consisted of a thin steel rod, with a maximum travel length of 150mm that moved in and out of a magnetic steel core. The calibration process involved recording values of displacement, associated with length of extension of the steel rod that were associated with a voltage output. The steel rod was fully extended out from the magnetic core. The LVDT was then positioned horizontally on a flat surface next to a meter ruler with increments marked on it. As the steel rod was pushed into the magnetic core, values of voltage were recorded using a digital voltmeter connected to the transducer amplifier unit.

The maximum voltage output from an LVDT was 10v and would lie, in most cases, between a positive and a negative voltage integer, allowing the steel rod to move in and out of the core via an equilibrium position of 0v
Prior to every explosive test, the amplification was always checked and in some cases adjusted, so that an output of 0v would occur when 70mm of the steel rod's length was extended out of the magnetic core. This defined the vertical distance between the bottom face of the primary slab and LVDT support structure, when the LVDT was connected. During progressive tests the vertical distance decreased, as damage and residual deflection increased.

3.5.1.1 Establishing a linear conversion factor

As the steel rod was pushed into the magnetic core, the recorded voltages were negative, but positive when the rod was pulled out. Each LVDT with its associated transducer amplifier yielded a linear relationship linking voltage with deflection, defined by equation (3.5.1).

$$v_{lvdt} = M_1 x_1 + C_v$$

Equation (3.5.1)

v_{lvdt} = Voltage associated with the output from an LVDT

M_1 = Gradient of the line

x_1 = Voltages recorded on the horizontal axis

C_v = Intercept voltage

The voltage-displacement plot associated with the calibration of an LVDT is illustrated in figure 3.5.1. The displacement associated with the equivalent of 1v was calculated by initially knowing the voltage intercept value. Two simultaneous equations with voltage input values of 0v and 1v were setup to calculate the equivalent displacement values. The difference in the displacement values would be associated with the equivalent of 1v difference and defined as the linear conversion factor.

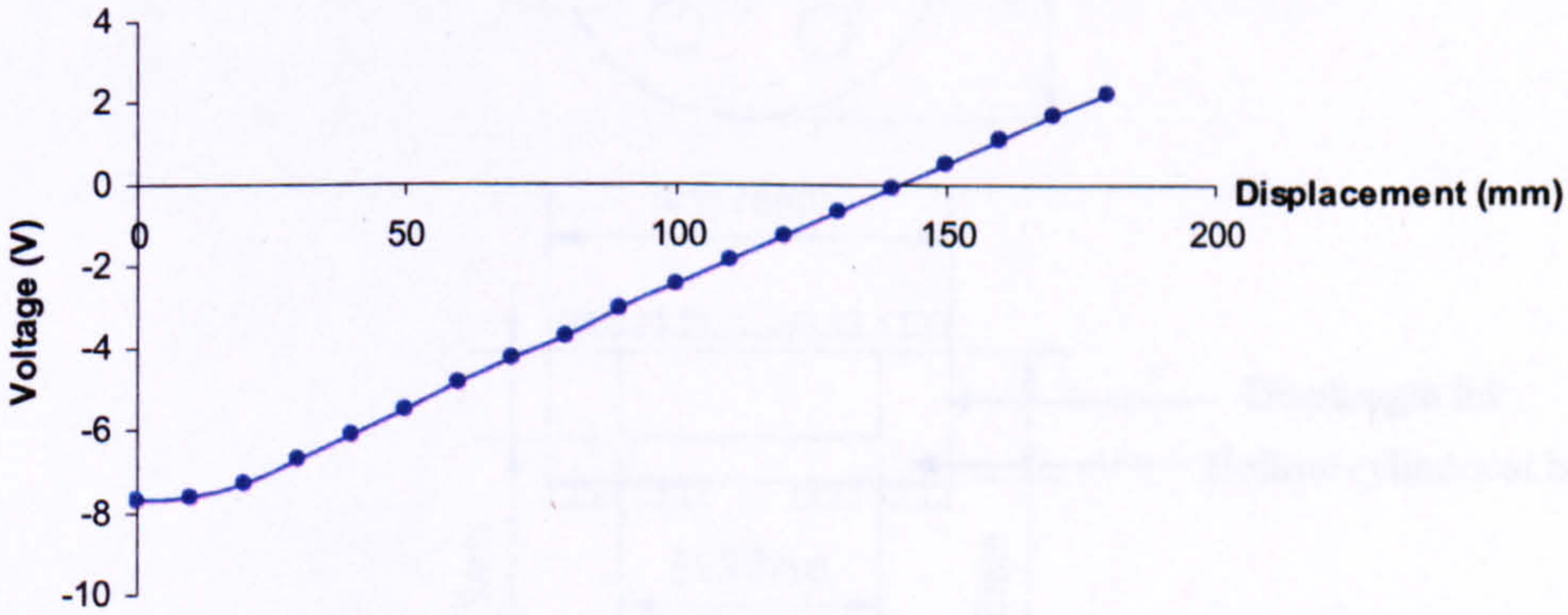

Figure 3.5.1Voltage-displacement calibration plot

It is evident from figure 3.5.1 that displacement values less than 20mm, associated within the voltage range –8v - -6.7v were non-linear.
The linear relationship was only valid within the range -6v – 2v. It is reasonable to state that a linear conversion factor could only be used within this range. Theoretically,

the relationship between rod displacement into the magnetic core and output voltage is linear, but in practice, as a result of errors in the instrumentation, the linear relationship over the entire range is not uniform. The experimental deflections of both the primary steel plate and primary reinforced concrete slab were all within the linear range. The non-linear relationship would have been taken into account if the steel rod travelled the last 20mm to full extension or compression within the core.

3.5.2 Calibration of the diaphragm pressure gauges

The gauges used by **Archer (1985)** were known as DPGs and used during the testing to measure pressure-time histories. The following describes their characteristics:

1. robust enough to function within the hostile environment,
2. strong enough to withstand impact forces from soil particles,
3. water proof,
4. promptly fixed if damaged without delaying the test programme.

Four DPGs were used during each explosive test. Each one had a different diaphragm lid thickness for the following reasons:

1. Thicker the lid – DPG positioned closer to the centre of the primary slab with less chance of it responding plastically.
2. Thinner the lid – DPG positioned at eccentricities from the centre of the primary slab. The eccentric positioning of the gauges was done by trial and error.

The geometry of a typical DPG is illustrated in figure 3.5.2.

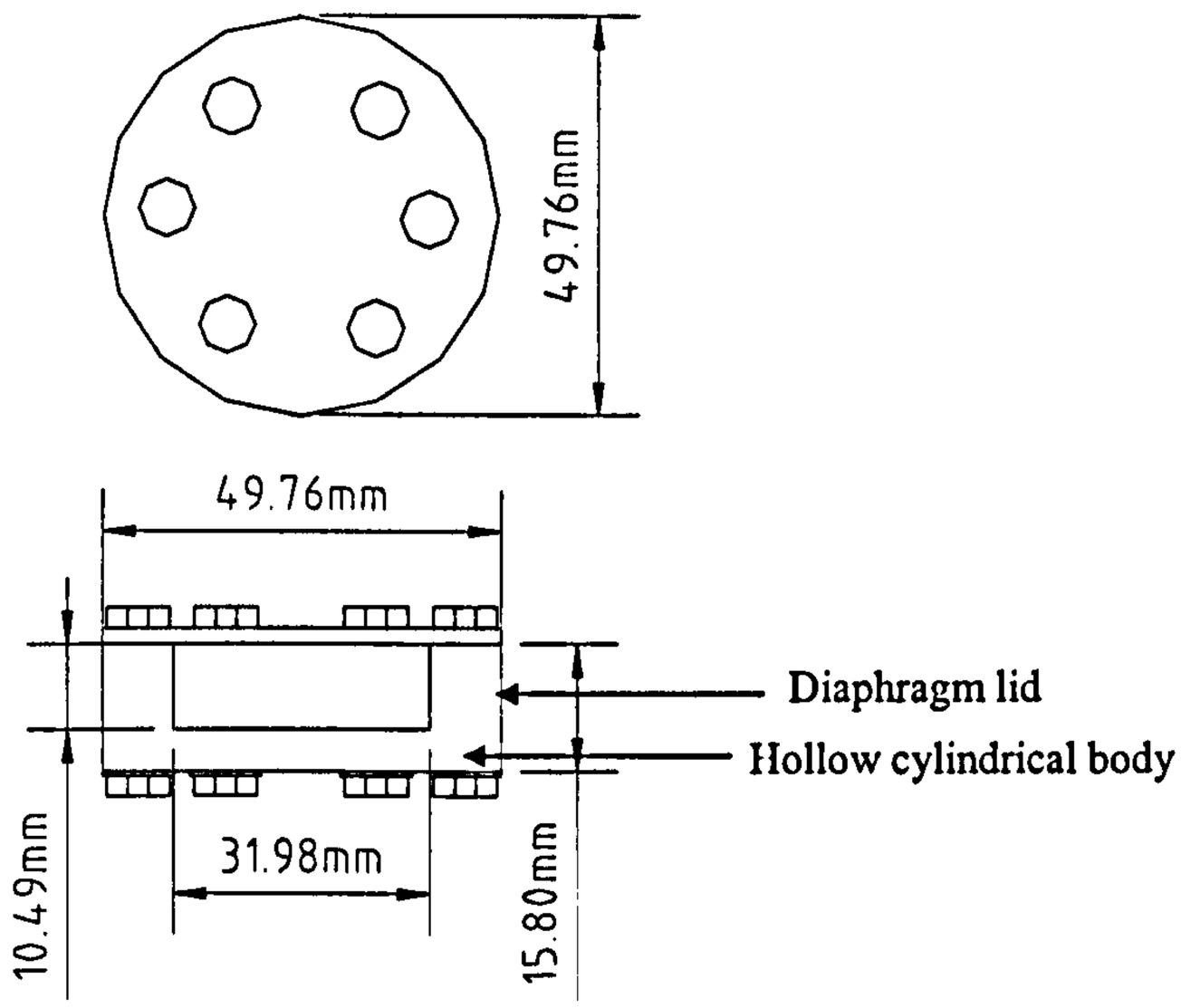

Figure 3.5.2 Plan and cross-sectional elevations of a DPG

The hollow cylindrical body was cut from a mild steel section. A hole was drilled into the sides of the body, connecting the strain gauge and resistor wires to a cable.

The circular diaphragm lid was cut out of a mild steel section. Sections were of varying thickness allowing different size circular lids to be cut.
The bottom face of the diaphragm lid was cleaned with acetone, to remove any impurities on the surface of the steel. A thin layer of cyano-acrylate glue was spread onto the cleaned surface and a strain gauge with a $120\,\Omega$ resistance was attached to it.
Once the glue had hardened, a lead wire was soldered to the strain gauge wires. The diaphragm lid was then bolted to the hollow cylindrical body, with five bolts positioned around the lid's circumference. The strain gauge was then connected into a wheatstone bridge setup.

3.5.2.1 Gas gun and calibration chamber design

A calibration chamber was designed that fitted onto the gas gun, initially used by **Warren (2002)**. A kulite pressure gauge HKM-375-5000 as illustrated in plate 3.5.1 was positioned within the gas gun and used to record the pressures that were released from the reservoir via the barrel of the gun. The kulite gauge had already been calibrated by the manufacturers, which yielded a calibration factor of (34 bar = 1v).

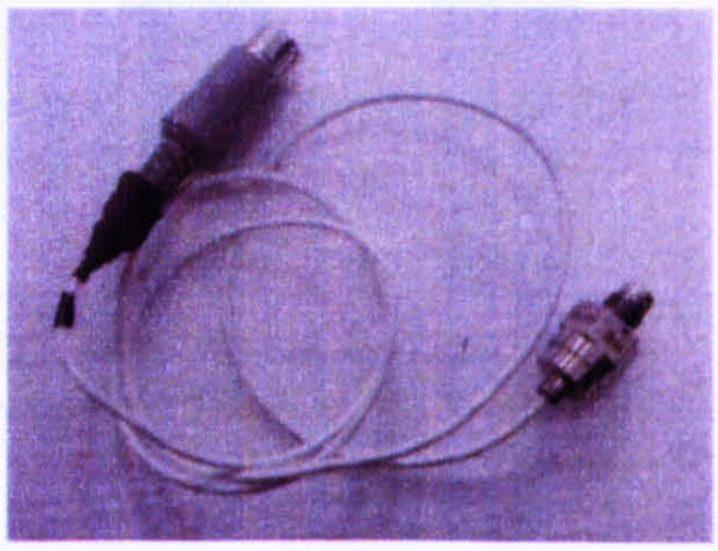

Plate 3.5.1Kulite pressure gauge

The calibration chamber as illustrated in figure 3.5.3 was designed as a closed system, so that when the shock front was released into it, the compressed air would be contained and equilibrate with time. The kulite gauge was positioned within the nozzle of the gas gun, measuring the pressure that entered the chamber. The chamber consisted of two sections:

1. The larger section contained the diaphragm lid.
2. The smaller section formed the chamber nozzle and screwed into the gas gun.

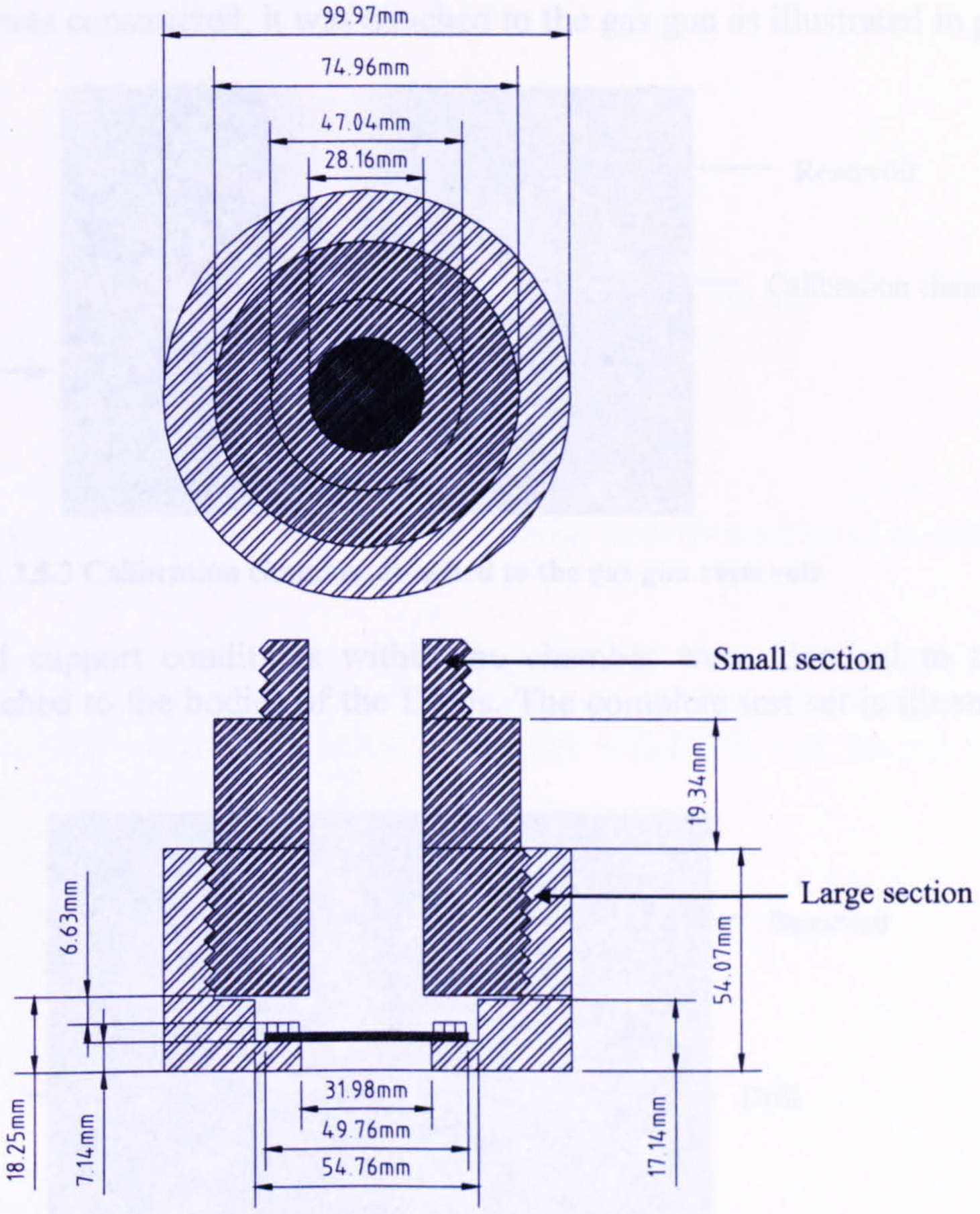

Figure 3.5.3 Plan and cross-sectional elevations of the calibration chamber

The larger section was clamped whilst a diaphragm lid, as illustrated in plate 3.5.2 was positioned into it. The smaller section was then screwed into the larger section.

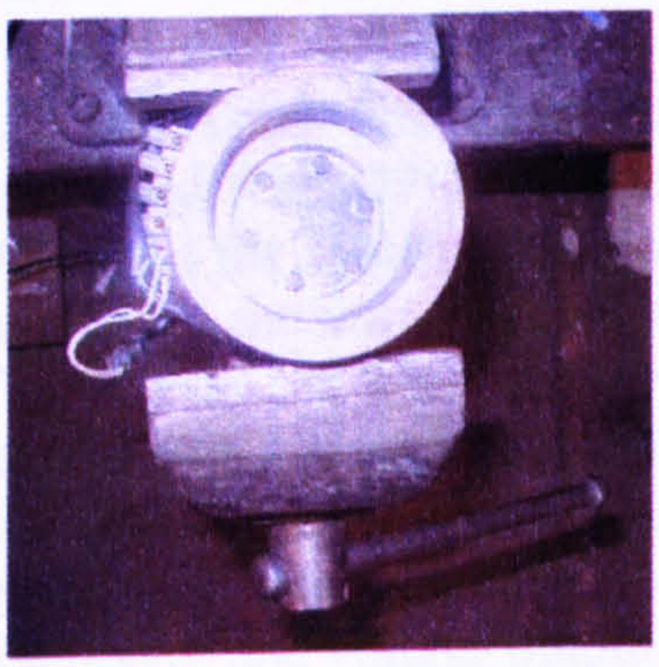

Diaphragm plate secured into the larger section

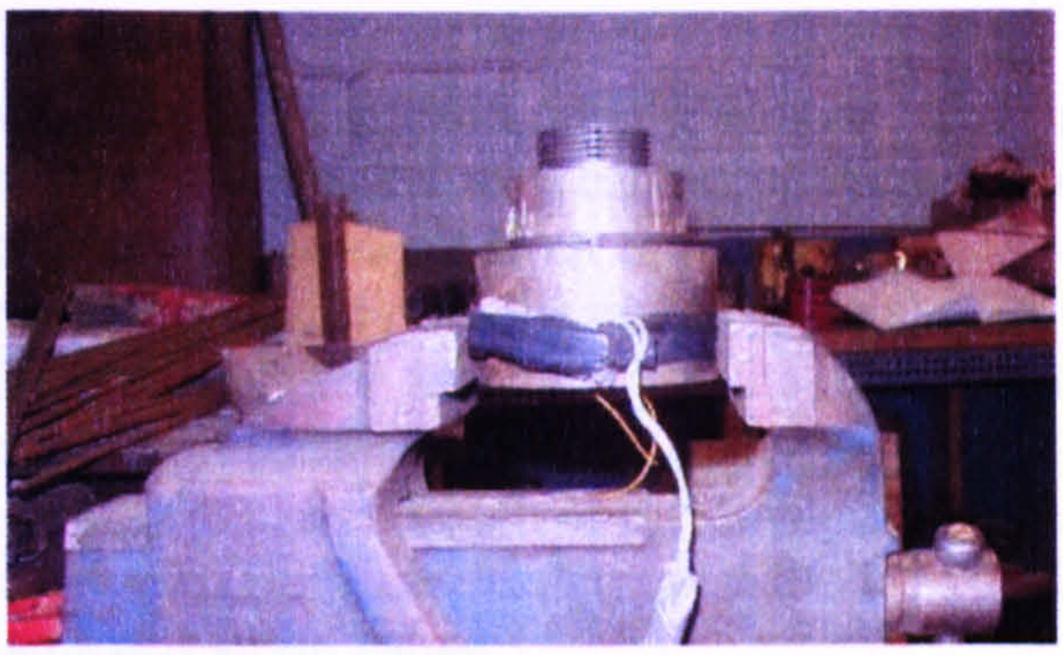

Chamber clamped and tightened

Plate 3.5.2 Securing the diaphragm into the chamber

Once the chamber was constructed, it was attached to the gas gun as illustrated in plate 3.5.3.

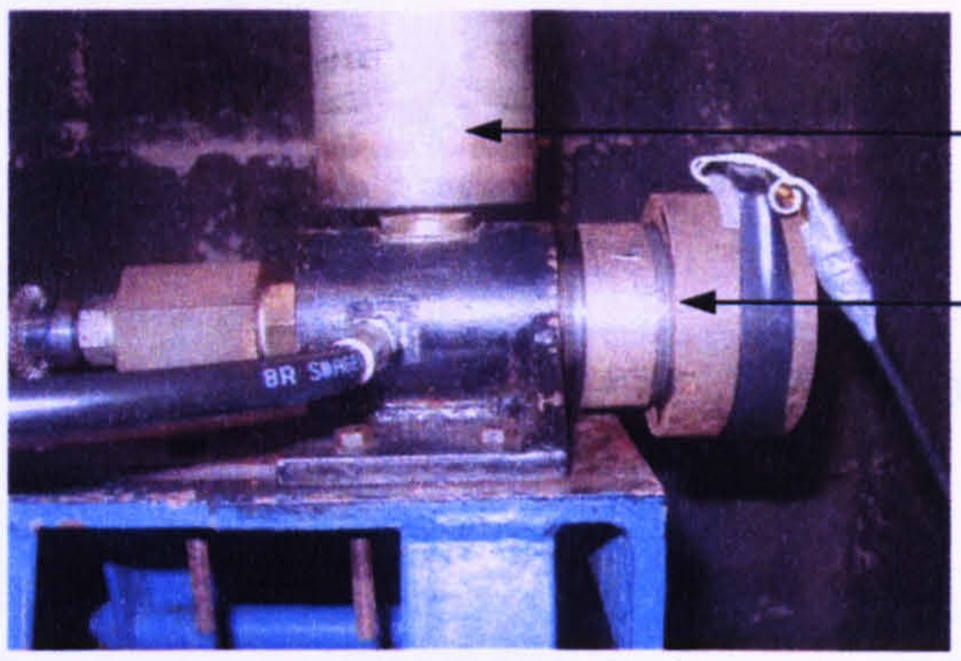

Plate 3.5.3 Calibration chamber attached to the gas gun reservoir

The diaphragm lid support conditions within the chamber were identical to those imposed when attached to the bodies of the DPGs. The complete test set is illustrated in plate 3.5.4.

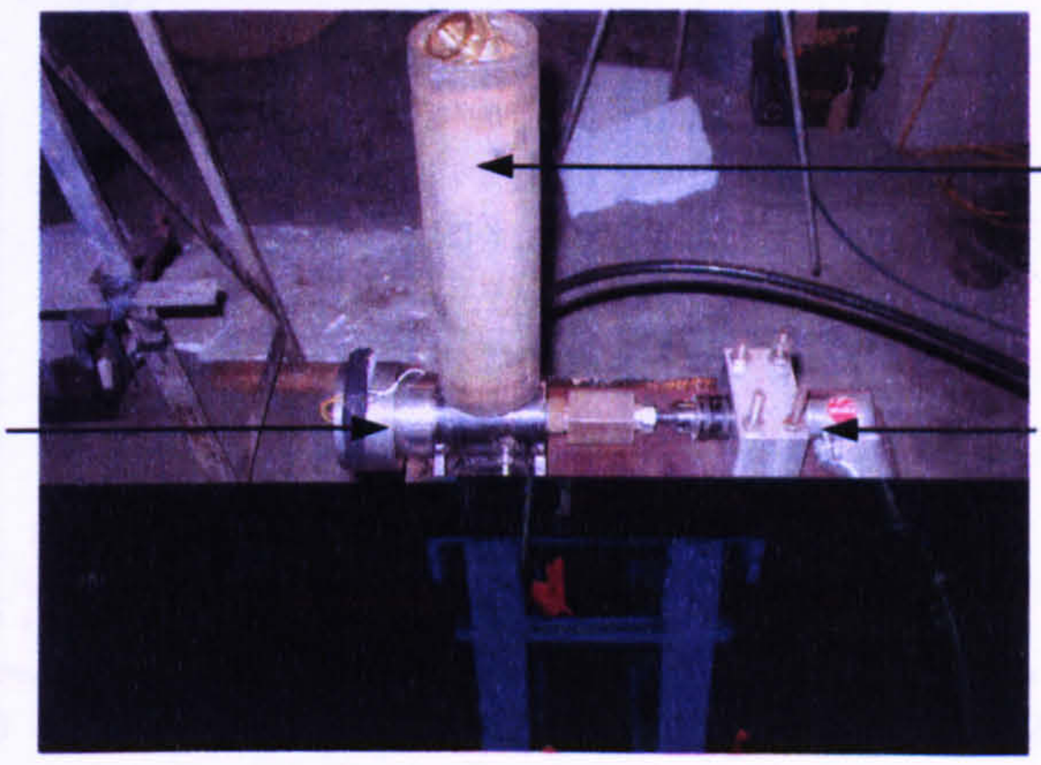

Plate 3.5.4 Gas gun

3.5.3 Calibration tests and results

All four DPG lids were calibrated statically in the calibration chamber. The lid associated with DPG1 was the thickest. It was subjected to a calibration pressure of 80bar. As the system was closed, the pressure-time output from the kulite gauge was equated to the voltage-time output from the diagram lid as illustrated in figure 3.5.4. The release of air was slow enough, ensuring the response of the diaphragms responded elastically rather than plastically.
Identical time bases were set on both the kulite gauge and each of the diaphragms. This ensured a direct relationship to be made between pressure exerted upon the face of the diaphragm and voltage output from the attached strain gauge.

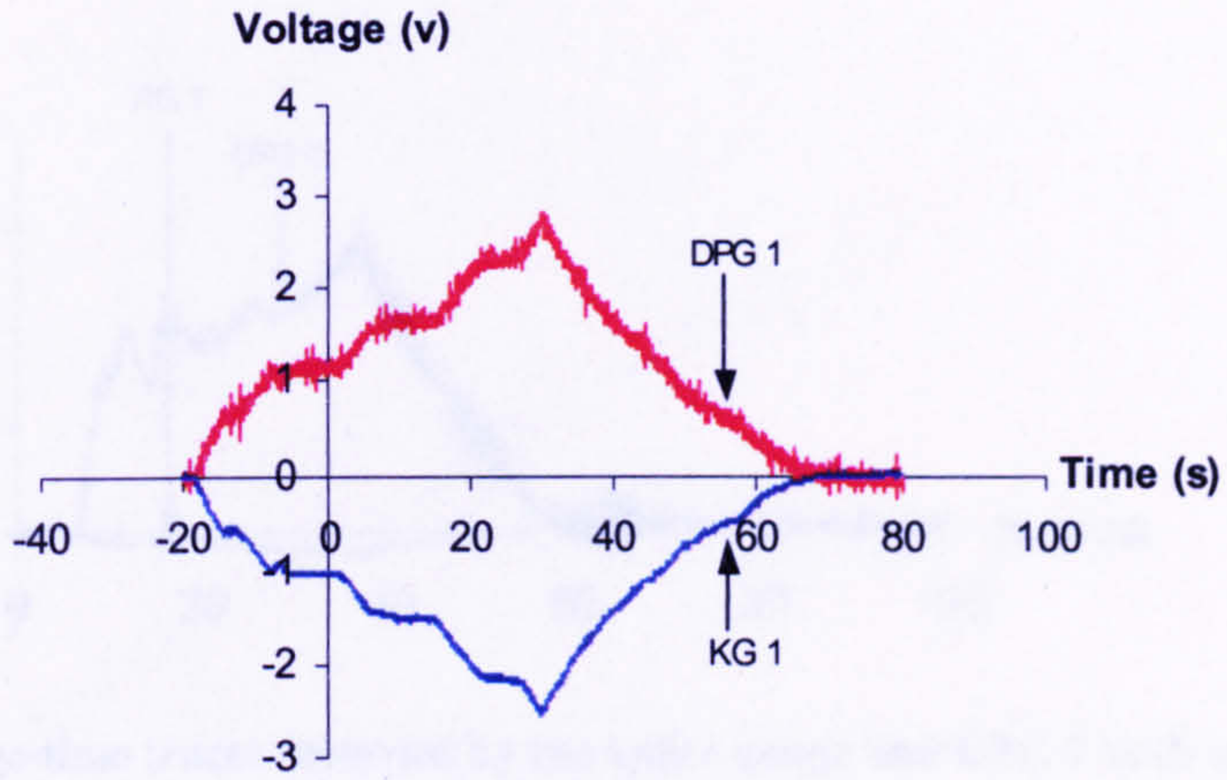

Figure 3.5.4 Voltage-time traces recorded by the kulite gauge and DPG1 subjected to static loading

The diaphragm lids associated with the remaining DPGs were approximately 65% thinner than that of DPG1. Instead, a maximum pressure of 20bar was used as the calibration pressure. The voltage-time traces associated with DPGs 2-4 and the kulite gauge are illustrated in figures 3.5.5-3.5.7.

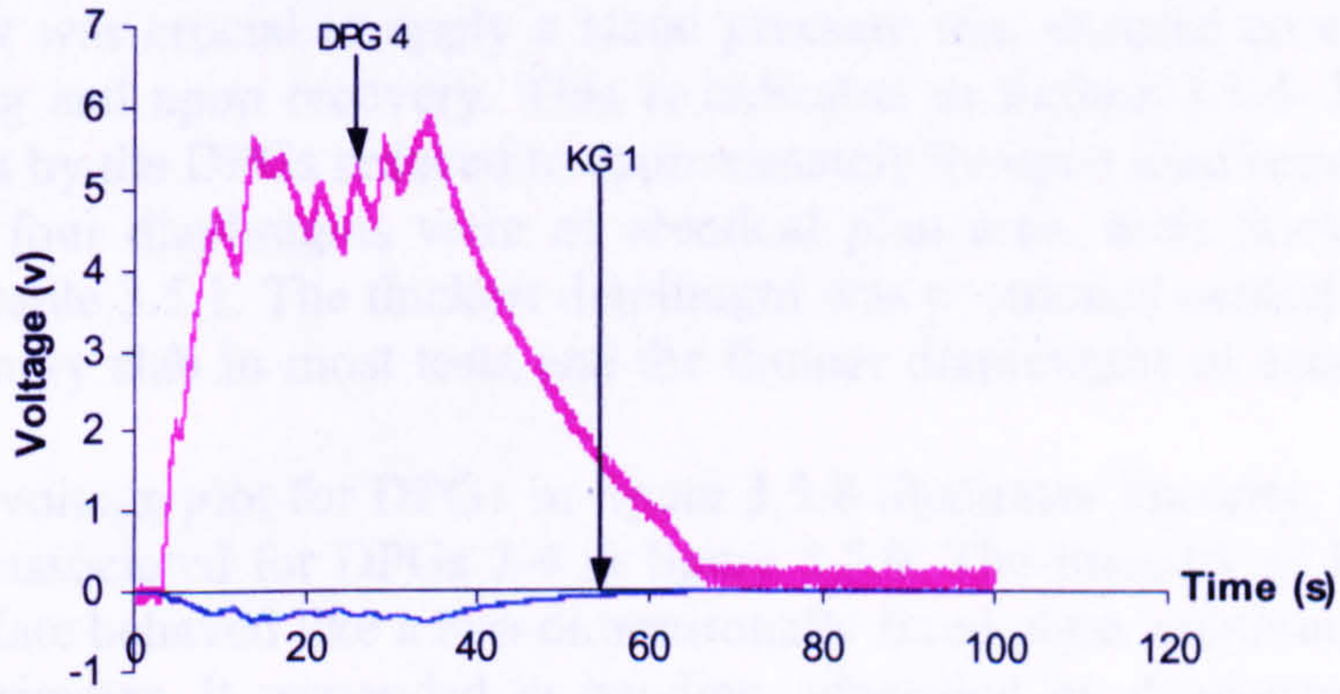

Figure 3.5.5 Voltage-time traces recorded by kulite gauge and DPG4 both subjected to static loading

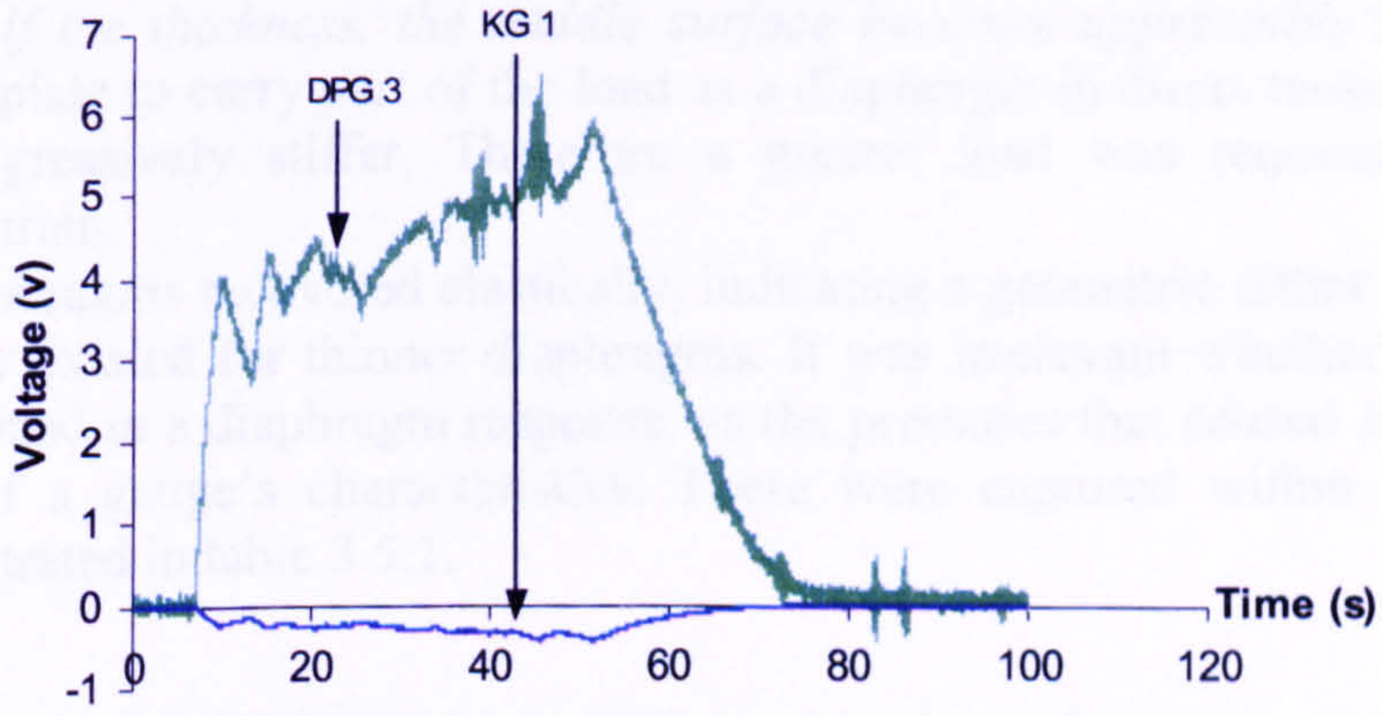

Figure 3.5.6 Voltage-time traces recorded by the kulite gauge and DPG 3 both subjected to static loading

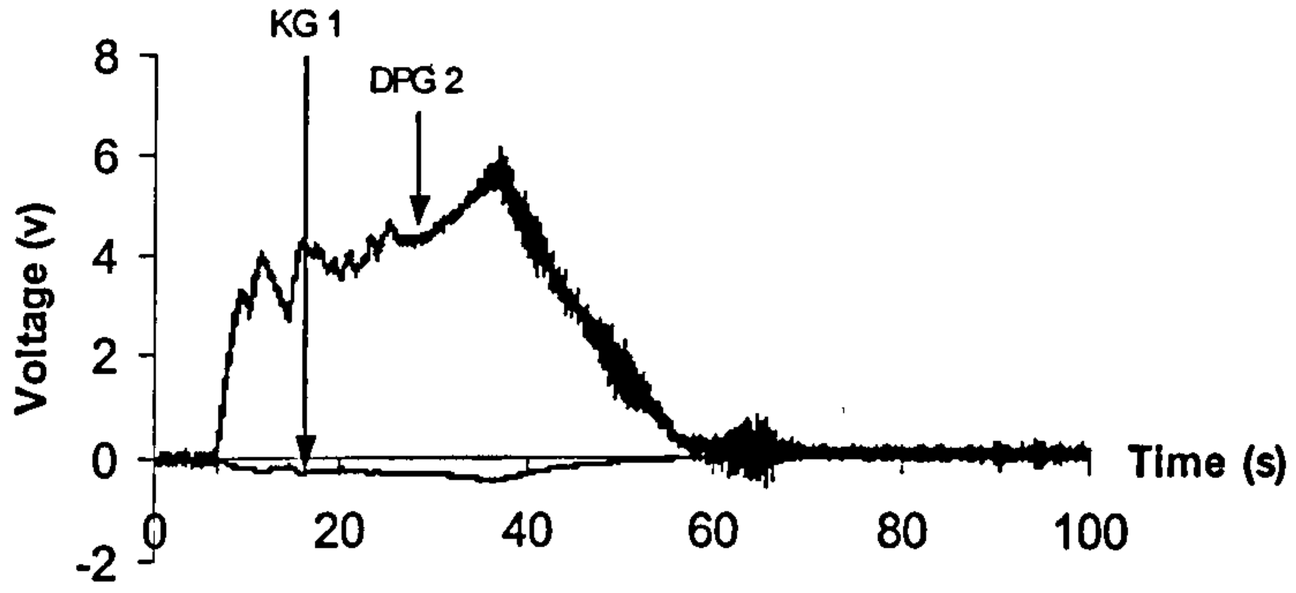

Figure 3.5.7 Voltage-time traces recorded by the kulite gauge and DPG 2 both subjected to static loading

Hysterisis effects were evident on the voltage-time traces in figures 3.5.4-3.5.7. This could have occurred for two reasons:

1. Non-uniform thickness of the diaphragm lids,
2. Horizontal sliding of the diaphragms due to loose screw connections.

Although all the diaphragms associated with each of the four DPGs had varying thicknesses, it was crucial to apply a static pressure that ensured an elastic response during loading and upon recovery. This is indicated in figures 3.5.4–3.5.7 where the voltage output by the DPGs reduced to approximately 0v upon load removal.
Although all four diaphragms were of identical plan area, their thickness varied as illustrated in table 3.5.1. The thickest diaphragm was positioned centrally upon the top face of a primary slab in most tests and the thinner diaphragms at eccentricities from the centre.
The pressure-voltage plot for DPG1 in figure 3.5.8 illustrates linearity, whereas a non-linearity was associated for DPGs 2-4 in figure 3.5.9. The linearity of DPG1 occurred because the plate behaved like a two-dimensionally fixed plate, continuously supported around its perimeter. It responded in bending, identified by displacement and strain therefore directly proportional to the applied load. The thinner diaphragms associated with DPGs 2-4 yielded parabolic pressure-voltage relationship curves.
Young & Budynas (2002) stated that '*when the deflection of the plate becomes larger than one-half the thickness, the middle surface becomes appreciably strained*'. This enabled the plate to carry part of the load as a diaphragm in direct tension, as the plate became progressively stiffer. Therefore a greater load was required to cause an increase in strain.
All four diaphragms recovered elastically, indicating a geometric rather than a material non-linearity existed for thinner diaphragms. It was irrelevant whether linear or non-linearity existed in a diaphragm response, as the pressures that caused a response were indicative of a gauge's characteristics. These were captured within the calibration factors, illustrated in table 3.5.1.

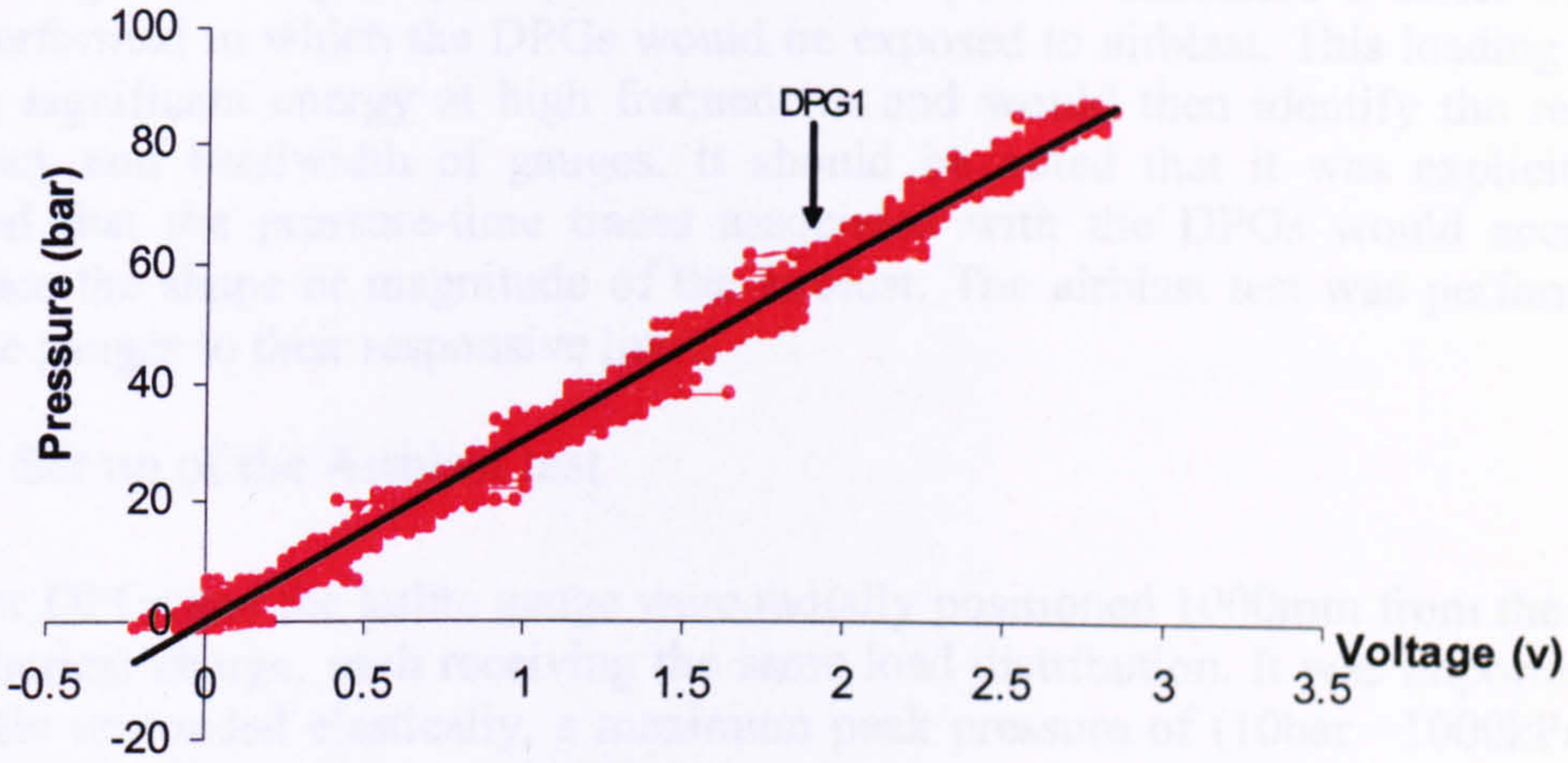

Figure 3.5.8 Pressure-voltage calibration relationship associated with the response of DPG1

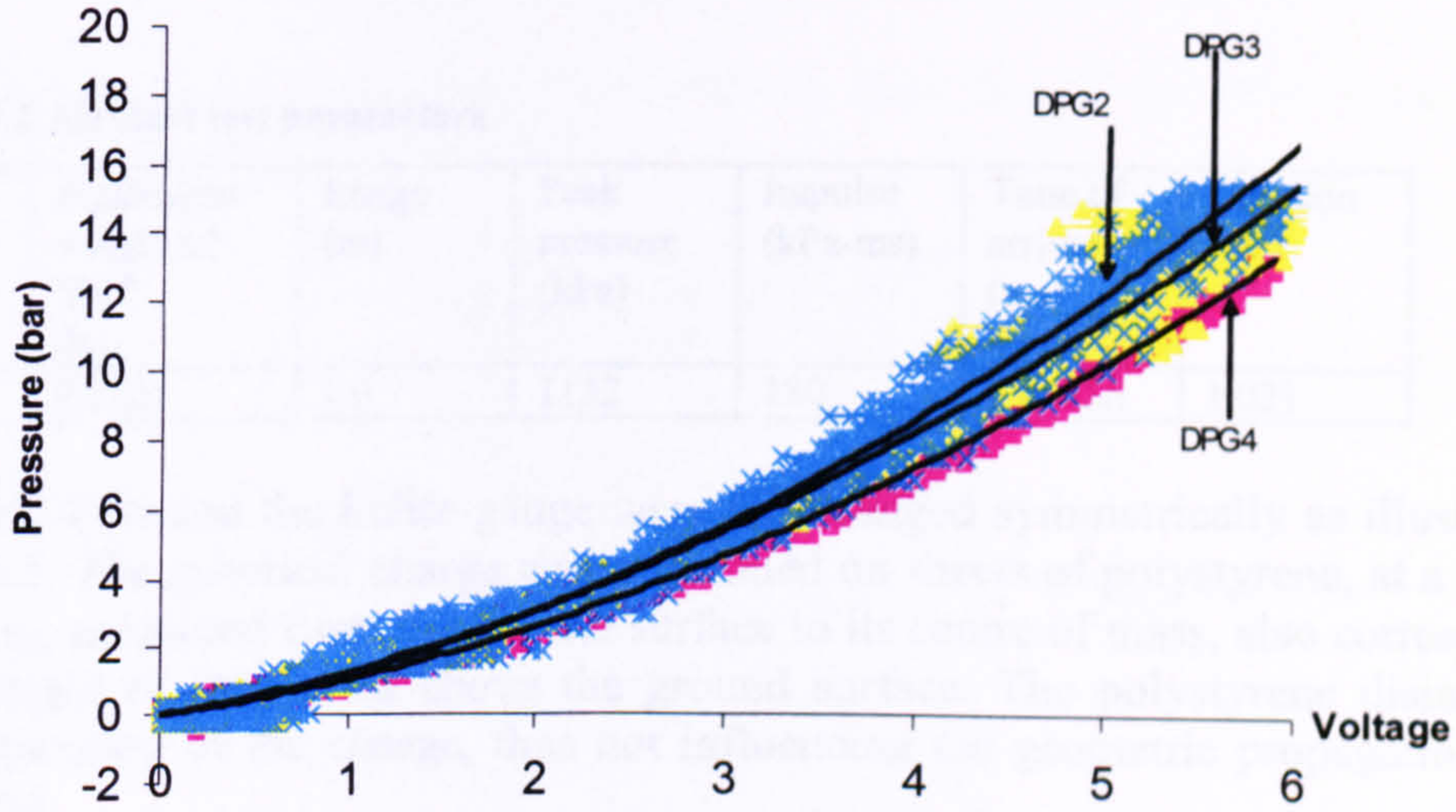

Figure 3.5.9 Pressure-voltage calibration relationship associated with the response of DPGs 2,3 and 4

The equations associated with the calibration plots from figures 3.5.8 and 3.5.9 are illustrated in table 3.5.1.

Table 3.5.1 Pressure-voltage calibration equations

Gauge	Plate thickness (mm)	Calibration equation
DPG1	2.02	$P=30.988v$
DPG2	0.64	$P=0.3107v^2+0.8986v$
DPG3	0.61	$P=0.2597v^2+1.0056v$
DPG4	0.7	$P=0.2491v^2+0.797v$

v = voltage P=Pressure

3.5.4 Validating the response of the diaphragm pressure gauges within an Airblast test

It was expected that the groundshock loading would contain little energy at relatively high frequencies. Performing groundshock loading on the DPGs without firstly

determining their frequency response was unacceptable. Therefore a series of trials were performed in which the DPGs would be exposed to airblast. This loading would contain significant energy at high frequencies and would then identify the resonant frequency and bandwidth of gauges. It should be noted that it was explicitly not expected that the pressure-time traces associated with the DPGs would accurately reproduce the shape or magnitude of the airblast. The airblast test was performed to push the gauges to their responsive limit.

3.5.4.1 Set up of the Airblast test

The four DPGs and the kulite gauge were radially positioned 1000mm from the centre of a spherical charge, each receiving the same load distribution. It was important that the DPGs responded elastically, a maximum peak pressure of (10bar =1000kPa) was assumed and inputted into CONWEP, to determine an approximate mass of the spherical charge. The input and output values from CONWEP are illustrated in table 3.5.2.

Table 3.5.2 Airblast test parameters

Charge weight (kg)	Equivalent weight of TNT (kg)	Range (m)	Peak pressure (kPa)	Impulse (kPa-ms)	Time of arrival (ms)	Duration (ms)
0.1737	0.2223	1.0	1132	180	0.85256	1.021

The four DPGs and the kulite gauge were all arranged symmetrically as illustrated in plate 3.5.5. The spherical charge was positioned on sheets of polystyrene, at a standoff of 500mm, measured from the ground surface to its centre of mass, also corresponding to the height of the DPGs above the ground surface. The polystyrene disintegrated upon detonation of the charge, thus not influencing the geometric propagation of the blast wave.

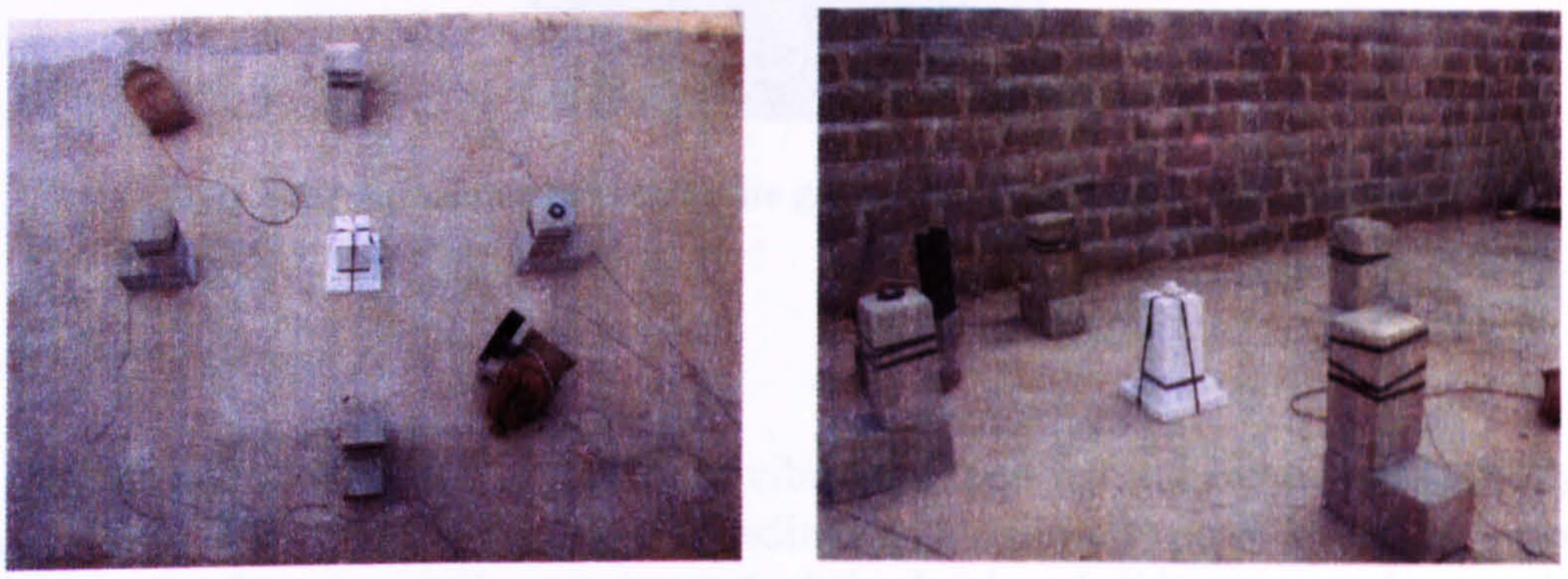

Plate 3.5.5 Airblast test setup

The four DPGs were mounted onto concrete blocks, using industrial tape, as illustrated in plate 3.5.6. The blocks were of a sufficient mass enabling them to remain vertical upon impact of the propagating blast wave.

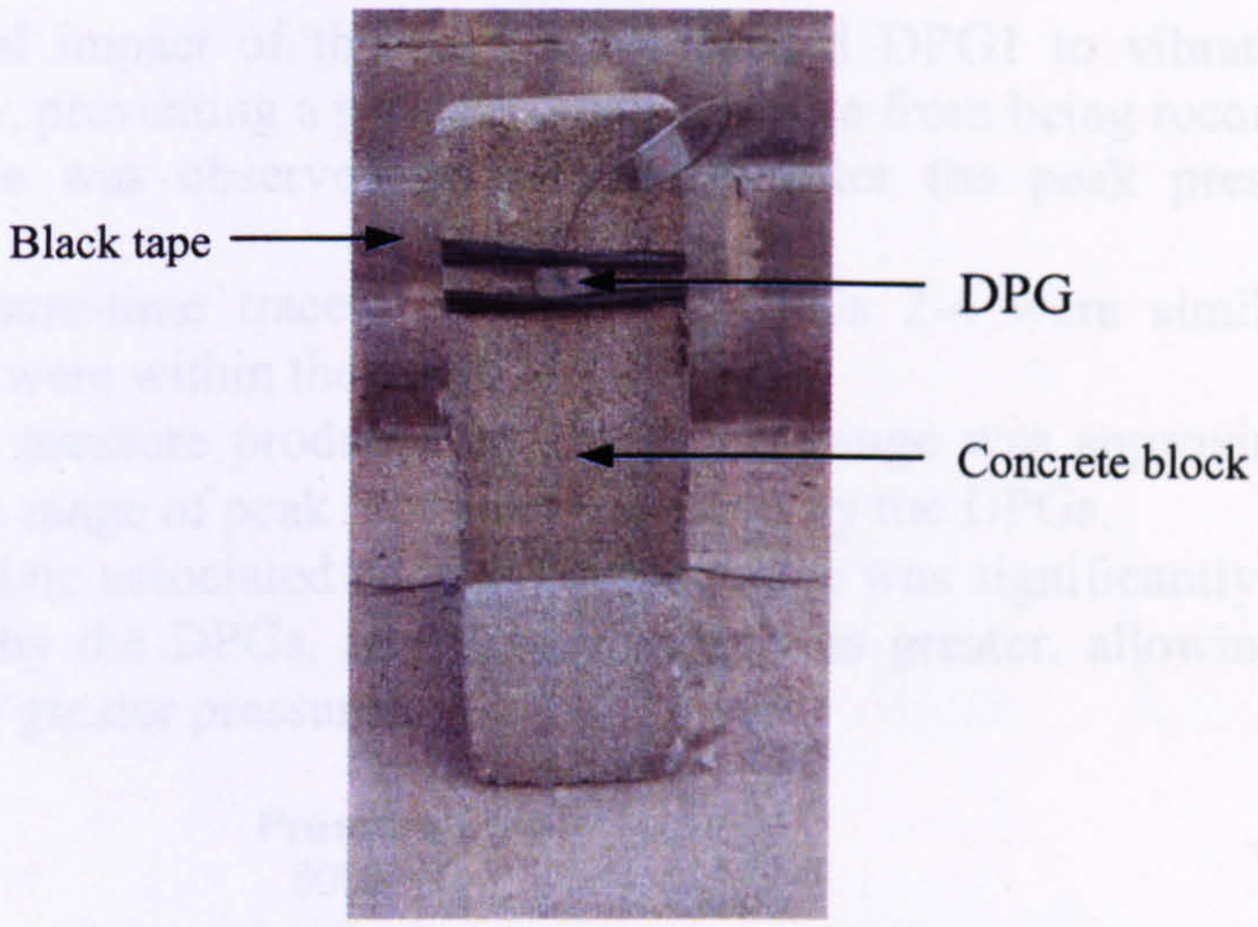

Plate 3.5.6 Attachment of a DPG to a concrete block

The kulite gauge was positioned flush with the front face of the steel element facing the charge, as illustrated in plate 3.5.7.

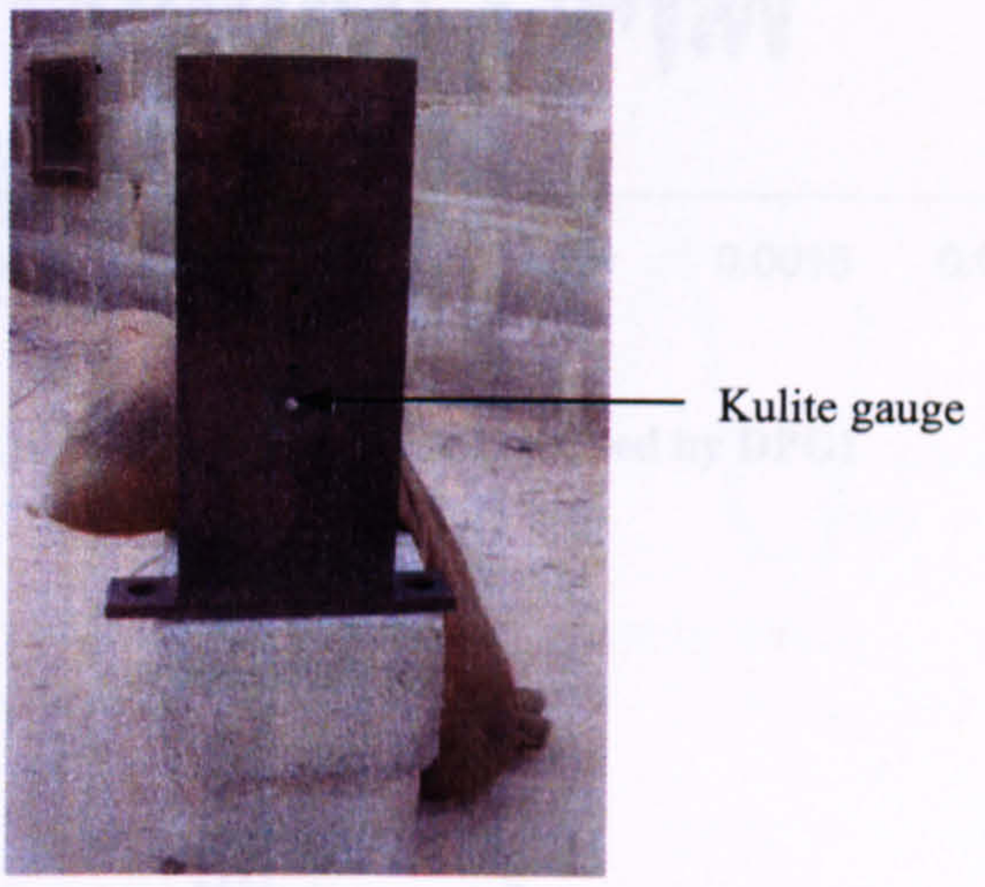

Plate 3.5.7 Attachment of the kulite gauge into a protective steel section

3.5.4.2 Airblast test results

The airblast test caused all four DPGs to vibrate at their natural frequencies. DPGs 2-4 responded to the blast wave by recording a maximum peak pressure prior to resonating. DPG1 resonated upon impact of the load and did not record a maximum peak pressure. Due to the large surface area and mass of the diaphragm lids, the gauges would not be suitable in measuring airblast. The primary concern was evaluating their suitability in measuring groundshock

The air blast test was performed to establish the range of frequencies the DPGs could respond to. As expected, the gauges could not pick up the high frequencies associated with airblast that were picked up by the kulite gauge. The pressure-time traces associated with all for DPGs and the kulite gauge are illustrated in figures 3.5.10–3.5.14. Comments relating to the figures are presented below:

1. The initial impact of the blast wave caused DPG1 to vibrate at its natural frequency, preventing a peak pressure response from being recorded.
2. Resonance was observed on DPGs 2-4 after the peak pressure had been recorded.
3. The pressure-time traces produced by DPGs 2-4 were similar. Their peak pressures were within the range 580–840kPa.
4. The peak pressure produced by the kulite gauge was approximately 900kPa, within the range of peak pressures produced by the DPGs.
5. The rise time associated with the kulite gauge was significantly less than those recorded by the DPGs, as it's bandwidth was greater, allowing it to respond quicker to greater pressures.

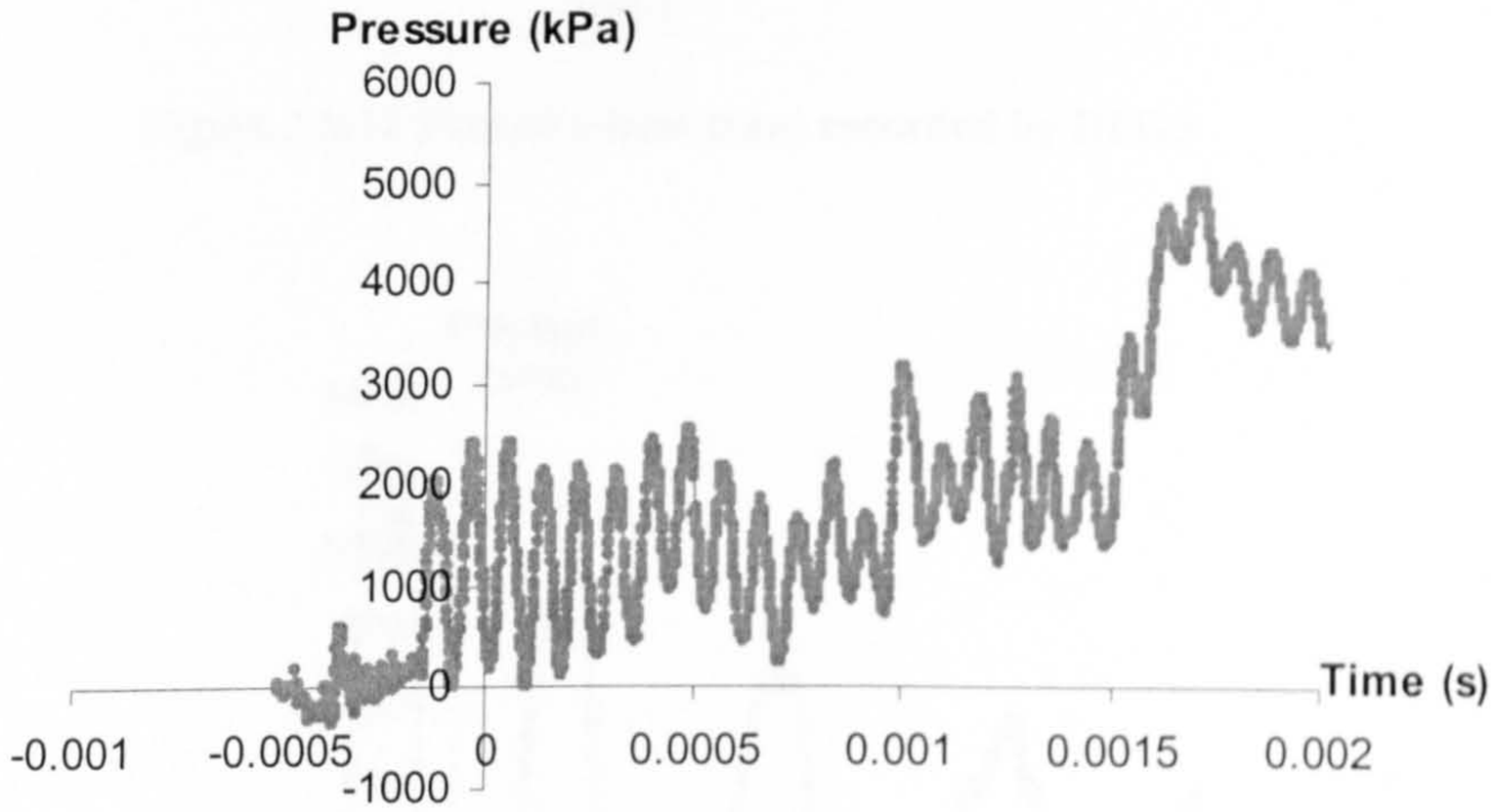

Figure 3.5.10 Pressure-time trace recorded by DPG1

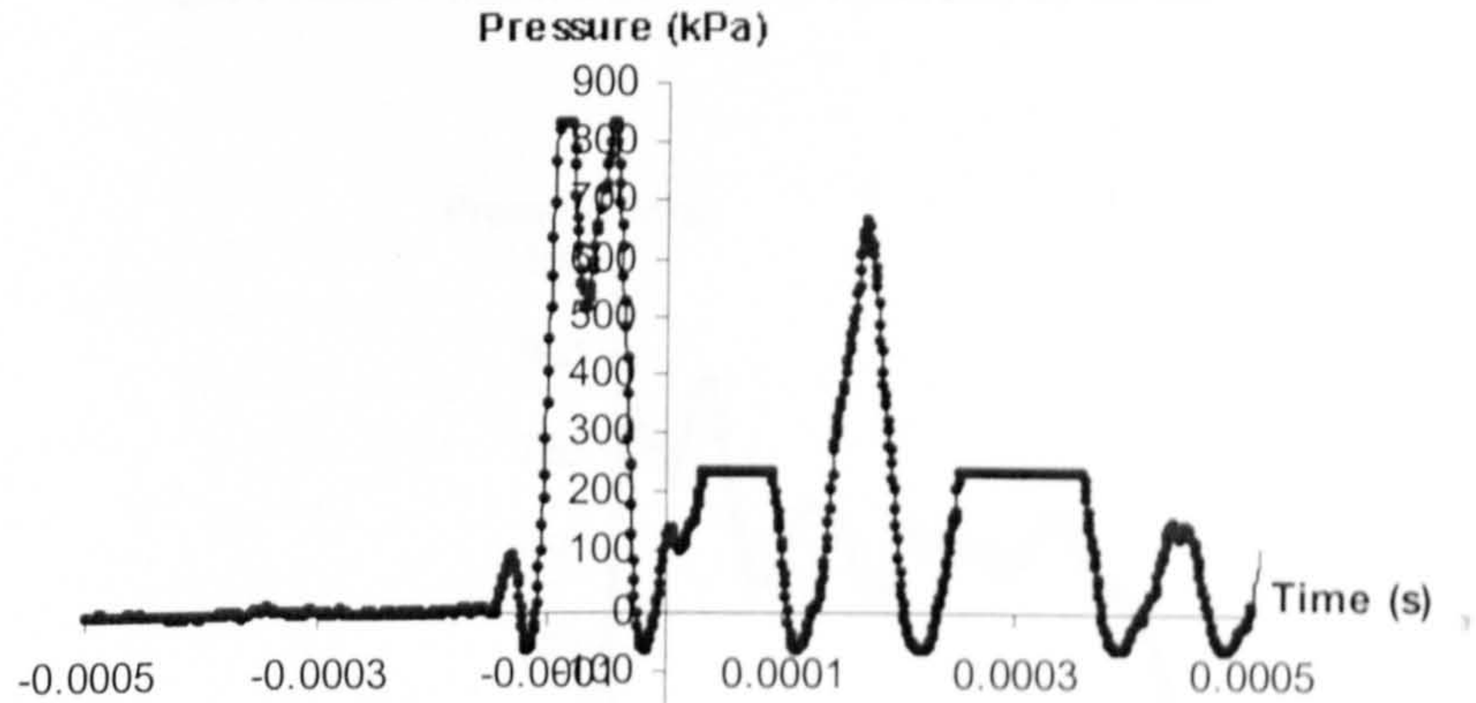

Figure 3.5.11 Pressure-time trace recorded by DPG2

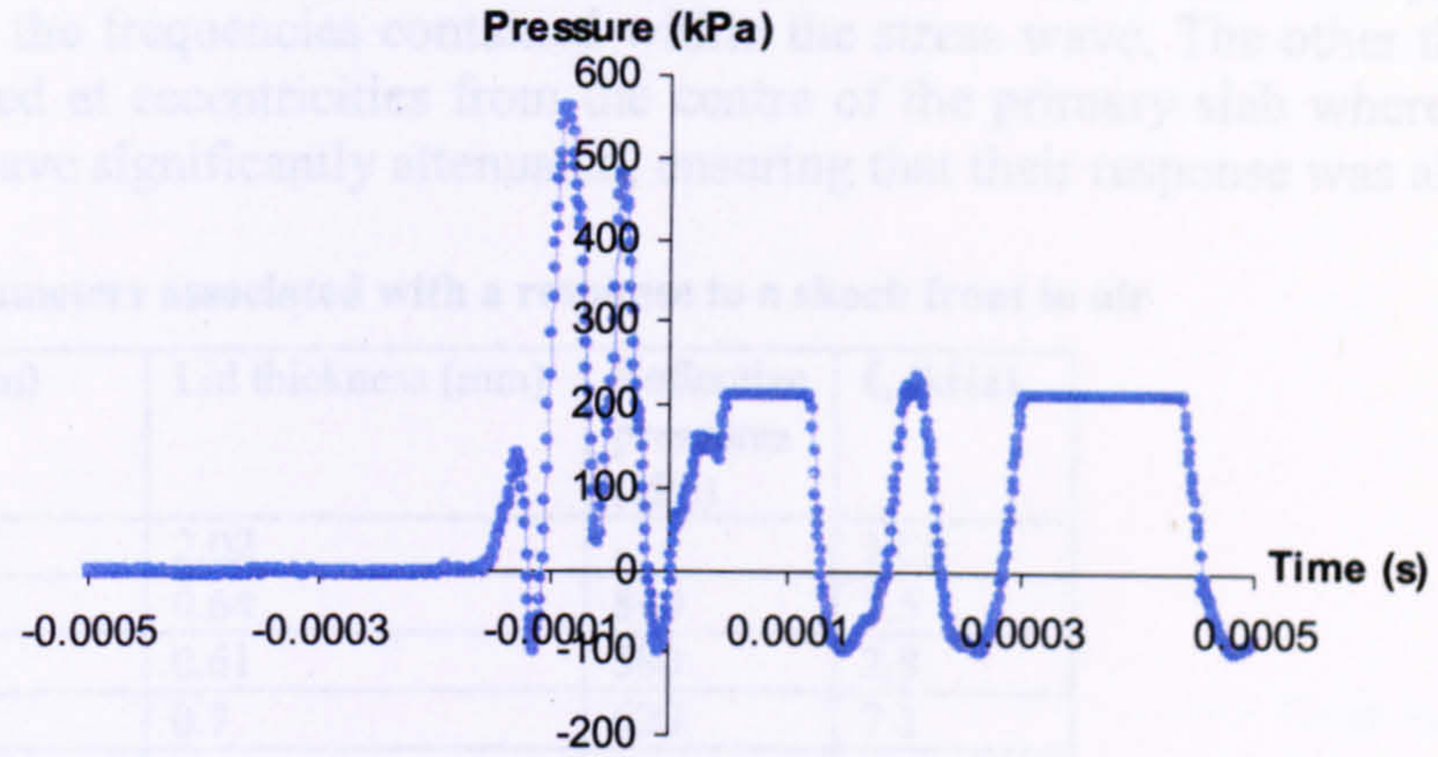

Figure 3.5.12 Pressure-time trace recorded by DPG3

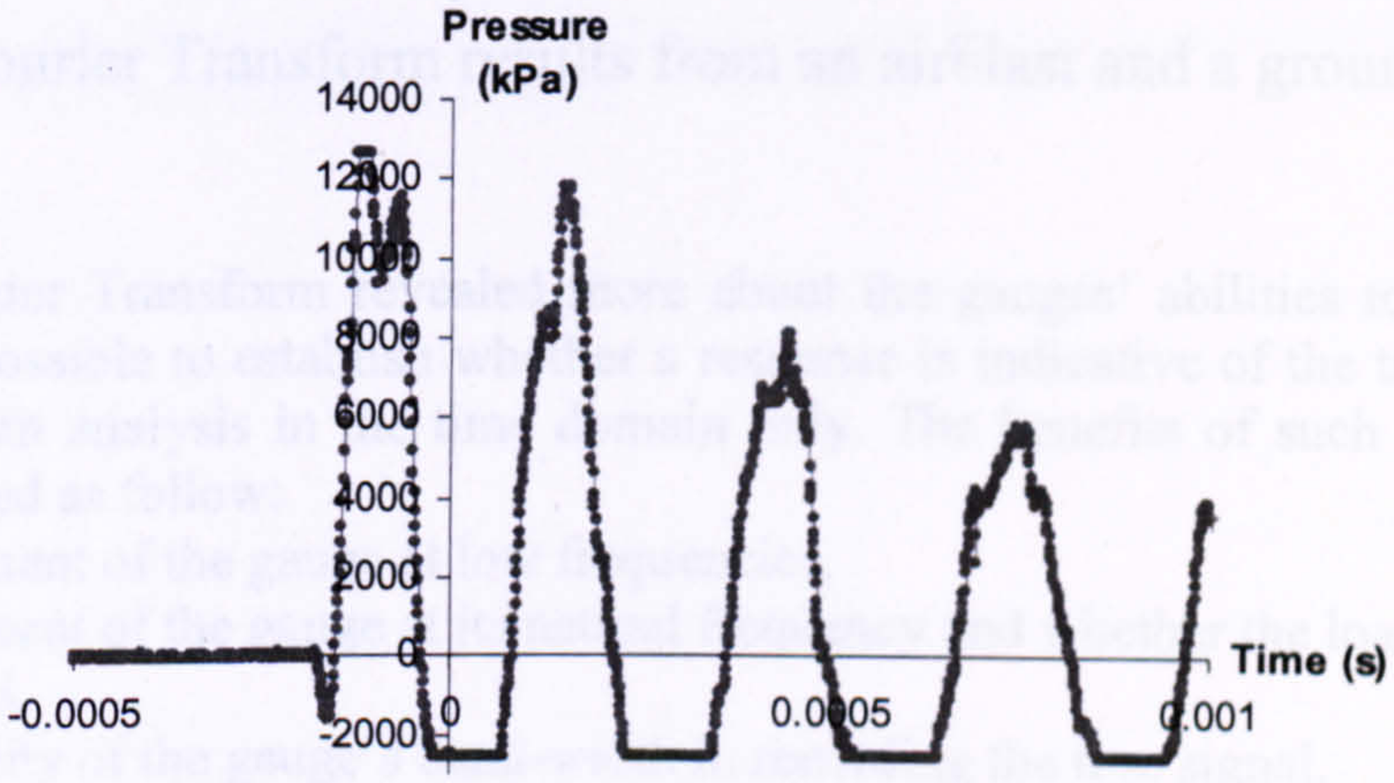

Figure 3.5.13 Pressure-time trace recorded by DPG4

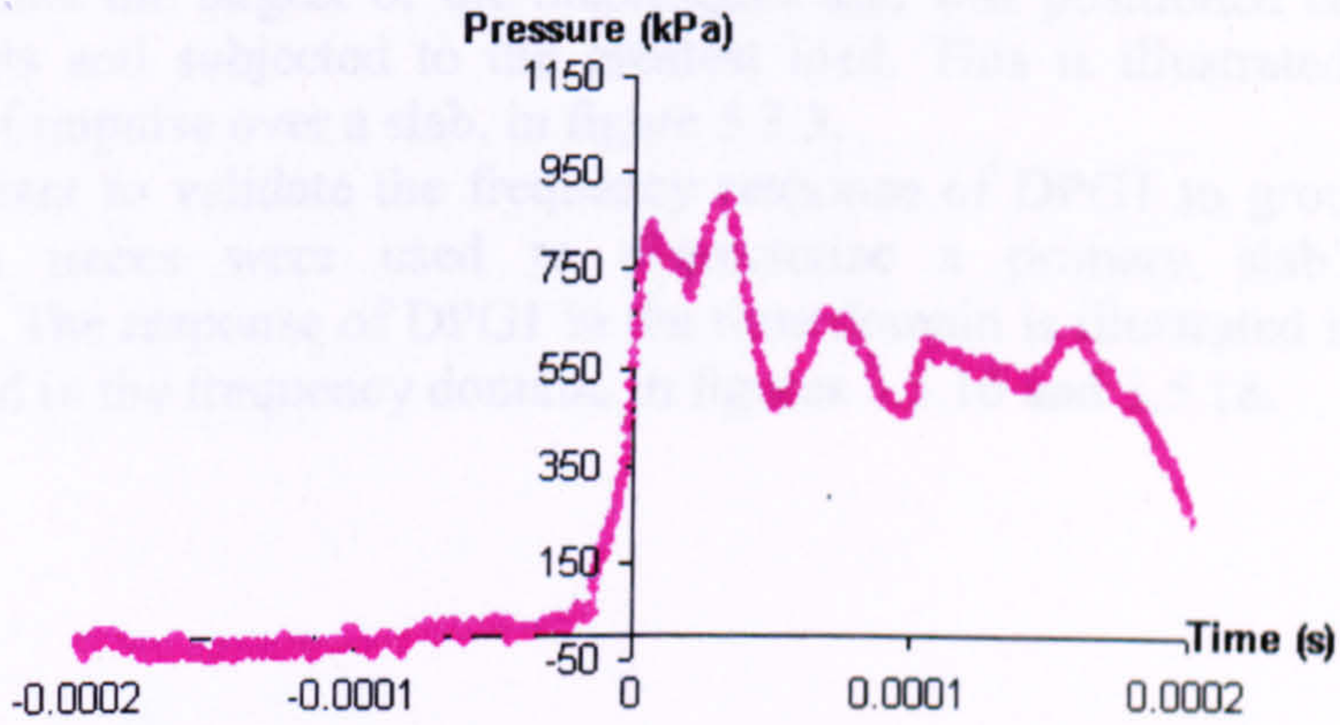

Figure 3.5.14 Pressure-time trace recorded by the kulite gauge

All four DPGs at some point during the airblast vibrated at their natural frequencies. Those natural frequencies are illustrated in table 3.5.3. DPG1 vibrated at the greatest natural frequency in comparison to the other gauges, due to its large diaphragm lid. It was positioned centrally on the top face of a primary slab during the explosive tests

because it was assumed that its thicker diaphragm would respond elastically, as well as responding to the frequencies contained within the stress wave. The other three DPGs were positioned at eccentricities from the centre of the primary slab where the stress wave would have significantly attenuated, ensuring that their response was also elastic.

Table 3.5.3 Parameters associated with a response to a shock front in air

Gauge	S (mm)	Lid thickness (mm)	Reflective pressures (kPa)	f_n (kHz)
DPG1	1000	2.02	-	12.5
DPG2	1000	0.64	840	3.5
DPG3	1000	0.61	580	2.8
DPG4	1000	0.7	620	7.1
KG	1000	-	900	-

S = Charge standoff
f_n = Natural frequency of response

3.5.5 Fast Fourier Transform results from an airblast and a groundshock test

The Fast Fourier Transform revealed more about the gauges' abilities to respond to load. It is impossible to establish whether a response is indicative of the true transient loading from an analysis in the time domain only. The benefits of such a procedure have been stated as follow:

1. excitement of the gauge at low frequencies,
2. excitement of the gauge at its natural frequency and whether the loading was damped,
3. suitability of the gauge's band-width in recording the true signal.

The pressure-time traces from both the airblast test and groundshock test RCIT3 recorded by DPG1 were analysed using the Fast Fourier Transform procedure.
DPG1 contained the largest of the diaphragms and was positioned centrally in most explosive tests and subjected to the greatest load. This is illustrated by the spatial distribution of impulse over a slab, in figure 5.3.3.
It was important to validate the frequency response of DPG1 to groundshock, as its pressure-time traces were used to characterise a primary slab's response to groundshock. The response of DPG1 in the time domain is illustrated in figures 3.5.15 and 3.5.17 and in the frequency domain, in figures 3.5.16 and 3.5.18.

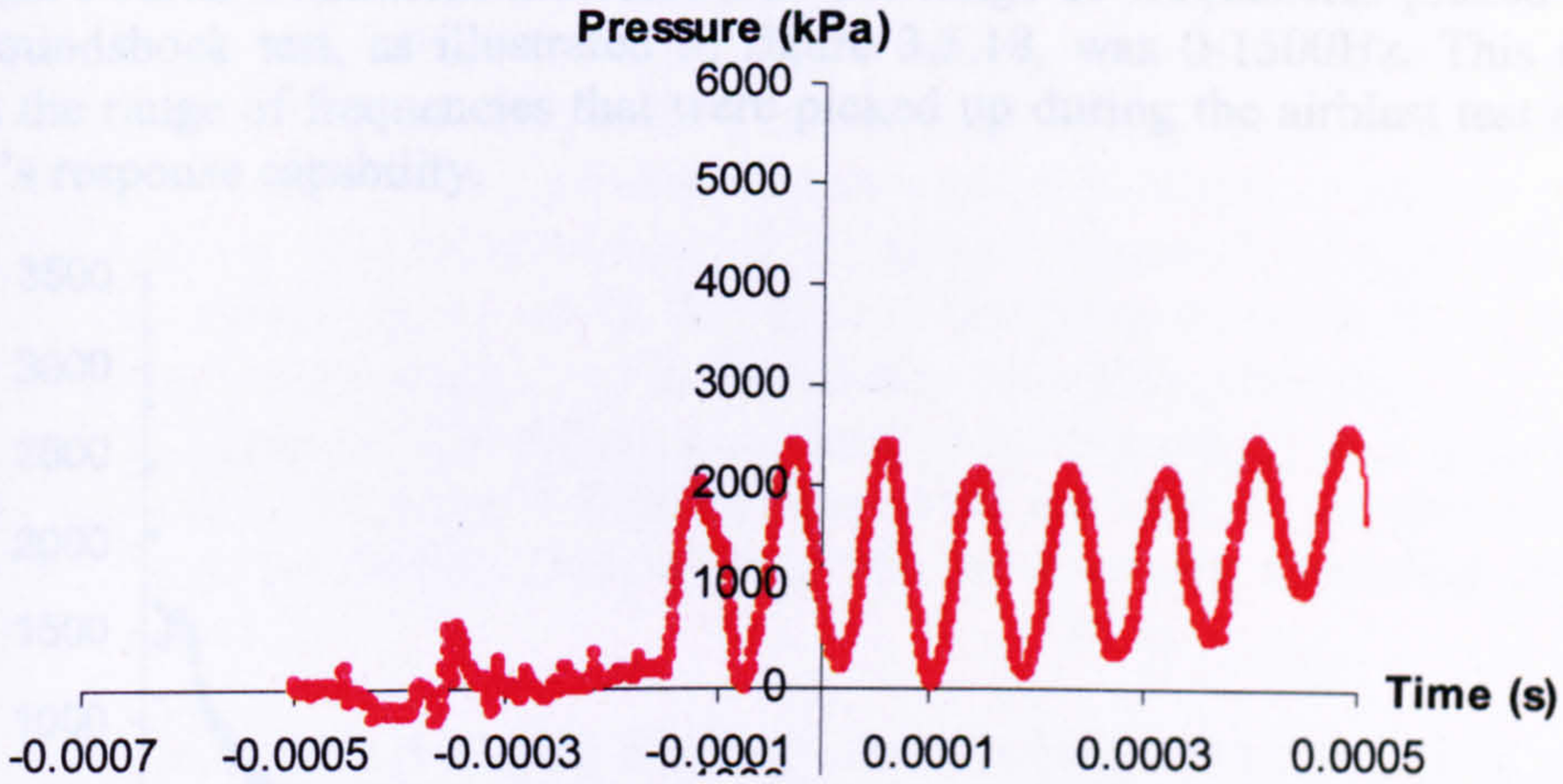

Figure 3.5.15 Pressure-time trace recorded by DPG1 in an airblast test

The Fast Fourier Transform indicated that DPG1s natural frequency was clearly 12500Hz, as illustrated in figure 3.5.16 but more importantly it managed to respond to frequencies within the range of 0-7000Hz.

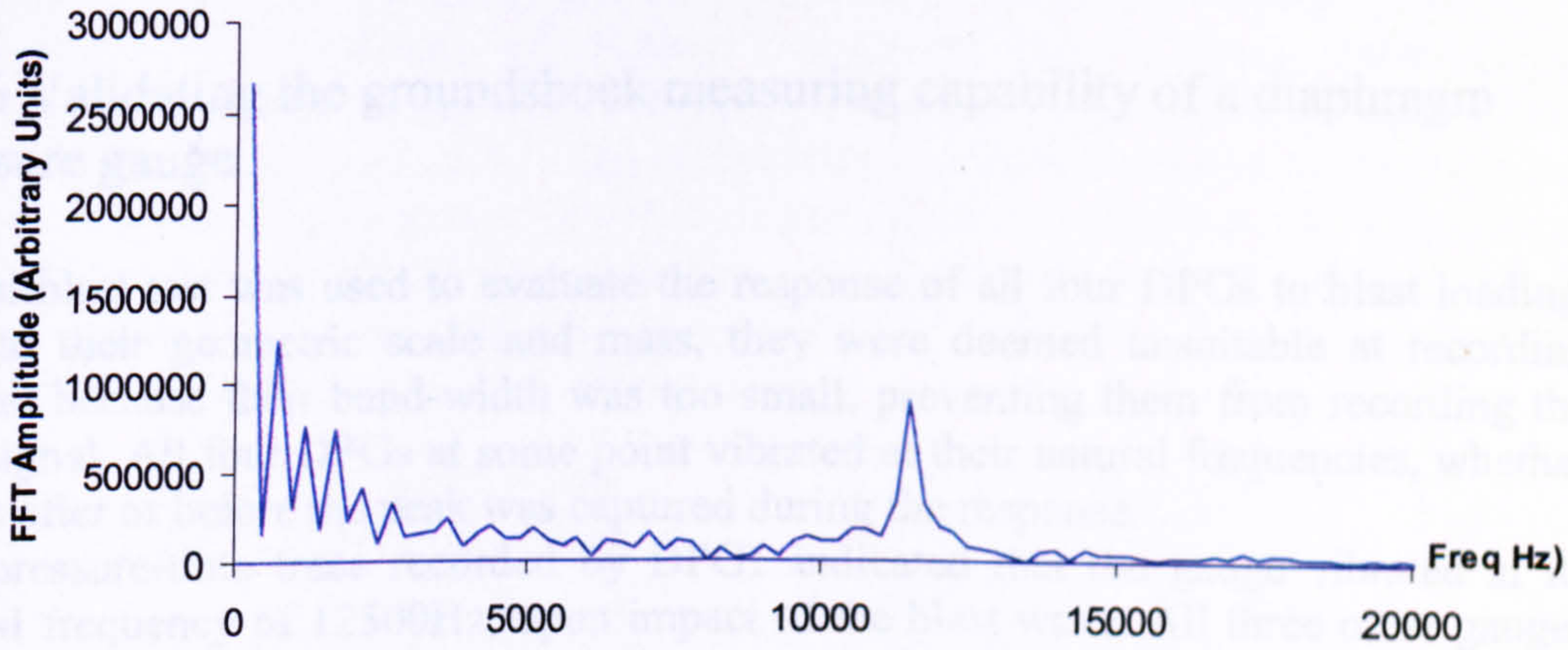

Figure 3.5.16 Fast-Fourier Transform analysis on the pressure-time results recorded by DPG1 during test an airblast test

The pressure-time trace from test RCIT3, as illustrated in figure 3.5.17, was chosen because DPG1 was not damaged in the test as it was in other tests, and because the trace recorded was simple, containing only a peak followed by decay. In tests with smaller charge standoffs, there was a series of peaks within a given trace, indicating other complex phenomena.

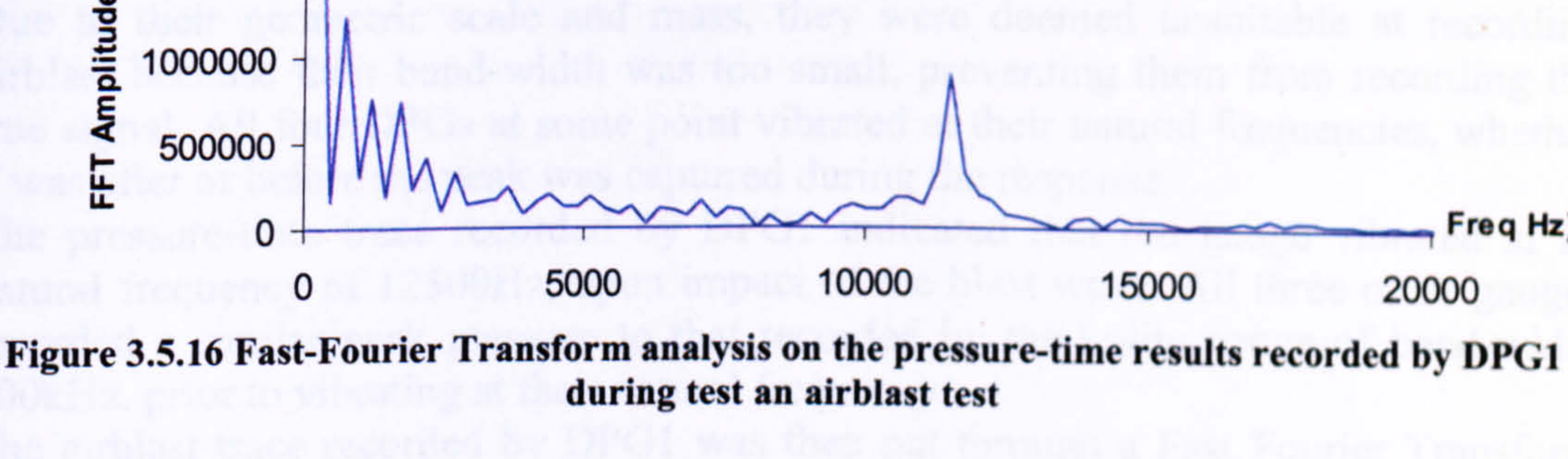

Figure 3.5.17 Pressure-time trace recorded by DPG1 from RCIT3

The Fast-Fourier-Transform indicated that the range of frequencies picked up during the groundshock test, as illustrated in figure 3.5.18, was 0-1500Hz. This range was within the range of frequencies that were picked up during the airblast test and within DPG1's response capability.

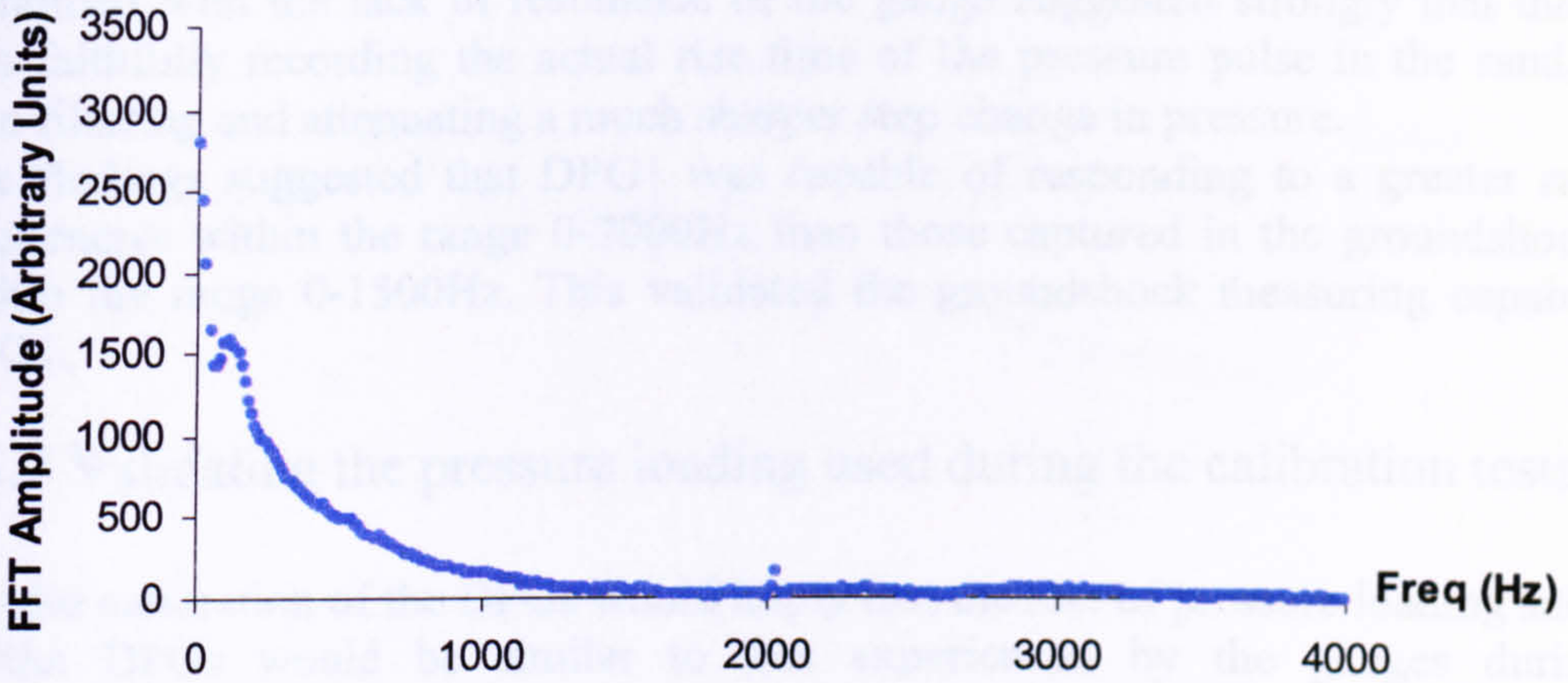

Figure 3.5.18 Fast-Fourier Analysis on the pressure-time results associated with DPG1 from test groundshock test RCIT3

3.5.6 Validating the groundshock measuring capability of a diaphragm pressure gauge

The airblast test was used to evaluate the response of all four DPGs to blast loading. Due to their geometric scale and mass, they were deemed unsuitable at recording airblast because their band-width was too small, preventing them from recording the true signal. All four DPGs at some point vibrated at their natural frequencies, whether it was after or before the peak was captured during the response.

The pressure-time trace recorded by DPG1 indicated that the gauge vibrated at its natural frequency of 12500Hz, upon impact of the blast wave. All three other gauges recorded a similar peak pressure to that recorded by the kulite gauge of band-width 300kHz, prior to vibrating at their natural frequency.

The airblast trace recorded by DPG1 was then put through a Fast Fourier Transform and analysed in the frequency domain. It was compared to the frequency domain data from groundshock test RCIT3, hence establishing whether the gauge was damping out the signal or whether the soil was attenuating it.

The lack of resonance in the response of DPG1 during groundshock test RCIT3 could have been due to the following:

1. The ground shock was attenuated during propagation, such that the signal itself contained no significant energy at frequencies close to the resonant frequency of the gauge.
2. The presence of the soil matrix in intimate contact with the membrane damped the membrane response and prevented the occurrence of resonance.

Either way, the lack of resonance in the groundshock data suggested that the results from the gauges were not unduly affected by dynamic amplification of the incident signal when buried in sand.

Ignoring the clear resonance in the airblast data, the characteristic rise time of the signal recorded by the DPG1 was about 32μs; that is, when exposed to a step change in pressure, the DPG responded in about 32μs. In comparison, the characteristic rise time of the pressure signal in the groundshock test was much longer, at around 550μs. This combined with the lack of resonance of the gauge suggested strongly that the gauge was faithfully recording the actual rise time of the pressure pulse in the sand, rather than filtering and attenuating a much sharper step change in pressure.
The findings suggested that DPG1 was capable of responding to a greater range of frequencies within the range 0-7000Hz than those captured in the groundshock tests within the range 0-1500Hz. This validated the groundshock measuring capability of DPG1.

3.5.7 Validating the pressure loading used during the calibration tests

A valid calibration of the DPGs would imply that the rate of pressure loading subjected to the DPGs would be similar to that experienced by the gauges during the groundshock tests.
A preliminary test performed on DPG1 during the calibration involved releasing a transient pressure into the chamber. The methodology behind this involved inserting a thin brass circular diaphragm which acted as boundary into the barrel of the gas gun, allowing the pressure to build up behind it. The brass diaphragm was then pierced using a manually operated drill, when 80 bars of pressure was ready to be released into the chamber. DPG1 was then removed from the calibration chamber and was replaced by an identical geometrically shaped diaphragm with a kulite gauge position flush to its top surface, as illustrated in plate 3.5.8. A pressure of 80 bar was then released into the chamber, causing the kulite gauge to respond.

DPG1

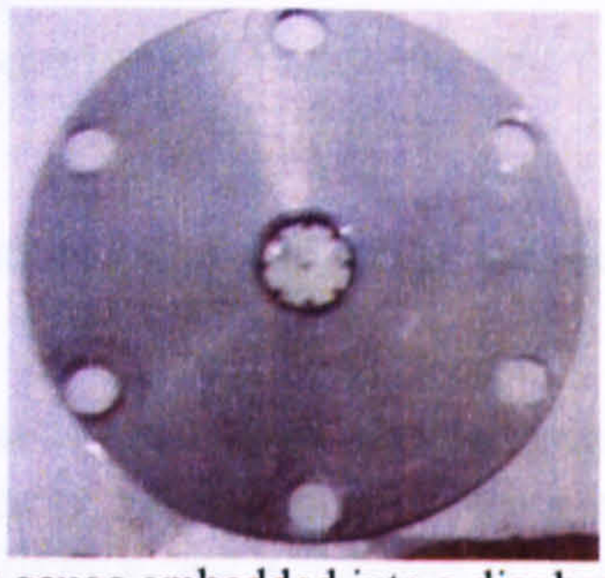

Kulite gauge embedded into a diaphragm

Plate 3.5.8 Kulite gauge inserted flush with the surface of a diaphragm

The voltage-time traces associated with the kulite gauge and DPG1, subjected to transient loading, are illustrated in figure 3.5.19. The response of both gauges to static loading is illustrated in figure 3.5.20.

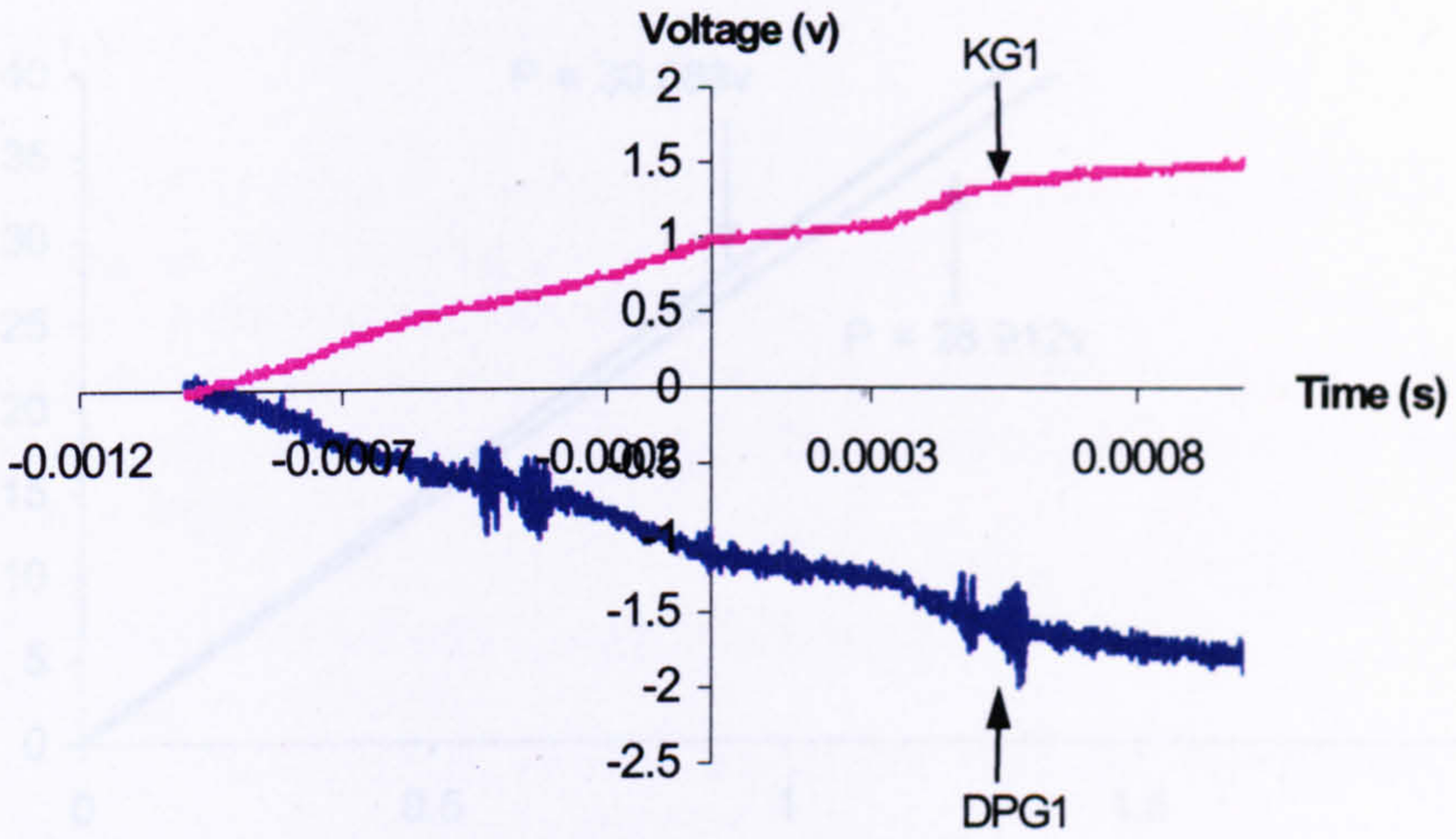

Figure 3.5.19 Voltage-time traces recorded by the kulite gauge and DPG1, subjected to transient loading.

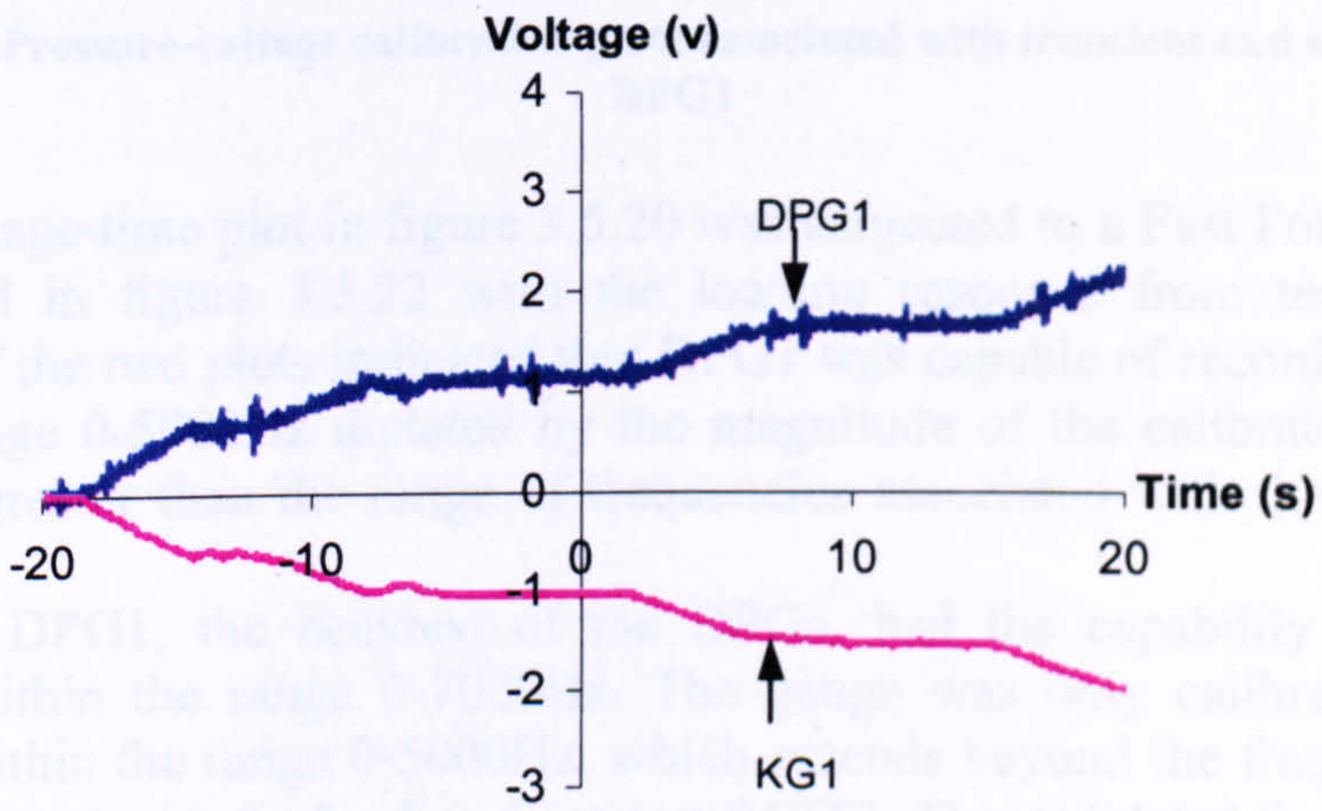

Figure 3.5.20 Voltage-time traces recorded by the kulite gauge and DPG1, subjected to static loading.

The pressure-voltage plots in figure 3.5.21 associated with the transient and static response of DPG1, both yield very similar linear relationships. As a result of this finding, the remaining DPGs were calibrated statically, for a number of reasons:

1. Greater control of the loading within the closed system of the calibration cell.
2. It was more difficult ensuring an elastic response of the diaphragms during transient loading.

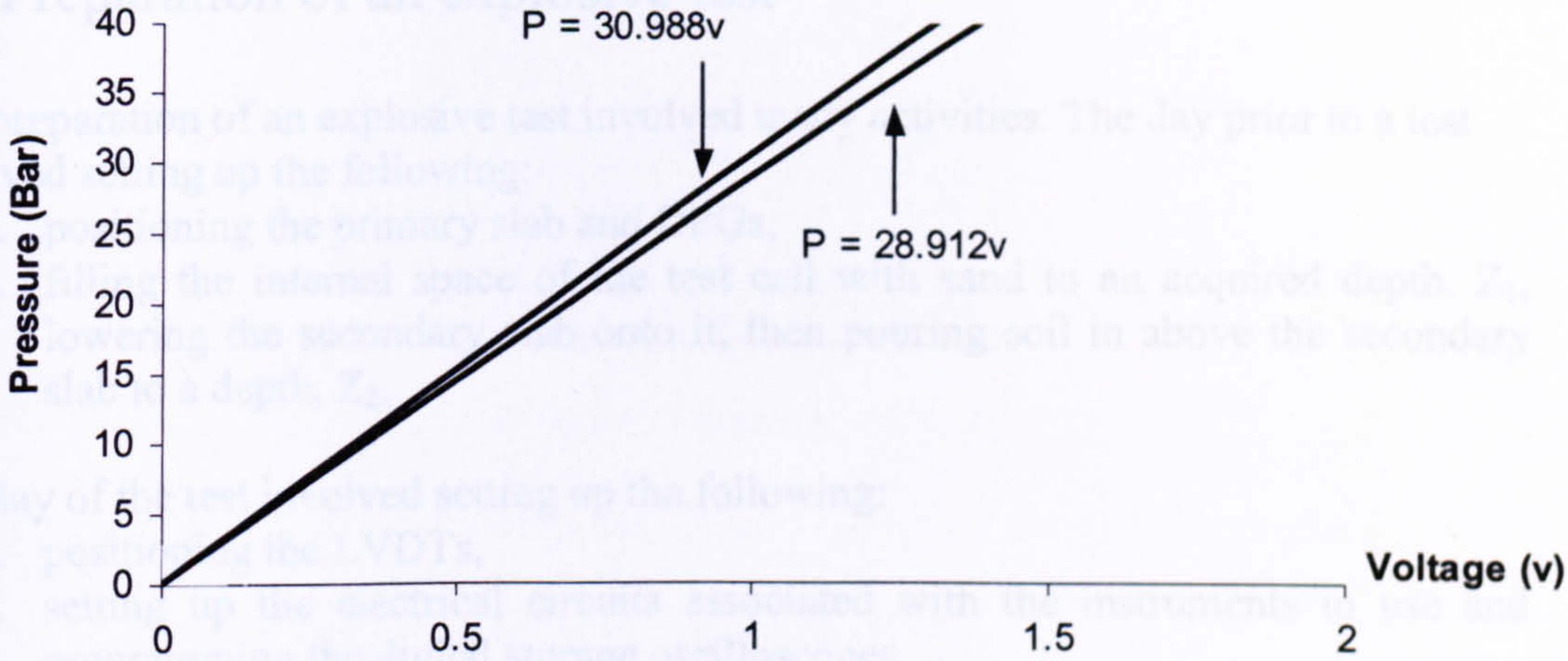

P=28.912v transient pressure calibration plot
P=30.988v static pressure calibration plot

Figure 3.5.21 Pressure-voltage calibration plots associated with transient and static loading of DPG1

The static voltage-time plot in figure 3.5.20 was subjected to a Fast Fourier Transform and illustrated in figure 3.5.22 with the loading response from test RCIT3. The comparison of the two plots indicated that DPG1 was capable of recording frequencies within the range 0-5000Hz dictated by the magnitude of the calibration load that is significantly greater than the range of frequencies associated with the load from test RCIT3.

Contextually, DPG1, the heaviest of the DPGs, had the capability of picking up frequencies within the range 0-7000Hz. The gauge was only calibrated to pick up frequencies within the range 0-5000Hz, which extends beyond the frequency range 0-1800Hz associated with the loading from test RCIT3. This validated the magnitude and the static loading used during the calibration procedure.

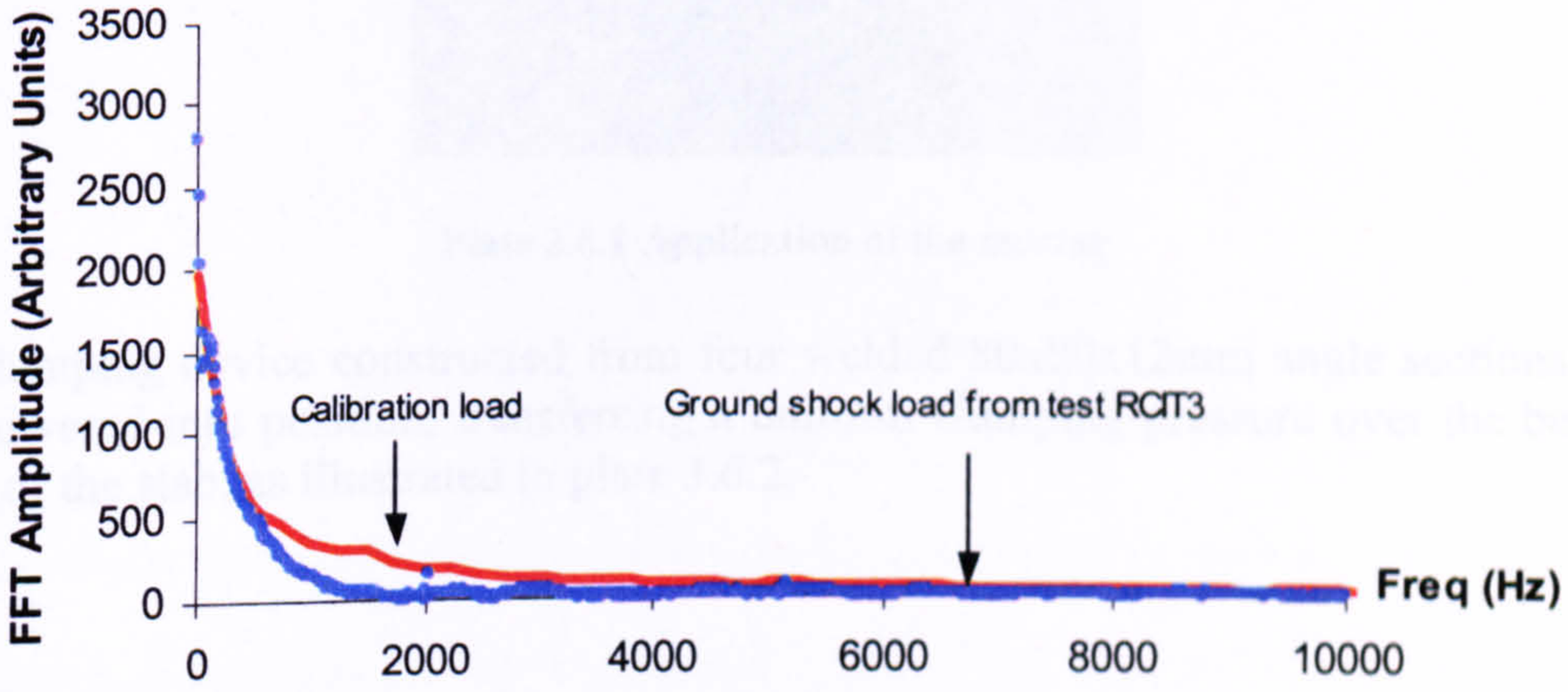

Figure 3.5.22 Comparison between the calibration and groundshock load within their frequency domains associated with the response of DPG1

3.6 Preparation of an explosive test

The preparation of an explosive test involved many activities. The day prior to a test involved setting up the following:

1. positioning the primary slab and DPGs,
2. filling the internal space of the test cell with sand to an acquired depth, Z_1, lowering the secondary slab onto it, then pouring soil in above the secondary slab to a depth, Z_2.

The day of the test involved setting up the following:

1. positioning the LVDTs,
2. setting up the electrical circuits associated with the instruments in use and programming the digital storage oscilloscopes,
3. positioning the charge.

3.6.1 Pre-test setup

A thin layer of mortar was initially applied to the top surface of the steel support frame that formed the bearing support for the primary slab. This compensated for the uneven bottom surface of the slab that was formed during casting. Another layer of mortar was then applied to the top face of the primary slab, as illustrated in plate 3.6.1. This took account of the uneven top surface that was formed during casting and ensured that the clamping system applied a uniform pressure around the perimeter of the slab.

Plate 3.6.1 Application of the mortar

The clamping device constructed from four welded 80x80x12mm angle sections, was then lowered into position, transferring a uniform clamping pressure over the bearing width of the slab, as illustrated in plate 3.6.2.

Plate 3.6.2 Clamping device

The next step involved positioning the DPGs on the top face of the primary slab as illustrated in plate 3.6.3. The eccentricities of the DPGs relative to the centre of the primary slab varied, depending upon the charge standoff.

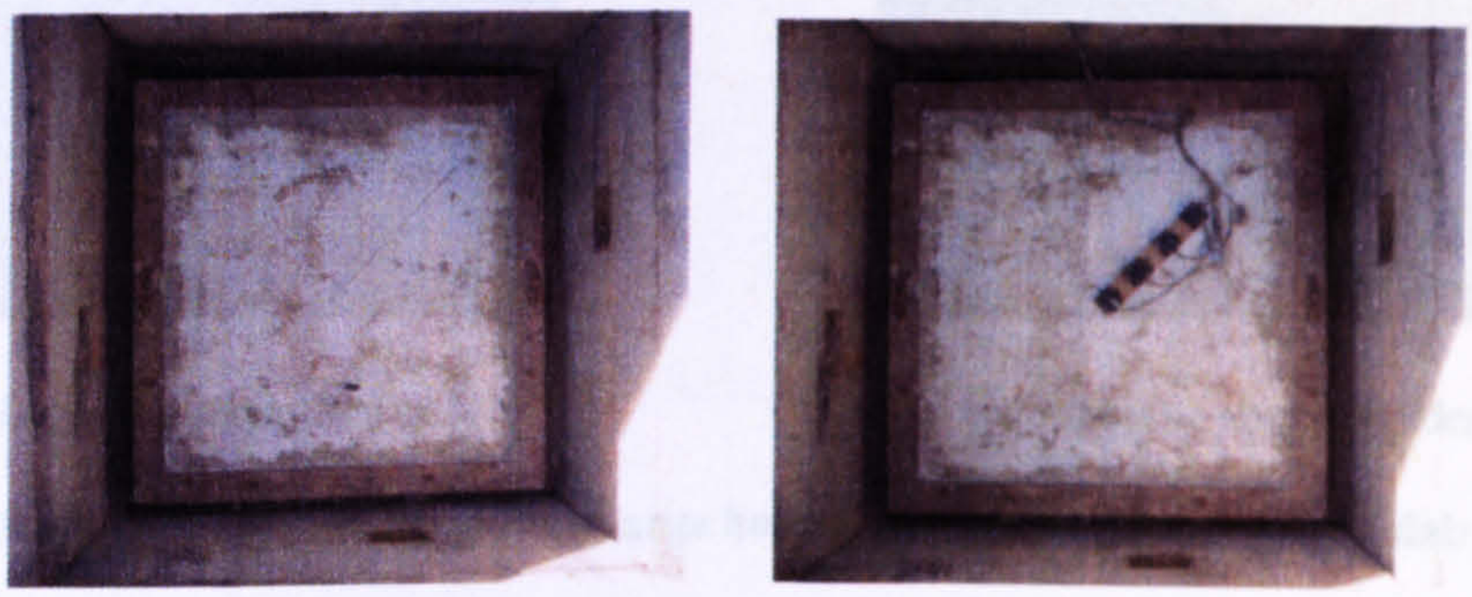

Plate 3.6.3 Positioning of the DPGs on the top face of the primary slab

Once the DPGs were positioned, a thin plastic bag was then inserted into the internal space of the test cell, to help contain the sand, followed by sheets of polystyrene, as illustrated in plate 3.6.4. The polystyrene ensured the confinement of soil volume over a plan area of 1000x1000mm.

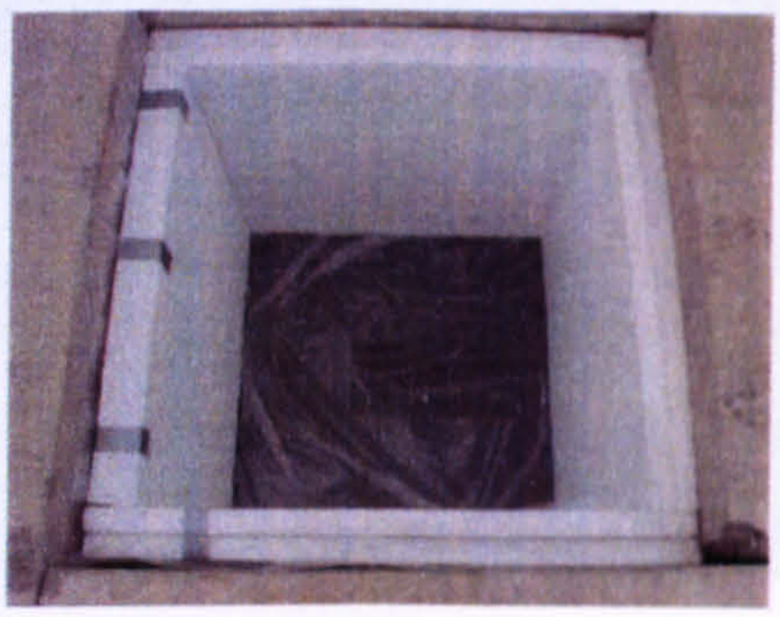

Plate 3.6.4 Positioning the polystyrene sheeting into the internal space of the test cell

The next task involved filling the internal space of the test cell with soil. This was performed manually using a shovel, compacting the soil in layers until the desired overburden depth was achieved. The effect of soil compaction on stress wave propagation has been discussed in detail in section 4.6. The degree of soil compaction was associated with values of density index, illustrated in table 4.6.6.The variability of such values in every test indicated a 'very dense' soil, in accordance with **Head**

(1992). The next major task involved drilling a hole through the secondary slab that was positioned on top of the first layer of soil overburden. The hole was drilled at an inclination of 70° to the horizontal, along plane O-B1 as illustrated in plate 3.6.5.
The charge holder illustrated in plate 3.6.5 was made of acetate and inserted into the drilled hole. It formed an inclined pathway through the soil overburden above the secondary slab. The charge could then be lowered down into the bottom of the charge holder, at a standoff above the primary slab. The charge holder prevented the charge from absorbing water contained within the soil that could have affected detonation.

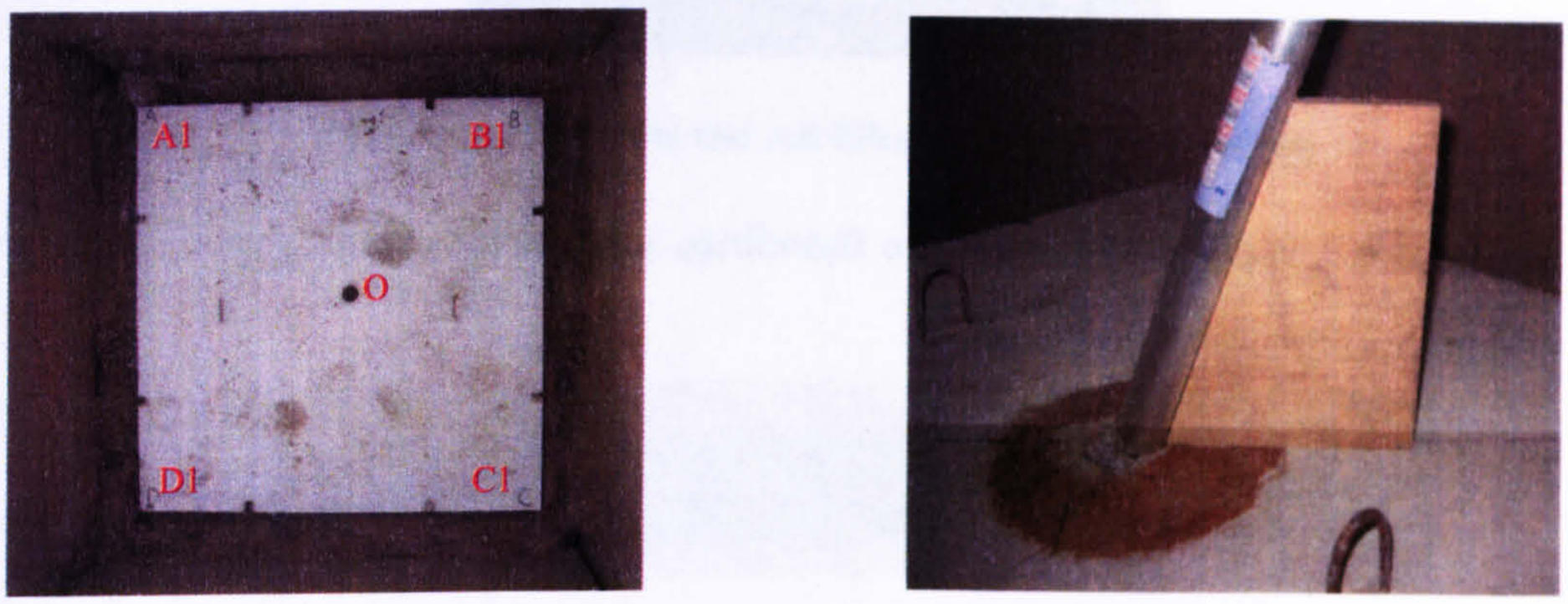

Plan of the secondary slab

Positioning the charge holder

Plate 3.6.5 Positioning of the charge holder relative to the secondary slab

The secondary slab containing the positioned charge holder was then lowered into the test cell on top of compacted soil overburden.
A second layer of polystyrene sheeting as illustrated in plate 3.6.6 was then inserted around the perimeter of the secondary slab.

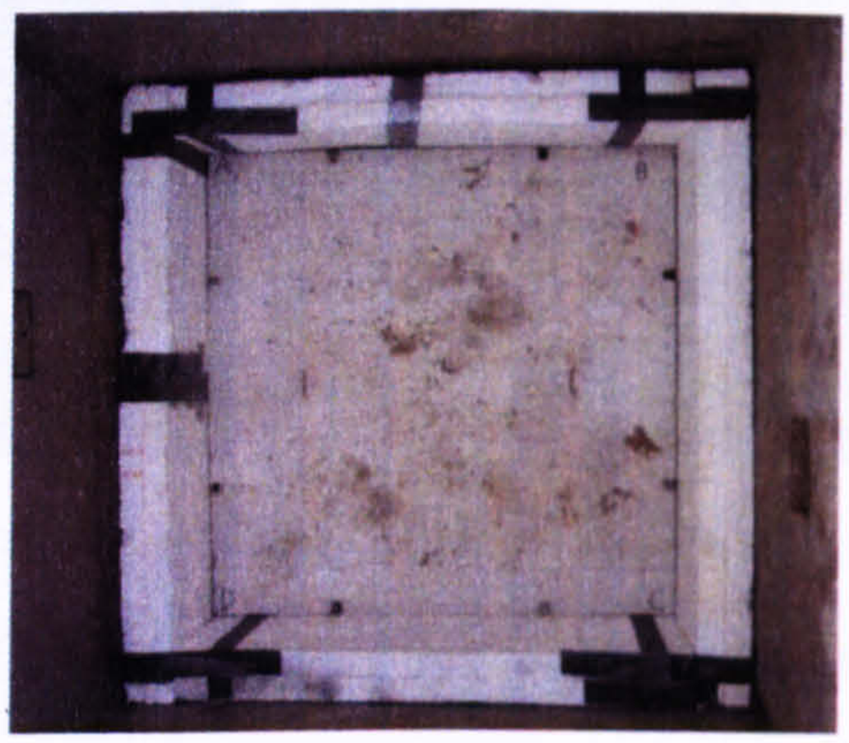

Plate 3.6.6 Positioning the second layer of polystyrene

The Soil overburden was levelled as illustrated in plate 3.6.7 followed by the lowering of the charge down into the charge holder. The charge holder was strong enough to cope with the lateral soil pressures imposed during soil compaction, preventing it from collapsing inwardly.

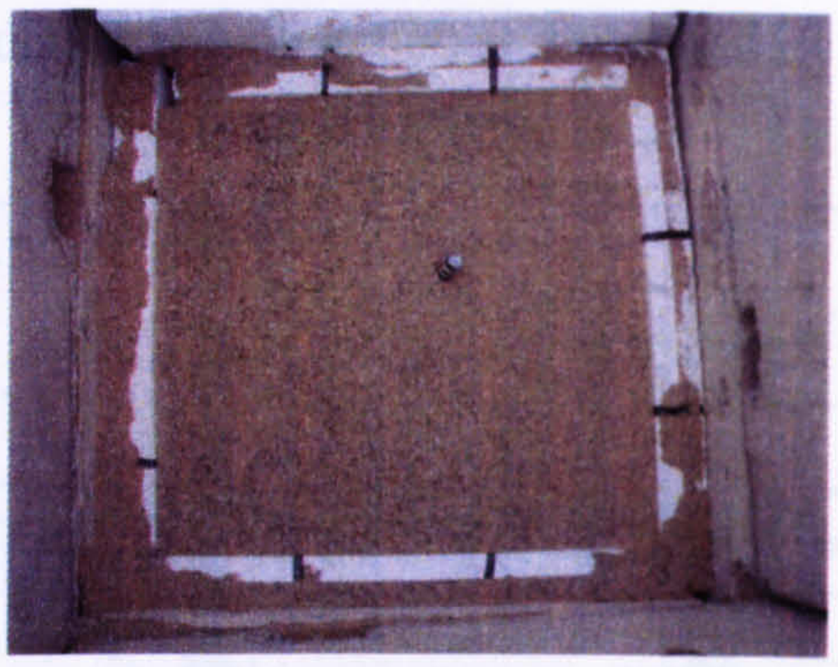

Plate 3.6.7 Plan of the test cell filled with both layers of soil

A charge template was made from cardboard as illustrated in plate 3.6.8, which was then filled with 183g of PE4.

Plate 3.6.8 Cylindrical charge mould

The detonator was then embedded within the charge then lowered into the charge holder as illustrated in plate 3.6.9.

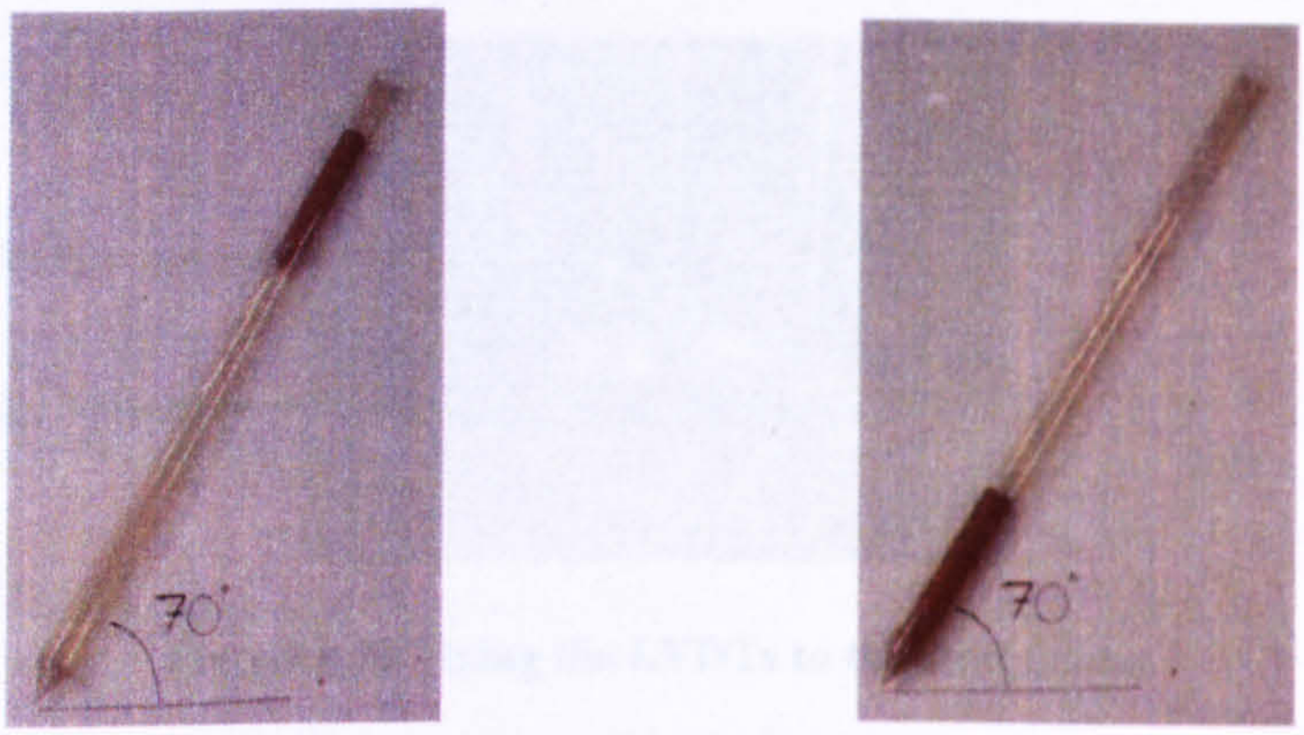

Entry of the charge into the charge holder Charge in position at a standoff from the primary slab

Plate 3.6.9 Movement of the charge down into the charge holder

The final test setup including instrumentation is illustrated in figure 3.6.1.

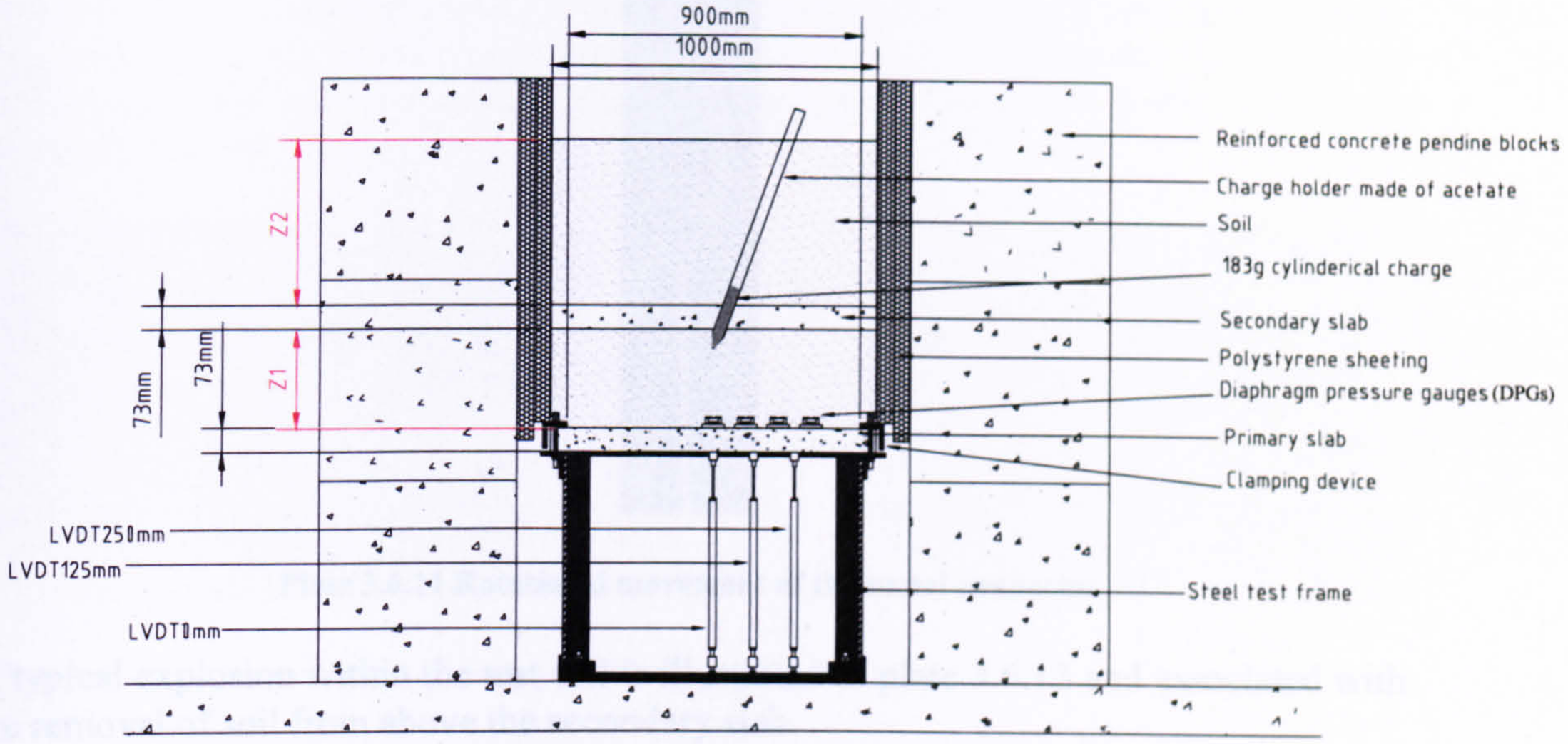

Z_1 = Soil overburden depth between the primary and the secondary slab
Z_2 = Soil overburden depth above the secondary slab

Figure 3.6.1 Cross-sectional elevation of an explosive test set up within the test cell

The deflection of the primary slab was recorded using LVDTs, connected through the concrete to the connectors on the bottom mesh. The LVDTs were bolted to the steel base plate that was welded to the steel test frame as illustrated in plate 3.6.10.

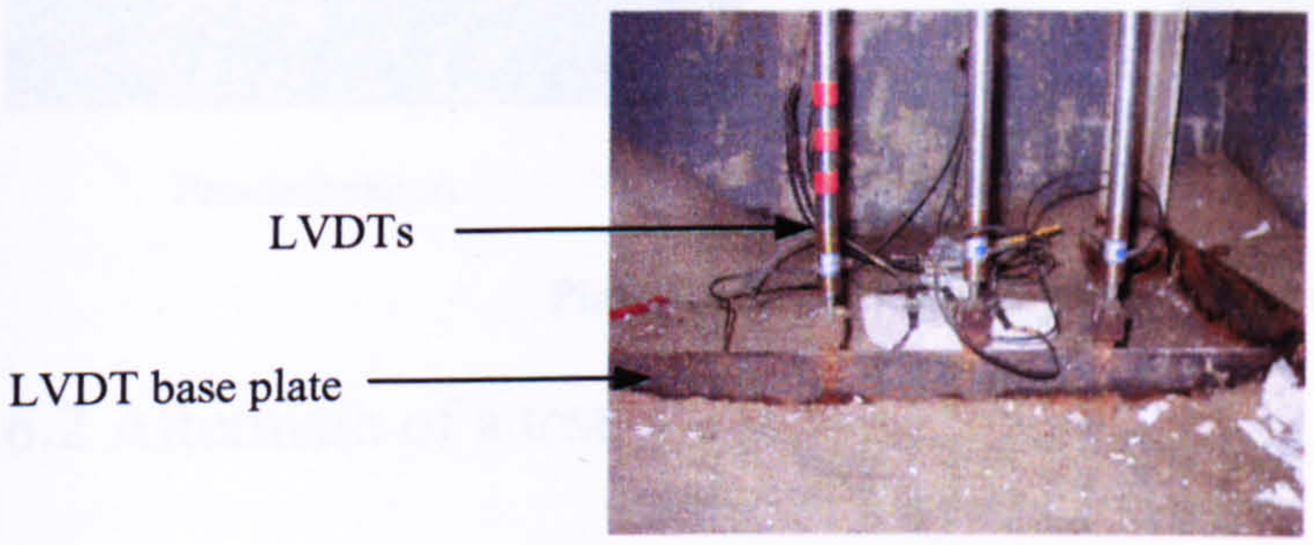

Plate 3.6.10 Fixing the LVDTs to the steel frame

Metal mountings were attached to each of the LVDTs as illustrated in plate 3.6.11. They allowed the LVDTs to be fixed in a vertical position beneath the bottom face of the primary slab but also giving it rotational stability during the bending of the slab. Without the ability to rotate, a fully fixed position would have caused the LVDTs to bend due to flexure of the slab.

Plate 3.6.11 Rotational movement of the metal connector

A typical explosion within the test cell is illustrated in plate 3.6.12 and associated with the removal of soil from above the secondary slab.

Pre-detonation

Post-detonation

Plate 3.6.12 Explosion within the test cell

3.6.2 Aftermath of a test

Once the test site was declared as being safe, the LVDTs were checked for damage and the formation of soil craters observed, as illustrated in plate 3.6.13. It was not within the objectives of the research to study the soil craters produced, leaving scope for further work.

Plate 3.6.13 Displacement of the soil

The loading produced within the test cell caused the pendine blocks to displace outwards, as illustrated in plate 3.6.14. Continuous displacement from each explosive test caused cracking of the blocks, but still ensured structural integrity. The displaced blocks had to be manoeuvred back into position prior to each test, which was a time consuming operation.

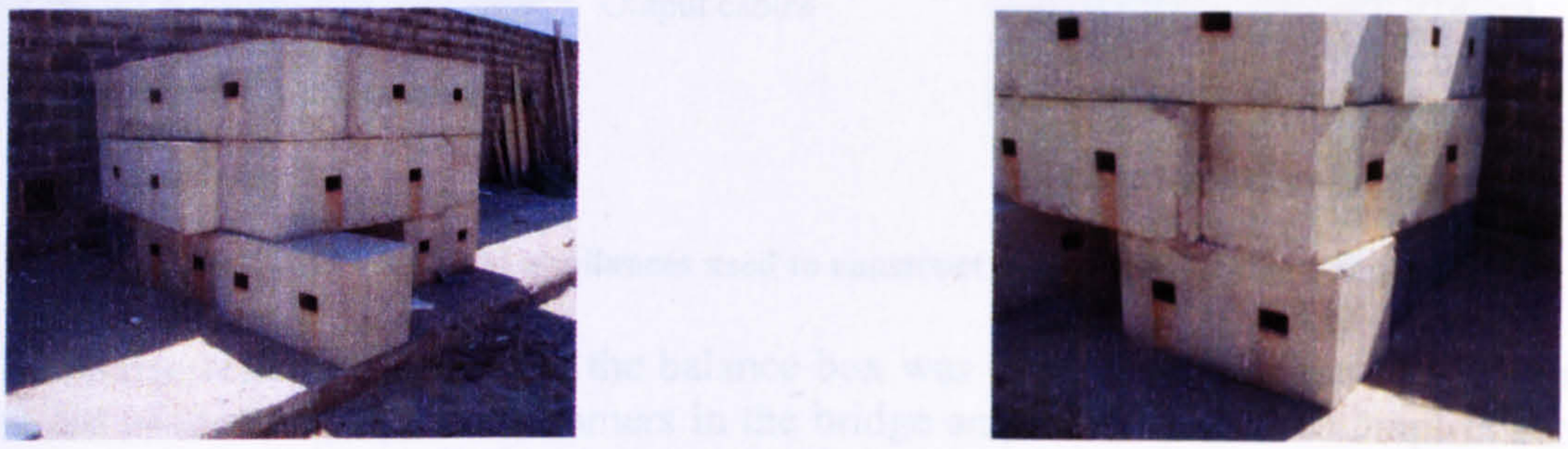

Plate 3.6.14 Damage to the displaced pendine blocks

3.6.3 Instrumentation setup

The instrumentation used during the experimental programme included:

1. linear variable displacement transducers – LVDTs,
2. diaphragm pressure gauges – DPGs,
3. strain gauges – SGs.

3.6.3.1 Linear variable differential transducer circuit setup

Each LVDT was connected to a transducer amplifier, powered externally by a connecting source. The induced output voltage was associated with the movement of the shaft in and out of the core that corresponded to the deflection of the primary slab After each test all three LVDTs and their circuits were checked for damage. All three LVDTs were positioned parallel together. The steel cores were pulled out by 70mm, corresponding to the length that was achieved when the LVDTs were positioned under the bottom face of the primary slab.

3.6.3.2 Diaphragm pressure gauge circuit setup

The strain gauges and DPGs had similar circuit setups. All strain gauges used had resistors connected to them, so that a change in strain would register a change in resistance. The active resistors had a maximum resistance of $120\,\Omega$, connected within a wheatstone bridge circuit. The cables attached to both types of instrumentation were connected to a balance box. It was used as a means of forming various wheatstone bridge circuits, as well as balancing them. It consisted of input terminals connecting to the cables of the instrumentation and output terminals with cables connecting to individual bridge amplifiers, as illustrated in plate 3.6.15.

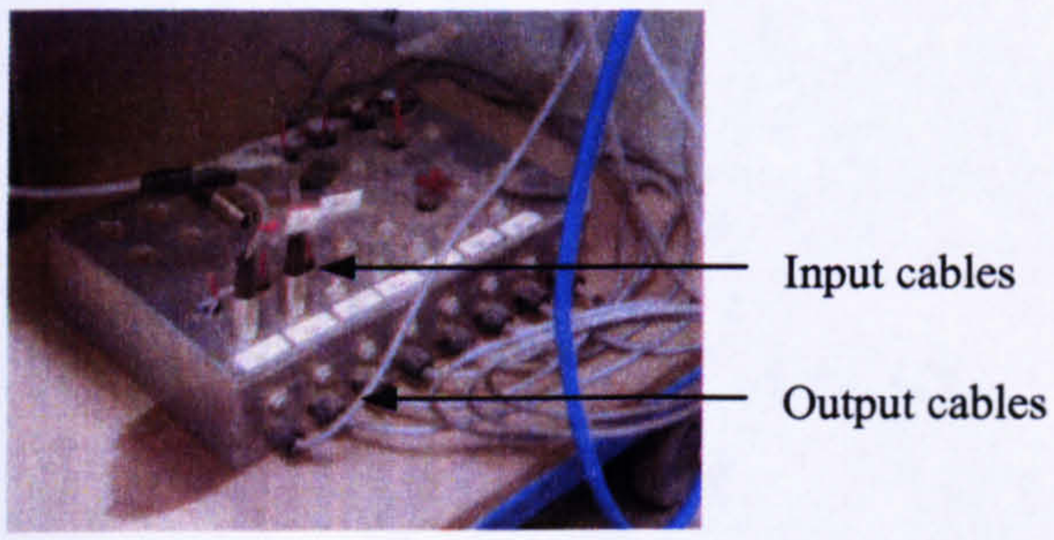

Balance box

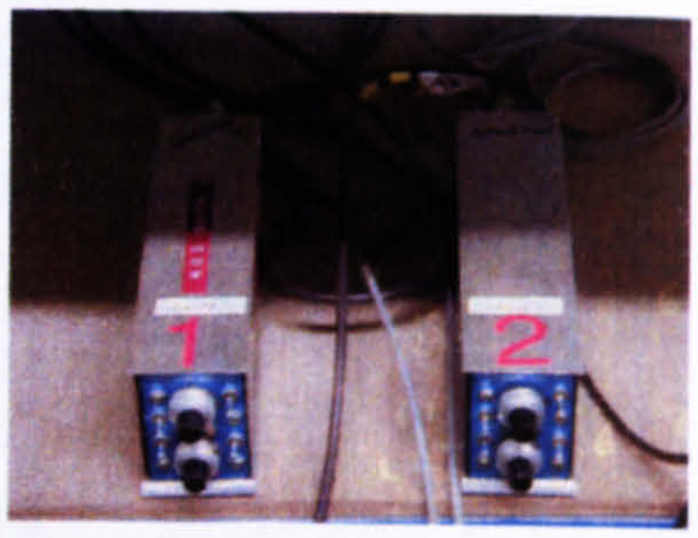

Bridge transducer amplifiers

Plate 3.6.15 Electrical appliances used to construct wheatstone bridge circuits

The coarse resistive trimmer in the balance box was used to balance the bridge, with the aid of medium and fine trimmers in the bridge amplifiers. Increased amplification ensured the trace had sufficient detail on the digital storage oscilloscope screen.
The bridge transducer amplifier was a type FE 359 TA and used throughout the experimental testing to supply a direct curent input voltage of 5v to a wheatstone bridge circuit. This was checked for accuracy using a digital voltmeter. Periodic rebalancing of the wheatstone bridge circuit was carried out during the instrumentation set-up prior to the detonation of the charge, to compensate for any drift taking place due to temperature change and any physical disruption to the wheatstone bridge circuit. On hot days it was common for the wheatstone bridge circuits to go out of balance, resulting in a re-balancing operation. The advantage of performing tests involving transient loading was that the load duration was short enough for the wheatstone bridge circuits to remain balanced.
Prior to each test, the response of all the DPGs were checked by connecting them into wheatstone bridge circuits, then manually exerting a pressure onto the diaphragms.
The digital voltmeter was then used to check the resistances of the resistors within the bodies of the DPGs. If the resistances were greater than 120Ω, it was assumed that there was a fault somewhere along the cable. If negligible resistances were identified, the resistor would be considered damaged and need a prompt repair before the next test.

3.6.3.3 Detonation of charge circuit setup

An L2A1 detonator was inserted into the cylindrical charge, 10mm below its surface. The detonator consisted of an exploding bridge wire that received a small voltage, causing its match head to ignite by the process of deflagration. A stress wave was then induced into the secondary explosive that increased in velocity. As the stress wave propagated through the booster pellet, a detonation reaction occurred. This simultaneously induced a shock front into the cylindrical charge of PE4, detonating it.
A break wire was then wrapped around the cylindrical charge, prior it being lowered down into the charge holder. The wire was connected to the trigger box, which in turn was linked to all digital storage oscilloscopes in use during a test. A single channel on each of the digital storage oscilloscopes was designated to recording the voltage-time trace for the snapping of the break. The snapping was associated with a sudden massive increase in voltage, due to an infinite resistance. The trigger voltage was set, in most tests, to 5v/division, ensuring that any electrical disturbances did not accidentally trigger the digital storage oscilloscopes prior to charge detonation. The

time duration between the detonation of the charge and response of each instrument could then be identified. These time values were essential in calculating approximate values for the loading wave velocities at various ranges in the soil, as described in section 4.6.2.1.

3.6.3.4 Digital storage oscilloscopes

Three digital storage oscilloscopes were used during the testing. Each scope was set to a direct current output, rather than an alternating curent output. A trace that has an alternating current output could be mistaken as the output from an instrument under load, due to the moving peaks. A direct current output from a non-responsive instrument would output a trace that was identified by a continuous flat line. It was easier to identify a change in the shape of a trace from a direct current output, rather than from an alternating current output.

Each oscilloscope in use during a test was set with a percentage of pre-trigger. This ensured that any phenomena associated with the response of the LVDTs, strain gauges and DPGs prior to detonation was recorded and differentiated from their true response under load. The pre-trigger was set between 10-20% of the total recorded time duration. It helped in eliminating any noise/electrical interference that might have been evident before detonation.

Setting the sensitivity was very important, as it determined whether the peaks of a trace were captured. Due to the unpredictable nature of the loading and the varying position of the charge, it was difficult to establish sensitivities that would ensure that all the peaks were captured. If the sensitivity was low, the voltage per division was increased, ensuring the entire trace was captured. The disadvantage limited the accuracy of the trace at crucial time intervals, capturing data points that appear jagged rather than smooth. This phenomenon is illustrated in figure 3.6.2.

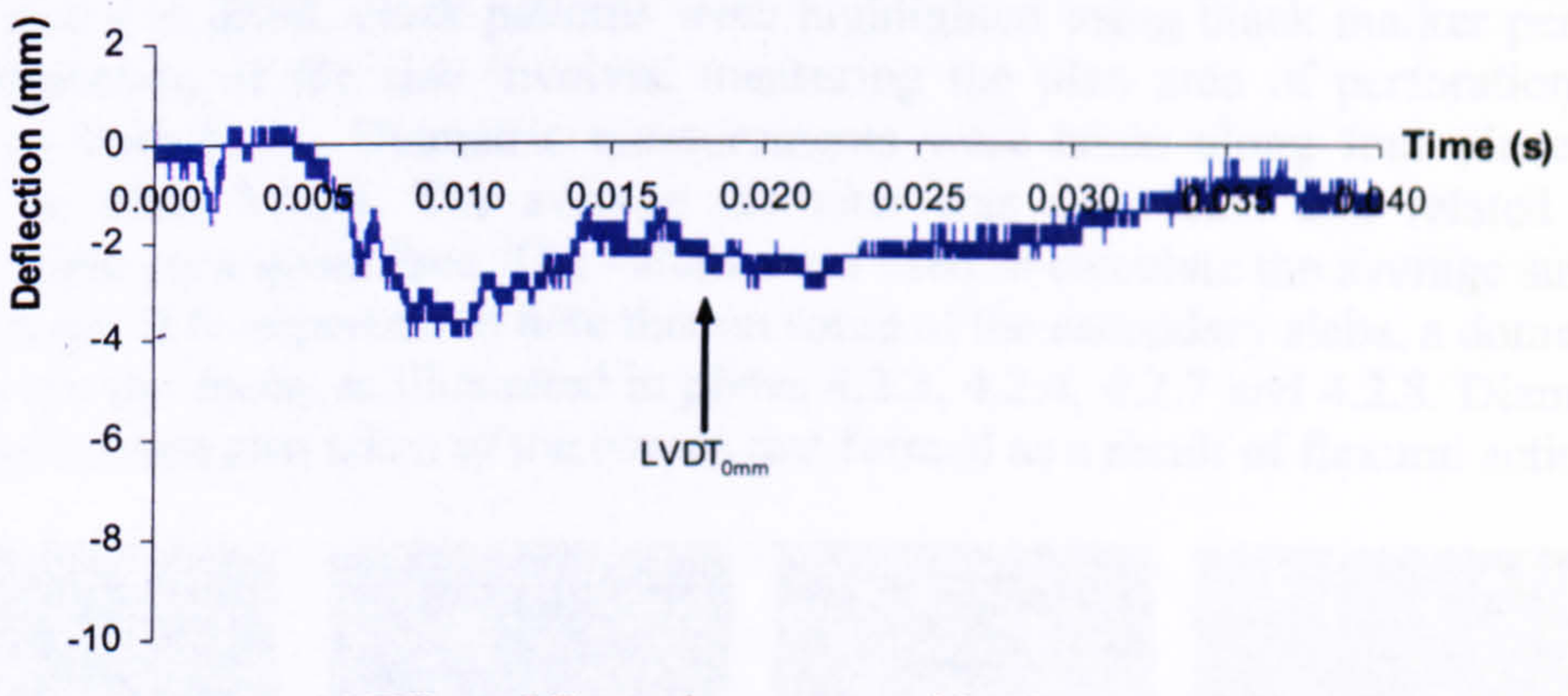

Figure 3.6.2 Effect of Capturing a trace with a low sensitivity

If the sensitivity was high the voltage per division decreased, increasing the accuracy of the data points, but increasing the probability of not capturing the peaks associated with the trace, as illustrated in figure 3.6.3.

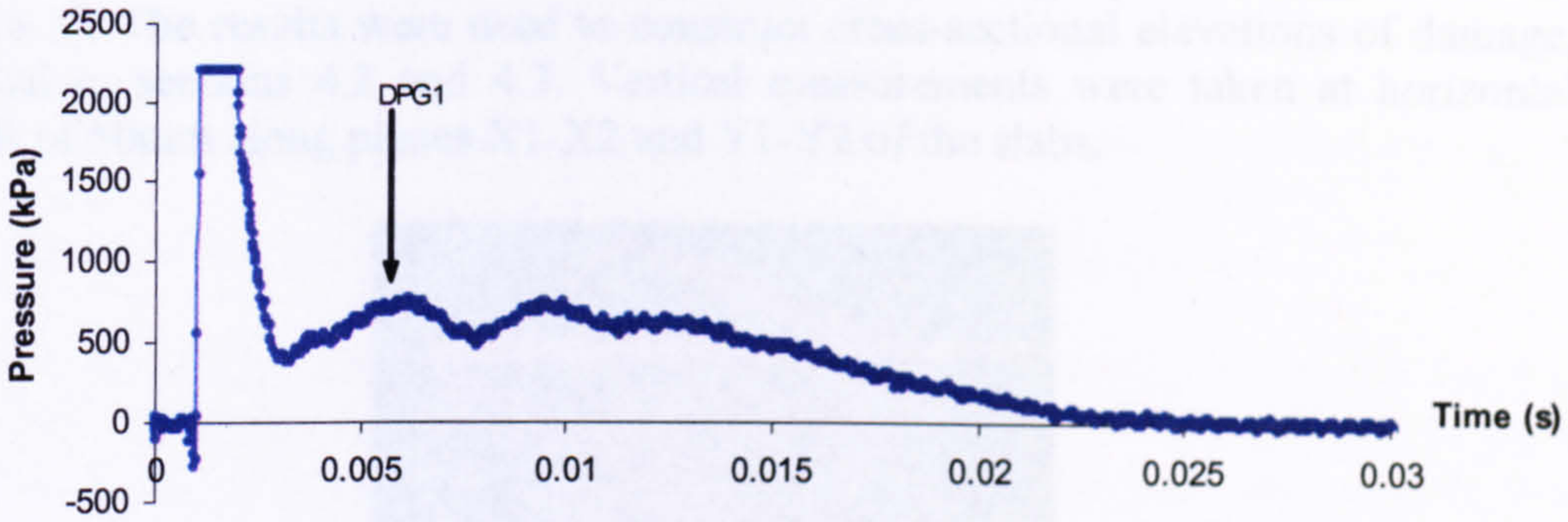

Figure 3.6.3 Effect of Capturing a trace with a high sensitivity

Setting the sensitivity was a trial and error procedure, which would improve as more of this work is undertaken.
The time base determined the rate at which the samples were recorded, within a range dictated by the sensitivity. A transient event would require a small time base, associated with a small time interval between captured samples. Time bases of magnitudes 5ms and 10ms were used. A static event would require a larger time base, as the duration between the capturing of samples would be large because of the slower response of the system under load.

3.6.4 Post test analysis

The disrupted soil overburden above the top face of the secondary slab was removed manually. The secondary slab was then removed carefully using the forklift truck and cleaned, using a pressurised water gun that removed black soot and sand that had been embedded within the cracks.
Once the slab had dried, crack patterns were highlighted using black marker pens. A damage inspection of the slab involved measuring the plan area of perforation and cratering on both faces. Diametric measurements were taken along four planes, as illustrated in plate 3.6.16. The average diameter was calculated that related to a particular crater on a given face. The values were used to calculate the average surface area of damage. It is important to note that on some of the secondary slabs, a dome was formed on the top faces, as illustrated in plates 4.2.3, 4.2.4, 4.2.7 and 4.2.8. Diametric measurements were also taken of the domes that formed as a result of flexural action.

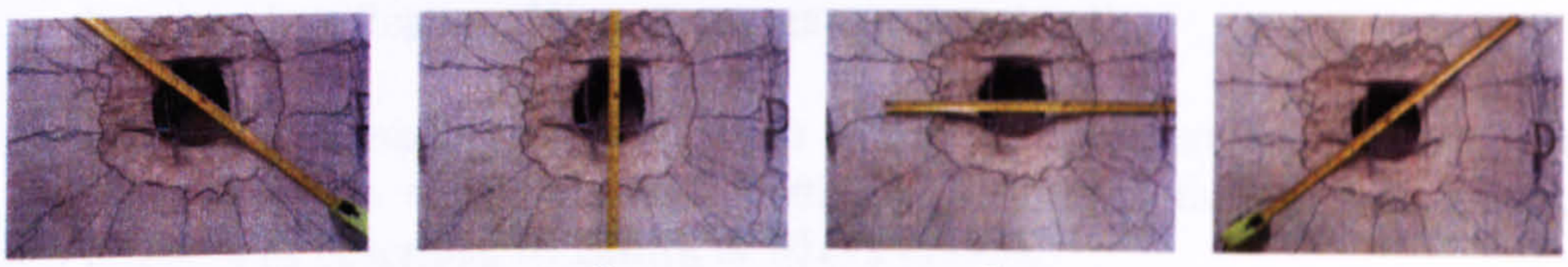

$ø_2$ **$ø_y$** **$ø_x$** **$ø_1$**

$ø_2$ =Diameter along plane A1-C1. $ø_y$ =Diameter in the along Y1-Y2 plane.
$ø_x$ =Diameter along plane X1-X2. $ø_1$ =Diameter along B1-D1 plane.

Plate 3.6.16 Measuring the surface plan area of damage associated with cratering and perforation

The primary and secondary slabs were both surveyed using a procedure illustrated in plate 3.6.17. The results were used to construct cross-sectional elevations of damage, illustrated in sections 4.2 and 4.3. Vertical measurements were taken at horizontal intervals of 50mm along planes X1-X2 and Y1-Y2 of the slabs.

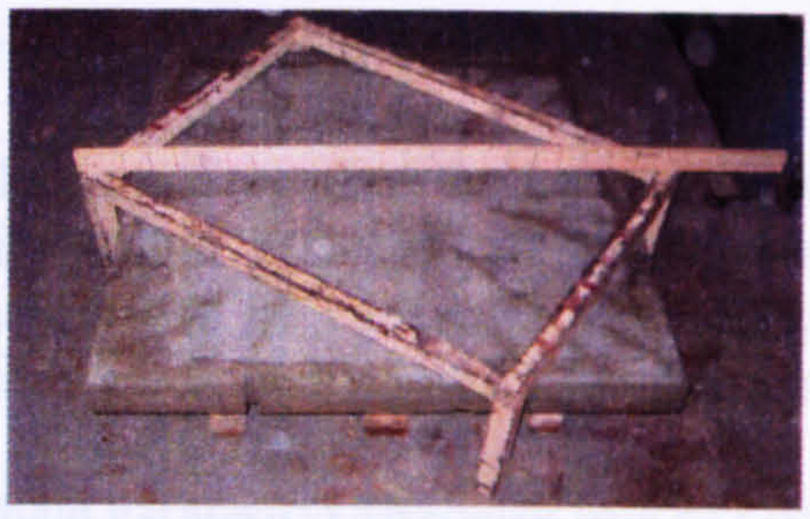

Plate 3.6.17 Method of surveying the slabs

3.7 Test repeatability

In total, 19 explosive tests were performed at a rate of approximately one every two weeks. In addition to the explosive tests, various other activities ran in parallel with the testing due to the limited duration available for the experimental work. Such activities involved construction of the reinforcement meshes, casting of the concrete, cube and cylinder testing, calibration of the LVDTs and DPGs and analysis of the damaged slabs.

If the explosive tests were carried out whist changing only one variable per test, a total of 84 tests would have been conducted, which would have been prohibited by the time available, without the suggestion of repeat testing.

An extended test matrix would still have been segregated into stages, but with different objectives and parameters, as illustrated in tables 3.7.1 and 3.7.2. Each Stage would also consist of a number of groups, which in turn would contain a number of tests.

An extended test matrix would involve separating measurements of loading recorded using pressure gauges and the damage identification of slabs into two phases. Both phases would involve the same number of tests and geometric setup.

1. Phase 1 (Primary steel plate) – measurements of load variation recorded using pressure gauges.
2. Phase 2 (Primary reinforced concrete slab) – measurement of deflection and damage identification. No pressure gauges involved.

The measurement of loading would involve an array of pressure transducers, inserted into the thickness of a steel plate and positioned flush with the top face, measuring face-on pressure as described by **Smith & Mays (1995).**

The results from both phases would be used to characterise the response of the primary slab with the aim of achieving a linear relationship as illustrated in figure 4.4.7. The maximum peak impulses recorded during phase 1 would be plotted against the maximum peak deflections recorded during phases 2.

The extended test matrix would be longer in duration to complete but containing fewer variables within a given test. Three important points would be considered when interpreting table 3.7.1.

1. Charge position parameter would only be used when a secondary slab is positioned and related to the charge standoff. As charge position varies, charge standoff also varies.
2. Only the charge standoff parameter would be used when a secondary slab is omitted.
3. Presence of a secondary slab would introduce the parameter Z_1.

The damaged primary slabs from Stage I of the test matrix were subjected to a varying number of cumulative hits within a soil overburden. A taller test cell would have allowed a greater depth of soil to be carried by the primary slab, ensuring all four charge positions were used in a cumulative attack for different values of Z_1.

Table 3.7.1 Variable and constant parameters associated with an extended test matrix

Stage	Charge standoff	Charge position	Z_1 (mm)	Z_2 (mm)	Secondary slab positioned	Secondary slab omitted	Primary slab positioned	Primary steel plate positioned
A	-	V	V_c	C	C	-	-	C
B	-	V	V_c	C	C	-		C
C	-	V	V_c	C	C	-	V_c	
D	-	C	C	V	V	-	-	C
E	V	-	-	-	-	C	-	C
F	V	-	-	-	-	C	C	-

C=constant
V=variable
V_c = Remains constant within a group of tests, but varies throughout the groups in the stage
Z_1 = Soil overburden a confined above and below the top face of the primary and bottom face of the secondary slab
Z_2 = Soil overburden above the top face of the secondary slab

Stage A would involve the identification of damaged secondary slabs, subjected to cumulative loading from variable charge positions. A primary steel plate would be used instead of a primary reinforced concrete slab for two reasons:

1. used solely to carry the soil overburden, rather than assessing its response,
2. faster turn around of tests with an undamaged steel plate remaining in position.

Stages B and C would be similar to Stage I and have identical test geometries. Stage B would determine the measurement of load across a steel plate. Stage C would identify the damage to a primary reinforced concrete slab, whilst a secondary slab was also subjected to cumulative loading. The results from both stages would be used to associate damage with loading.

The damaged primary slabs subjected to cumulative loading from Stage I indicated a lesser degree of damage because a fresh secondary slab was replaced during the cumulative loading. This would not occur in Stage C.

Stage D would be similar to Stage II but with a positioned primary steel plate instead of a primary reinforced concrete slab. The results would determine the influence a variation in the soil overburden above a secondary slab had to the loading across the primary steel plate.

Stages E and F would indicate a similarity with Stage III. Both would be geometrically similar with the admittance of a secondary slab. Stage E would involve a primary steel

plate in measuring the loading. Stage F would involve damage identification of a primary reinforced concrete. The results from both stages would be used to associate damage with loading. The results from Stages B, C and Stages E, F would be used to identify the energy absorption ability of a secondary slab, based upon results from Stage I tests RCIT9-11 and Stage III. The extended test matrix would allow a greater number of data points to be analysed, rather than a limited number. An indication of the tests within a stage and their core objectives are illustrated in table 3.7.2.

Table 3.7.2 Identification of stages from the original test matrix

Stage	Number of groups	Number of tests	Objectives
A	4	16	Identifying the damage to a reinforced concrete secondary slab associated with variable charge positions. Assess whether a reduction in Z_1 influences the damage to a secondary slab due to stress wave reflection from the steel primary plate
B	4	16	Determining the loading magnitude across a primary steel plate when secondary slabs are subjected to cumulative loading for different values of Z_1
C	4	16	Identifying the damage to a reinforced concrete primary slab when both the primary and secondary slabs are subjected to cumulative loading for different values of Z_1.
D	1	4	Assess whether a reduction in Z_2 influences the damage to the secondary slab as well as the loading across the steel plate
E	4	16	Determining the loading magnitude across a primary steel plate, with variable charge standoffs and admitted secondary slabs.
F	4	16	Identifying the damage to a primary reinforced concrete slab, subjected to cumulative loading from variable charge standoffs and admitted secondary slabs.

Z_1 = Soil overburden a confined above and below the top face of the primary and bottom face of the secondary slab
Z_2 = Soil overburden above the top face of the secondary slab

Even with this rationalisation, a total of 19 tests still had to be conducted, this being the minimum considered sensible for a parametric study. The possibility of six stages of testing would have increased the number of data points, allowing any spurious points to be identified and eliminated easier. Stages A-F were instead reduced to Stages I, II and III. The limitation on duration precluded the possibility of a comprehensive series of repeat tests. As each test contained results associated with more than one variable, it was crucial to set up each test with prudence as well as identifying the extent to which the variability of parameters would influence the loading. Such parameters are stated as follow:

1. concrete strength,
2. soil compaction,
3. soil moisture content.

The consistencies of these parameters during experimental testing have all been discussed in Chapter 4 and 5 with reference to the following:

1. influence on groundshock loading,
2. damage identification of the primary and secondary slabs.

The ability of all the instrumentation used to respond accurately to groundshock has been discussed in section 5.1. Re-calibration also occurred on a regular basis, ensuring all instrumentation was functional at the start of an explosive test. This yielded an overall confidence in the quality of the experimental results.

Chapter Four

Results

4.1 Positioning of instrumentation and orientation of the primary and secondary slabs

The geometry of both the primary and secondary slabs were identical, as illustrated in figure 4.1.1. The corner reference points A1, B1, C1, D1 were essential when differentiating between the top and bottom faces. The diagonals of a slab were associated with planes O-A1, O-B1, O-C1 and O-D1, orthogonal axes along planes O-Y1, O-Y1, O-X1 and O-X1 and quadrants A1, B1, C1 and D1.
The primary slab contained DPGs positioned on its top face along plane O-B1 and LVDTs on the bottom face along plane O-X2
The secondary slab contained an artificially inclined drilled hole, at an offset from the centre. Charges were variably positioned within the hole.

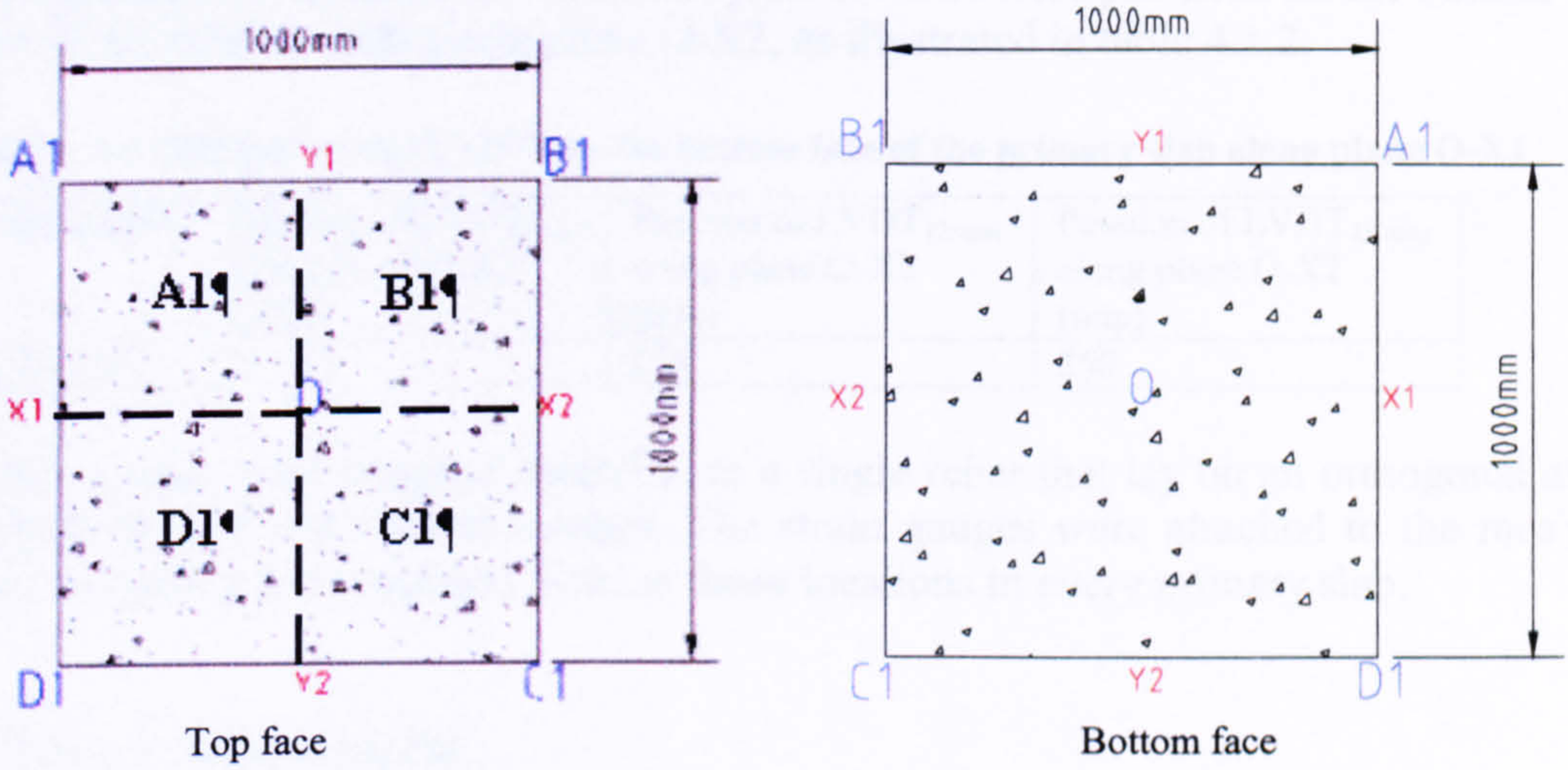

Figure 4.1.1 Reference points on the top and bottom faces of a primary and a secondary slab

4.1.1 Positioning of the instrumentation

Pressure-time histories were recorded by DPGs positioned at designated positions along plane O-B1, as illustrated in table 4.1.1. The DPGs were associated with diaphragms of a variable thickness. The thinnest associated with DPG3, positioned the furthest away from the centre of the slab responding to loading of a smaller magnitude as compared to that experienced by DPG1.

Table 4.1.1 Positions of the DPGs on the top face of the primary slab along plane O-B1

Test number	Charge standoff (mm)	Position of DPG1 along plane O-B1 (mm)	Position of DPG2 along plane O-B1 (mm)	Position of DP3 along plane O-B1 (mm)	Position of DPG4 along plane O-B1 (mm)
RCIT1	540	0	370	470	270
RCIT2	440	0	200	300	100
RCIT3	350	0	200	300	100
RCIT4	300	0	200	300	100
RCIT5	340	0	200	300	100
RCIT6	240	0	200	300	100
RCIT7	150	0	200	300	100
RCIT8	100	0	200	300	100
RCIT9	190	0	200	300	100
RCIT10	90	150	350	450	250
RCIT11	0	150	350	450	250
RCIT12	113	150	350	450	250
RCIT13	13	200	350	450	250
RCIT17	190	0	200	300	100
RCIT18	90	150	350	450	250
RCIT19	0	150	350	450	250

The deflection-time histories recorded by the LVDTs were positions on the bottom face of the primary slab along plane O-X2, as illustrated in table 4.1.2.

Table 4.1.2 Positions of the LVDTs on the bottom face of the primary slab along plane O-X1

Test number	Position of $LVDT_{0mm}$ along plane O-X2 (mm)	Position of $LVDT_{125mm}$ along plane O-X2 (mm)	Position of $LVDT_{250mm}$ along plane O-X2 (mm)
RCIT1-19	0	125	250

Strain gauges were attached centrally, to a single rebar that lay on an orthogonal axis in both the top and bottom meshes. The strain gauges were attached to the meshes prior to casting and remained fixed at those locations in every primary slab.

4.2 Secondary slabs

Stage I of the test matrix was segregated into groups of tests. Each group contained a number of tests that were dictated by charge positions. Groups 1 and 2 contained 4 tests, dictated by four charge positions. Subsequent groups contained fewer tests, as the soil overburden above the primary slab was reduced.

It is important to state that although a perforation might be observed on the plan area of a secondary slab, its cross-sectional elevations do not illustrate this in all cases. This is because the perforation would have formed at an offset from the centre of the slab. Some of the slabs were damaged during transportation preventing them from being surveyed accurately.

4.2.1 Damaged secondary slabs from Stage I group 1 of the test matrix

The soil overburden confined between the top and bottom face of the primary and secondary slab in group 1 was 500mm. The soil overburden above the secondary slab remained constant at 500mm.

4.2.1.1 Test RCIT1

The damage to both faces of secondary slab RCB73IT1 is illustrated in plate 4.2.1.

Top face: Circumferential cracks surrounded the central area of the slab. Square cracks occurred outside the circumferential crack zone. No cracks were present near the corner perimeters in quadrants A, C and D.

Bottom face: An increase in crack number and concentration. Radial cracks initiated from the circumference of the crater, perpendicular and propagate outwards. These radial cracks did not appear to extend to the boundaries of the slab. There also appeared to be discontinuous circumferential cracks confined between radial cracks.

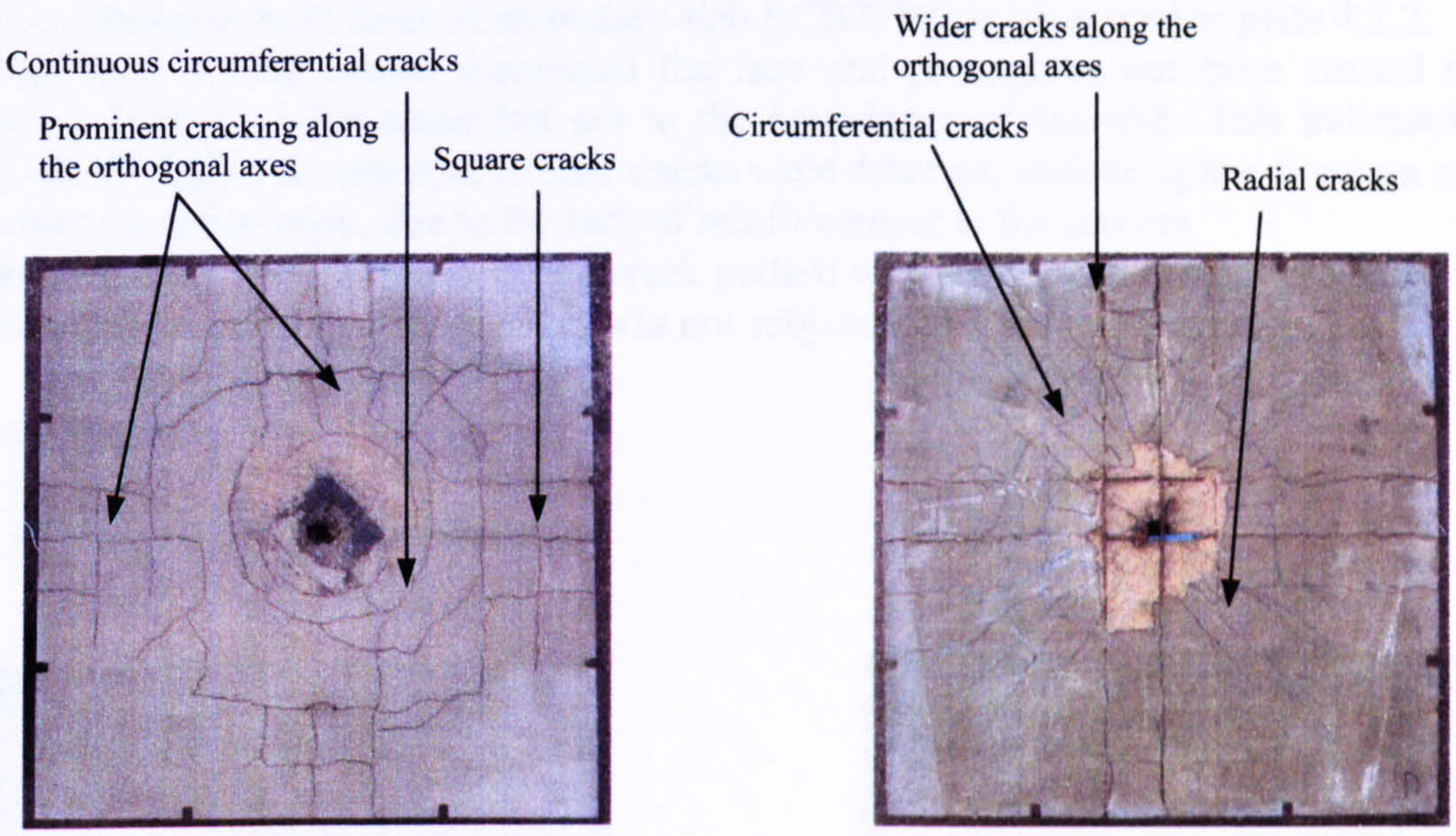

Plate 4.2.1 Top and bottom faces of secondary slab RCB73IT1

Cross-sections through slab RCB73IT1 are illustrated in figure 4.2.1.

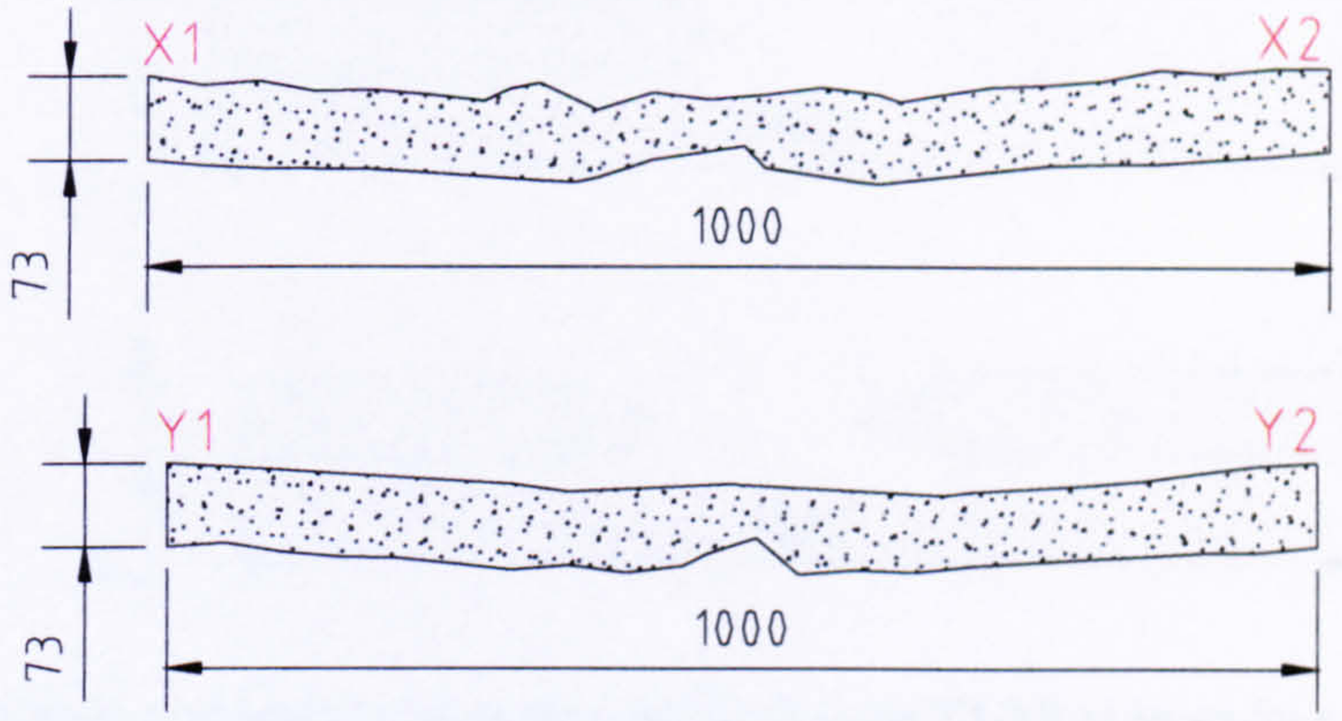

Figure 4.2.1 Cross-sectional elevation through X1-X2 and Y1-Y2 of secondary slab RCB73IT1

4.2.1.2 Test RCIT2

The damage to both faces of secondary slab RCB73IT2 is illustrated in plate 4.2.2.
Top face: Radial cracks dominated the face and propagated out from around the circumference of the crater but not to the boundaries of the slab. This indicated a localised region of response. Corner cracks were detected, indicating the direction of a reflective stress wave, due to the lack of reinforcement at the corners
Bottom face: The geometry of the crack pattern was very similar to that produced on the top face, implying that the slab was not subjected to a flexural response.

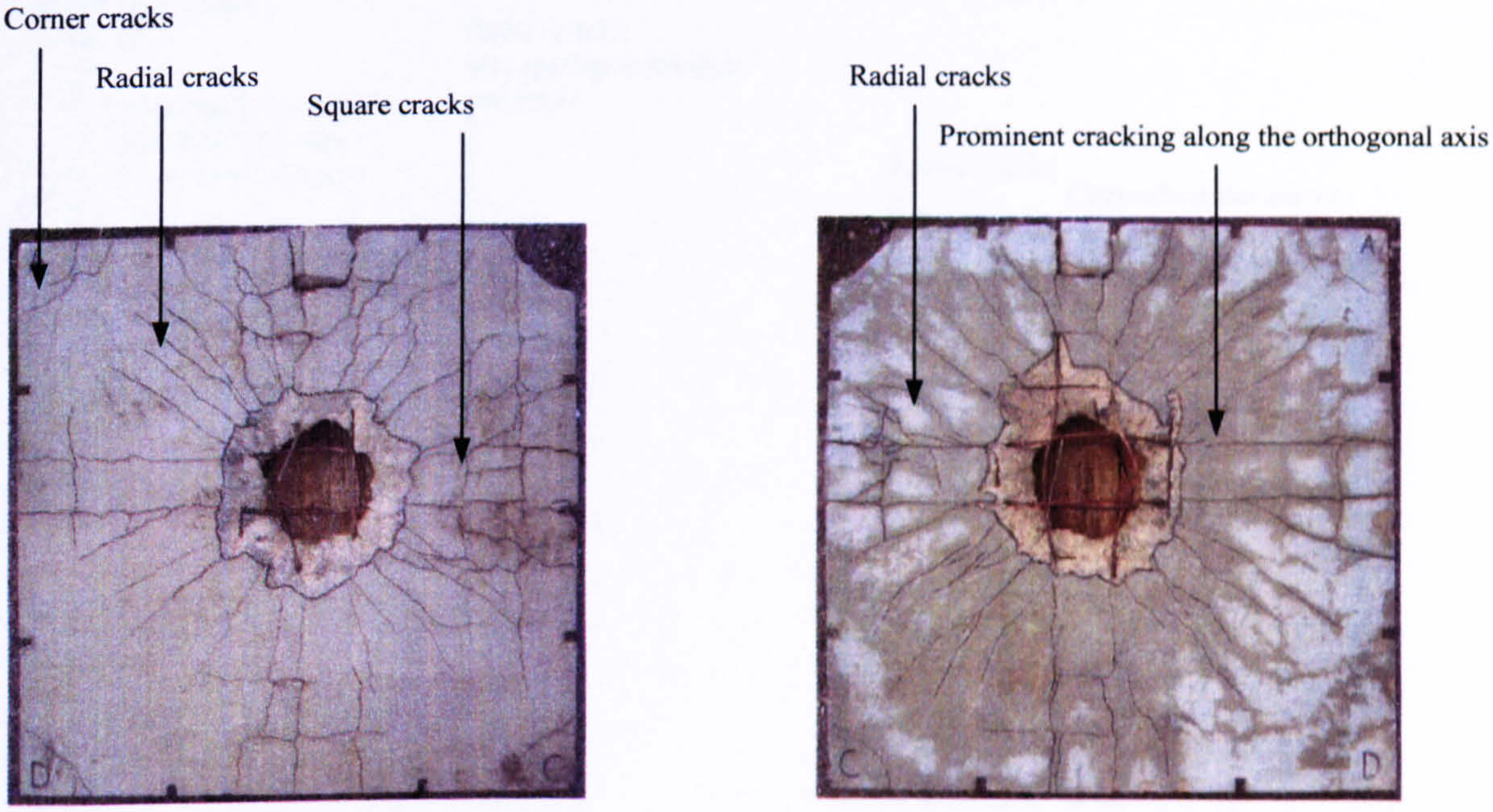

Plate 4.2.2 Top and bottom faces of secondary slab RCB73IT2

Cross-sections through slab RCB73IT2 are illustrated in figure 4.2.2.

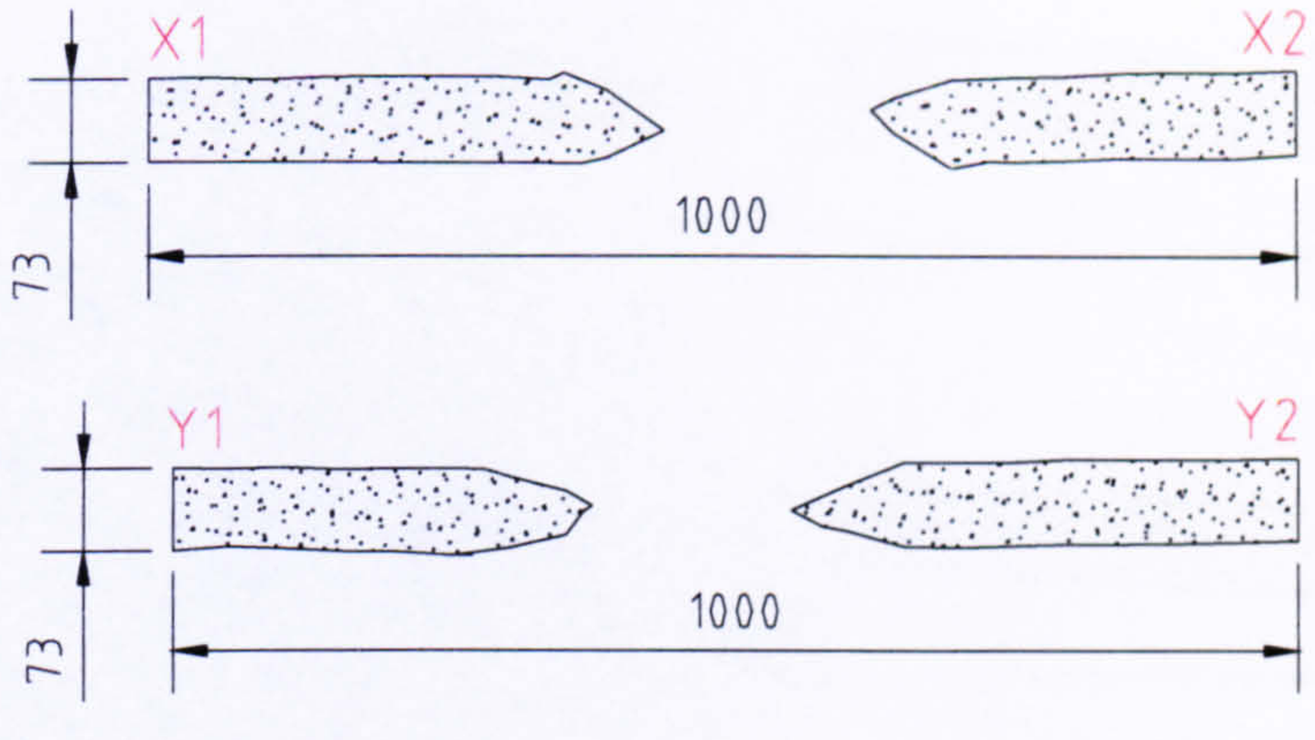

Figure 4.2.2 Cross-sectional elevation through X1-X2 and Y1-Y2 of secondary slab RCB73IT2

4.2.1.3 Test RCIT3

The damage to both faces of secondary slab RCB73IT3 is illustrated in plate 4.2.3.
Top face: Large concentration of radial cracks dominated the entire surface, apart from within quadrant D. They propagated from the circumference of the crater out to the perimeter of the slab. A dome region was formed, indicating a local flexural response by a large discontinuous circumferential crack
Bottom face: Widely spaced circumferential cracks appeared to propagate at a radial distance away from the crater. Rebar cracks were evident at reference points X1, X2, Y1 and Y2.

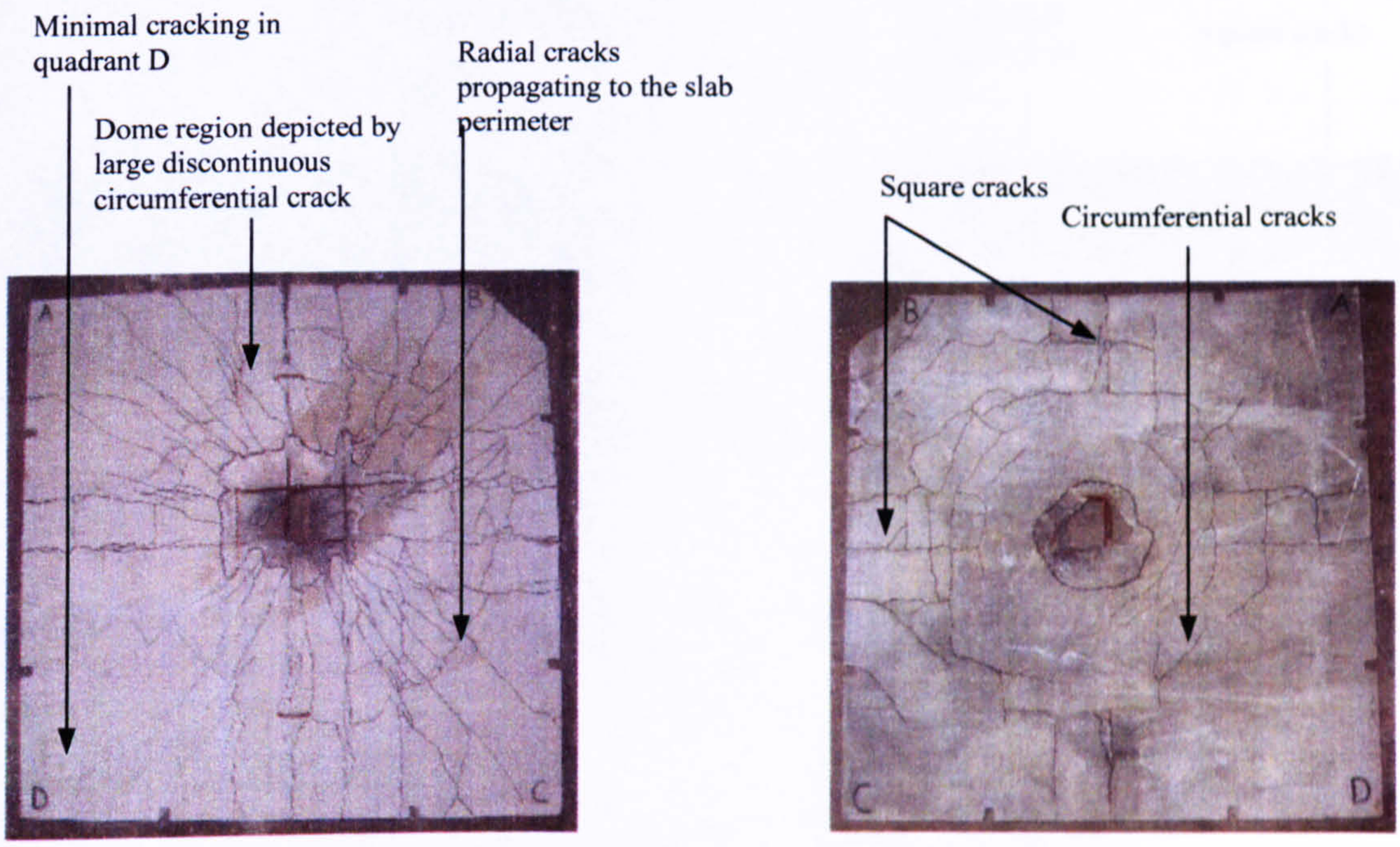

Top face

Bottom face

Plate 4.2.3 Top and bottom faces of secondary slab RCB73IT3

Cross-sections through slab RCB73IT3 are illustrated in figure 4.2.3.

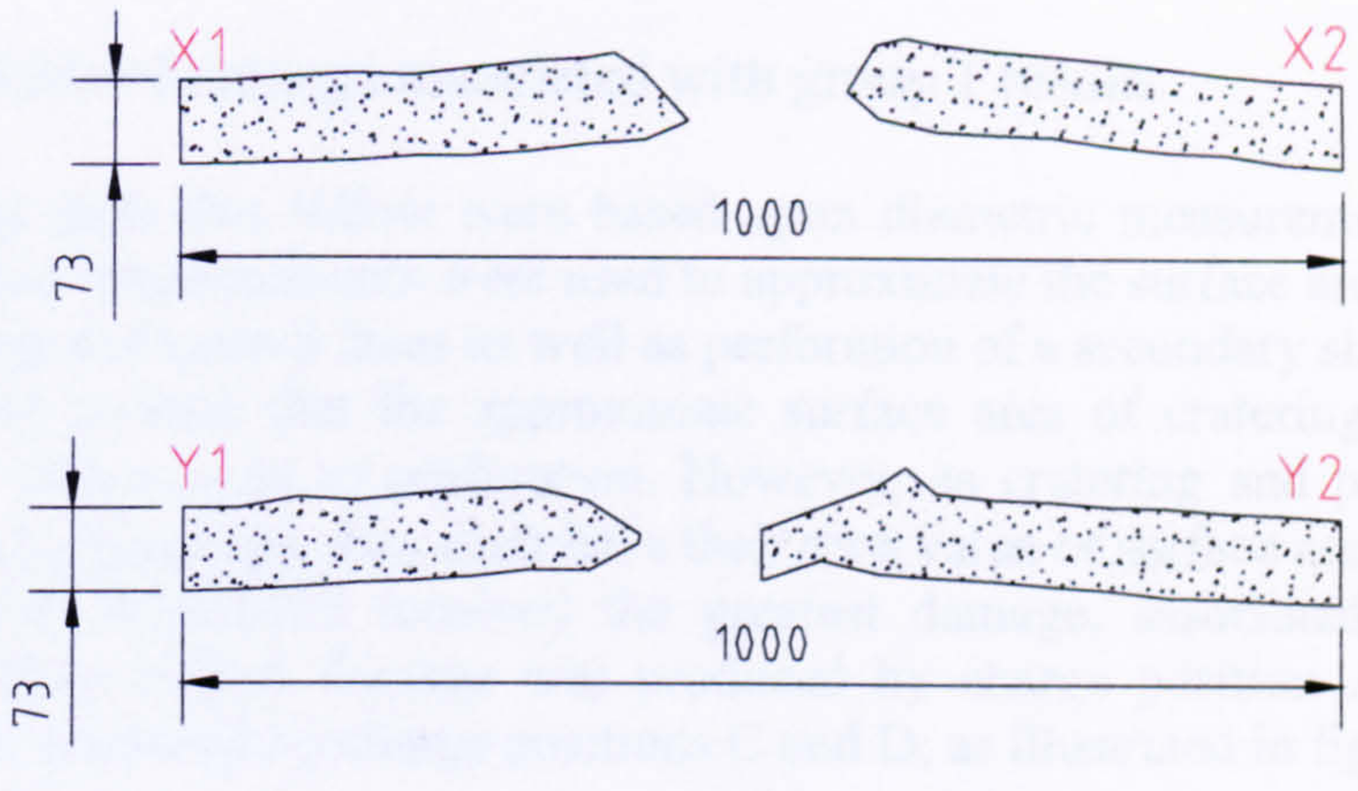

Figure 4.2.3 Cross-sectional elevation through X1-X2 and Y1-Y2 of secondary slab RCB73IT3

4.2.1.4 Test RCIT4

The damage to both faces of secondary slab RCB73IT4 is illustrated in plate 4.2.4.
Top face: Continuous radial cracks propagated from around the circumference of the crater to the sides of the slab. Cracking appeared to be consistent in all four quadrants.
Bottom face: Widely spaced circumferential cracks were concentrated centrally on the face. Radial cracks did not appear to be evident. Square cracks were evident at reference points X1, X2, Y1 and Y2.

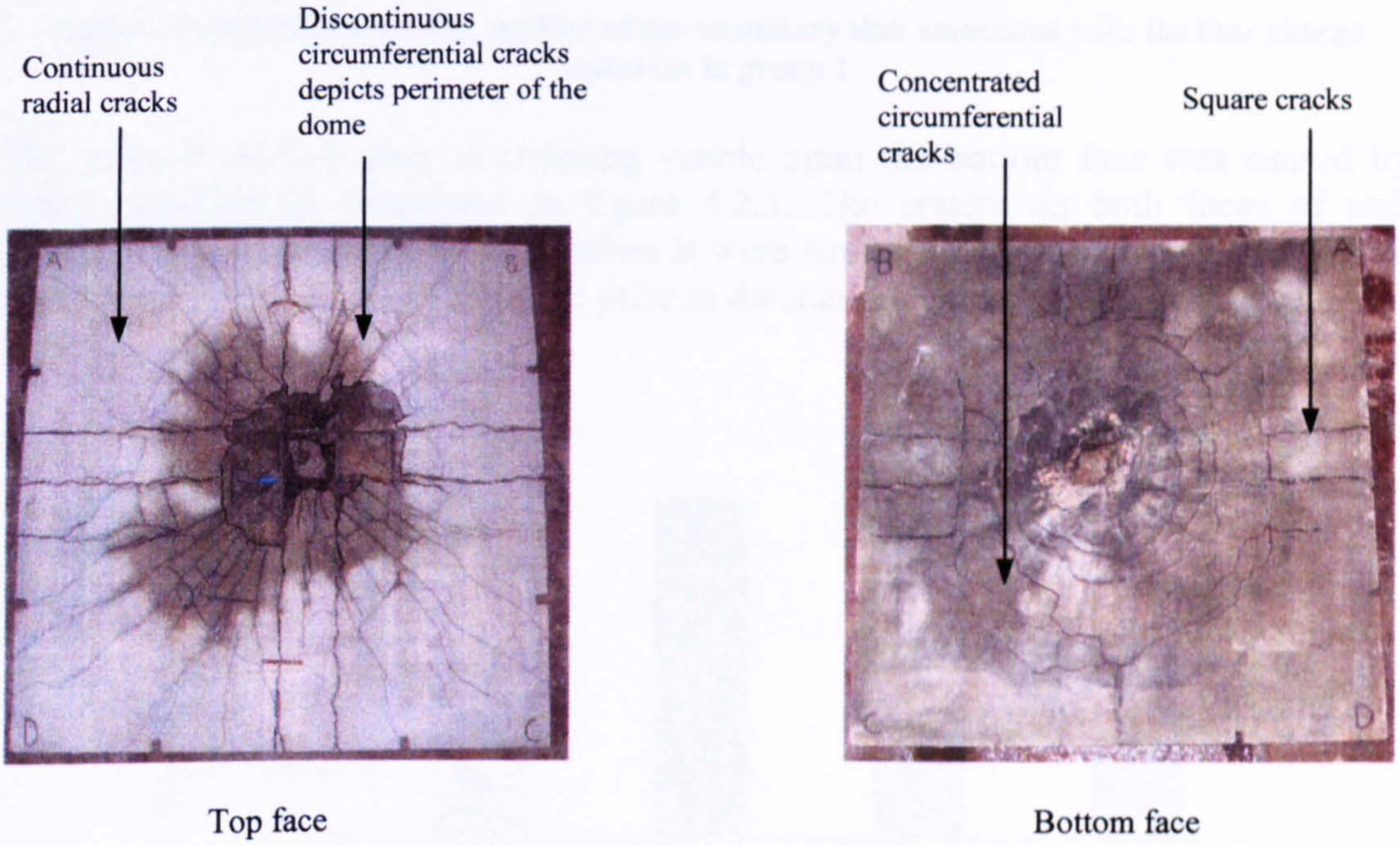

Plate 4.2.4 Top and bottom faces of secondary slab RCB73IT4

4.2.1.5 Analysis of damage associated with group 1 results

The graphical plots that follow were based upon diametric measurements, recorded manually. These measurements were used to approximate the surface area of cratering on both the top and bottom faces as well as perforation of a secondary slab.
It is important to state that the approximate surface area of cratering included the approximate surface area of perforation. However, as cratering and perforation are different forms of damage, they each have their own value of surface area.
Secondary slab RCB73IT2 received the greatest damage, associated with charge position B. The smallest damage was produced by charge position A and similar damages were produced by charge positions C and D, as illustrated in figure 4.2.4.

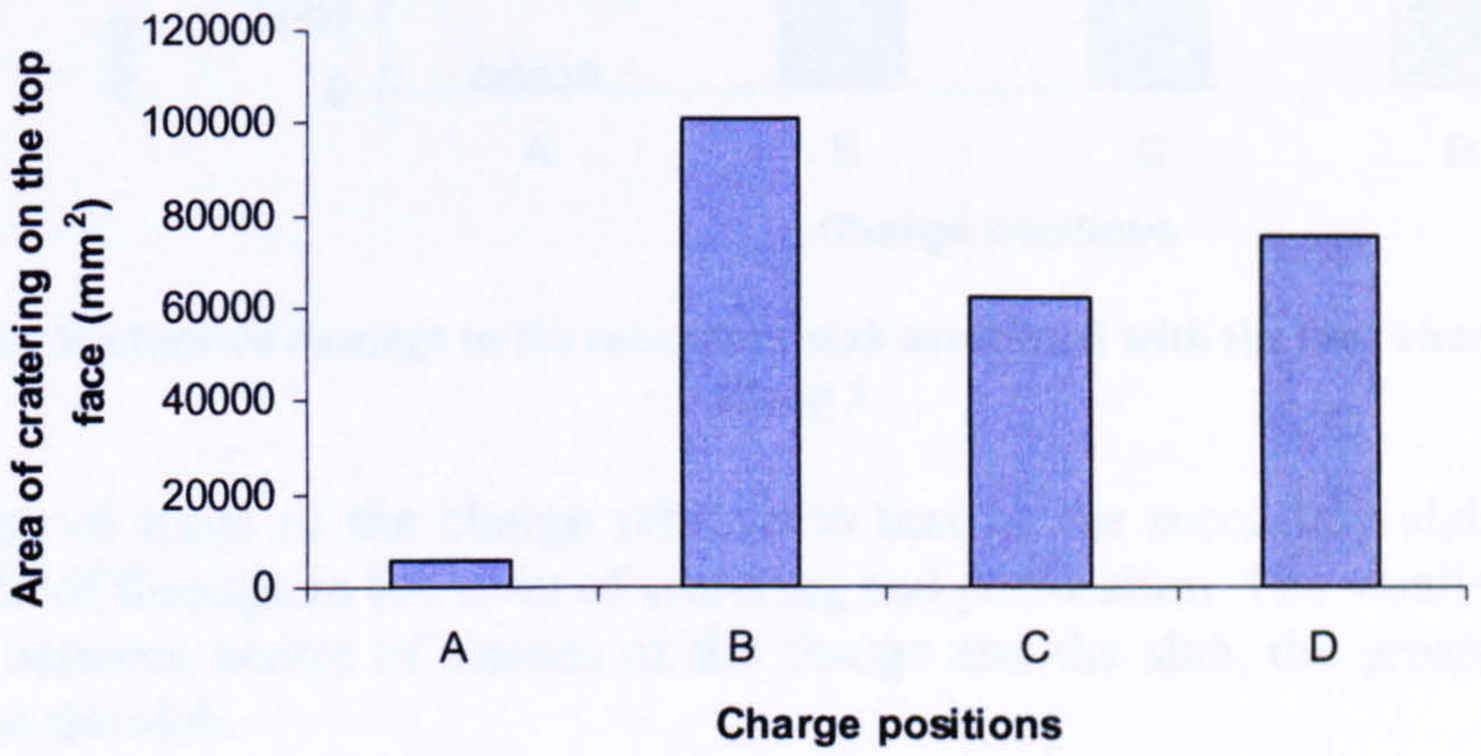

Figure 4.2.4 Cratering on the top face of the secondary slab associated with the four charge positions in group 1

The greatest surface area of cratering visible upon the bottom face was caused by charge position B, illustrated in figure 4.2.5. The craters on both faces of slab RCB73IT2 subjected to charge position B were similar in surface area. There was an equal distribution of charge volume prior to detonation, above and below the centre of mass of the slab.

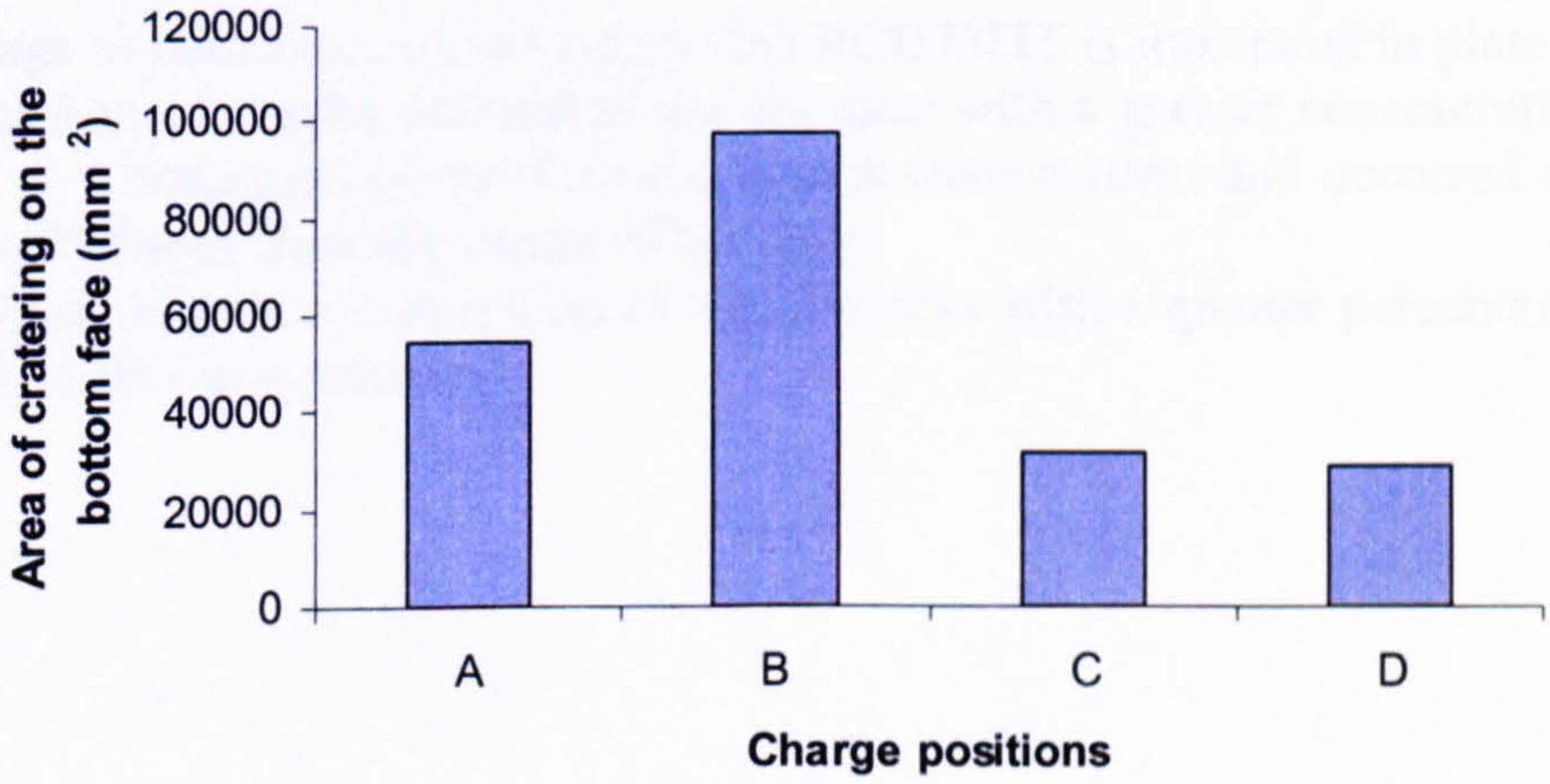

Figure 4.2.5 Cratering on the bottom face of the secondary slab associated with the four charge positions in group 1

Charge position B caused the greatest surface area of perforation, three times greater in area than the second greatest damage, caused by charge position C, as illustrated in figure 4.2.6.

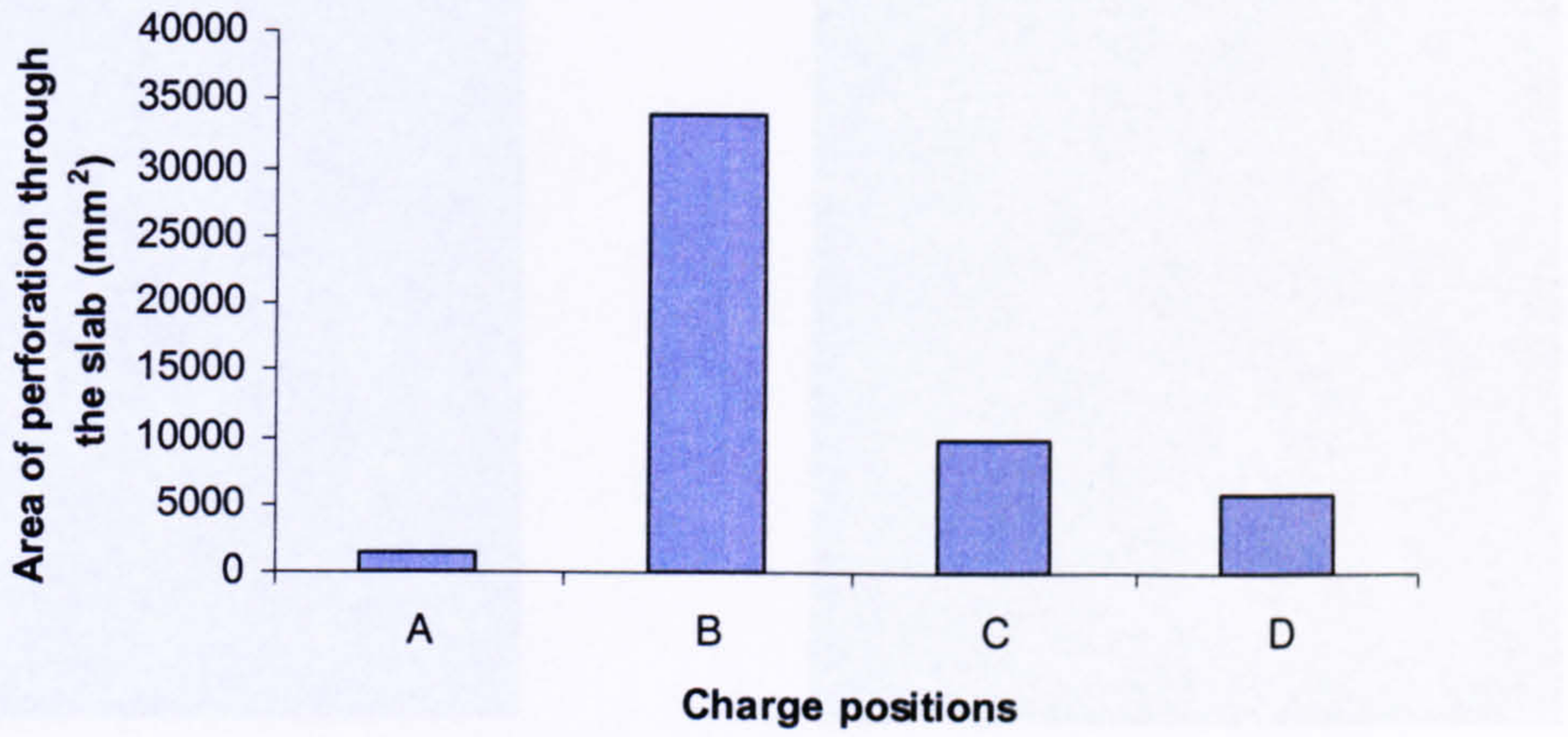

Figure 4.2.6 Perforated damage to the secondary slab associated with the four charge positions in group 1

The centre of mass of the charge relative to that of the secondary slab dictates the magnitude of damage in the form of cratering and perforation. The smaller the vertical distance between centre of masses of the charge and the slab, the greater the overall damage to the slab.

4.2.2 Damaged secondary slabs from Stage I group 2 of the test matrix

The soil overburden confined between top and bottom face of the primary and secondary slab in group 2 was 300mm. The soil overburden above the secondary slab remained constant at 500mm.

4.2.2.1 Test RCIT5

The damage to both faces of secondary slab RCB73IT5 is illustrated in plate 4.2.5.
Top face: Square cracks dominated the top face with a greater concentration within quadrant B. Continuous circumferential cracks were evident and occurred at a radial distance of 500mm from the centre of the slab.
Bottom face: Heavy concentration of radial cracks with a greater percentage of steel rebar was visible in quadrant B.

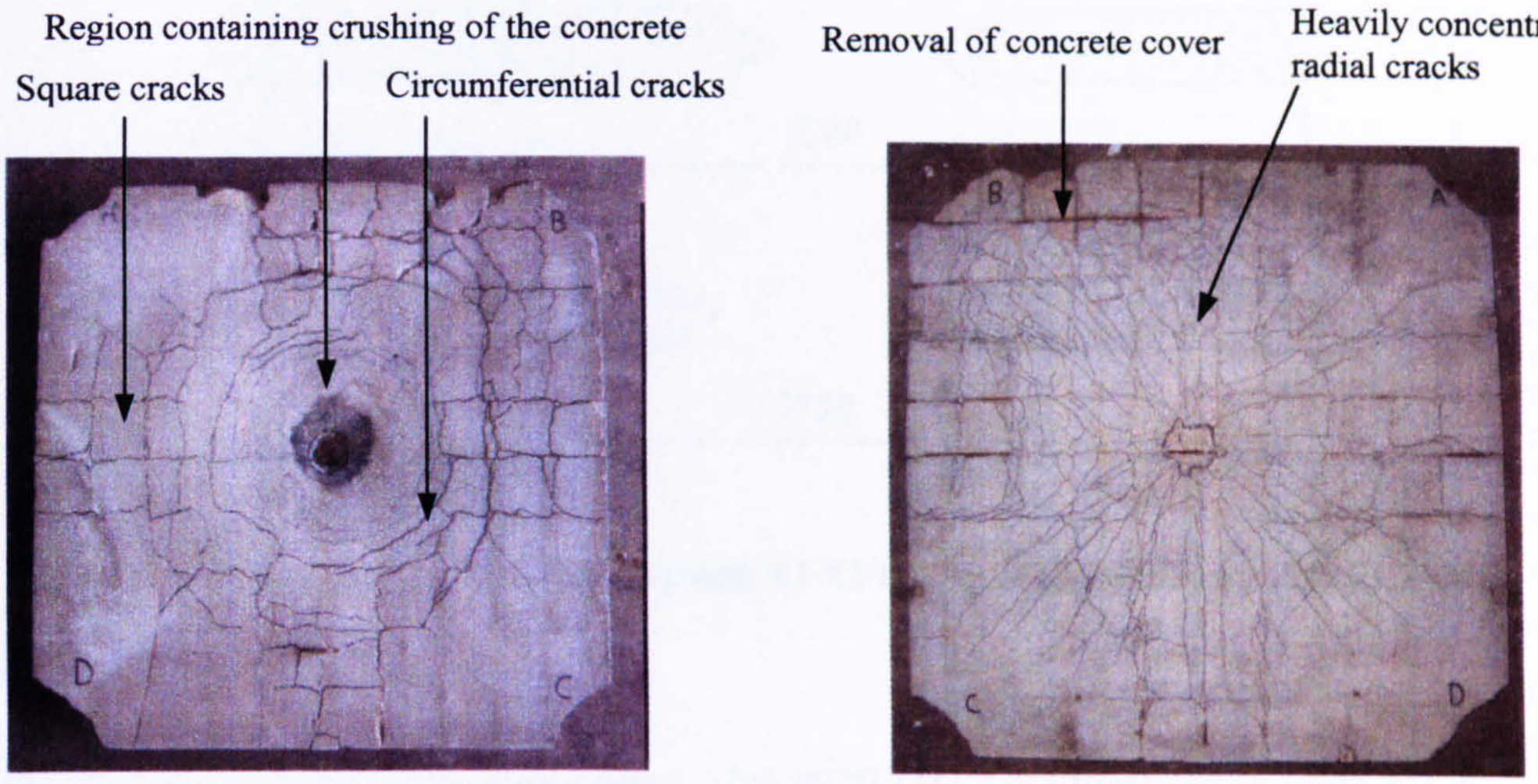

Top face Bottom face

Plate 4.2.5 Top and bottom faces of secondary slab RCB73IT5

4.2.2.2 Test RCIT6

The damage to both faces of secondary slab RCB73IT6 is illustrated in plate 4.2.6.

Top face: Sparse crack profile. Square cracks were evident along the orthogonal axes as well as widely spaced radial cracks propagating from around the crater circumference at approximately 150mm. Circumferential cracks did not appear to be evident.

Bottom face: Similar crack profile as illustrated on the top face with longer radial cracks.

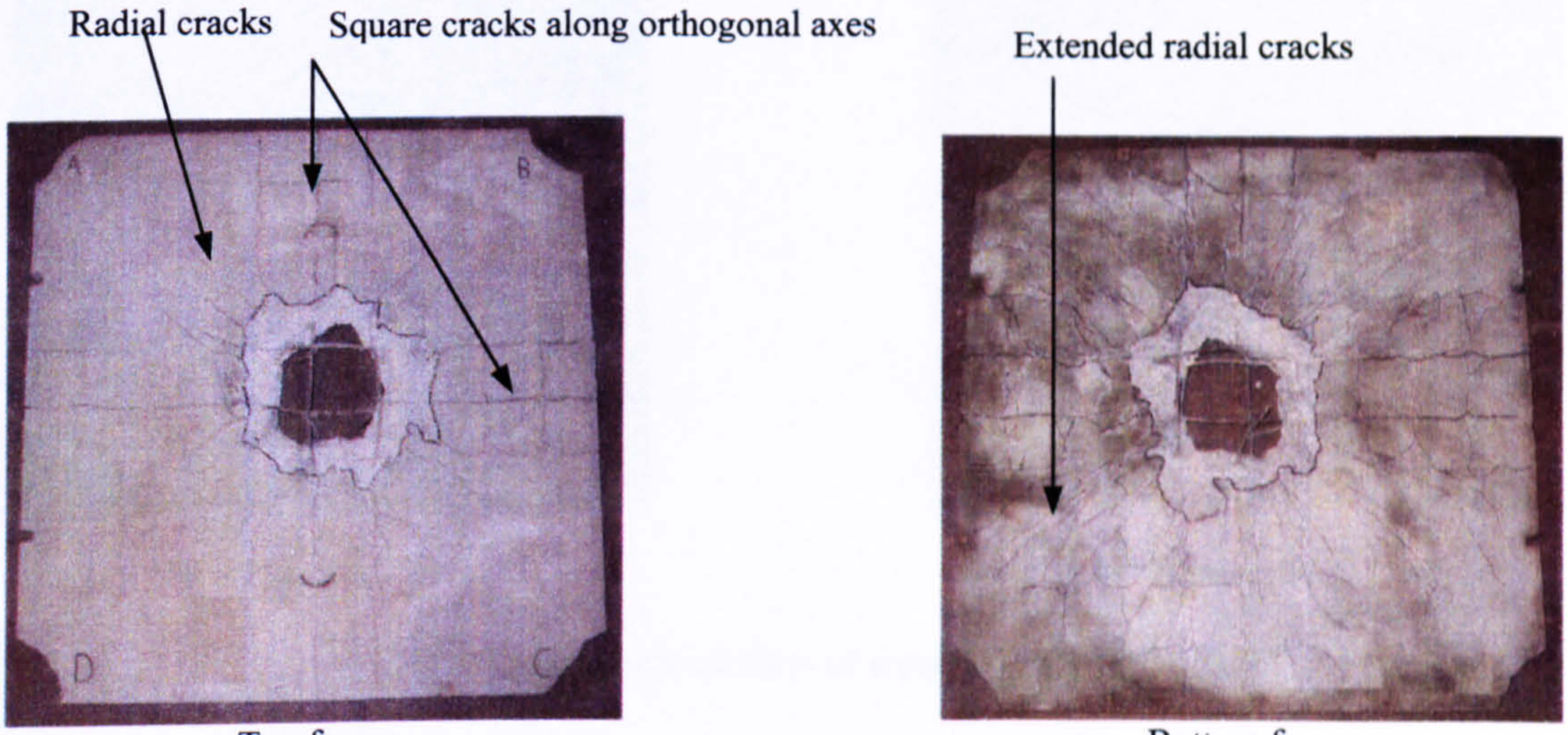

Top face Bottom face

Plate 4.2.6 Top and bottom faces of secondary slab RCB73IT6

Cross-sections through slab RCB73IT6 are illustrated in figure 4.2.7

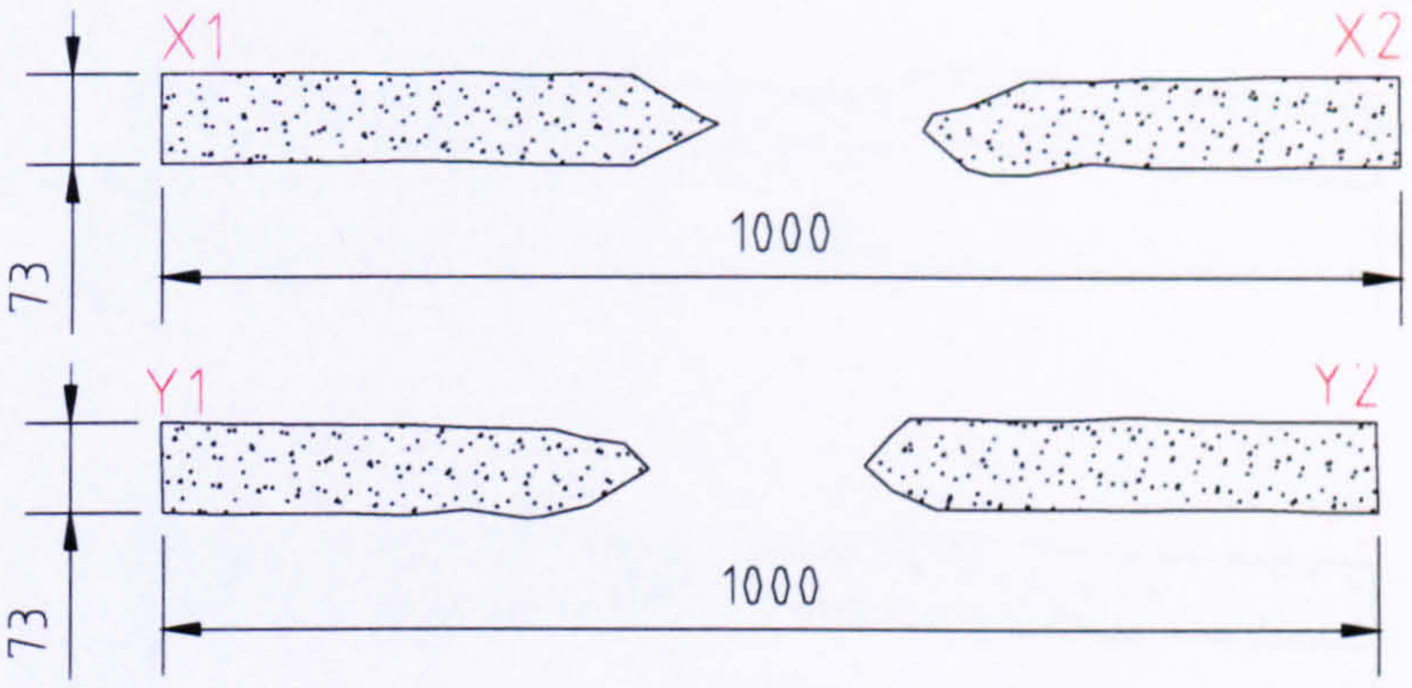

Figure 4.2.7 Cross-sectional elevation through X1-X2 and Y1-Y2 of secondary slab RCB73IT6

4.2.2.3 Test RCIT7

The damage to both faces of secondary slab RCB73IT7 is illustrated in plate 4.2.7.
Top face: Large concentration of radial cracks propagated the perimeter of the slab. Discontinuous circumferential cracks outlined the circumference of a dome.
Bottom face: Circumferential cracks appeared to form around the crater. Square cracks propagated outside the circumferential crack region to the sides of the slab along the orthogonal axes.

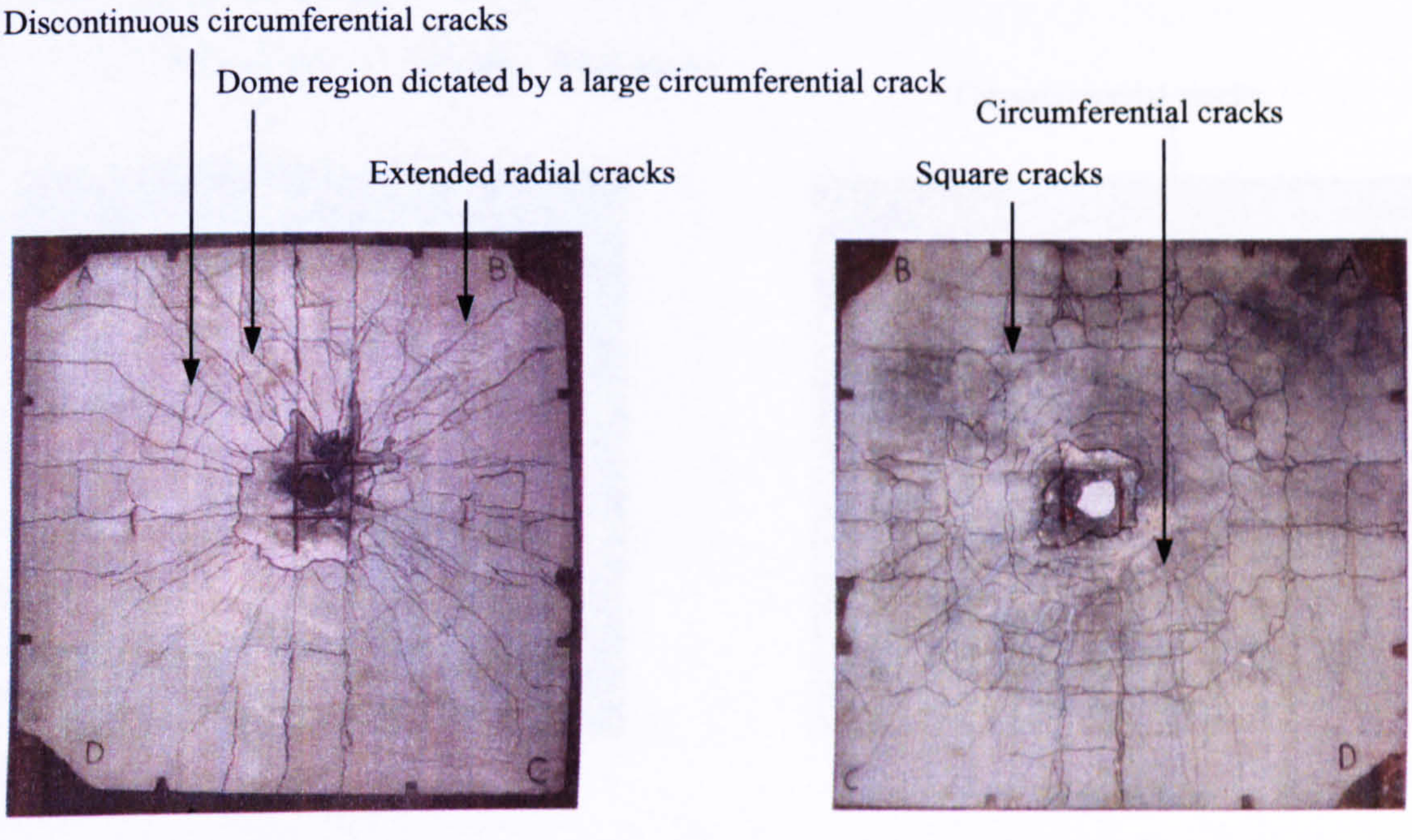

Plate 4.2.7 Top and bottom faces of secondary slab RCB73IT7

Cross-sections through slab RCB73IT7 are illustrated in figure 4.2.8.

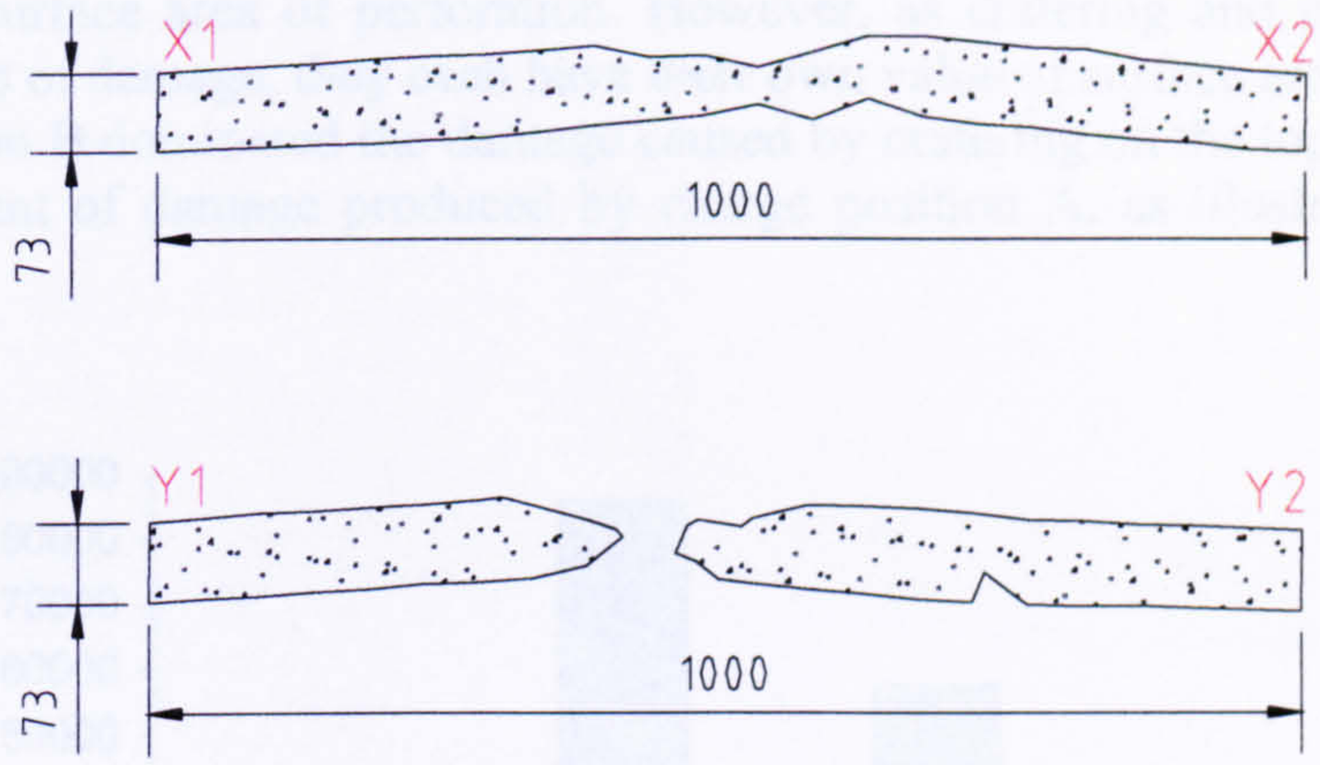

Figure 4.2.8 Cross-sectional elevation through X1-X2 and Y1-Y2 of secondary slab RCB73IT7

4.2.2.4 Test RCIT8

The damage to both faces of secondary slab RCB73IT8 is illustrated in plate 4.2.8.
Top face: Majority of the radial cracks propagated from around the circumference of the crater to the perimeter of the slab. A discontinuous circumferential crack illustrates a dome formation.
Bottom face: Circumferential cracks propagated out from the centre of the slab at a radial distance of approximately 250mm.

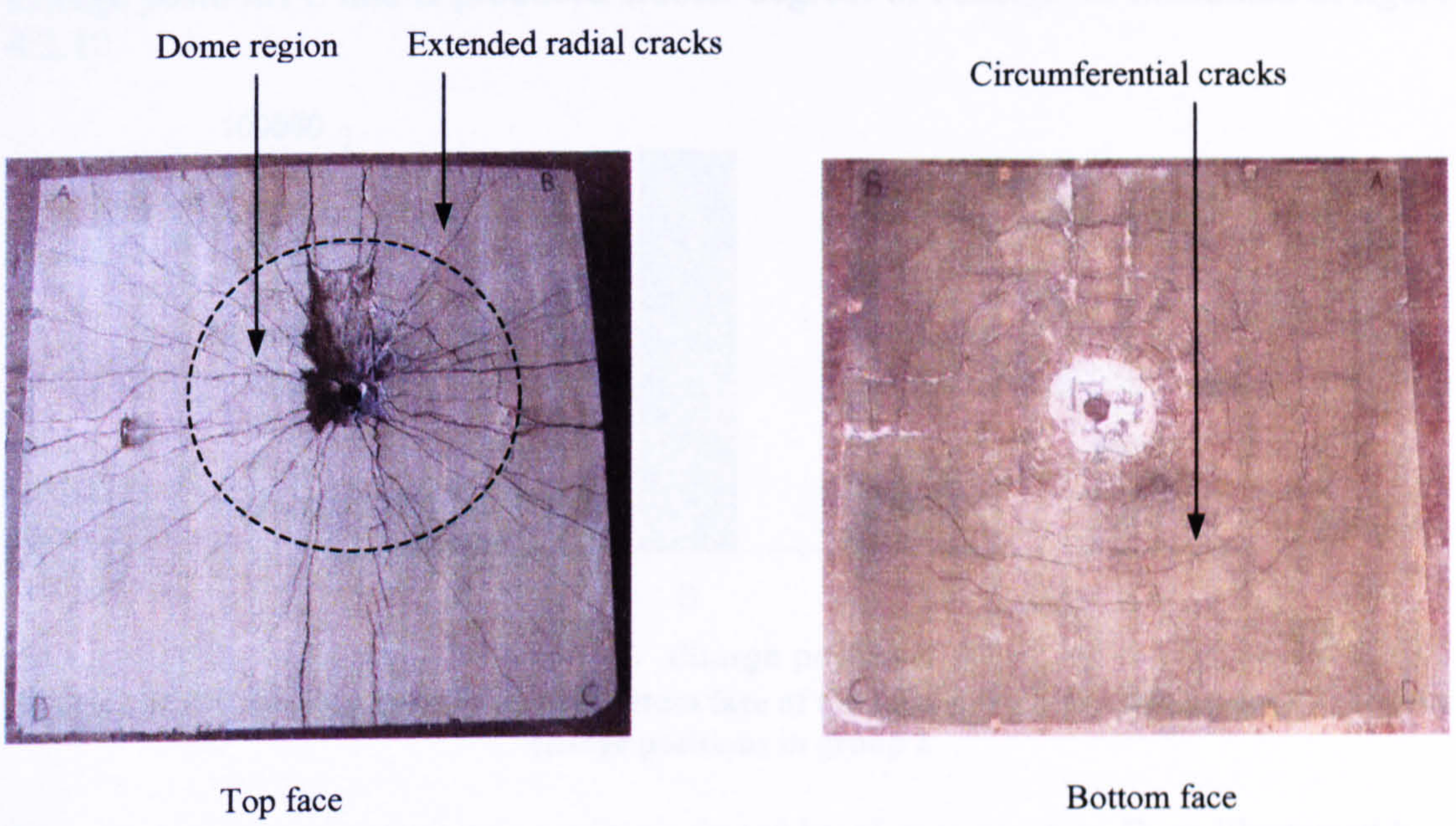

Plate 4.2.8 Top and bottom faces of secondary slab RCB73IT8

4.2.2.5 Analysis of damage associated with group 2 results

The graphical plots below are based upon diametric measurements, recorded manually. They have been used to approximate the surface area of cratering on both the top and bottom faces of a secondary slab as well as the surface area of perforation.

It is important to state that the approximate surface area of cratering includes the approximate surface area of perforation. However, as cratering and perforation are different forms of damage, they each have their own value of surface area.
Charge position B dominated the damage caused by cratering on the top face with the smallest amount of damage produced by charge position A, as illustrated in figure 4.2.9.

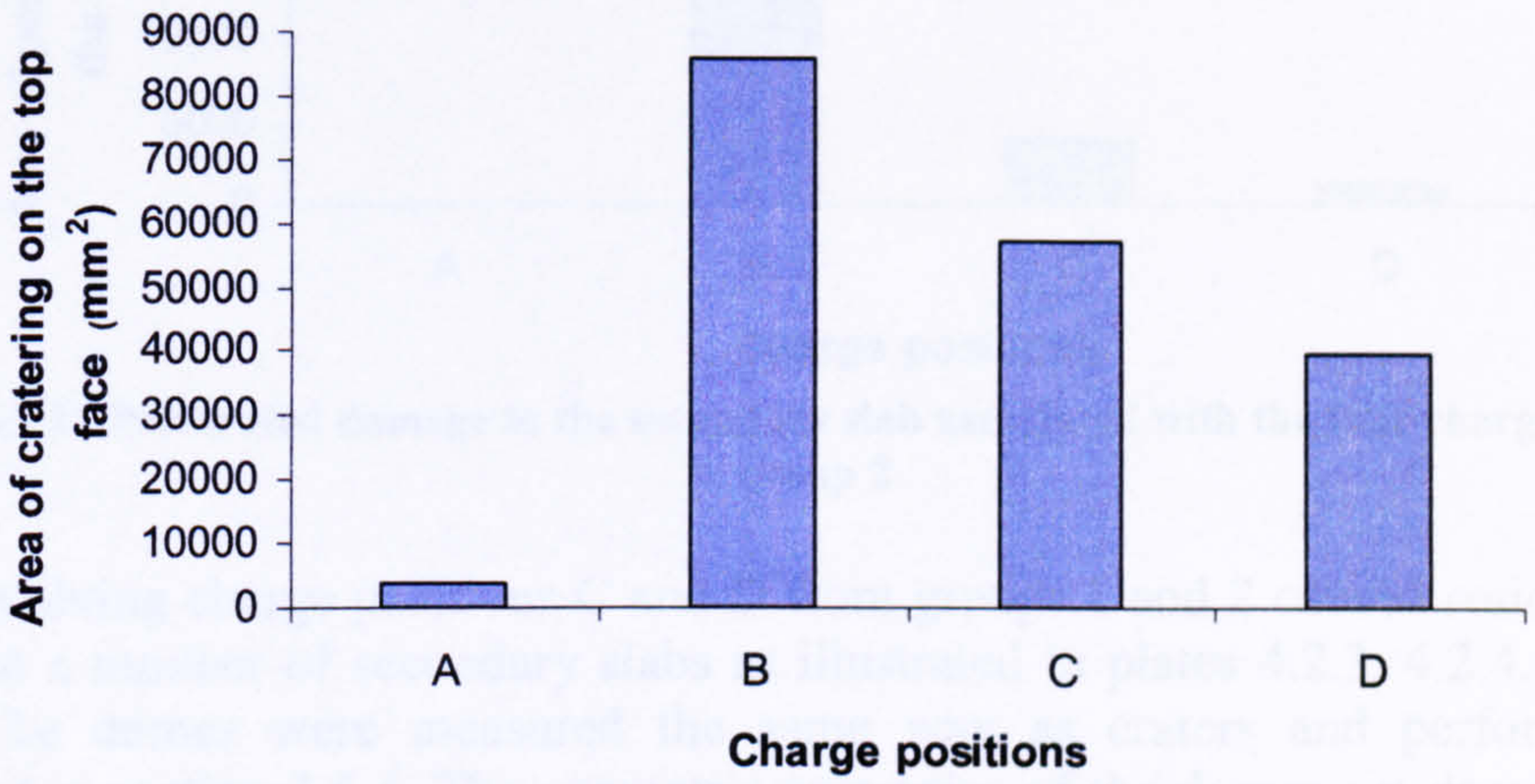

Figure 4.2.9 Crater damage on the top face of the secondary slab associated with the four charge positions

Charge positions C and D produced similar degrees of damage, as illustrated in figure 4.2.10.

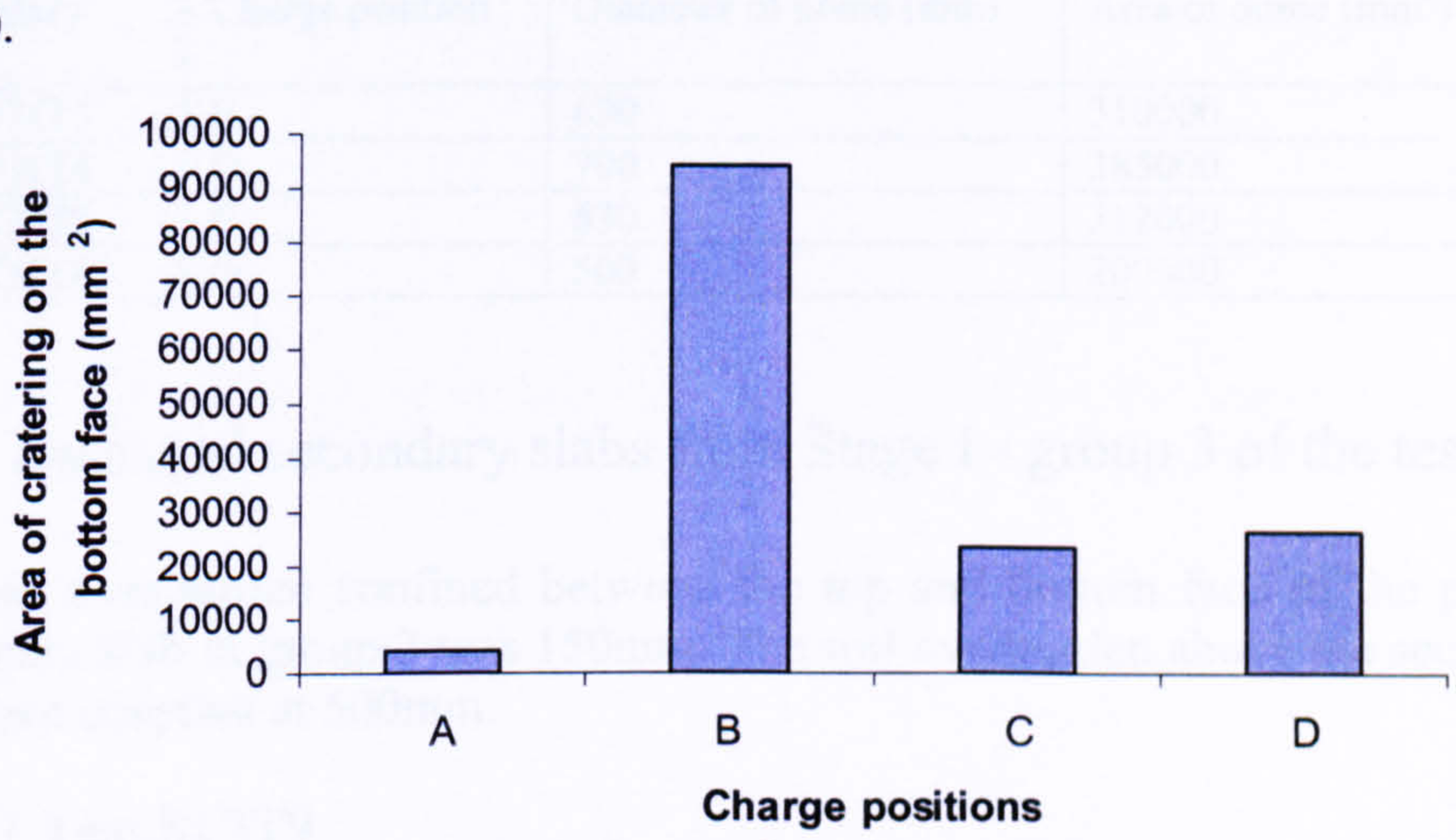

Figure 4.2.10 Cratering damage on the bottom face of the secondary slab associated with the four charge positions in group 2

The maximum perforation was again produced by charge position B, as illustrated by figure 4.2.11 with a negligible perforation associated with charge position A.

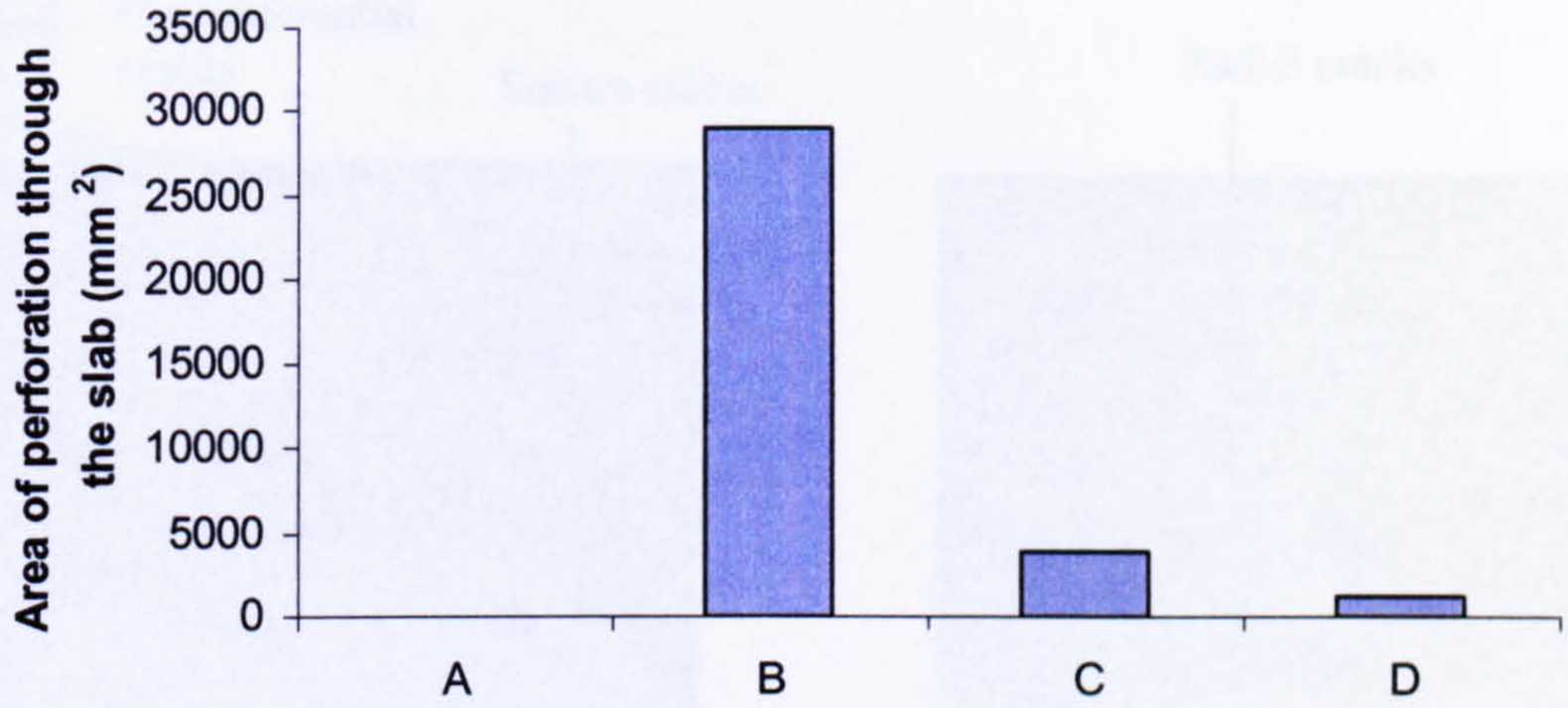

Figure 4.2.11 Perforated damage to the secondary slab associated with the four charge positions in group 2

Tests involving charge positions C and D from groups 1 and 2 caused residual dome effects to a number of secondary slabs as illustrated in plates 4.2.3, 4.2.4, 4.2.7 and 4.2.8. The domes were measured the same way as craters and perforations, as described in section 3.6.4. The geometric properties of the domes are documented in table 4.2.1.

Table 4.2.1 Secondary slabs that produced damage in the form of a dome effect

Secondary slabs	Charge position	Diameter of dome (mm)	Area of dome (mm^2)
RCB73IT3	C	630	310000
RCB73IT4	D	700	385000
RCB73IT7	C	630	312000
RCB73IT8	D	500	200000

4.2.3 Damaged secondary slabs from Stage I - group 3 of the test matrix

The soil overburden confined between the top and bottom face of the primary and secondary slab in group 3 was 150mm. The soil overburden above the secondary slab remained constant at 500mm.

4.2.3.1 Test RCIT9

The damage to both faces of secondary slab RCB73IT9 is illustrated in plate 4.2.9.
Top face: Square cracks and circumferential cracks dominated the surface. Corner cracks were evident around reference points B, C and D. These were associated with the violation of the concrete's elastic limit. The geometry of the corner crack in quadrant B depicts the profile of an inward travelling stress wave.
Bottom face: Radial cracks dominated the face, propagating out from around the crater

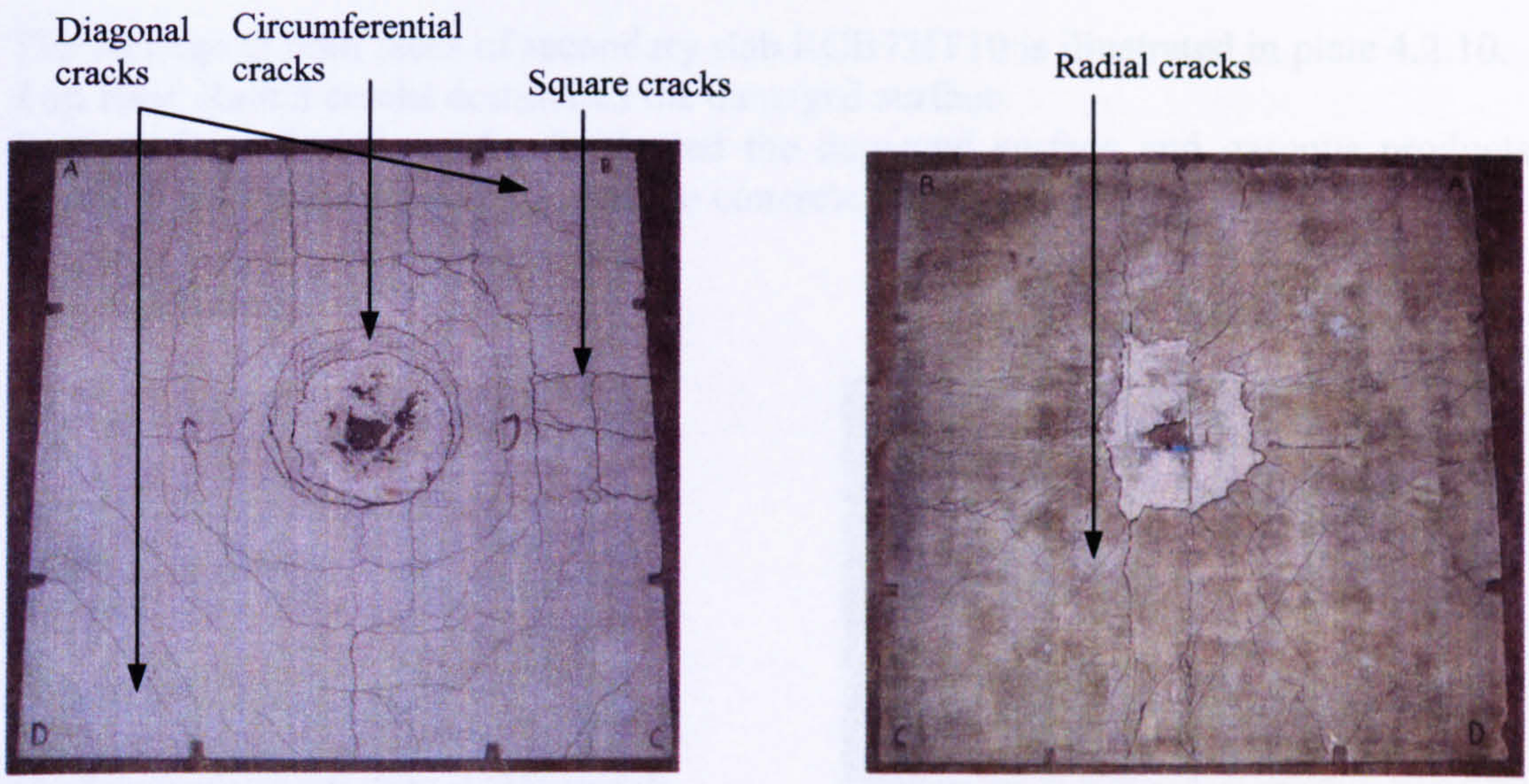

Top face

Bottom face

Plate 4.2.9 Top and bottom faces of secondary slab RCB73IT9

A cross-section through slab RCB73IT9 is illustrated in figure 4.2.12.

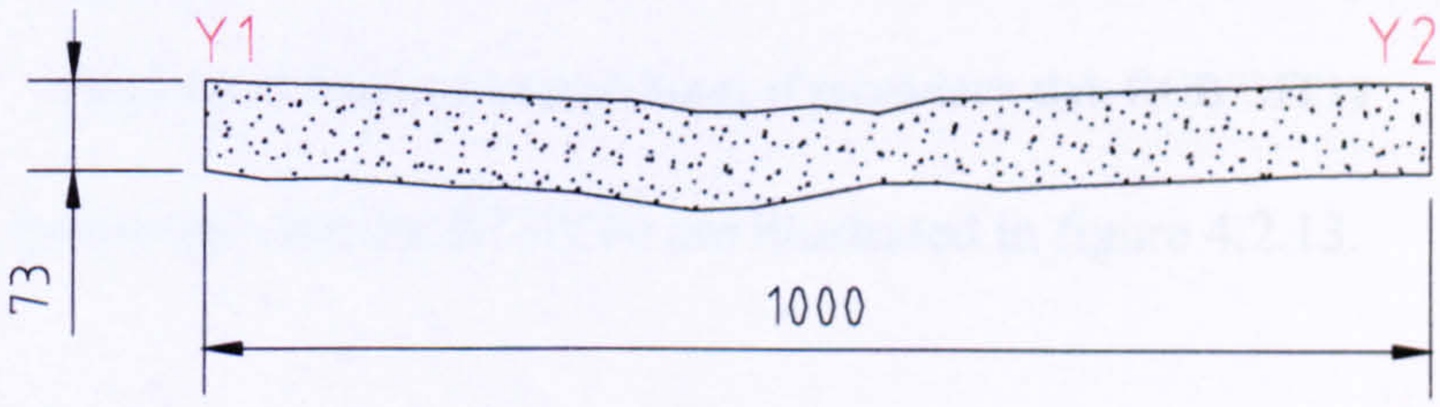

Figure 4.2.12 Cross-sectional elevation through X1-X2 and Y1-Y2 of secondary slab RCB73IT9

4.2.3.2 Test RCIT10

The damage to both faces of secondary slab RCB73IT10 is illustrated in plate 4.2.10.
Top face: Radial cracks dominated the damaged surface
Bottom face: Radial cracks dominated the damaged surface and gaseous products caused significant discolouration of the concrete face.

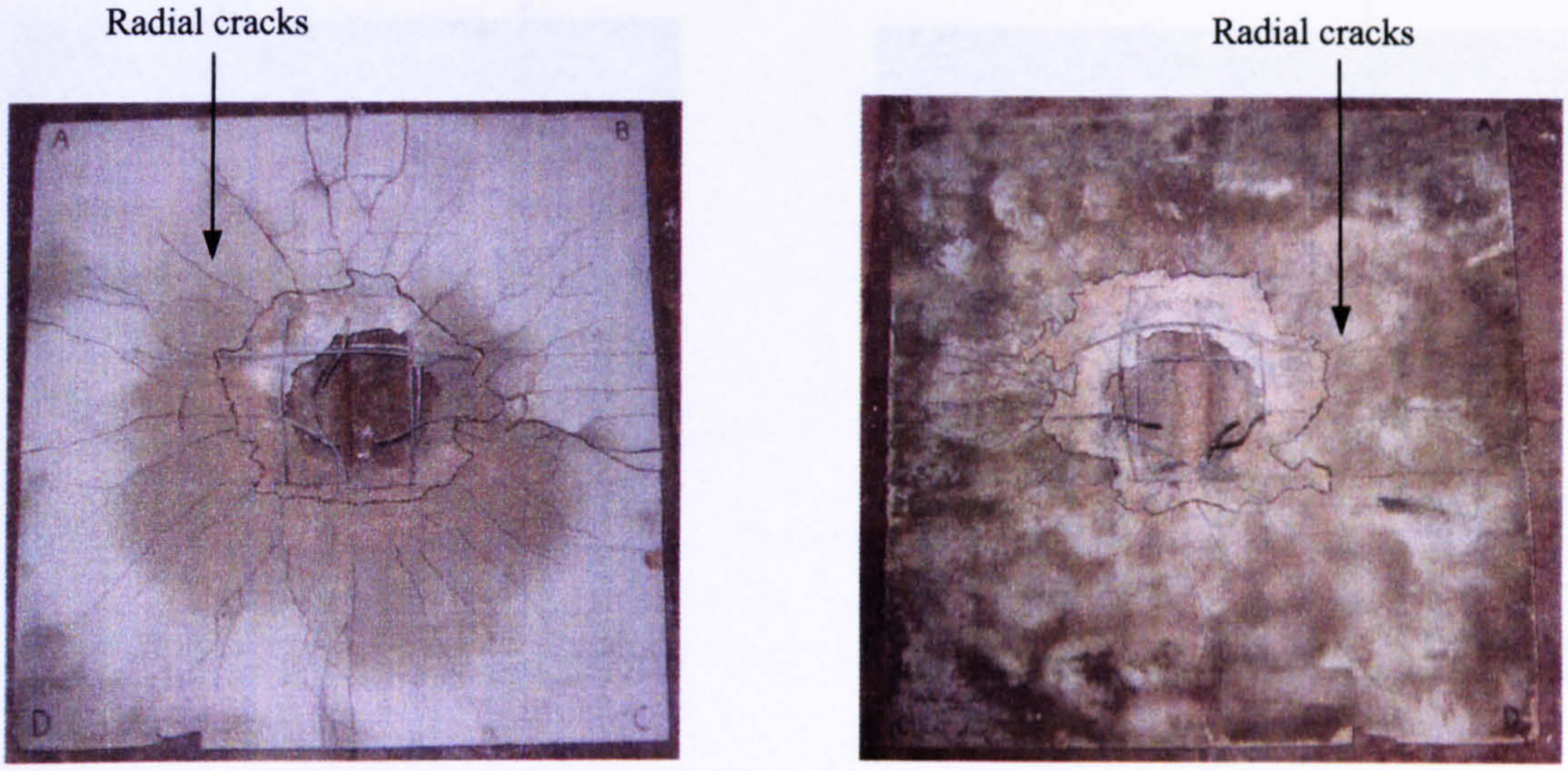

Top face

Bottom face

Plate 4.2.10 Top and bottom faces of secondary slab RCB73IT10

Cross-sections through slab RCB73IT10 are illustrated in figure 4.2.13.

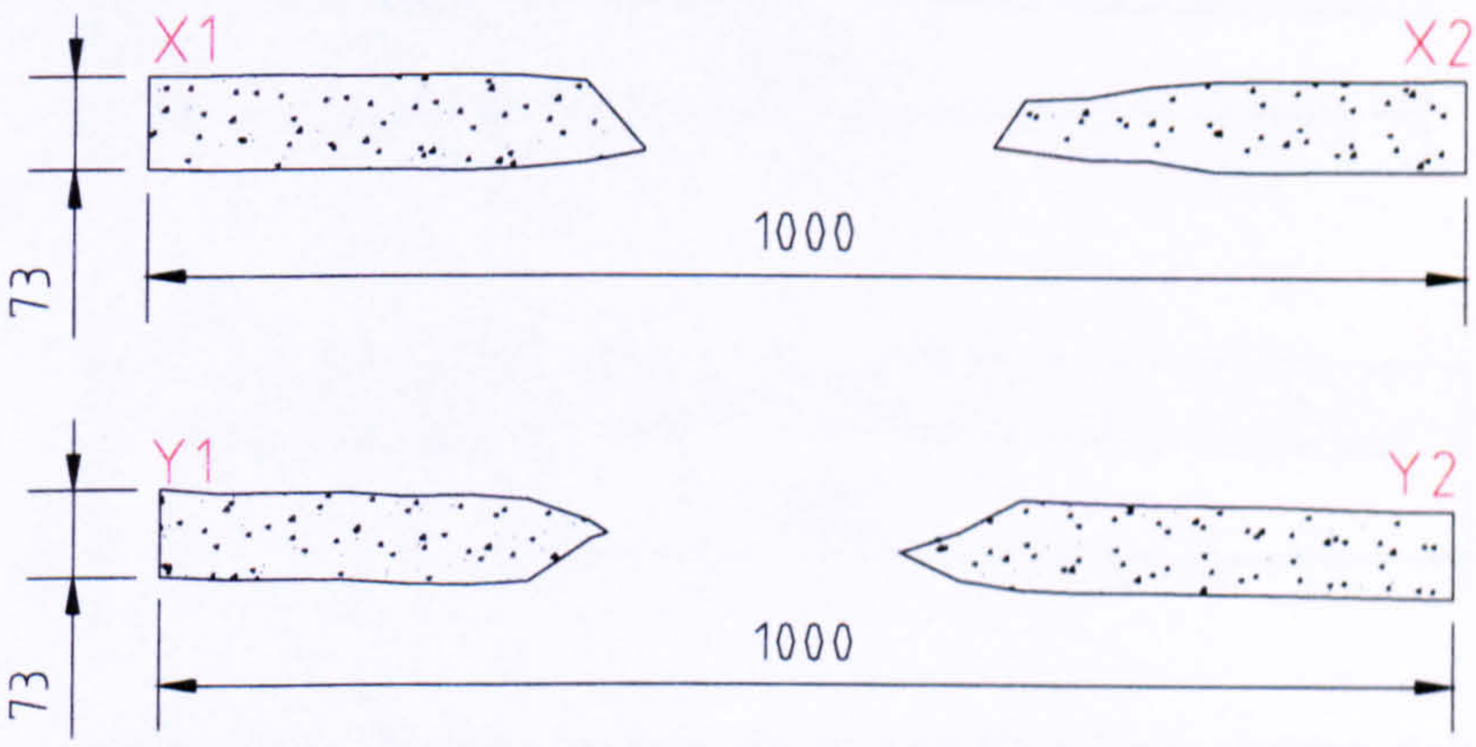

Figure 4.2.13 Cross-sectional elevation through X1-X2 and Y1-Y2 of secondary slab RCB73IT10

4.2.3.3 Test RCIT11

The damage to both faces of secondary slab RCB73IT11 is illustrated in plate 4.2.11.
Top face: Square cracks were wide, along the orthogonal axes. Radial cracks propagated from the crater to the sides of the slab. Circumferential cracks were

contained between two radial cracks, suggesting that the radial cracks formed first, preventing the expansion of the circumferential cracks.
Bottom face: Continuous circumferential cracks were present but barely visible, due to the discolouration of the slab, caused by the smoke from the charge detonation.

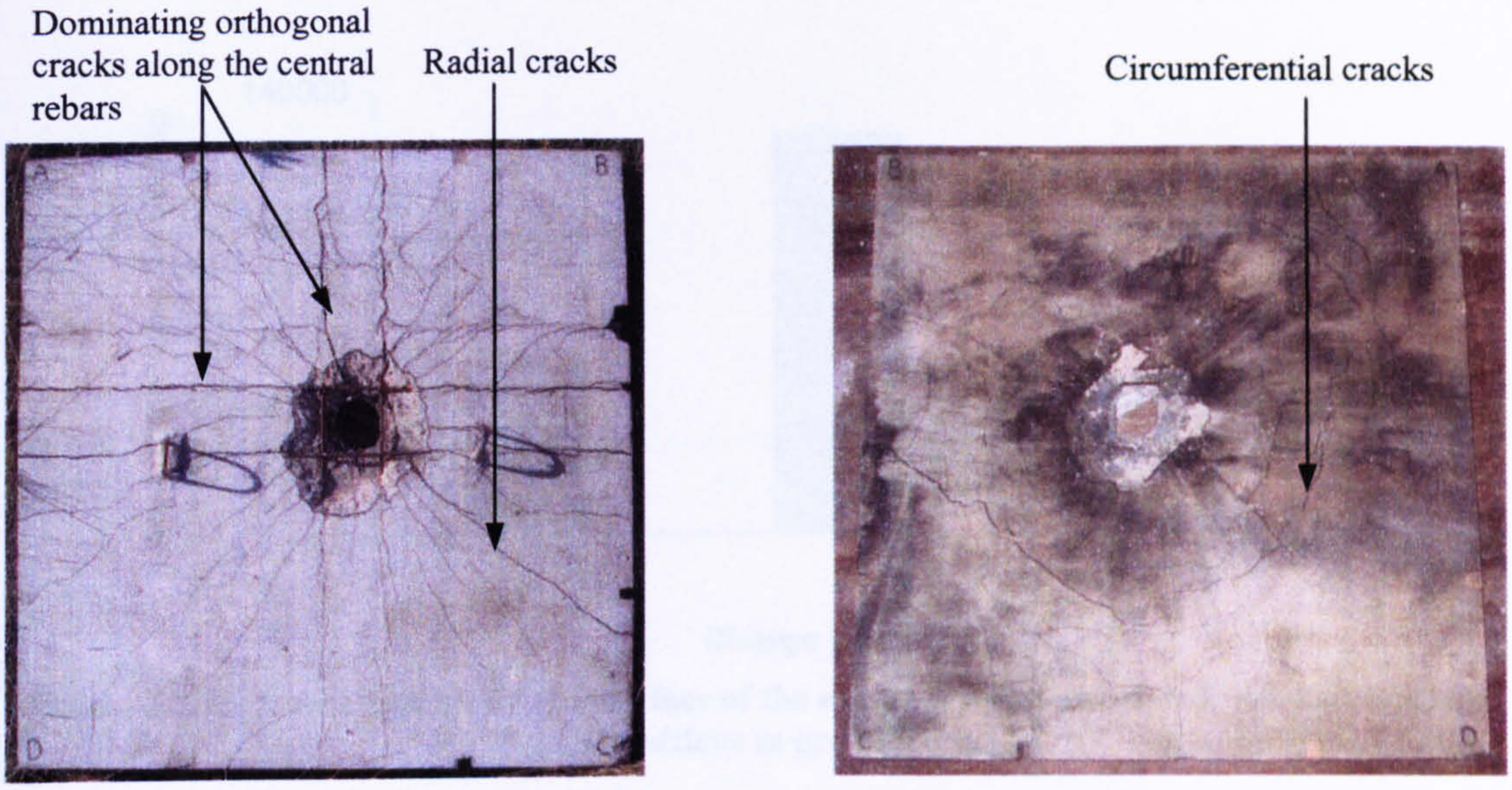

Top face

Bottom face

Plate 4.2.11 Top and bottom faces of secondary slab RCB73IT11

Cross-sections through slab RCB73IT11 are illustrated in figure 4.2.14.

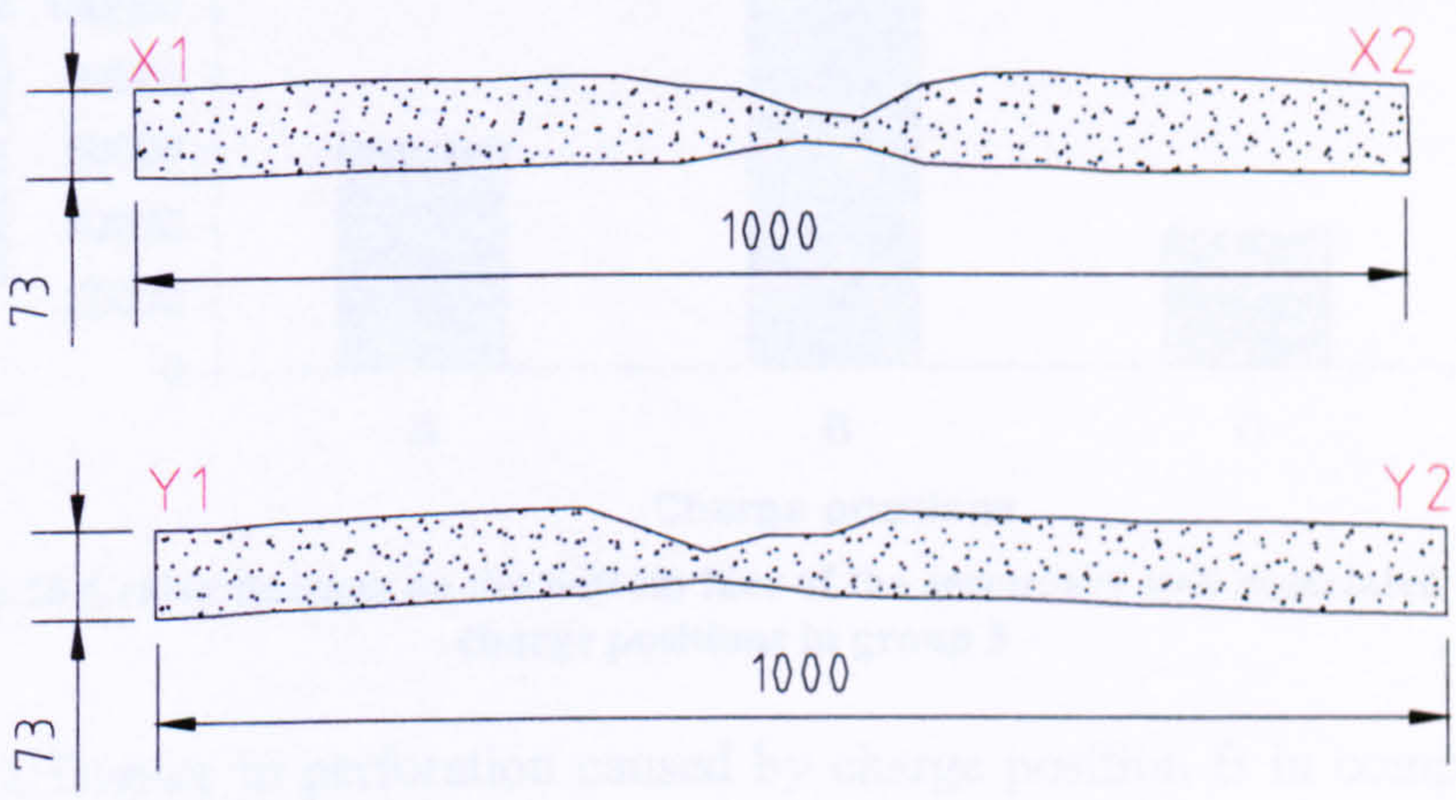

Figure 4.2.14 Cross-sectional elevation through X1-X2 and Y1-Y2 of secondary slab RCB73IT11

4.2.3.4 Analysis of damage associated with group 3 results

The graphical plots that follow are based upon diametric measurements, recorded manually, used to approximate the surface area of cratering on both the top and bottom faces of a secondary slab as well as the surface area of perforation. It is important to state that the approximate surface area of cratering includes the

approximate surface area of perforation. However, as cratering and perforation are different forms of damage, they each have their own value of surface area.
Charge position A caused a perforation that was greater than that caused by charge position C, as illustrated in figure 4.2.15. Previous tests did not illustrate this finding

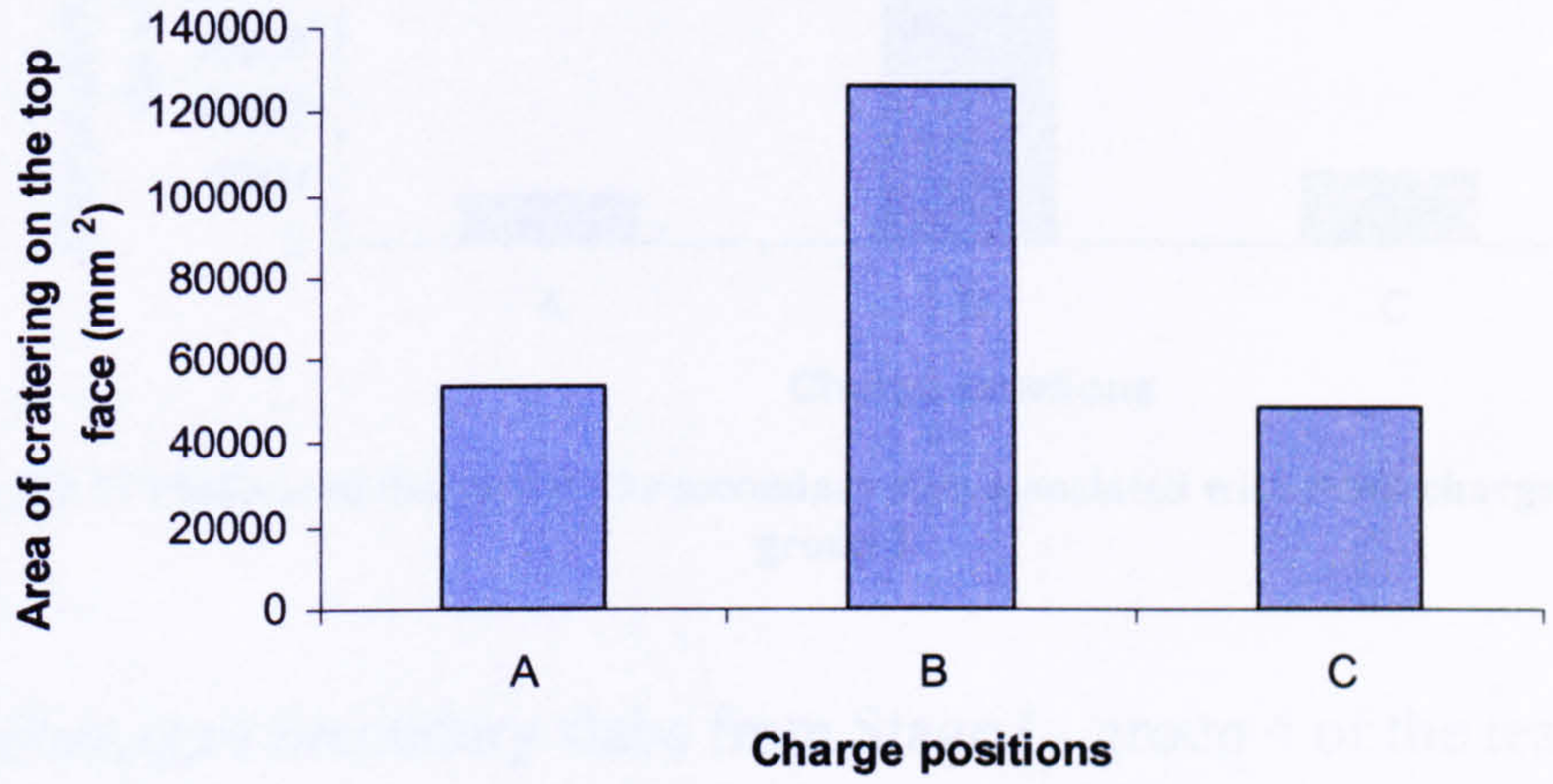

Figure 4.2.15 Crater damage on the top face of the secondary slab associated with three charge positions in group 3

The damage caused by charge positions A, B and C is illustrated in figure 4.2.16.

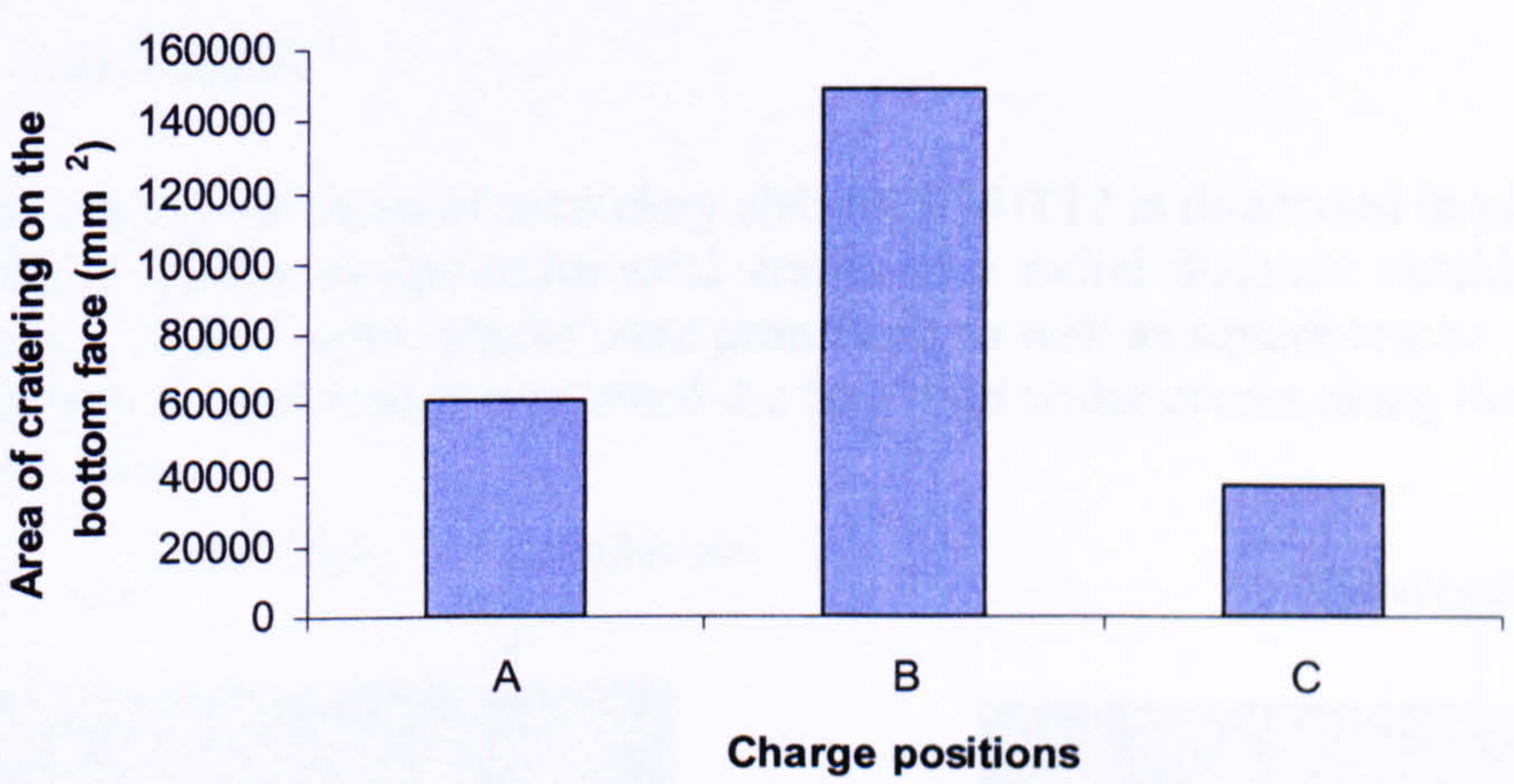

Figure 4.2.16 Crater damage on the bottom face of the secondary slab associated with three charge positions in group 3

The large difference in perforation caused by charge position B in comparison to A and C is consistent throughout the group of tests as illustrated in figure 4.2.17.

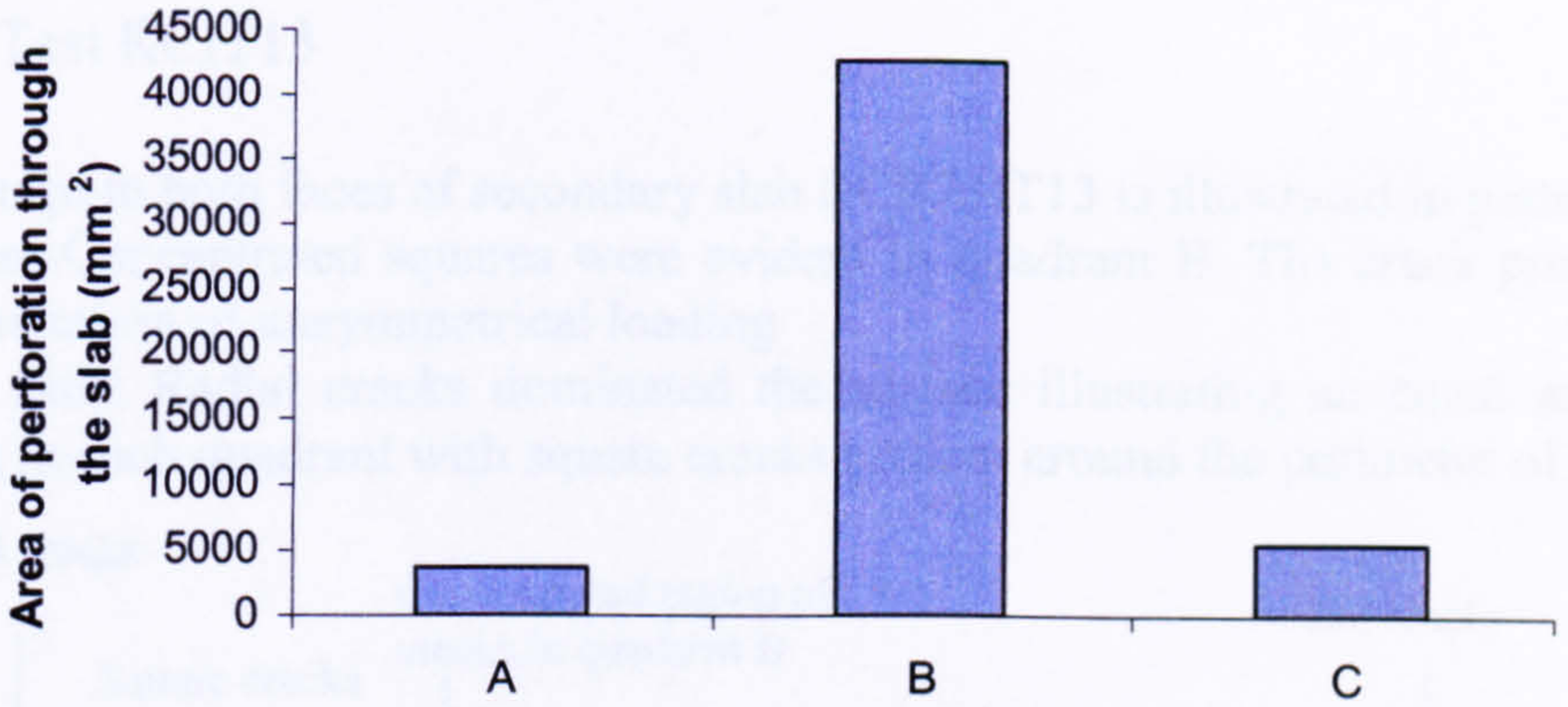

Figure 4.2.17 Perforated damage to the secondary slab associated with three charge positions in group 3

4.2.4 Damaged secondary slabs from Stage I - group 4 of the test matrix

The soil overburden confined between top and bottom face of the primary and secondary slab in group 4 was 73mm. The soil overburden above the secondary slab remained constant at 500mm.

4.2.4.1 Test RCIT12

The damage to both faces of secondary slab RCB73IT12 is illustrated in plate 4.2.12.
Top face: Continuous circumferential cracks at a radial distance outside the crater zone were visible. Corner cracks were prominent as well as square cracks.
Bottom face: Radial cracks consumed the face with wider cracks along the orthogonal axes.

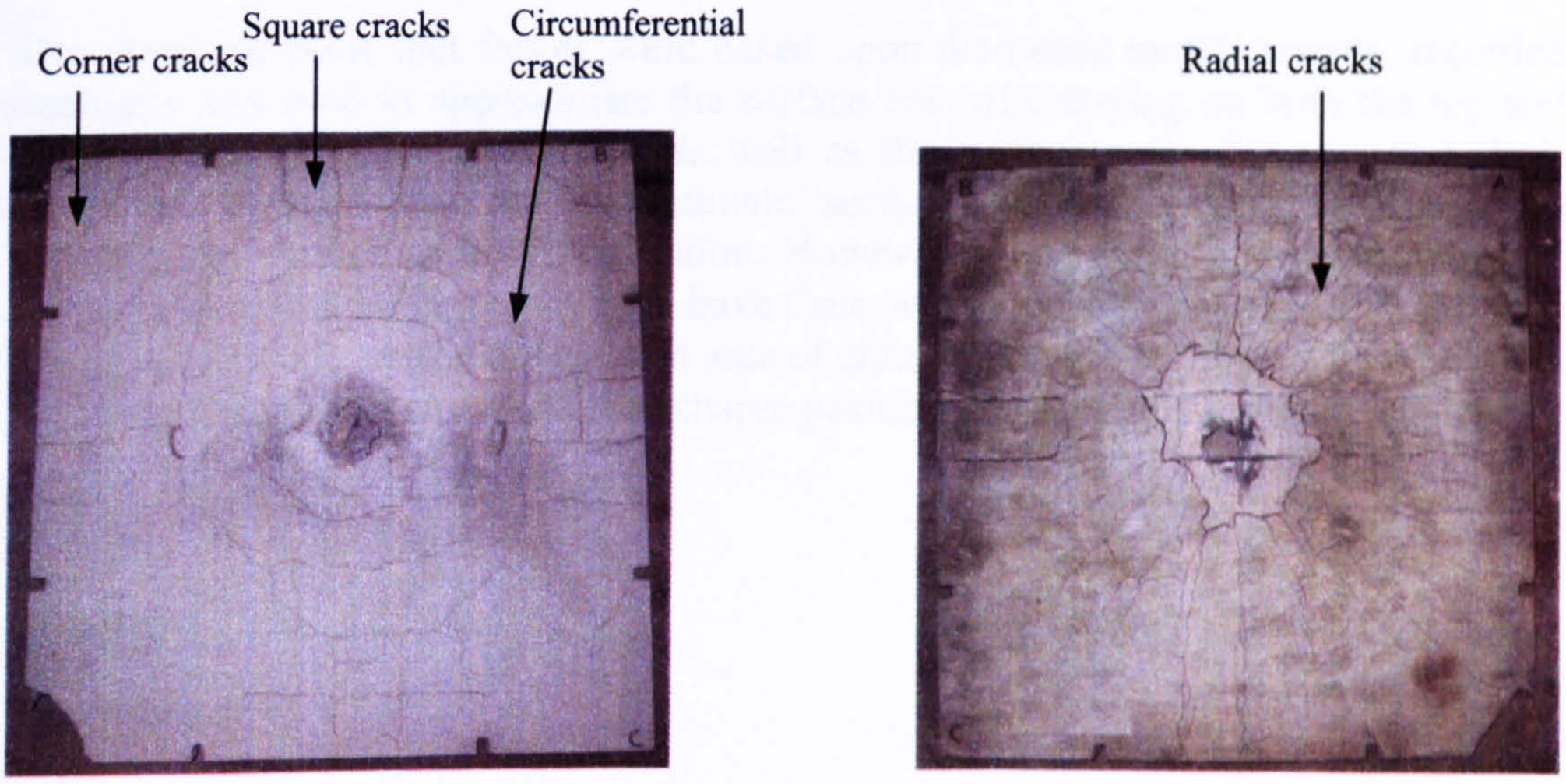

Plate 4.2.12 Top and bottom faces of secondary slab RCB73IT12

4.2.4.2 Test RCIT13

The damage to both faces of secondary slab RCB73IT13 is illustrated in plate 4.2.13.
Top face: Concentrated squares were evident in quadrant B. The crack profile gave clear illustration of unsymmetrical loading
Bottom face: Radial cracks dominated the surface illustrating an equal amount of cracking in each quadrant with square cracks present around the perimeter of the slab.

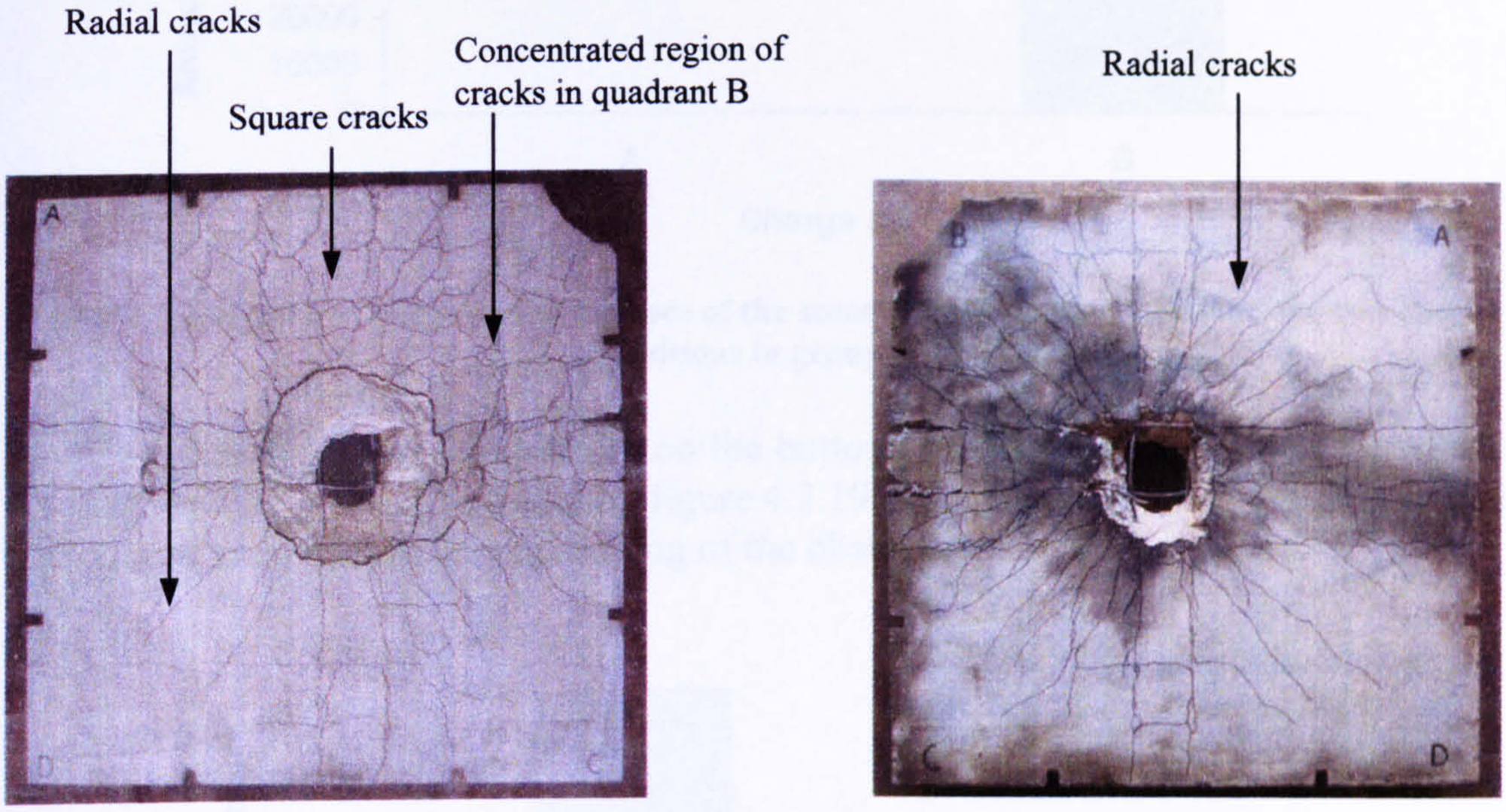

Top face Bottom face

Plate 4.2.13 Top and bottom faces of secondary slab RCB73IT13

4.2.4.3 Damage analysis associated with group 4 results

The graphical plots that follow were based upon diametric measurements, recorded manually and used to approximate the surface area of cratering on both the top and bottom faces of a secondary slab as well as the surface area of perforation. It is important to state that the approximate surface area of cratering includes the approximate surface area of perforation. However, as cratering and perforation are different forms of damage, they each have their own value of surface area.
Charge position B caused the greatest area of cratering on the top face, with negligible cratering formed as a result of using charge position A, illustrated in figure 4.2.18.

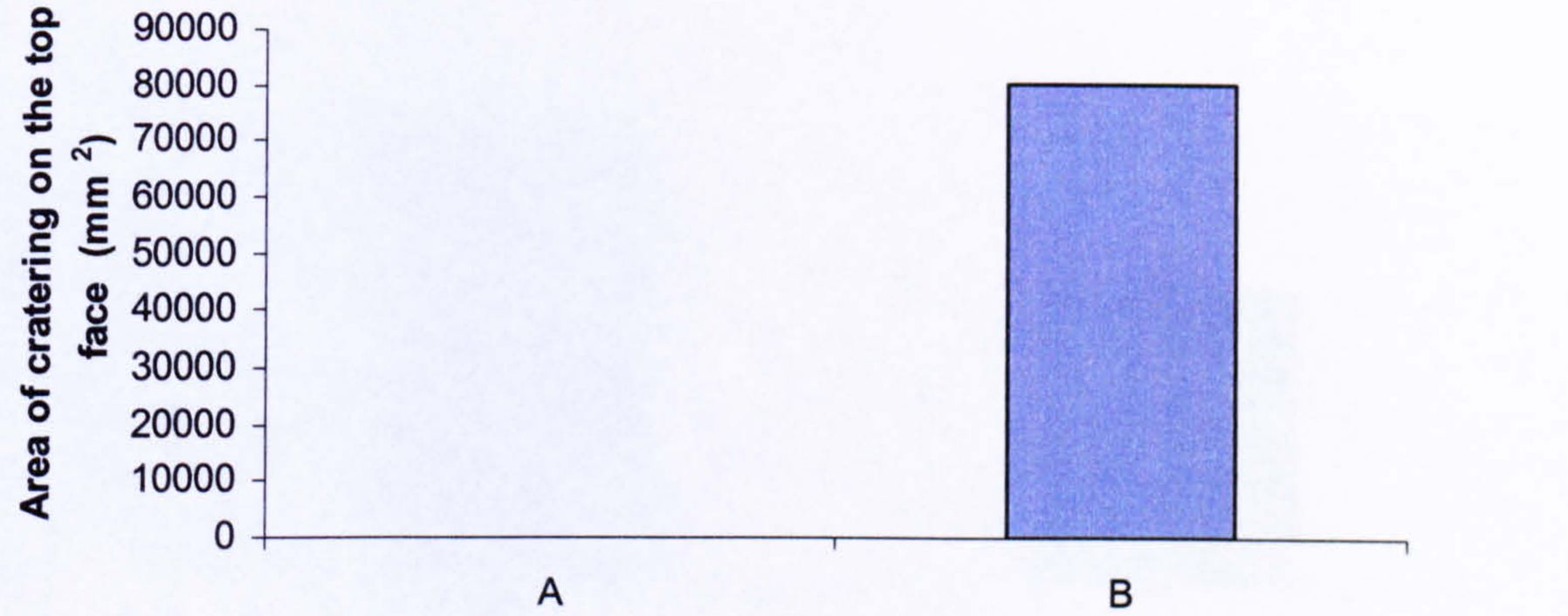

Figure 4.2.18 Crater damage on the top face of the secondary slab associated with the two charge positions in group 4

An unexpected increase in cratering on the bottom face by charge position A, caused the greatest damage as illustrated by figure 4.2.19. This is not consistent with previous test results, questioning the positioning of the charge.

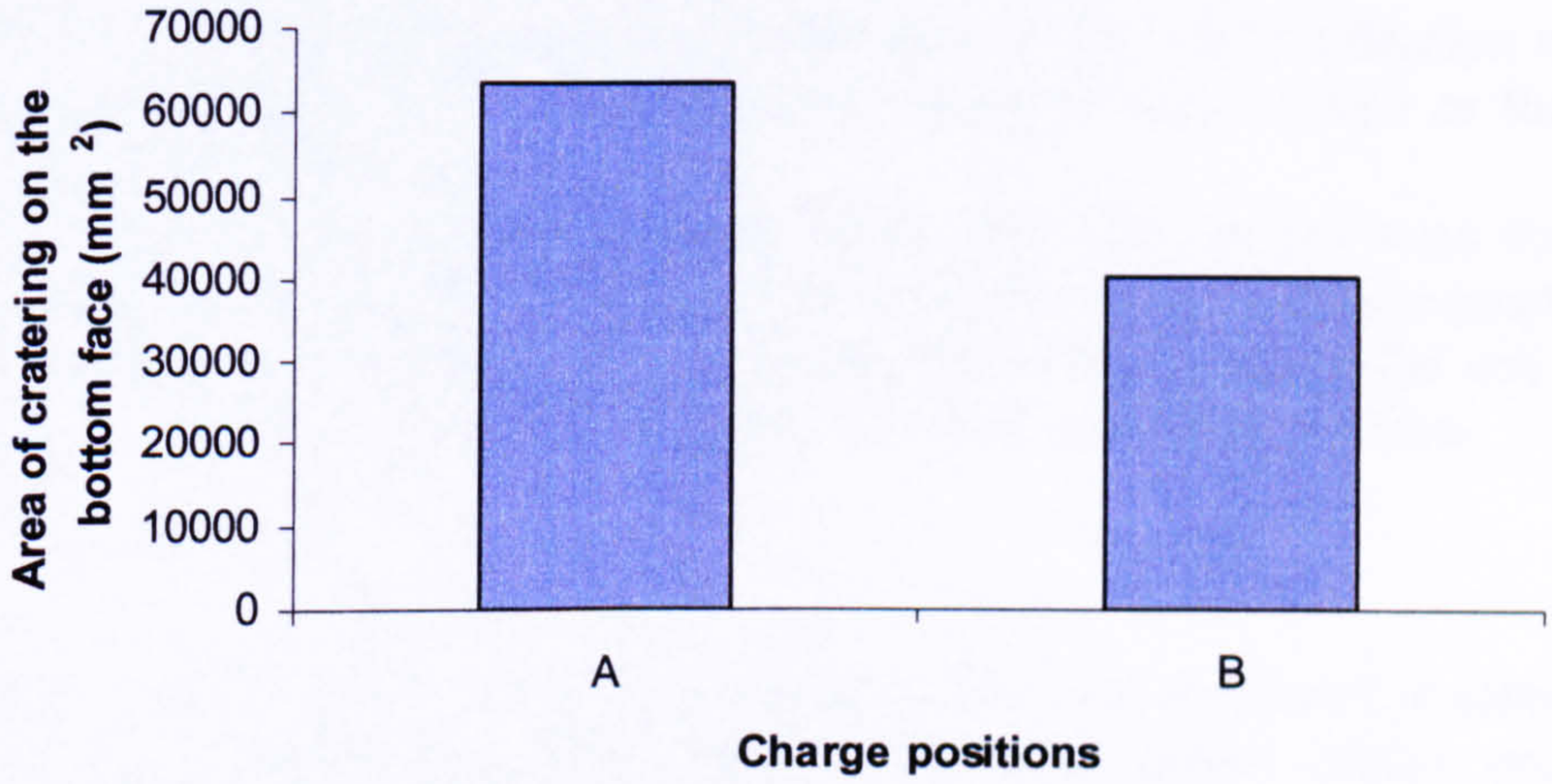

Figure 4.2.19 Crater damage on the bottom face of the secondary slab associated with the two charge positions in group 4

The maximum damage caused by perforation up until now was associated with charge position B. Charge position A caused the greatest damage in this case, as illustrated in figure 4.2.20.

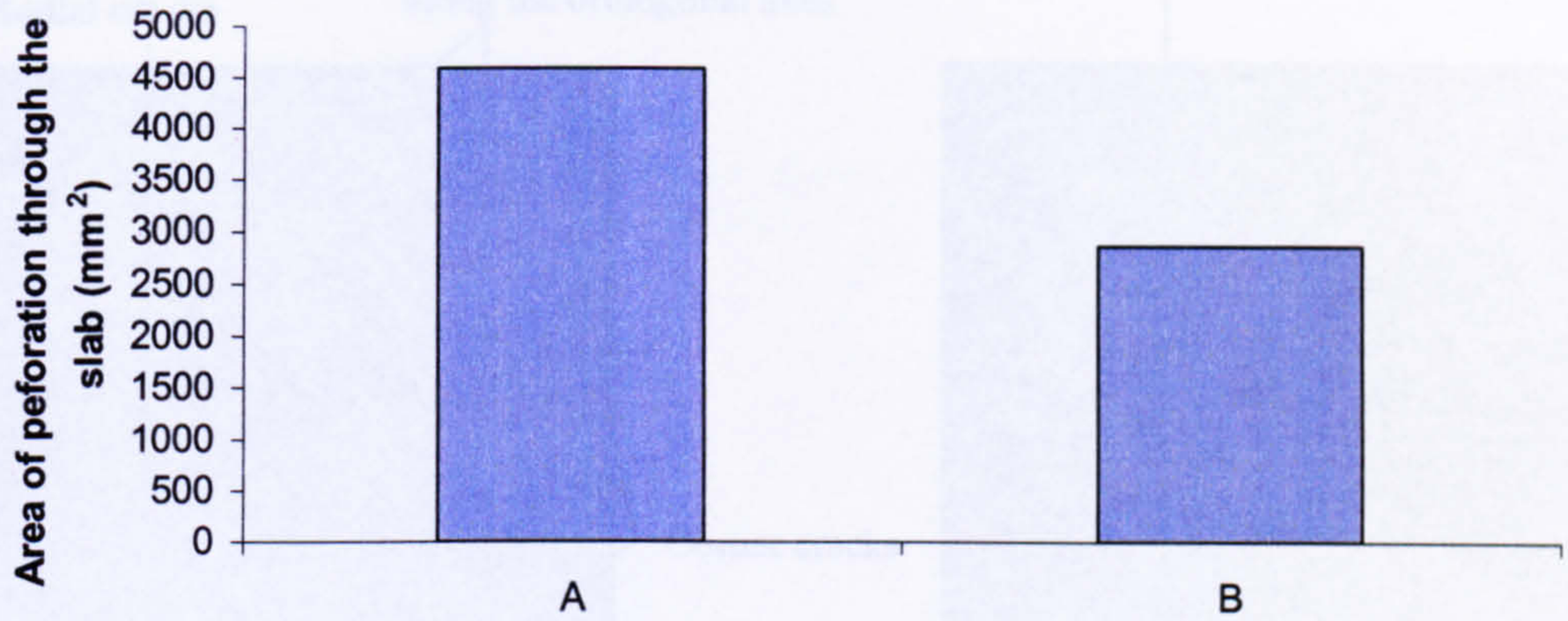

Figure 4.2.20 Perforated damage to the secondary slab associated with the two charge positions in Group 4

4.2.5 Damaged secondary slabs from Stage II of the test matrix

Stage II involved identifying whether a reduction in the soil overburden above the secondary slab influenced the damage to the secondary slab as well as the loading across the primary slab.
Test setups were dictated by the geometry of test RCIT10 that produced the greatest overall damage to the secondary slab with the implementation of charge position B.
The soil overburden above the secondary slab was 500mm, whilst the soil confined between top and bottom face of the primary remained constant at 500mm,

4.2.5.1 Test RCIT14

The damage to both faces of secondary slab RCB73IT14 is illustrated in plate 4.2.14.
Top face: Dominated by square cracks, with minor radial cracks propagating outwards from the circumference of the crater but not to the perimeter of the slab. The square cracks indicated that a greater area of concrete yielded, with the load transferring to the steel rebars. Circumferential cracks were not evident.
Bottom face: Dominated by radial cracks. Circumferential and square cracks were not evident.

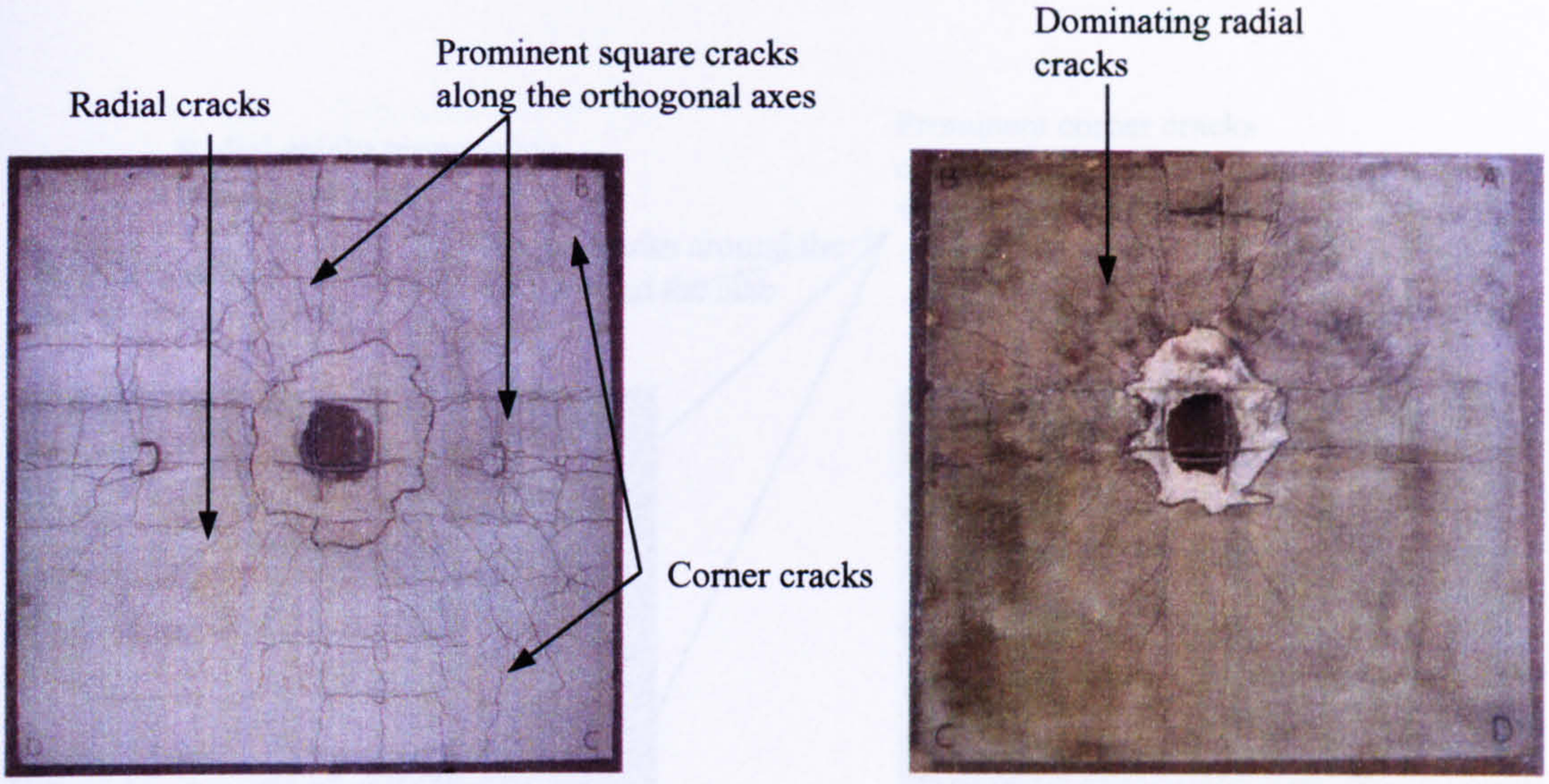

Plate 4.2.14 Top and bottom faces of secondary slab RCB73IT14

Cross-sections through slab RCB73IT14 are illustrated in figure 4.2.21.

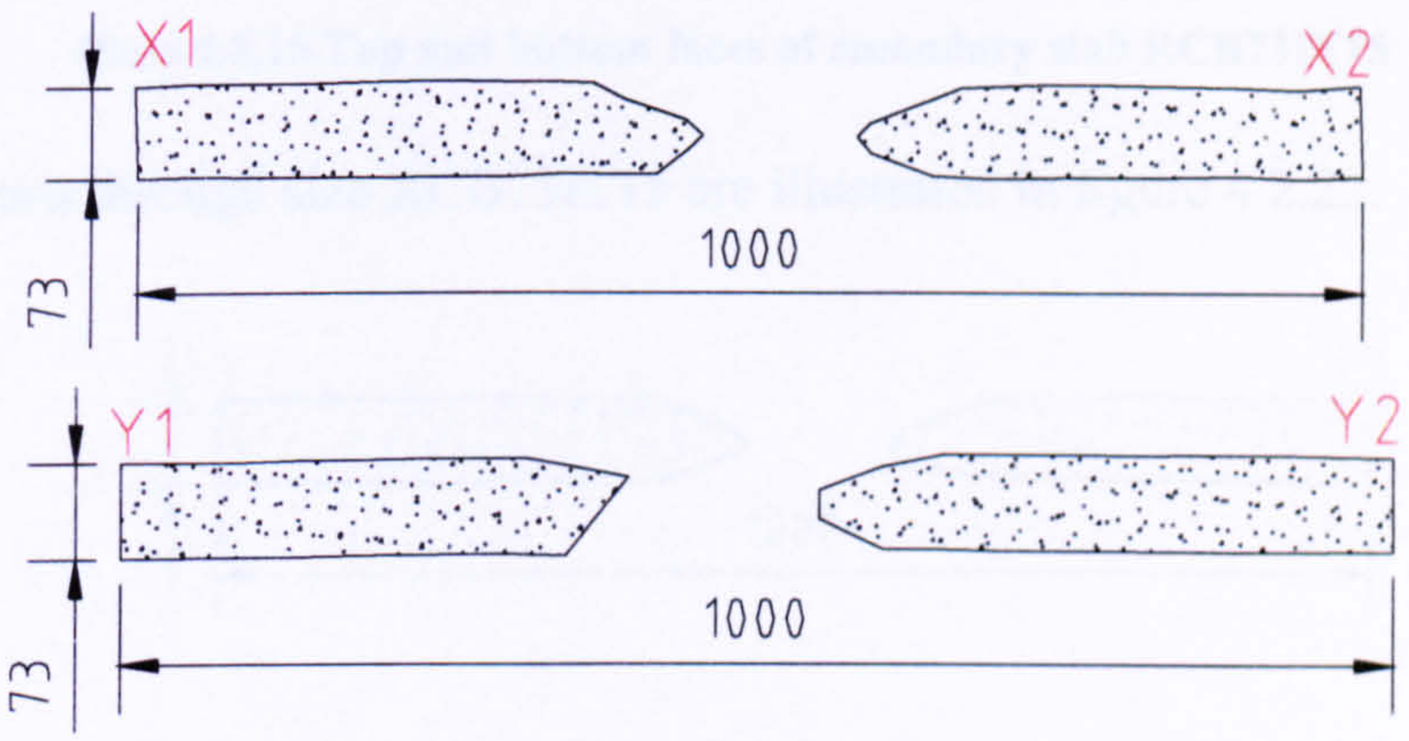

Figure 4.2.21 Cross-sectional elevation through X1-X2 and Y1-Y2 of secondary slab RCB73IT14

4.2.5.2 Test RCIT15

The damage to both faces of secondary slab RCB73IT15 is illustrated in plate 4.2.15.

Top face: Radial cracks appeared to dominate the central region of the slab followed by a large circumferential crack of radius 250mm as well as multiple corner cracks in corner B. The corner cracks indicated failure of the concrete caused by reflected stress waves. Dominant cracking was evident along the two orthogonal axes, with a concentrated amount of cracking in quadrant B.

Bottom face: Radial cracks propagated outwards, approximately the same radial distance as the cracks on the top face. Cracking in general was less severe compared to top face.

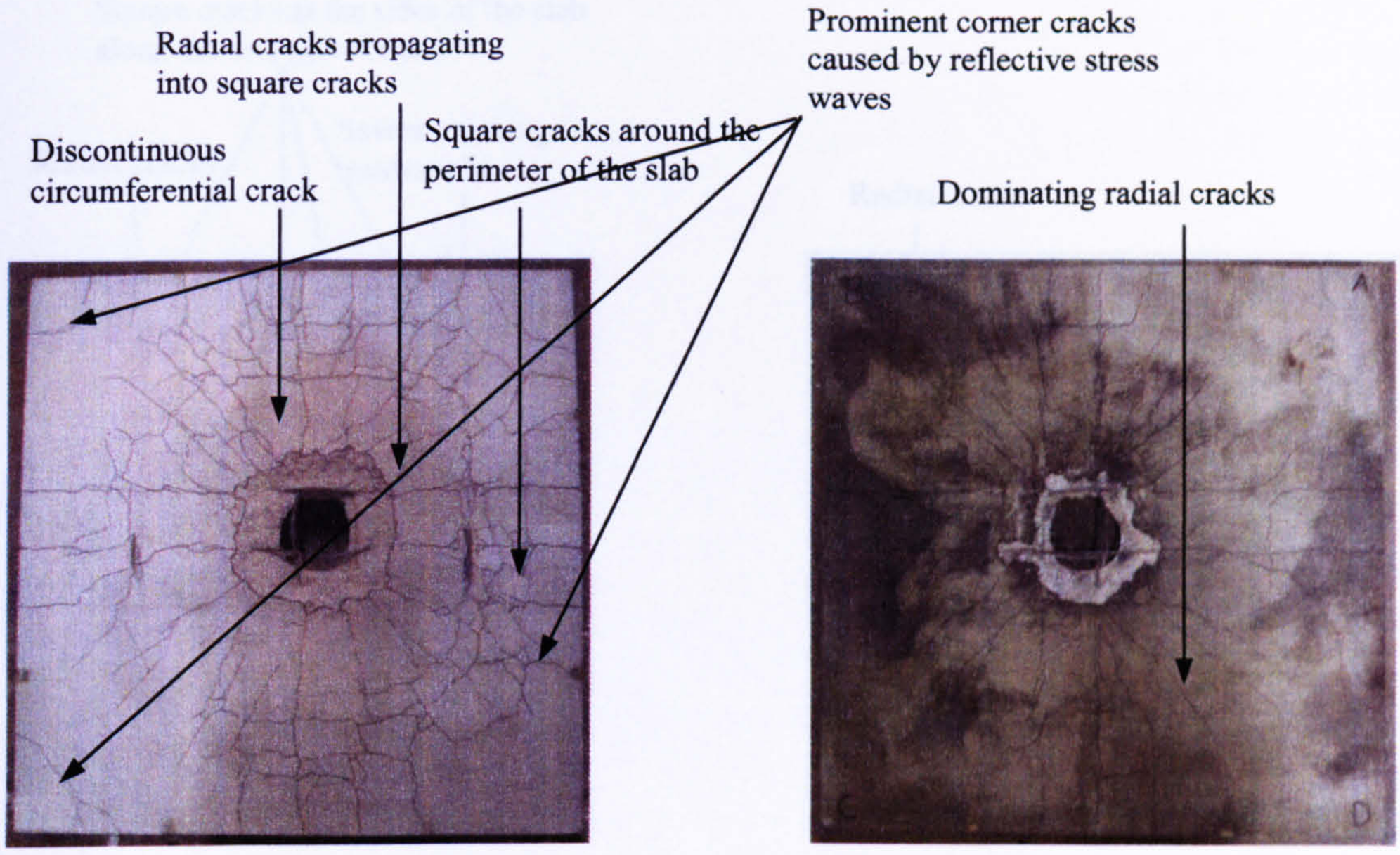

Top face Bottom face

Plate 4.2.15 Top and bottom faces of secondary slab RCB73IT15

Cross-sections through slab RCB73IT15 are illustrated in figure 4.2.22.

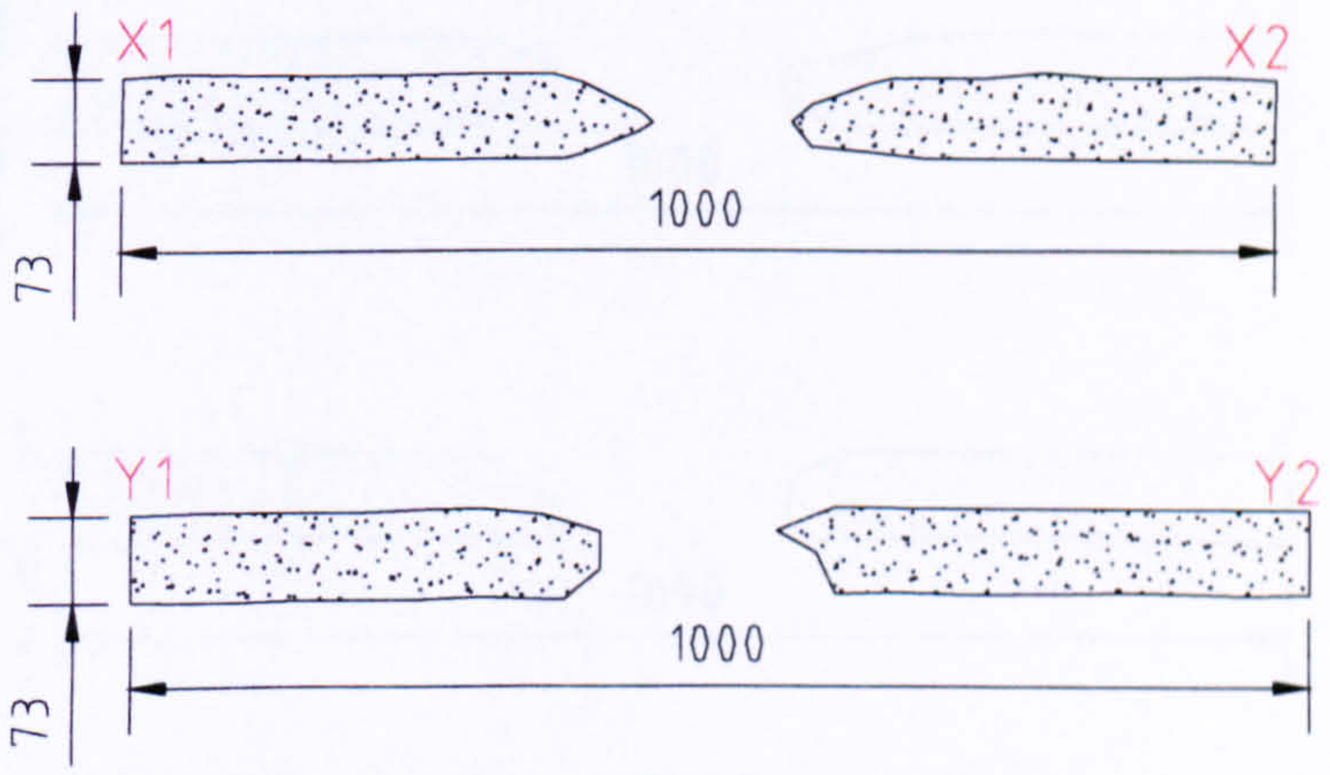

Figure 4.2.22 Cross-sectional elevation through X1-X2 and Y1-Y2 of secondary slab RCB73IT15

4.2.5.3 Test RCIT16

The damage to both faces of secondary slab RCB73IT16 is illustrated in plate 4.2.16.
Top face: Square cracks were evident as well as discontinuous circumferential cracks between equally spaced radial cracks.
Bottom face: Radial cracks propagated outwards and mild square cracks were evident along the orthogonal axes.

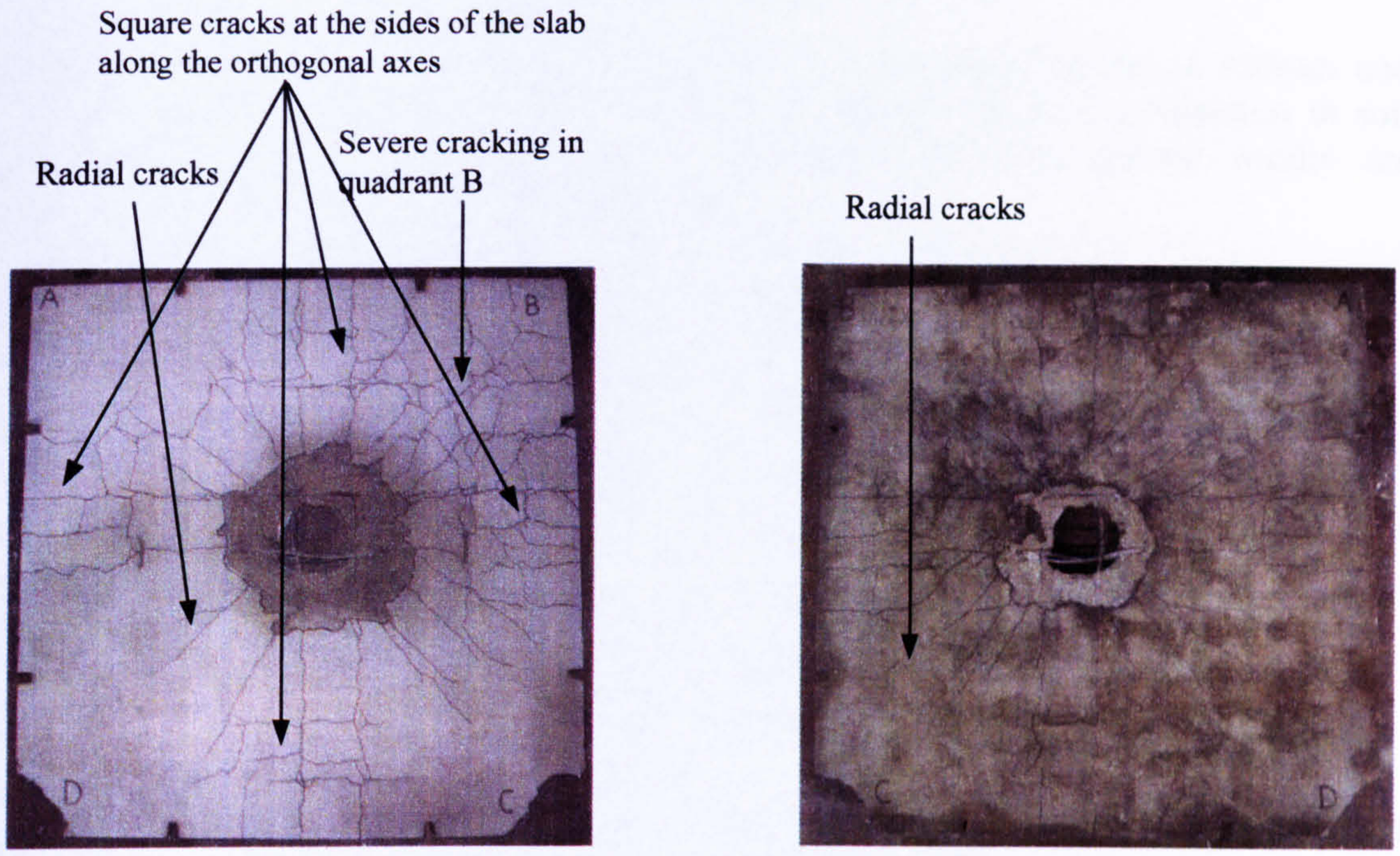

Top face

Bottom face

Plate 4.2.16 Top and bottom faces of secondary slab RCB73IT16

Cross-sections through slab RCB73IT16 are illustrated in figure 4.2.23.

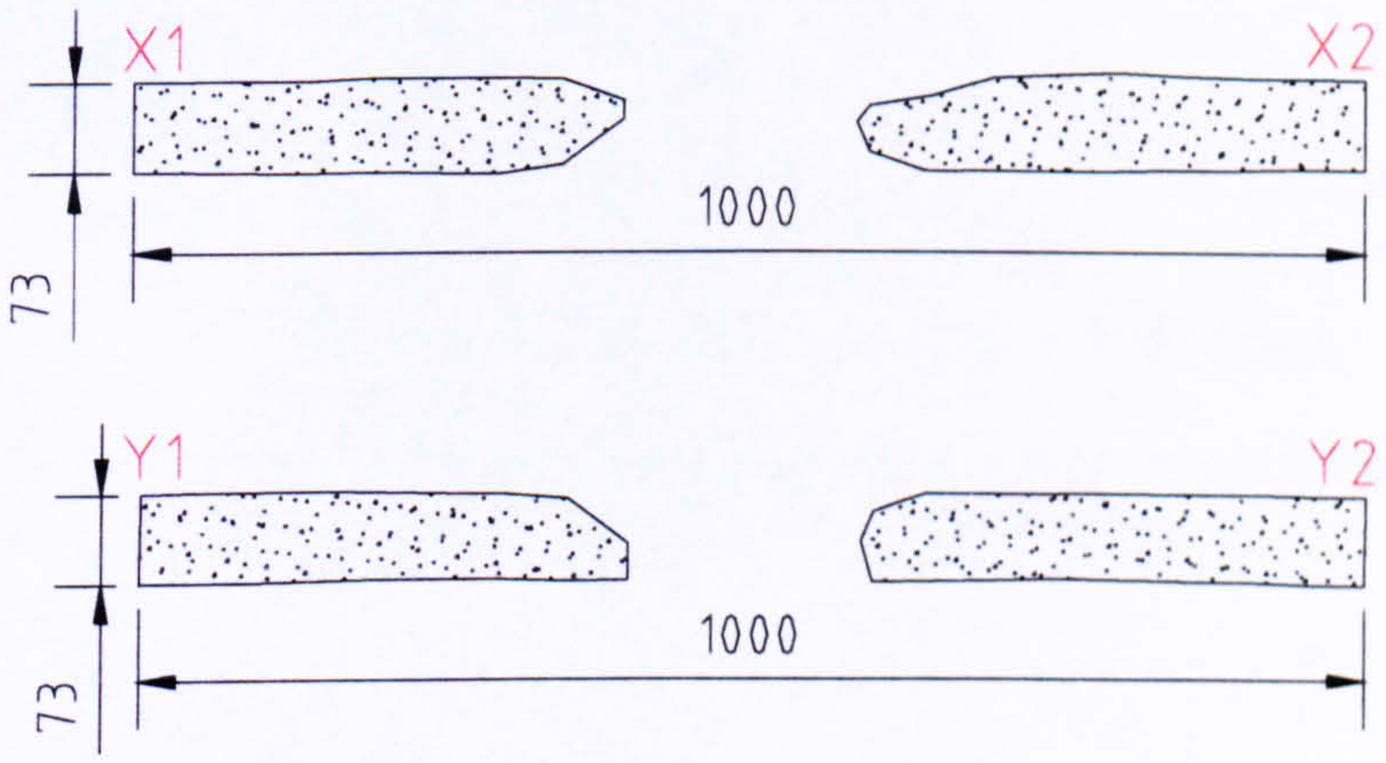

Figure 4.2.23 Cross-sectional elevation through X1-X2 and Y1-Y2 of secondary slab RCB73IT16

4.2.5.4 Damage analysis associated with Stage II results

The graphical plots that follow are based upon diametric measurements, recorded manually, used to approximate the surface area of cratering on both the top and bottom faces of a secondary slab as well as the surface area of perforation. It is important to state that the approximate surface area of cratering includes the approximate surface area of perforation. The curves in figures 4.2.24–4.2.26 were constructed from four data points. The inclusion of the data point associated with a

soil overburden of 500mm suggested that a decrease in the parameter influenced the damage. However, if this data point were removed, the remaining three data points would not suggest this phenomenon.
More tests would need to be performed at soil overburden depths of 300mm and 500mm, above the secondary slab, in order to validate whether a reduction in soil overburden affects the damage to a secondary slab. The current results are inconclusive, leaving scope for further work.

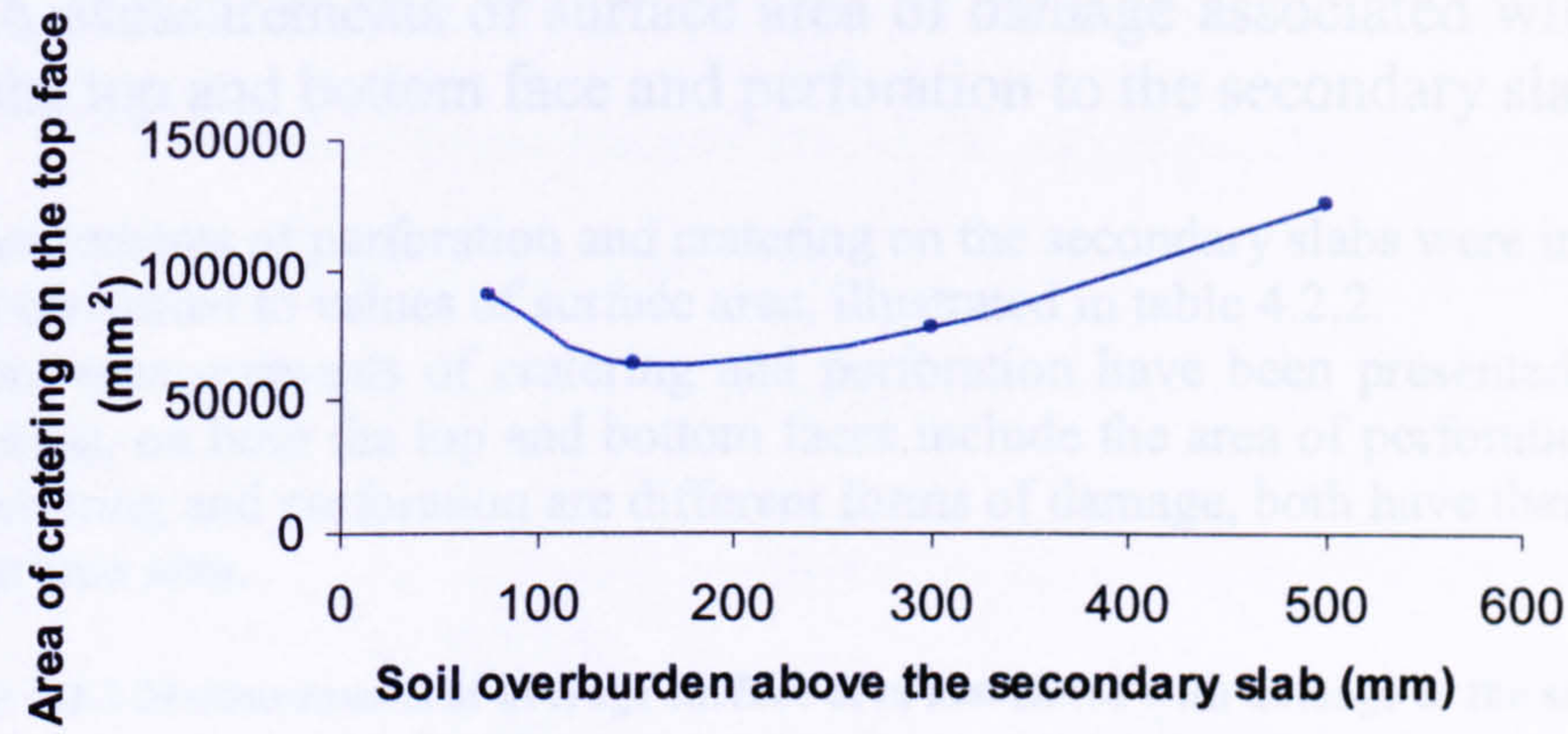

Figure 4.2.24 Area of cratering on the top face of the secondary slab associated with depth of soil overburden above the secondary slab

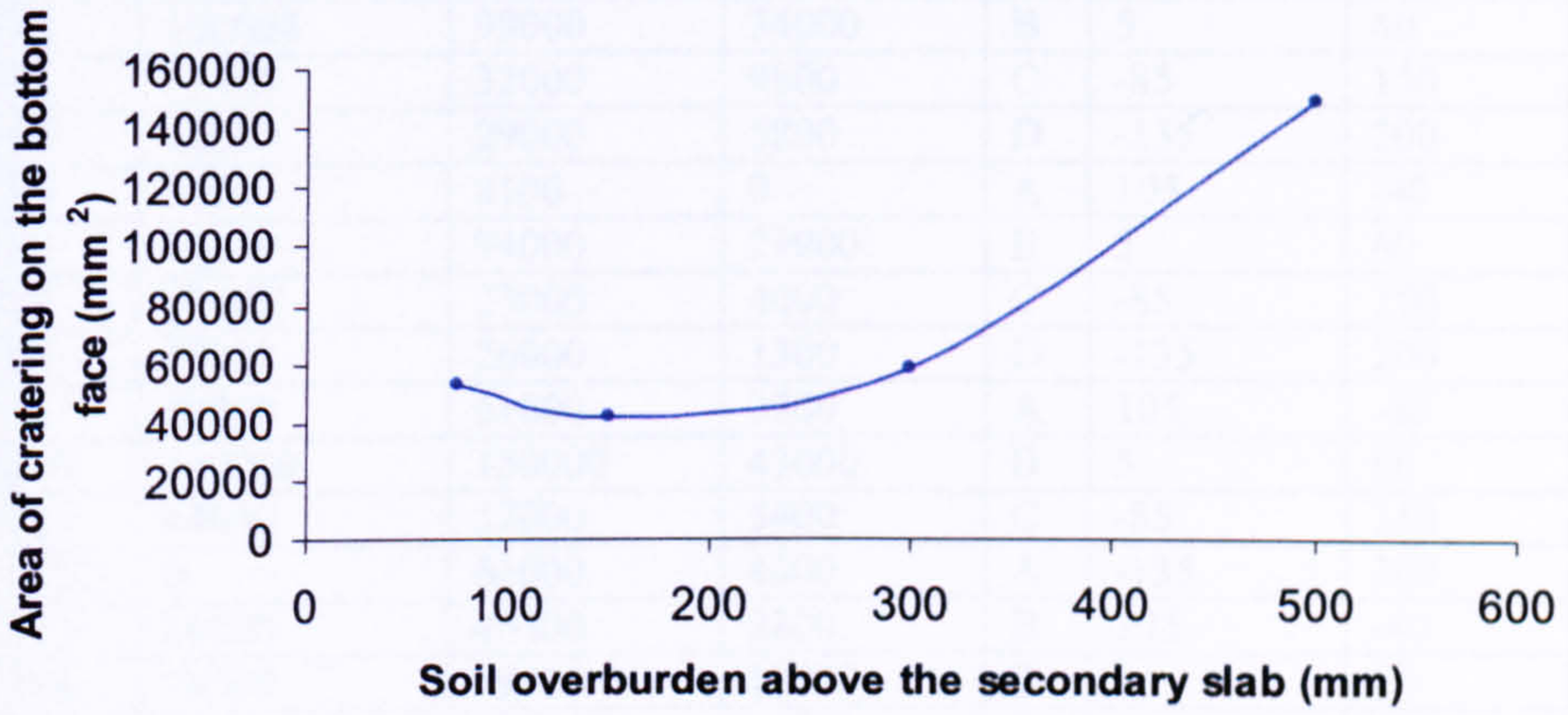

Figure 4.2.25 Area of cratering on the bottom face of the secondary slab associated with depth of soil overburden above the secondary slab

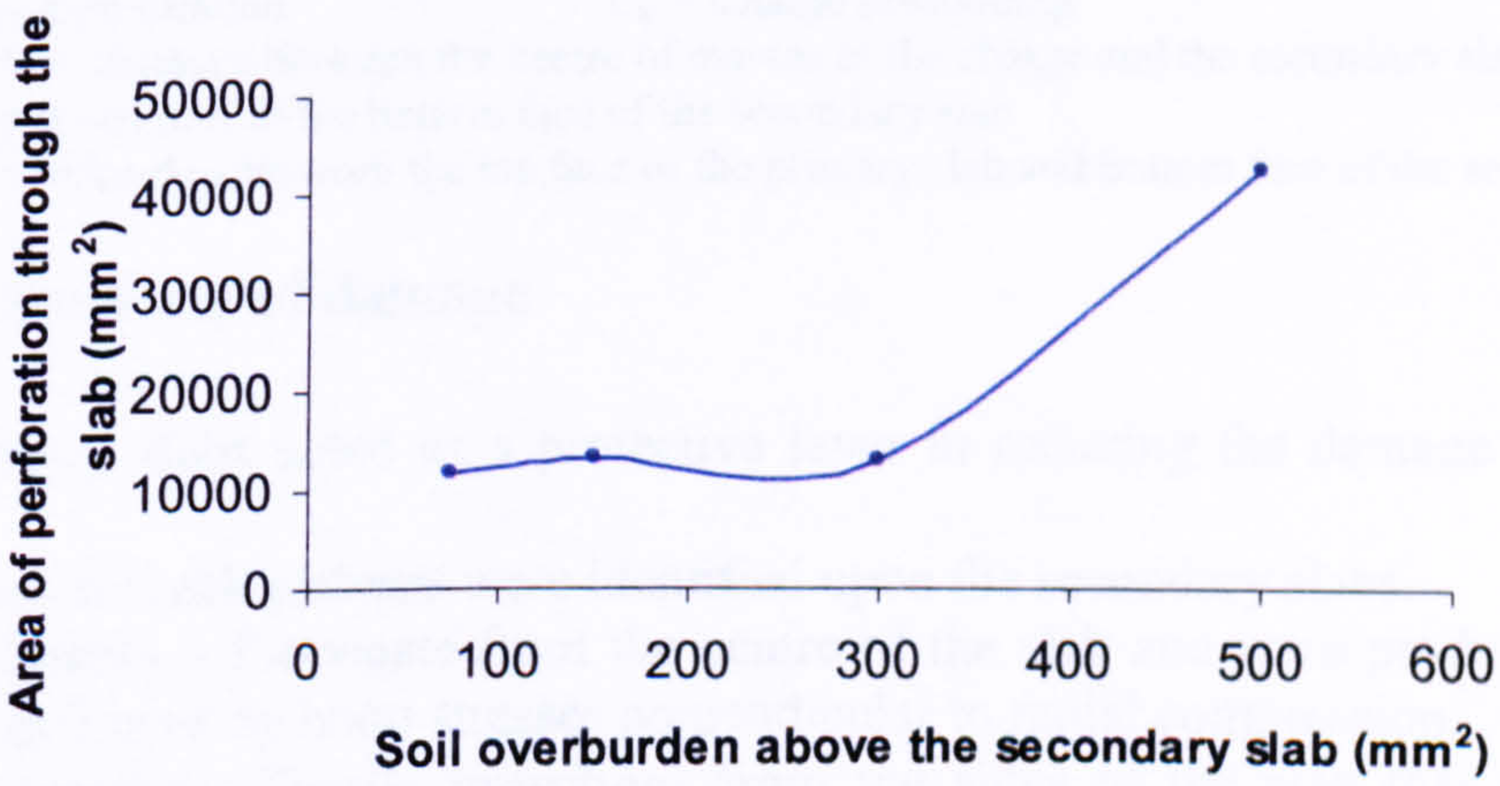

Figure 4.2.26 Area of perforation within the secondary slab associated with depth of soil overburden above the secondary slab

Due to problems with the DPGs used during Stage II, it was impossible to assess the loading across the primary slab as the soil overburden was reduced. It was decided to perform a number of hydrocode simulations in AUTODYN2D to initially establish, rather than to model, the effect caused by reducing the soil overburden above the secondary slab. The results from this are described in section 4.4.3.2.

4.2.6 Measurements of surface area of damage associated with cratering on the top and bottom face and perforation to the secondary slabs

Measurements of perforation and cratering on the secondary slabs were initially taken, then converted to values of surface area, illustrated in table 4.2.2.
Where measurements of cratering and perforation have been presented, the area of cratering, on both the top and bottom faces include the area of perforation. However, as cratering and perforation are different forms of damage, both have their own values of surface area.

Table 4.2.2 Measurements of average surface area associated with damage to the secondary slabs

Test number	A_{ct} (mm^2)	A_{cb} (mm^2)	A_p (mm^2)	C_p	Y_{cc} (mm)	S_{bb} (mm)	Z_l (mm)
RCIT1	5900.	54000	1370	A	105	-40	500
RCIT2	100008	98000	34000	B	5	60	500
RCIT3	62400	32000	9800	C	-85	150	500
RCIT4	76000	29000	5800	D	-135	200	500
RCIT5	3700	4100	0	A	105	-40	300
RCIT6	86000	94000	29000	B	5	60	300
RCIT7	57000	23000	4000	C	-85	150	300
RCIT8	40000	26000	1300	D	-135	200	300
RCIT9	54000	61000	3800	A	105	-40	150
RCIT10	130000	150000	43000	B	5	60	150
RCIT11	49000	37000	5400	C	-85	150	150
RCIT12	0	63000	4600	A	-135	200	75
RCIT13	80000	40000	2800	B	105	-40	75
RCIT14	78000	59000	13000	B	5	60	150
RCIT15	64000	42000	13000	B	5	60	150
RCIT16	90000	53000	11800	B	5	60	150

A_{ct} = Area of cratering on the top face A_{cb} = Area of cratering on the bottom face
A_p = Area of perforation C_p = Charge positioning
Y_{cc} = Vertical distance between the centre of masses of the charge and the secondary slab
S_{bb} = Charge standoff to the bottom face of the secondary slab
Z_l = Soil overburden between the top face of the primary slab and bottom face of the secondary slab

4.2.7 Overview of damage

A secondary slabs acted as a protective layer in reducing the damage to a primary slabs.
A number of crack patterns were identified upon the secondary slabs.
Radial cracks – Propagate from the centre of the slab and were produced either by flexural action or by hoop stresses perpendicular to radial compression.
Corner cracks - Tensile reflections from the sides of the slab that exceeded the tensile resistance of the concrete. These cracks occurred within the corner regions.

Square cracks – Visibly prominent along the orthogonal axes of the slab, indicating the shortest distance in stress wave propagation. The cracks indicated a direct transfer of load from the concrete into the steel. They covered the entire the plan area on most slabs, and geometrically resembled the reinforcement mesh.

Circumferential cracks – Propagated around the circumference of a crater and penetrated the surface of the slab. Those furthest away from the crater or the epicentre of the slab may have been related to the phenomena associated with the formation of a dome, associated with a flexural response. Two types of circumferential cracks were also identified:

1. discontinuous circumferential cracks trapped perpendicular between two radial cracks,
2. continuous circumferential cracks without the interruption of radial cracks.

Three main crack patterns were continuously identified on the faces of the secondary slabs as illustrated in table 4.2.3.

Table 4.2.3 Differentiating between the types of cracks present on the faces of secondary slabs associated with the charge positions

	Top face			Bottom face		
Charge positions	Radial cracks	Circumferential cracks	Square cracks	Radial cracks	Circumferential cracks	Square cracks
A	x	√	√	√	√	x
B	√	x	x	√	x	x
C	√	√	x	x	√	√
D	√	√	x	x	√	√

x = Cracks not present
√ = Cracks present

Charge positions were also associated with percentages of charge volumes, illustrated in table 4.2.4 and embedded within the following:

1. soil overburden above the secondary slab,
2. thickness of the secondary slab,
3. soil overburden contained between the primary and secondary slabs.

Table 4.2.4 Proportion of the charge's volume embedded relative to a secondary slab

Charge positions	Charge proportion within Z_1 (%)	Charge proportion within the secondary slab (%)	Charge proportion within Z_2 (%)	Vertical distance between centre of masses of the charge and secondary slab (mm)
A	0	5	95	105
B	33	49	18	5
C	77	23	0	-85
D	100	0	0	-135

Z_1 = Soil overburden contained between the primary and secondary slab
Z_2 = Soil overburden above the secondary slab

Even though charge position A had 5.18% of its volume embedded within the slab, the damage to the slab was less compared to charge position D with 100% of its volume embedded within the soil overburden below the secondary slab.

if enough explosive is coupled with the soil underneath the concrete slab, a larger flexural type crater is formed with regions of enhanced penetrability, as observed by **Cameron *et al* (2000).** This was observed on secondary slabs RCB73IT4 and RCB73IT8, where the charge was positioned below the bottom face of the slab.
By approximately positioning a charge so that a third of its volume was embedded within each of the three layers, the overall damage significantly increased. The proportion of charge embedded within the soil overburden beneath the secondary slab inflicted an additional heave force through the bottom face. This had the effect of weakening it, combined with a sufficient volume of charge within its thickness, causing internal damage.
Charge positions C and D both appeared to have produced similar magnitudes of overall damage as illustrated in plates 4.2.3, 4.2.4, 4.2.7 and 4.2.8.
Even though the volume of charge embedded within the thickness of the secondary slab was greater in C then in D, the magnitude of damage produced by charge positions C and D were comparable. This indicated that a greater volume of charge mass embedded within the thickness of the slab caused a greater surface area of visible damage, even though internal damage might have been greater.
Wood (1961) commented on the nature of cracks that formed on reinforced concrete slabs when subjected to explosive loading. He described the face of the slab that is in contact with the greatest proportion of the charge, being forced into compression and yield lines in the form of circumferential cracks occurring on the surface as a result of radial forces. The opposite face then goes into tension, exhibiting radial cracks, caused by circumferential forces. These types of cracks were visible on the top and bottom faces of the secondary slabs that were subjected to charge position A in tests RCIT1, 5, 9 and 12.
Pope (2002) presented a damaged slab in figure 2.9.1 with radial and circumferential cracks visibly evident on its top face as a result of airblast. The same types of cracks were also been identified on the top faces of secondary slabs when charge position A was implemented in tests RCIT1, 5, 9 and 12 in table 4.2.5.

Table 4.2.5Top face of secondary slabs with radial and circumferential cracks

	RCB73IT1	RCB73IT5	RCB73IT9	RCB73TI12
Top face of secondary slabs caused by charge position A	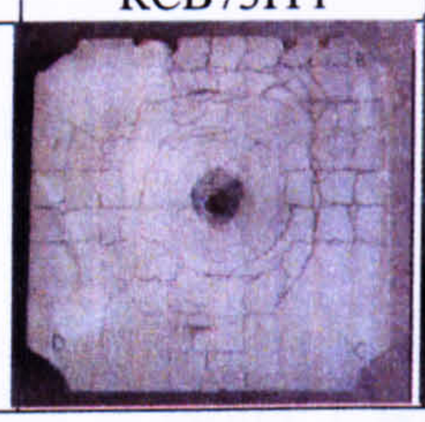	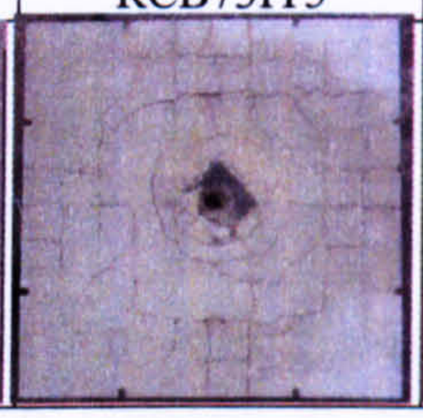	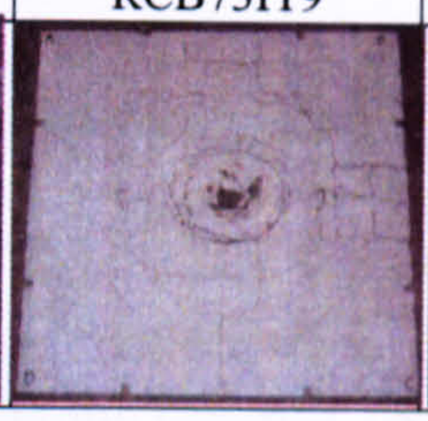	

Renick (2000) considered a number of damage mechanisms that were employed when a charge was detonated within an air/concrete/soil experimental set-up. One particular mechanism that was observed upon secondary slab RCB73IT7 in test RCIT7, was flexure. A typical cross-sectional elevation of slab RCBI73T7 in figure 4.2.27 illustrated this phenomenon.

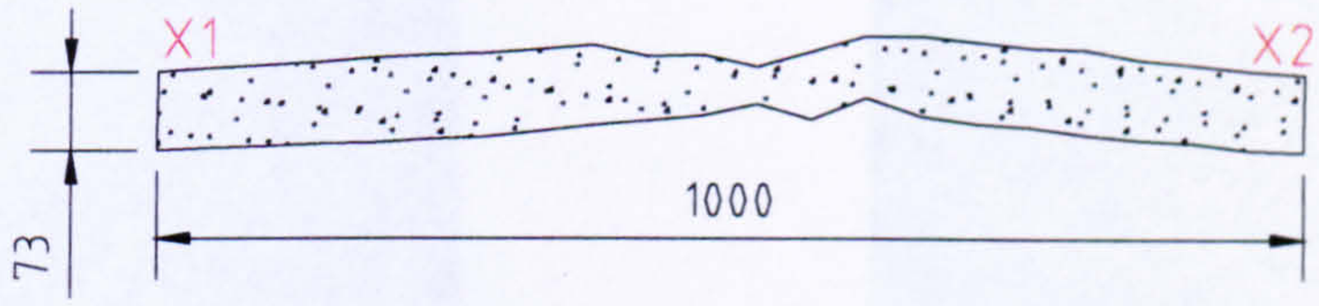

Figure 4.2.27 Cross-sectional elevation through X1-X2 of secondary slab RCB73IT7 indicating flexure

The four modes of damage described by **Deng *et al* (2004)** have been observed on the damaged secondary slabs using charge position A in tests RCIT1, 5, 9 and 12.
Duranovic (1994) illustrated a number of damaged reinforced concrete slabs in figure 2.9.5 that were subjected to airblast. The damage contained square cracks on both faces and radial cracks on the bottom face, which was in context with the damage to slabs in tests RCIT1, 5, 9 and 12.

4.3 Primary slabs

Four primary slabs were used throughout Stage I, each subjected to a number of cumulative hits as illustrated in table 4.3.1. The soil overburden above the secondary slab remained fixed at 500mm, whilst the soil overburden above the primary slab varied.

Table 4.3.1 Cumulative hits associated with the damage sustained by the primary slabs.

Group	Tests	Test descriptions	Primary slabs	Number of cumulative hits	Soil overburden between the primary and secondary slabs (mm)
1	1-4	RCIT1-4	RCR73IT1-4	4	500
2	5-8	RCIT5-8	RCR73IT5-8	4	300
3	9-11	RCIT9-11	RCR73IT9-11	3	150
4	12-13	RCIT12-13	RCR73IT12-13	2	75

4.3.1 Cumulative damage subjected to the primary slab used in Stage I - group 1 of the test matrix

The soil overburden confined between top and bottom face of the primary and secondary slab in group 1 was constant at 500mm.The soil overburden above the secondary slab remained constant at 500mm
The damage to both faces of primary slab RCR73IT1-4 is illustrated in plate 4.3.1.
Top face: Corner and short cracks around the supports were vaguely evident as well as thin square cracks over the face.
Bottom face: Radial cracks propagated from the centre of the slab, illustrating early signs of weakening.

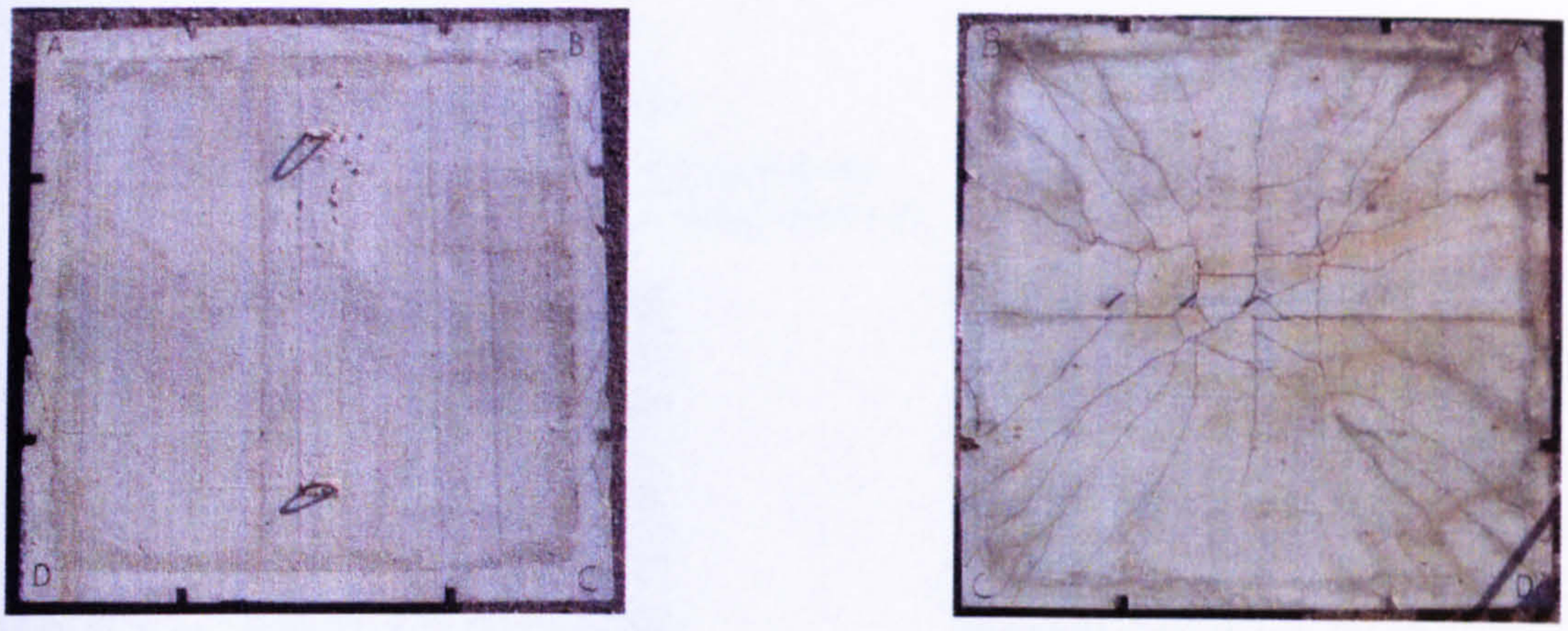

Top face Bottom face

Plate 4.3.1 Top and bottom faces of primary slab RCR73IT1-4

Cross-sections through slab RCR73IT1-4 are illustrated in figure 4.3.1.

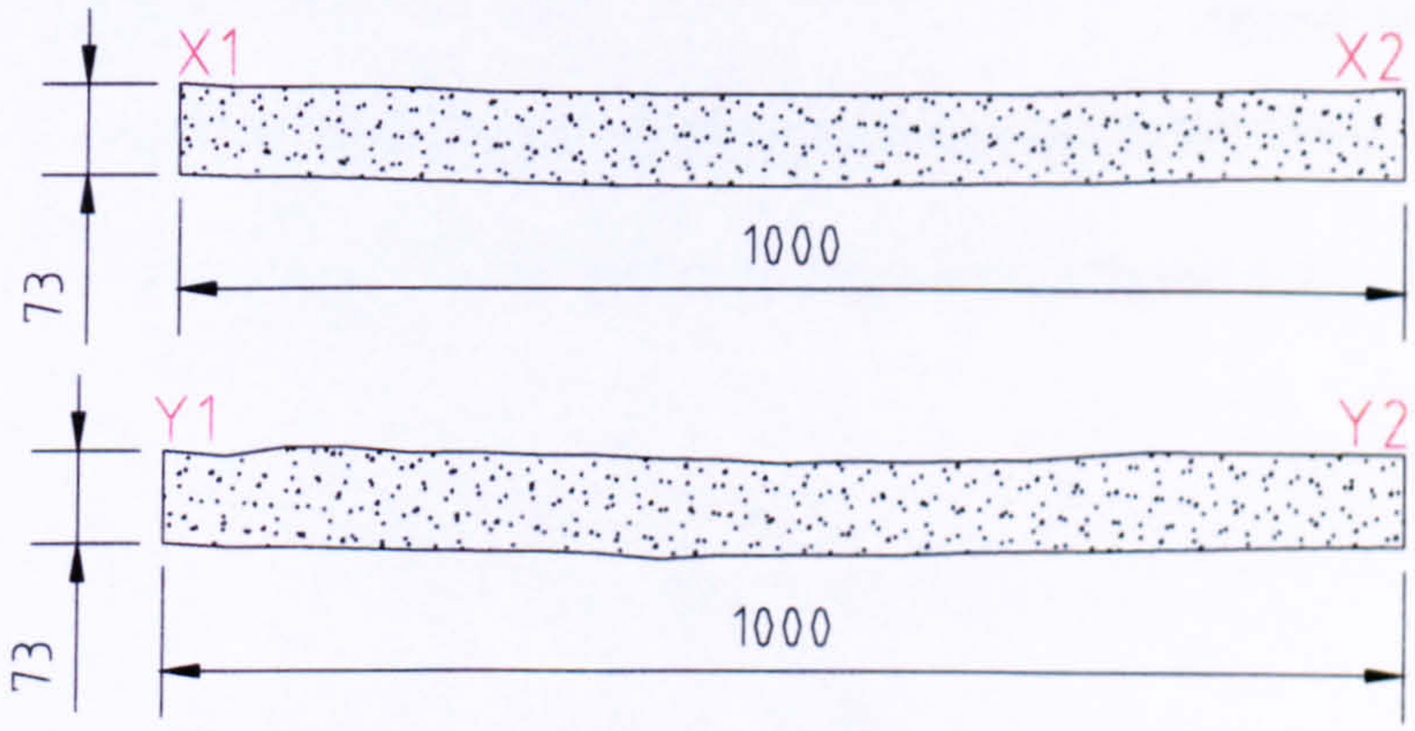

Figure 4.3.1 Cross-sectional elevation through X1-X2 and Y1-Y2 of primary slab RCR73IT1-4

4.3.2 Cumulative damage subjected to the primary slab used in Stage I-group 2 of the test matrix

The soil overburden confined between top and bottom face of the primary and secondary slab in group 2 was constant at 300mm. The soil overburden had decreased by 40% from an original value of 500mm. The soil overburden above the secondary slab remained constant at 500mm.

The damage to both faces of primary slab RCR73IT5-8 is illustrated in plate 4.3.2.

Top face: Fully developed corner cracks on all four corners were evident. Rotation was evident along support B1-C1. A central square area formed, with irregular radial cracks and cratering propagating from the four corners, perpendicular with the corner cracks.

Bottom face: Wide radial cracks propagated deep into the thickness of the slab, dominating the surface and exposing the rebars over the entire face.

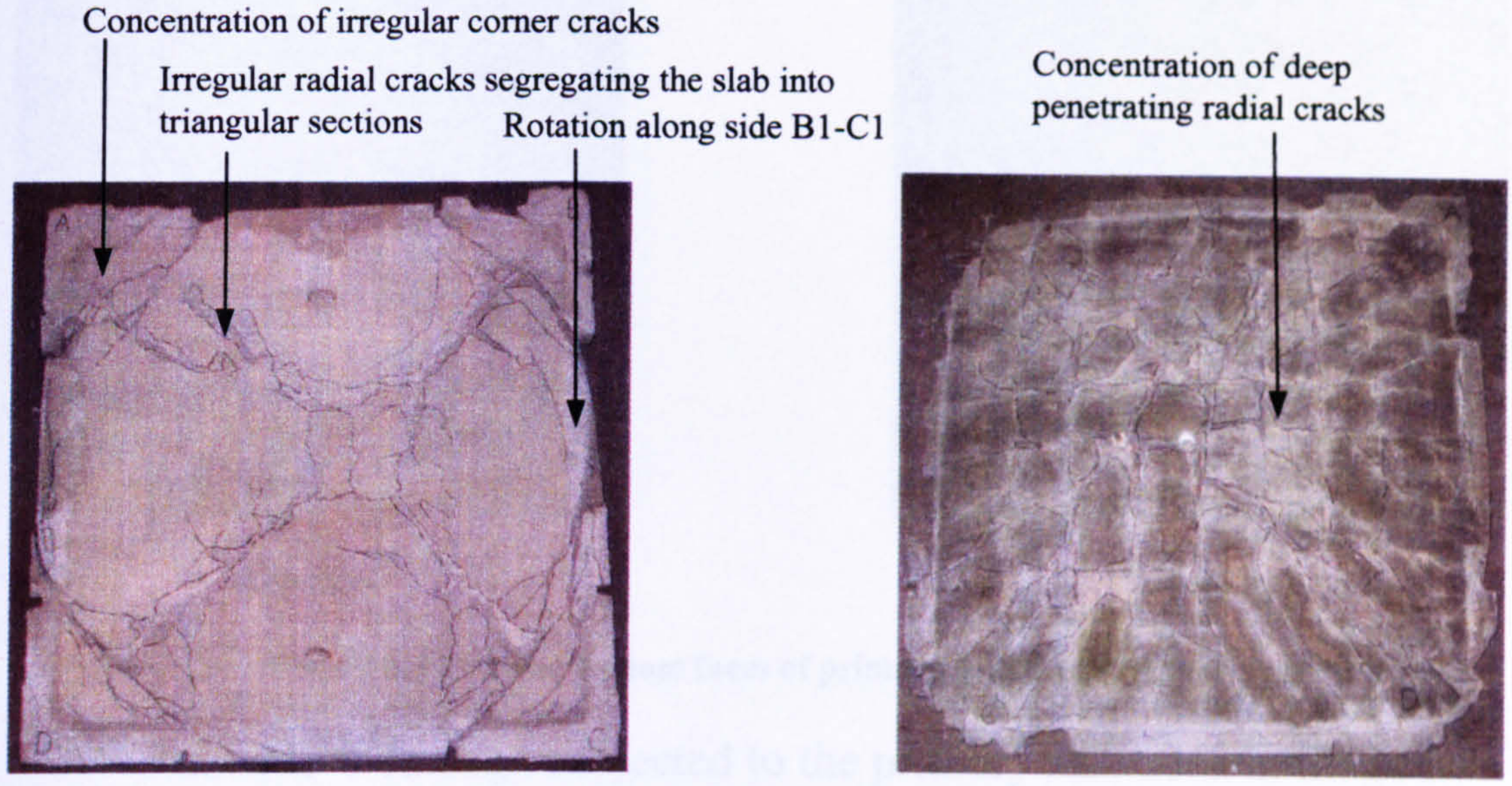

Plate 4.3.2 Top and bottom faces of primary slab RCR73IT5-8

A cross-section through slab RCR73IT5-8 is illustrated in figure 4.3.2

.

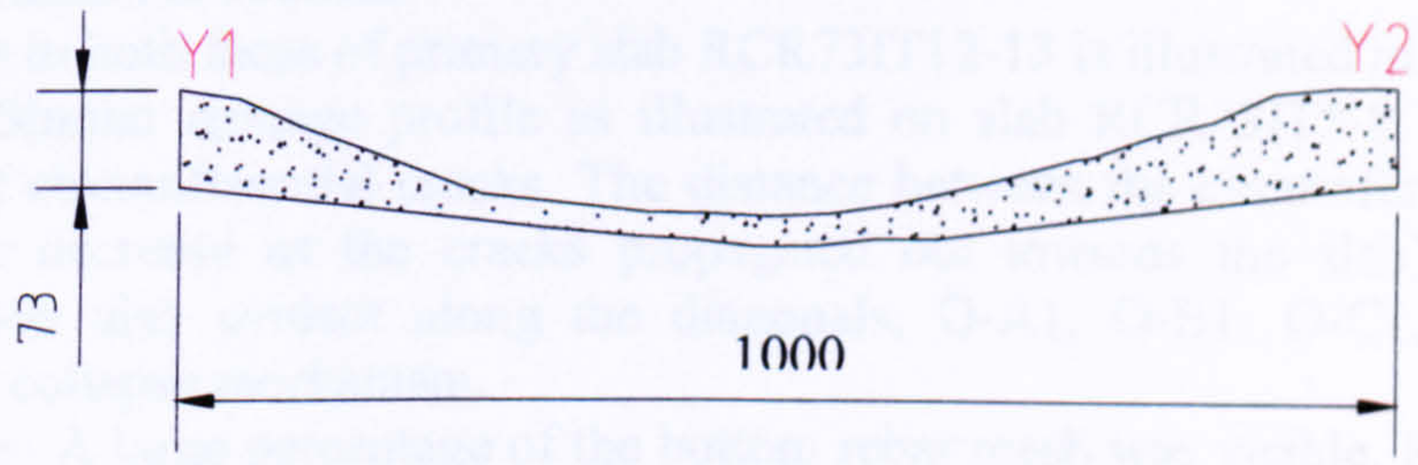

Figure 4.3.2 Cross-sectional elevation through Y1-Y2 of primary slab RCR73IT5-8.

4.3.3 Cumulative damage subjected to the primary slab used in Stage I-group 3 of the test matrix

The soil overburden confined between top and bottom face of the primary and secondary slab in group 3 was constant at 150mm. The soil overburden had decreased by 70% from an original value of 500mm. The soil overburden above the secondary slab remained constant at 500mm. The damage to both faces of primary slab RCR73IT9-11is illustrated in plate 4.3.3.

Top face – The concrete cover had significantly reduced, preventing crack profiles from being identified. The support conditions could no longer prevent rotation

Bottom face – Deep penetrating radial cracks propagated from the central region of the slab out towards the perimeter.

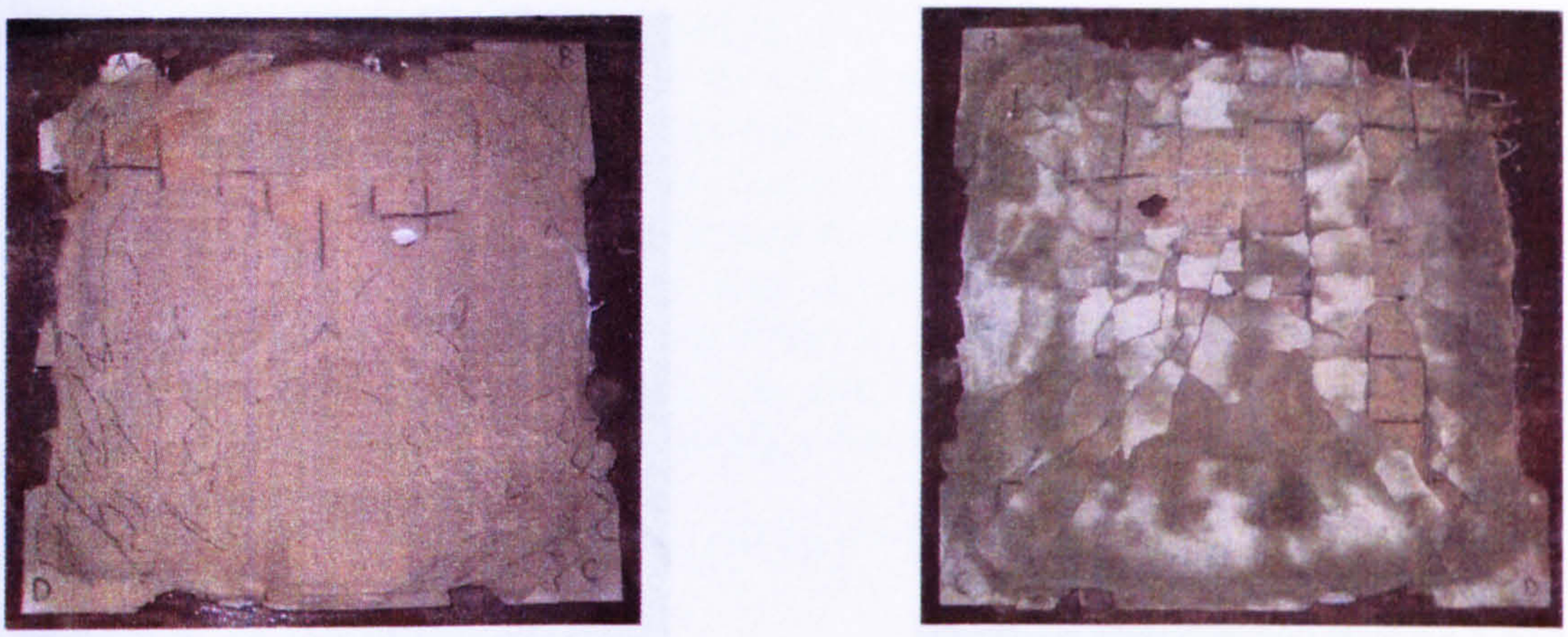

Top face Bottom face

Plate 4.3.3 Top and bottom faces of primary slab RCR73IT9-11.

4.3.4 Cumulative damage subjected to the primary slab used in Stage I-group 4 of the test matrix

The soil overburden confined between top and bottom face of the primary and secondary slab in group 4 was constant at 73mm. The soil overburden decreased by 85% from an original value of 500mm. The soil overburden above the secondary slab remained constant at 500mm.

The damage to both faces of primary slab RCR73IT12-13 is illustrated in plate 4.3.4.

Top face: Similar damage profile as illustrated on slab RCR73IT5-8 but with the inclusion of circumferential cracks. The distance between the circumferential cracks appeared to decrease as the cracks propagated out towards the slab's perimeter. Cratering was also evident along the diagonals, O-A1, O-B1, O-C1, and O-D1, indicating a collapse mechanism.

Bottom face: A large percentage of the bottom rebar mesh was visible. Radial cracks were evident around the perimeter. The bottom mesh appeared to be retaining the damaged concrete. Slip action was also visible that caused the top rebars to deform. The rebars in the top face were pulled into the slab at the angle to the horizontal during flexural action. This caused a de-bonding movement at the ribbed steel-concrete interface, causing the perpendicular rebar hooks, which pointing downwards to bend outwards. This caused the hook angle to increase byto rotation, as illustrated in plate 4.3.5.

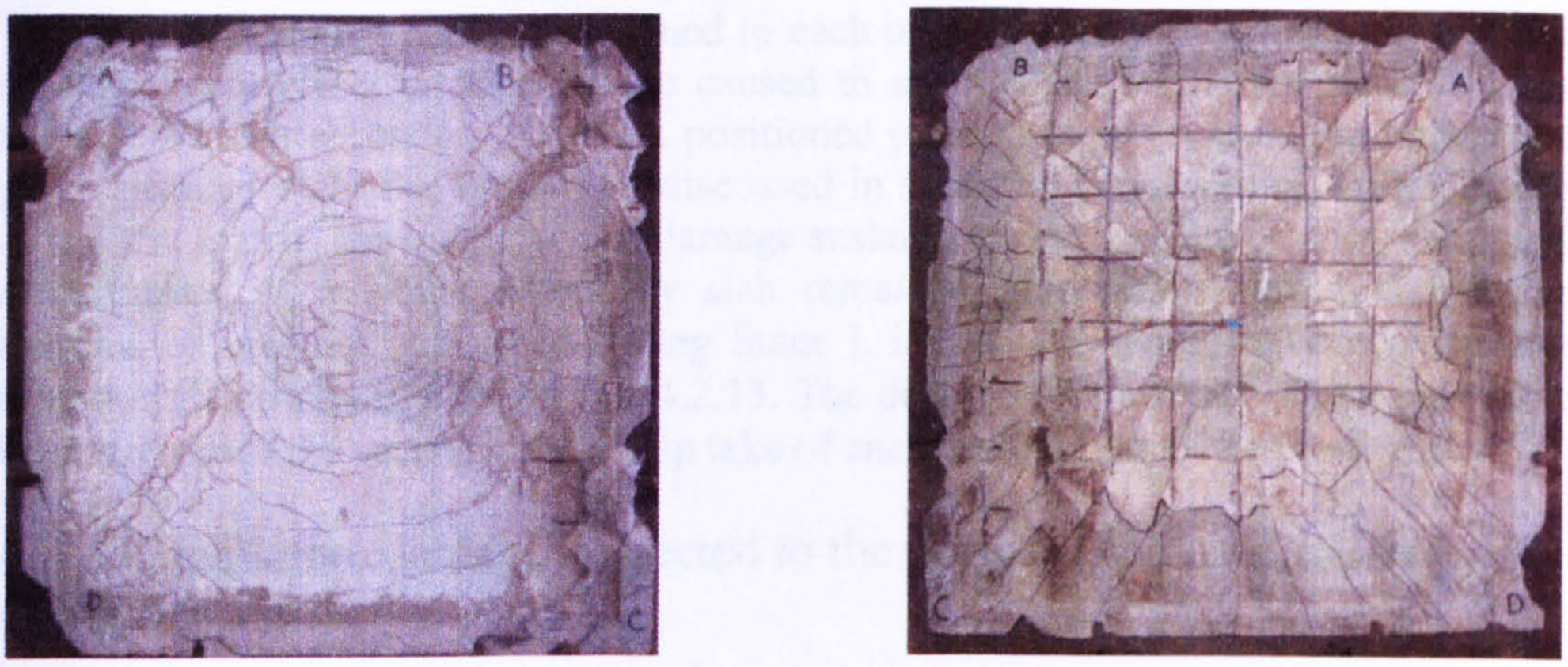

Top face Bottom face

Plate 4.3.4 Top and bottom faces of primary slab RCR73IT12-13.

Cross-sections through slab RCR73IT12-13 are illustrated in figure 4.3.3.

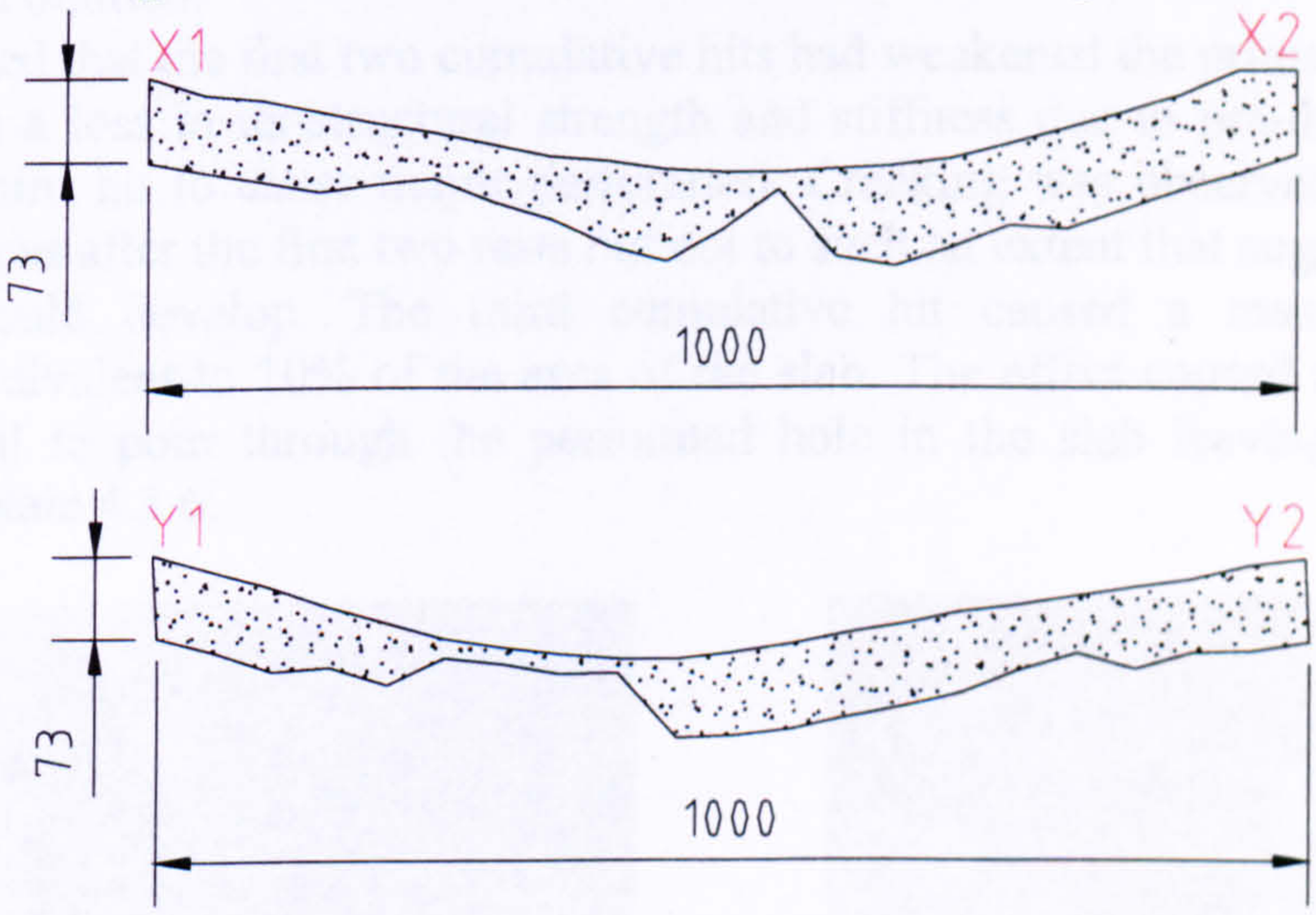

Figure 4.3.3 Cross-sectional elevation through X1-X2 and Y1-Y2 of primary slab RCR73IT12-13.

Section of concrete held in position by the steel mesh

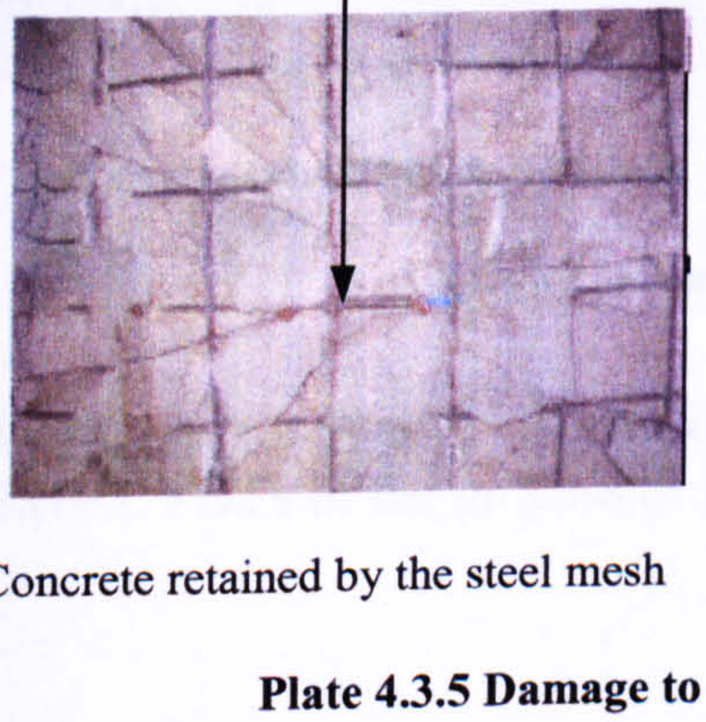

Concrete retained by the steel mesh

Slip on a rebar in the top mesh

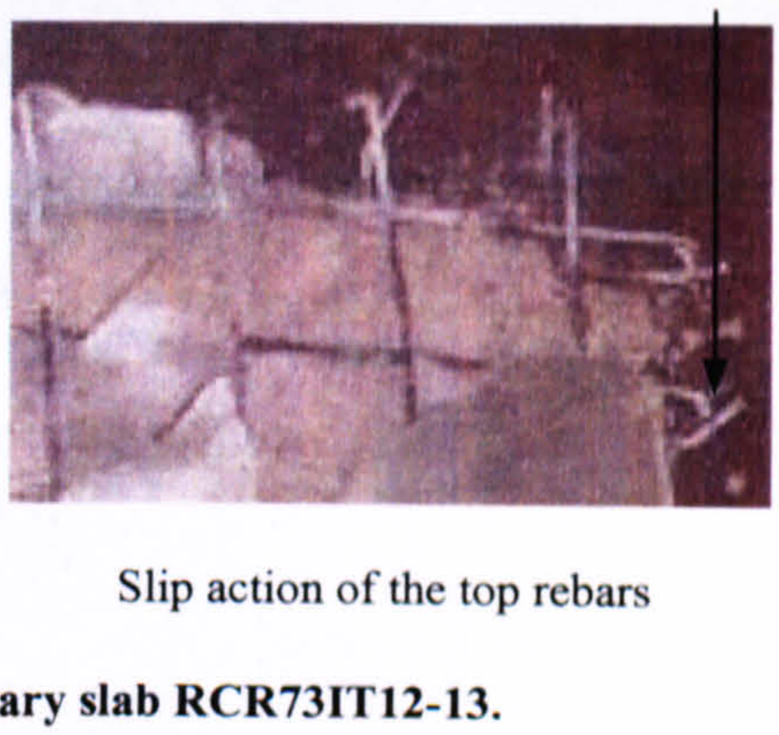

Slip action of the top rebars

Plate 4.3.5 Damage to the bottom face of primary slab RCR73IT12-13.

The final cumulative damage sustained to each of the primary slabs from Stage I has no significant effect on the damage caused to each of the secondary slabs. This is because a fresh secondary slab was positioned prior to every cumulative hit upon a given primary slab. For reasons as discussed in section 3.7 concerning the reduction of the test matrix, the magnitude of damage sustained to each of the primary slabs was a minimum. If a single secondary slab remained in position during cumulative loading, as was not performed during Stage I, its damage would have been greater than that illustrated in plates 4.2.1–4.2.13. The damage to a primary slab would have been greater as the secondary slabs up take of energy would have been less.

4.3.5 Cumulative damage subjected to the primary slab used in Stage III of the test matrix

This was the final stage of the test matrix. Three tests were performed without the use of positioned secondary slabs. The charge standoffs varied from 190mm, 90mm and 0mm, identical to the values used in tests RCIT9-11. The objective was to compare the severity of damage subjected to two primary slabs, when secondary slabs are positioned and omitted.

It was suspected that the first two cumulative hits had weakened the primary slab such that there was a loss in its structural strength and stiffness due to pre-damage. This allowed the third hit to cause major perforation. Cracking was observed on the top and bottom faces after the first two tests but not to such an extent that suggested that a perforation could develop. The third cumulative hit caused a massive central perforation equivalent to 10% of the area of the slab. The effect caused a cylindrical volume of soil to pour through the perforated hole in the slab leaving a void, as illustrated in plate 4.3.6.

Plan elevation of the test cell

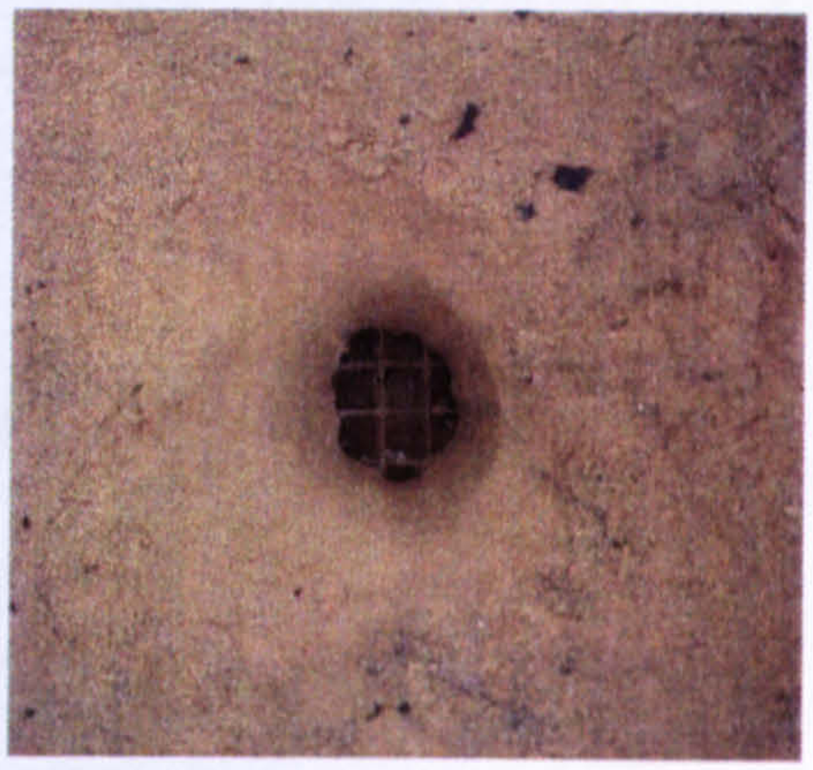

Cylindrical cavity in the soil overburden

Plate 4.3.6 Plan elevation of the test cell with a soil void.

The third cumulative hit caused a large deflection of the primary slab, damaging all three LVDTs in the process as illustrated in plate 4.3.7.

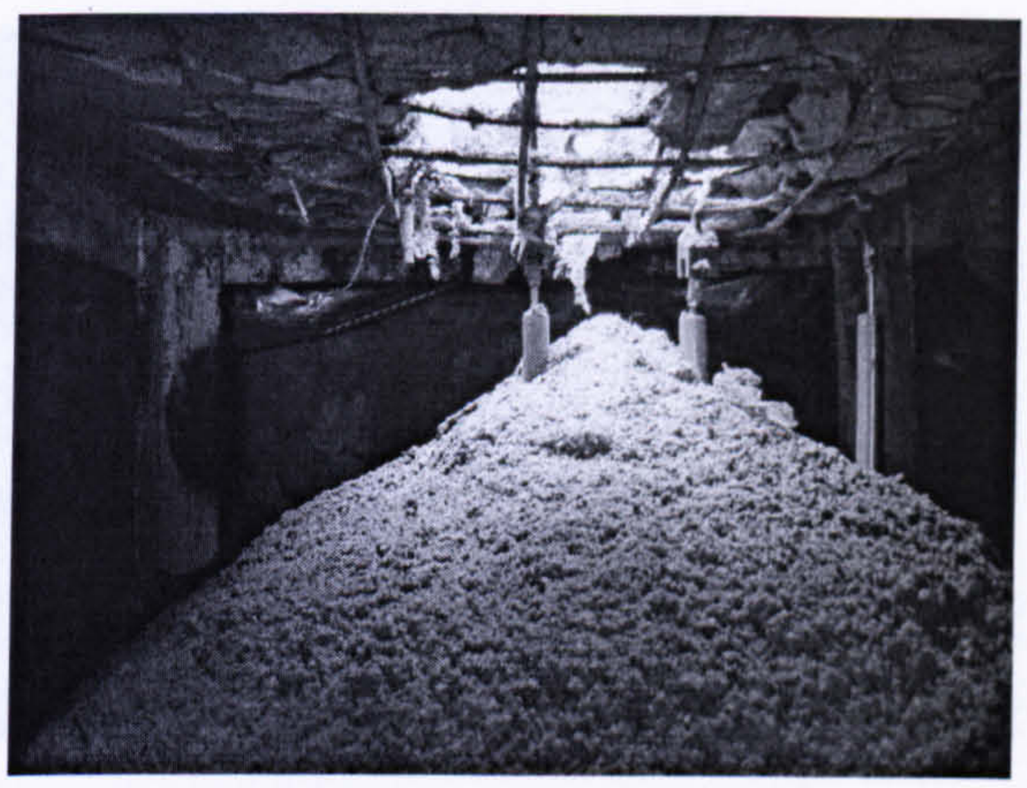

Plate 4.3.7 Infill of soil beneath the primary slab.

Regions of damage to the top and bottom faces of slab RCR73IT17-19 have been illustrated in plates 4.3.8–4.3.11, followed by plan elevations in plate 4.3.12.

Top face: Punching shear failure, which perforated the slab, followed by subsequent scabbing on the bottom face, caused the greatest damage. The cross-sectional elevation of the slab illustrated inclined planes that passed through the thickness of the slab associated with shear failure. Once the large mass of concrete had been removed from the centre, the overall compressive strength decreased. This caused diaphragm action also known as catenary action of the slab forcing the load to be carried by the steel reinforcement. This phenomenon caused tensile failure of the concrete.

The circumferential cracks which propagated out from around the perforated hole, were caused by radial stresses, perpendicular to the crack plane, that caused flexural action of the slab.

The large circumferential crack around the perforation indicated a plane of weakness, illustrated in plate 4.3.8, where the load exceeded the tensile capacity of the concrete. The circumferential cracks indicated subsequent failure planes that did not penetrate the entire thickness of the slab.

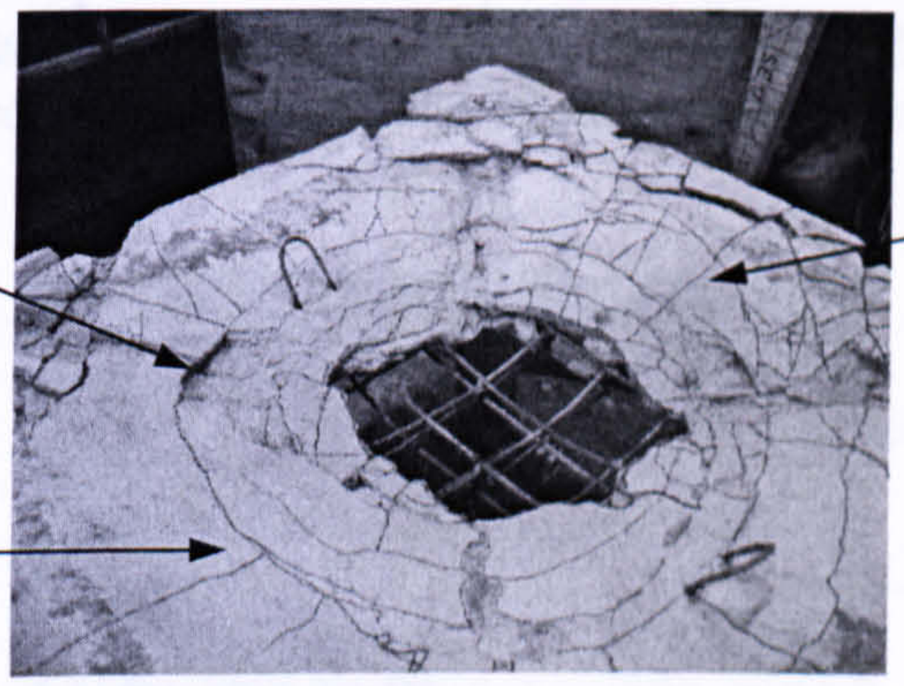

Plate 4.3.8 Magnified damage profile of the top face of the primary slab.

Yield failure and crushing as illustrated in plate 4.3.9 were observed along the diagonal planes O-A1, O-B1, O-C1 and O-D1 of the slab were identified. These are also common on slabs subjected to static loading, as discussed by **Park (2000)** and **Wood (1961)** in section 2.9.

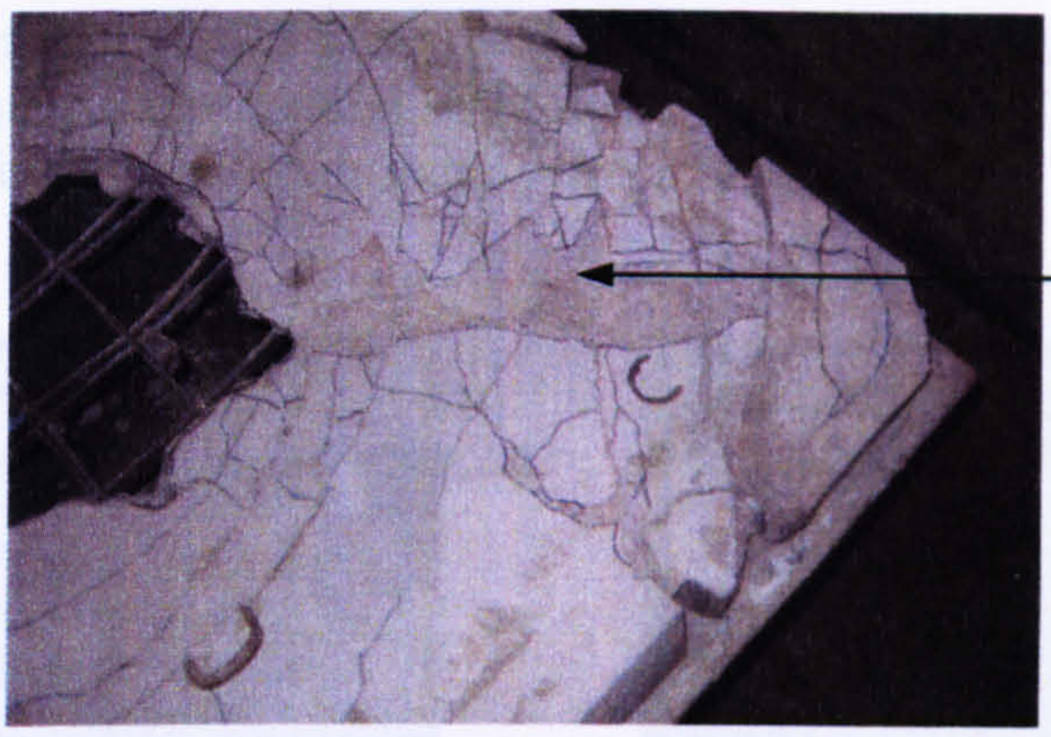

Plate 4.3.9Crush zones along the diagonals

All four sides of the slab were clamped into position using welded angle sections. The support conditions were assumed fixed. After three cumulative hits it appeared that rotation of the sides occurred as illustrated by plate 4.3.10.

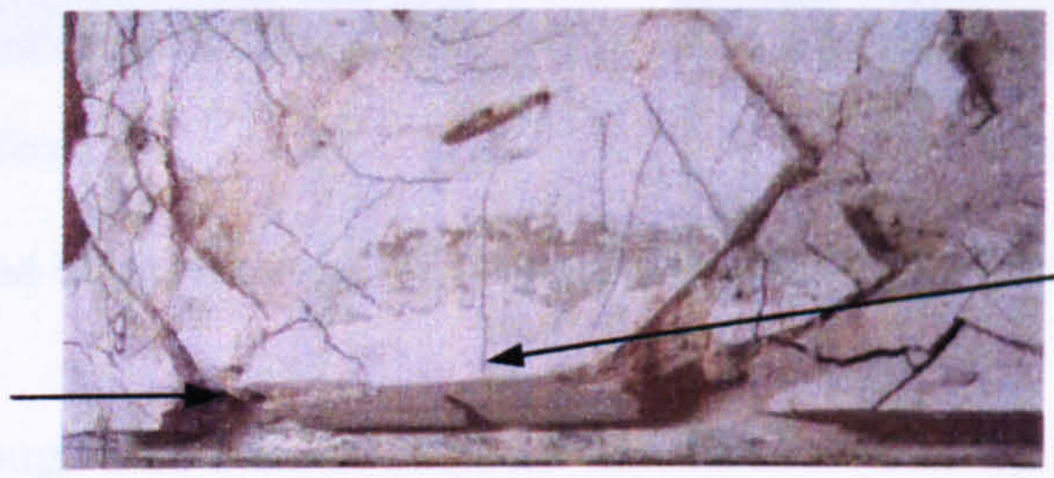

Plate 4.3.10 Rotation of side A1-B1.

The clamping system employed two bolts per side of the primary slab positioned at intervals of 350mm. The drilled holes that contained the clamping bolts, as illustrated in plate 4.3.11 formed an initial point of weakness during flexural response.
Rotation was evident between two bolted positions on a single side. This implied the slab was not fully fixed in position. In retrospect, a larger number of bolts should have been employed per side on the clamping device, to ensure full fixity. The cumulative attack severely damaged the corner regions of the primary slab as illustrated in plate 4.3.11.

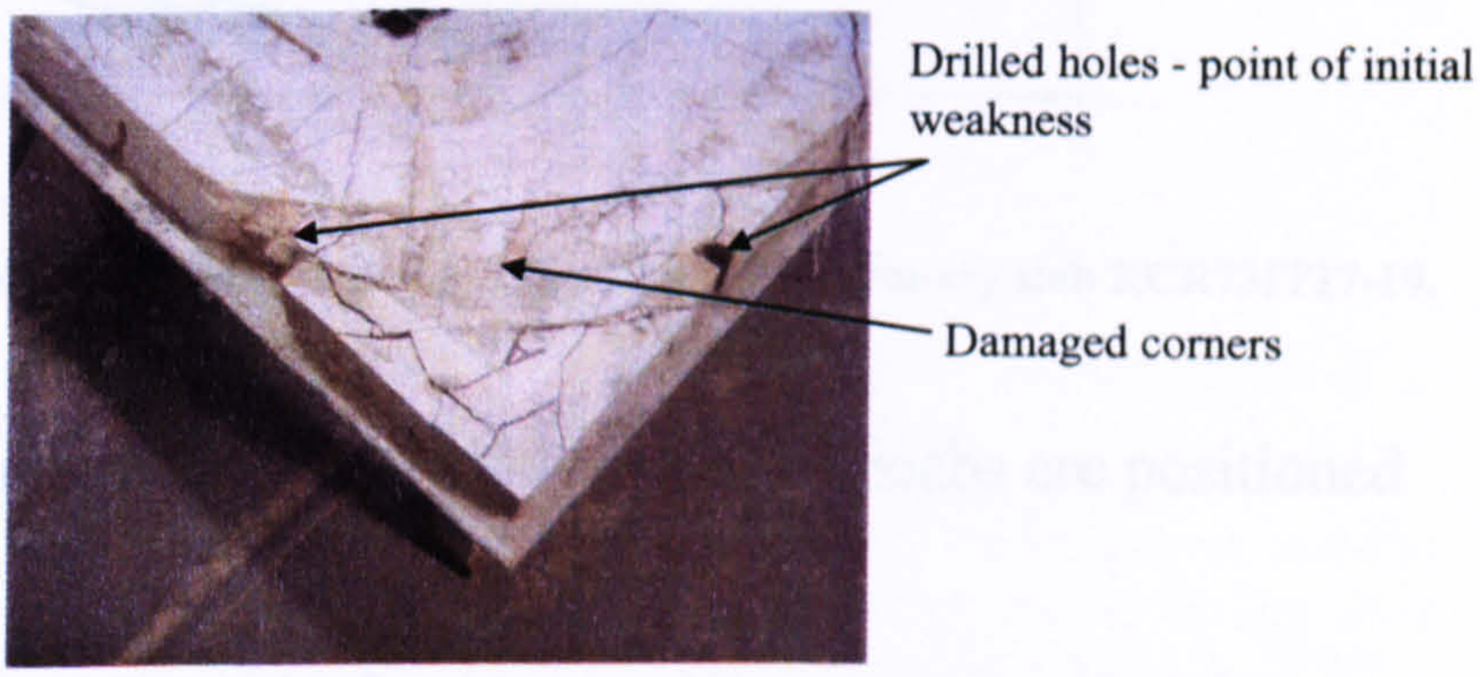

Plate 4.3.11 Severe damage around the corners of the primary slab.

Bottom face: The radial cracks penetrated deep into the thickness of the slab and were wider than the circumferential cracks on the top face. This was due to the increase in circumferential stresses acting perpendicular to the crack planes on the bottom face.

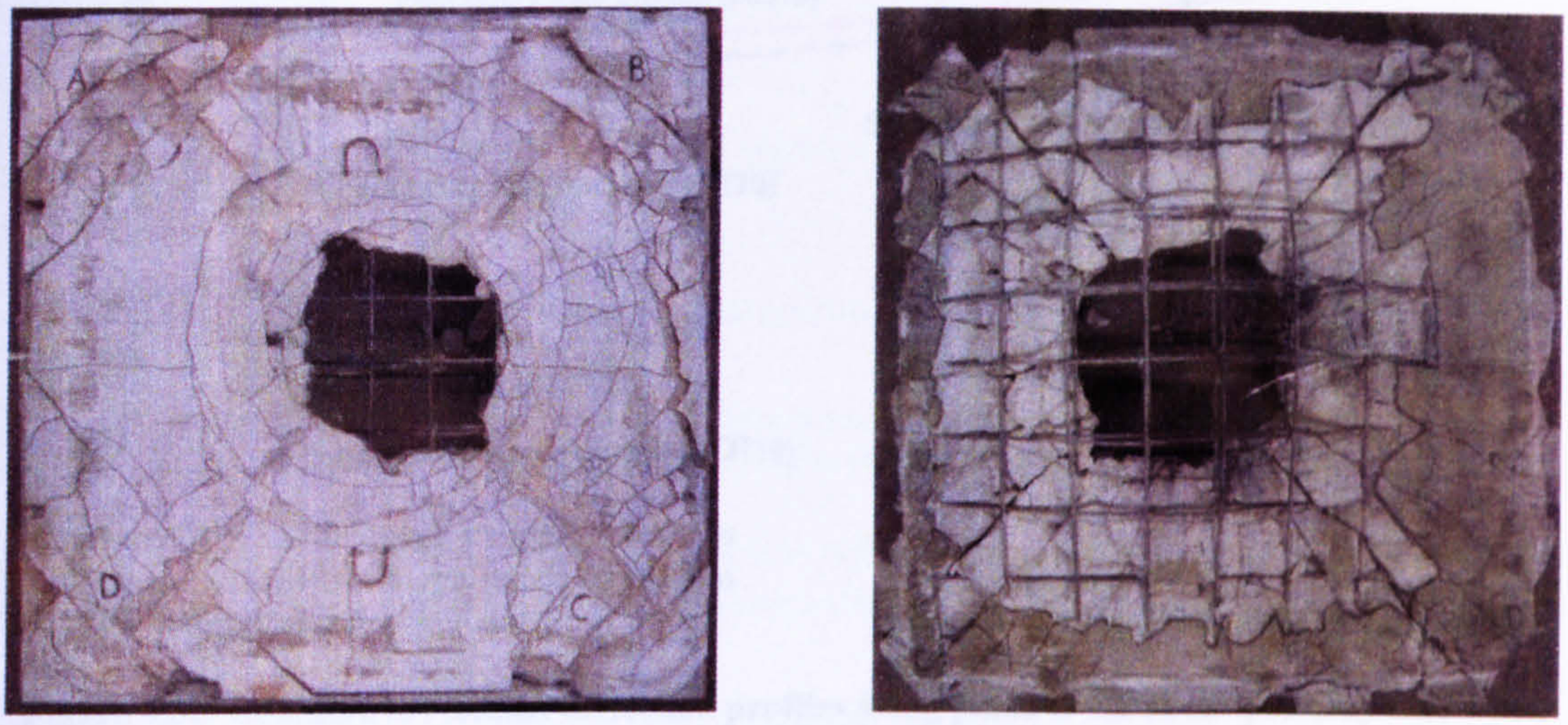

Top face

Bottom face

Plate 4.3.12 Top and bottom faces of the primary slab RCR73IT17-19 with a secondary slab omitted.

Cross-sections through slab RCR73IT17-19 are illustrated in figure 4.3.4.

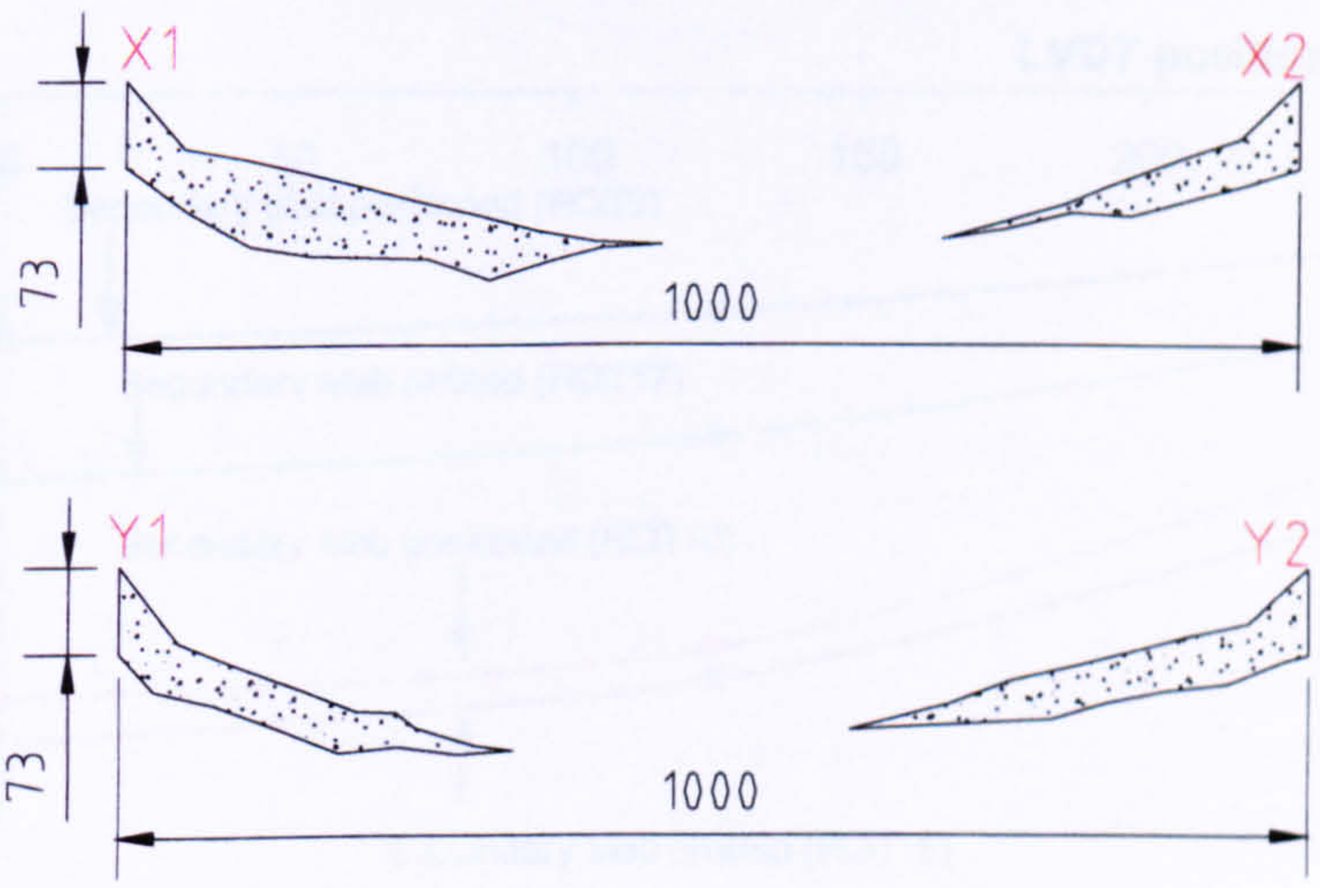

Figure 4.3.4 Cross-sectional elevation through X1-X2 and Y1-Y2 of primary slab RCR73IT17-19.

4.3.6 Response of the primary slabs when secondary slabs are positioned and omitted

It is evident from figure 4.3.5 that the first hit caused the greatest residual difference between the two primary slabs that were protected and unprotected. Due to the damaged LVDTs from test RCIT19 it was not possible to compare the residual deflective difference associated with the third cumulative hit.

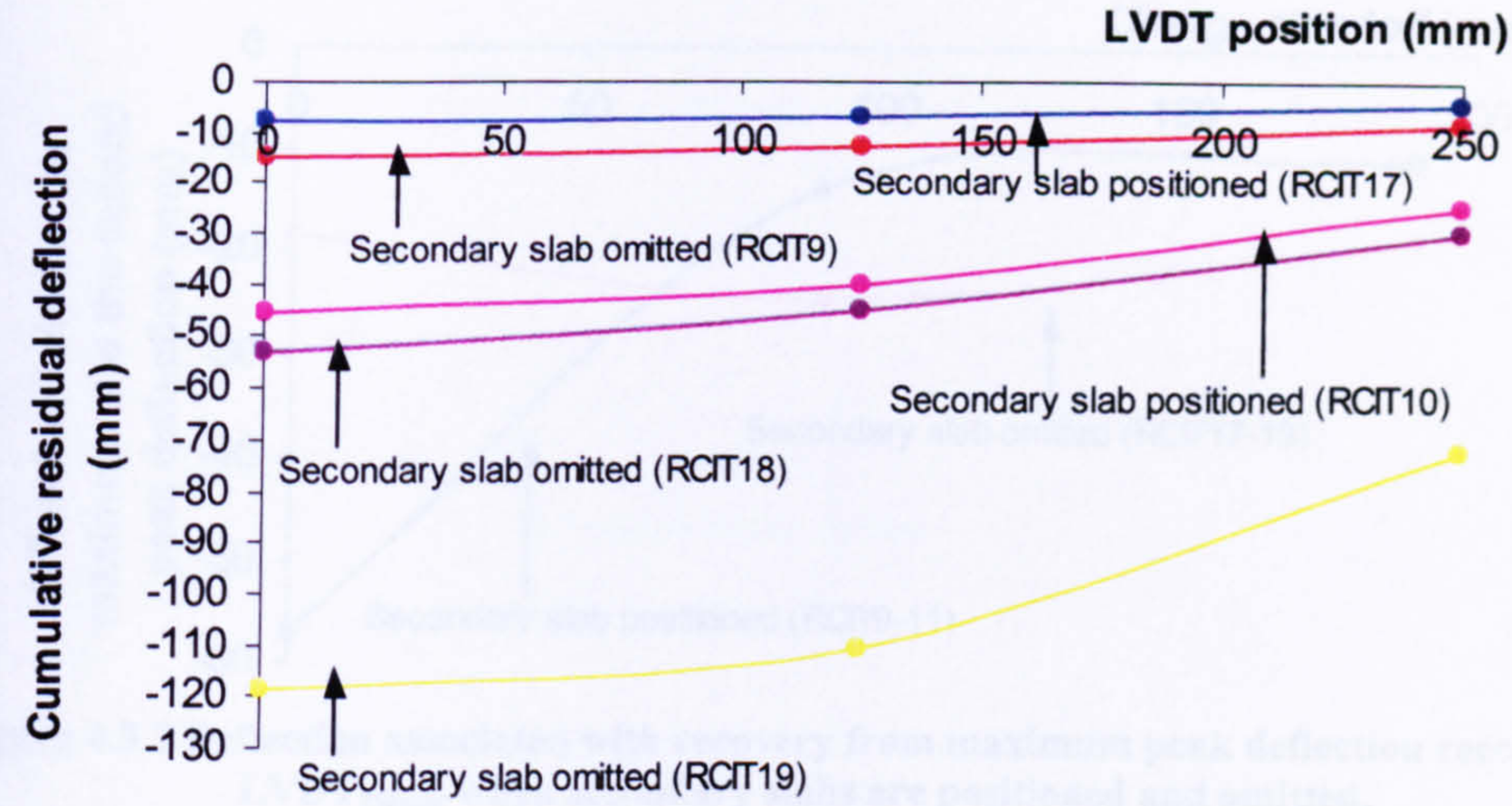

RCIT9 and RCIT17 - Charge standoff = 190mm
RCIT10 and RCIT18 - Charge standoff = 90mm
RCIT19 - Charge standoff = 90mm

Figure 4.3.5 Cumulative residual deflection profiles along plane O-X2 of the primary slab when secondary slabs are positioned and omitted.

There was a greater input of energy into the primary slab on the second hit, as a greater proportion of the charge was beneath the secondary slab. This increase in energy is indicated by a smaller difference between the maximum deflection curves from tests RCIT10 and RCIT18 as illustrated in figure 4.3.6.

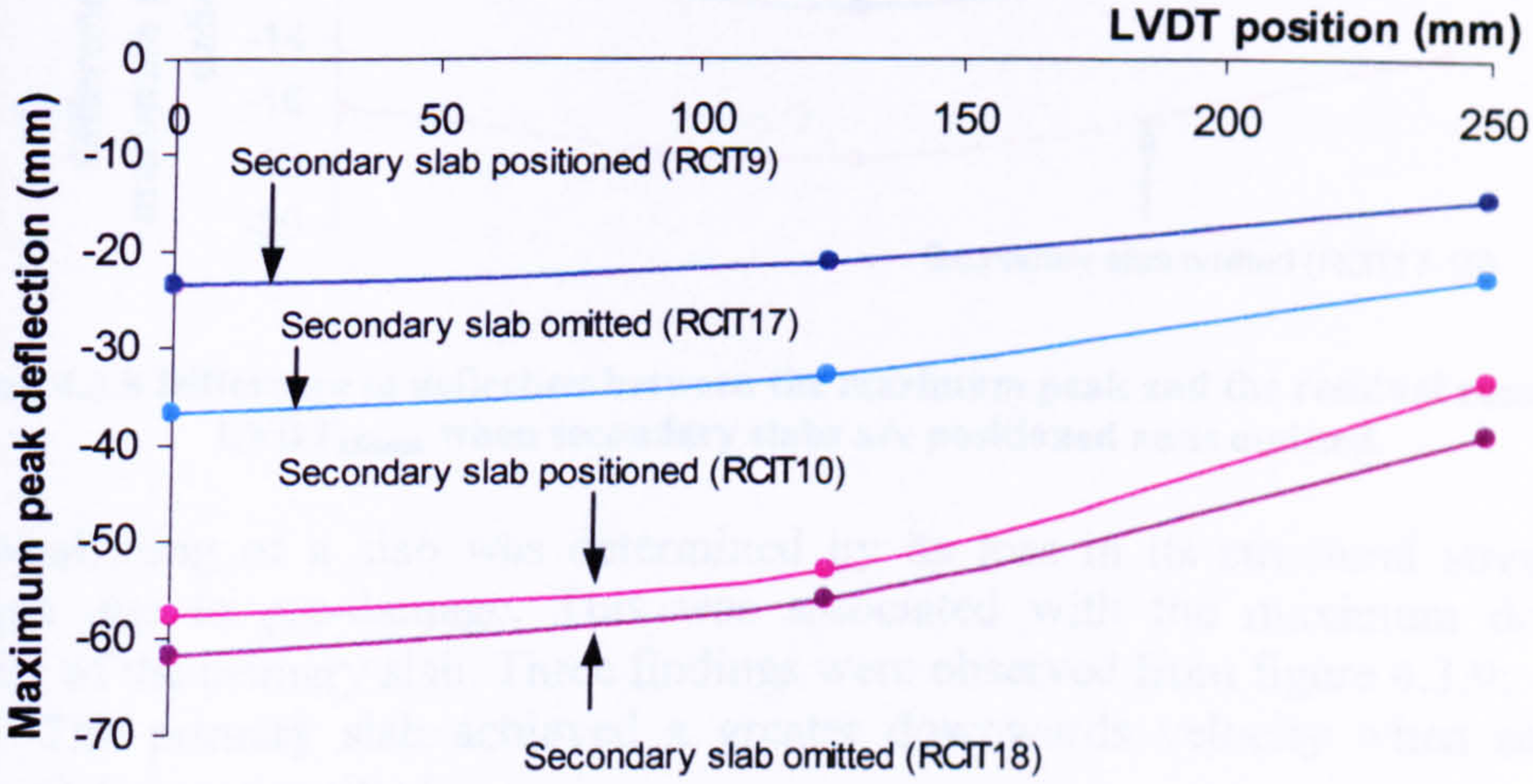

RCIT9 and RCIT17 - Charge standoff = 190mm
RCIT10 and RCIT18 - Charge standoff = 90mm

Figure 4.3.6 Maximum peak deflection profiles of primary slabs when secondary slabs are positioned and omitted.

The difference between the maximum and second peak of deflection was consistent during tests RCIT17-19 as illustrated in figure 4.3.7, where secondary slabs were omitted. A larger difference was observed on the curve associated with tests RCIT9-11 for standoffs <100mm. when secondary slabs were positioned.

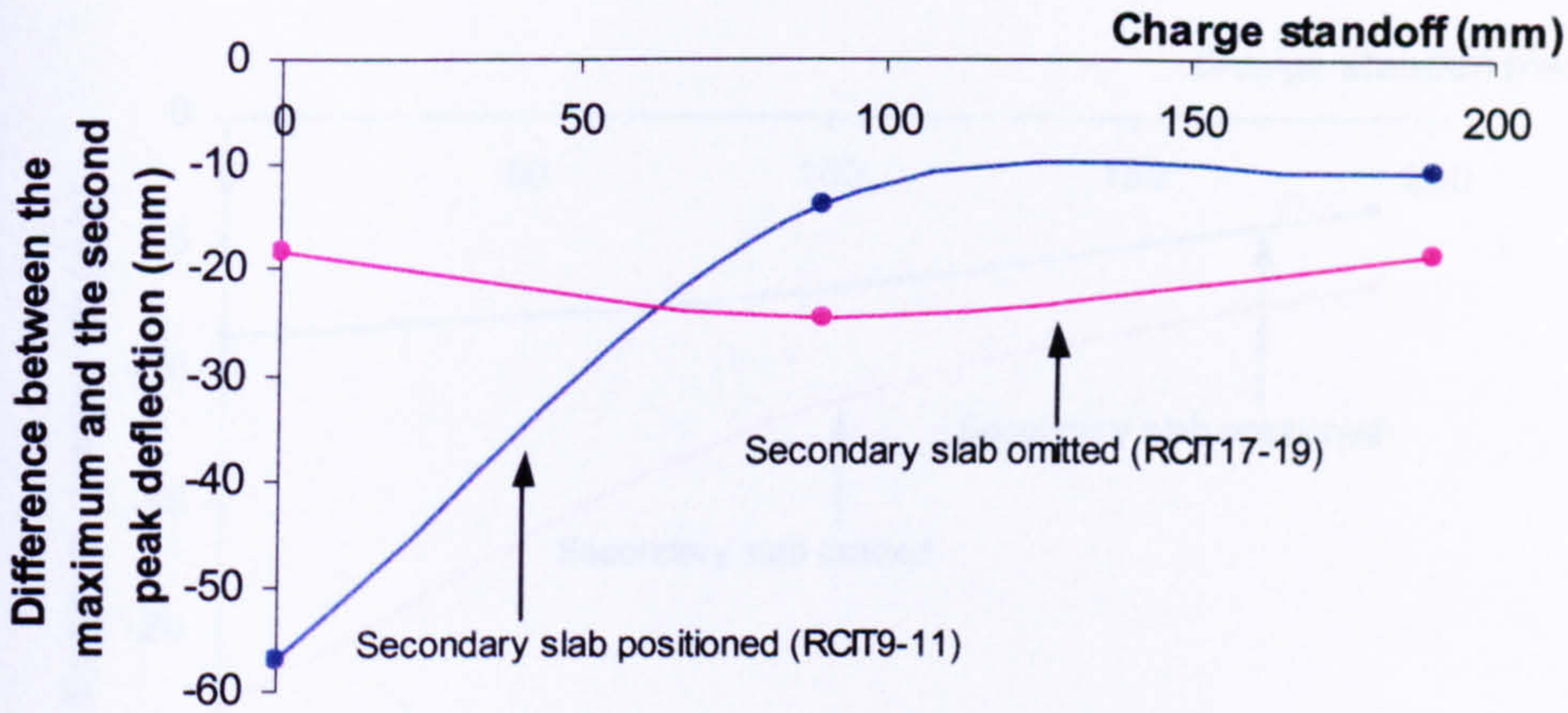

Figure 4.3.7 Deflection associated with recovery from maximum peak deflection recorded by $LVDT_{250mm}$ when secondary slabs are positioned and omitted.

There appears to be a consistent difference between the maximum peak and residual deflections, irrespective of a positioned secondary slab, as illustrated in figure 4.3.8.

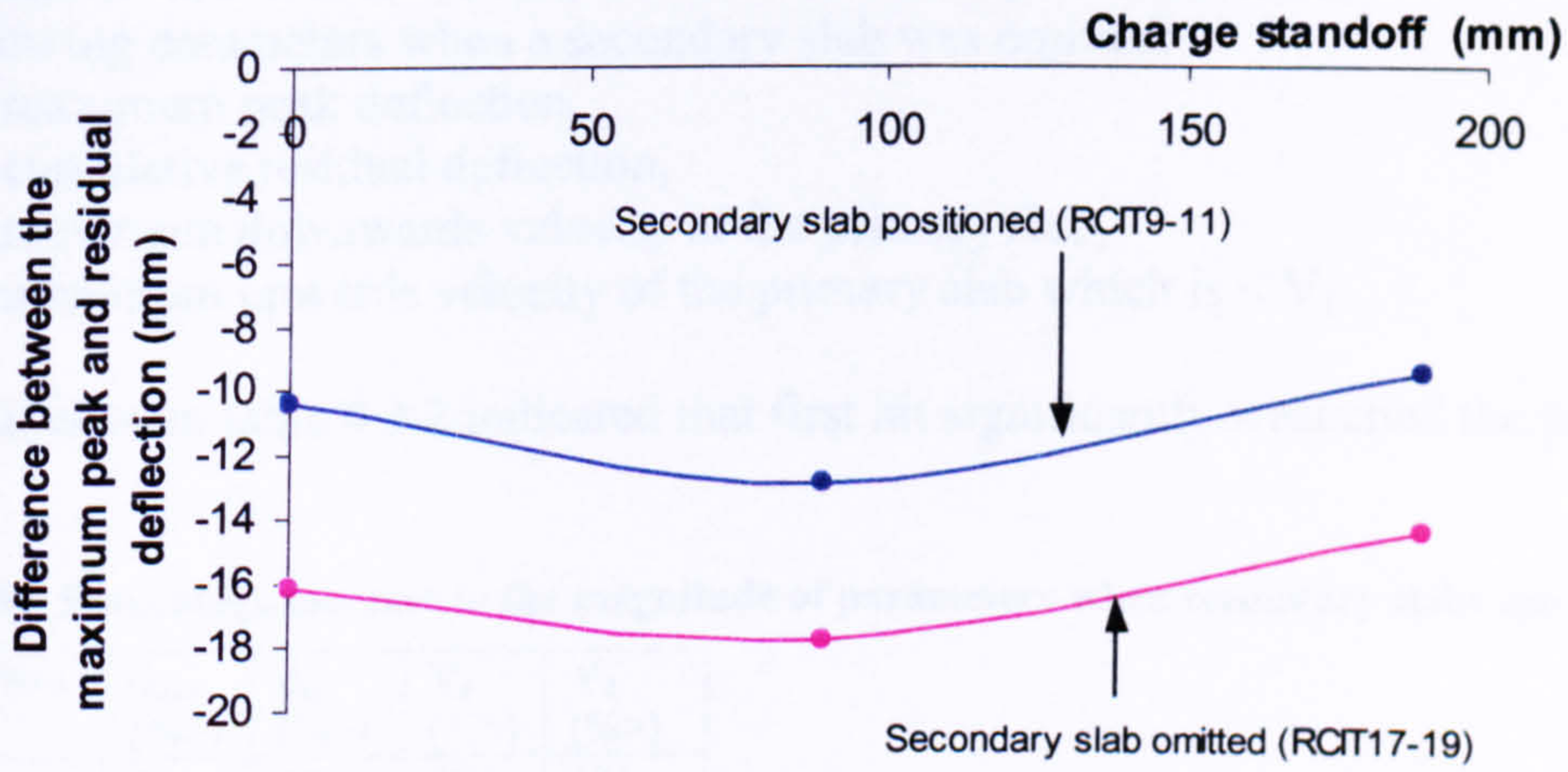

Figure 4.3.8 Difference in deflection between the maximum peak and the residual recorded by $LVDT_{250mm}$ when secondary slabs are positioned ands omitted.

The weakening of a slab was determined by its loss in its structural strength and stiffness due to pre-damage. This was associated with the maximum downward velocity of the primary slab. Three findings were observed from figure 4.3.9:

1. The primary slab achieved a greater downwards velocity when secondary slabs were omitted.
2. There was a consistent difference in velocity on both curves within a standoff range of 90mm and 190mm.
3. Within the range 0mm-90mm a change in standoff caused a greater change in the velocity when secondary slabs were omitted.

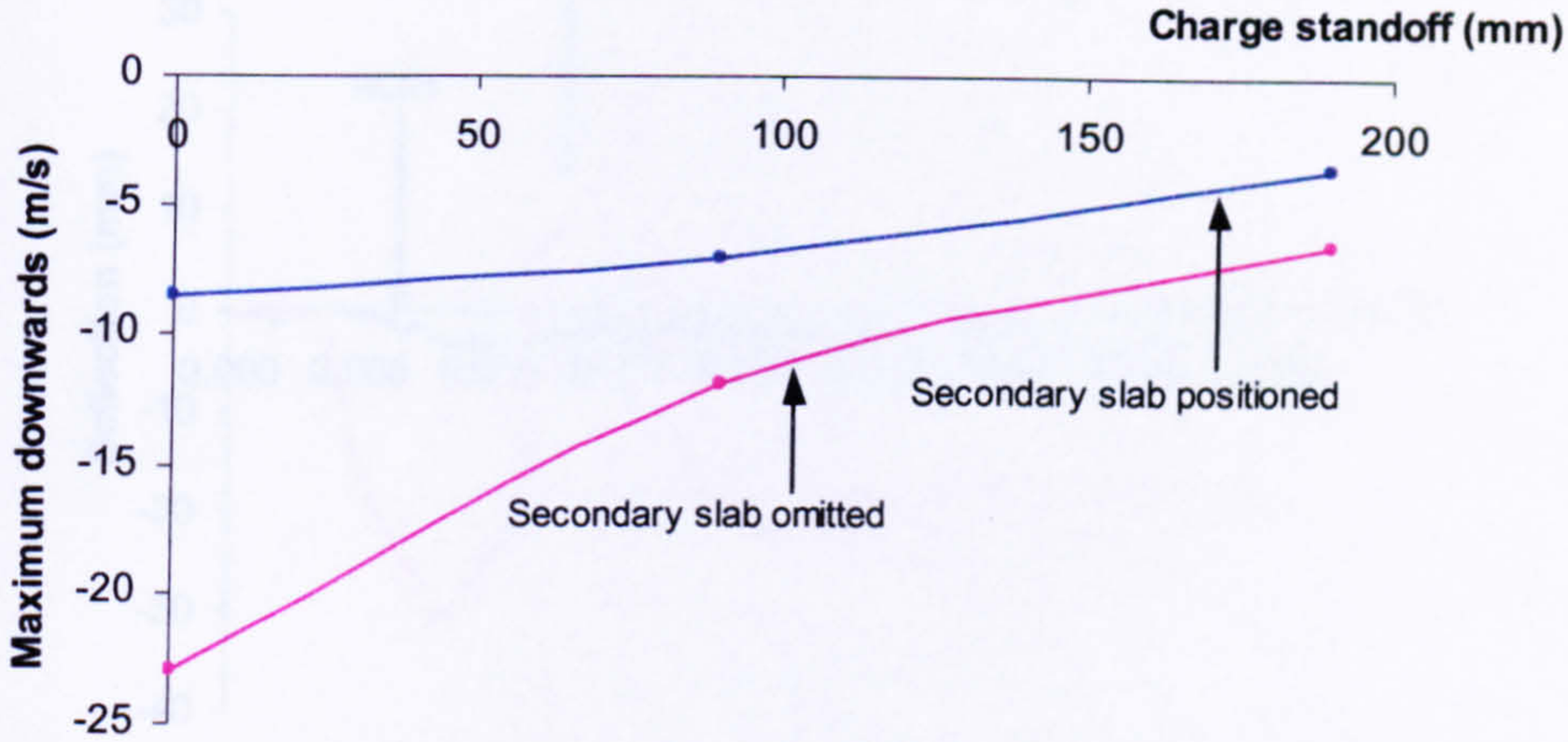

Figure 4.3.9 Maximum downwards velocity of a primary slab recorded by $LVDT_{0mm}$ when secondary slabs are positioned and omitted.

Results from tests RCIT9-10 and RCIT17-18 were used to establish the variation in the following parameters when a secondary slab was omitted:

1. maximum peak deflection,
2. cumulative residual deflection,
3. maximum downwards velocity of the primary slab,
4. maximum upwards velocity of the primary slab which is $< V_1$

The values from table 4.3.2.indicated that first hit significantly weakened the primary slab.

Table 4.3.2 Percentage increase in the magnitude of parameters when secondary slabs are omitted

Cumulative hits	d_{max} (%>)	d_{cr} (%>)	V_1 (%>)	V_2 (%>)
1	56	85	59	121
2	7.4	16	39	59

d_{max} = Maximum peak deflection
d_{cr} = Cumulative residual deflection
V_1 = Maximum downwards velocity of the primary slab
V_2 = Maximum upwards velocity of the primary slab

4.3.7 Phenomena associated with the response of the instrumentation

As the charge standoff decreased the spatial distribution of loading was concentrated centrally on the top face of the primary slab, which increased the chance of damage to the three LVDTs.

Fully capturing a trace was dependent upon the setting of the sensitivity on the digital storage oscilloscopes. The trace recorded in test RCIT2, illustrated in figure 4.3.10 was damaged and contained irregular peaks.

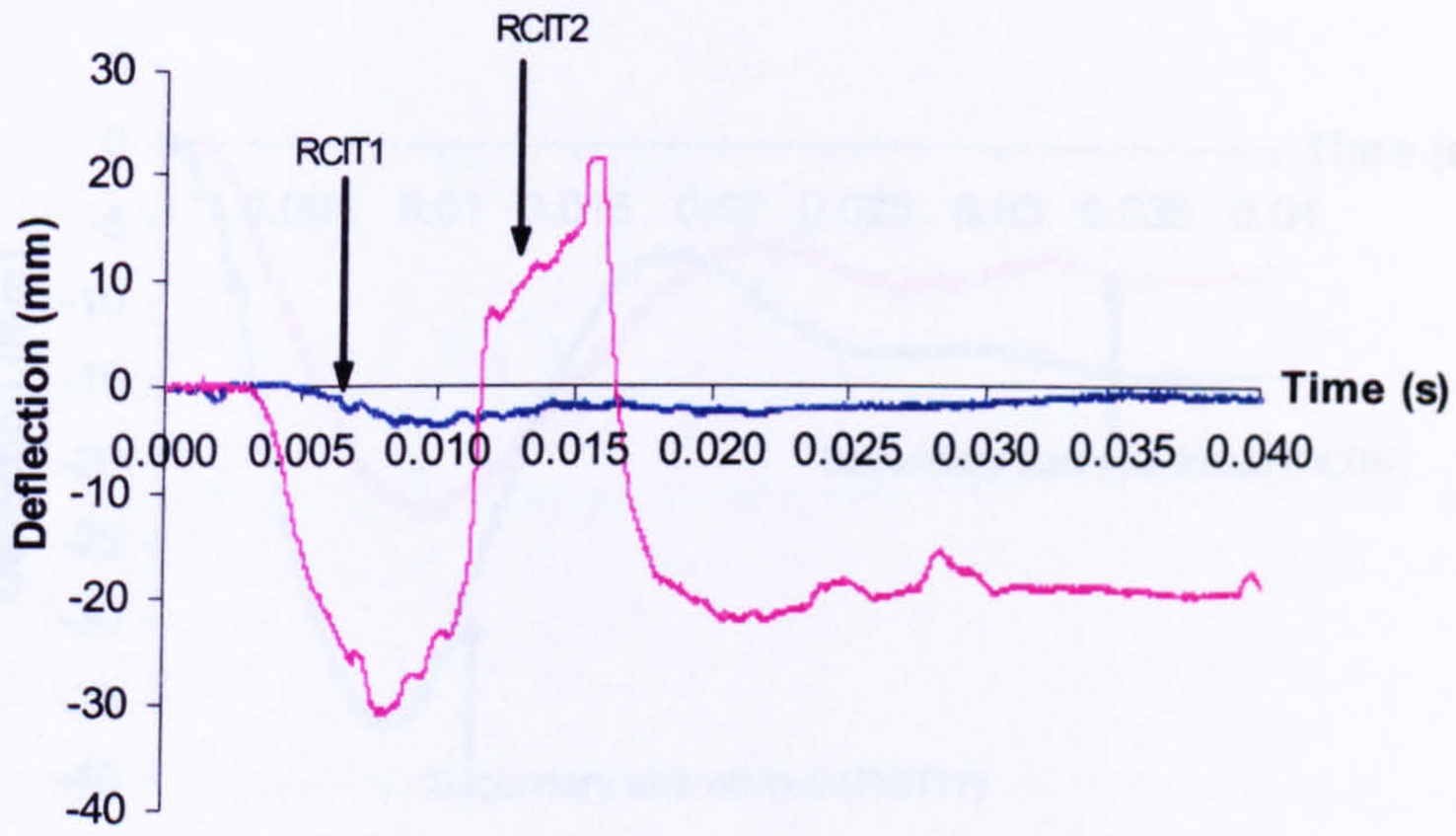

Figure 4.3.10 Deflection-time traces recorded by $LVDT_{250mm}$ during tests RCIT1-2

A loss in structural strength and stiffness was observed by a maximum peak deflection increase of approximately 20mm after each cumulative hit. illustrated in figure 4.3.11.

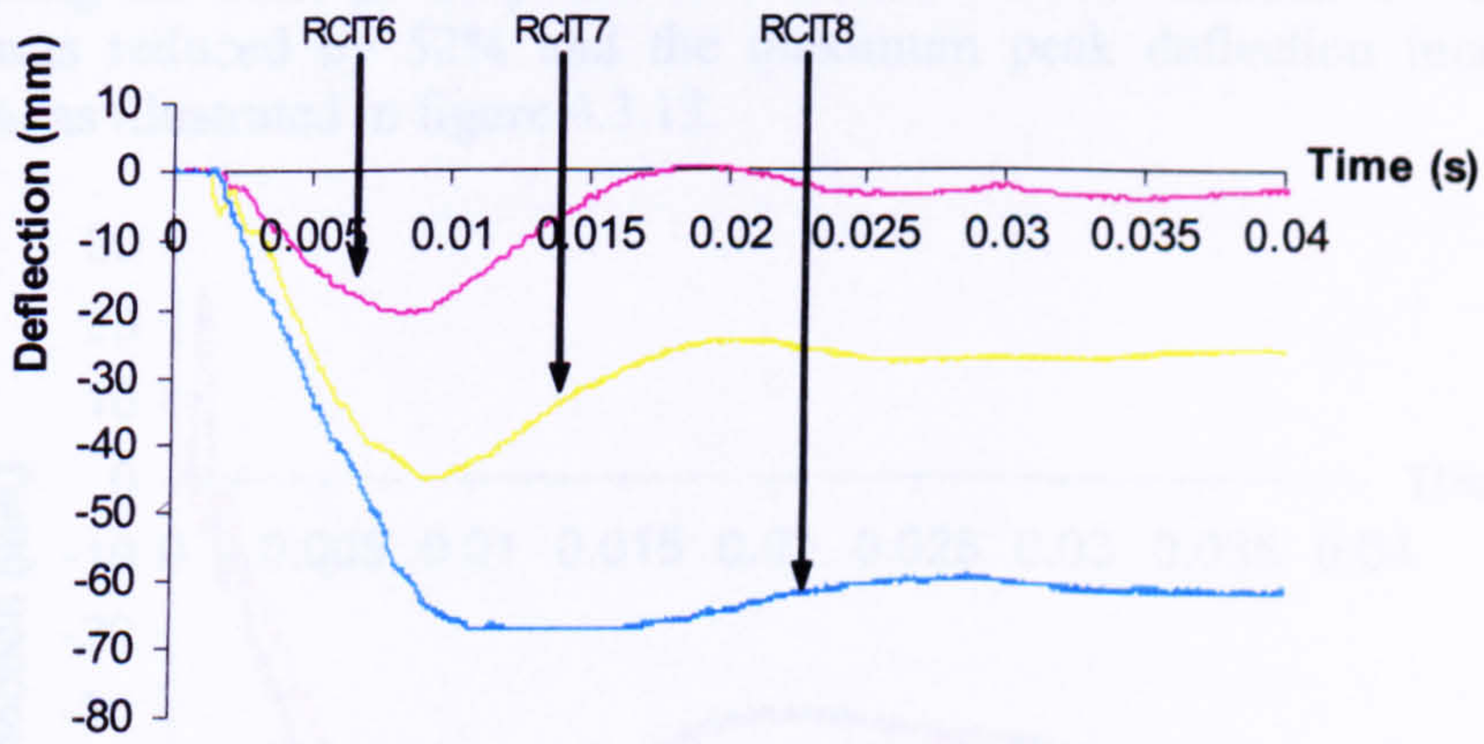

Figure 4.3.11 Deflection-time traces recorded by $LVDT_{0mm}$ during tests RCIT6-8

When a secondary slab was omitted, the following characteristics were observed:

1. The maximum peak deflection was greater.
2. The duration between maximum peak deflection and the initial recovered deflection was smaller.
3. The residual deflection was greater.

By omitting the secondary slab that was initially positioned 150mm above the top face of the primary slab in test RCIT9, the maximum peak deflection increased by a further 57% as illustrated in figure 4.3.12.

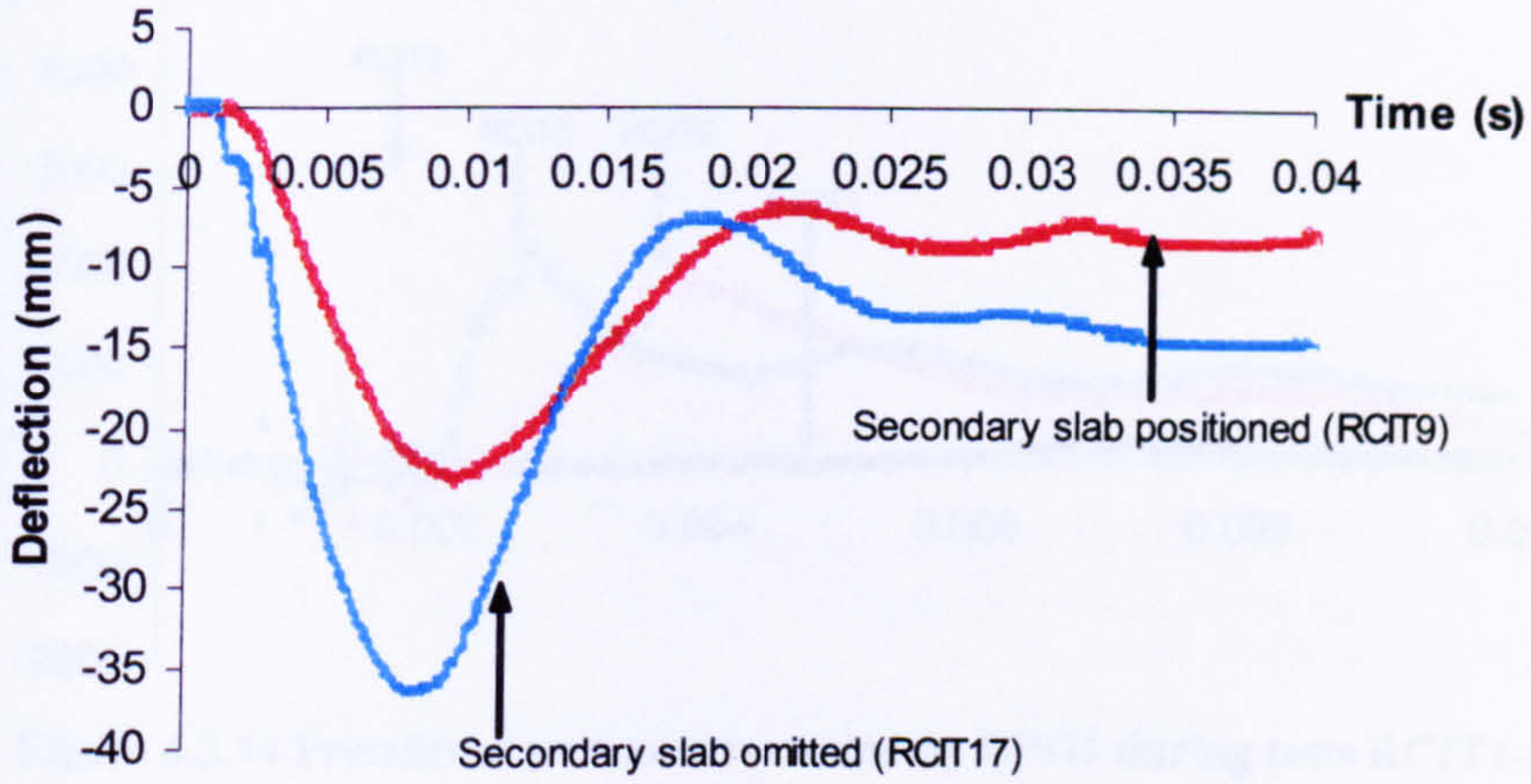

RCIT9 - Charge standoff = 190mm
RCIT17 - Charge standoff = 190mm

Figure 4.3.12 Deflection-time traces recorded by $LVDT_{0mm}$ during tests RCIT9 and RCIT17

By subjecting the same primary slab to a further second cumulative hit, the charge standoff was reduced by 52% and the maximum peak deflection increased by a further 7%, as illustrated in figure 4.3.13.

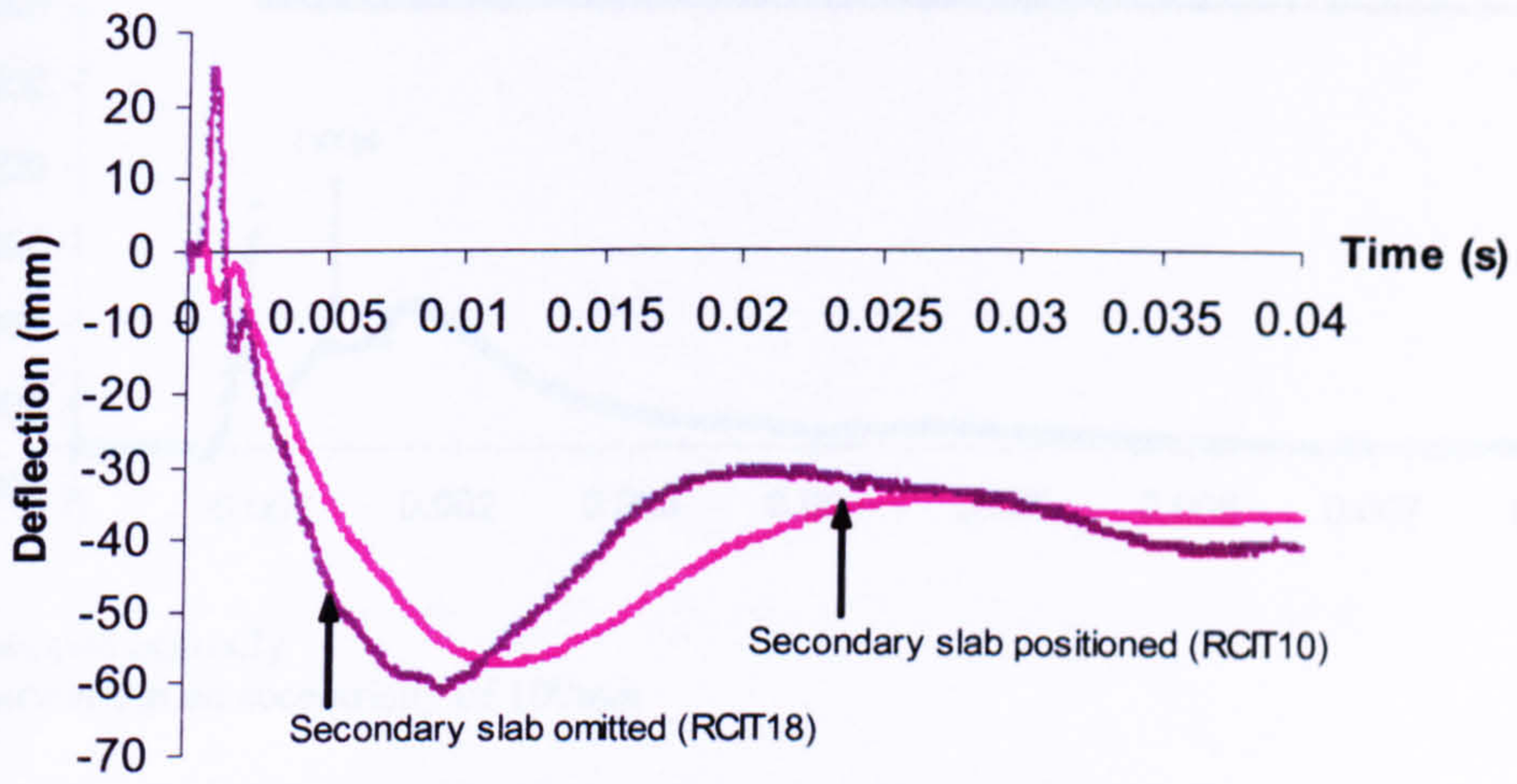

RCIT10 and RCIT18 - Charge standoff = 90mm

Figure 4.3.13 Deflection-time traces recorded by $LVDT_{0mm}$ during tests RCIT10&18

The pressure-time traces illustrated in figure 4.3.14 were recorded by DPG1, positioned centrally on the top face of a primary. The curves all illustrate a slow decay from the maximum peak pressure. The following was assumed regarding the recovery of the diaphragms:

1. If there was a soil void surrounding the top face of the diaphragms during recovery, the rate of recovery would have been greater.
2. If the soil were forced back onto the top face of the diaphragms at the point of recovery with an impact force, the rate of diaphragm recovery would have been slower.

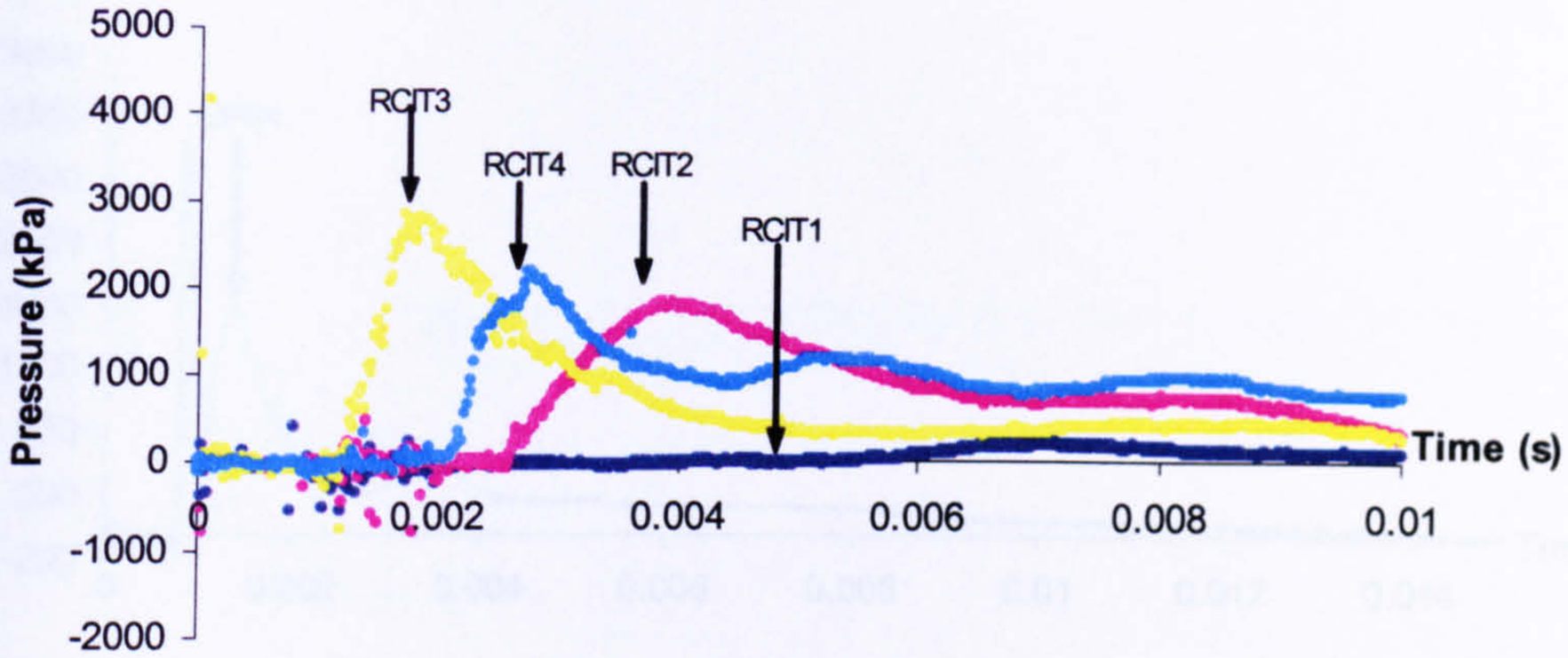

Figure 4.3.14 Pressure-time traces recorded by DPG1 during tests RCIT1-4

The pressure-time trace associated with DPG1 from figure 4.3.15 illustrates an initial rate of pressure increase then a constant pressure output for a duration. The sensitivity was set too high preventing a maximum peak pressure and the rest of the trace from being recorded. Choosing a sensible sensitivity is crucial in recording a trace but very difficult when dealing with time varying loads.

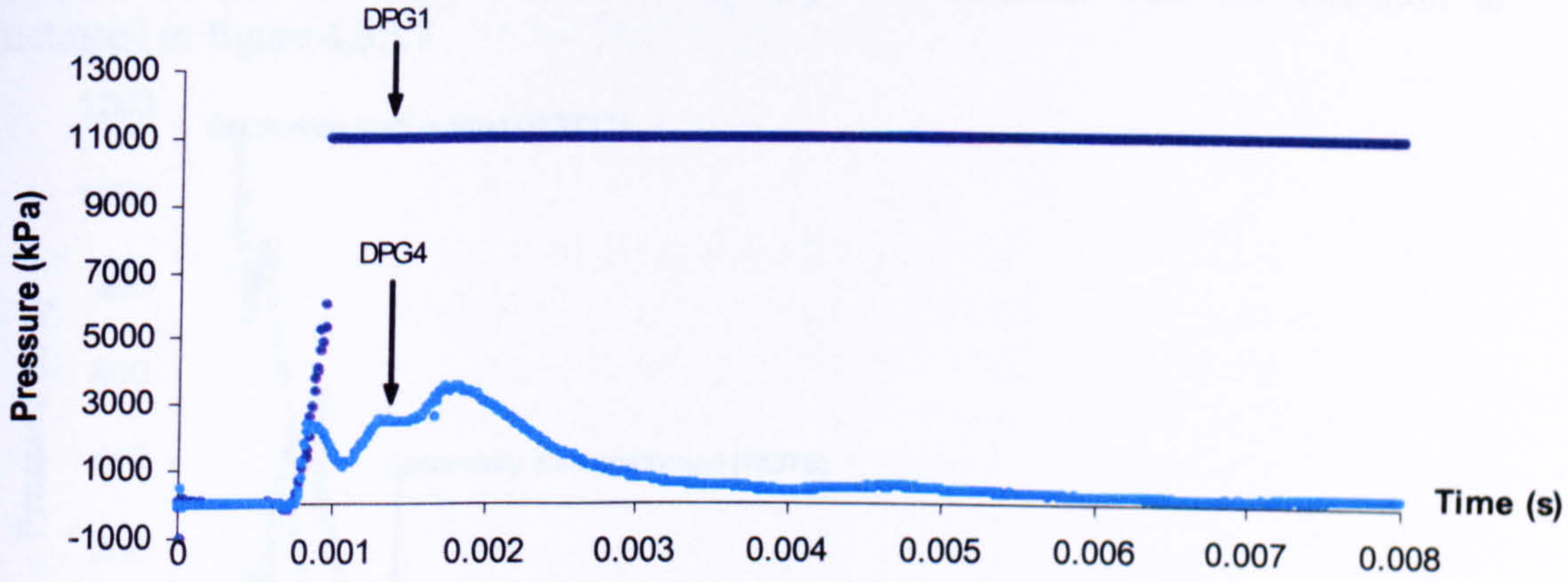

DPG1 positioned centrally
DPG 4 positioned at an eccentricity of 100mm

Figure 4.3.15 Pressure-time traces during test RCIT9

The majority of the pressure-time traces contained ambiguous peak pressures as illustrated in figures 4.3.16 and 4.3.17 during an elastic response. DPG4 in test RCIT10 was subjected to loading at a charge standoff of 90mm, whilst DPG2 in tests RCIT9 and RCIT17 was subjected to loading at a charge standoff of 190mm. The increase in the number of peak pressures identified within a trace could have been due to reflected stress waves from the internal sides of the test cell. As the DPGs were not flush with the top face of the primary slab, peaks could have been associated with lateral movement of the gauges. The soil used to fill the internal space of the test cell was not homogeneous and contained a variation in aggregate sizes up to a maximum of 5mmm, as illustrated in sieve analysis in figure 4.6.1. Impact of the larger particles could also have caused the sporadic peaks.

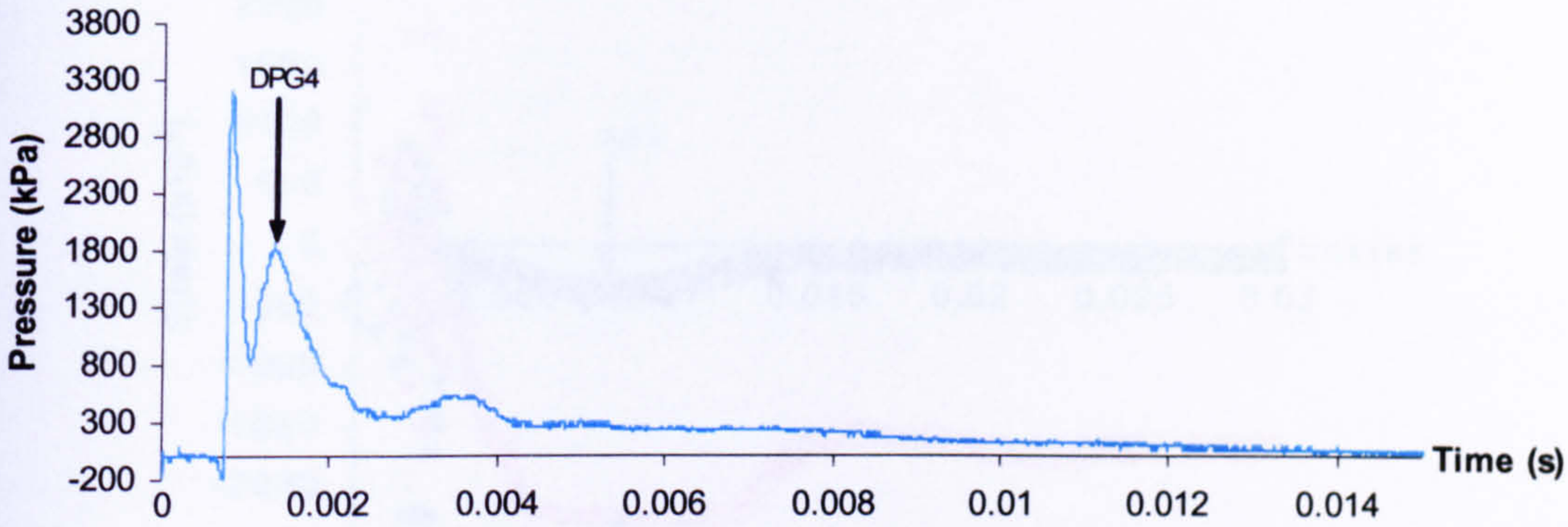

DPG 4 positioned at an eccentricity of 200mm from the centre of the slab

Figure 4.3.16 Pressure-time trace from test RCIT10 indicating sporadic peaks

Some of the traces captured contained interference that could have been associated with electrical interference or even external noise from to the explosion. The wires embedded within cables attached to the DPGs detached in a number of tests due to stress wave impact. An increase of a further 144% in the maximum peak pressure was observed in test RCIT17, when a secondary was omitted. This phenomenon is illustrated in figure 4.3.17

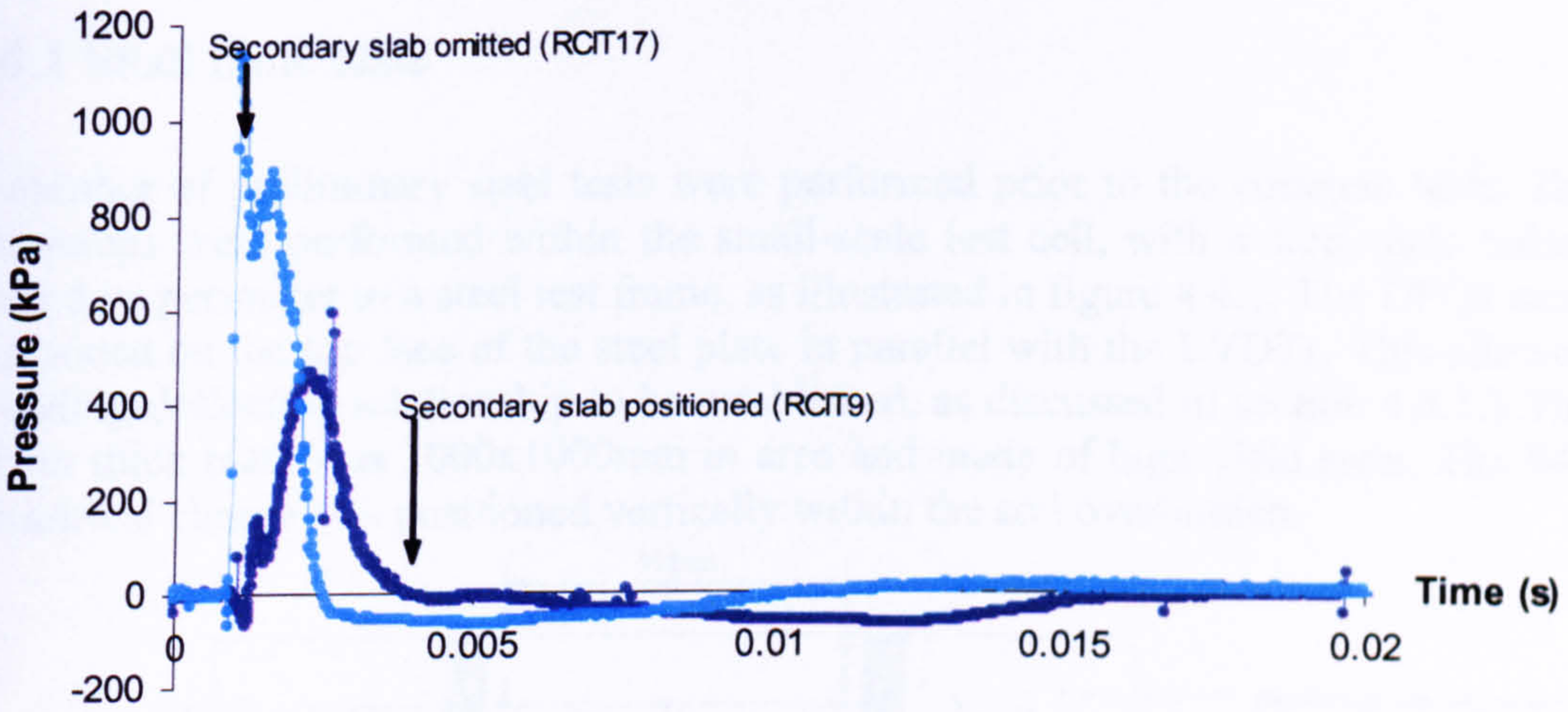

DPG 2 positioned at an eccentricity of 200mm from the centre of the slab
RCIT9 and RCIT17 – Charge standoff = 190mm

Figure 4.3.17 Pressure-time traces recorded by DPG2 in tests RCIT9 and RCIT17

If either of the LVDTs or DPGs were damaged during a test they could be fixed with relative ease in time for the next test. If a strain gauge was severely damaged nothing could be done to it as it was embedded within the primary slab. It has been put forward that strain gauges embedded in reinforced concrete slabs should not be used in future tests of an explosive nature for the following reasons:

1. If damaged they could not be retrieved and fixed.
2. Considerable interference preventing a response time from being determined.
3. It was difficult to identify whether their response was indicative of the entire slab or whether the rebar they were attached to had detached from the concrete.
4. They were not useful in determining an accurate response of the slab.

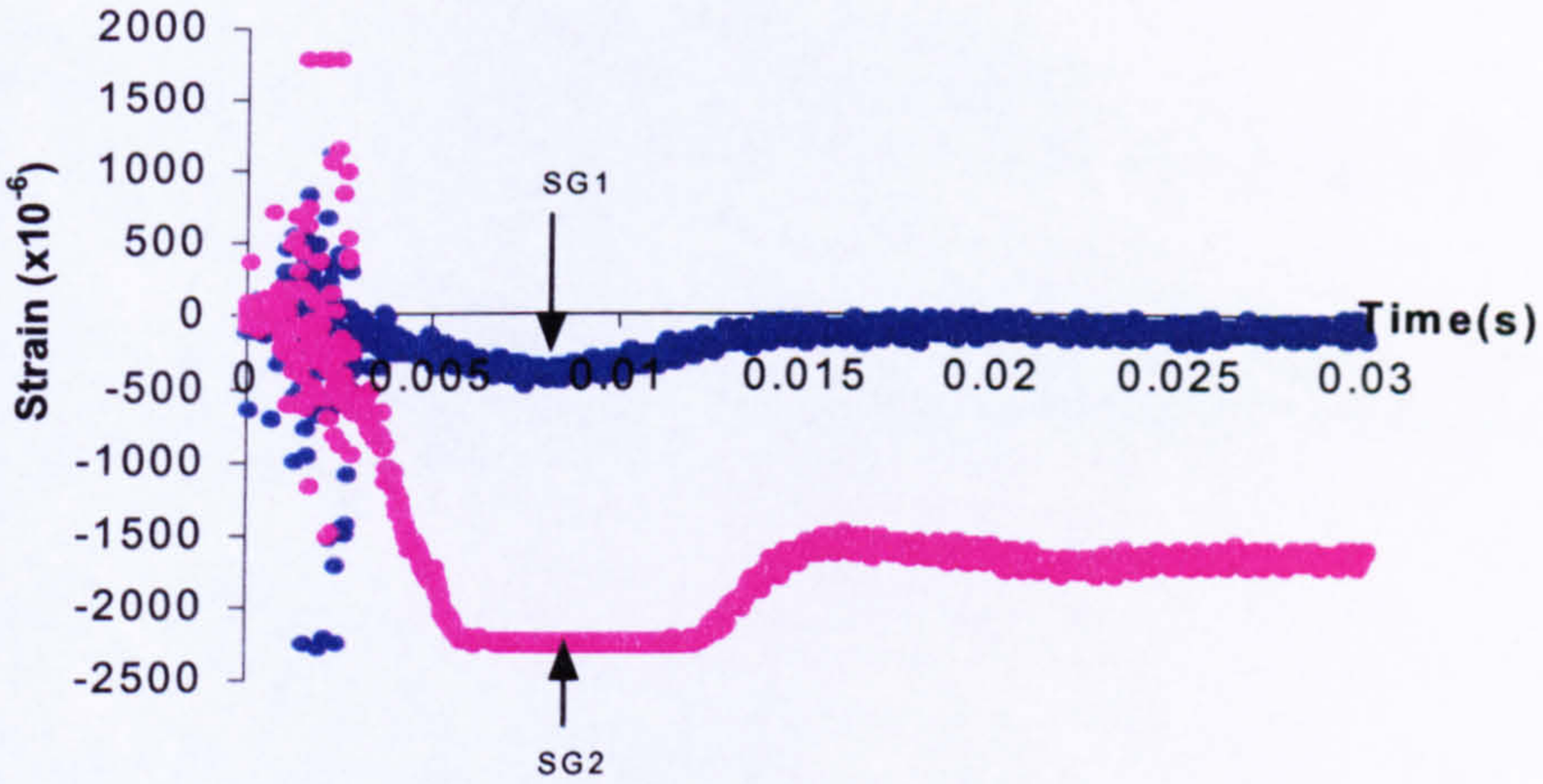

SG1=Strain gauge in top mesh
SG2=Strain gauge in bottom mesh

Figure 4.3.18 Strain-time traces recorded by SG1 and SG2 during test RCIT3

4.4 Characterising the structural response caused by groundshock loading and identification of parameters

4.4.1 Steel plate tests

A number of preliminary steel tests were performed prior to the concrete tests. The test setups were performed within the small-scale test cell, with a steel plate bolted around its perimeter to a steel test frame, as illustrated in figure 4.4.1. The DPGs were positioned on the top face of the steel plate in parallel with the LVDTs. This allowed a loading-deflection relationship to be established, as discussed in section 4.4.1.1.The 10mm thick plate was 1000x1000mm in area and made of high yield steel. The 94g cylindrical charge was positioned vertically within the soil overburden.

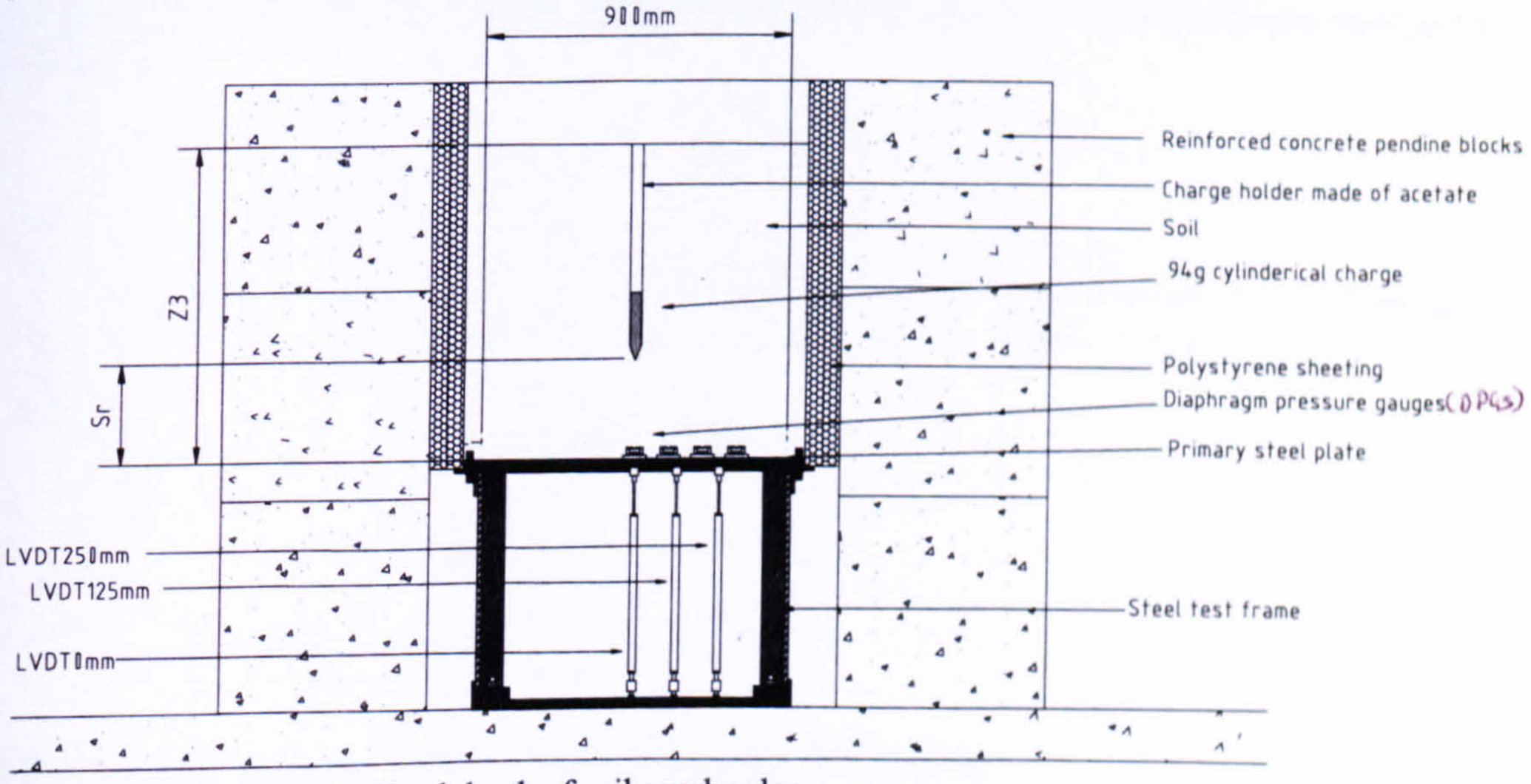

S = Charge standoff Z_3 = Total depth of soil overburden

Figure 4.4.1Cross-sectional elevation of a steel test set up within the test cell

The steel plate tests were performed for two reasons:

1. To characterise structural response to groundshock.
2. To evaluate the response and workability of the DPGs and LVDTs prior to being used in the concrete tests.

Four steel plate tests were performed within a soil overburden depth of 1000mm. The charge standoffs were large enough ensuring the plate responded elastically. The steel test matrix is indicated in table 4.4.1.

Table 4.4.1Steel test matrix

T_n	S_r (mm)	Z_3 (mm)	W (g)	θ	t_{rs} (mm)
ST1	600	1000	94	90°	10
ST2	500	1000	94	90°	10
ST3	300	1000	94	90°	10
ST4	150	1000	94	90°	10

T_n = Test number
ST = Steel Test
S_r = Charge standoff
Z_3 = Total depth of soil overburden
W = Mass of the charge
θ = Charge angle of inclination to the horizontal
t_{rp} = Thickness of the primary steel plate

The deflection and pressure time histories recorded using the central $LVDT_{0mm}$ and DPG1 were associated with tests ST2-4. The central LVDT was positioned on the bottom face of the steel plate and the central DPG positioned on the top face of the primary plate. This allowed the load induced into the steel plate to be related to deflection. The deflection and pressure results were used to calculate ratio values of load duration and natural frequency of the response, hence allowing response of the plate to be characterised. The parameters associated with a deflection-time history are illustrated in figure 4.4.2. The parameters associated with the symbol (δ) are related to deflection.

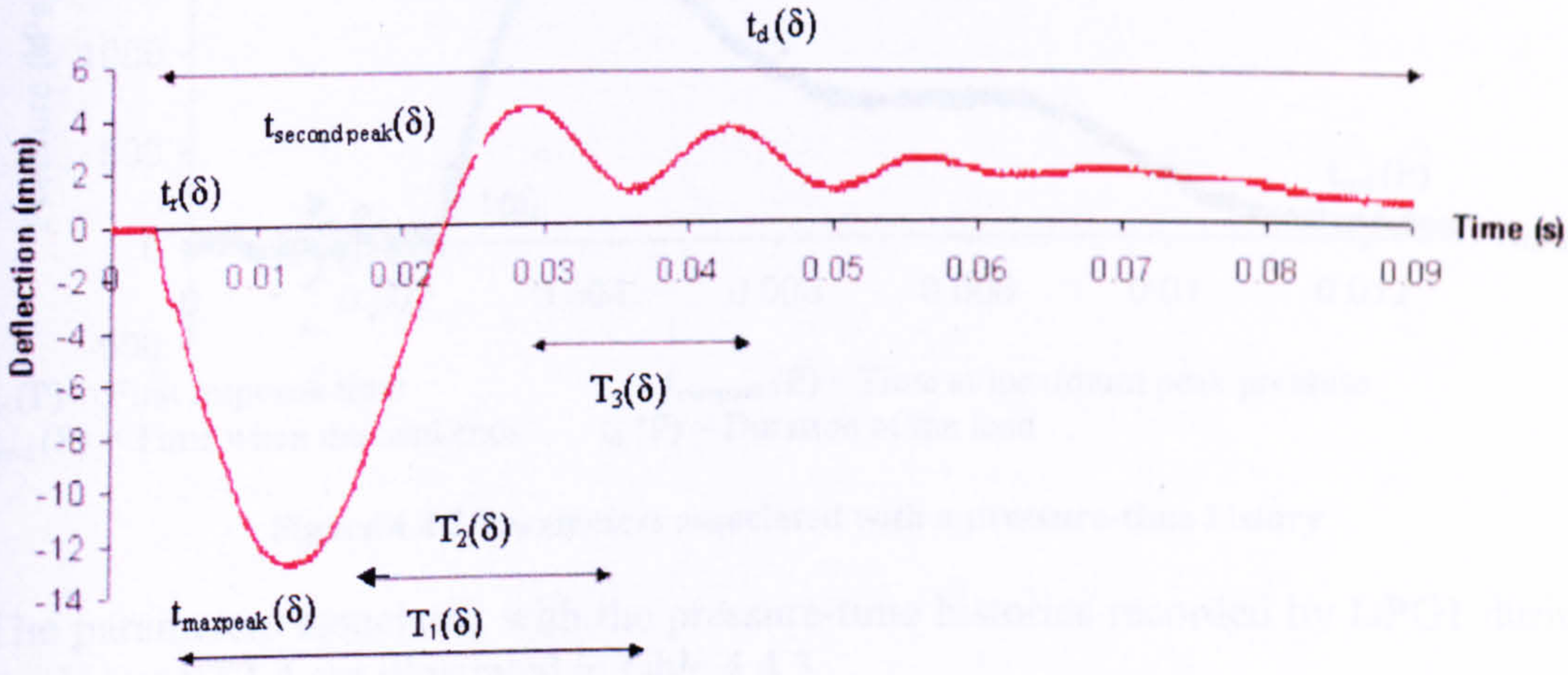

$t_r(\delta)$ = Response time $t_{maxpeak}(\delta)$ = Time at maximum peak deflection
$t_{second\ peak}(\delta)$ = Time at the second peak $t_d(\delta)$ = Duration of the response $T_1(\delta)$ = First natural period of oscillation $T_2(\delta)$ = Second natural period of oscillation

Figure 4.4.2 Parameters associated with a deflection-time history

The parameters associated with the deflection-time history recorded by the central LVDT from tests ST2-4 are tabulated in table 4.4.2. The results from test ST1 were not available due to problems with the digital storage oscilloscope

Table 4.4.2 Parameters of duration from deflection-time histories in steel tests

Test	S (mm)	$t_r(\delta)$ (ms)	$t_{maxpeak}(\delta)$ (ms)	$t_{second\ peak}(\delta)$ (ms)	$t_{end}(\delta)$ (ms)	$t_d(\delta)$ (ms)	T_1 (ms)	T_2 (ms)	T3 (ms)	T4 (ms)
ST2	500	3.1	13.7	30	88	58	34	24	15	14
ST3	300	1.9	9.2	22	60	58.1	29	22	15	-
ST4	150	1.1	5.5	18	55.3	54.2	24	20	15	-

S_r = Charge standoff
$t_r(\delta)$ = First response time
$t_{maxpeak}(\delta)$ = Time at maximum peak deflection
$t_{second\ peak}(\delta)$ = Time at the second peak
$t_{end}(\delta)$ = Time when the response ends
$t_d(\delta)$ = Duration of the response
T_1 = First natural period of oscillation
T_2 = Second natural period of oscillation

During the deflection of the primary plate, the natural period of response decreased as time of the response elapsed, as indicated in table 4.4.2. This occurred for two reasons:

1. reduction in internal energy as the plate moved against its self-weight,
2. reduction in internal energy as the plate moved against the weight of soil overburden.

The first natural period occurred during the maximum peak deflection and initial recovery of the plate. The second and third natural frequencies occurred once the load was removed. The parameters that determined a particular pressure-time history recorded by a DPG have been assigned to a trace and are illustrated in figure 4.4.3. The parameters associated with the symbol (P) are related to pressure.

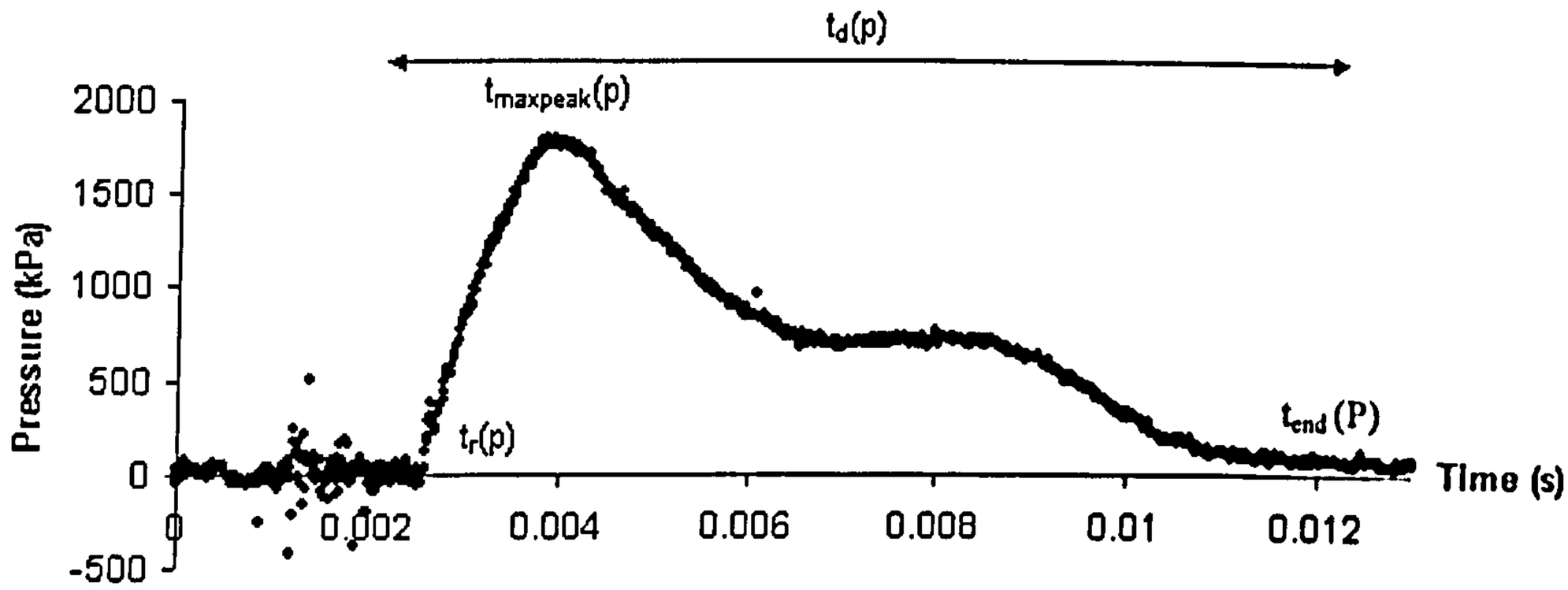

t_r (P) = First response time
$t_{maxpeak}$ (P) = Time at maximum peak pressure
t_{end} (P) = Time when the load ends
t_d (P) = Duration of the load

Figure 4.4.3 Parameters associated with a pressure-time history

The parameters associated with the pressure-time histories recorded by DPG1 during steel tests ST2-4 are illustrated in table 4.4.3.

Table 4.4.3 Parameters of duration from pressure-time histories in steel tests

Test	t_r (P) (ms)	$t_{max\ peak}$ (P) (ms)	t_{end} (P) (ms)	t_d (P) (ms)
ST2	2.0	10	20	18
ST3	1.2	6.7	16.2	15
ST4	0.4	1.4	10	9.6

t_r (P) = First response time $t_{maxpeak}$ (P) = Time at maximum peak pressure
t_{end} (P) = Time when the load ends t_d (P) = Duration of the load

The duration of the loading recorded by DPG1 and the natural period of oscillation of the primary plate, recorded by the central $LVDT_{0mm}$, have both been used to evaluate the ratio of t_d/T. The ratios of load duration and natural period of response are illustrated in table 4.4.4.They have been calculated from values in tables 4.4.2 and 4.4.3.

Low & Hao (2001) *stated that 'for a structure subjected to an impulsive load, the first displacement peak would be the most severe'.* This was observed in all the deflection-time histories recorded by the LVDTs illustrated in figures A.1.1-A.1.24 in the Appendix. **Low & Hao (2001)** also stated that *'the first displacement peak is considered in analysing structural response to impulsive loading'.* The first natural period of response has been used to calculate ratio values of load duration to natural period of response.

Table 4.4.4 Ratio values of t_d/T from tests ST2-4

Test	$t_d(P)/T_1(\delta)$	Type of response
ST2	0.53	Impulsive end of the dynamic range
ST3	0.52	Impulsive end of the dynamic range
ST4	0.40	Impulsive

t_d (P) = Duration of the load
T_1 = First natural period of response

The ratio values of 0.53 and 0.54 in table 4.4.4 are only slightly above the **Clough & Penzien (1993)** suggested limit for an impulsive response.
A half sine-wave impulse load distribution in accordance with **Clough & Penzien (1993)** approximates the pressure-time history profiles recorded by DPG1 during steel tests ST2-4 as illustrated in figure 4.4.4.
The reasons for this are stated as follow:

1. The rise to peak pressure is not instantaneous in comparison to an airblast response associated with a triangular loading distribution.
2. There are irregular and subsequent peaks before and after a maximum peak pressure.
3. The pressure varied between 200-300kPa for a duration before a significant decay in pressure is observed.

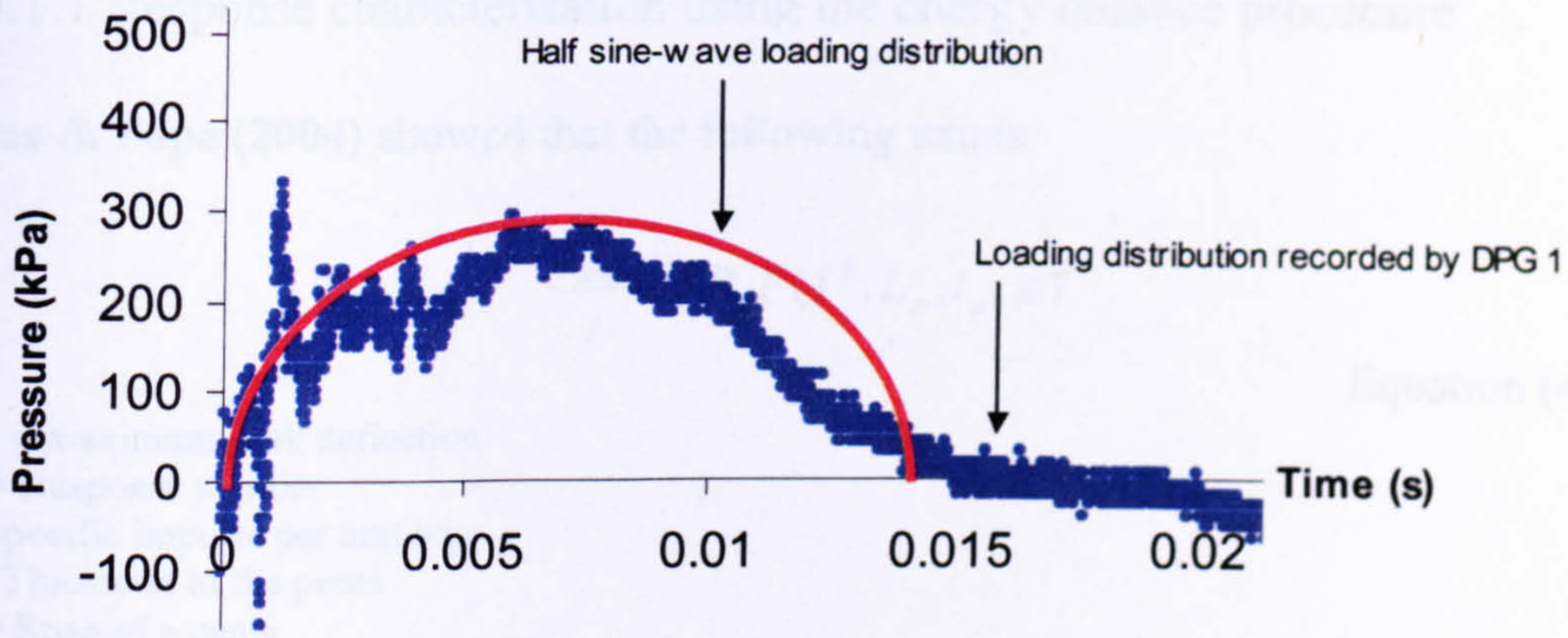

Figure 4.4.4 Comparison between an idealised half sine-wave loading distribution and a pressure-time history profile recorded by DPG1 during steel test ST2

The results from table 4.4.4 indicate an impulsive response. The ratio values of load duration to natural period of response in equation (4.4.1) are either equal to or less than 0.5.

$$\frac{t_d}{T} \leq 0.5$$

Equation (4.4.1)

t_d = Load duration
T = Natural period of response

Theoretically an ideally impulsive or a quasi-static response would be defined by equations (4.4.2) and (4.4.3) respectively.

$$\text{(Impulsive response)}\ \frac{t_d}{T} = 0$$

Equation (4.4.2)

$$\text{(Quasi-static response)}\ \frac{t_d}{T} = \infty$$

Equation (4.4.3)

t_d = Load duration
T = Natural period of response

Clearly as td/T approaches the ideal limit in equation (4.4.2) the assumption of impulsive behaviour will become progressively more valid, with the converse applying as the ratio increases. Therefore equation (4.4.1) must be viewed as no more than a guideline. Determination of what is an acceptably low value of td/T to justify the assumption of impulsive behaviour must be a matter of engineering judgement.

4.4.1.1 Response characterisation using the energy balance procedure

Tyas & Pope (2004) showed that the following exists:

$$\frac{d_{\max}}{t} \propto R_n F(I^2, L_p, t_p, \rho)$$

Equation (4.4.2)

d_{max} = maximum peak deflection
R_n = Response number
I =Specific impulse per unit area
t_p = Thickness of the panel
L_p = Span of a panel
ρ = Density

The reinforced concrete primary slabs used throughout the l testing were all identical in geometry. This neglected the need for a response number as discussed in section 2.3.2.
A full spatial distribution of impulse was not achieved due to the lack of DPGs and channels on the digital oscilloscopes. This would have been essential, as the loading was unsymmetrical upon the top face of a primary slab and could not be assumed to be equal along the diagonal planes.
Tyas & Pope (2004) showed that the central peak impulse dominated the response of a slab, when impulse is highly spatially concentrated. A hypothesis stating the following iwas a reasonable approximation

$$d^2_{\max} \propto I^2$$

Equation (4.4.3)

$$d_{\max} \propto I$$

Equation (4.4.4)

d_{max} = maximum peak deflection
I = Impulse

The energy balance procedure, initially adopted by **Pope (2002)** was a way of characterising the response of the plate. It equates the induced load to the strain energy in the plate. A linear relationship would indicate an impulsive response.
Impulse values were calculated from the pressure-time traces recorded by the DPG1 positioned at an eccentricity of 100mm from the centre of the plate. The spatial distribution of impulse along the top face of the steel plate is illustrated in figure 4.4.5. Observations from figure 4.4.5 are stated as follow:

1. A decrease in the charge standoff was related to a reduction in impulse.
2. The values of impulse associated with the three different charge standoffs showed similarities at progressing distances away from the centre of the plate.
3. Significant impulse values were recorded along the DPG plane between 0mm and 100mm.
4. Significant reduction in impulse at eccentricities greater than 200mm indicated stress wave attenuation.

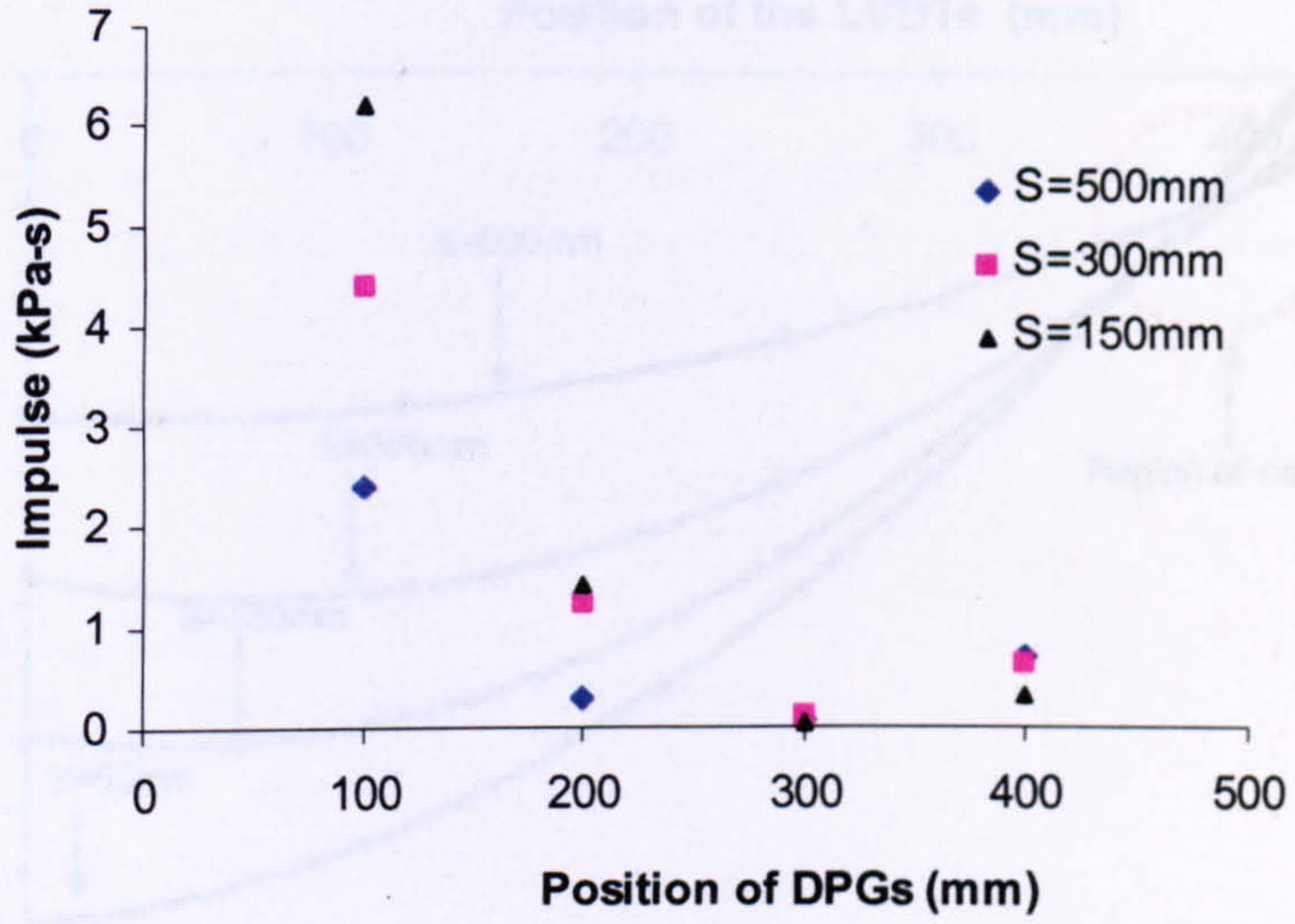

S=Charge standoff

Figure 4.4.5 Impulse recorded at different positions on the top face of the steel plate

DPG1 was not positioned centrally on the top face of the steel plate, as there was a danger of it being damaged from the groundshock at close-in standoff positions. It was instead positioned at an eccentricity of 100mm along the DPG plane to ensure its survival.

Findings from the steel tests and a physical assessment of the gauge suggested that DPG1 could have been positioned at the centre of the plate and was centrally positioned in most of the concrete tests. The positioning of the gauges along the DPG plane was a trial procedure, ensuring an undamaged elastic response of the diaphragms.

The deflected profiles of the plate, illustrated in figure 4.4.6 associated with the time at which the central peak deflection occurred, were caused by the different charge standoffs positions. As the charge standoff decreased, the central peak deflection increased, as more energy was induced into the plate.

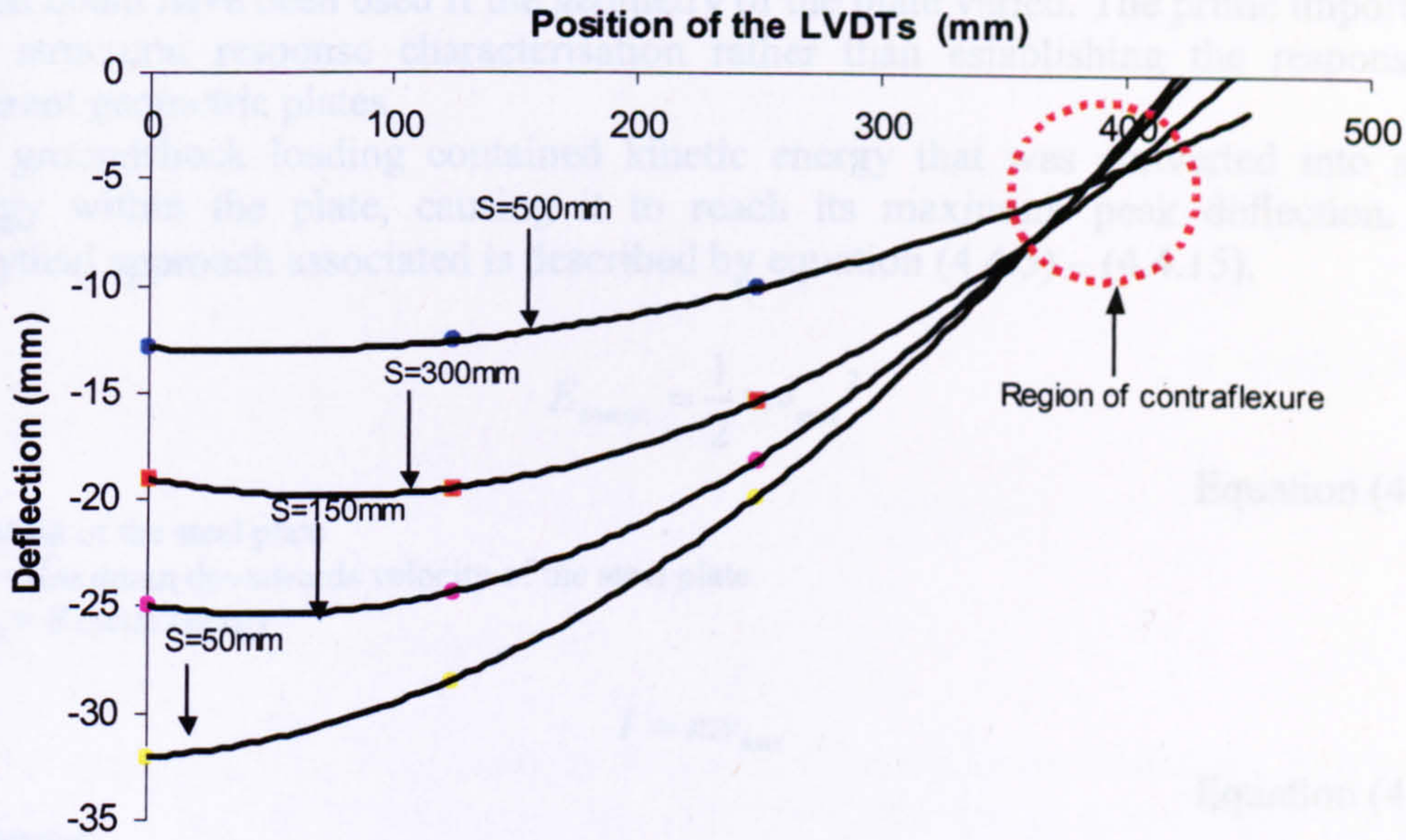

S =charge standoff

Figure 4.4.6 Maximum deflected profiles of the primary steel plate associated with charge standoff positions

The deflection of the plate along the LVDT plane illustrated in figure 4.4.6, between 0-100mm, appeared to remain consistent for charge standoffs between 150-500mm. These maximum impulses recorded by DPG1, positioned at an eccentricity of 100mm along the DPG plane, were taken from figure 4.4.5 and associated with the maximum peak deflections. The linear relationship in figure 4.4.7 demonstrated that impulse is sensitive to a variation in charge standoff, hence validating the linear relationship in equation (4.4.4).

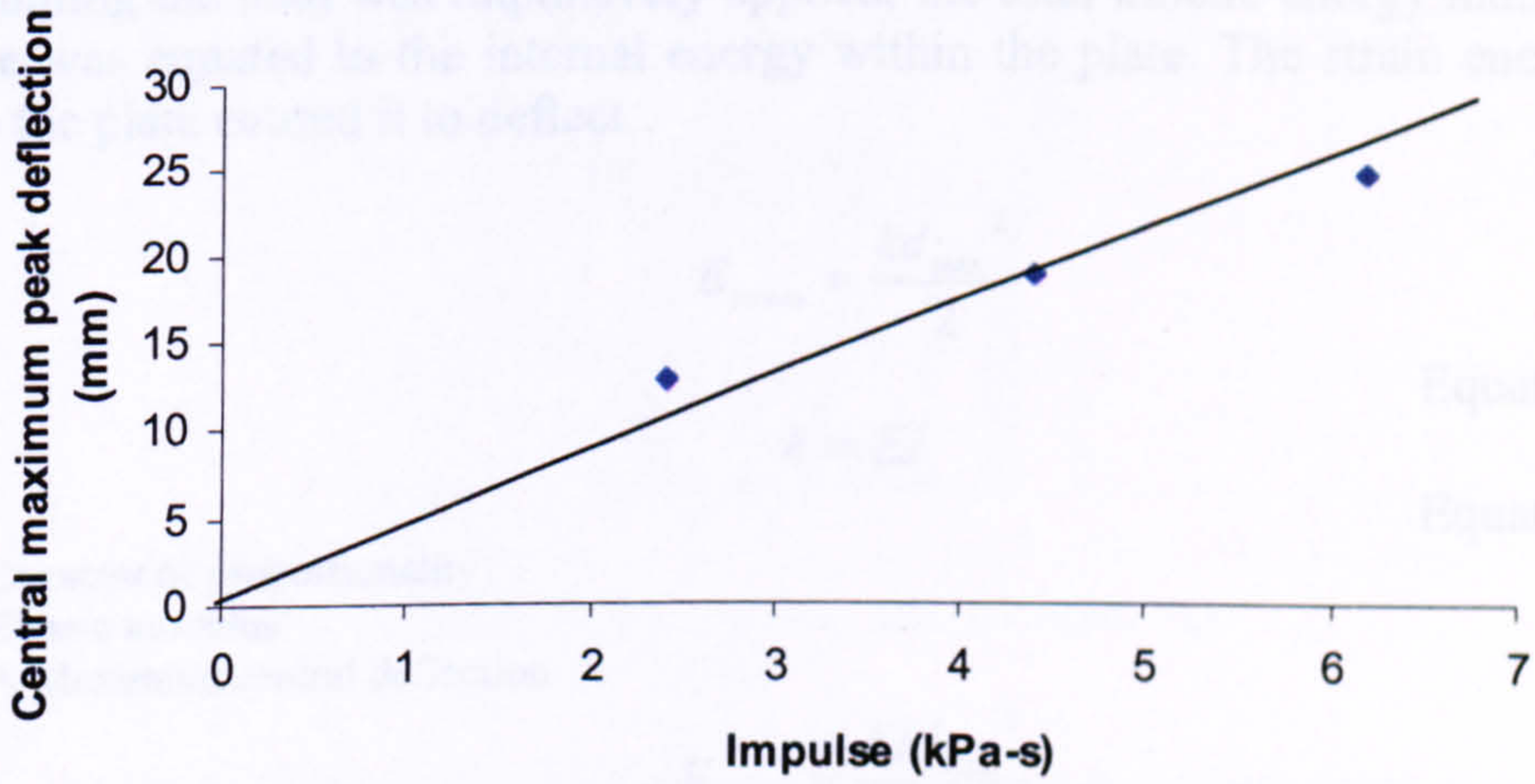

Figure 4.4.7 Central maximum peak deflection associated with impulses induced into the primary steel plate

The linear relationship in figure 4.4.7 not only puts this work in context with that performed by **Pope (2002)**, but also agrees with the theoretical analysis of conservation of energy balance described by **Tyas & Pope (2003),** presented below. The linear relationship in figure 4.4.7 could have been presented using a response

number as discussed initially by **Zhao (1998)** then used by **Tyas & Pope (2004)** which could have been used if the geometry of the plate varied. The prime importance was structural response characterisation rather than establishing the response of different geometric plates.

The groundshock loading contained kinetic energy that was converted into strain energy within the plate, causing it to reach its maximum peak deflection. The analytical approach associated is described by equation (4.4.5) – (4.4.15).

$$E_{kinetic} = \frac{1}{2} m v_{\max}^{\ 2}$$

Equation (4.4.5)

m = Mass of the steel plate
v_{max} = Maximum downwards velocity of the steel plate
$E_{kinetic}$ = Kinetic energy

$$I = m v_{\max}$$

Equation (4.4.6)

I = Impulse

$$v_{\max} = \frac{I}{m}$$

Equation (4.4.7)

$$E_{kinetic} = \frac{1}{2} m \left(\frac{I}{m} \right)^2$$

Equation (4.4.8)

$$E_{kinetic} = \frac{I^2}{2m}$$

Equation (4.4.9)

Assuming the load was impulsively applied, the total kinetic energy induced into the plate was equated to the internal energy within the plate. The strain energy induced into the plate caused it to deflect.

$$E_{strain} = \frac{k d_{\max}^{\ 2}}{2}$$

Equation (4.4.10)

$$k = EI$$

Equation (4.4.11)

k = Constant of proportionality
E = Elastic modulus
d_{max} = Maximum central deflection

$$E_{strain} = \frac{E I d_{\max}^{\ 2}}{2}$$

Equation (4.4.12)

Equating the strain energy in the plate to the induced kinetic energy,

$$\frac{EId_{\max}^{\ 2}}{2} = \frac{I^2}{m}$$

Equation (4.4.13)

$$d_{\max}^{\ 2} \propto I^2$$

Equation (4.4.14)

$$d_{\max} \propto I$$

Equation (4.4.15)

4.4.2 Reinforced concrete tests

The geometric set up of the concrete tests was different to the steel tests. The loading was un-symmetrical as the charge was positioned, relative to a secondary reinforced concrete slab, at an inclination of 70° to the horizontal as illustrated in figure 4.4.8. The DPGs were positioned along diagonal plane O-B1, with reference to figure 4.1.1 that coincided with the plane of the charge. The drilled hole that penetrated into the thickness of the slab for positioned charges did not cut through the rebars in the top face. This would have occurred if the hole had been drilled into plane O-X2, coinciding with the plane in which the LVDTs were positioned. This approach would have weakened the slab's tensile capacity prior to detonation and was discarded.

Z_1 = Soil overburden confined between the primary and secondary slab
Z_2 = Soil overburden above the secondary slab

Figure 4.4.8 Cross-sectional elevation of a concrete test set up within the test cell

The experimental data from the first four concrete tests was used to determine the response of the primary slab RCR73IT1-4. A test matrix for those tests is indicated in table 4.4.5. The results from tests RCIT5-13 were not included in the analysis due to incomplete data associated with the pressure-time histories from DPG1 and the deflection-time histories recorded by $LVDT_{0mm}$.

Table 4.4.5 Test matrix for concrete tests RCIT1-4

T_n	S_r (mm)	Z_1 (mm)	Z_2 (mm)	W (g)	θ	t_{bs} (mm)	t_{rs} (mm)	C_p
RCIT1	540	500	500	183	70°	73	73	A
RCIT2	440	500	500	183	70°	73	73	B
RCIT3	350	500	500	183	70°	73	73	C
RCIT4	300	500	500	183	70°	73	73	D

T_n = Test number
S_r = Charge standoff
Z_1 = Depth of soil overburden between the primary and secondary slabs
Z_2 = Depth of soil overburden above the secondary slab
W = Mass of the charge
θ = Charge angle of inclination
t_{rs} = Thickness of the primary reinforced concrete slab
t_{bs} = Thickness of the secondary reinforced concrete slab
C_p = Charge position

The parameters associated with a deflection-time history recorded by $LVDT_{0mm}$ are tabulated in table 4.4.6.

Table 4.4.6 Parameters of duration from deflection-time histories in concrete tests

Test	S_r (mm)	$t_r(\delta)$ (ms)	$t_{maxpeak}(\delta)$ (ms)	$t_{second\ peak}(\delta)$ (ms)	$t_{end}(\delta)$ (ms)	$t_d(\delta)$ (ms)	T_1 (ms)	T_2 (ms)
RCIT1	540	4.8	10	15	35	30.2	15	12.5
RCIT2	440	3.8	8.6	16.6	40	36.2	19	14
RCIT3	350	2.5	8.7	16.3	35	32.5	19	13.4
RCIT4	300	3.3	8.9	17.6	40	36.7	20	14

S_r = Charge standoff
$t_r(\delta)$ = First response time
$t_{maxpeak}(\delta)$ = Time at maximum peak deflection
$t_{second\ peak}(\delta)$ = Time at the second peak
$t_{end}(\delta)$ = Time when response ends
$t_d(\delta)$ = Duration of the response
T_1 = first natural period of oscillation
T_2 = Second natural period of oscillation

The parameters associated with the pressure-time histories recorded by DPG1 positioned centrally on the top face of the primary slab are illustrated in table 4.4.7.

Table 4.4.7 Parameters of duration from pressure-time histories in concrete tests

Test	$t_r(P)$ (ms)	$t_{max\ peak}(P)$ (ms)	$t_{end}(P)$ (ms)	$t_d(P)$ (ms)
RCIT1	5.4	7	12.2	6.8
RCIT2	2.6	4.1	13.1	10.5
RCIT3	3.5	1.9	12.7	9.2
RCIT4	1.2	1.8	11.3	10.1

$t_r(P)$ = Response time
$t_{maxpeak}(P)$ =Time at maximum peak pressure
$t_{end}(P)$ = Time when the load ends
$t_d(P)$ = Duration of the load

The ratio values of load duration and natural frequency of response are illustrated in table 4.4.8.

Table 4.4.8 Ratio values of t_d/T from tests RCIT1-4

Test	t_d (P)/T_1 (δ)	Response
RCIT1	0.54	Impulsive end of the dynamic range
RCIT2	0.55	Impulsive end of the dynamic range
RCIT3	0.48	Impulsive
RCIT4	0.50	Impulsive end of the dynamic range

An idealised half sine-wave impulse load distribution in accordance with **Clough & Penzien (1993)** approximates a typical pressure-time history profile, as illustrated in figure 4.4.9, recorded by DPG2.

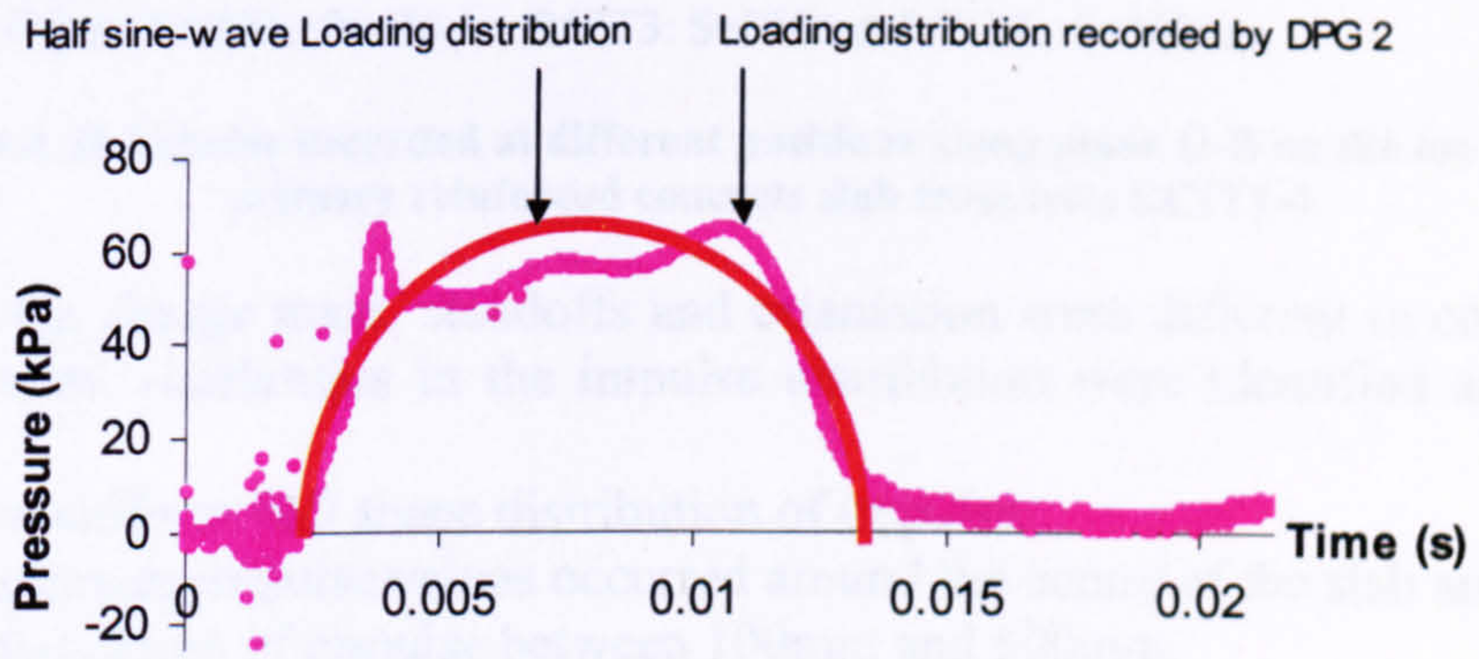

Figure 4.4.9 Comparison between a half sine-wave loading distribution and the pressure-time history profile recorded by DPG2 during concrete test RCIT2

The results from table 4.4.8 indicate that the ratio values of load duration to natural period of response are either equal to or less than 0.5, associated with an impulsive response.

$$\frac{t_d}{T} \leq 0.5$$

Equation (4.4.16)

It is important to note that an idealised rectangular loading distribution would also be defined by equation (4.4.16).

Khan & Keller (1997) stated that '*additional soil mass from the overburden tends to increase the natural period which directs the blast loading to the impulsive regime*'. This statement backs up the impulsive response finding together with the fact that primary slab RCR73IT1-4 carried a total depth of soil overburden of 1000mm, which was greater than the depth of soil carried by the other primary slabs.

Due to mechanical problems with the central $LVDT_{0mm}$, the maximum peak deflections were not captured and therefore could not be compared to the maximum impulse values recorded by DPG1. This prevented an energy balance analysis from being performed.

The spatial distribution of impulse along the top face of the primary slab is illustrated in figure 4.4.10.

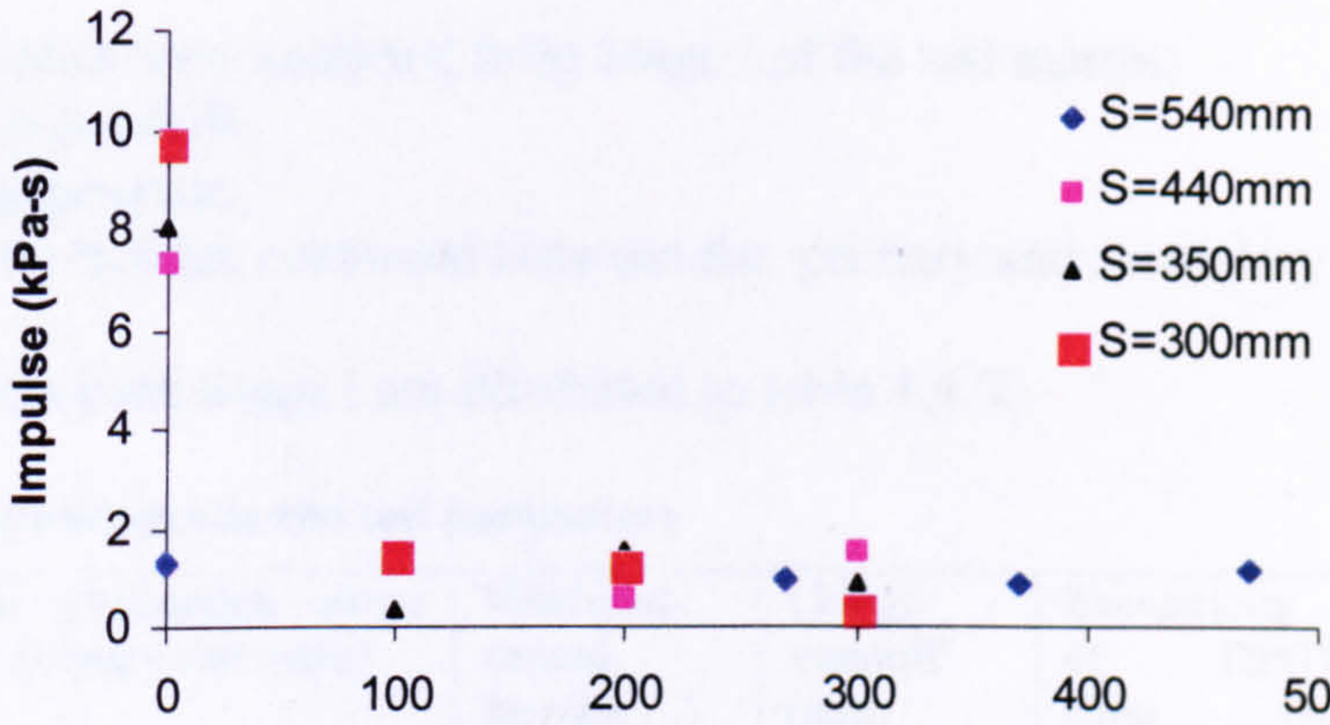

S = charge standoff
RCIT1: S=540mm RCIT2: S=440mm RCIT3: S=350mm RCIT4: S=300mm

Figure 4.4.10 Impulse recorded at different positions along plane O-B on the top face of the primary reinforced concrete slab from tests RCIT1-4

Although the charge mass, standoffs and orientation were different in comparison to the steel tests, similarities in the impulse distribution were identified and stated as follow::

1. non-uniform bell shape distribution of impulse,
2. maximum impulse values occurred around the centre of the slab and plate
3. stabilization of impulse between 100mm and 500mm.
4. decrease in charge standoff led to an increase in impulse.

The steel and concrete tests both yielded an impulsive response from calculations of t_d/T. This suggested that the concrete test results would have also yielded a linear relationship from an energy balance procedure, if the maximum peak deflections were captured. A lack of experience in setting the sensitivity on the digital oscilloscopes during the earlier tests prevented the maximum peak deflections from being recorded.

4.4.3 Experimental parameters affecting groundshock

It has already been established that the response has been characterised as impulsive, implying that the primary slab responds once the load has significantly decayed. The experimental parameters that affected the magnitude of loading across the top face of the primary slab are described as follow:

1. soil overburden contained between the primary and secondary slabs,
2. soil overburden above the secondary slab,
3. charge standoff,
4. presence of a secondary slab,
5. charge position relative to the secondary slab.

4.4.3.1 Analysis of parameters that influenced impulse from Stage I of the test matrix

Three parameters were analysed from Stage I of the test matrix:

1. charge standoff,
2. charge position,
3. soil overburden contained between the primary and secondary slabs.

Impulse results from Stage I are illustrated in table 4.4.9.

Table 4.4.9 Impulse results and test parameters

Tests	Soil overburden above the primary slab (mm)	Maximum central impulse (kPa-s)	Charge standoff (mm)	Eccentricity of DPG1 from the centre (mm)	Charge position
RCIT1	500	1.35	540	0	A
RCIT2	500	7.32	440	0	B
RCIT3	500	7.4	350	0	C
RCIT4	500	9.77	300	0	D
RCIT5	300	2.63	340	0	A
RCIT6	300	8.41	240	0	B
RCIT7	300	10.3	150	0	C
RCIT8	300	15.5	100	0	D
RCIT9	150	7.65	190	0	A
RCIT10	150	11.34	90	150	B
RCIT11	150	26.5	0	150	C
RCIT12	75	8.18	113	150	A
RCIT13	75	11.23	13	200	B

The results from Stage I of the test matrix as illustrated in table 4.4.9 have been graphically represented in figures 4.4.11-4.4.14. DPG1 in tests RCIT9-11 was positioned at an eccentricity from the centre of the primary slab.
The greater the proportion of charge below the bottom face of the secondary slab, the greater the magnitude of impulse at the centre of the primary slab, as illustrated in figure 4.4.11. At charge standoffs $\geq$300mm the difference in impulse associated with charge positions B and C was small. At a charge standoff $\geq$350mm, the difference in impulse values between charge positions A and B was large and consistent. This suggested that the positioning of the charge above the top face of the secondary slab had a significant affect in reducing the central impulse on the primary slab. At charge standoffs $\leq$100mm the charge position below the bottom face of the secondary slab became critical, causing a significant increase in the central impulse on the primary slab.

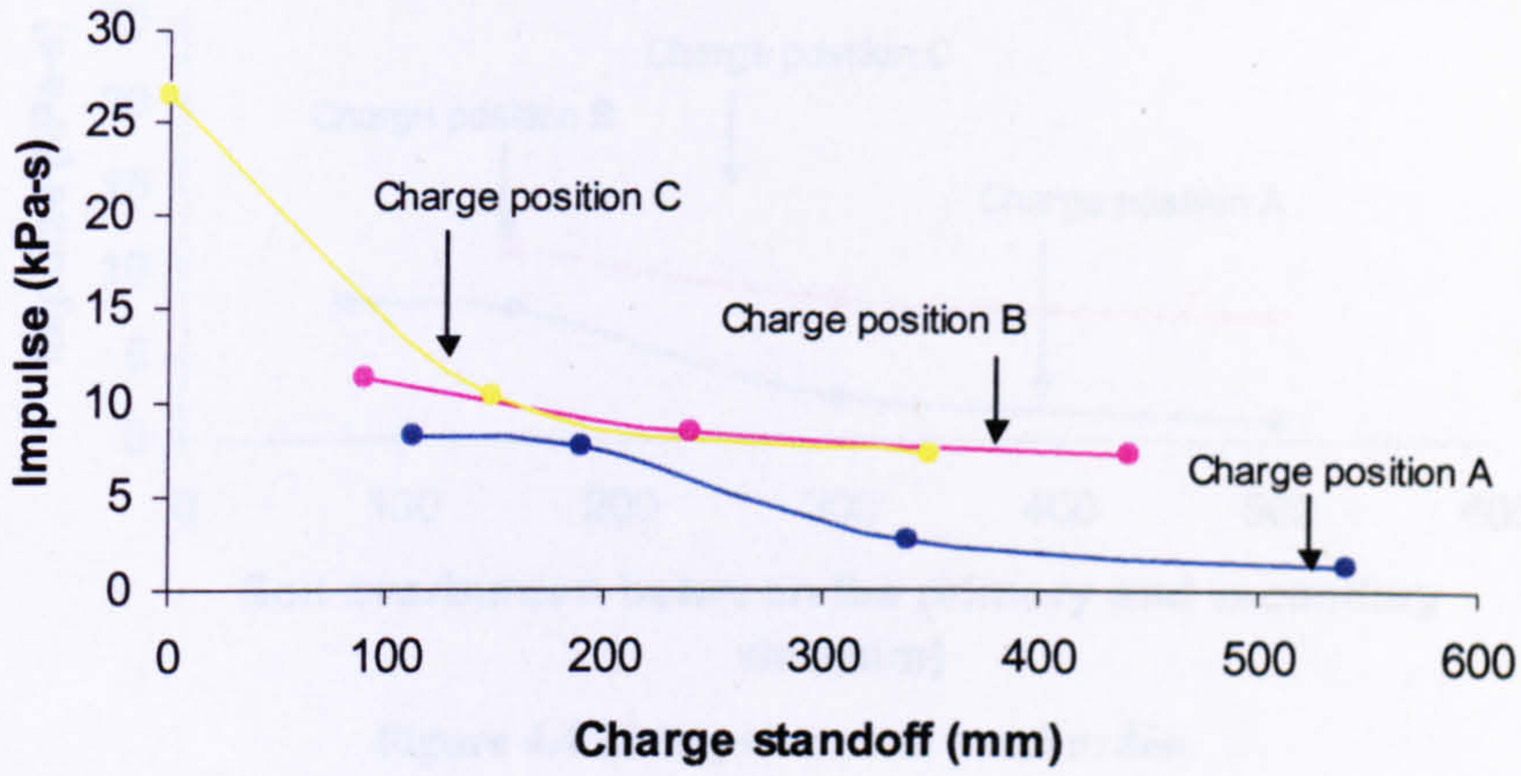

Figure 4.4.11 Impulse v charge standoff

At smaller soil overburden depths, a primary slab experienced a larger central impulse, from a stress wave that had attenuated less, whilst travelling along a smaller wave path. The greater the proportion of the charge beneath the secondary slab (charge positions C and D) the larger the impulse. The curves that depict such a phenomenon are illustrated figure 4.4.12

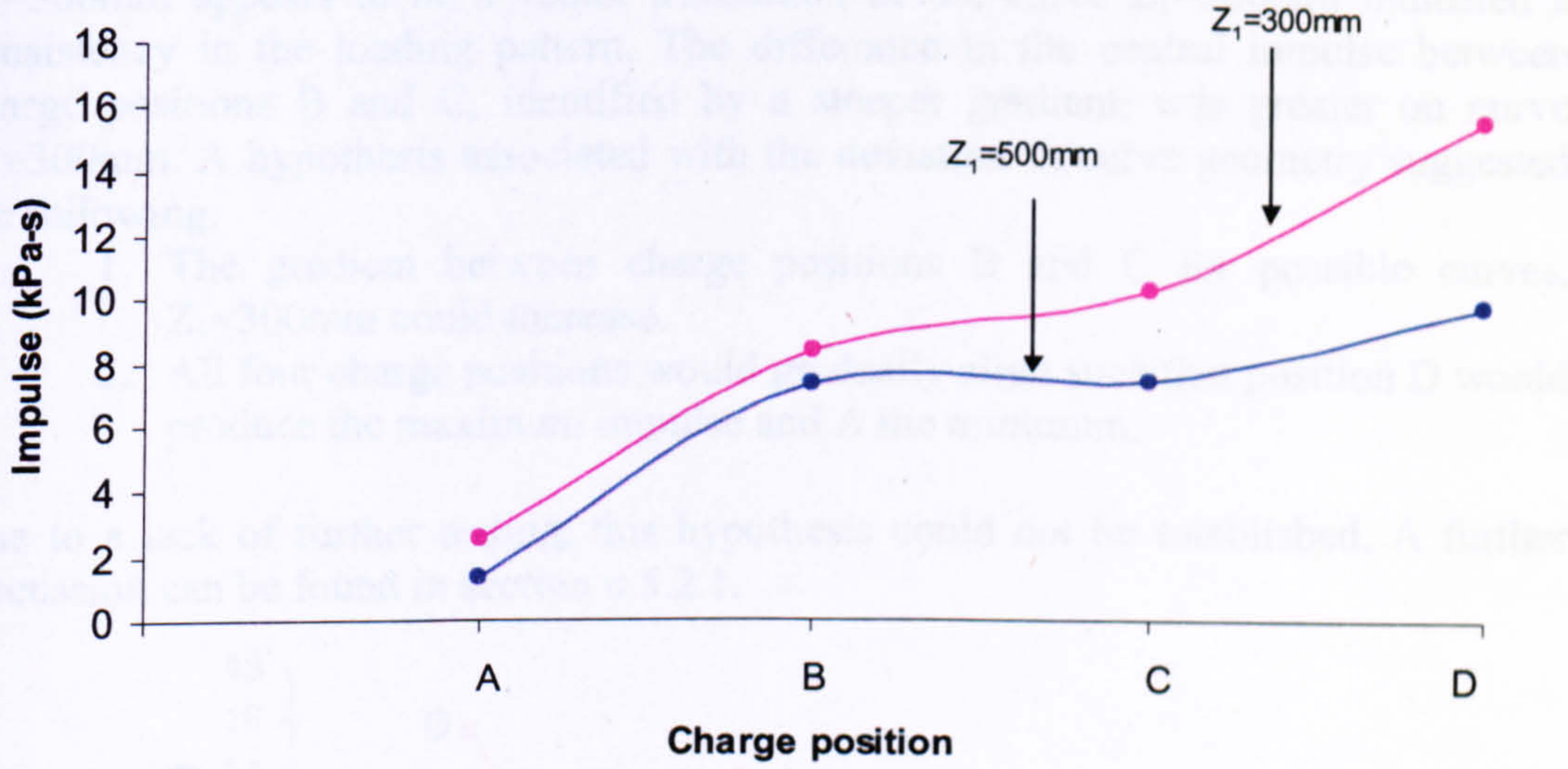

Z_1= Soil overburden contained above the top face of the primary slab and below the bottom face of the secondary slab

Figure 4.4.12 Impulse v charge position

Charge positions B and C caused similar central impulses on the primary slab when the soil overburden was ≤350mm, as illustrated in figure 4.4.13. Soil overburden values ≥350mm, which contained charge positions A, B and C did not significantly alter the impulse.

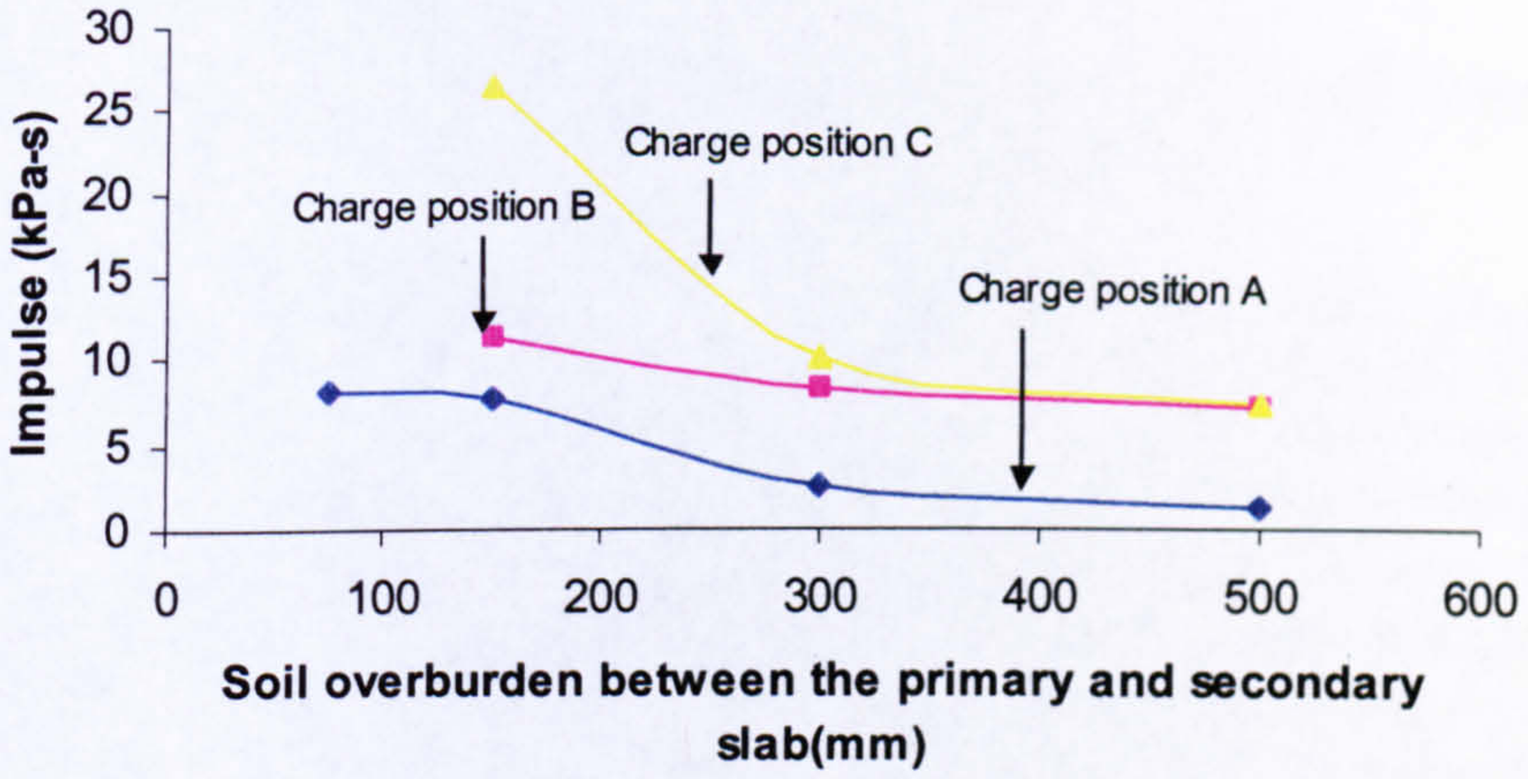

Figure 4.4.13 Impulse v soil overburden

The geometric similarity of curves Z_1=300mm and Z_1=500mm in figure 4.4.14 implies that there was a consistent phenomena identified in groundshock loading. The effect of using charge positions B and C caused a small difference in the central impulse on the primary slab associated with curve Z_1=500mm. This difference increased when the soil overburden decreased. A 10mm difference in the charge standoff position, between charge positions A and C at standoffs of 350mm and 340mm, caused a 6kPa-s difference in the impulse. The curve associated with Z_1=300mm appears to be a vector translation of the curve Z_1=500mm indicated a consistency in the loading pattern. The difference in the central impulse between charge positions B and C, identified by a steeper gradient, was greater on curve Z_1=300mm. A hypothesis associated with the deviation in curve geometry suggested the following:

1. The gradient between charge positions B and C for possible curves, Z_1<300mm could increase.
2. All four charge positions would gradually align such that position D would produce the maximum impulse and A the minimum.

Due to a lack of further testing, this hypothesis could not be established. A further discussion can be found in section n 5.2.1.

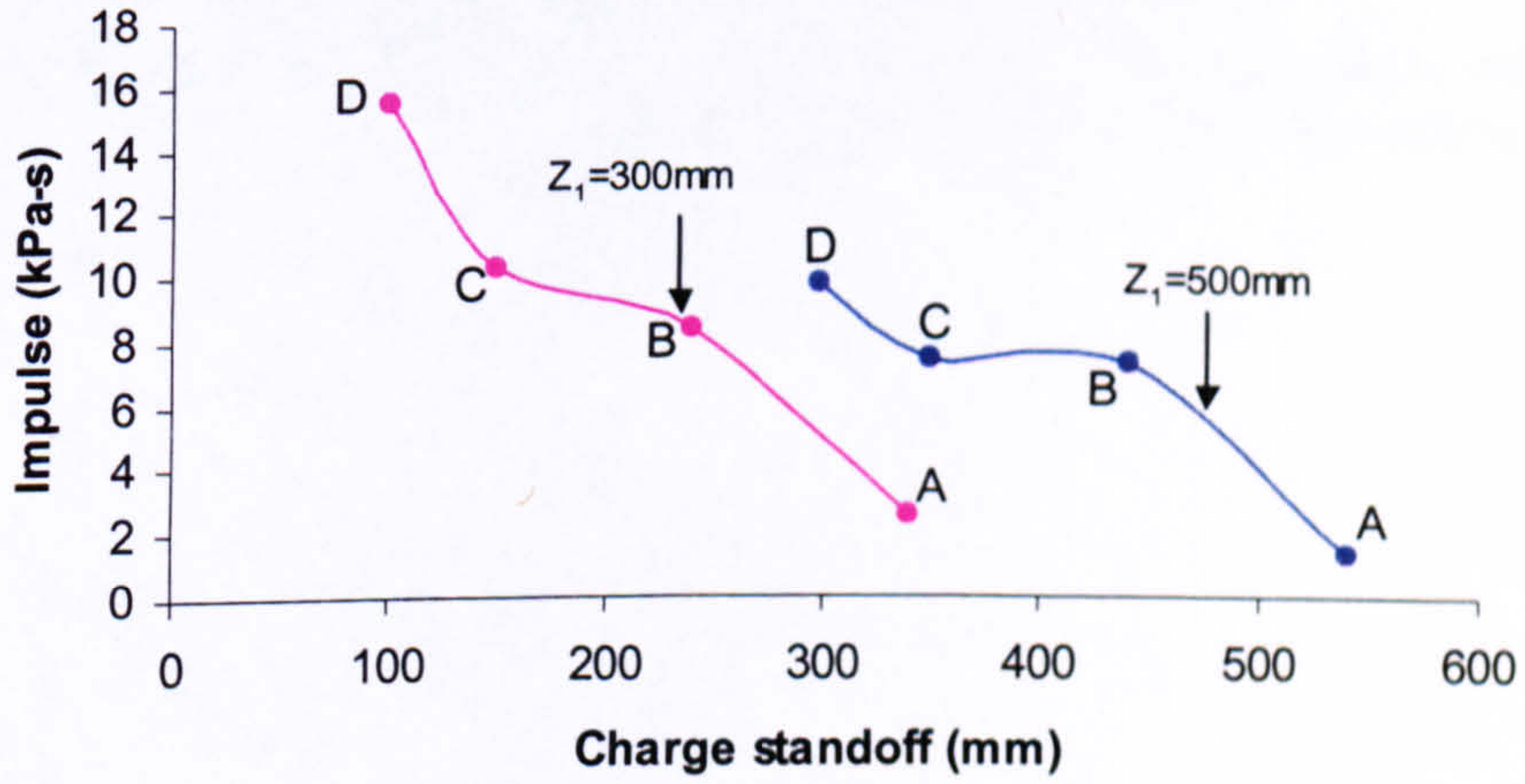

Z_1= Soil overburden contained between the primary and secondary slabs

Figure 4.4.14 Impulse v charge standoff

4.4.3.2 Analysis of parameters that influence impulse from Stage II of the test matrix: Numerical simulations using AUTODYN2D

The soil overburden above the secondary slab was varied within Stage II of the test matrix. The graphical results from Stage II, in section 4.3 did not conclusively indicate that a reduction in the soil overburden would affect the severity of damage to the secondary slab. Due to a problem with the DPGs, variability in the soil overburden could not be associated with the loading. Due to a lack of time and an intense experimental schedule, it was impossible to continue evaluating this phenomenon.

It was decided to run a number of simulations numerically, using AUTODYN2D, to establish whether a reduction in the soil overburden affected the severity of damage to the secondary slab, as well as the loading across the top face of the primary slab.

It was of no direct interest to model the experimental tests, but instead to identify whether the soil overburden parameter influenced the damage and loading parameters. If the experimental setup was being modelled, AUTODYN3D would have been used, to take account of the unsymmetrical nature the tests.

This would have taken longer to setup and would have taken weeks, with the possibility of the simulation crashing. It is unknown whether the damage to the primary and secondary slabs would be significantly different if a 2D rather than a 3D version was used.

It was decided to use AUTODYN2D based upon work performed experimentally and numerically by **Chapman *et al* (1994)** and **Ma *et al* (1999).** The authors used AUTODYN2D to simulate what was a three-dimensional situation, two-dimensionally, using axial symmetry and implementing a cylindrical charge vertically. It has been stated by **Chapman *et al* (1994)** that *'Axial symmetry was employed, as it produced a better model of the physical situation'*. It was concluded that there was good agreement experimentally and numerically with the first two peaks of the waveform that would be associated with causing structural damage. *'AUTODYN2D has potential as a tool for investigation of complex blast wave propagation problems'* as also stated by **Chapman *et al* (1994)**.

The hydrocode simulations in AUTODYN2D could not be performed to increase the scope of data recorded from the experimental tests. This was due to a difference in geometry between the numerical and experimental test setups.

Due to the axial symmetry in AUTODYN2D a vertical charge could only be used. A comparison between charges positioned experimental and numerically is illustrated in figure 4.4.15.

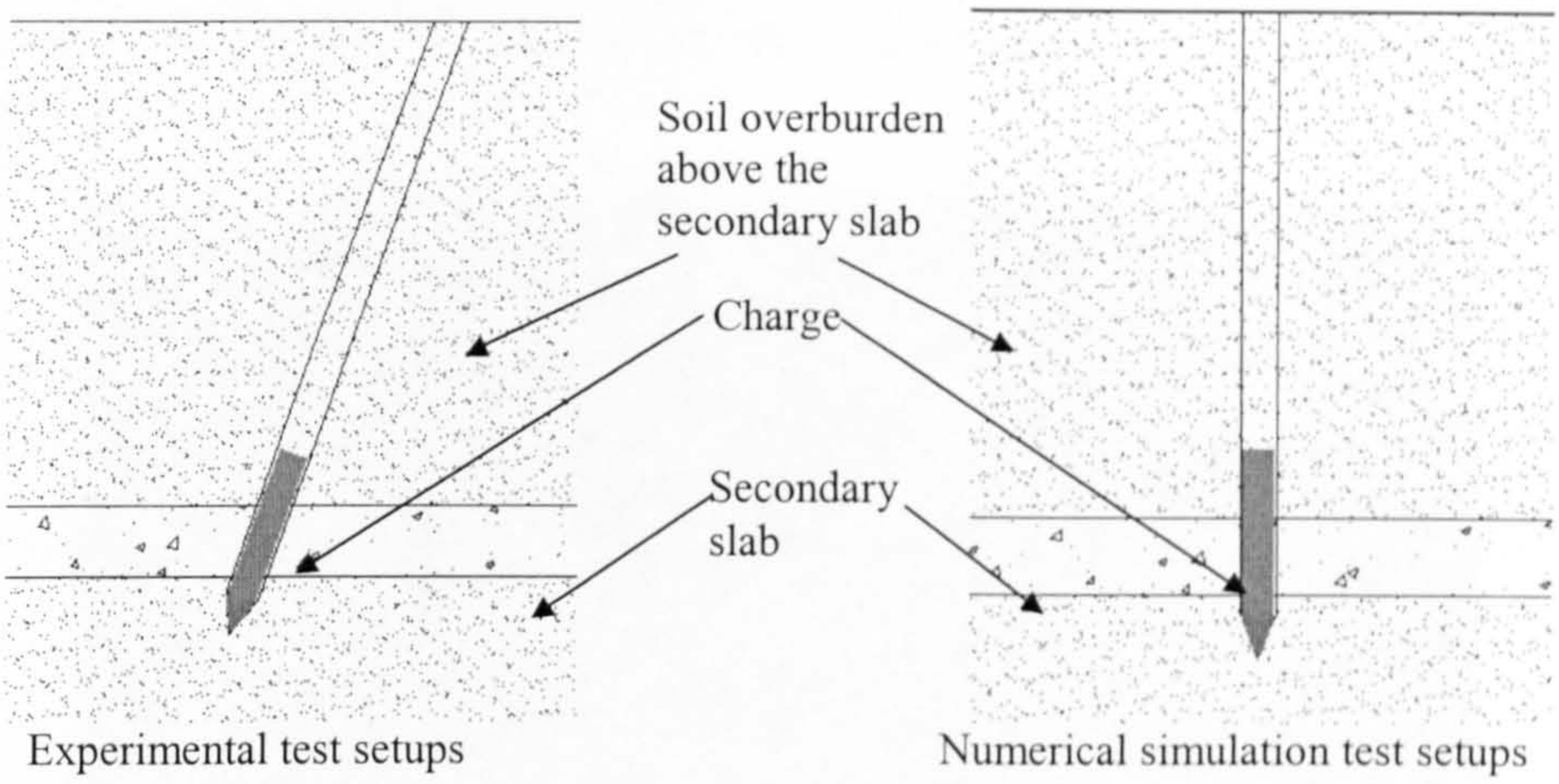

Figure 4.4.15 Charge positions relative to a secondary slab in the experimental and numerical test setups

The simulation setup in AUTODYN2D was axial symmetrical, as illustrated in figure 4.4.16 containing coloured shapes that represented different materials. The geometry presented in figure 4.4.14 is essentially a 90° anti-clockwise rotation of the geometry of the 'numerical simulation test setup' in figure 4.4.15 with axial symmetry.

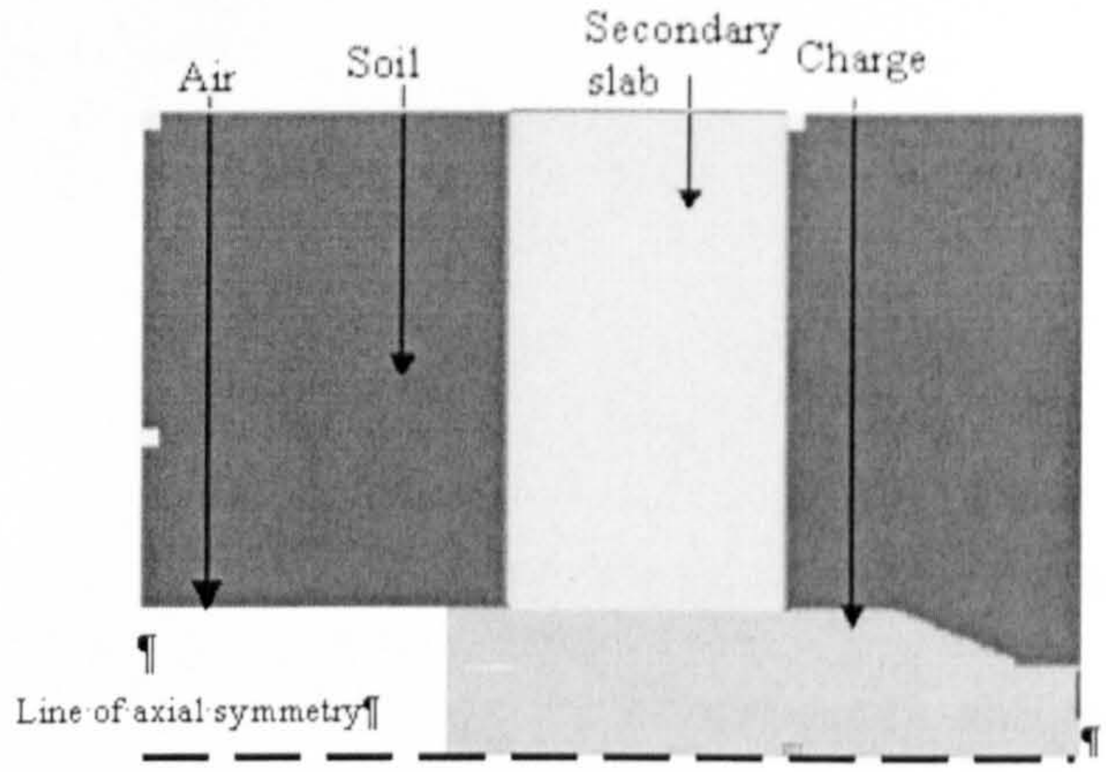

dark blue = soil used as overburden green = Explosive charge light blue = Concrete
white = Air

Figure 4.4.16 Charge positions relative to a secondary slab in the experimental and numerical test setups.

A grid in the shape of a rectangular block was constructed, containing the soil, charge and the concrete secondary slab, as illustrated in figure 4.4.17.
A sensitivity analysis was performed by setting up simulations with different size meshes and comparing the recorded peak pressures at fixed target points to the variation in mesh size. The importance of carrying out such a procedure has been discussed by **Tyas & Pope (2004)** and **Chapman *et al* (1994)**. The soil used represented the actual soil used during the testing. The secondary slabs used in all the simulations did not have reinforcement. The main importance was establishing whether the damage to a secondary was dependent upon the variation in soil overburden above the secondary slab.

The implementation of a rigid surface in place of a primary slab decreased the running time of the simulations. Target points were positioned on the surface, mimicking DPGs, as illustrated in figure 4.4.17.

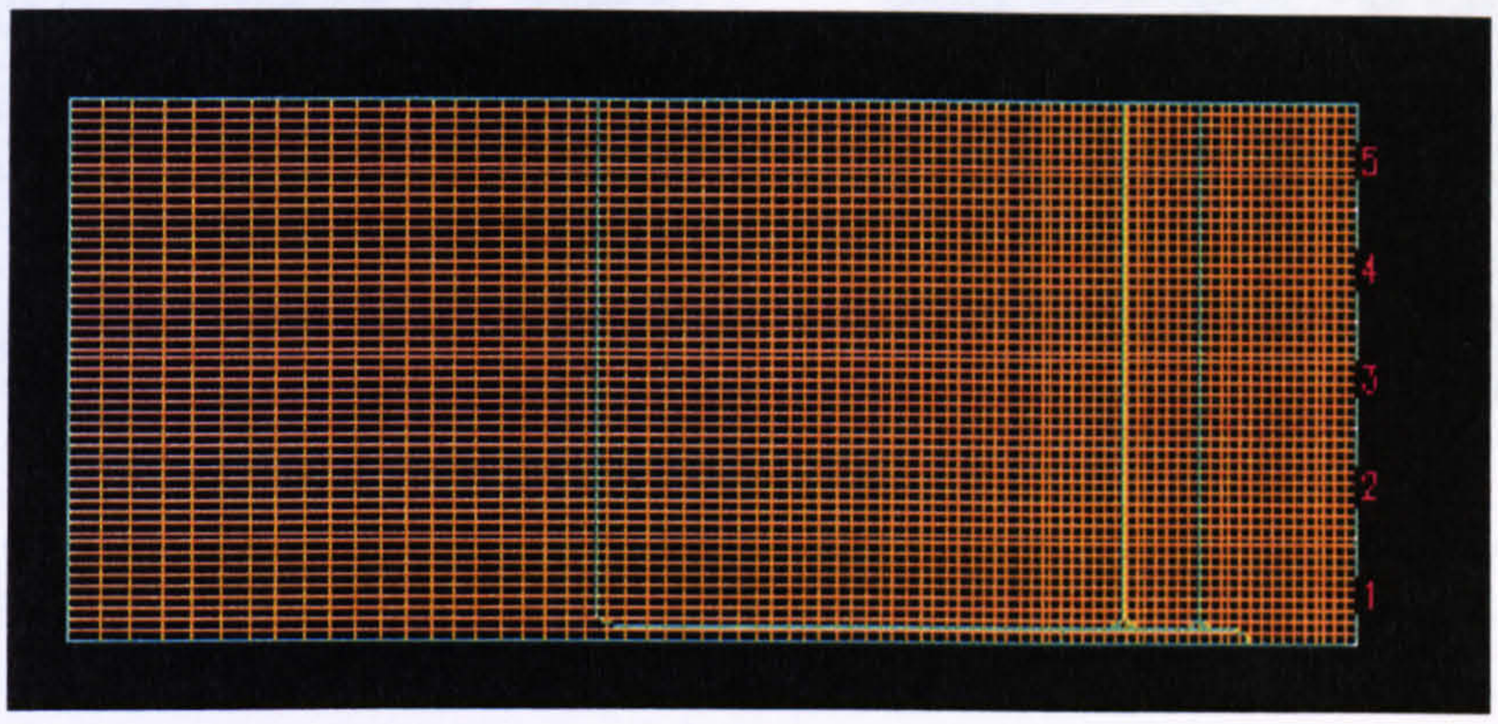

Figure 4.4.17 Positioning of the target points on the rigid surface.

Five target points in total were used and positioned at eccentricities from the centre of the surface as illustrated in table 4.4.10.

Table 4.4.10 Positioning of the target points on the rigid surface in an AUTODYN2D simulation

Target points	Eccentricity from the centre of the slab (mm)
1	0
2	100
3	200
4	300
5	400

The target points were positioned in such a way as movement was only recorded in the direction of the propagating stress wave.
The first few simulations run were part of the sensitivity analysis on the mesh size. All simulation profiles were built on meshes that varied in resolution, which were then filled with a material. The greater the mesh resolution, the greater the number of cells incorporated into a geometric profile, consisting of sub-geometries and the quicker the running time of the simulation. The smaller the mesh resolution, the opposite occurred. A number of identical geometric test profiles were setup, with different mesh resolutions. Square meshes of sizes, 10x10mm, 5x5mm, 2x2mm and 1.5x1.5mm were all setup and run. Configurations of meshes 10x10mm and 5x5mm are illustrated in figure 4.4.18.

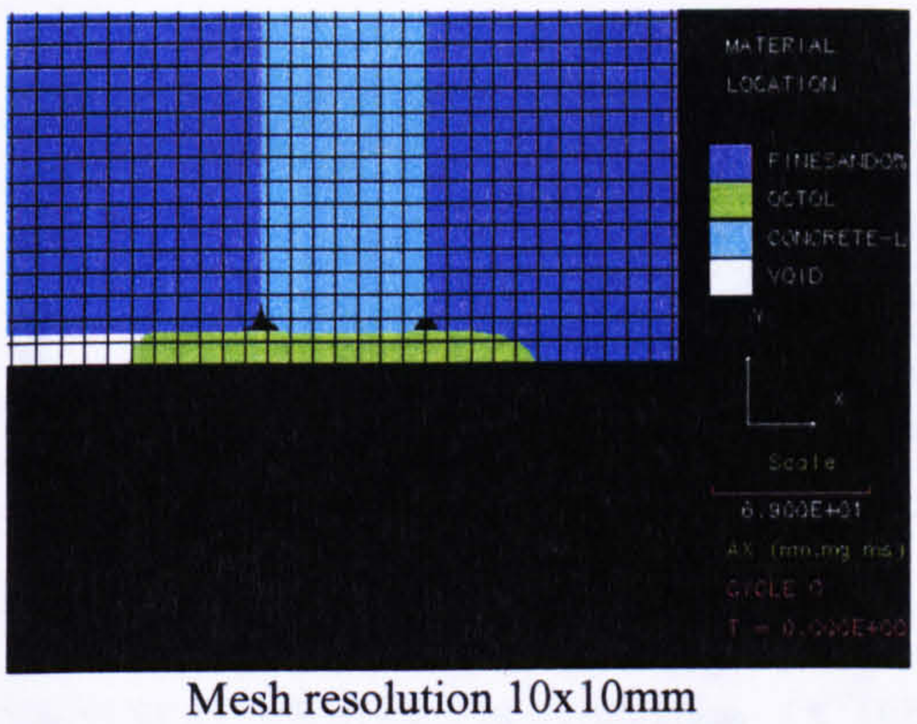

Mesh resolution 10x10mm

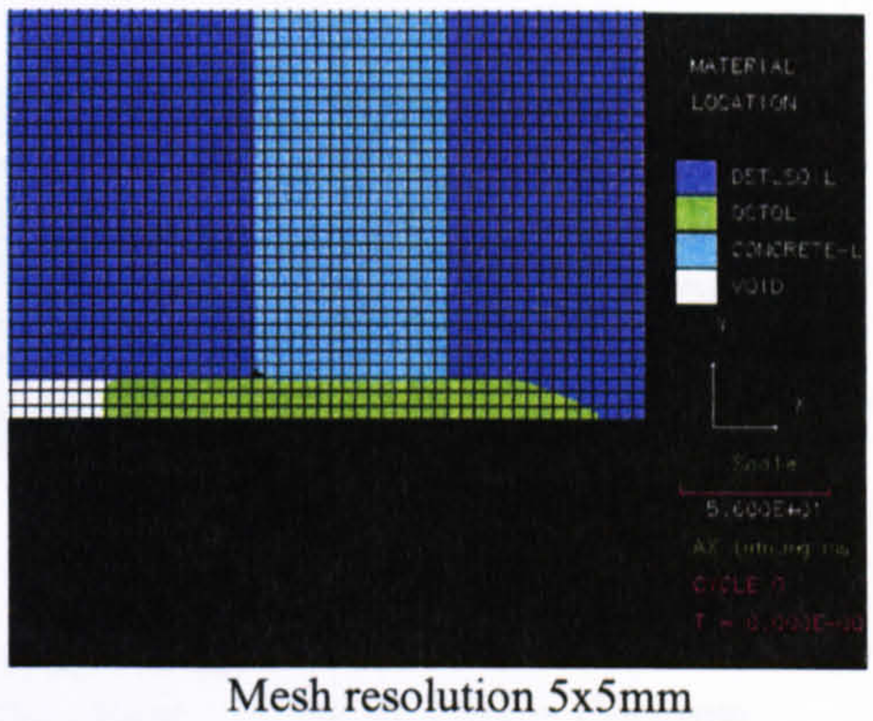

Mesh resolution 5x5mm

DSTLSOIL = soil used as overburden OCTOL = Explosive charge CONCRETE-L = Concrete
VOID = Air

Figure 4.4.18 Different mesh resolutions used to in simulations

The peak pressures recorded by the target points associated with the variation in mesh sizes are illustrated graphically in figure 4.4.19. Target points associated with mesh sizes 1.5x1.5mm and 2x2mm recorded similar peak pressures, compared to a variation in mesh sizes 5x5mm and 10x10mm.

It was decided to set up mesh sizes of 2x2mm for all the simulations involving a decrease in the soil overburden above the secondary slab.

The graphical findings presented by **Chapman *et al* (1994)** in figure 2.8.3 are similar to those illustrated in figure 4.4.19 and stated as follow:

1. Difference in peak pressure recorded within larger mesh sizes (10x10mm and 5x5mm) is greater.
2. Difference in peak pressure recorded within smaller mesh sizes (2x2mm and 1.5x1.5mm) is less.

It was concluded that a further decrease in mesh resolution below a 2x2 mesh would not affect the recorded peak pressures, but would increase the duration of the simulation.

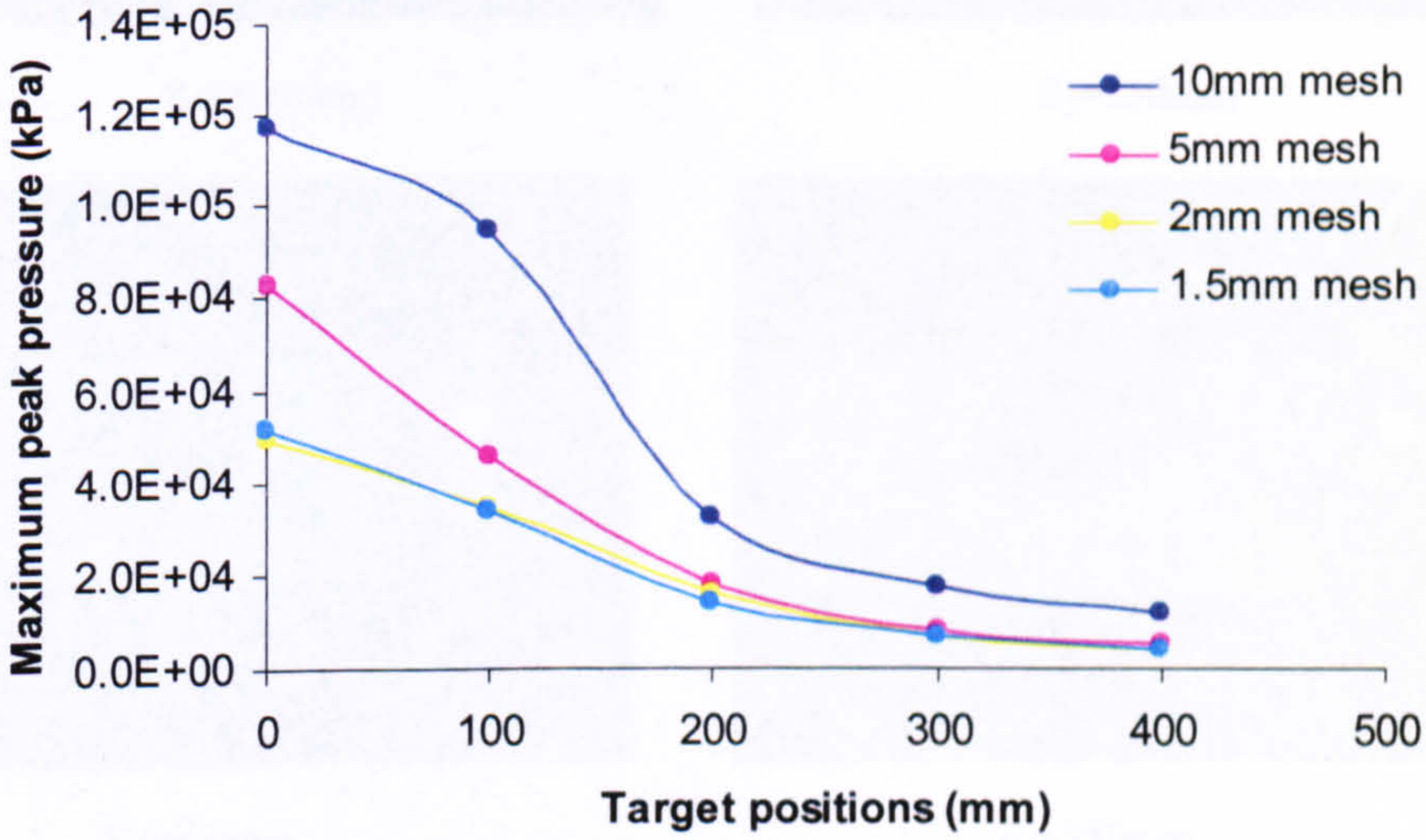

Figure 4.4.19 Maximum peak pressure recorded at the target points

The geometric profile of the secondary slab prior to a numerical detonation was very different to that at the end of the test. A comparison is illustrated in figure 4.4.20.

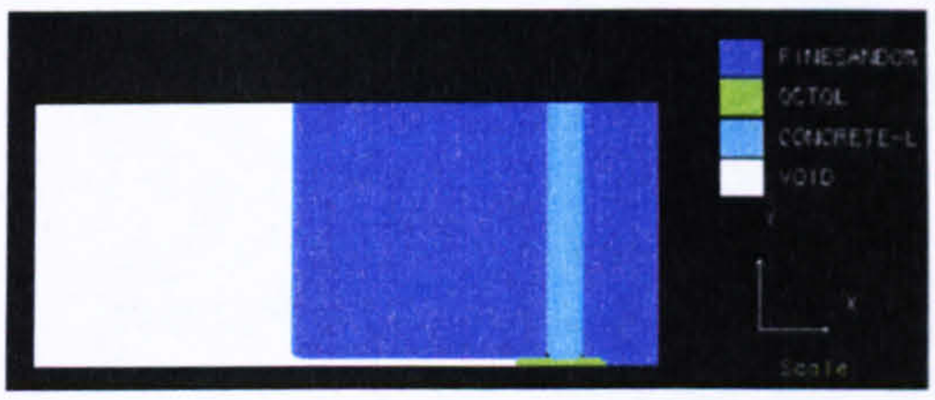

At time t=0

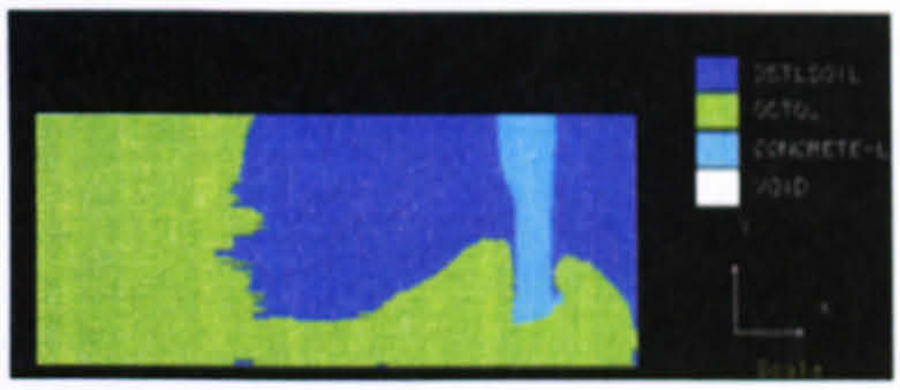

At time $t=t_{end}$

t=0 = Prior to detonation of the charge $t=t_{end}$ = End of the simulation
DSTLSOIL = Soil used as overburden OCTOL =Explosive charge CONCRETE-L = Concrete
VOID = Air

Figure 4.4.20 Geometric configuration of the numerical simulation

The final damage to the secondary slabs from the AUTODYN2D simulations are illustrated in figure 4.4.21. The damaged slabs within the range of 300-500mm all illustrated similar profiles, consisting of cratering on the top face and minor cratering on the bottom face of the slab. The damaged slabs associated with Z_2=300mm and Z_2=200mm illustrated two dissimilar profiles. The slab associated with Z_2=200mm indicated a reduced degree of cratering on the top face. The greatest change in damage profile occurred within the range 75-200mm. The damaged slabs indicated an increase in the degree of residual hogging, with increased distortion.

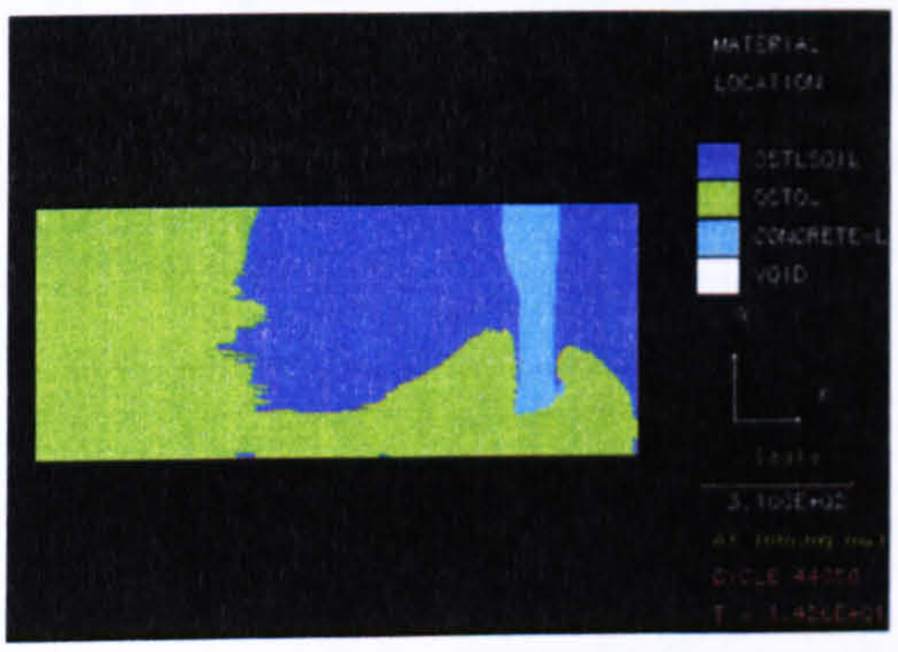

Z_2=500mm

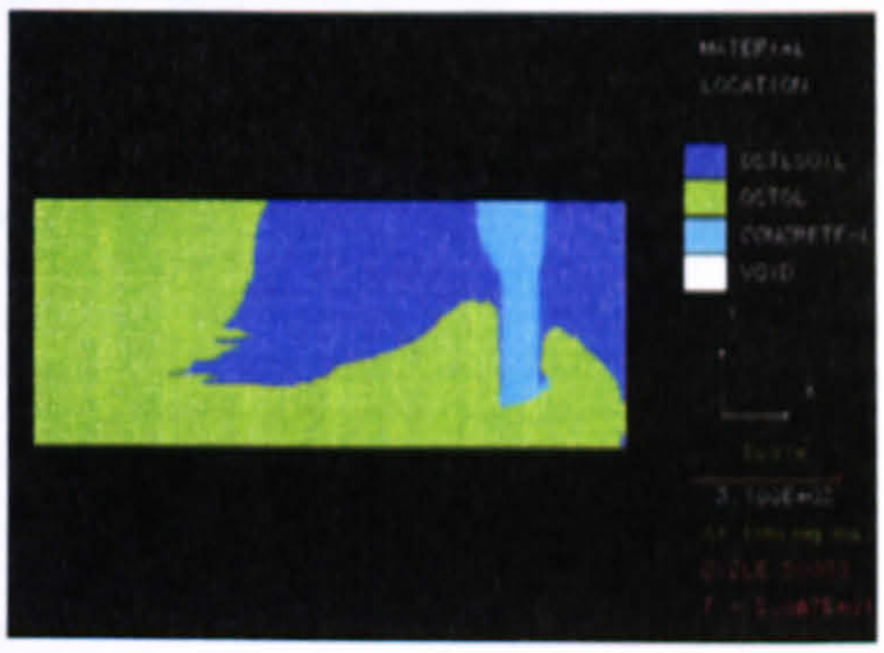

Z_2=450mm

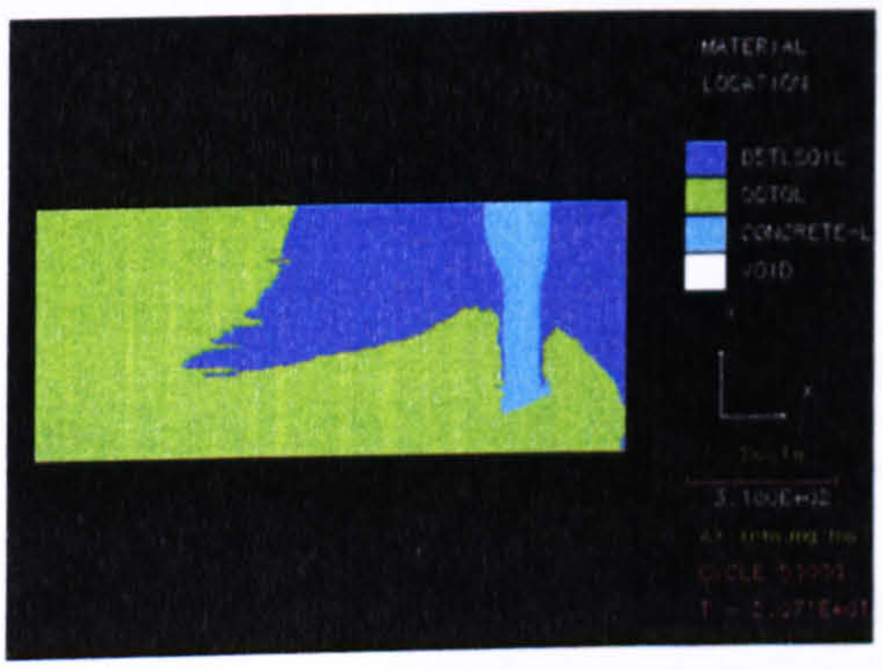

Z_2=400mm

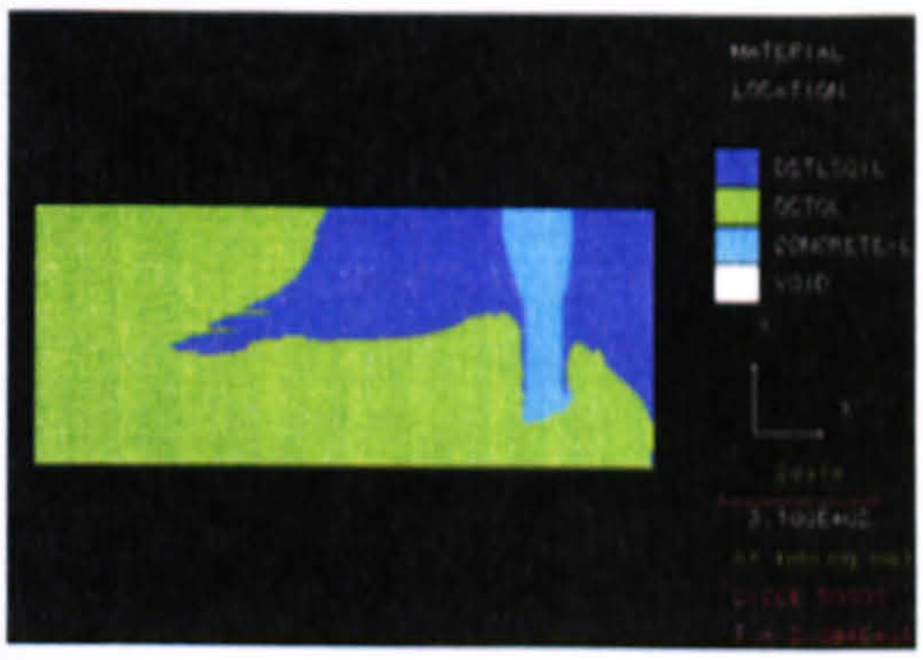

Z_2=350mm

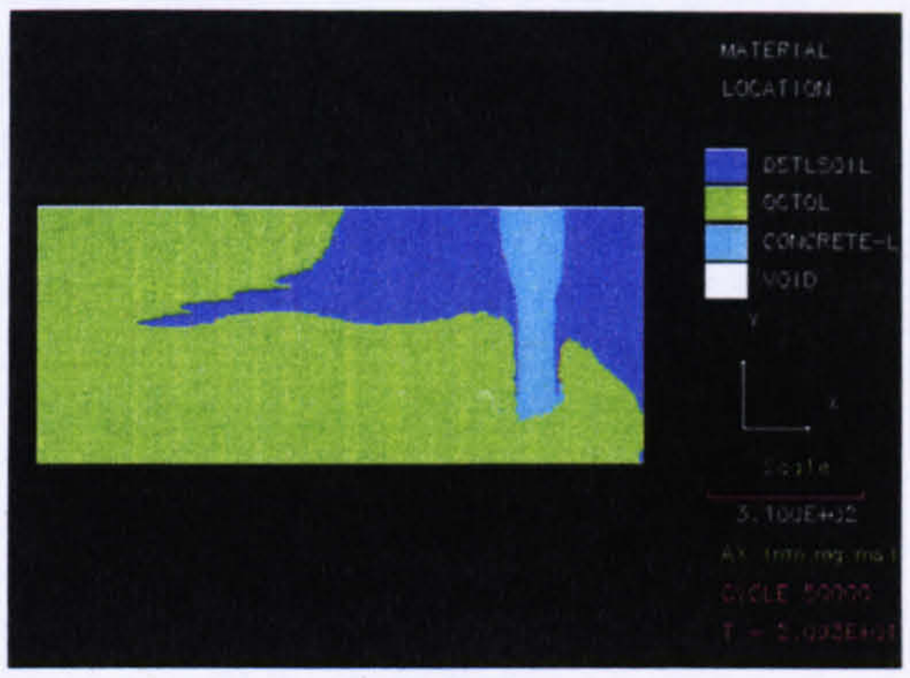

Z_2=300mm

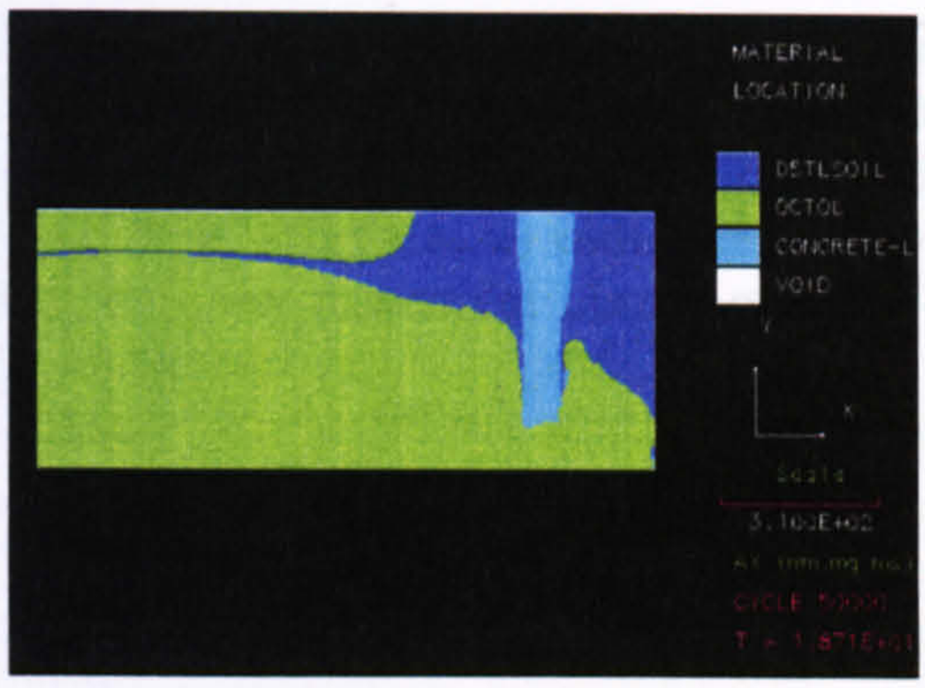

Z_2=200mm

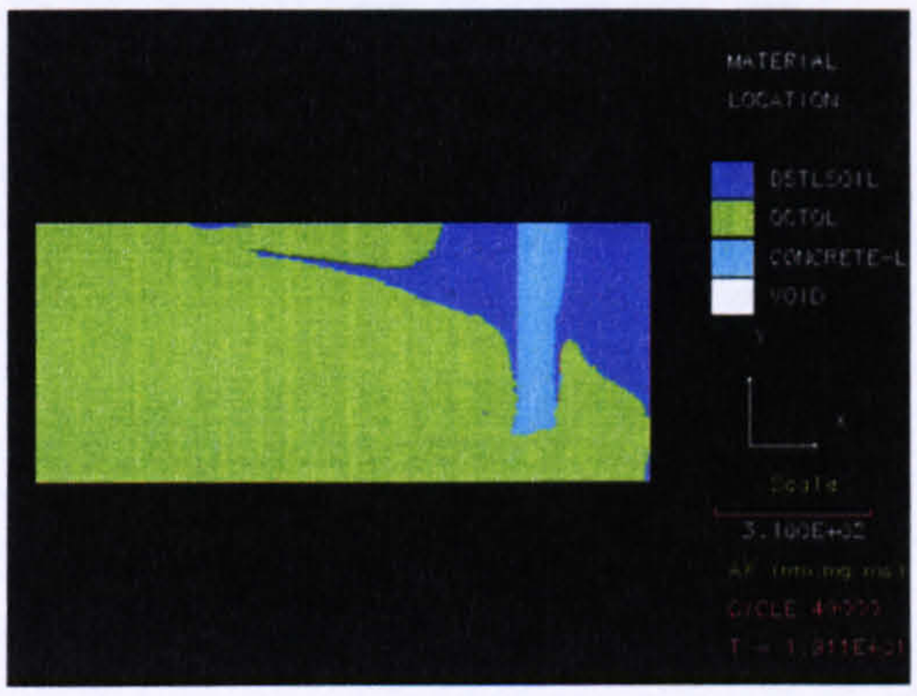

Z_2=150mm

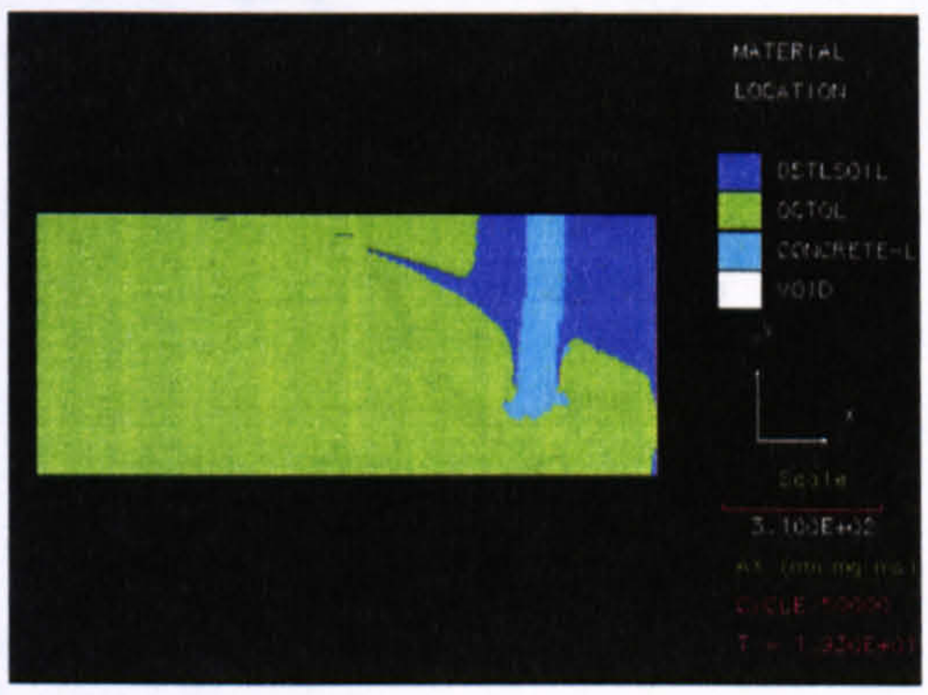

Z_2=100mm

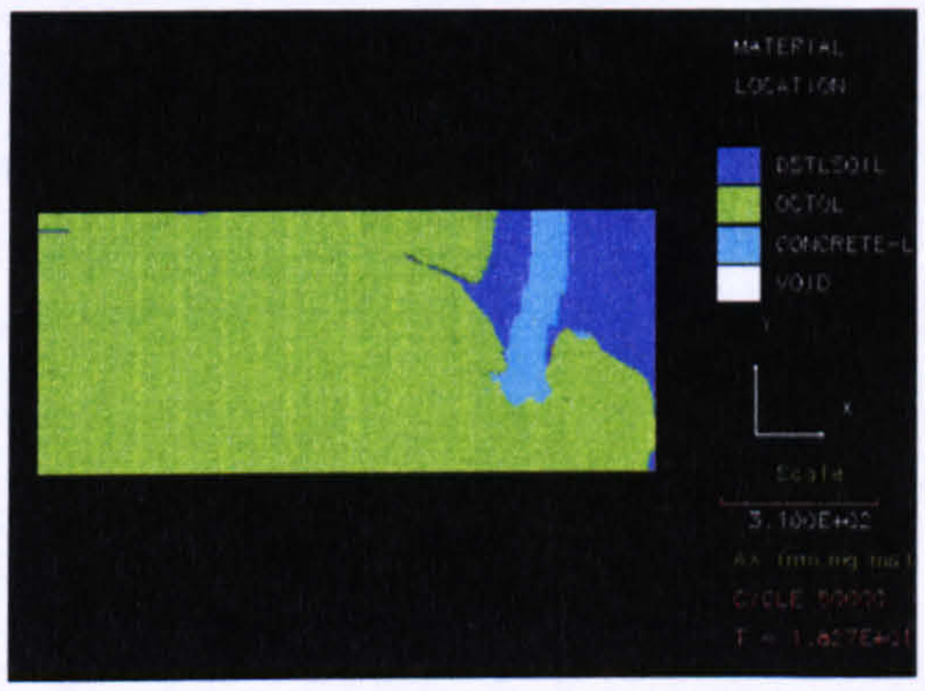

Z_2=75mm

Z_2 = Soil overburden above the secondary slab
DSTLSOIL = soil used as overburden
OCTOL = Explosive charge
CONCRETE-l = Concrete
VOID = Air

Figure 4.4.21 Damaged secondary slabs associated with a reduction in the soil overburden above their top face.

It has been established that there was a variation in the geometry of damage inflicted upon the secondary slabs as the soil overburden varied. More importantly, the reduction of the soil overburden and consequence damage did not appear to influence the loading across the rigid surface where the target points were positioned as illustrated in figure 4.4.22.

The approximate impulse calculated from the pressure-time histories in figure 4.4.20 was 5kPa-s. The numerical simulations performed were geometrically based upon test RCIT9 that involved a soil overburden depth of 500mm above the secondary slab. The impulse recorded by DPG1 during the test was 7.7kPa-s, as indicated in table 4.4.9. This implied that there was a similarity with the numerical output of 5kPa-s, hence demonstrating a confidence in the DPG results.

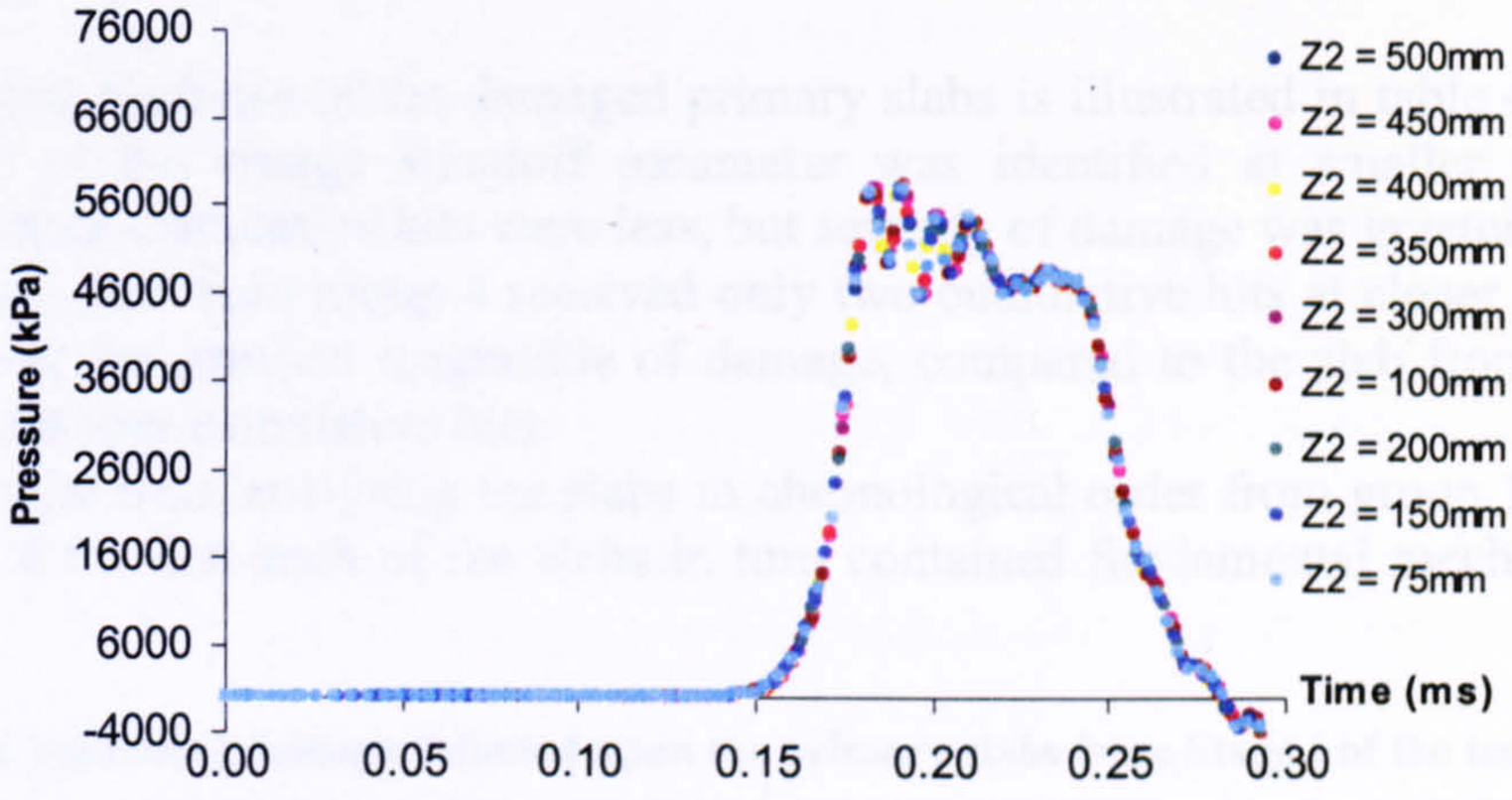

Figure 4.4.22 Pressure-time histories recorded by target point 1 during the reduction in soil overburden above the secondary slab

4.5 Damage classification and phenomena of primary reinforced concrete slabs

It has already been established that groundshock loading caused primary slab RCR73IT1-4 to respond impulsively. The lack of experimental data due to instrumentation damage at close charge standoffs prevented a full analysis in determining the response of primary slabs RCR73IT5-8, RCR73IT9-11 and RCR73IT12-13.

The parameters that influenced the loading are stated as follow:

1. soil overburden contained above the top face of the primary slab and below the bottom face of the secondary slab,
2. charge standoff,
3. charge position relative to the secondary slab,
4. positioning of a secondary slab.

It was found that impulse is dependent upon the charge standoff, with greater impulses produced at smaller charge standoffs. It is therefore hypothesized that damage could be proportional to impulse. This work has been put into context with the work performed by **Hader (1983)** and **McVay (1988),** both characterising the damage to reinforced concrete slabs. Their experimental work was presented graphically, differentiating between spall, breach and no damage, associated with varying thicknesses of slab and standoff distances from close-in spherical charges.

Four primary slabs were subjected to cumulative loading using charges positioned relative to secondary slabs during Stage I of the test matrix. It is important to state that the cumulative hits subjected to each of the primary slabs varied for two reasons:

1. As soil overburden below the secondary slab decreased from an initial value of 500mm, not all charge positions could be implemented, that led to a standoff above the primary slab.
2. It was of interest to compare the severity of damage to primary slabs that were subjected to fewer cumulative hits at smaller standoffs.

Photographic evidence of the damaged primary slabs is illustrated in table 4.5.1. The sensitivity of the charge standoff parameter was identified at smaller values of standoff where cumulative hits were less, but severity of damage was greater.
The primary slab from group 4 received only two cumulative hits at closer standoffs, but achieved the greatest magnitude of damage, compared to the slab from group 1 that received four cumulative hits.
It was evident from analysing the slabs in chronological order from group 1 to group 4 in table 4.5.1 that each of the slabs in turn contained fundamental mechanisms of damage.

Table 4.5.1Cumulative damage inflicted upon the primary slabs from Stage I of the test matrix

	Group 1 tests	Group 2 tests	Group 3 tests	Group 4 tests
Top face	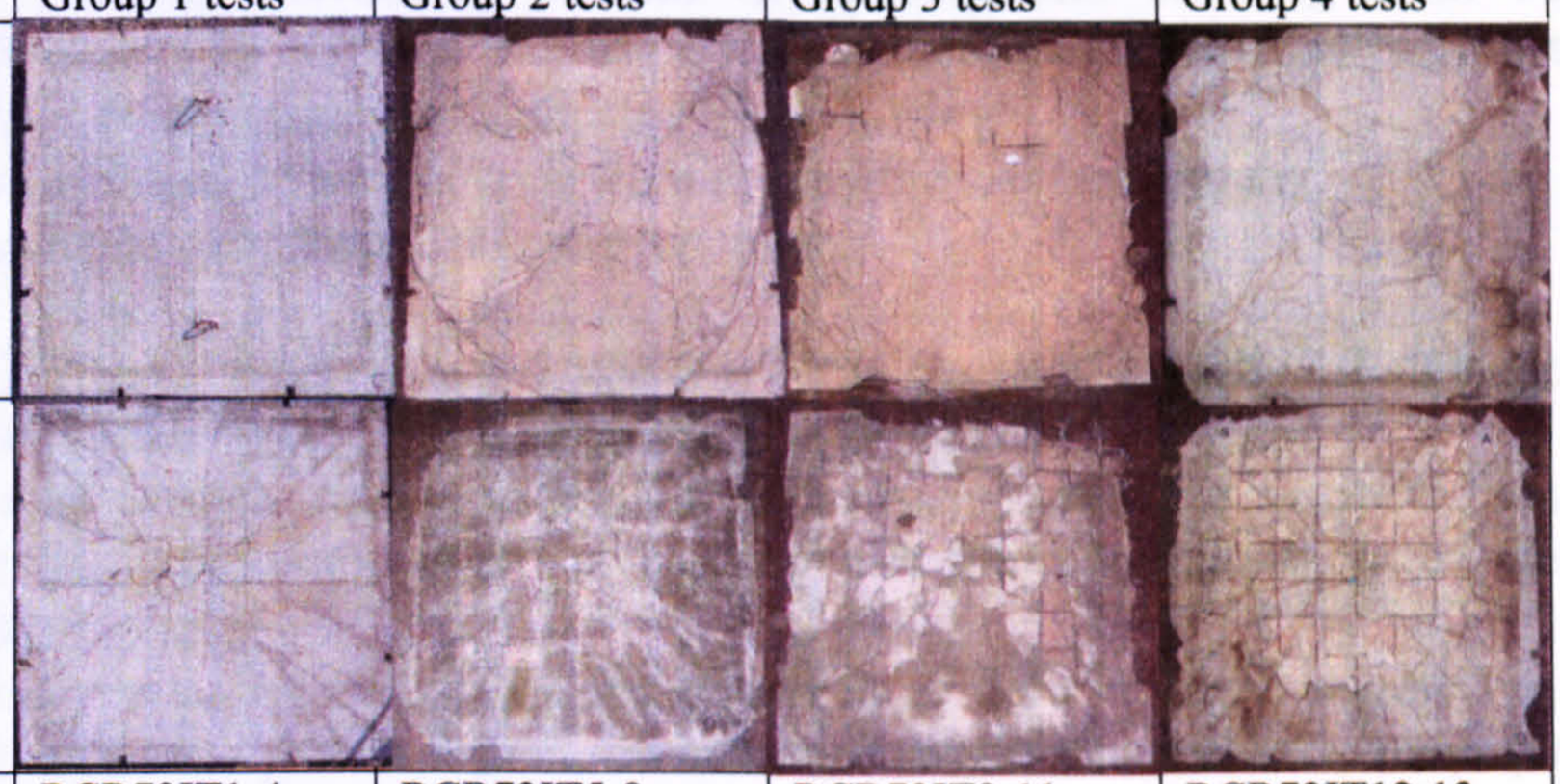			
Bottom face				
Slab	RCR73IT1-4	RCR73IT5-8	RCR73IT9-11	RCR73IT12-13
Cumulative hits	4	4	3	2
Charge standoffs (mm)	540,440,350,300	340,240,150,100	190,90,0	113,13

4.5.1 Analysis of damage to the top face of the primary slabs

Slab RCR73IT1-4 from group 1 received the smallest magnitude of damage compared to that received from the other slabs. A visual inspection indicated the following:

1. Cracks were narrow and small in quantity.
2. Cracking was only apparent around the perimeter of the slab forming non-continuous corner cracks.

Slab RCR73IT5-8 from group 2 contained a greater severity to than slab RCR73IT1-4. A visual inspection indicated the following:

1. Corner cracks were longer and thicker.
2. Spalling was evident within the corner regions.
3. Second mode of damage appeared to be diagonal cracks normal to the corner cracks, propagating in towards the centre of the slab. These cracks segregated the slab into quadrants.
4. The central region of the slab contained a discontinuous square crack with its four corners extending into the diagonal cracks.

The central cracked region appeared to indicate the start of a breach pattern emerging. The pattern of cracking appeared to be symmetrical, but the faintly visible cross, drawn in ink at the centre of the slab, corresponded to the centrally positioned DPG1, did not correspond with the centre of the geometry of the square breach pattern. This was the only indication that demonstrates that the loading was not uniform, implying that the difference of 20°between a vertically positioned charge and a 70° inclined charge appeared to alter the geometry of damage by off-setting what could have been a symmetrical pattern, into a non-symmetrical pattern relative to the centre of the slab. It is unfortunate that slab RCR73IT9-11 from group 3 did not illustrate a clear representation of damage, due to the reduction in the concrete cover which has been significantly reduced, preventing patterns of spalling and cracking from being identified. However, the damage that has been produced is greater than that on slab RCR73IT5-8. A visual inspection indicated the following:

1. Severe removal of the concrete from around the slab's perimeter.
2. Exposure of reinforcement in the top mesh.

Slab RCR73IT12-13 from group 4 contained the greatest severity of damage in comparison to all the slabs. A visual inspection indicated the following:

1. Diagonal corner cracks progressed into spalls, with the greatest damage occurring along plane O-B1, coinciding with the plane in which the charge was positioned.
2. Central region geometrically changed from a definite small square region, expanding to a greater region, containing many circular cracks, propagating from around the centre of the slab out towards the perimeter.
3. Continuous and discontinuous circumferential cracks dominated the slabs surface.

The visual inspection of the primary slabs enabled all the major planes of damage, known as yield lines, to be identified. The yield lines have been drawn on the top faces of the primary slabs, illustrated in table 4.5.2. The greater the numbers of different yield line patterns the greater the severity of damage to the slab. The damage caused by small charge standoffs were associated with a concentrated spatial distribution of load around the centre of the slab.

The primary slab associated with cumulative hits from group 3 was not present in table 4.5.2 as the damage had significantly removed the concrete cover on the top face, preventing the yield lines from being observed.

At small charge standoffs the spatial distribution of loading was concentrated over the central region of the slab, preventing the entire slab from responding globally. This caused local flexural action of the slab, forming circumferential cracks and severe

crushing. The geometry of yield lines on each of the slabs in table 4.5.2 indicated a progressive sequence of cumulative damage mechanisms.

Table 4.5.2 Simplistic crack patterns inflicted upon the primary slabs in Stage I.

	Group 1 tests	Group 2 tests	Group 4 tests
Top face	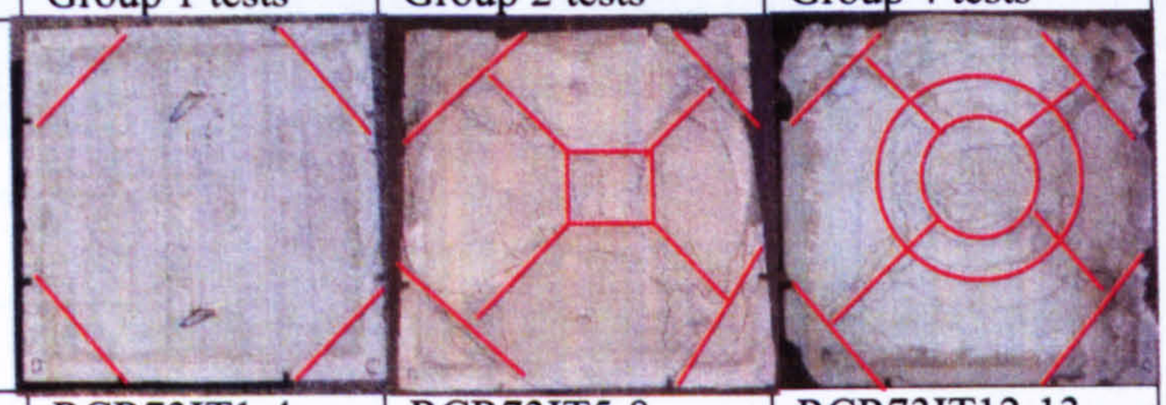		
Slab	RCR73IT1-4	RCR73IT5-8	RCR73IT12-13
Chronological order of the damage modes	1.Corner cracks	1.Corner cracks & spalling. 2.Diagonal cracks 3.Central square cracking	1.Corner cracks and spalling. 2.Diagonal cracks and spalling. 3.Central circumferential cracking 4.discontinuous circumferential cracking within the four quadrants
Cumulative hits	4	4	2
Charge standoffs (mm)	540,440,350,300	340,240,150,100	113,13

4.5.2 Analysis of damage to the bottom face of the primary slabs

The geometry of damage to the bottom face of each of the primary slabs appeared to remain consistent with radial cracks penetrating from the centre of the slab to the perimeter as, illustrated in table 4.5.3.

Crack depth and width varied in each of the primary slabs. The main feature that differentiated all four slabs in terms of damage severity was scabbing. This was defined by the area of concrete cover removed from within each of the individual 100x100mm small square grids contained within the entire square bottom mesh.

There was a significant increase in scabbing to slabs RCR73IT5-8, RCR73IT9-11, RCR73IT12-13 compared to that inflicted upon slab RCR73IT1-4. This could have been due to the distribution of loading concentrated centrally rather than globally.

It was possible to give an approximate quantitative account of the degree of scabbing to the bottom faces of the primary slabs. However, the degree of scabbing achieved after the cumulative hits on each of the slabs would have been calculated as a percentage of surface area of concrete removed from the bottom face and would be very approximate.

Extended time on the research project could have led to a procedure for significantly quantifying the degree of scabbing to the bottom faces of the primary slabs. This gives scope for future work.

Table 4.5.3 Cumulative damage inflicted upon the primary slabs in Stage I.

Bottom face	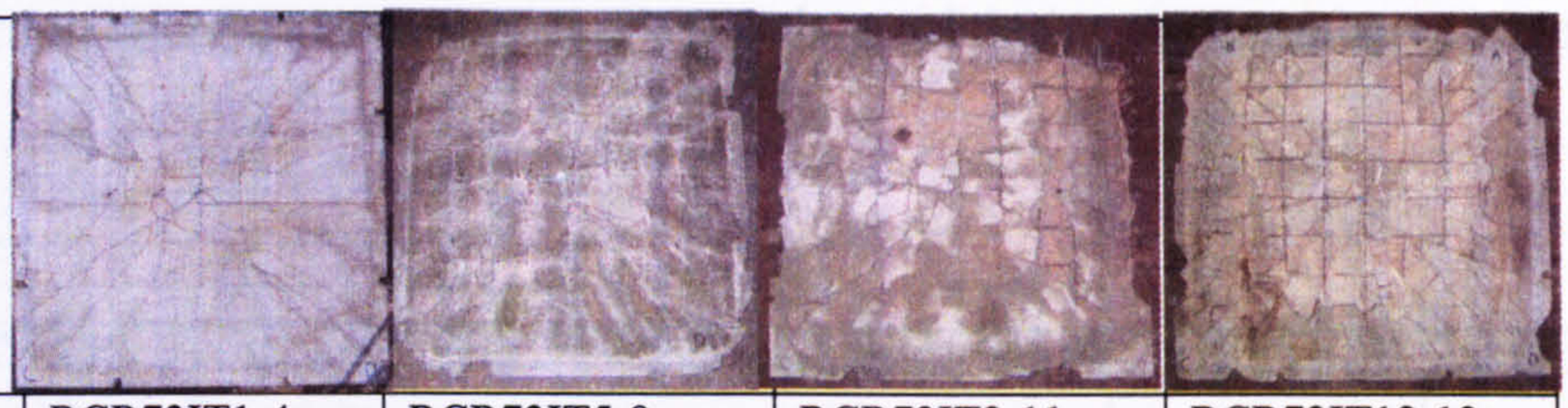			
Slab	RCR73IT1-4	RCR73IT5-8	RCR73IT9-11	RCR73IT12-13
Cumulative hits	4	4	3	2
Charge standoffs (mm)	540,440,350,300	340,240,150,100	190,90,0	113,13

The damage to the top and bottom faces of the slabs have been classified and illustrated in table 4.5.4. The procedure adopted was not universal to damaged concrete slabs. However, the idea was taken from the work performed by **Duranovic (1994)**.

Table 4.5.4 Four modes of damage classification associated protected primary slabs when secondary slabs were positioned.

Group	Damage mode	Top face	Bottom face	Reduction in soil overburden above the primary slab	Cumulative hits
1	I	Negligible cracks	Minor hair line cracks	0%	4
2	II	Central punching action, craters along the diagonals, corner cracks, residual sagging of the slab	Wide radial cracks	40%	4
3	III	Reduced concrete cover, residual sagging of the slab	Reduced concrete cover and disintegrated slab perimeter	70%	3
4	IV	Significant bending of the central region, dictated by circumferential cracks, cratering along the diagonals	Significantly reduced concrete cover	85%	2

4.5.3 Cumulative weakening of primary slabs and the affect of omitting secondary slabs from within the soil environment

Stage III of the test matrix consisted of three tests, performed on primary slab RCR73IT17-19 with secondary slabs omitted. The damage to the slab was compared to the damage encountered by primary slab RCR73IT9-11, associated with positioned secondary slabs.

A comparison of the two different test set-ups is illustrated in figure 4.5.1. Each charge position represented a single hit on the primary slab, with or without the use of

a secondary slab. The three secondary slabs in the left drawing of figure 4.5.1 illustrate the total number of fresh secondary slabs used during the cumulative attack.

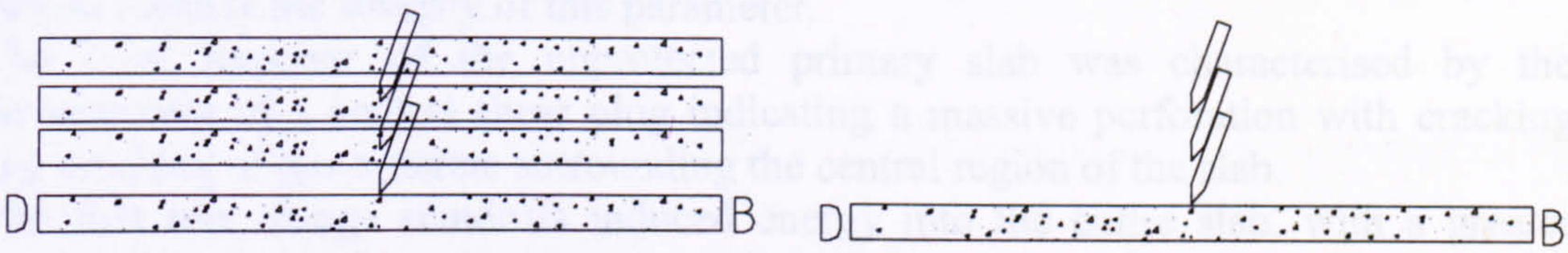

Secondary slabs positioned

Secondary slabs omitted

Figure 4.5.1 Positioning the cylindrical charges at three fixed standoffs relative to a primary slab when secondary slabs are positioned and omitted

The objective was to consider the effectiveness a secondary slab had in reducing the damage to the primary slab as well as the cumulative loading affect associated with primary slab weakening.

By omitting a secondary slab from within the soil overburden and detonating a statically positioned inclined cylindrical charge of mass 183g at a standoff of 190mm, the central deflection of the primary slab increased by 60%. The second cumulative hit increased the peak deflection by a further 5%, implying that the first hit significantly weakened the slab, enabling the initial downwards velocity of the primary slab upon impact to increase as the charge's standoff decreased.

The first two hits at standoffs 190mm and 90mm caused the unprotected primary slab to endure minor cracking to the top and bottom faces. The third cumulative hit involved a contact charge, which caused a massive perforation as illustrated in table 4.5.5.

It was unexpected, as the damage caused by previous hits did not indicate such potential damage.

Table 4.5.5 Damage comparison to two primary slabs subjected to cumulative loading with secondary slabs omitted and positioned within the soil overburden.

	Secondary slabs omitted	Secondary slabs positioned
Top face	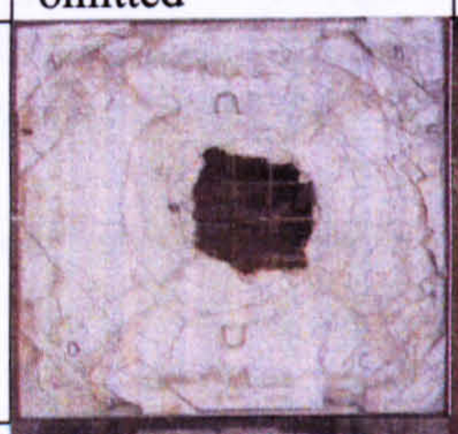	
Bottom face		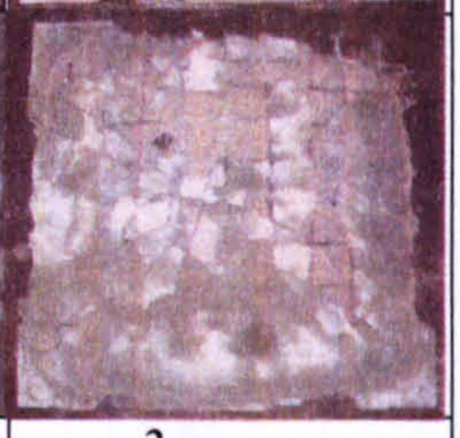
Hits	3	3

It is reasonable to assume that the third cumulative hit, a contact charge, would have induced similar magnitudes of loading into both the primary slabs. The first and second cumulative hits would have caused weakening to both the primary slabs, with a greater degree inflicted upon the unprotected primary slab.

Slab weakening was, and is, difficult to quantify from visual inspection, without cross-sectioning the slabs. Non-destructive procedures such pundit tests would have helped identify the severity of this parameter.
The local response of the unprotected primary slab was characterised by the development of a central shear plug indicating a massive perforation with cracking and crushing of the concrete surrounding the central region of the slab.
The first two charge standoffs induced energy into the entire slab, with a greater degree of cracking concentrated centrally. The third hit caused a central distribution of load, which initiated the formation of a shear plug, trapping a proportion of the energy within the plug and causing it to fly out with a velocity.

4.5.4 Magnitude of damage associated with groundshock loading

It is evident from the top and bottom faces of the primary slabs that the cumulative damage inflicted upon the slabs from groups 1-4, in chronological order, increased.
It has been proven using ratios of t_d/T and the energy balance procedure that primary slab RCR73IT1-4 responded impulsively to groundshock loading. It was not analytically proven that the other primary slabs within Stage I responded impulsively, as incomplete data prevented an analysis from being performed. These slabs RCR73IT5-8 – RCR73IT12-13 all suffered significantly greater damage as illustrated in table 4.5.1, which also affected the response of the instrumentation. However, due to a greater accuracy in measuring impulse as discussed in section 2.3.3, the severity of damage to all the primary slabs was also associated with a cumulative impulse recorded by DPG1. DPG1 was positioned at eccentricities from the centre of primary slabs RCR73IT5-8, RCR73IT9-11 and RCR73IT12-13 as illustrated in table 4.5.6 to reduce the chance of damage to the gauge. The increase in damage to the primary slabs was due to an increase in cumulative impulse history, sustained during cumulative loading, by reducing the charge standoffs. The results from table 4.5.1 and table 4.5.6 indicate that the charge standoff parameter, rather than the number of cumulative hits, determined the severity of damage to a primary slab. An increase in impulse and slab damage has been associated with a decrease in both the number of cumulative hits and charge standoff values. The impulse per hit was greater; therefore the cumulative impulse history was also significantly greater.

Table 4.5.6 Test parameters

Tests	Soil overburden above the primary slab and below the secondary slab (mm)	Maximum Impulse (kPa-s)	Charge standoff (mm)	Eccentricity of DPG1 from the centre (mm)	Charge position
RCIT1	500	1.35	540	0	A
RCIT2	500	7.32	440	0	B
RCIT3	500	7.4	350	0	C
RCIT4	500	9.77	300	0	D
RCIT5	300	2.63	340	0	A
RCIT6	300	8.41	240	0	B
RCIT7	300	10.3	150	0	C
RCIT8	300	15.5	100	0	D
RCIT9	150	7.65	190	0	A
RCIT10	150	11.34	90	150	B
RCIT11	150	26.5	0	150	C
RCIT12	75	8.18	113	150	A
RCIT13	75	11.23	13	200	B

4.6 Variability of the material parameters and soil compaction

4.6.1 Concrete strengths

All the concrete slabs used during testing were of identical geometry, containing the same percentage and layout of reinforcement and cast from the same mix design. During a single casting operation, six concrete slabs were cast. Each slab mould was filled with concrete from a single batch. Excess concrete from the batch was used to fill a number of cylinders and cube moulds. The concrete cylinders and cubes were subjected to indirect tensile and compression testing, indicating the static tensile and compressive strengths of the slab on the day of an explosive test. The results from the static testing are illustrated in table 4.6.1.

Table 4.6.1 Static compressive and tensile strengths of cubes and cylinders associated with the strength of an associated slab on the day of an explosive test.

Primary slabs	Average compressive strengths (N/mm^2)	Average tensile strengths (N/mm^2)	Secondary slabs	Average compressive strengths (N/mm^2)	Average tensile strengths (N/mm^2)
RCR73IT1-4	44	5.5	RCB73IT1	44	5.2
			RCB73IT2	42	4.8
			RCB73IT3	43	4.8
			RCB73IT4	42	5.4
RCR73IT5-8	43	5.6	RCB73IT5	41	5.2
			RCB73IT6	45	4.8
			RCB73IT7	43	5.6
			RCB73IT8	44	5.6
RCR73IT9-11	45	5.4	RCB73IT9	44	5.4
			RCB73IT10	41	5.4
			RCB73IT11	42	5.5
RCR73IT12-13	40	5.2	RCB73IT12	40	5.3
			RCB73IT13	40	5.3
RCR73IT14-16	43	5.7	RCB73IT14	38	5.1
			RCB73IT15	43	5.2
			RCB73IT16	43	4.9
RCR73IT17-19	42	6.3	RCB73IT17	44	4.9
			RCB73IT18	44	5.2
			RCB73IT19	43	5.4

Statistical interpretation of the primary slab data shows that:

1. The difference between the maximum and minimum compressive and tensile strengths for all four slabs was $5N/mm^2$ and $1.12N/mm^2$ respectively.
2. Mean compressive and tensile strengths were $43N/mm^2$ and $5.6N/mm^2$ respectively.
3. The ratio of compressive to tensile strength was approximately 8.0.

Statistical interpretation of the secondary slab data

1. The difference between the maximum and minimum compressive and tensile strengths for all the slabs was $5N/mm^2$ and $0.5N/mm^2$ respectively.
2. Mean compressive and tensile strengths were $44N/mm^2$ and $5.2N/mm^2$ respectively.
3. The ratio of compressive to tensile strength was approximately 8.0.

The compressive and tensile material strengths of the cubes and cylinders represent strengths associated with relatively slow loading rates. The effect on strength of rapid loading rates applied to the slabs as a result of stress wave propagation was beyond the scope of the research and not investigated. Values of standard deviation and coefficients of variation are illustrated in table 4.6.2.

Table 4.6.2 Statistical data relating to the concrete strengths

	Primary slab data		Secondary slab data	
Parameters	Compressive strength data	Tensile strength data	Compressive strength data	Tensile strength data
Mean	42.8N/mm^2	5.6N/mm^2	42N/mm^2	5.2N/mm^2
Standard deviation	1.72	0.38	1.8	0.26
Coefficient of variation	4%	6%	4%	5%
Percentage of data within 1 Standard deviation	67%	67%	79%	58%
Percentage of data within 2 Standard deviation	100%	100%	95%	100%
Percentage of data within 3 Standard deviation	100%	100%	100%	100%

Kong & Evans (1987) stated that '*the poorer the quality control, the higher the standard deviation*'. The quality of control of concrete samples has been related to the standard deviation, as illustrated in table 4.6.3.

Table 4.6.3 Standard deviation values under different conditions (Kong & Evans, 1987).

Conditions	Standard deviation (N/mm^2)
Good control with weight batching, use of graded aggregates, etc. Constant supervision	4-5
Fair control with weight batching. Use of two sizes of aggregates. Occasional supervision.	5-7
Poor control. Inaccurate volume batching of all-in aggregates. No supervision.	7-8 and above

The standard deviation values from table 4.6.2 are all <1.8N/mm^2. In context with table 4.6.3 this suggests that the data illustrated in table 4.6.1 was within conditions of 'Good control' according to **Kong & Evans (1987). ACI 318-95 (1996)** contains a similar representation for quality of control of concrete samples, as previously described by **Kong & Evans (1987).** The standard deviation has been associated with the 'standard of control' illustrated in table 4.6.4 taken from **ACI 318-95 (1996).** The values in table 4.6.4 appear to be valid for concrete samples up to 45MPa. The results from table 4.6.2 have been associated with a standard of control that relate to the range of values within 'Laboratory trial mixes' illustrated in table 4.6.4.

Table 4.6.4 Classification of standard of control for concretes with strengths up to 45MPa (ACI 214-277, 1996)

Standard of control	Overall standard deviation	
	In the field	Laboratory trial mixes
Excellent	<3	<1.5
Very good	3-3.5	1.5
Good	3.4-4	1.5-2
Fair	4-5	2-2.5
Poor	>5	>2.5

According to table 4.6.4 the compressive strengths of the primary and secondary slabs on the day of an explosive test are associated with a standard of control as 'Good', and 'Excellent' for the tensile strengths.

4.6.2 Soil compaction and moisture contents

The sieve analysis for the gravely sand (1271RL/Concrete sand Grade MR Lees) illustrated in figure 4.6.1 indicated that 95% of the aggregate tested contained a maximum particle size of 5mm.

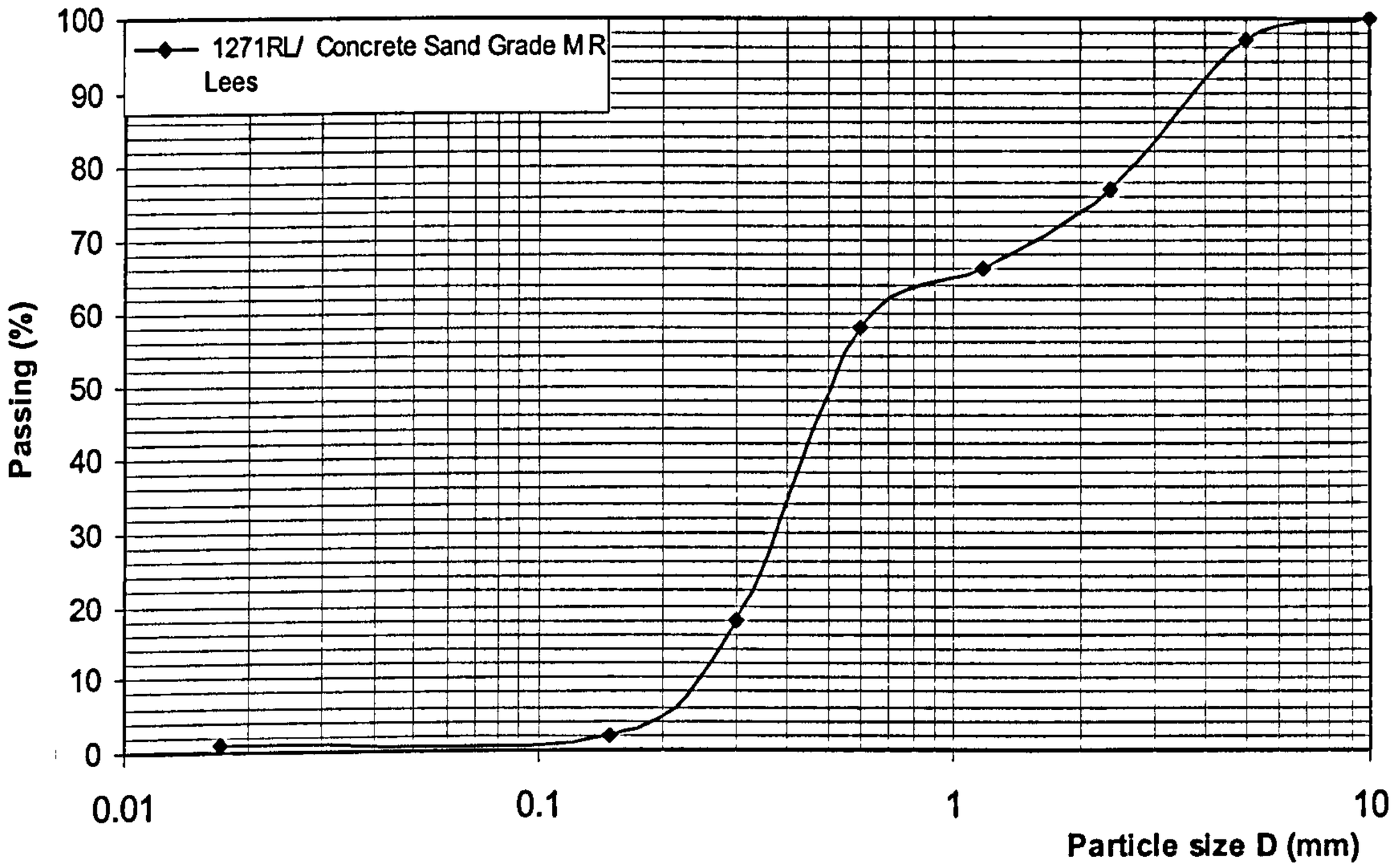

Figure 4.6.1 Sieve analysis of the sand

The internal space of the test cell was manually filled in layers of soil using a shovel. Each layer was compacted in turn, by flattening the soil surface with the flat face of the shovel until there were enough soil layers for a specific soil overburden depth within the test cell. Although this method was not to any recognised standard, acceptably consistent soil compaction was achieved as explained below and in section 4.6.2.1.Static soil compaction tests were performed using identical soil to that filling the test cell. Soil samples were tested in a saturated and a dry state to determine the maximum and minimum soil bulk densities, according to the procedures documented

in **BS1377 Part 4:4.3 (1990)** for gravels, taken from **Head (1992).** The purpose was to compare soil bulk density values in a wet and dry state, defined as maximum and minimum, illustrated in table 4.6.5 with soil bulk densities taken from the soil overburden, illustrated in table 4.6.6. The variation in the density index values as illustrated in table 4.6.6 indicate the degree of manual soil compaction. In establishing the maximum wet bulk density, the soil was fully saturated in deionised water and manually scooped into the steel container in three stages, with each stage being compacted using the vibro-hammer. During the compacting stage, water seeped out from around the circumference of the container that was attached to a steel base plate, as well as spilling over the top. This would have decreased the saturation of the soil, but the very nature of compaction involves reducing the volume of voids. In establishing the minimum dry bulk density, soil was initially oven dried for 24 hours, then in three stages, poured into the cylindrical container attached to a base plate from a height of 500mm, compacting under its own self-weight. In total, 12 tests were performed, 3 tests associated with each of the 4 bulk density parameters illustrated in table 4.6.5.

Table 4.6.5 Maximum and minimum soil bulk densities

State of soil	Minimum bulk density (kg/m^3)	Maximum bulk density (kg/m^3)
Wet	1517	1602
Dry	1357	1528

Prior to each explosive test, four soil samples were taken from the manually compacted soil overburden within the test cell to establish average moisture contents. Soil samples were taken using cylindrical steel containers of a known internal volume at varying soil depths. The moisture content of the soil samples was achieved using the procedures outlined in **BS 1377-9 (1990)** Test 1(A). The samples were initially wet weighed then oven dried. The oven's thermostat was set to a constant temperature of 108° C, which was checked regularly and within the specified range of 105-110° C. The samples were positioned on the top shelf, enabling the air to circulate around the containers preventing overheating of the soil, as specified by the code. The code specified that drying should continue until the samples had reached a constant mass. The samples remained in the oven for a duration of 24 hours, in which time the moisture had completed evaporated. This was determined by a negligible change in mass, checked at two 2 hour intervals after 24 hours. The samples were removed and left to cool in a cabinet for two reasons:

1. Warm air currents can lead to inaccuracies with a sensitive balance.
2. In an open environment dry soil can absorb moisture from the atmosphere, which would influence the dry mass reading.

The moisture content was calculated using equation (4.6.1).

$$w = \frac{m_{cw} - m_{cd}}{m_{cd} - m_c} x100\%$$

Equation (4.6.1)

m_{cw} = mass of container and wet soil
m_{cd} = mass of container and dry soil
m_c = mass of container
w =soil moisture content

The range of average soil moisture contents from the soil overburden from each of the explosive tests are illustrated in table 4.6.6.
It was also of interest to calculate the density index of the soil prior to each charge detonation, to evaluate the consistency of soil compaction. The density index expresses the degree of compactness of a cohesionless soil with respect to the loosest and densest conditions of it. A soil in the loosest state would have a relative density of 0% whilst in the densest state 100%. The dry unit weight of a soil does not, by itself, reveal whether the soil is loose or dense, due to the influence of particle shape and gradation on this property. Only when viewed against the possible range of variation, in terms of relative density, can the unit weight be related to the compaction effort used to place the soil within the internal space of the test cell. The density index is defined by equation (4.6.2).

$$I_D = \frac{\rho_D - \rho_{D,\min}}{\rho_{D,\max} - \rho_{D,\min}} \frac{\rho_{D,\max}}{\rho_D}$$

Equation (4.6.2)

I_D = Density index.

ρ_D = Density of the insitu soil sample taken from soil overburden within the test cell.

$\rho_{D,\min}$ = Minimum dry density taken from the compaction tests.

$\rho_{D,\max}$ = Maximum dry density taken from the compaction tests.

The results from table 4.6.6 include the variation in the density index and moisture content from tests RCIT1-RCIT19.

Table 4.6.6 Wet and dry bulk densities with a degree of saturation

Test	Wet bulk density (kg/m^3)	Dry bulk density (kg/m^3)	Moisture content (%)	Density index (%)
1	1611	1525	5	98
2	1626	1513	7	92
3	1606	1510	6	91
4	1625	1518	7	94
5	1615	1520	6	96
6	1611	1507	6	89
7	1606	1522	5	97
8	1604	1526	5	99
9	1615	1522	6	97
10	1602	1508	6	89
11	1626	1514	7	92
12	1583	1520	4	95
13	1645	1512	8	91
14	1634	1526	7	98
15	1570	1515	4	93
16	1550	1503	3	87
17	1535	1500	2	85
18	1564	1507	4	89
19	1572	1511	4	91

Head (1992) related the degree of soil compaction to the state of the soil type as illustrated in table 4.6.7.
The density index results from table 4.6.6 indicated that the soil prior to compaction was within the 'very dense' range. This suggested that any mechanical means of

compaction would not have made a significant difference to the soil bulk density, thus justifying the manual procedure that was implemented.
The density index values calculated from all the tests illustrated in table 4.6.6 indicated that the soil was compacted to 'very dense' in every test, according to table 4.6.7. This suggested broad confidence in the consistency of the placement methods used for the insitu tests.

Table 4.6.7 Density index range associated with soil description (Head, 1992)

Description	Density index range (%)
Very loose	0-15
Loose	15-35
Medium	35-65
Dense	65-85
Very dense	85-100

In justifying the variability of data in table 4.6.6, statistical parameters were calculated as given in table 4.6.8. The results from tables 4.6.6 and 4.6.8 were then put into context with the literature.

Table 4.6.8 Variation in the standard deviation of the soil data

Parameters	Wet bulk density data	Dry bulk density data	Moisture content data
Mean	1600kg/m^3	1515kg/m^3	5.4%
Standard deviation	29.8 kg/m^3	7.8 kg/m^3	1.6%
Coefficient of variation	1.9%	0.5%	29.3%
Percentage of data within 1 Standard deviation	68%	74%	63%
Percentage of data within 2 Standard deviations	100%	100%	95%
Percentage of data within 3 Standard deviations	100%	100%	100%

The wet and dry bulk densities were highly consistent with very low coefficient of variations. The moisture content variability requires more explanation.
Famiglietti *et al* (1999) attempted to characterise the variability in moisture content of natural insitu sandy soil. From the vast amount of measurements taken, it was established that the coefficient of variation for the moisture content lay within the range 20–35%.
Plassmeyer & Nkongolo (2000) performed a statistical analysis on the water content, soil bulk density and air content parameters recorded during experimental work on prepared test specimens of soil. The authors stated that '*the water content showed the highest variability with a coefficient of variation of 42.9%*'. The coefficient of variation for the moisture contents calculated from tests outlined within this thesis also showed the highest variability as illustrated in table 4.6.8. This suggested that the parameter has a greater variability than the bulk density, and indicates that a high moisture content variability is not inconsistent with a low variability of other parameters. **Famiglietti *et al* (1999)** and **Plassmeyer & Nkongolo (2000)** mentioned that the coefficient of variation for the soil bulk densities varied between 1.5-5% indicating a similarity with those presented in table 4.6.8. Their data lay on a normal distribution curve. A normal distribution is associated with 68.26% of the data within one standard deviation, 95.44% within two standard deviations and 99.74% within three standard deviations, as indicated by **Kong & Evans (1987).** The distribution for moisture content given in table 4.6.8 is very close to this, suggesting a normal

distribution. The standard deviation data associated with the wet and dry bulk densities from table 4.6.8 also suggested a normal distribution.
Kirda & Reichardt (1985) investigated field spatial variability of soil moisture contents. The coefficient of variation of the measurements ranged from 6.8-14.9%, indicating '*rather high variability in soil moisture content*'. **Hyde (1991)** stated that '*soil water content can have a profound influence on groundshock propagation in cohesive soil, particularly if the moisture content is 25% or greater*'. Although the moisture contents in table 4.6.6 were taken from a granular rather than cohesive soil, **Hyde (1991)** equated a '*loose, dry sand and gravel with low relative density*' to a density approximately 1500kg/m^3. All of the wet densities illustrated in table 4.6.6 were greater than 1500kg/m^3, suggesting that the soil could be classified as '*sandy loam, loess, dry sand and backfill*' with an associated density of 1630 kg/m^3. None of the values from table 4.6.6 exceeded a wet bulk density of 1630kg/m^3.
Hyde (1991) stated that '*effects of water in sands with low relative densities can produce effects similar to those seen in cohesive soils*'. **Hyde (1991)** and **Wang & Lu (2004)** mentioned that the soil moisture contents would effect stress wave propagation in relatively wet soils. They did not comment on any effect caused to stress wave propagation at values <10%.
It has been concluded that the variation in data illustrated in table 4.6.8 is comparable to that found in the literature. However, no specific comments have been made that relate a change in stress wave propagation to moisture contents <10%. Further investigations characterising the ability of soil with variable moisture content to transmit groundshock is required. However this was beyond the scope of the research performed. Such data could then be used to update the semi-empirical code CONWEP as discussed in the literature.

4.6.2.1 Overriding effect transient stress wave propagation has on initial soil compaction

When a charge is detonated in soil, the explosive gas products exert an incredibly instantaneous high pressure on the surrounding soil that expands, causing a stress wave to propagate. The stress wave advances via grain to grain contact in the soil environment causing the soil particles to move with a velocity less than the velocity of the stress wave, known as the loading wave velocity.
The compressive stress wave compresses the soil particles above the insitu level of compaction, achieved prior to detonation. It decreases the volume of air retained and increases the bulk density of the surrounding soil.
Experimental data has been used to prove that the initial compacted state of the soil did not affect the propagation of the stress wave.
The first piece of experimental evidence involved calculations of the loading wave velocity. These were made based upon wave path lengths as illustrated in figure 4.6.2. The wave path was defined as the distance from the centre of mass of the charge to the centre on the top face of each of the DPGs positioned along plane O-B1 on the top face of the primary slab.

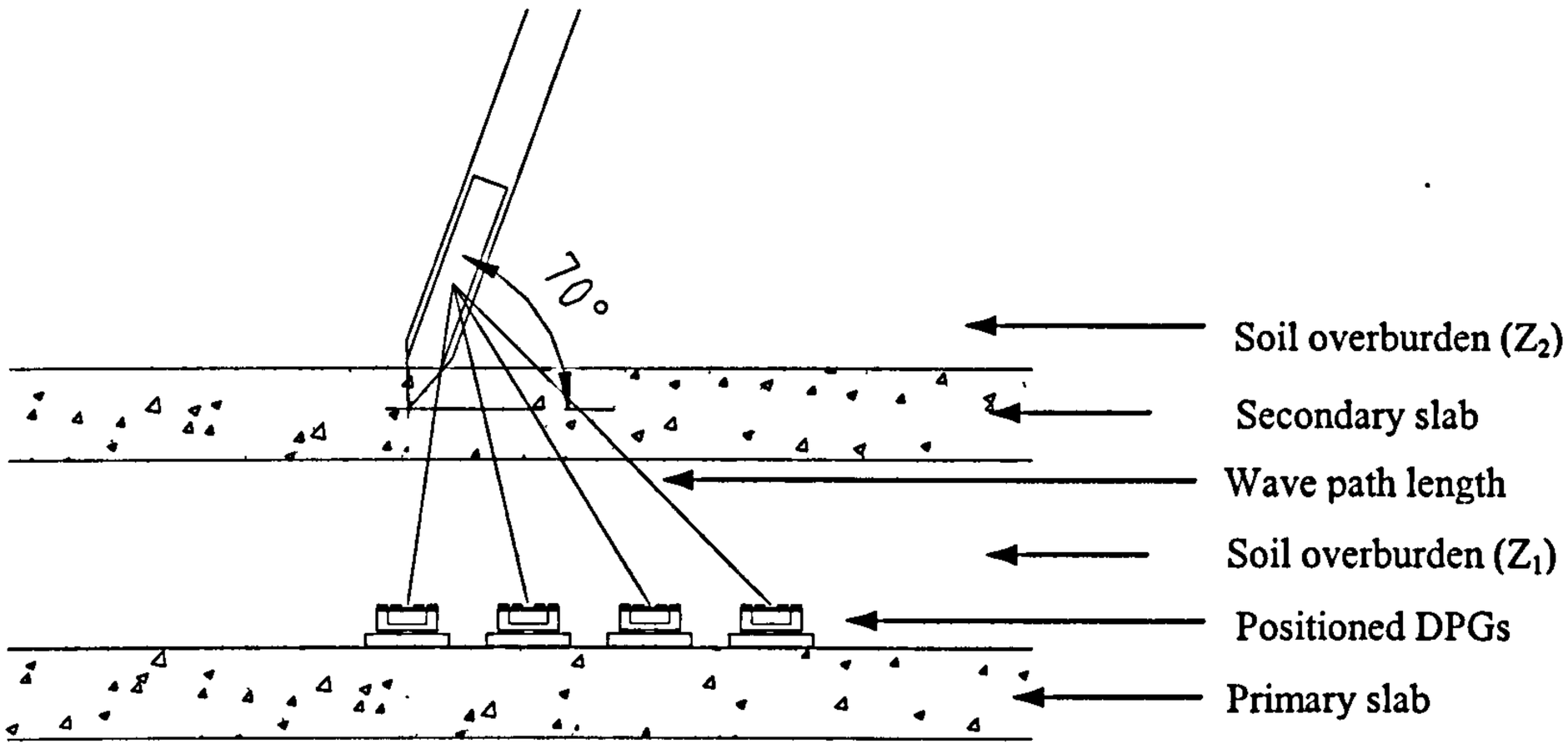

Figure 4.6.2 Position of the charge relative to the secondary slab indicating the variable wave path lengths

The attenuation of the loading wave velocity and the effect it had on the soil was investigated using data from tests RCIT9 and RCIT17. Both tests were geometrically identical, apart from the fact that a secondary slab was omitted from test RCIT17, causing a greater amount of energy to be induced into the soil overburden. This suggested that the loading wave velocity was larger in the case of an omitted secondary slab. Velocities were calculated from the wave path lengths from figure 4.6.2 and the time taken for the wave to travel from the source to the DPGs.
Trend lines were assigned to the data in figure 4.6.3, illustrating both plots converging together at approximately 140m/s, indicating the seismic velocity for the soil.

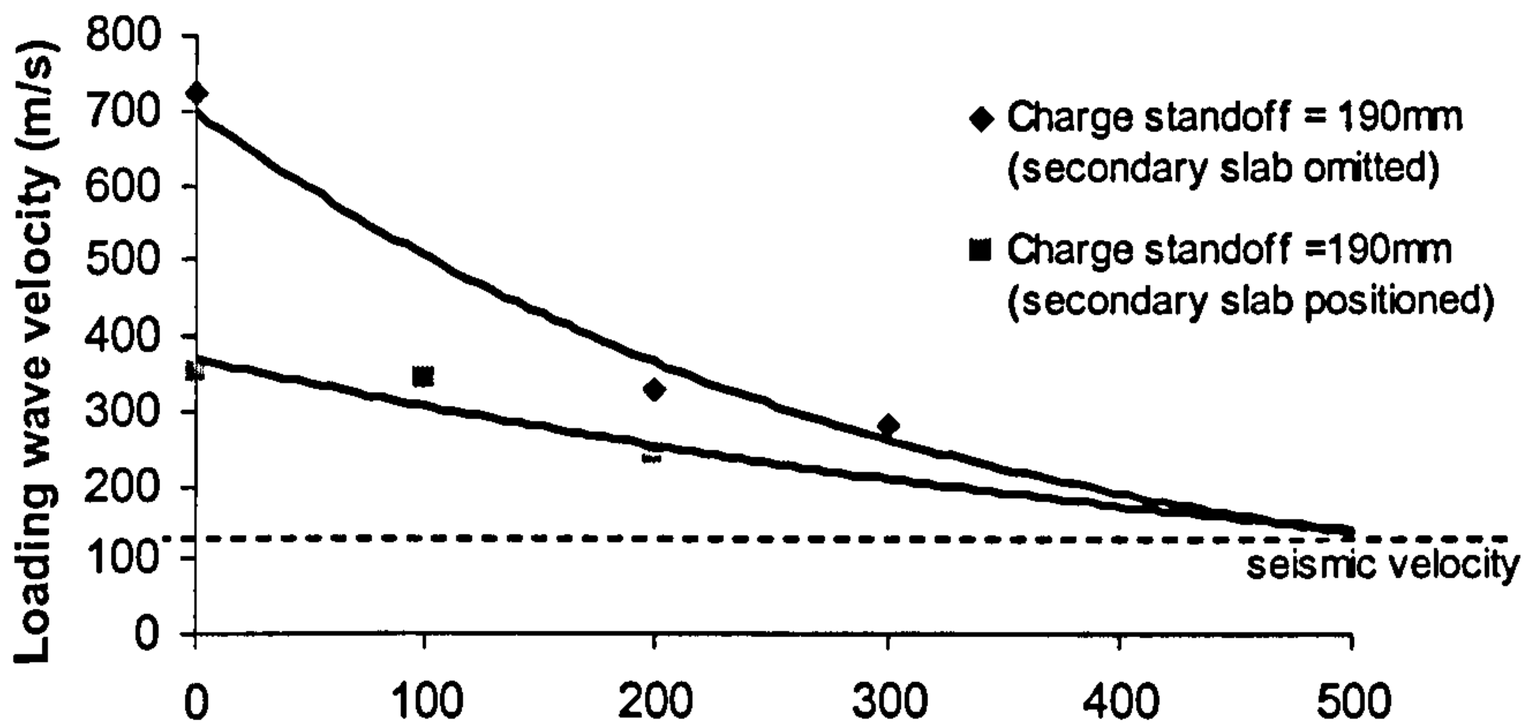

Figure 4.6.3 Exponential decay trends of the loading wave velocity when secondary slabs are omitted and positioned

Stress wave attenuation has been discussed by **Smith & Hetherington (1994)** commenting on the decaying loading wave velocity with range away from the source, equilibrating with what is known as the seismic velocity. The results from figure 4.6.3 indicated three important findings:

1. Loading wave velocity decayed into the seismic velocity in the far field environment.
2. The greater the energy initially induced into the soil overburden below the charge, the greater the loading wave velocities and increased compaction of the soil.
3. Omitting the secondary slab allowed more energy to be induced into the soil, increasing the loading wave velocities, which increase the degree of compaction above an insitu value.

The findings from figure 4.6.3 have been put into context with those by **Zhongqi & Yong (2003)** in figure 4.6.4. An increase in the peak void ratio with scaled distance indicates that stress wave propagation is causing soil compaction. However, at a scaled distance of $1 mkg^{-1/3}$, the change in the rate of peak void ratio decreases, implying that the stress wave has significantly attenuated. The levelling of the peak void ratio at 0.73 indicates that the loading wave velocity is equilibrating with the seismic velocity.

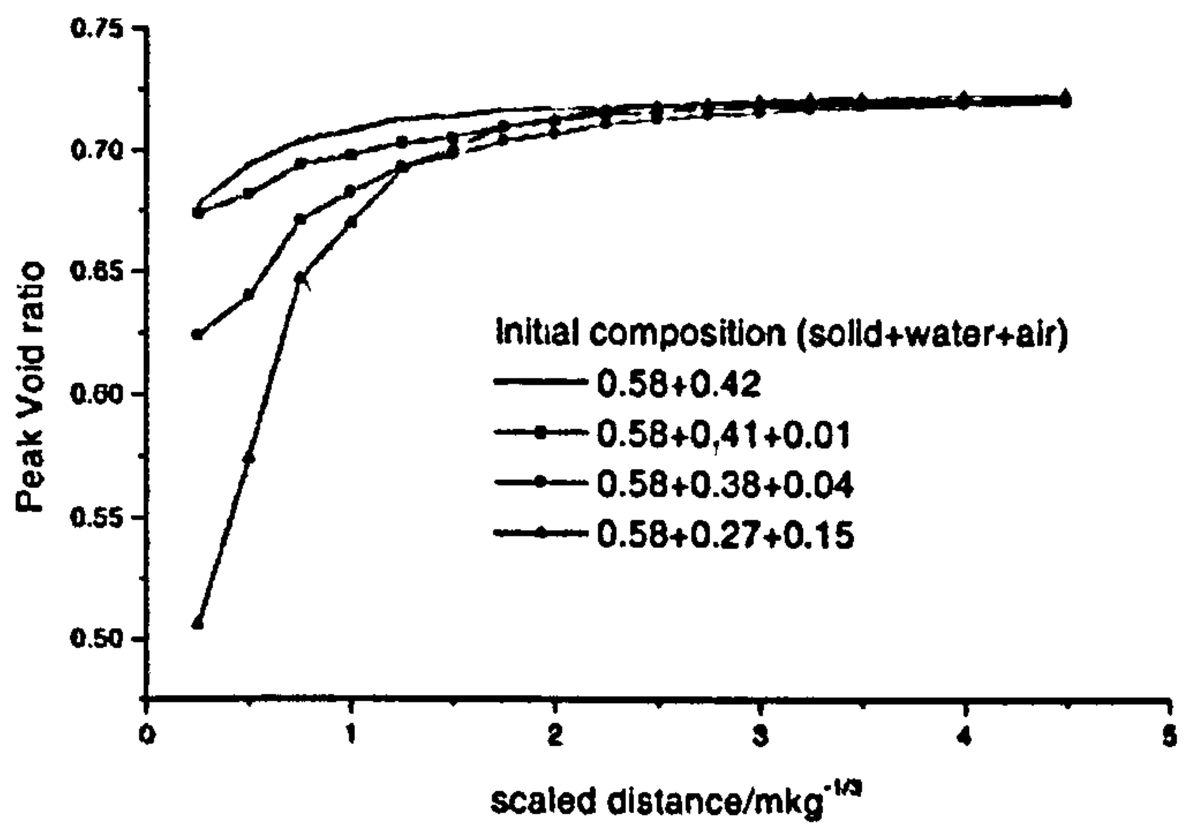

Peak Void ratio corresponding to peak pressure at different locations

Figure 4.6.4 Change in characteristic soil properties as a function of scaled range under blast loading (Zhongqi & Yong, 2003)

The semi-empirical program CONWEP, based upon a huge collection of experimental data, only contains values of seismic velocity from a library source and does not take into account the depreciation of the loading wave velocity, as illustrated in figure 4.6.3. This underestimates the magnitude of pressures within the near field environment, as the loading wave parameter would be associated with the value of seismic velocity and expressed in the following equation of stress with a smaller magnitude.

$$\sigma = \rho C u$$

Equation (4.6.3)

σ = Free field stress
ρ = Bulk density of the soil
C= Loading wave velocity
u= Particle velocity

CONWEP does not take into account compaction. It contains a range of soil densities in its materials library associated with different soils, but not a range of densities for a particular soil associated with variable stresses. The change in soil bulk density with stress has instead been investigated by **Pullen & Newman (1995),** which addresses soil compaction. Materials such as soil that are subjected to varying stress within a gauged reactive confinement cell, (GREAC cell), yield information in the form of an equation of state curve, which illustrates a stress-density relationship. They describe the response of the material to changes in density and induced stress during loading and un-loading. These relationships are implemented into the user sub-routines of programmes such as the finite element non-linear programme, AUTODYN2D.
The soil used as overburden within the test cell during explosive testing was subjected to a gauge reactive cell test. The results from GREAC cell testing would be applied to the following:

1. Integrating the data into an AUTODYN2D subroutine, for running simulations based upon the geometric setup as discussed in section 4.4.3.2.
2. Understanding soil compaction.

The equation of state curve associated with the sand is illustrated in figure 4.6.5, yielding three important features:

1. A non-linear increase in soil bulk density was associated with compaction as stress is increased.
2. At full compaction the soil bulk density was 2150kg/m^3 and will effectively remain at the value even if the applied stress of 290MPa is modestly increased.
3. The soil bulk density reduces by 2%, once the load has been removed, from the density associated with the maximum stress, causing residual stresses to remain locked into the soil structure.

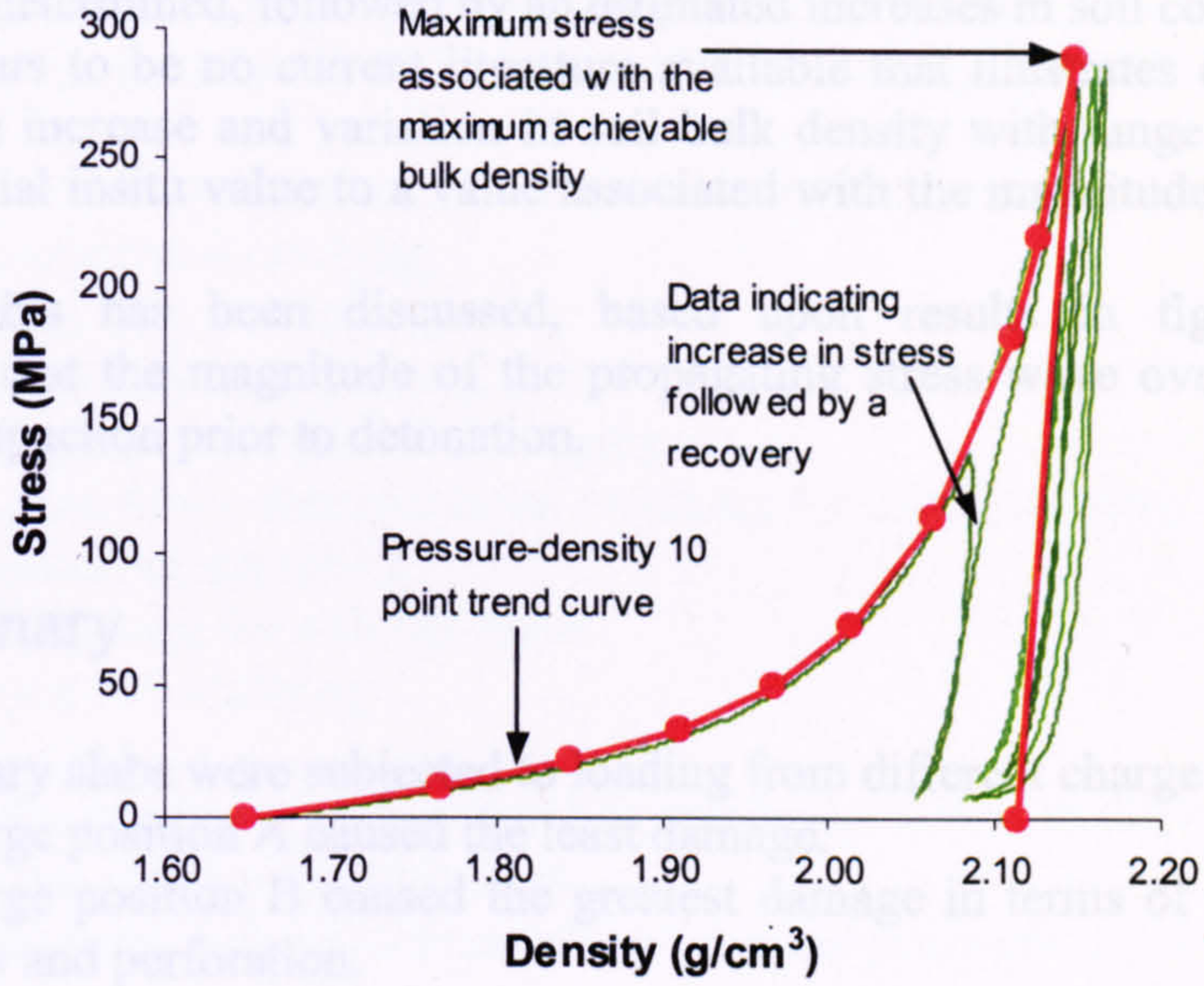

Figure 4.6.5 Experimental GREAC cell data – Variation in soil bulk density with applied stress

The features from figure 4.6.5 have helped to understand soil compaction caused by stress wave propagation in the following ways:

1. After detonation of the charge, the soil locally surrounding the space once occupied by the charge experiences an instantaneous increase in density, caused by the stress wave, many magnitudes greater than the stress associated with the insitu density.
2. The stress wave compacts the soil it travels through, by increasing its density above the insitu density to a value associated with its attenuating stress at a given interval of time.

Zhongqi & Yong (2003) commented on the near field environment containing significantly high magnitudes of stress, increasing the soil density by compaction.
Both the near and far field loadings are dependent upon the ratio of charge standoff to the effective span of the primary slab as discussed by **Pope (2002).** The experimental tests performed were all within a near field environment as the charge standoff was less than the effective span of the primary slab. Within the near field environment, the soil deformation mechanisms that occur involve the 'solid phases' as discussed by **Zhongqi & Yong (2003).** The solid phase is considered deformable, in view of the fact that the duration of the loading is very short and there is not enough time to squeeze the air and water out of the skeleton. The authors also stated that '*the greater the air content in the soils, the larger the reduction of the void ratio under the blast pressures*', suggesting that even if the soil in the near field environment was not compacted prior to the detonation of the charge, the induced stress wave would compact the soil to a density associated with the level of induced stress at that interval of time, irrespective of the initial compaction.
The detonation of the cylindrical charge would have caused an instantaneous rise in soil stress associated with an equivalent increase in density. The variation in pressure surrounding the charge upon detonation was unknown, as DPGs positioned that close would have been damaged. The DPGs measured a variation in reflected pressures upon the primary slab and were not positioned side-on, in any test, to the direction of

the stress wave. This prevented free-field soil pressures surrounding the primary slab from being determined, followed by an estimated increases in soil compaction.
There appears to be no current literature available that illustrates or even discusses directly, the increase and variation in soil bulk density with range from the source, from an initial insitu value to a value associated with the magnitude of a propagating stress wave.
However, this has been discussed, based upon results in figures 4.6.3-4.6.5, concluding that the magnitude of the propagating stress wave overrides any initial form of compaction prior to detonation.

4.7 Summary

The secondary slabs were subjected to loading from different charge positions:

1. Charge position A caused the least damage.
2. Charge position B caused the greatest damage in terms of cratering on both faces and perforation.
3. Charge positions C and D caused a heaving forcing on the bottom face of the slab. This caused a residual dome to be formed on the top face, indicating a plane of weakness.

Four main types of crack patterns were identified upon the faces of the secondary slabs:

1. circumferential cracks,
2. radial cracks,
3. square cracks,
4. corner cracks.

Numerical simulations were performed in AUTODYN2D to identify, rather than model, the influence a change in soil overburden above the secondary had to the loading upon the primary slab. The following, based a fixed charge position, was identified:

1. A change in the thickness of the soil overburden above the secondary slab did not significantly alter the damage to the secondary slab.
2. A change in the thickness of the soil overburden above the secondary slab did not influence the loading across the primary slab.

The average impulse calculated from the numerical simulations based upon an altered geometric test setup to that performed experimentally was 5kPa-s. This was within the same order of magnitude indicated by the impulse results from tests RCIT1-4 demonstrating a confidence in the DPG results.
It was established that the finer the mesh setup in AUTODYN2D the greater the accuracy of the pressure-time histories recorded by the target points, with an increase in the duration of the simulations.

Four primary slabs in total were each subjected to cumulative loading. Slab RCR73IT1-4 received mild cracking on both faces, where as the common trends of damage upon slabs RCR73IT5-8, RCR73IT9-11 and RCR73IT12-13 were described as :

1. wide and deep radial cracks on the bottom face,
2. circumferential cracking,
3. irregular corner cracking,
4. irregular diagonal cracking,
5. development of a central shear plug,
6. reduction of the concrete cover exposing the reinforcement,
7. slip action of the rebars,
8. rotation along the slab perimeter,
9. spalling and scabbing.

The greater the number of cumulative hits, the harder is was to differentiate between different modes of failure mechanisms.
The following from deflection-time, strain-time and pressure-time histories was observed:

1. The importance of setting the sensitivity on the digital storage oscilloscopes in capturing an entire trace.
2. The increase in deflection parameters associated with the response of a primary slab when secondary slabs were omitted.
3. The multiple peaks identified on the pressure-time histories and associated with gauge movement, impact from aggregates and interaction with the non-symmetrical stress waves.

The steel plate test results indicated that the steel plate responded impulsively to groundshock loading. This was identified from two procedures using:

1. energy balance procedure,
2. calculations of load duration and natural period of response.

The results from concrete tests RCIT1-4 indicated that primary slab RCRI73T1-4 responded impulsively, from calculation of the ratio values that were similar to those achieved from the steel tests. Similarity in the ratio values was used to assume that a linear energy balance relationship would also be associated with slab RCRI73T1-4. This was also backed up by a similarity in the geometry of the impulse distribution across the top faces of both the steel plate and reinforced concrete slab.
Due to incomplete experimental data associated damaged instrumentation during tests RCIT5-13, an impulsive response of primary slabs RCRI73T5-8, RCRI73T9-11 and RCRI73T12-13 was not proven.
The internal weakening of a primary slab defined as a loss in strength and stiffness was unidentifiable from the degree of external damage.
The damage to the primary slabs subjected to cumulative attack was due to the cumulative impulse history. Less cumulative hits at smaller charge standoffs caused a greater severity of damage to the slab.
The compressive and tensile concrete strength data was associated with the strength of a fresh primary and secondary slab on the day of an explosive test. The variability of data was associated with a standard of control defined as 'Good' in accordance with the literature.

The soil bulk densities and moisture contents varied throughout the experimental testing. The variability was associated with a coefficient of variation and put into context with the literature. The distribution of data was associated with a normal distribution. The literature indicated that the moisture content can have a profound effect on stress wave propagation. However, the effect of moisture content values <10% on stress wave propagation, was not mentioned.

The variation in the density index values in accordance with the literature, suggested that the degree of soil compaction prior to detonation in the soil in each test, was similar. It was also concluded that the degree of soil compaction prior to charge detonation in each test did not affect the increase in soil compaction caused by stress wave propagation.

Chapter Five

Discussion

5.1 Quality of the experimental results

The instrumentation used in any explosive event involving time varying loads must be able to respond quickly enough and possess a sufficiently high capture rate. For this reason certain instruments were used with the confidence that they would capture the true response. Three types of instrumentation were used through out the testing:

1. diaphragm pressure gauges (DPGs),
2. linear variable differential transducers (LVDTs),
3. strain gauges (SGs).

The Nyquist criterion was used to ensure that the sampling rate was such that the true response was captured. If samples were recorded at time intervals of Δt, the maximum possible frequency that could be pick up corresponded to the Nyquist frequency

$$f = \frac{1}{2\Delta t}$$

Equation (5.1.1)

f= Nyquist frequency
Δt = Sampling rate

This implies that if the frequencies associated with the response of a structure were less than the Nyquist frequency, the true response would be captured.
It has been shown in the following sub-chapters that the capture rate set for all three instruments ensured that the trace histories captured were indicative of the response.
The digital storage oscilloscopes were set with a 10% pre-trigger, allowing the instrumentation to start recording prior to detonation. This ensured that if a response was captured within this 10% duration it could be associated with interference and ignored. It was only after the break wire had broken that the instruments captured what was considered as a true response.

5.1.1 Diaphragm pressure gauges

It was not of interest to evaluate the response of the DPGs caused by the static soil overburden pressures alone. Instead, they were used to evaluate the reflective pressures caused by stress wave propagating.
Prior to charge detonation the circuits associated with all four DPGs were balanced using a wheatstone bridge circuit outputting a constant voltage. This indicated that their response would be primarily due to the effects of groundshock only.
The DPGs were positioned normal to the incoming stress wave measuring face-on pressure. The gauges were not positioned side-on to the stress wave throughout the

testing as illustrated in figure 2.7.1. This meant that free-field pressures were not established.
If cost was not an option the gauges could have been manufactured with built in accelerometers as discussed by **Dongen & Weerheijm (1992).** This would have allowed both face-on and side-on pressures to be established.
The pressure-time plots recorded by the DPGs during the groundshock loading also illustrated multiple peak pressures as discussed by **Zhongqi & Yong (2003).** A number of possible reasons are stated as follow:

1. impact of larger soil particles,
2. stress waves reflecting from the internal sides of the test cell,
3. arrival of the stress waves of different magnitudes due the inclined positioning of the charge,
4. vibration of the DPG bodies, even though they were taped to the top face of the primary slab.

The calibrations of the DPGs were performed in a specifically designed chamber. Their load response range was determined from both an airblast and a groundshock test. It was established that the soil damped out the higher frequencies, contained in groundshock.
However, it was necessary to consider that the response of the DPGs themselves might also have filtered out (or magnified) certain frequencies. Therefore, it was decided to expose the DPGs to an air blast test, the loading from which would certainly contain very high frequency components. The purpose of this test was to determine the frequency response of the DPGs and, specifically, to highlight any resonance and/or damping effects.
The results from the airblast test in section 3.5.4.2, involving all four DPGs and a kulite gauge, (the latter specifically designed to respond to such high frequencies) are illustrated in figures 3.5.10-3.5.14, indicating that the DPGs did not respond effectively to the high frequencies. A Fast-Fourier-Transform analysis was applied to the pressure-time history associated with the response of DPG1, as illustrated in figure 5.1.1. The objective was to evaluate the range of frequencies the gauge could successfully record from the airblast test, assigning a detectable frequency range and hence bandwidth to the gauge.
DPG1 contained the thickest and heaviest diaphragm, compared to those attached to the other three DPGs. The Fast-Fourier-Transform analysis in figure 5.1.1 indicated that its bandwidth was too small and that it oscillated at its natural period of vibration during the loading, preventing the true airblast signal from being recorded. The Fast-Fourier-Transform analysis indicated two points:

1. The natural frequency of DPG1 was ~12.5kHz.
2. DPG1 had the ability of responding within a range of 0-7000Hz.

A Fast-Fourier-Transform was applied to the pressure-time histories of DPG1, as the gauge was always positioned centrally on the top face of the primary slab in most of the explosive tests. It was subjected to a greater load than the other three gauges, positioned at eccentricities from the centre of the slab. Its response was crucial in validating the linear energy balance relationship; discussed in section 4.4. This helped vindicate an impulsive response of primary slab RCR73IT1-4. The impulses recorded by the other three gauges during the explosive tests were also used to illustrate a similarity in impulse load distribution, identified by **Pope (2002).** The author also used the energy balance procedure to indicate an impulsive response.

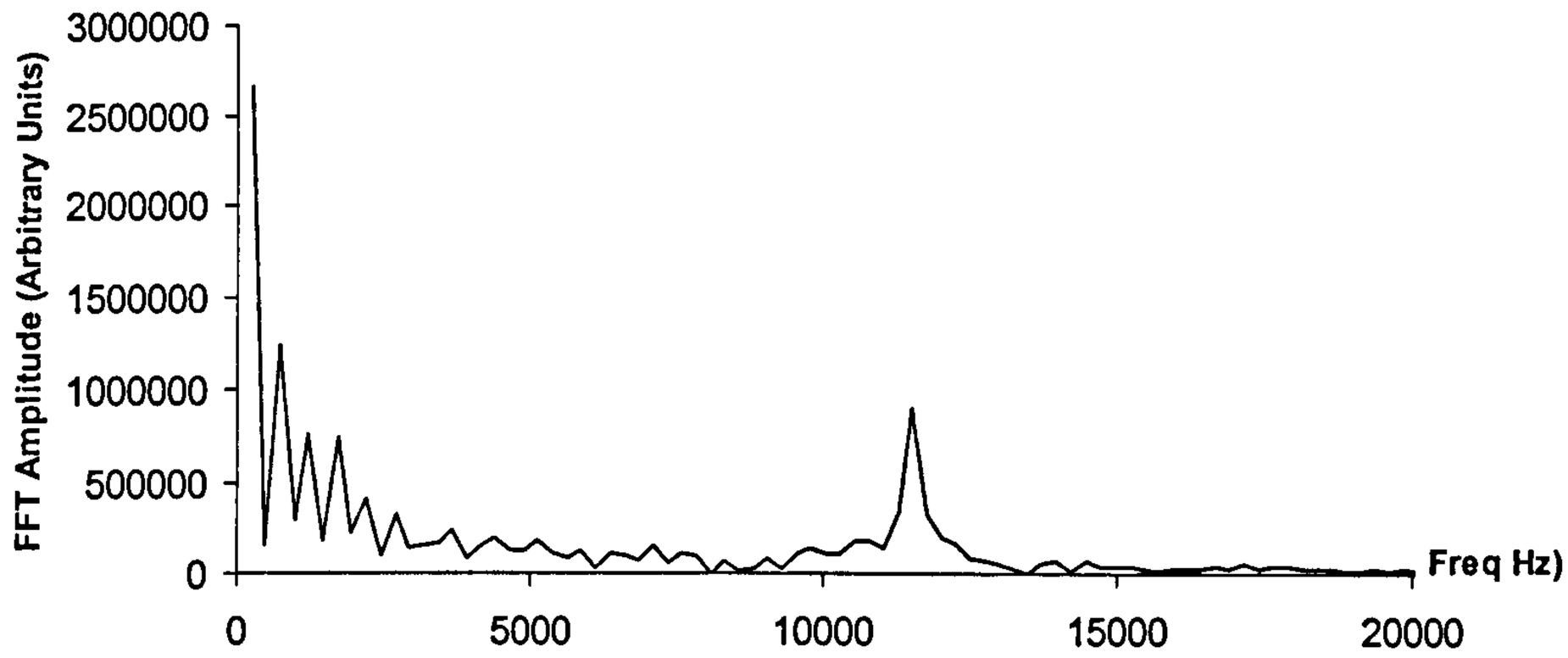

FFT=Fast Fourier Transform

Figure 5.1.1 Fast-Fourier -Transform analysis on the pressure-time results associated with DPG1 from test the airblast test

During the calibration procedure a static load of 80bars caused DPG1 to respond elastically. A smaller static pressure of 20bar caused the other three DPGs to also respond elastically, as their diaphragms were thinner.

A Fast-Fourier-Transform was then applied to the pressure-time history associated with the calibration load for DPG1. It indicated that the gauge would be able to respond to frequencies within the range of 0-5000Hz. The frequency load calibration plot was then compared to the frequency plot associated with the pressure-time history from explosive test RCIT3, as illustrated in figure 5.1.2. The two graphical plots indicated that the frequency of response recorded from test RCIT3 was within the range of 0-1500Hz, and well within the calibrated load range of 0-5000Hz.

Both ranges were also within the gauges detectable range of 0-7000Hz, identified from the airblast test. This validated DPG1's capability of recording groundshock.

DPG1's diaphragm was thicker than those associated with the other three gauges. This theoretically indicated that its mass and size would inhibit its response to greater frequencies. It has been proven that for the range of frequencies associated with groundshock, DPG1's response was indicative of the loading. This indicated that the thinner diaphragms, of smaller mass associated with the other three gauges, also responded to those frequencies. However, due to stress wave attenuation, they would have responded to loads containing smaller frequencies.

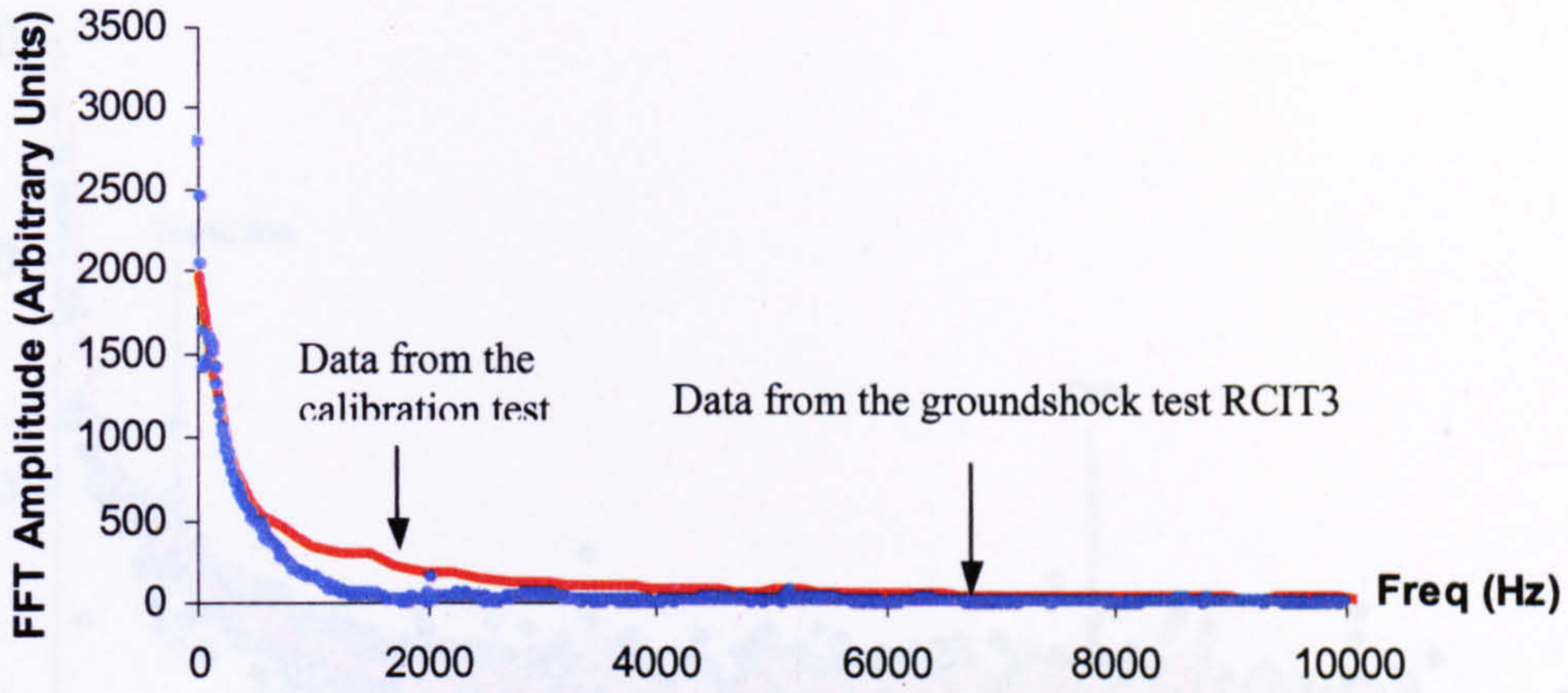

FFT=Fast Fourier Transform

Figure 5.1.2 Comparison between the calibration and groundshock load within their frequency domains associated with the response of DPG1

5.1.2 Linear variable displacement transducers

The LVDTs used during explosive testing were chosen based upon precedence from authors, **Pope (2002)**, **Duranovic (1994)** and **Archer (1985).** The authors all gathered reliable data from using the LVDT model and on that basis were used to evaluate the response of primary reinforced concrete slabs during groundshock.

The LVDTs were the most reliable of the instrumentation used to record a response, during groundshock. However, the output data was unreliable when the following occurred:

1. full compression of the shaft's travel length into the core preventing further deflection of the slab,
2. perforation of the primary slab.

At time intervals of $\Delta t = 10\,\mu s$ throughout the duration of the response each LVDT outputted a voltage associated with a value of deflection. This characterised the true response of the primary slab at a designated position. The Nyquist frequency associated with the sampling rate of the LVDTs was 50kHz. This meant that if the primary slab responded to frequencies less than 50kHz its true response would be captured. The Fast-Fourier-Transform curve illustrated in figure 5.1.3 was associated with the central deflection-time history of a primary slab. The amplitude of the FFT components decayed rapidly as the frequency increased. In the range 10-15kHz, the amplitudes were less than 1% at a frequency of 100Hz. This indicated that very little energy was contained within the higher frequencies and that the Nyquist frequency had not been violated. This validated the suitability of an LVDT, responding at a sampling rate of $\Delta t = 10\,\mu s$, to groundshock loading.

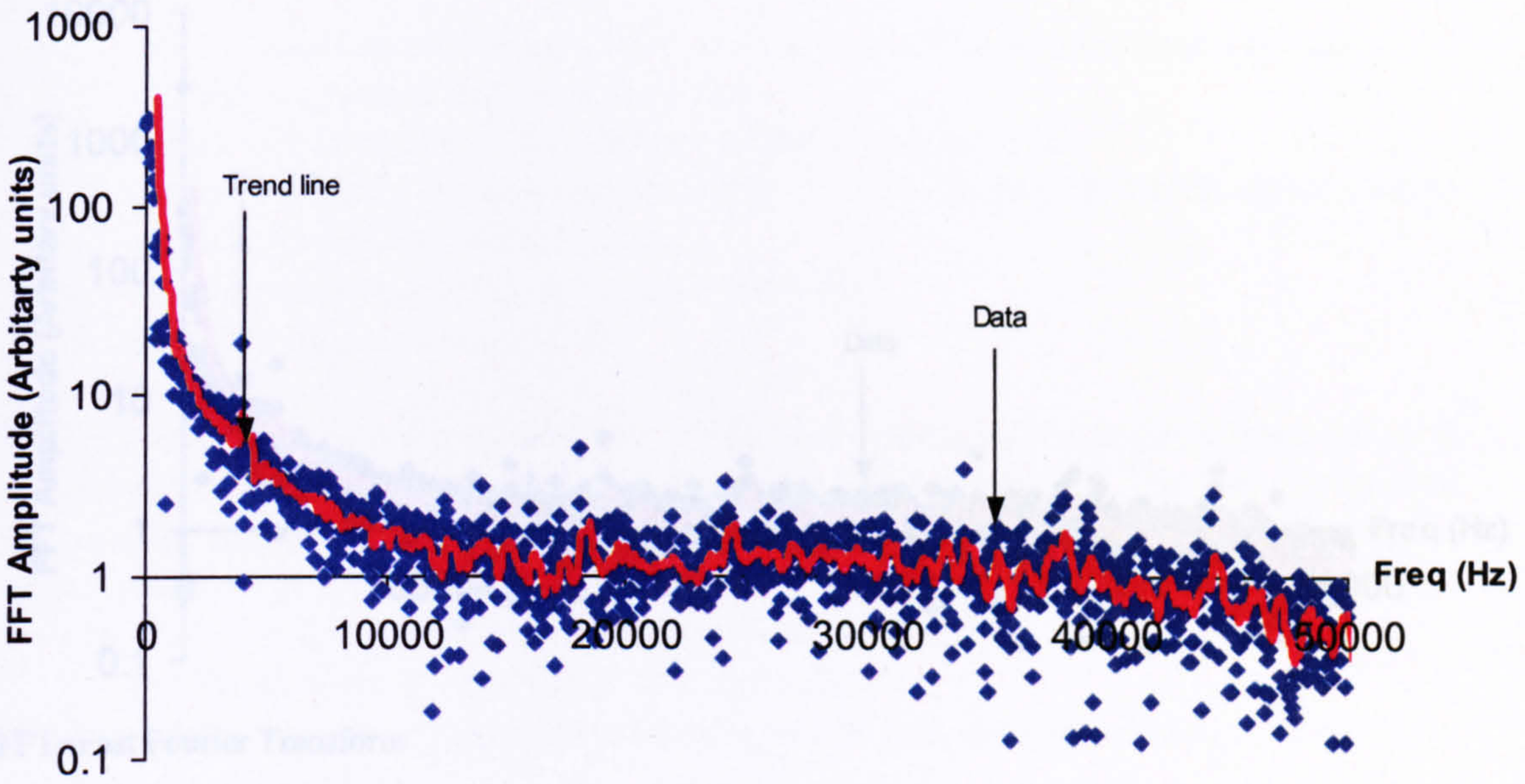

FFT=Fast Fourier Transform

Figure 5.1.3 Fast-Fourier-Transform analysis on the central deflection-time history associated with a sampling rate of $10\mu s$

The LVDTs were each re-calibrated at the end of each group of tests that involved the same primary slab . If damaged beyond the point of repair, a new LVDT was calibrated and used. Prior to each test all three LVDTs were connected to the digital storage oscilloscopes and their shafts were moved in and out of the core to ensure that a voltage output was being produced.

5.1.3 Strain gauges

Tyas (1999) used the same size and type of strain gauges that were attached to the steel reinforcement within the primary slabs. The author indicated that the 5mm strain gauges with the Fylde bridge amplifiers have a 3 decibel bandwidth >100KHz. This indicated that a significant range of frequencies would be captured.
The strain gauges were calibrated at the manufacturers, yielding a calibration factor that was applied to the voltage output data.
At time intervals of $\Delta t = 10\,\mu s$ throughout the duration of the response, each strain gauge outputted a voltage that was converted to a value of strain. Therefore the maximum possible frequency the strain gauge could respond to was 50kHz, according to the Nyquist Criterion.
The Fast-Fourier-Transform curve illustrated in figure 5.1.4 was associated with the strain-time history of a strain gauge attached to the central rebar in the top mesh of a primary slab.
It was evident that the amplitude of the Fast-Fourier-Transform components decayed rapidly as the frequency increased. There was significant decay after 15kHz, which was less than the Nyquist frequency of 50kHz. This validated the suitability of the strain gauges and sampling rate, in outputting a true response.

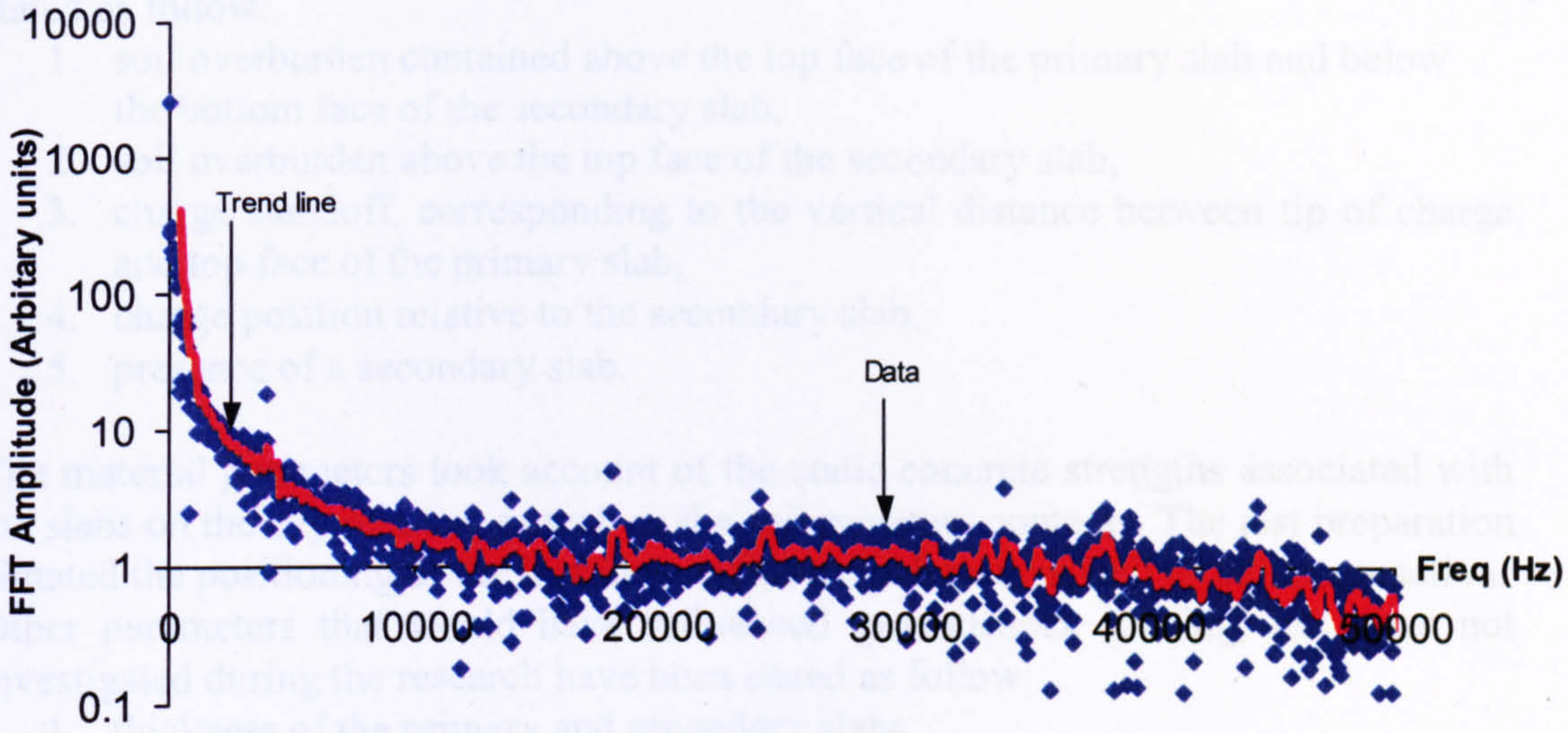

FFT=Fast Fourier Transform

Figure 5.1.4 Fast-Fourier-Transform analysis on the central top mesh strain-time history associated with a sampling rate of $10\mu s$

The data retrieved from the strain gauges was not as useful as that from the LVDTs and DPGs. This was primarily because of the difficulty in interpreting the resulting data (if any). The difficulty occurred for two reasons:

1. If the strain gauges were damaged they could not be fixed and information relating to the internal response of the slab could not be analysed.
2. As the severity of slab damage increased, the concrete-steel bond weakened, causing the strain gauges to illustrate a response that was not indicative of the reinforced concrete slab moving as a single entity. This instead illustrated the movement of the steel rebars.

Recommendations for further testing should neglect the strain gauges and instead increase the number of DPGs over the top face of the primary slab. This would allow a greater understanding of loading that caused the damage.

5.2 Parameters affecting loading and structural response of the primary slab

Parameters that have been investigated, are stated as follow:

1. geometric,
2. material,
3. test preparation.

The geometric parameters that influenced groundshock loading were considered and stated as follow:

1. soil overburden contained above the top face of the primary slab and below the bottom face of the secondary slab,
2. soil overburden above the top face of the secondary slab,
3. charge standoff, corresponding to the vertical distance between tip of charge and top face of the primary slab,
4. charge position relative to the secondary slab,
5. presence of a secondary slab.

The material parameters took account of the static concrete strengths associated with the slabs on the day of a test as well as the soil moisture contents. The test preparation dictated the positioning of the instrumentation in each test, as well as soil compaction. Other parameters that would have influenced groundshock loading, but were not investigated during the research have been stated as follow:

1. thickness of the primary and secondary slabs,
2. static concrete strengths dependent upon the mix design,
3. soil bulk density,
4. charge mass,
5. charge geometry,
6. charge inclination.

5.2.1 Geometric parameters

The experimental data retrieved from the testing was used to determine trends as well as hypothesising other possible trends. Due to the complexity of the experimental test setup and unsymmetrical distribution of loading, a theoretical approach from first principles involving the response of the primary slab and stress wave propagation was not performed.

From Stage I of the test matrix involving positioned secondary slabs, three parameters were found to have influenced the loading across the primary slab:

1. soil overburden between the primary and the secondary slab,
2. charge standoff,
3. charge position relative to the secondary slab.

These three parameters caused the central impulse on the top face on the primary slab to vary according to figures 4.4.11 – 4.4.14.

The graphical results from figure 4.4.14 indicated a geometric trend in the curves. A hypothesis based upon this trend was integrated into those results and illustrated in figure 5.2.1. Two of the impulse-charge standoff plots, Z_1=300mm and Z_1=500mm from figure 5.2.1 were established from the experimental data. The other two curves, Z_1<300mm and Z_1>500mm were hypothesized plots, based upon a general trend, and with a label entitled 'Assumed geometric profile'. The hypothesised 'Assumed geometric profiles' were approximated from the change in gradients that connected points A, B, C and D together as the soil overburden varied. The specific value of soil overburden that could be associated with each of the two 'Assumed geometric profiles' was unknown. Further testing would yield specific geometric evidence of such curves.

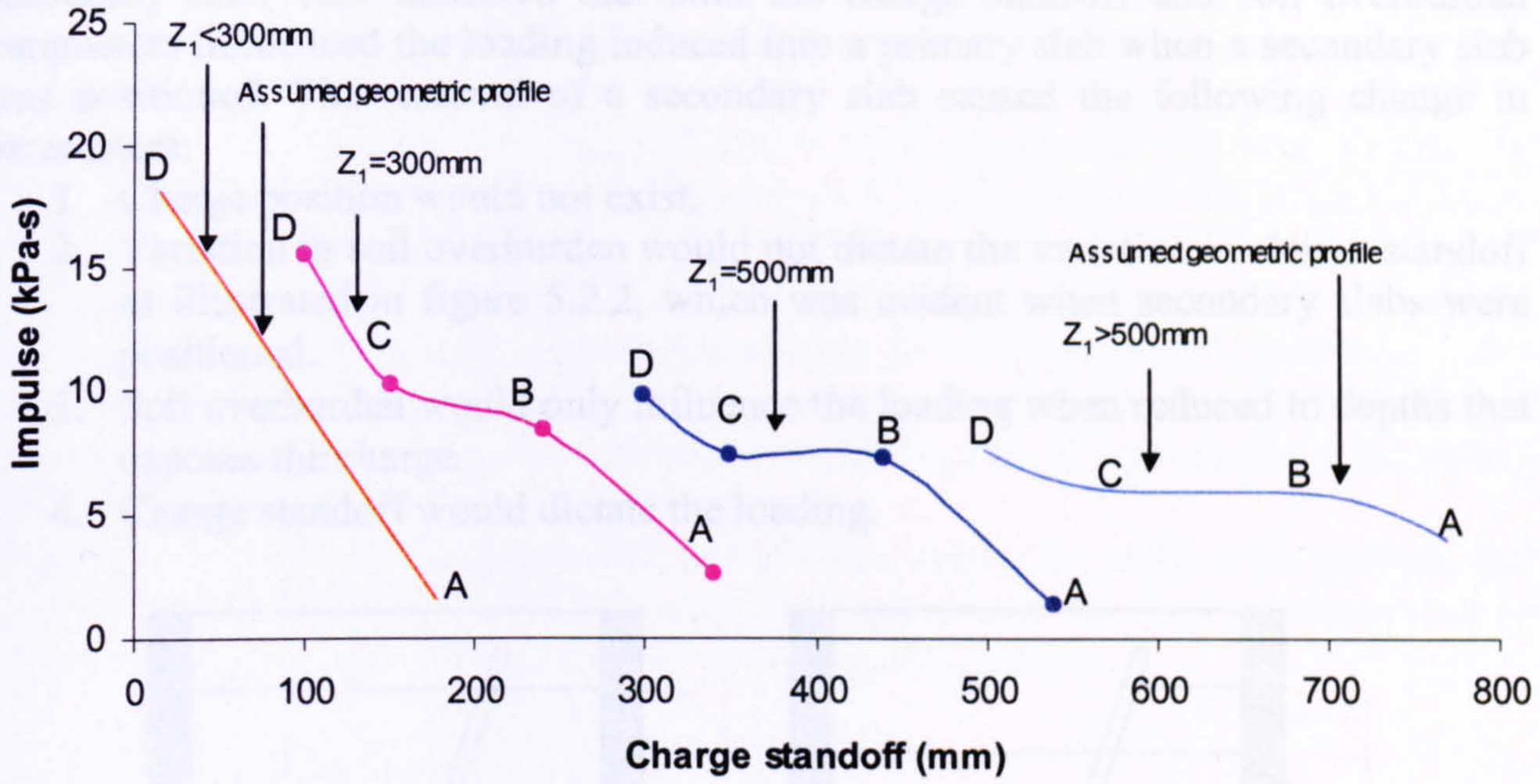

Z_1=Soil overburden between the top face of the primary slab and bottom face of the secondary slab

Figure 5.2.1 Variation in Impulse with charge standoff as soil overburden above the primary slab varies

The geometric trend in the plots was dictated by charge positions B and C. As charge standoff decreased, the gradient of the line linking points B and C increased. Curves associated with Z_1=300mm and Z_1=500mm illustrate this phenomena. The curve associated with Z_1>500mm was hypothesized. It indicated the following in comparison to the other curves:

1. Negligible difference in impulse caused by charge positions B and C,
2. smaller difference in impulse caused by charge positions A, B and C, D.

The curve associated with Z_1<300mm was also hypothesized, indicating a possible geometry between impulse and charge standoff. It indicated that each charge position has a significant effect on the central impulse on the primary slab, increasing the sensitivity of the charge position parameter. A generic identification of the two hypothesised curves indicated the following:

1. Curve Z_1>500mm - all four charge positions relative to a secondary slab have a similar effect on the impulse. The charge standoffs were outside a range, which caused the charge position parameter to be less sensitive.
2. Curve Z_1<300mm – all four charge positions had a different effect on the impulse that increased in magnitude with a decrease in charge standoff. Stress wave attenuation was less at closer standoffs, reducing the wave path and increasing the sensitivity of the charge position parameter.

The presence of a secondary slab divided the total soil overburden depth into two layers:

1. Z_1 - soil overburden between the primary and secondary slab,
2. Z_2 - soil overburden above the secondary slab.

The four charge positions, A, B, C and D, identified by their proportion of volume relative to a secondary slab were also associated with charge standoff values. Such values varied with a variation in soil overburden depth, above and below the

secondary slab. This indicated that both the charge standoff and soil overburden parameters influenced the loading induced into a primary slab when a secondary slab was positioned. The removal of a secondary slab caused the following change in parameters:

1. Charge position would not exist.
2. Variation in soil overburden would not dictate the variation in charge standoff as illustrated in figure 5.2.2, which was evident when secondary slabs were positioned.
3. Soil overburden would only influence the loading when reduced to depths that exposes the charge.
4. Charge standoff would dictate the loading.

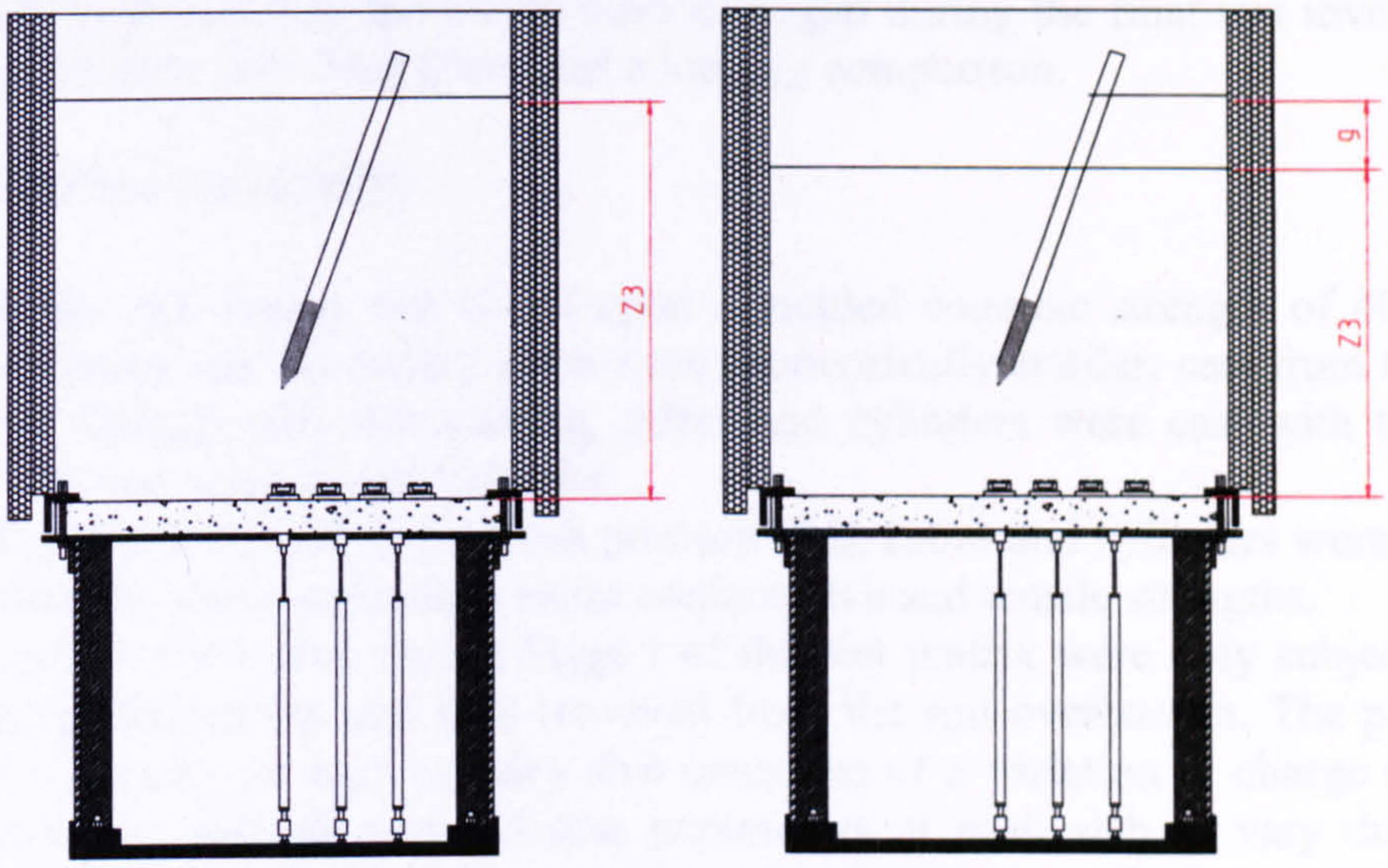

Z_3 = Total soil overburden carried by the primary slab
g = Percentage reduction in soil overburden.

Figure 5.2.2 Reduction in the total soil overburden parameter

The sensitivity associated with the charge standoff and soil overburden parameters have been analysed in terms of percentage variation of impulse, illustrated in table 5.2.1.

Table 5.2.1 Percentage variation in soil overburden and central impulse induced into the primary slab

			Percentage variation (%)
Charge position	Z_1=500mm	Z_1=300mm	40% decrease
A	1.35kPa-s	2.6kPa-s	93% increase
B	7.3kPa-s	8.4kPa-s	15% increase
C	8.1kPa-s	10.3kPa-s	27% increase
D	9.8kPa-s	15.5kPa-s	58% increase

It is important to state that a percentage variation could not be calculated for soil overburden depths 75mm and 150mm due to an inconsistency with the positioning of DPG1.

The change in the position of DPG1 was made in order to prevent the gauge from being damaged during groundshock, but prevented a direct impulse comparison with variation in soil overburden depths.
The results from table 5.2.1 suggested that a 40% decrease in the soil overburden, caused an increase in impulse. Charge positions A and D provided the largest increase in impulse whilst B and C had less of an effect. For two out of four charge positions, the percentage increase in impulse was significantly greater than the percentage reduction in soil overburden. This suggested that the charge standoff parameter, (also associated with charge position parameter, when a secondary slab is positioned) was more sensitive than the soil overburden parameter between the primary and secondary slabs.
Stage III involved a comparison of loading when secondary slabs were omitted and positioned. Unfortunately the DPGs were damaged during the final test involving an omitted secondary slab. This prevented a loading comparison.

5.2.2 Material variability

The concrete mix design was based upon a yielded concrete strength of 40N/mm^2. Both the primary and secondary slabs were geometrically similar, cast from the same mix ratios. During each slab casting, cubes and cylinders were cast with the same concrete that was used to cast the slabs.
On the day of a test involving a fresh primary slab, cubes and cylinders were crushed to determine the slabs' equivalent static compressive and tensile strengths.
The secondary slabs used during Stage I of the test matrix were only subjected to a single charge detonation and then removed from the soil overburden. The pattern of cumulative loading on each primary slab consisted of a variation in charge standoff. This caused the strength and stiffness parameters of each slab to vary during the cumulative loading, independent upon the slab's initial strength. It was beyond the scope of the work to evaluate the degree of this variation.
The variability of the compressive and tensile strengths associated with the primary and secondary slabs is illustrated in figures 5.2.3 and 5.2.4. The compressive and tensile strengths associated with the primary and secondary slabs were cast with a standard of control defined as 'Good' as suggested by **Kong & Evans (1987)** and **ACI 318-95 (1996)**. This meant that the strength parameter was considered as having a negligible effect on the damaged slabs.

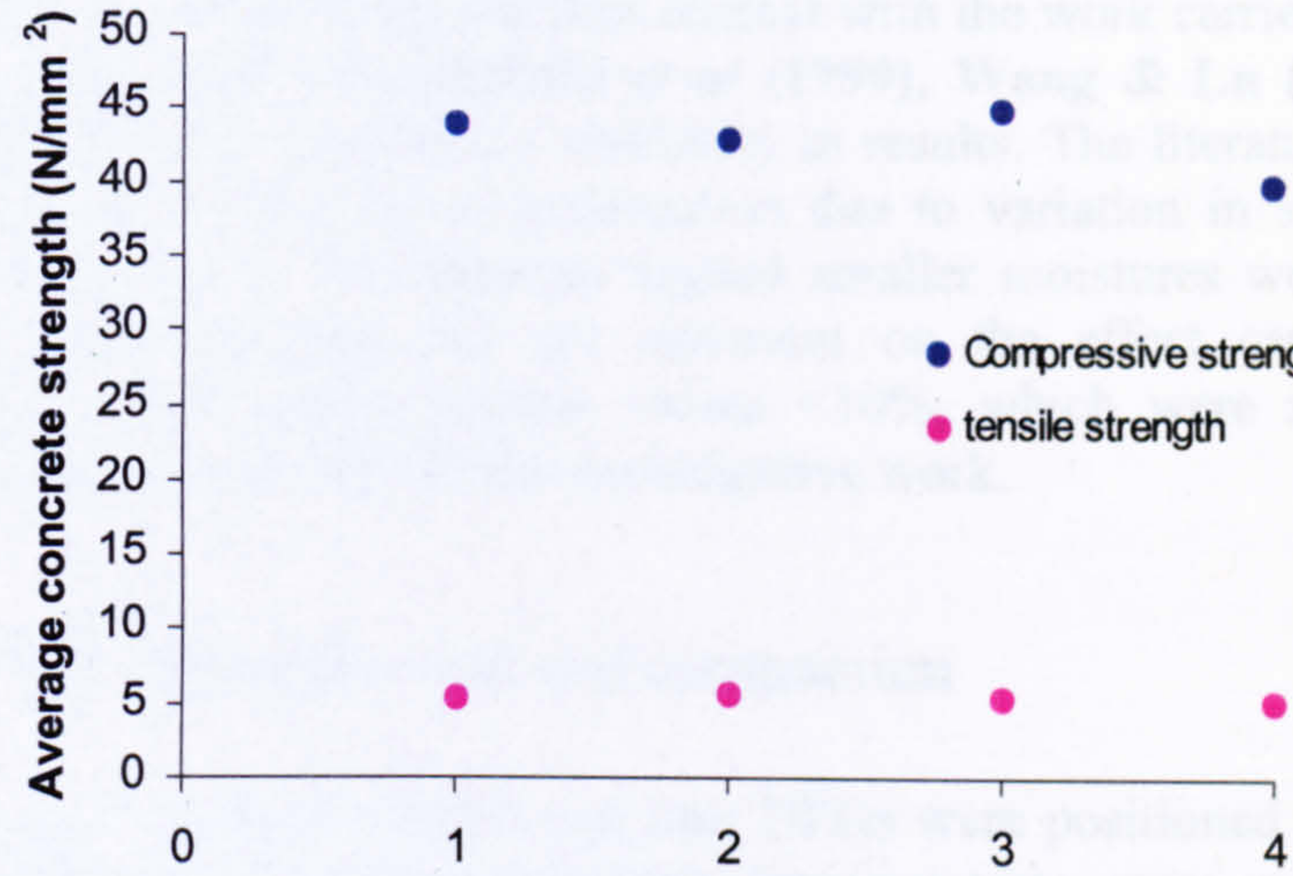

1 – Primary slab RCR73IT1-4: 2 - Primary slab RCR73IT5-8: 3 - Primary slab RCR73IT9-11:
4 - Primary slab RCR73IT112-13

Figure 5.2.3 Variation in concrete strengths associated with each primary slab used in Stage I of the test matrix prior to loading

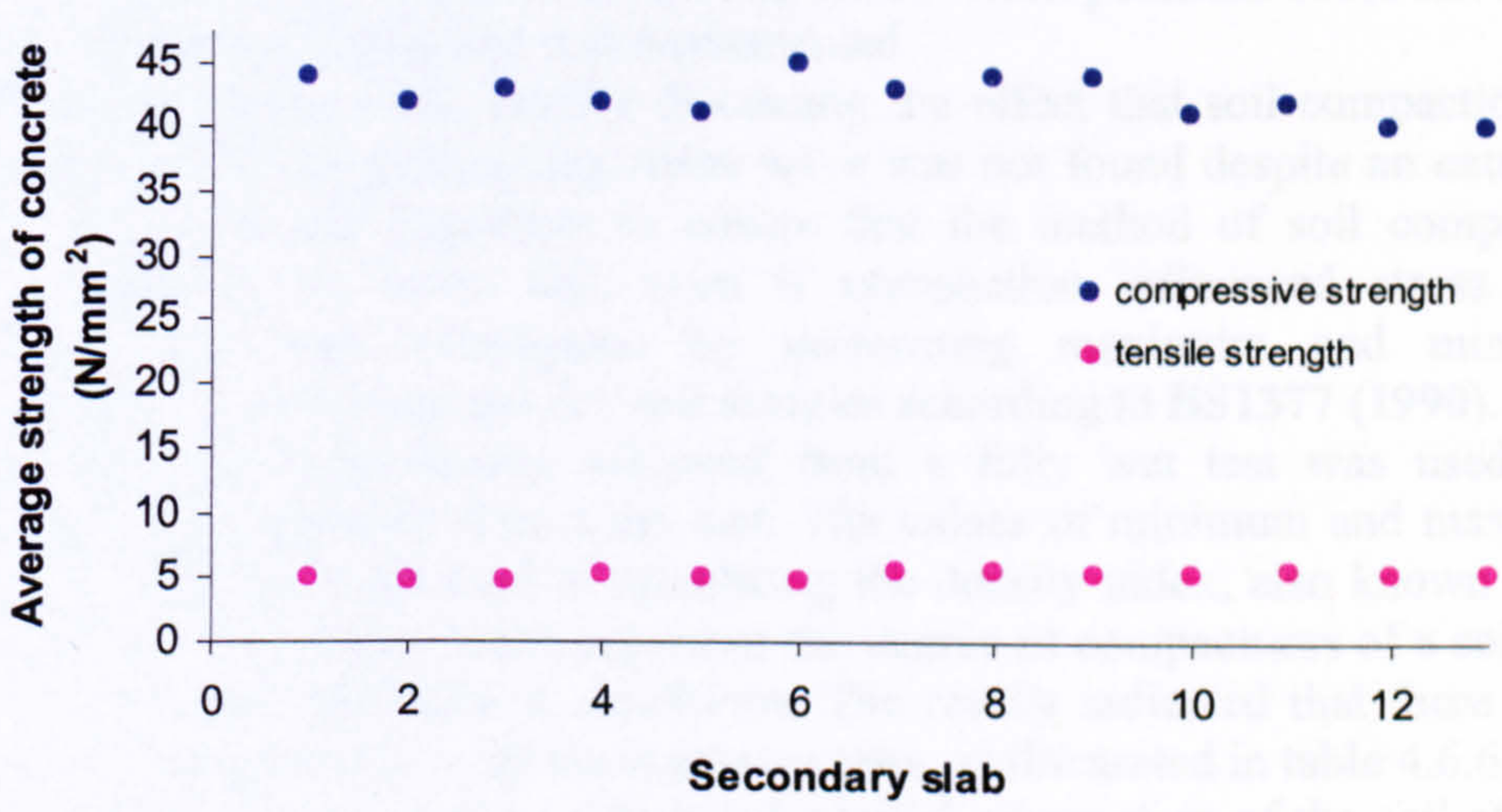

1 – Secondary slab RCB73IT1: 2 - Secondary slab RCB73IT2: 3 - Secondary slab RCB73IT3
4 - Secondary slab RCB73IT4: 5 – Secondary slab RCB73IT5: 6 - Secondary slab RCB73IT6
7 - Secondary slab RCB73IT7: 8 - Secondary slab RCB73IT8: 9 - Secondary slab RCB73IT9
10 - Secondary slab RCB73IT10: 11 - Secondary slab RCB73IT11: 12 - Secondary slab RCB73IT12
13 - Secondary slab RCB73IT13

Figure 5.2.4 Variation in concrete strengths associated with the secondary slabs used in Stage I of the test matrix prior to loading

The soil used during the explosive tests was not considered dry. The cost of ordering dry soil would have been too expensive. However, the advantage of dry soil would have eliminated the moisture content parameter.
Insitu soil samples were taken at different depths during soil compaction from within the test cell and the moisture contents in accordance with **BS 1377-9 (1990)** Test

1(A). The moisture contents varied between 2-8%. The variability was expressed as a coefficient of variation and put into context with the work carried out by **Plassmeyer & Nkongolo (2000), Famiglietti *et al* (1999), Wang & Lu (2004)** and **Kirda & Reichardt (1985)** suggesting a similarity in results. The literature also indicated the effect caused to stress wave propagation due to variation in soil moisture content. Other statements in the literature argued smaller moistures would cause an effect. However, the literature did not comment on the effect caused to stress wave propagation at moisture content values <10%, which were measured during the testing, leaving scope for further investigative work.

5.2.3 Test preparation and soil compaction

In each test, the three LVDTs and four DPGs were positioned upon a primary slab. All instruments, if not damaged from previous tests, were put through responsive checks and used in proceeding tests.

In both the steel and the concrete tests the method of soil compaction remained consistent. It is important to state that a flat-based vibrator was not available to compact the soil in layers. It was decided, under the conditions given, that the layers of soil carried by the primary slab would be shovelled into the test cell and manually compacted using the flat face of the shovel until the total overburden depth was achieved. This procedure ensured that the DPGs were positioned on the top face of the primary slab were not moved during compaction. Their positions could have been altered if a mechanical procedure was implemented.

Authoritative published work directly discussing the effect that soil compaction has on the magnitude of the propagating stress wave was not found despite an extensive literature review. It was important to ensure that the method of soil compaction remained consistent in every test, even if compaction influenced stress wave propagation. This was investigated by performing maximum and minimum compaction tests on fully wet and dry soil samples according to **BS1377 (1990).**

The maximum soil bulk density achieved from a fully wet test was used as a comparison to that achieved from a dry test. The values of minimum and maximum dry soil bulk densities were used in calculating the density index, also known as the relative density. The density index expresses the degree of compactness of a soil with respect to the loosest and densest conditions. The results indicated that there was a consistency of compactness in all the explosive tests, as illustrated in table 4.6.6.

The next step involved evaluating whether the initial compaction of the soil affected the attenuating magnitude of propagating stress wave. The following was used to evaluate this:

1. Equation of state curve illustrated in figure 5.2.5.
2. Loading velocity curve illustrated in figure 5.2.6.

The equation of state curve illustrated in figure 5.2.5 describes how the increase in applied stress changes the soil's bulk density. The increase in density indicates soil compaction within a fully confined environment; dictated by the boundary conditions within gauged reactive confinement cell, (GREAC cell) test. A detailed explanation of such a test has been described by **Pullen & Newman (1995).** An equation of state curve illustrates a material's behaviour at significantly high stresses, indicative of an explosive event. Curves of this description have been integrated into the material library of AUTODYN2D, a well respected non-linear finite element programme that

has shown similarity with experimental data. **Chapman *et al* (1994), Tyas & Pope (2004)** and **Ma *et al* (1999)** have all commented on its accurate simulation outputs, based upon the equation of state curves, hence giving confidence in the (GREAC cell) procedure. The observations from figure 5.2.5 have been stated as follow:

1. The increase in applied stress increased the bulk density non-linearly.
2. The increase in stress between 0-50MPa caused the greatest increase in bulk density.

Upon detonation of the charge the maximum peak stress in the soil surrounding the charge was instantaneously reached. The stress would have increased from an insitu compacted value to a maximum stress associated with the energy from a 183g charge of PE4.

It is difficult to state a value of that stress as it was not measured, but it would lie somewhere on the equation of state curve. The equation of state curve in figure 5.2.5 does not take into account the attenuation of stress with range, which would have indicated a variation in soil bulk density.

The loading wave velocity curves in figure 5.2.6 were established from the determination of each DPGs' response time at their associated range along the top face of the primary slab. The response time was calculated as being the difference between the response of the gauge due to stress wave propagation and the time at which the charge detonated.

The curves in figure 5.2.6 indicate a depreciation of the loading wave velocity with range. The loading wave velocity is proportional to the magnitude of stress according to 5.2.1. The decrease in the stress from a large magnitude at the point of source with range indicates attenuation as described by **Ahmed (1994).** The loss of stress with range and time would still be large enough to compact the soil above its insitu value.

It is unknown whether the stress associated with the seismic velocity would still significantly compact the soil above its insitu value. Further testing would need to be performed.

The DPGs did not measure side-on pressures as defined by equation (5.2.1) during any of the tests. The DPGs instead measured face-on pressures. A maximum peak reflective pressure of 17MPa was recorded by DPG1 at an eccentricity of 150mm in from the centre of the slab where a contact charge was positioned in test RCIT11. This implied that the stress around the source must have been significantly greater than the depreciated reflective stress of 17MPa. However, an actual value was not determined due to the inability in positioning the DPGs close enough to the source.

$$\sigma = \rho C u$$

Equation (5.2.1)

σ = Free field stress
ρ = Bulk density of the soil
C = Loading wave velocity
u = Particle velocity

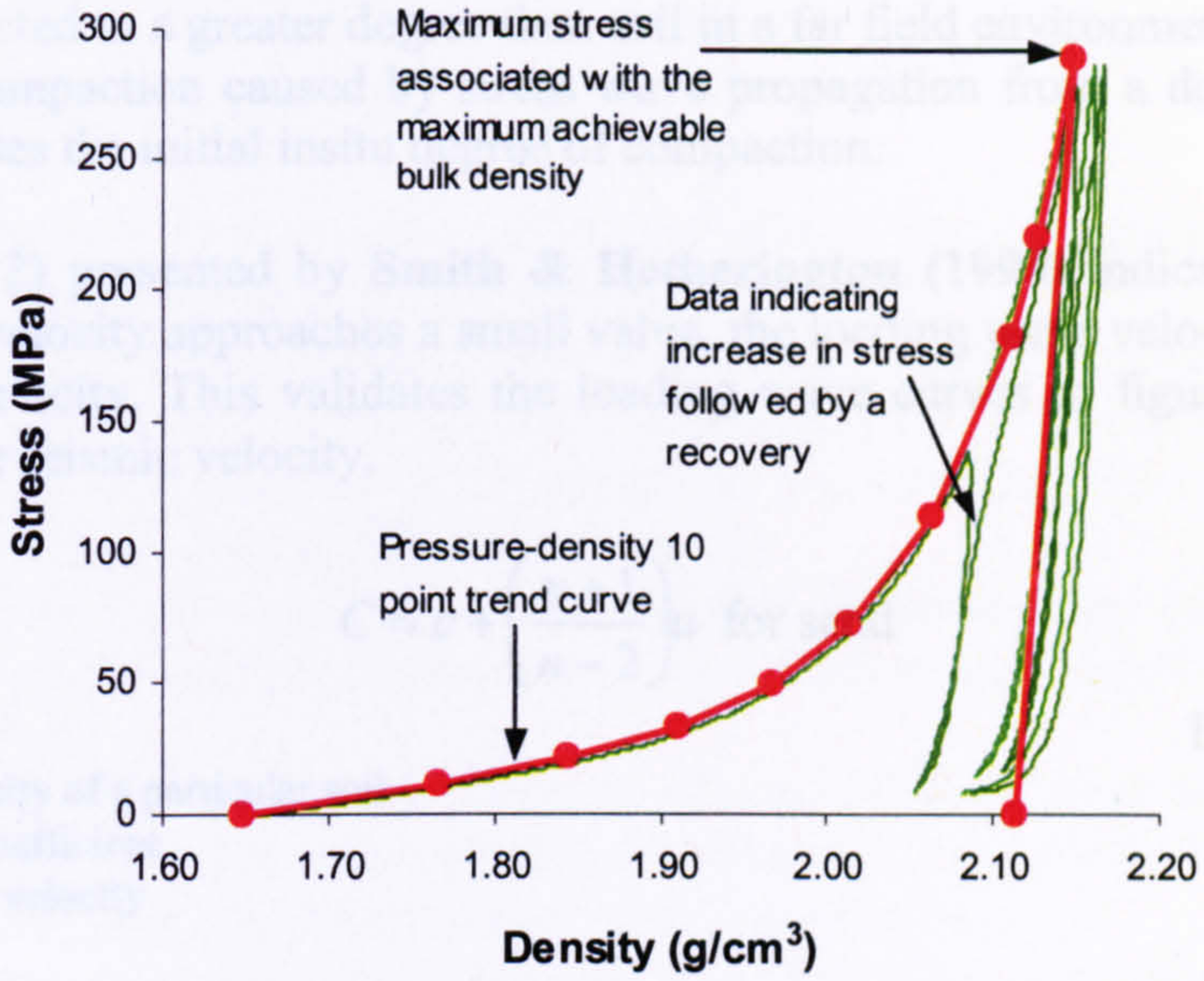

Figure 5.2.5 Experimental GREAC cell data – Variation in the soils bulk density with applied stress.

The second piece of evidence relates to figure 5.2.6. The main observations are stated as follow and have been based upon the geometry of the test configurations:

1. The variation in stress associated with the loading wave velocity attenuated into the seismic velocity.
2. The seismic velocity occurred at a range of 500mm from the centre of the slab along plane O-B1. This corresponded to a charge standoff of approximately 535mm.

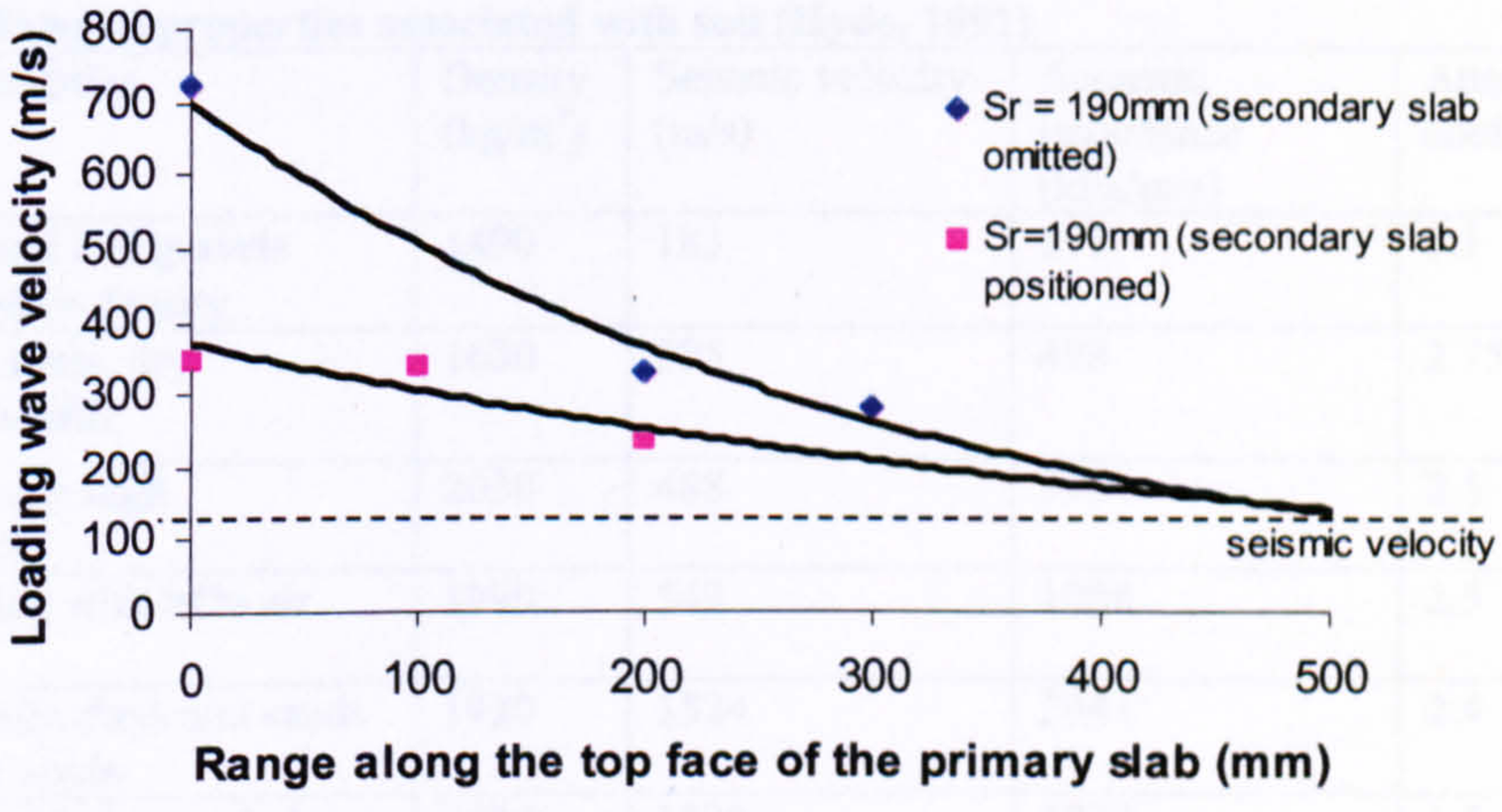

Figure 5.2.6 Exponential decay trends of the loading wave velocity when secondary slabs are omitted and positioned

The accuracy of the curves in figure 5.2.6, as well as the range in which the loading wave velocity approached the seismic velocity, would have been greater if a larger number of DPGs were positioned over a wider range along plane O-B1.
It is reasonable to suggest that further compaction of the soil above the insitu state would be less, and perhaps in some cases negligible, when the stress wave propagates at the seismic velocity. The following has been observed:

1. Soil within the near field environment described by **Pope (2002)** was compacted to a greater degree than soil in a far field environment
2. Soil compaction caused by stress wave propagation from a detonated charge overrides the initial insitu degree of compaction.

Equation (5.2.2) presented by **Smith & Hetherington (1994)** indicates that as the peak particle velocity approaches a small value, the loading wave velocity approaches the seismic velocity. This validates the loading wave curves in figure 5.2.6, which level out at the seismic velocity.

$$C = c + \left(\frac{n+1}{n-2}\right)u \text{ for sand}$$

Equation (5.2.2)

c = Seismic velocity of a particular soil
n = attenuation coefficient
u = Peak particle velocity

It was important to ensure that the soil overburden in each test was compacted to the same degree, as suggested by **Head (1992).** The literature revealed that calculations of the density index would give an indication of compactness consistency throughout the tests. It has been identified that CONWEP does not take account of the attenuating loading wave velocity with range.
It instead gives a value for the seismic velocity associated with a soil bulk density. It is unclear whether the soil prior to detonation relates to the bulk densities indicated in table 5.2.2 or whether the soil bulk densities relate to the environment in which the stress wave has already propagated through and compacted. The assumption is that the latter is incorrect.

Table 5.2.2 Material properties associated with soil (Hyde, 1991)

Material description	Density (kg/m^3)	Seismic velocity (m/s)	Acoustic impedance (kPa/m/s)	Attenuation coefficient
Loose, dry sand and gravels with low relative density	1490	183	271	3.1
Sandy loam, loess, dry sands, and backfill	1630	305	498	2.75
Dense sand with high relative density	2030	488	995	2.5
Wet sandy clay with >4% air voids	1990	549	1086	2.5
Saturated sandy clays and sands with <1% air voids	1920	1524	2941	2.4
Heavy saturated clays and clay shales	2030	1829	3732	1.5

The maximum loading wave velocities recorded by the central DPG when a secondary slab was positioned and omitted, were 380m/s and 700m/s respectively.
The presence of a secondary slab appears to reduce the loading wave velocity by approximately 50%. This loss of energy is accounted for in damage mechanisms and stress wave attenuation.

5.3 Steel and concrete tests

5.3.1 Purpose of the steel plate tests

Steel tests were performed to characterise the response of a steel plate to groundshock loading, when a 94g charge of PE4 was detonated.
The steel plate was thick enough to ensure that the response was elastic allowing a fast turn around of tests. The size of the charge used was substantial enough to cause the plate to respond and the DPGs to capture the pressure-time histories but not large enough to damage any of the instrumentation.
The results were used within an energy balance procedure that indicated a linear relationship between central maximum peak deflection and impulse indicating an impulsive response.
The response was also confirmed from ratio values of load duration and natural period of structural response. The ratio values were either less or slightly above the **Clough & Penzien (1993)** suggested limit for an impulsive response.
The results from the concrete tests formed the main theme of the thesis. Each charge was positioned at an inclination relative to a secondary slab throughout Stage I of the test matrix. The charge was detonated at a constant angle of inclination of 30° to the vertical during every explosive test and put into context within the range of $15° < \theta < 45°$ as indicated by **National Defence Research Committee (1946)**. The main differences between the steel plate and reinforced concrete tests are stated as follow:

1. Concrete tests - charge inclination and presence of a secondary slab within the soil environment.
2. Steel tests – vertically positioned charge without secondary slabs.

Damaged instrumentation and incomplete capturing of traces by the DPGs and LVDTs during the concrete tests prevented an energy balance procedure from being performed.
As both the steel and concrete tests indicated impulsive loading from the ratio values it was assumed that the incomplete concrete test results would have also indicated a linear energy balance relationship.
Both the steel and concrete tests were performed within the near-field environment. This was determined from ratio values of charge standoff to effective length of the target discussed by **Pope (2002).**
Near field loading has the effect of causing a travelling hinge to propagate outwards, towards the supports, to form on a steel plate as discussed by **Pope (2002).** This was evident during the deflection of the steel plate in test ST4 at intervals of time that progressed from t_1 to t_5 as illustrated in figure 5.3.1

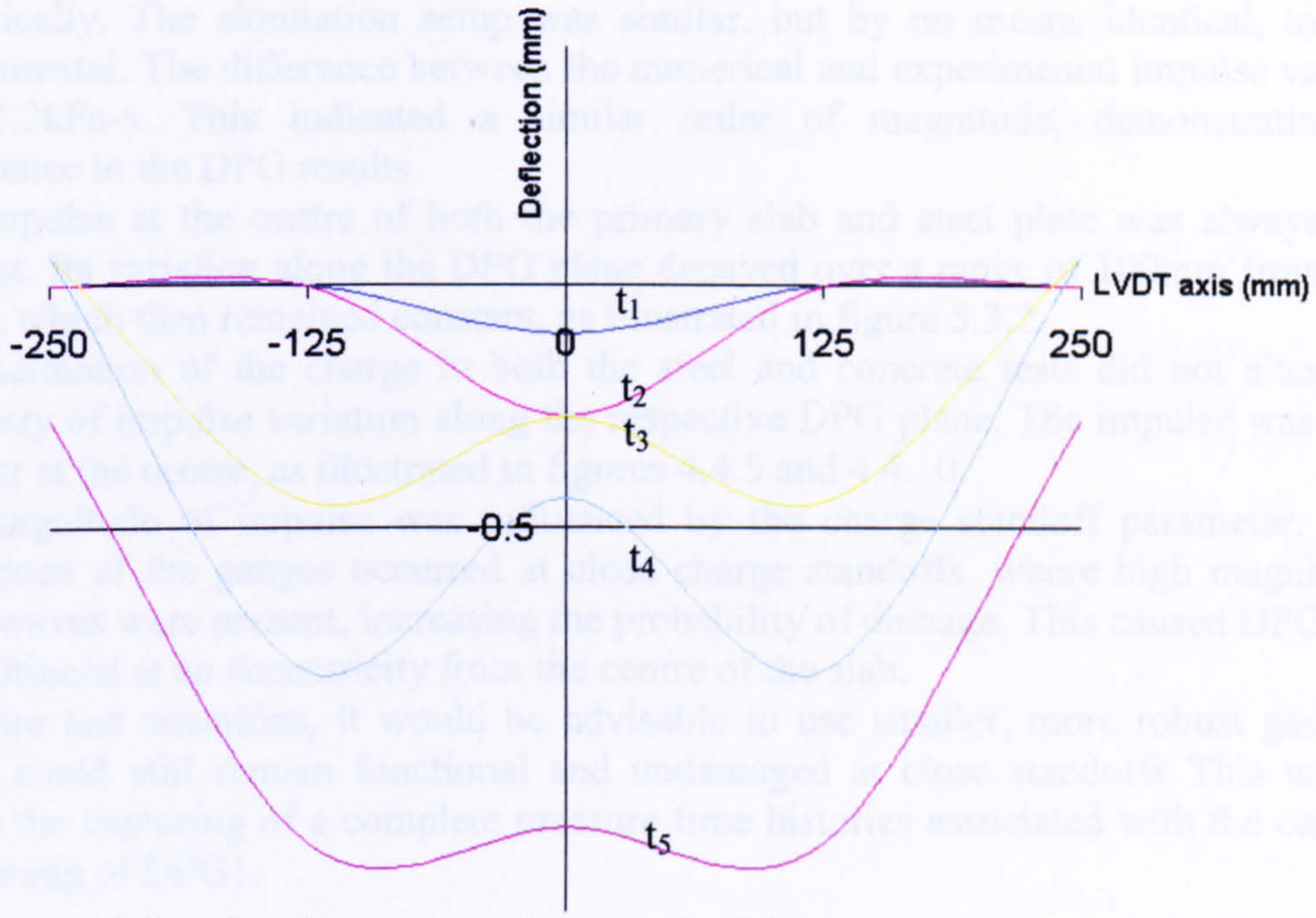

t_1, t_2, t_3, t_4 ,t_5 = deflected profiles at progressing intervals of time

Figure 5.3.1 Moving hinge on the primary steel plate subjected to groundshock loading

5.3.2 Reliability of the pressure-time data recorded using the diaphragm pressure gauges

The DPGs were positioned on the top face of a primary slab along plane O-B1 in which the inclined charge was positioned. Due to a lack of channels on the digital storage oscilloscopes, only four DPGs could only be used in each test. A greater number of DPGs would have allowed a better understanding of the variation in loading that caused the damage to the primary slabs.

It has been concluded that primary slab RCR73IT1-4 subjected to four cumulative hits responded impulsively. There is greater degree of accuracy in calculating the impulse as explained in section 2.3.2 than there would be in determining the maximum peak pressure associated with a quasi-static response.

In cases where the geometric profile of data points illustrated the convergence of a peak pressure, it was reasonable to assume that the peak was representative of a true response. In the case of multiple peaks as discussed by **Zhongqi & Yong (2003)** the cause of the individual peaks were hypothesised. This made it difficult to identify the initial peak caused by the propagating stress wave, which was assumed to be the greatest, but was not always observed in this way as illustrated in figures A.1.40 (b), A.1.42, A.1.46 (b), A.1.47 (a), A.1.47 (b), A.1.48 (b), A.1.51, A.1.52 and A.1.59.

A number of pressure-time histories illustrated in figures A.1.45, A.1.46 (a), A.1.48 and A.1.51 did not capture the peak pressure. The sensitivity set on the digital oscilloscopes was too great, as discussed in section 3.6.3.4. With more experience in this area, there is a possibility that the human error in setting the sensitivity could be improved, ensuring that the entire trace is captured.

The geometry of the tests within Stage II of the test matrix was based upon test RCIT9, with the implementation of charge position B. The impulse recorded by DPG1 in test RCIT9 was 7.7kPa-s in comparison to its value of 5kPa-s, recorded

numerically. The simulation setup was similar, but by no means identical, to the experimental. The difference between the numerical and experimental impulse values was 2.2kPa-s. This indicated a similar order of magnitude, demonstrating a confidence in the DPG results.

The impulse at the centre of both the primary slab and steel plate was always the greatest. Its variation along the DPG plane decayed over a range of 100mm from the centre, which then remained constant, as illustrated in figure 5.3.2.

The inclination of the charge in both the steel and concrete tests did not alter the geometry of impulse variation along the respective DPG plane. The impulse was still greatest at the centre, as illustrated in figures 4.4.5 and 4.4.10.

The magnitude of impulse was influenced by the charge standoff parameter. The limitations of the gauges occurred at close charge standoffs, where high magnitude stress waves were present, increasing the probability of damage. This caused DPG1 to be positioned at an eccentricity from the centre of the slab.

In future test situations, it would be advisable to use smaller, more robust gauges, which could still remain functional and undamaged at close standoffs This would ensure the capturing of a complete pressure-time histories associated with the central positioning of DPG1.

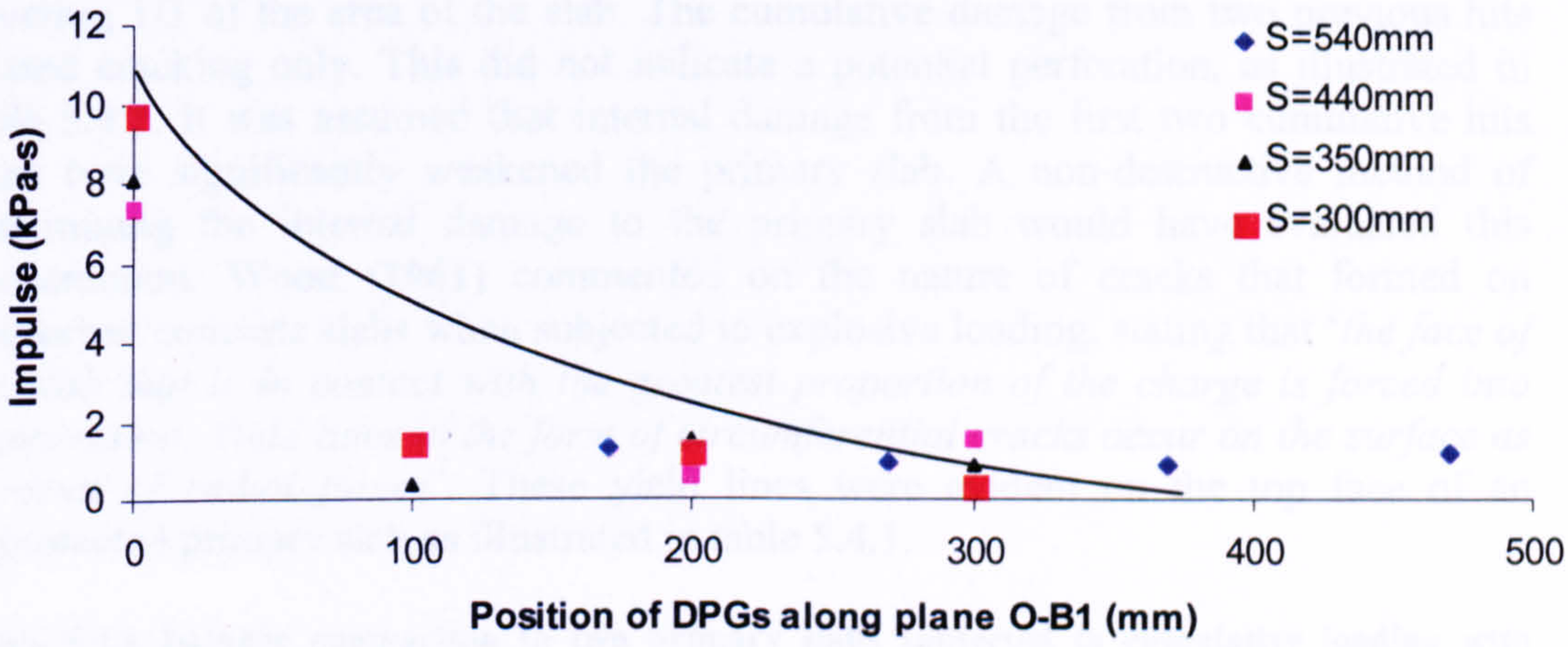

S= charge standoff

Figure 5.3.2 Impulse recorded at different positions along plane O-B1 on the top face of the primary reinforced concrete slab from tests RCIT1-4

The geometric distribution of loading identified on the top face of a primary slab, illustrated in figure 5.3.2 is similar to that identified by **Pope (2002).** He stated that '*in the near field environment the loading decays rapidly from an epicentral peak to much lower values at the panel perimeter'*. A pictorial understanding of this is illustrated in figure 5.3.3

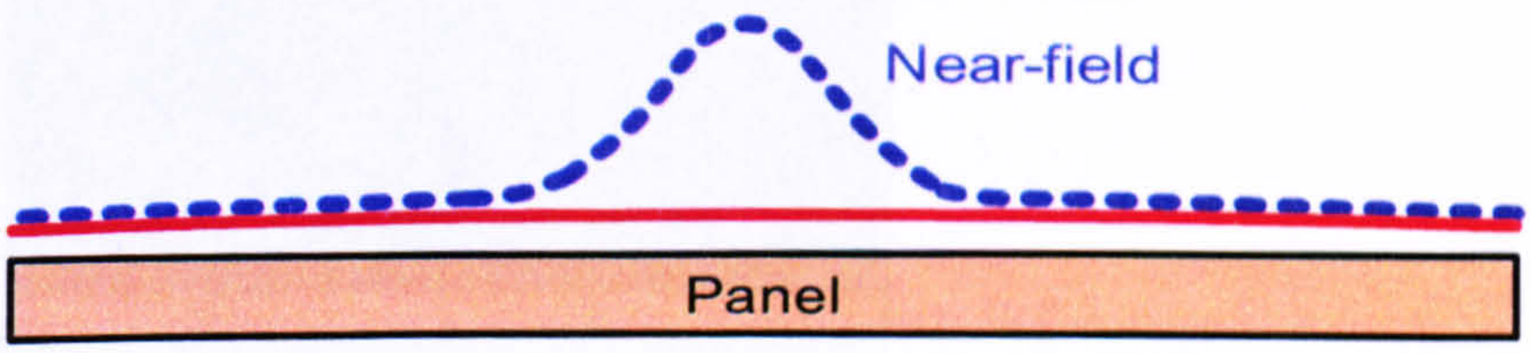

Figure 5.3.3 Distribution of specific impulse from near field loading (Pope, 2002)

5.4 Response of the reinforced concrete primary slab

5.4.1 Structural damage associated with groundshock loading

The implementation of charges relative the secondary slab involved drilling a hole into the slab. This allowed different charge positions to exist relative to the slab. The drilled hole would have instantly set up planes of weakness within the slab, which would have increased in severity after detonation. The influence of the damage caused by the pre-weakening was not evaluated. The drilled hole represented the penetration of a weapon prior to detonation. The initial loading induced into a primary slab was caused by charge position A. Cumulative loading was then induced by charge positions B, C and D. The individual contribution of damage caused by individual charge positions B, C and D was unknown, as there was not enough time to investigate this further. The results from Stage III of the test matrix involved omitted secondary slabs and were compared to a series of identical tests with positioned secondary slabs. Unfortunately a comparison of impulse could not be performed due to damaged instrumentation. The final third cumulative hit to a protected and unprotected primary slab involved a contact charge. The protective primary slab indicated further damage, whilst the unprotected slab endured a massive perforation, covering 1/3 of the area of the slab. The cumulative damage from two previous hits caused cracking only. This did not indicate a potential perforation, as illustrated in table 5.4.1. It was assumed that internal damage from the first two cumulative hits must have significantly weakened the primary slab. A non-destructive method of determining the internal damage to the primary slab would have evaluated this phenomenon. **Wood (1961)** commented on the nature of cracks that formed on reinforced concrete slabs when subjected to explosive loading, stating that '*the face of the slab that is in contact with the greatest proportion of the charge is forced into compression. Yield lines in the form of circumferential cracks occur on the surface as a result of radial forces*'. These yield lines were evident on the top face of an unprotected primary slab as illustrated in table 5.4.1.

Table 5.4.1 Damage comparison to two primary slabs subjected to cumulative loading with secondary slabs omitted and positioned within the soil overburden

	Secondary slabs omitted	Secondary slabs positioned
Top face		
Bottom face		
Hits	3	3

Secondary slabs omitted – unprotected primary slab
Secondary slabs positioned – protected primary slab

Deng *et al* (2004) differentiated between the effects of perforation and punching of concrete fragments. A concrete fragment expelled by punching action would have a greater mass travelling at a larger velocity. This would have a detrimental effect on the internal space within a structure. The damage to the unprotected primary slab RCR73IT17-19 as illustrated in table 5.4.1 indicated punching action of the concrete. This caused the removal of a concrete section, evident after the test. Anti-scabbing plates attached to the bottom face of a slab as used by **Pope (2002)** would have prevented this.

The findings from Stage III of the test matrix indicated that the impulse histories rather than a single induced impulse, caused by a contact charge, significantly increased the severity of damage to a primary slab with the assistance of internal weakening.

5.4.2 Classification of damage mechanisms

If a time limit had not governed the experimental work, the test matrix would have been significantly extended. This would have allowed the variation of a single parameter per test, as discussed in section 3.7, whilst the other parameters remained constant. There was no opportunity to do this and so the test matrix had to be significantly reduced.

The final cumulative damage encountered by each of the primary slabs was of a smaller magnitude of damage than would have been experienced if a single secondary slab remained in position.

If a procedure that yielded this were adopted, it would not have been possible to evaluate the damage to the secondary slabs caused by the four charge positions. All four primary slabs used during Stage I of the test matrix were damaged to different degrees of severity for the following reasons:

1. number of varying cumulative hits associated with charge positions,
2. decrease in the charge standoff,
3. decrease in the soil overburden below the secondary slab.

It was evident from the damaged primary slabs in table 5.4.2 that a decrease in the charge standoff, soil overburden and the number of cumulative hits, increases the severity of damage to a primary slab. The damaged primary slabs from Stage I all illustrated a sequence of yield line mechanisms that dictated the damage mode. These were caused by an increase in the magnitude of load, which decreased spatially upon the top face at smaller charge standoffs.

The damage to each of the primary slabs has been associated with the cumulative impulse history corresponding to the sum of induced loads, sustained during the cumulative attack.

An impulsive response was only associated with slab RCR73IT1-4. It was likely that slabs RCR73IT5-8, RCR73IT9-11 and RCR73IT12-13 responded dynamically. This was not proven due to a lack of data. A measurement of impulse defined as the cumulative impulse history was associated with final degree of damage to all four slabs, as illustrated in figure 5.4.2.

Due to the small charge standoffs positioned relative to slabs RCR73IT9-11 and RCR73IT12-13, DPG1 was not positioned centrally on the top face of the primary slab. Instead it was positioned at an eccentricity along plane O-B1. This prevented an accurate comparison with the other cumulative impulse histories, but ensured the gauge's survival.

The increase in damage from slab RCR73IT1-4 to slab RCR73IT5-8 was associated with a central cumulative impulse history difference of 10kPa-s (36.8-26.5kPa-s).
Slab RCR73IT9-11 experienced a cumulative impulse history of 45.5kPa-s recorded at an eccentricity of 150mm from the centre of the slab.
The central cumulative impulse history was not established for slab RCR73IT9-11 and has not been indicated in table 5.4.2. However, the predicated central impulse would have been >45.5kPa-s. The increase in damage from slab RCR73IT5-8 to slab RCR73IT9-11 was associated with an increase in the cumulative impulse history >10kPa-s (45.5-36.8kPa-s). The exact value was unknown.

Table 5.4.2 Cumulative damage inflicted upon the primary slabs in Stage I

	Group 1 tests	Group 2 tests	Group 3 tests	Group 4 tests
Top face				
Bottom face				
Slab	RCR73IT1-4	RCR73IT5-8	RCR73IT9-11	RCR73IT12-13
Z_1 (mm)	500mm	300mm	150mm	75mm
Z_2 (mm)	500mm	500mm	500mm	500mm
Cumulative hits	4	4	3	2
Charge standoffs (mm)	540,440,350,300	340,240,150,100	190,90,0	113,13
Central impulse histories (kPa-s)	1.3, 7.3, 8.1, 9.8	2.6, 8.4, 10.3, 15.5		
Magnitude of the central cumulative impulse history (kPa-s)	26.5	36.8	*>45.5*	*

Z_1 = Soil overburden contained between the primary and secondary slabs
Z_2 = Soil overburden above the secondary slab
*****Variability of DPG1s eccentric positioning prevented a cumulative impulse history from being established.*

Pope (2002) and **Duranovic (1994)** both commented on the presence of circumferential and radial cracks, which were apparent upon slabs subjected to airblast. These crack patterns were also observed upon the damaged primary slabs in table 5.4.2. The increase in damage associated with concentration of different crack patterns have been identified as following a suggestive trend. The chronological order is described as follow:

1. corner cracks,
2. diagonal cracks,
3. central square crack – Region occupied within a plastic hinge,
4. central circumferential crack – Region occupied within a plastic hinge,
5. discontinuous circumferential cracks.

Primary slab RCR73IT9-11 associated with group 3 tests has been excluded from table 5.4.3 because crack patterns were not visible on the surface, as the concrete cover has been reduced. This was due to slab impact upon the ground of the test site during its removal from within the test cell. An improved slab removal scheme should be considered during future testing in similar environments.
Slabs with a greater degree of damage contained crack patterns that were evident on less damaged slabs, but also contained a greater number of different crack patterns as illustrated in table 5.4.3.

Table 5.4.3 Simplistic crack patterns inflicted upon the primary slabs in Stage I.

	Group 1 tests	Group 2 tests	Group 4 tests
Top face	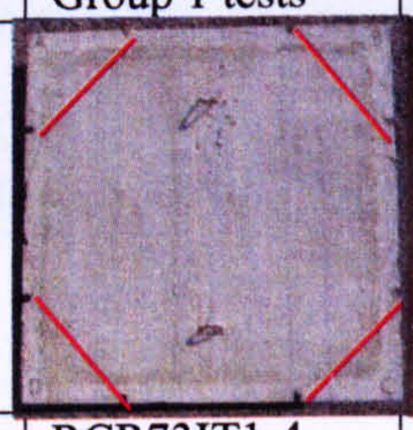	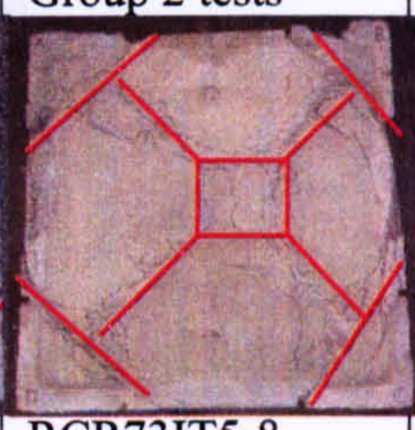	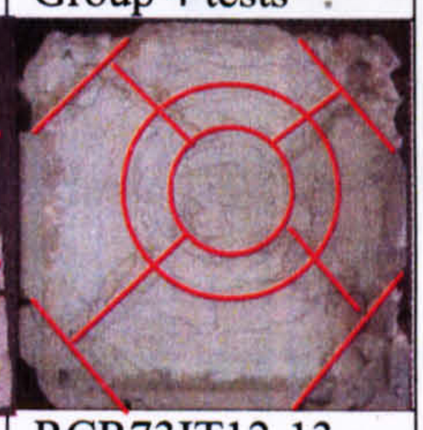
Slab	RCR73IT1-4	RCR73IT5-8	RCR73IT12-13
Chronological order of crack developments	1.Corner cracks	1.Corner cracks & spalling 2.Diagonal cracks 3.Central square cracking	1.Corner cracks and spalling 2.Diagonal cracks and spalling 3.Central circumferential cracking 4.Discontinuous circumferential cracking within the four quadrants
Cumulative hits	4	4	2
Charge standoffs (mm)	540,440,350,300	340,240,150,100	113,13

The severity of damage to the bottom face was linked with the formation of a plastic hinge on the top face, as illustrated in plate 5.4.1. The spreading out of the plastic hinge from the centre of the slab indicated a greater area of the slab that no longer responded elastically. Slab RCR73IT1-4 contained hairline cracks upon the top face, as well as an undamaged cross-sectional elevation as illustrated in figure…. It was assumed that the response was elastic.
The plastic zones have been clearly indicated on slabs RCR73IT5-8 and RCR73IT12-13 in plate 5.4.1. A 'square' region, offset from the centre of slab RCR73IT5-8, has indicated the area surrounding plastic deformation. A 'circular' region upon slab RCR73IT12-13 has indicated a greater area of plastic deformation.

The plastic zones were identified much clearer upon the top face of a primary slab as the bottom face only indicated radial cracking and scabbing. The geometry of damage to both faces differed for two reasons:

1. Bottom face - flexural response as well as stress wave reflection from a free surface.
2. Top face - flexural response due to load transfer from soil to concrete.

Damage mechanisms in the form of local shear and spalling, which occur within a near field environment as described by **Krauthammer (1999)** were also evident upon slab RCR73IT12-13 in plate 5.4.1.

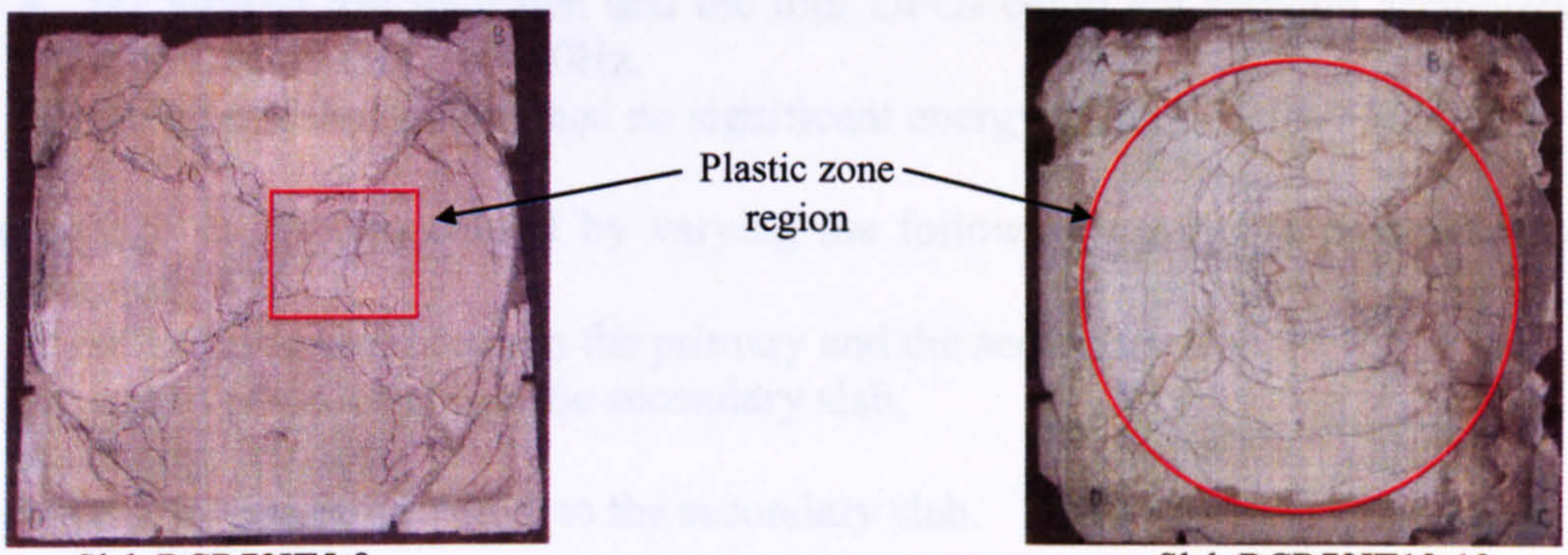

Plate 5.4.1 Identification of the plastic zone on two primary slabs

An elastic and three simplistic plastic hinge mechanisms are illustrated in table 5.4.4. The mechanisms are not symmetrical due to the non-symmetrical distribution of the loading, but indicate approximate regions of concrete plasticity.

Table 5.4.4 Plastic hinge formation on the top face of the primary slabs

	Group 1 tests	Group 2 tests	Group 3 tests	Group 4 tests
Plastic hinge formation along plane X1-X2				
Slab	RCR73IT1-4	RCR73IT5-8	RCR73IT9-11	RCR73IT12-13
Mechanism identification	Elastic response after 4 tests	Expanding plastic hinge after 4 cumulative hits	Greater central region acquiring a plastic hinge after 3 cumulative hits	Totally plastic after 2 cumulative hits

The bottom face of the primary slabs contained an abundance of radial cracks only. However the variability of the following was observed:

1. concentration of cracks,
2. width of a crack,
3. depth of crack,
4. exposure of the reinforcement.

5.5 Summary

The findings from the calibration of the DPGs are that

1. the Fast-Fourier-Transform analysis indicated DPG1 had a natural frequency of 12500Hz,
2. the Fast-Fourier-Transform analysis indicated that DPG1 could respond accurately to transient pneumatic loading within the range 0-7000Hz,
3. the Fast-Fourier-Transform analysis indicated that DPG1 could respond to frequencies associated with groundshock within the range 0-5000Hz,
4. the airblast test indicated that the four DPGs could not respond accurately to high frequencies >10000Hz,
5. the groundshock contained no significant energy at frequencies >5000Hz.

The change in impulse caused by varying the following geometric parameters was investigated:

1. soil overburden between the primary and the secondary slab,
2. soil overburden above the secondary slab,
3. charge standoff,
4. charge position relative to the secondary slab.

The charge standoff values associated with each charge position varied with variation in soil overburden depth below the secondary slab. This indicated that both the charge standoff and soil overburden parameters influenced the loading applied to a primary slab.
When a secondary slab was omitted the charge position parameter ceased to exist and the variation in soil overburden did not influence the variation in charge standoff. However, the soil overburden only influenced the loading when it was reduced to depths that exposed the charge to the air.
The presence of a secondary slab reduced the loading wave velocity by approximately 50% identified during the implementation of charge positions A, B and C. Analysis of the geometric parameters indicated the following:

1. There was a greater percentage increase in impulse associated with charge position A than there was in a reduction of soil overburden beneath the secondary slab.
2. Charge positions A and D indicated the largest increase in impulse whilst B and C were less.

The variability of the concrete strengths was interpreted from values of standard deviation and associated with a standard of control defined as 'Good', in accordance with standard criteria. The distribution of bulk density and moisture content data implied a normal distribution. The variability of the bulk density and moisture content was expressed as a coefficient of variation. These values were put into context with values from the literature and similar trends were identified. The moisture content can have a significant effect on stress wave propagation as mentioned in the literature. Moisture contents much larger than those presented in this thesis were reported in published literature and were said to influence stress wave propagation. No specific comments in the literature were made that discussed the effect caused to stress wave propagation at moisture contents <10%. Therefore it suggested that the moisture contents recorded did not affect stress wave propagation.

The variability in the density index values suggested that there was a similar degree of soil compaction prior to detonation in all the explosive tests. It was then demonstrated that the initial degree of soil compaction did not influence the propagation of the stress wave. The high transient stresses associated with the stress wave would have overridden any initial degree of compaction.

Steel plate test data indicated a linear relationship between impulse and maximum peak deflection. This together with low t_d/T values gives strong support to the assumption that the steel plate response to groundshock was impulsive.

Test data from tests RCIT1-4 on a primary slab also indicated an impulsive response based upon t_d/T ratio values. The energy balance procedure was not performed due to a lack of data.

Pressure-time histories were recorded by the DPGs and the following found:

1. A numerical simulation performed in AUTODYN2D gave an impulse, which was of a similar magnitude to that recorded experimentally, giving a confidence in the DPG results.
2. The impulse at the centre of both the primary slab and steel plate was always the greatest. Its variation along the DPG plane decayed over a range of 100mm from the centre, thereafter remaining constant.
3. The inclination of the charge in both the steel and concrete tests did not alter the geometry of impulse variation along the respective DPG plane. The impulse was still greatest at the centre.
4. The limitations of the gauges occurred at close charge standoffs where high magnitude stress waves were present, which increased the chance of damage.

The following relates to the damage of a primary slab:

1. Primary slab RCR73IT1-4 was subjected to four cumulative hits and responded impulsively. This implied that the slab responded once the load had significantly depreciated.
2. The impulse histories rather than a single induced impulse caused by a contact charge significantly increased the severity of damage to a primary slab by internal pre-weakening.
3. A decrease in the charge standoff, soil overburden and the number of cumulative strike parameters increased the severity of damage to a primary slab.
4. The damaged primary slabs all illustrated a sequence of yield line mechanisms that suggested a global bending response mode.
5. Circumferential and radial cracks were apparent upon the damaged primary slabs as well as on slabs subjected to airblast as indicated in the literature.
6. Slabs with a greater degree of damage contained crack patterns that were evident on less damaged slabs, but contained a greater number of different crack patterns associated with a greater magnitude of loading.
7. It was evident that the severity of damage to the bottom face of a primary slab was linked to the formation of a plastic hinge on the top face. The spreading out of the plastic hinge from the centre of the slab indicated a greater area of the slab that no longer responded elastically.

It is arguable that there were intermediate stages of damage severity during cumulative attack upon the primary slabs. These were not investigated but the final degree of damage was. The final degree of damage upon the top face of primary slabs varied in severity and a chronological order of crack patterns were observed:

1. corner cracks,
2. diagonal cracks,
3. central square crack – Region occupied within a plastic hinge,
4. central circumferential crack – Region occupied within a plastic hinge,
5. discontinuous circumferential cracks.

Chapter Six

Conclusions

The conclusions relate to the following:

1. The structural response of the steel plate and reinforced concrete slabs.
2. The variability of both the material and geometric parameters in influencing groundshock loading.
3. The soil compaction.
4. The severity of damage subjected to the primary and secondary slabs.

1 (a) The pressure-time history profiles recorded by the DPGs during groundshock approximated an idealised half sine-wave load function.

1 (b) Groundshock loading did not excite DPG1's natural frequency; Airblast loading did. This indicated that the soil damped the higher frequencies contained within the propagating stress wave.

1 (c) Two methods were used to evaluate an impulsive response of the steel plate and primary slab RCR73IT1-4. An intial energy balance procedure illustrated a linear relationship between the maximum induced kinetic energy and the maximum strain energy in the plate. Such a relationship indicated an impulsive response. The second method involved ratio value calculations of load duration to natural period of response. All the values were within or very close to the impulsive range, suggested in the literature.

1 (d) The second method in determining an impulsive response was applied to the concrete data associated with slab RCR73IT1-4, used during tests RCIT1-4. A lack of results due to damaged instrumentation prevented the initial method from being performed. All the ratio values were or close to the impulsive range. Due to incomplete DPG and LVDT data, an impulsive response was not determined for the other three primary slabs RCR73IT5-8, RCR73IT9-11 and RCR73IT12-13 in preceding tests. At smaller charge standoffs the primary slabs experienced a greater degree of damage, affecting their strength and stiffness parameters. This would have influenced the response and possibly caused the slabs to respond even more impulsively due to a progressive increase in natural period as damaged increased. This suggestion was supported by the increase in the natural period exhibited in tests RCIT1-4.

2 (a) The variability of the soil bulk density and moisture content parameters was defined in terms of a coefficient of variation and put into context with the literature, which suggested a similarity in variability. The literature contained moisture content values, larger than those stated in this thesis that were said to cause a profound influence on stress wave propagation. There was a lack of literature regarding the effect caused to stress wave propagation at moisture content values <10%. This suggested that values of this order have a negligible effect on stress wave propagation.

2 (b) The variability of the concrete compressive and tensile strength data was described in terms of a standard deviation and classified as being within a 'Good' standard of control.

2 (c) The positioning of a secondary slab introduced parameters associated with charge position and two soil overburden depths, above and below the secondary slab.

2 (d) At soil overburden depths >500mm beneath a secondary slab the variability of charge positions A–D relative to the slab had a negligible effect on the central impulse on the primary slab. At values <300mm, the difference in central impulsive caused by the four change positions increased.

2 (e) The charge standoff parameter was the most sensitive in influencing the magnitude of groundshock.

2 (f) The numerical simulations performed in AUTODYN2D suggested that the soil overburden above the top face of the secondary slab caused a change to the damage geometry of a secondary slab. However, a negligible change in the loading distribution across the primary was identified.

3 (a) The density index values in accordance with the literature indicated that the degree of soil compaction during the setup of each explosive test was similar.

3 (b) The magnitude of the propagating stress wave overrides any initial form of soil compaction prior to charge detonation. This was due to the extremely high stresses induced into the soil after detonation, (which would have been well above the initial insitu soil stresses.)

4 (a) The evaluation of damage mechanisms upon the primary slabs increased in severity at smaller values of charge standoffs, also causing damage to the instrumentation.

4 (b) The damage to the secondary slabs was qualitatively analysed with the identification of a number of crack patterns. The position of a charge relative to the slab dictated the sequence of crack patterns on both faces.

4 (c) The four primary slabs from Stage I contained damage mechanisms that were associated with the spatial distribution and magnitude of a cumulative load.

4 (d) The removal of a secondary slab during cumulative loading caused unnoticeable internal weakening The extent to which was unidentifiable from the external damage that caused a loss in structural strength and stiffness.

Chapter Seven

Future work

7.1 Improvements to the experimental testing

More DPGs positioned over the top face of the primary slab would have helped to associate damage with a spatial distribution of load, rather than just along the plane that experienced the greatest load distribution.
It was observed during the explosive tests that the clamped supports around the perimeter of the primary slab, as illustrated in plate 3.6.2, did not provide full fixity. Slip and rotation at the supports were discovered after a number of cumulative hits. The effect it had to the overall damage in the form of cracking, cratering and perforation was unknown. A more rigid method of fixing the primary slab, or a measurement of slip/rotation should be used in any future work
The use more LVDTs positioned on the bottom face of a primary slab would help determine a spatial variation in deflection. Three-dimensional plots of deflection could then be associated with damage. However, an increased number of LVDTs would be cost dependent as well as requiring a greater number of channels on the digital storage oscilloscopes.
The strain gauges attached to the reinforcement within the primary slabs should have been neglected for two reasons:

1. Once damaged during a cumulative series of loadings, they could not be replaced and were deemed unusable.
2. The strain-time histories were not as valuable in assessing structural response.

7.2 Advancement in associated research

7.2.1 Soil compaction

The importance of soil compaction prior to charge detonation has been evaluated as having a negligible influence on stress wave propagation. However, there is a lack of literature that discusses changes in soil bulk density caused by stress wave propagation. A procedure could be considered using a Split-Hopkinson-Pressure-Bar to assess the increase in soil bulk density throughout a soil filled bar. The results from Split-Hopkinson-Pressure-Bar tests could be used to construct an equation of state model, as is illustrated in figure 4.6.5 for different ranges of loading magnitude and loading rates.

7.2.2 Weakening of a primary slab

It has been concluded that cumulative loading weakens the internal structure of the primary slab, even though this might not be visible on the surface. Non-destructive procedures such as pundit testing would have helped identify and even quantify the internal damage. A greater degree of internal damage would indicate a decrease in the elastic modulus, consequently decreasing the stress wave velocity through the slab.

The degree of internal damage could then be related to the stress wave propagation velocity through the slab.

7.2.3 Cumulative loading on primary and secondary slabs

The final damage experienced by the primary slabs caused by cumulative loading was of a smaller magnitude, to that which would have been caused if a single secondary slab remained in position during the loadings.
In a real situation a cumulative attack from the air would strike a single secondary slab a number of times.
A further series of tests could involve positioning a secondary slab within the soil overburden and leaving it during a series of cumulative loadings. The damage inflicted upon the primary slab could then be compared to the damage sustained by a primary slab from Stage I of the test matrix, which involved the implementation of a fresh secondary slab after each charge detonation.

7.2.4 Further ideas

Tests performed at a larger scale would use the scaling law by exploring its validity for buried structures for predictions of maximum impulse and damage. The experimental setup could be modelled using the non-linear finite element programme AUTODYN to predict impulse and damage.
The damage to both the secondary and primary slabs could be analysed with a varying slab thickness.
High-bandwidth, fibre optic pressure sensors have been designed by **MacPherson *et al* (2000).** The gauges are small enough to be positioned flush within a thick steel plate. A geometric formation of these gauges over the plan area of a steel plate would help identify the spatial variation in loading associated with an inclined charge. The loading at small charge standoffs could also be evaluated and then associated with the deflection of a primacy slab. This would have helped characterise the response of primary slabs RCR73IT5-8, RCR73IT9-11 and RCR73IT12-13, which was not identified due instrumentation problems at lower values of charge standoff.
During the experimental work more than one parameter was being assessed during a single test. In a proposed investigation the charge standoff would remain constant in three situations when;

1. secondary slab is omitted,
2. secondary slab is directly above the charge,
3. secondary slab is directly below the charge.

A geometric layout of the test configuration with an omitted secondary slab is illustrated in figure 7.1.1 and the positioned slabs in figure 7.1.2. The charge standoff parameter would remain constant during the tests. Although a primary slab is indicated in both figures 7.1.1 and 7.1.2 it could be replaced with a thick steel plate that would respond elastically.
Two objectives would be considered:

1. To establish whether varying the position of the secondary slab affects the structural response.
2. To establish whether the magnitude of loading upon the primary slab varies with the position of a secondary slab.

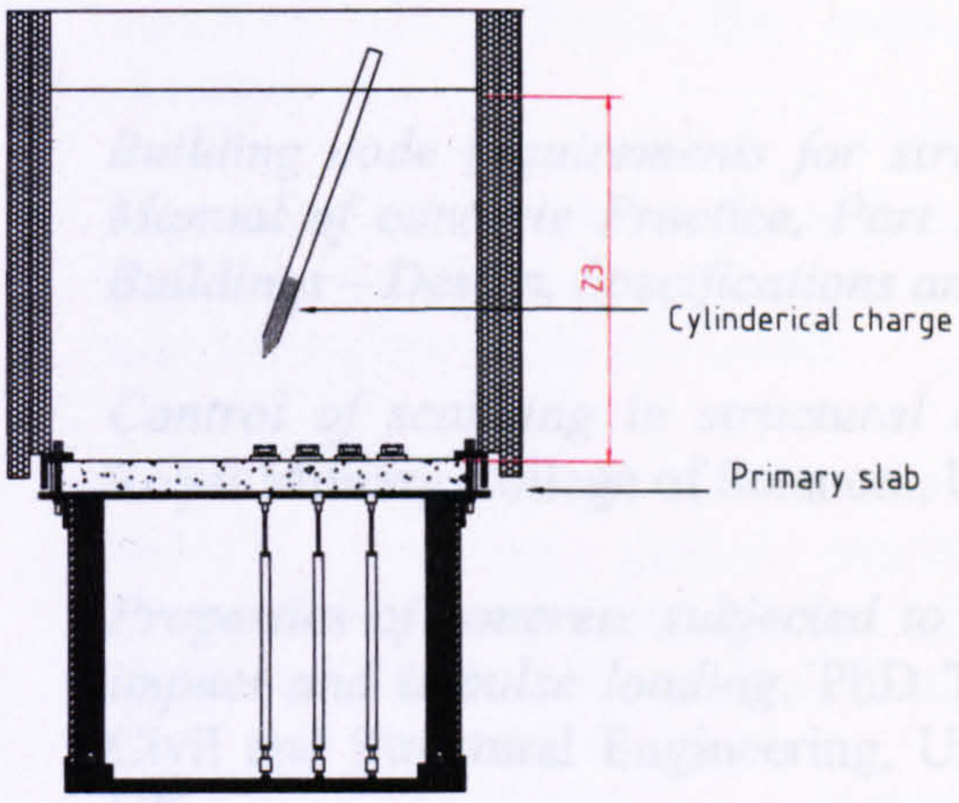

Z_3 = Total soil overburden carried by a primary slab when a secondary slab is not present

Figure 7.1.1 Geometric setup up with an omitted secondary slab

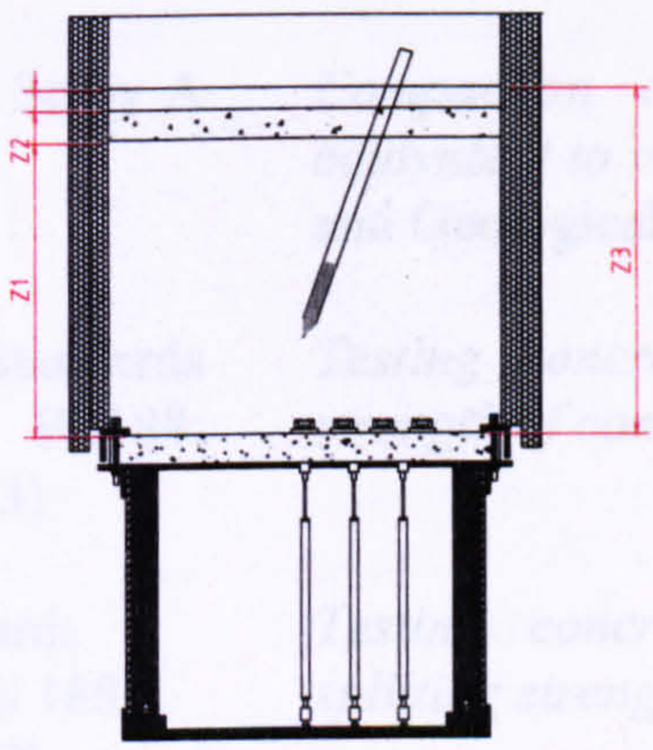

Test a) Secondary slab above the charge

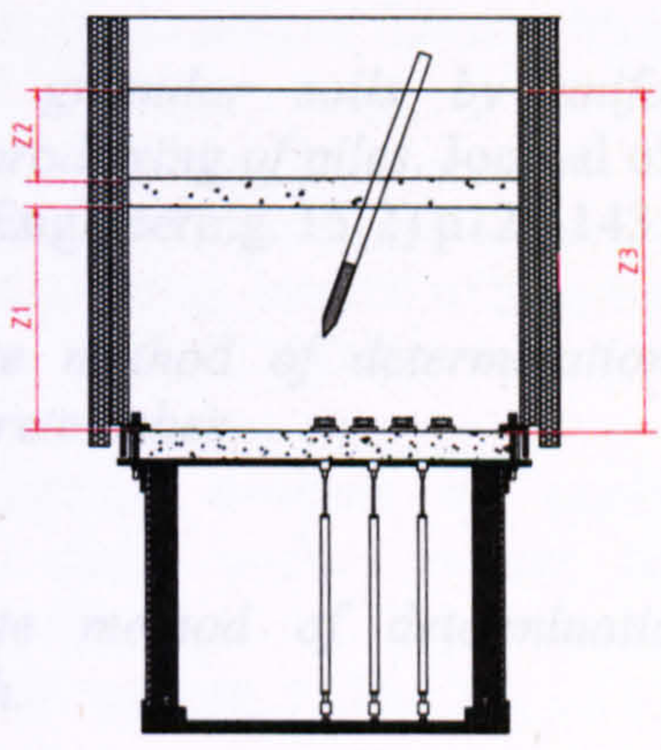

Test b) Secondary slab above the charge

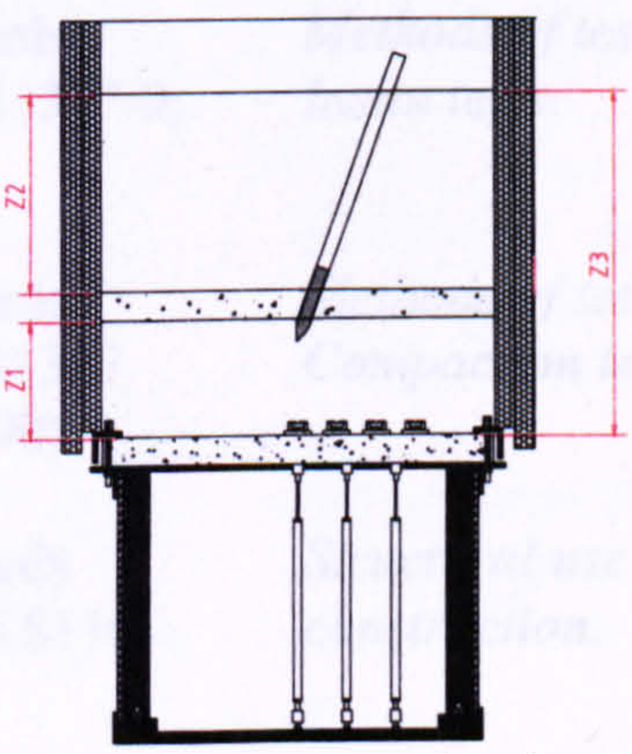

Test c) Secondary slab relative to the charge

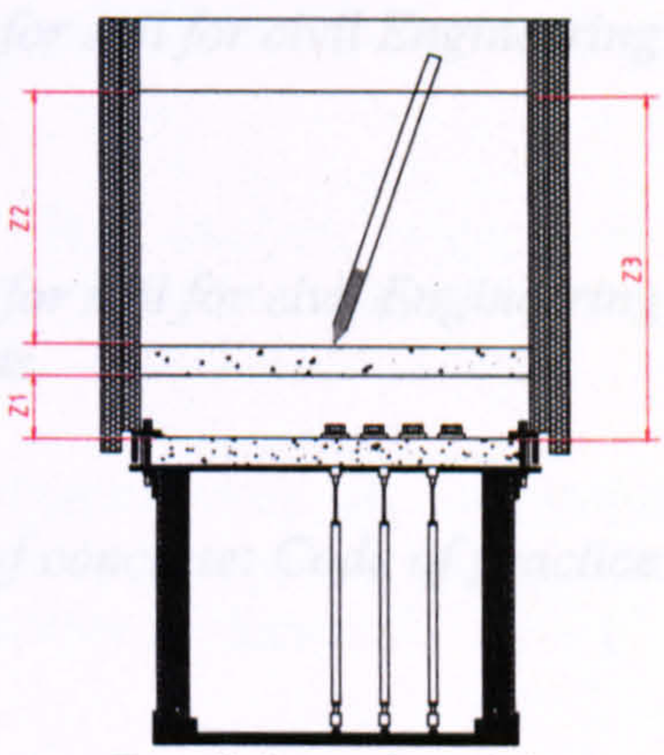

Test d) Secondary slab below the charge

Z_1 = Soil overburden contained between the primary and the secondary slab
Z_2 = Soil overburden above the secondary slab
Z_3 = Total soil overburden carried by a primary slab when a secondary slab is not positioned

Figure 7.1.2 Geometric setup of proposed tests

References

ACI 318-95 (1996) — *Building code requirements for structural concrete, ACI Manual of concrete Practice, Part 3: Use of concrete in Buildings – Design, Specifications and Related Topics.*

Ahmed I (1994) — *Control of scabbing in structural concrete.* MSc thesis, Royal Military College of Sciences, UK.

Archer B (1985) — *Properties of concrete subjected to explosively generated impact and impulse loading.* PhD Thesis, Department of Civil and Structural Engineering, University of Sheffield, UK.

AUTODYN theory manual (1998) — Available from Century Dynamics. Horsham, West Sussex, UK.

Bement R & Selby A (1997) — *Compaction of granular soils by uniform vibration equivalent to vibrodriving of piles.* Journal of Geotechnical and Geological Engineering. 15(2) p121-143.

British Standards Institution, BS188: Part 116 (1983) — *Testing concrete method of determination of crushing strength of concrete cubes.*

British Standards Institution, BS 1881: Part 117 (1983) — *Testing concrete method of determination of tensile splitting strength.*

British Standards Institution, BS1377-9, (1990) — *Methods of test for soil for civil Engineering purposes. Insitu tests.*

British Standards Institution, BS1377 Part 4:4.3 (1990) — *Methods of test for soil for civil Engineering purposes. Compaction tests.*

British Standards Institution, BS 8110 (1997) — *Structural use of concrete: Code of practice for design and construction.*

British Standards Institution, BS 4449 (1997) — *Specification for carbon steel bars for the reinforcement of concrete*: Annex E - Inspection testing and certification.

British Cement Association (2000) — Specifying concrete to BS EN 206-1 / BS 8500.

Buell JW (1984) *Steel fibre reinforcement to control spalling in structural concrete.* MSc Thesis, The Royal Military College of Science, UK.

Bull J W & Woodford C H (2000) *Stress and displacement effects due to subsurface barriers laid under cement concrete runways.* Journal of Computers and Structures. 78(4) p375–383.

Cameron R.K (2000) *A methodology for modelling the sequential impact of modern precision guided munitions-phase II.* 16th international symposium on the military aspects of blast and shock, Keble college, Oxford. p283-287.

Chapman T.C, Rose T.A & Smith P.D (1994) *Blast wave simulation using AUTODYN2D: A parametric study.* International Journal of Impact Engineering. 16(4) p777-787.

Clough R & Penzien J (1993) *Dynamics of structures: Second Edition.* McGraw-Hill Book Co.

Davies M R & Williams, A J (1992) *Centrifuge modelling the protection of buried structures subjected to blast loading.* Journal of Structures under shock and impact. 13(7) p237-248.

Deng G, Jun D & Zhang X (2004) *Numerical simulation analysis on explosion damage shapes of RC slabs under contact detonation.* 2nd International Conference on Protection of Structures against Hazards, Singapore. p155-158.

Dongen P & Weerheijm J (1992) *Interaction of ground shock with soil pressure transducers.* Journal of Structures under Shock and Impact. 3(2) p625-633.

Duranovic N (1994) *Validation of blast analysis algorithms.* PhD Thesis, Department of Civil and Structural Engineering, University of Sheffield, UK.

Famiglietti J, Devereaux C, Laymon T & Tsegaye P (1999) *Ground-based investigation of soil moisture variability within remote sensing footprints during the southern Great Plains.* Water Resources Research. 35(6) p1839-1851.

Gary G, Klepaczko J & Zhao H (1995) *Generalisation of split Hopkinson Bar technique to use viscoelsatic bars.* International Journal of Impact Engineering. 16(3) p529-530.

Hader H (1983) *Effects of bare and cased explosive charges on reinforced concrete walls.* Proceedings of the first International Symposium of Interaction of Non-nuclear Munitions with Structures, Colorado, USA. p231-246.

Hanssen A.G, Enstock L & Langseth M (2002) *Close-range blast loading of aluminium foam panels.* International Journal of Impact Engineering. 27(5) p593-618.

Head K.H (1992) *Soil Classification and compaction tests: Manual of soil laboratory testing, Volume 1, Second Edition.* Pentech Press limited.

Heap J.C (1964) *Bending of circular plates under a variable symmetrical load.* ANL-6882 Physics AEC Research and Development report, Argonne National Laboratory, Illinois, USA. p569-583.

Horvath V, Janosi I & Vella P (1996) *Anomalous density dependence of static friction in sand.* Physical review E. 54(2) p2005-2009.

Hu J, Wang A, Dong J, Deng G & Yang K (2004) *Experimental investigation on contactile explosion damage effect to fiber reinforced concrete slabs with soil bedding cushion.* 2nd International Conference on Protection of Structures against Hazards, Singapore. p199-203.

Hyde D.W (1991) *Conventional Weapons Effects Program.* US Army, Vickburg Waterways Experiment Station, Vicksburg, Mississippi, USA.

Khan P.K & Keller M.D (1997) *Behaviour and evaluation of an existing underground structure subjected to impulsive loads from an internal explosion.* 2nd Asia-Pacific Conference on Shock & Impact Loads on Structures. Melbourne, Australia. p205-211.

Kong F.K & Evans R.H (1987) *Reinforced and Prestressed Concrete: 3rd Edition.* Chapman & Hall Ltd, Hong Kong. p62-64.

Krauthammer T (1999) *Modern protective structures-Design, analysis and evaluation.* Course Notes from Penn State University, USA

Lam N, Mendis P & Ngo T (2004) *Response spectrum solutions for blast loading.* Electronic Journal of Structural Engineering. 4(6) p28-44.

Low H & Hao H (2001) *Reliability analysis of reinforced concrete slabs under explosive loading.* Journal of Structural Safety. 23(2) p157-178.

Macpherson W.N, Gander M.J, Barton, J.S, Jones J.C, Owen C.L, Watson A.J & Allen R.M (2000) *Blast-pressure measurement with a high-bandwidth fibre optic pressure sensor.* Journal of Measurement Science and Technology. 11(9) p95-102.

Ma G.W, Hao H & Zhou Y.X (1999) — *Numerical simulation of underground explosion.* Proceedings of the Joint Singapore-Norway Technical Workshop on Ground Shock, Singapore. p97-106.

McVay M (1988) — *Spall damage of concrete structures.* Published by Dept of the Army, US Army Corps of Engineers, USA.

National Defence Research Committee (1946). — *Effects on impact and explosion.* Summary Technical Report of Division 2, Volume 1, Washington DC, USA.

Nevile A M (1981) — *Properties of concrete: 2nd Edition.* Published by Pitman, UK.

Park R (2000) — *Reinforced concrete slabs, Second Edition.* John Wiley & Sons Inc, Canada.

Perry S H, Dinic G & Bischoff P.H (1992) — *Formation of full depth cracks in concrete slabs subjected to hard impact.* Conference of Structures under Shock and Impact II, Trinity College, Dublin. p73-82.

Pope D.J (2002) — *Response prediction of plate-reinforced concrete panels exposed to near-field blast.* PhD Thesis, University of Sheffield, UK.

Plassmeyer C & Nkongolo N (2000) — *Investigation into the Spatial Distribution of Soil Bulk Density, water and Air Contents.* Canadian Journal of Soil Science. 2(3) p3-10.

Pullen A & Newman J (1996) — *Dynamic Properties of Shocked Geological Materials: Final Technical Report.* Published by DERA Farnborough, UK.

Renick J.D (2000) — *Cumulative damage in layered targets.* 16th International Symposium Military Aspects of Blast and Shock, Keble College, Oxford. p23-33.

Smith P.D & Mays G.C (1995) — *Blast Effects on Buildings.* Thomas Telford Ltd, London, UK.

Smith P.D and Hetherington J.G (1994) — *Blast Ballistic Loading of Structures.* Butterworth-Heinemann Ltd, Oxford, UK.

Tedesco J.W, Hayes J R & Landis D.W (1987) — *Dynamic response of layered structures subject to blast effects of non-nuclear weaponry.* Journal of Computers & Structures. 26(1/2) p79-86.

TM 5-855-1 (1985) — *Fundamentals of protective design for conventional weapons*. US Army Technical Manual, HQ Dept of the Army, Washington DC, USA.

TM 5-1300 (1991) — *Design of structures to resist the effects of accidental explosions*. Dept of the Army, Washington DC, USA.

Tyas A (1999) — *Scientific Evaluation of special equipments*. PhD Thesis, University of Sheffield, UK.

Tyas A and Pope D (2003) — *The Energy Take-Up Of Panels Subjected To Near-Field Blast*. Published in the 1st International Conference on Extreme Loading on Structures, Toronto, Canada. p80-88.

Tyas A & Pope D (2004) — *Response Of Steel Plate Panels To Near-Field Blast Loading*. Published in the 2nd Asia-Pacific Conference on Protection of Structures Against Hazards, Singapore. p83-91.

Watson A.J, Hobbs B & Wright S J (1989) — *Scaling explosive damage to reinforced concrete beams and slabs*. Proceedings of the first International Conference on Structures under Shock and Impact, Cambridge, USA. p15-28.

Warren J (2002) — *A study of the formation and stability of impulsively driven viscous jets*. PhD thesis, Department of Civil and Structural Engineering, University of Sheffield, UK.

Wood R.H (1961) — *Plastic and elastic design of slabs and plates*. Thames and Hudson Ltd, London, UK.

Wright S.J (1991) — *The vulnerability of reinforced concrete elements to explosive loading*. PhD Thesis, Department of Civil and Structural Engineering, University of Sheffield, UK.

Yamaguchi H, Morishita M, Ando T, Tanaka H & Ito T (1999) — *Damage evaluation of the underground reinforced concrete members subjected to explosive loading*. 9th International Symposium on the Interaction of the Effects of Munitions with Structure, Japan. p108-117.

Young W.C & Budynas R.G (2002) — *Roark's formulas for stress and strain*: Seventh edition. McGraw-Hill Companies Inc., Singapore.

Yuetang Z, Mingyang W & Qianqihu Y (1999) — *Wave propagation in a partly saturated soil*. 9th International Symposium on the Interaction of the Effects of Munitions with Structures, Berlin-Strausberg. p222-230.

Zhao Y.P (1998) — *Suggestion of a new dimensionless number for dynamic plastic response of beams and plates*. Archive of Applied Mechanics. 68(7) p524-538.

Zhongqi W & Yong L (2003) *Numerical analysis on dynamic deformation mechanism of soils under blast loading*. Journal of Soil Dynamics and Earthquake Engineering. 23(2) p705-714.

Wang Z & Lu Y (2004) *Numerical Investigation of Effects of Water Saturation on Blast Wave Propagation in Soil Mass*. Journal of Engineering Mechanics. 130(5) p551-561.

Zimmerman H.D, Nguyen C.T & Hookham P.A (1999) *Investigation of spherical vs cylindrical charge shape effects on peak free-air overpressure and impulse*. 9th International Symposium on Interaction of the Effects of Munitions with Structures, Berlin-Strausberg. p334-342.

Appendices

A.1 Analysis of the deflection, strain and pressure results associated with the response of the primary slabs

The raw experimental data recorded using the LVDTs, DPGs and SGs is contained in this section. The positioning of the instrumentation used during an experimental test is illustrated in tables A.1.1 and A.1.2.

Table A.1.1 Positions of the DPGs on the top face of the primary slab along plane O-B1.

Test number	Charge standoff (mm)	Position of DPG1 (mm)	Position of DPG2 (mm)	Position of DP3 (mm)	Position of DPG4 (mm)
RCIT1	540	170	370	470	270
RCIT2	440	0	200	300	100
RCIT3	350	0	200	300	100
RCIT4	300	0	200	300	100
RCIT5	340	0	200	300	100
RCIT6	240	0	200	300	100
RCIT7	150	0	200	300	100
RCIT8	100	0	200	300	100
RCIT9	190	0	200	300	100
RCIT10	90	150	350	450	250
RCIT11	0	150	350	450	250
RCIT12	113	150	350	450	250
RCIT13	13	150	350	450	250
RCIT17	190	0	200	300	100
RCIT18	90	150	350	450	250
RCIT19	0	150	350	450	250

The LVDTs were used to record deflection-time histories at fixed positions on the bottom face of the primary slab along plane O-X2. Three LVDTs were used per test set at fixed positions, as illustrated in table A.1.2.

Table A.1.2 Positions of the LVDTs on the bottom face of the primary slab along plane O-X2.

Test number	Position of $LVDT_{0mm}$ (mm)	Position of $LVDT_{125mm}$ (mm)	Position of $LVDT_{250mm}$ (mm)
RCIT1-19	0	125	250

Strain gauges were attached centrally, to a single rebar that lay on an orthogonal axis in both the top and bottom meshes of a primary slab.

A.1.1 Deflection-time trace results

Group 1 results – Individual test analysis
Comments relating to figure A.1.1 are described below:

1. All three LVDTs show a similarity in response due to a greater spatial distribution of loading across the top face of the primary slab.
2. The jagged traces illustrated were caused by setting the sensitivity too low.

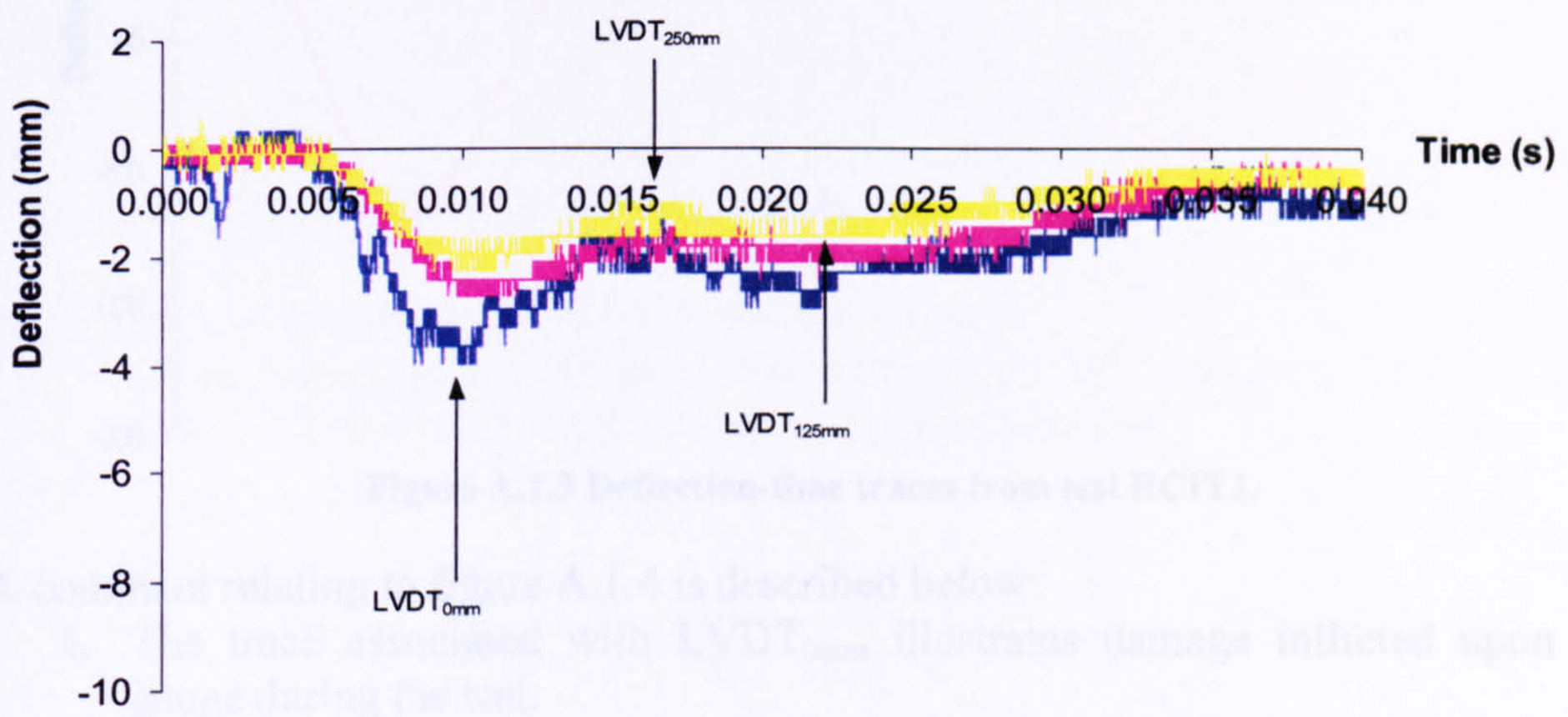

Figure A.1.1 Deflection-time traces from test RCIT1.

Comments relating to figure A.1.2 are described below:

1. Similar magnitudes of the second peak were produced by the LVDTs even though there were differences in maximum peak deflections.
2. Both of the traces illustrate a second peak deflection below what was the datum level of the primary slab. The force causing the slab to move upwards was less than the force of inertia associated with the primary slab.

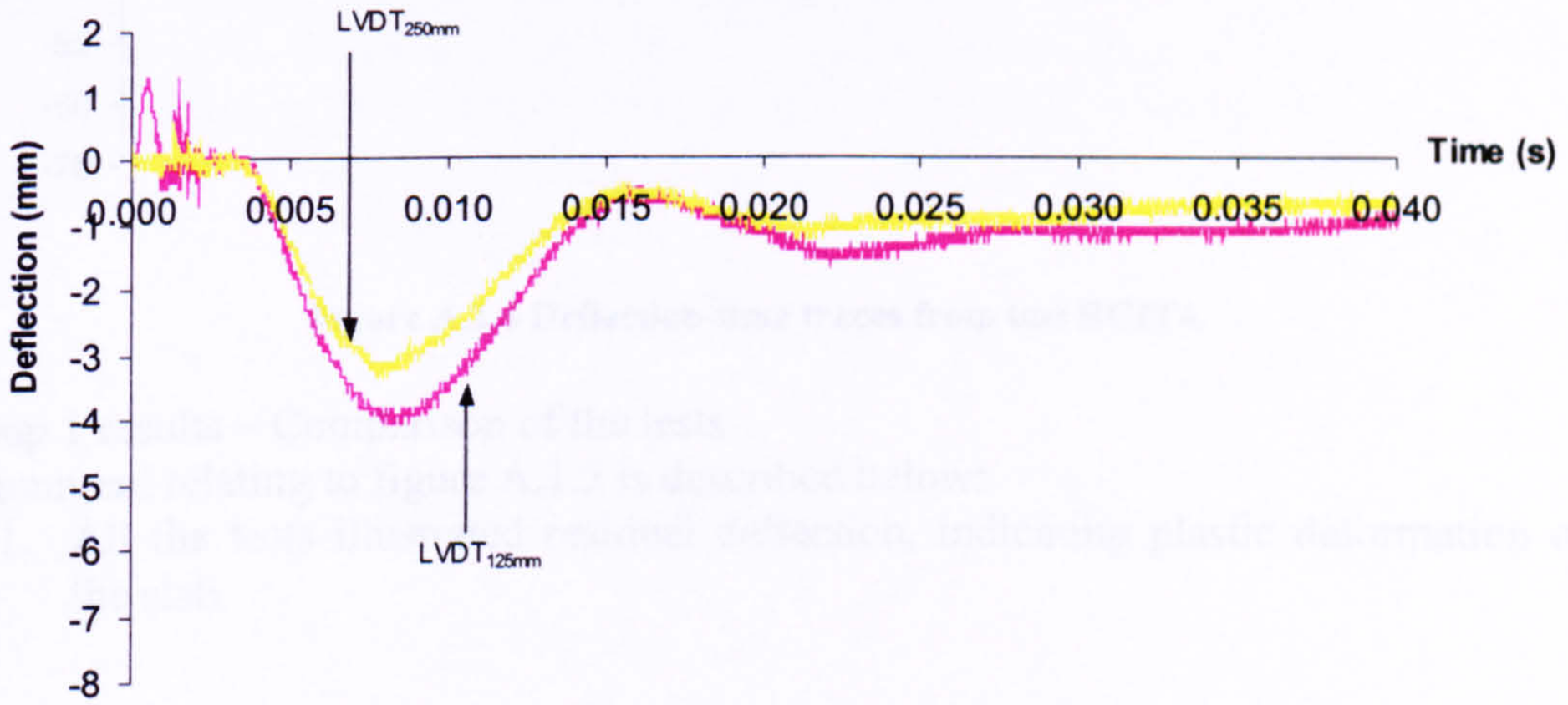

Figure A.1.2 Deflection-time traces from test RCIT2.

A comment relating to figure A.1.3 is described below:

1. After three tests the primary slab displaced at the first mode of vibration, which is indicated by the LVDTs having similar times during the first cycle of vibration.

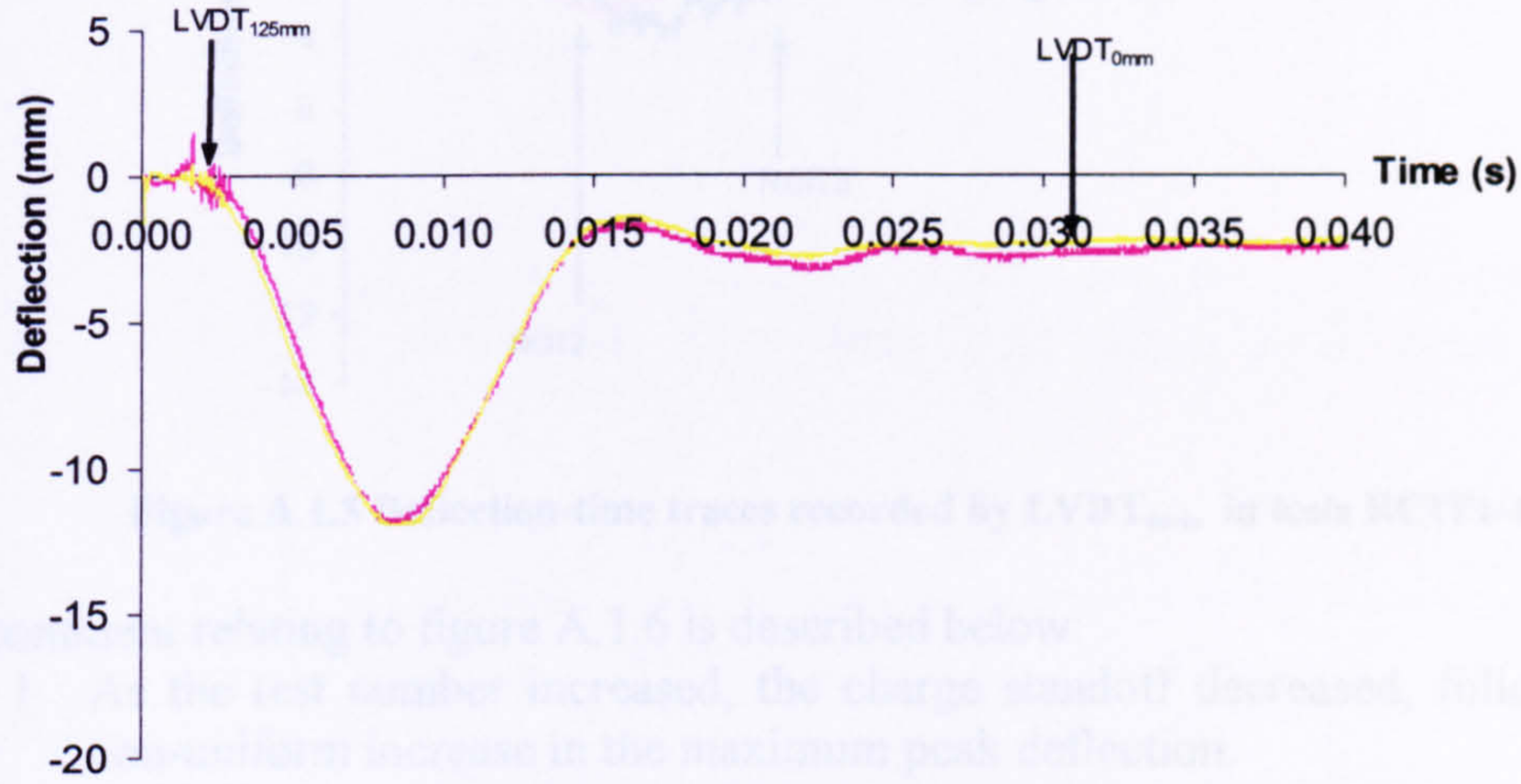

Figure A.1.3 Deflection-time traces from test RCIT3.

A comment relating to figure A.1.4 is described below:

1. The trace associated with $LVDT_{0mm}$ illustrates damage inflicted upon the gauge during the test.

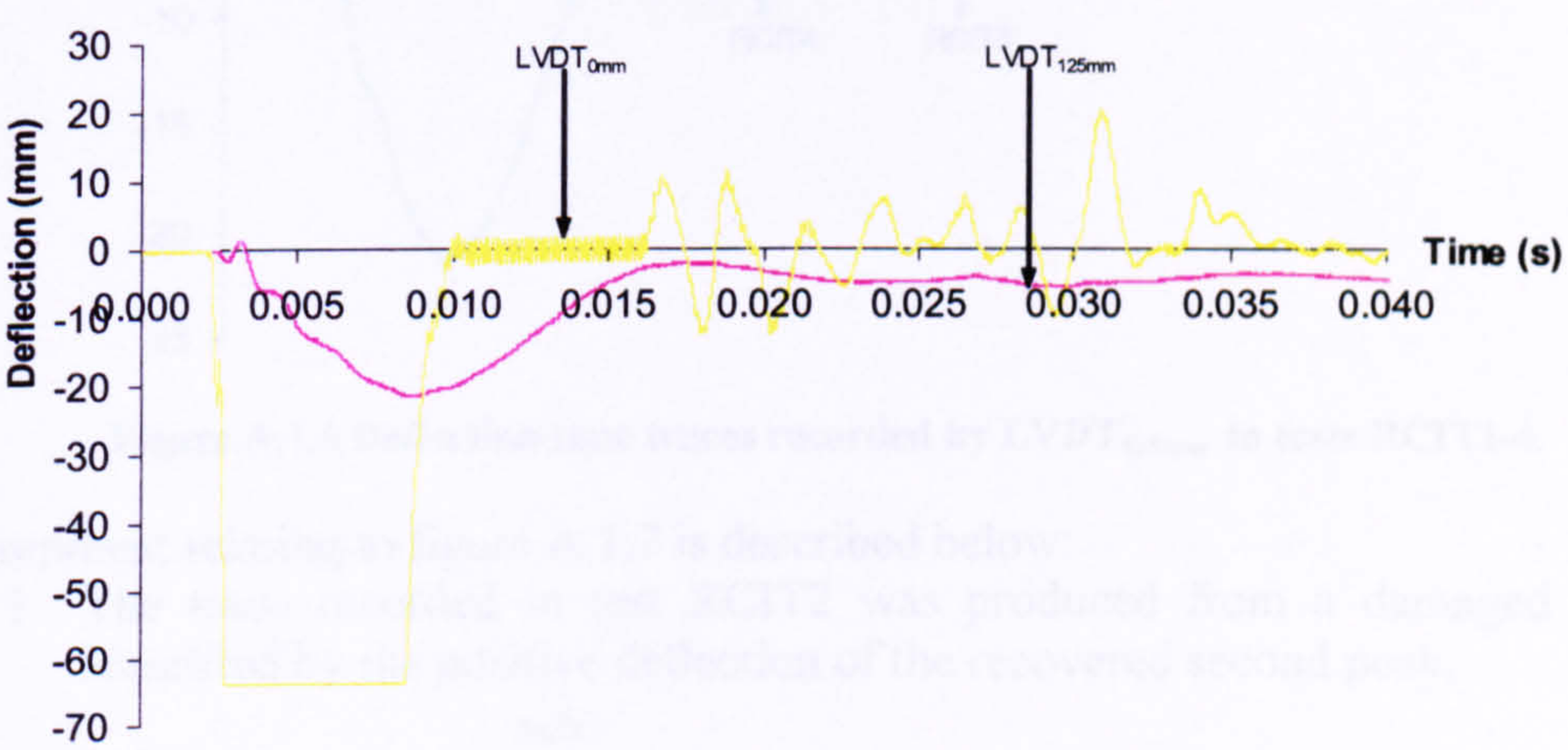

Figure A.1.4 Deflection-time traces from test RCIT4.

Group 1 results – Comparison of the tests

A comment relating to figure A.1.5 is described below:

1. All the tests illustrated residual deflection, indicating plastic deformation of the slab.

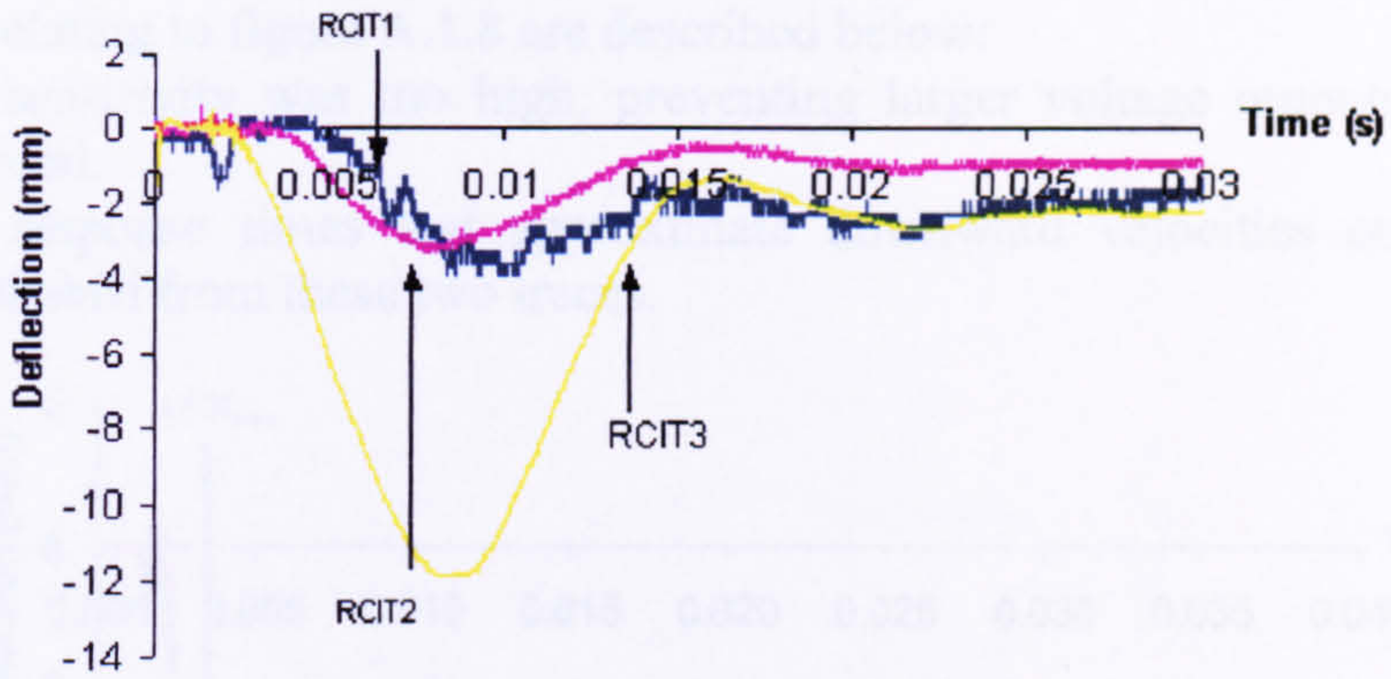

Figure A.1.5 Deflection-time traces recorded by $LVDT_{0mm}$ in tests RCIT1-4.

A comment relating to figure A.1.6 is described below:

1. As the test number increased, the charge standoff decreased, followed by a non-uniform increase in the maximum peak deflection.

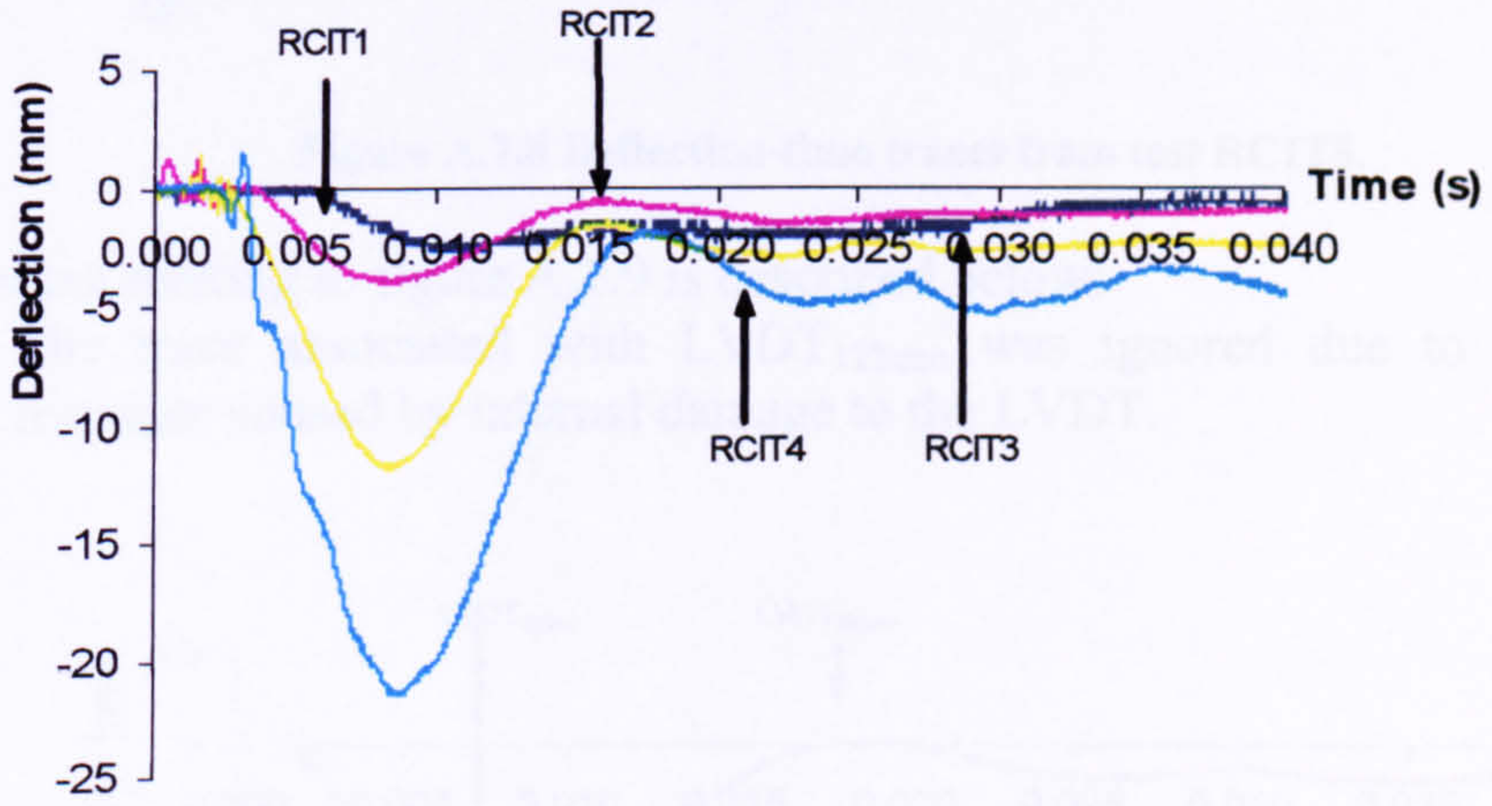

Figure A.1.6 Deflection-time traces recorded by $LVDT_{125mm}$ in tests RCIT1-4.

A comment relating to figure A.1.7 is described below:

1. The trace recorded in test RCIT2 was produced from a damaged LVDT, identified by the positive deflection of the recovered second peak.

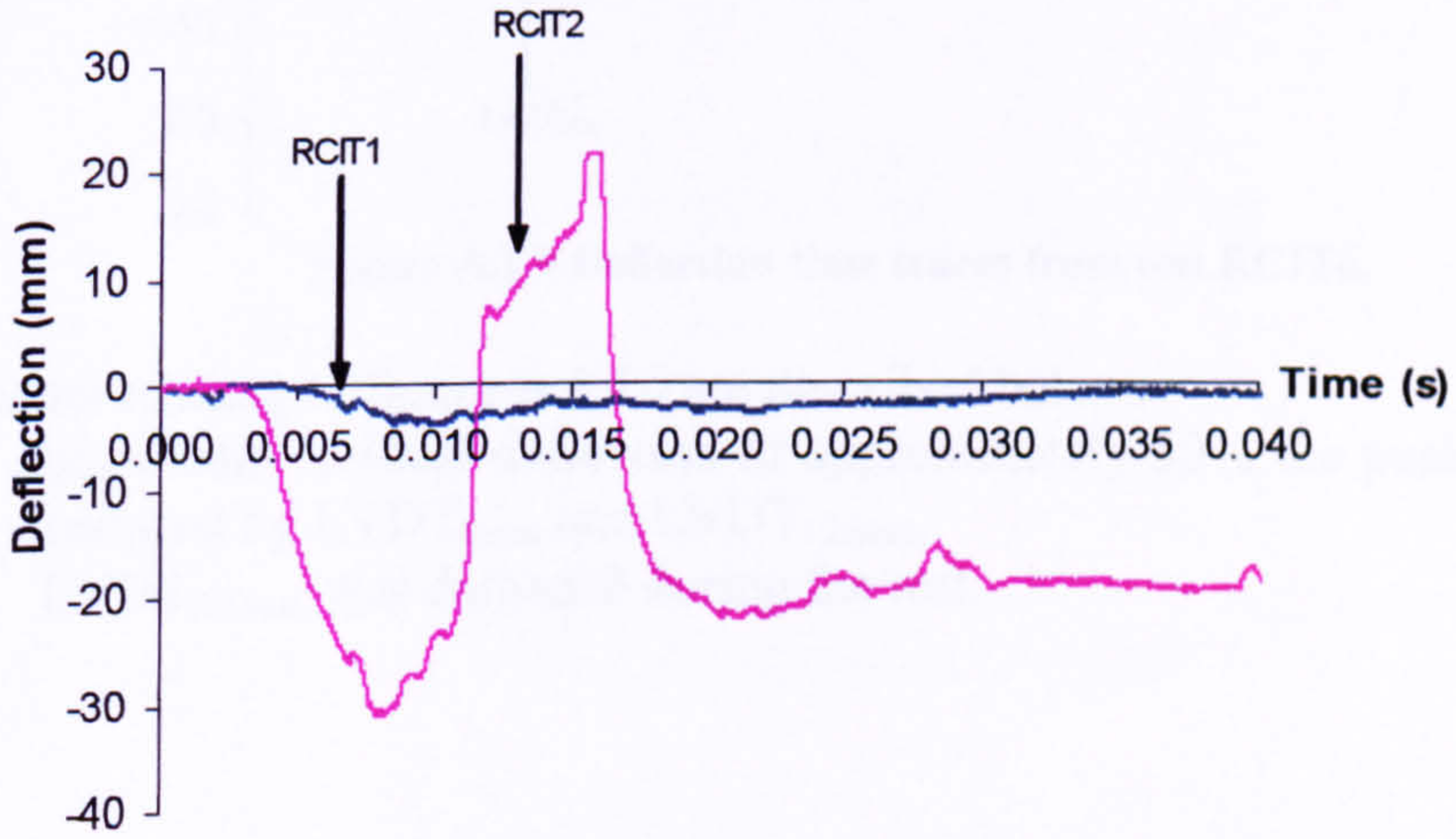

Figure A.1.7 Deflection-time traces recorded by $LVDT_{250mm}$ in tests RCIT1-2.

Group 2 results – Individual test analysis.

Comments relating to figure A.1.8 are described below:

1. The sensitivity was too high, preventing larger voltage outputs from being recorded.
2. The response times and approximate downward velocities could only be established from these two traces.

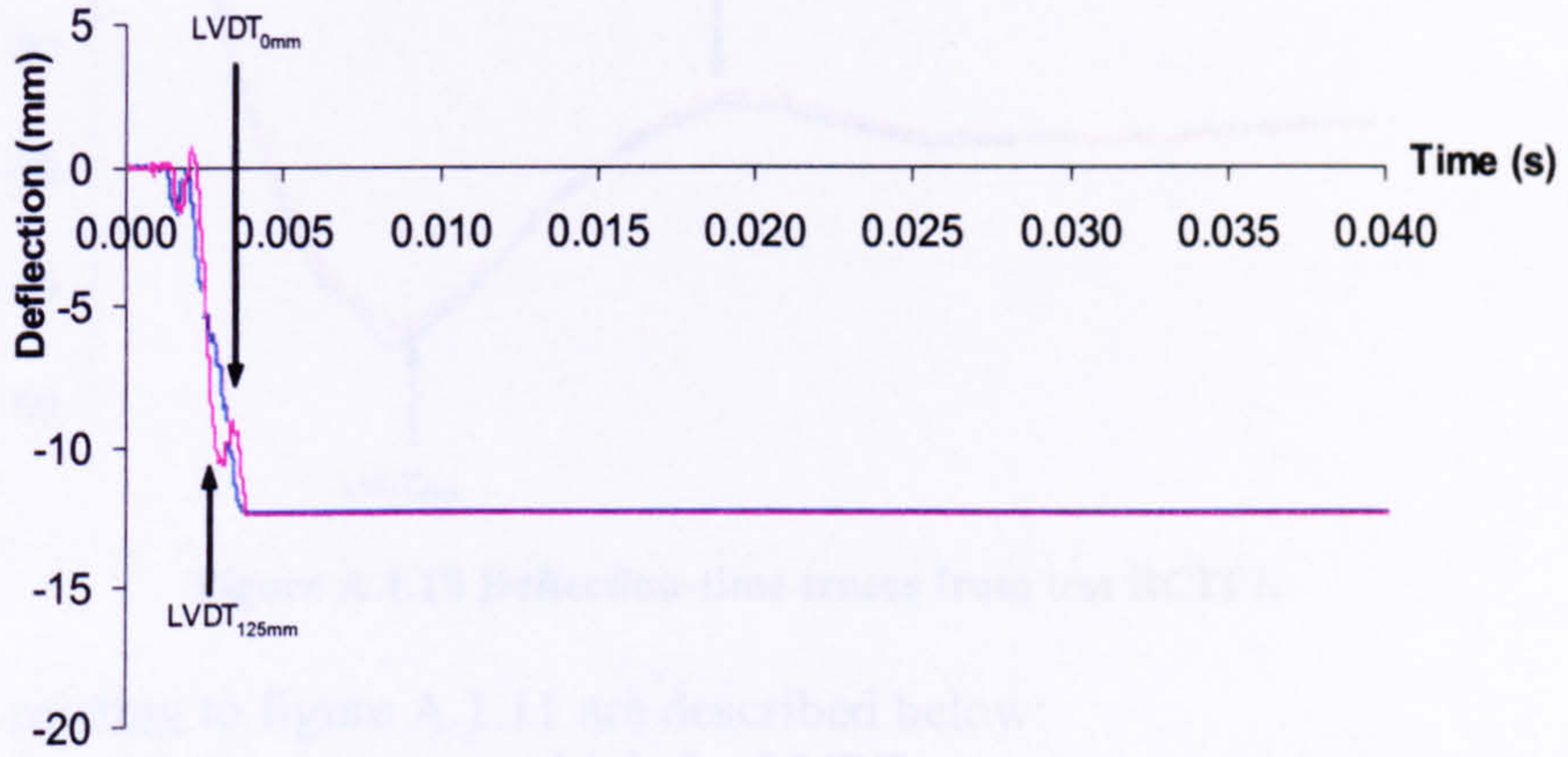

Figure A.1.8 Deflection-time traces from test RCIT5.

A comment relating to figure A.1.9 is described below:

1. The trace associated with $LVDT_{125mm}$ was ignored due to an inaccurate response caused by internal damage to the LVDT.

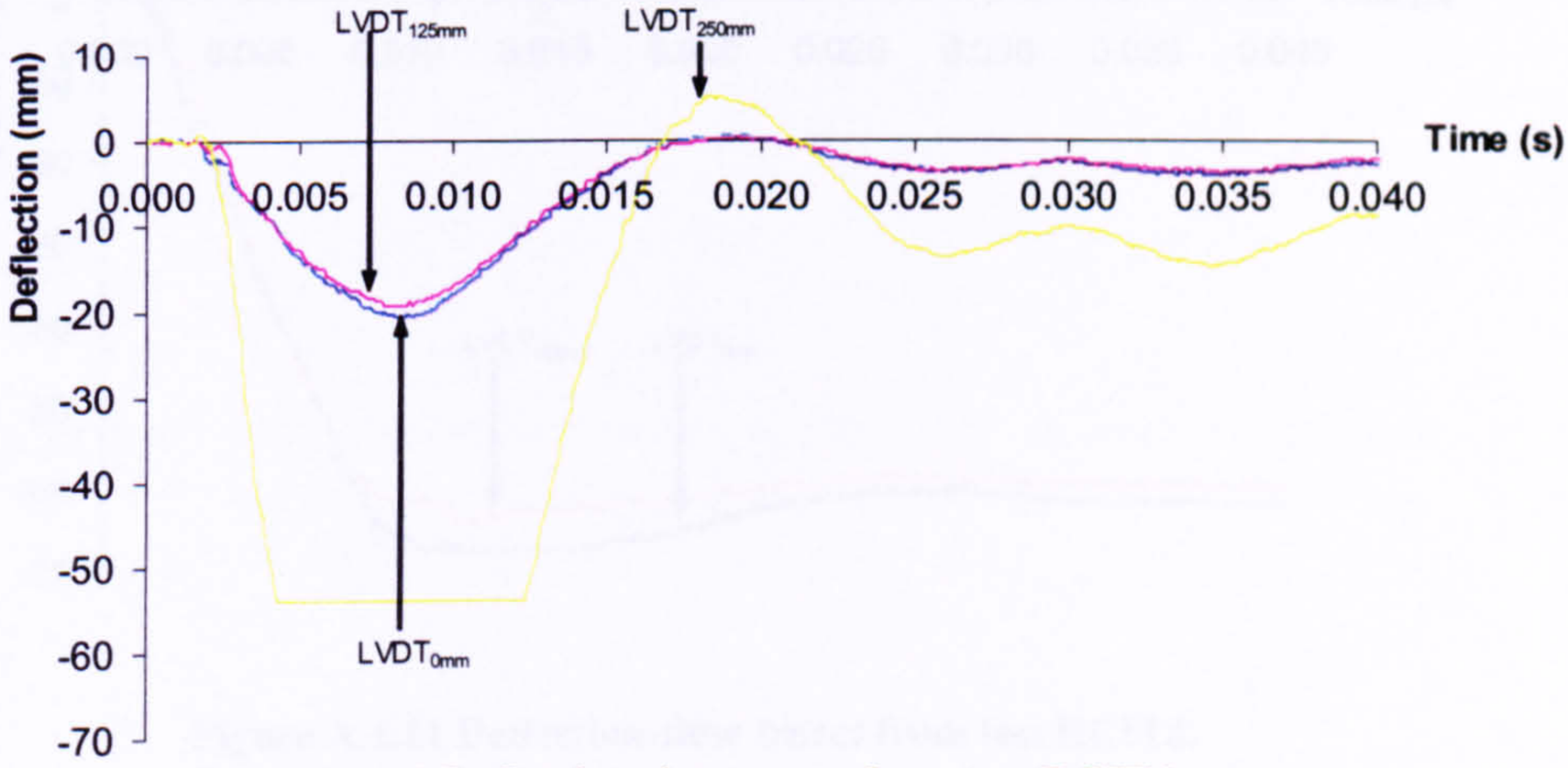

Figure A.1.9 Deflection-time traces from test RCIT6.

Comments relating to figure A.1.10 are described below:

1. Significant residual deflection of approximately 50% the peak deflection was recorded by $LVDT_{0mm}$ and $LVDT_{125mm}$.
2. $LVDT_{250mm}$ was damaged during the test.

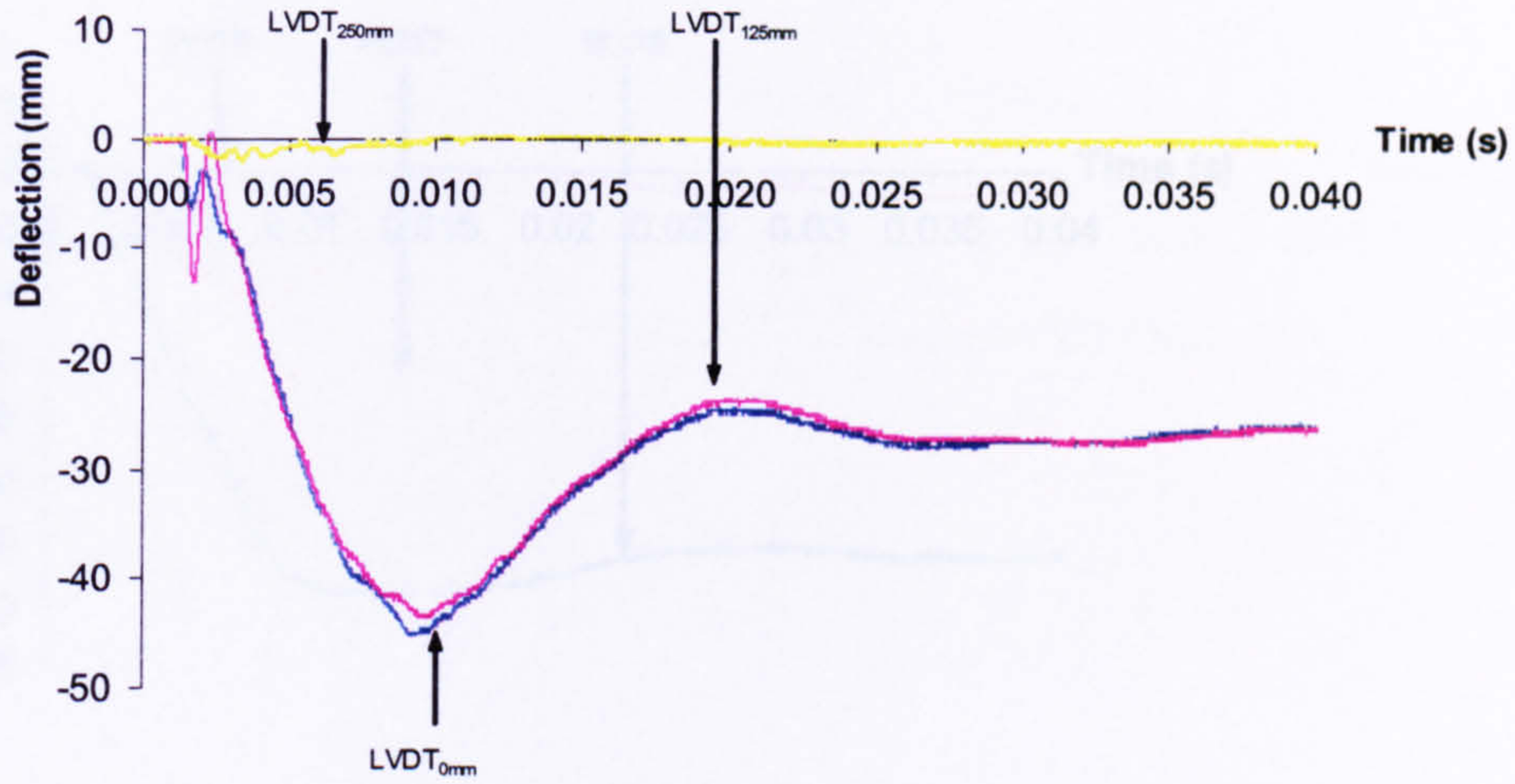

Figure A.1.10 Deflection-time traces from test RCIT7.

Comments relating to figure A.1.11 are described below:

1. The sensitivity was set too high for $LVDT_{0mm}$, preventing the peak deflection from being recorded.
2. The difference in the residual deflection compared to the peak deflection recorded by $LVDT_{125mm}$ significantly decreased.

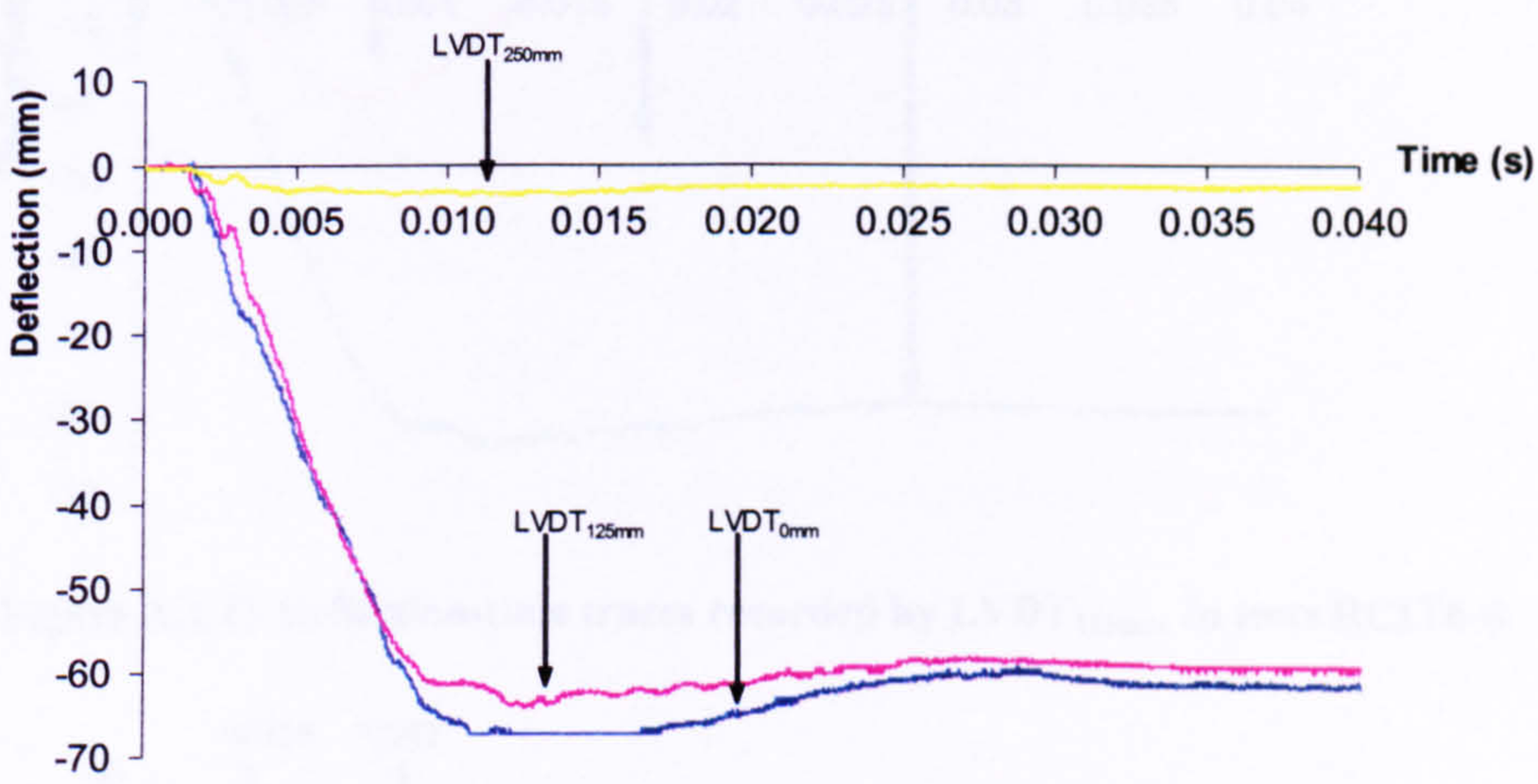

Figure A.1.11 Deflection-time traces from test RCIT8.

Group 2 results – Comparison of the tests.

Comments relating to figure A.1.12 are described below:

1. The downward velocity of the primary slab increased with an increase in test number.
2. The number of peaks recorded by $LVDT_{0mm}$ during the response of the primary slab decreased as the test number increased.

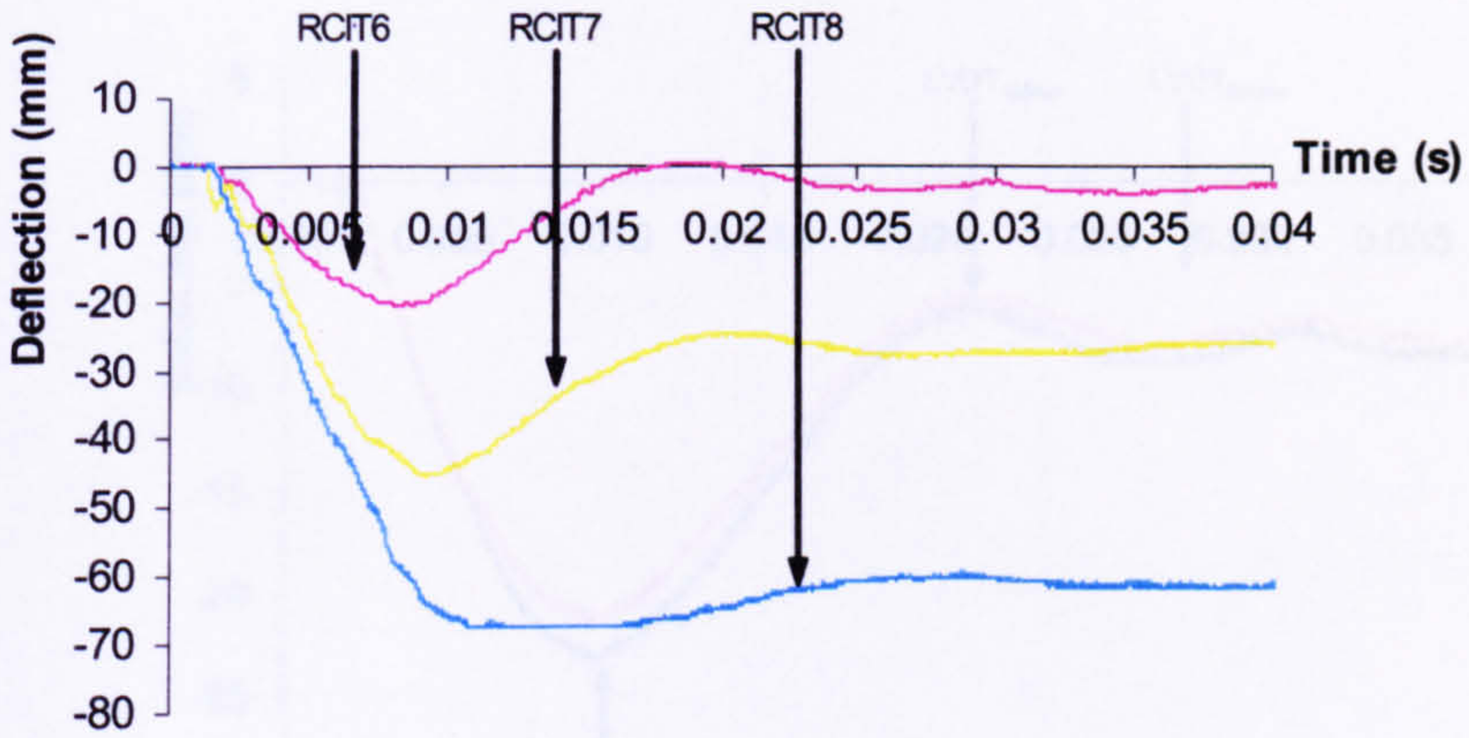

Figure A.1.12 Deflection-time traces recorded by $LVDT_{0mm}$ in tests RCIT6-8.

A comment relating to figure A.1.13 is described below:

1. Further plastic deformation occurred as the initial recovered peak had a larger value of deflection.

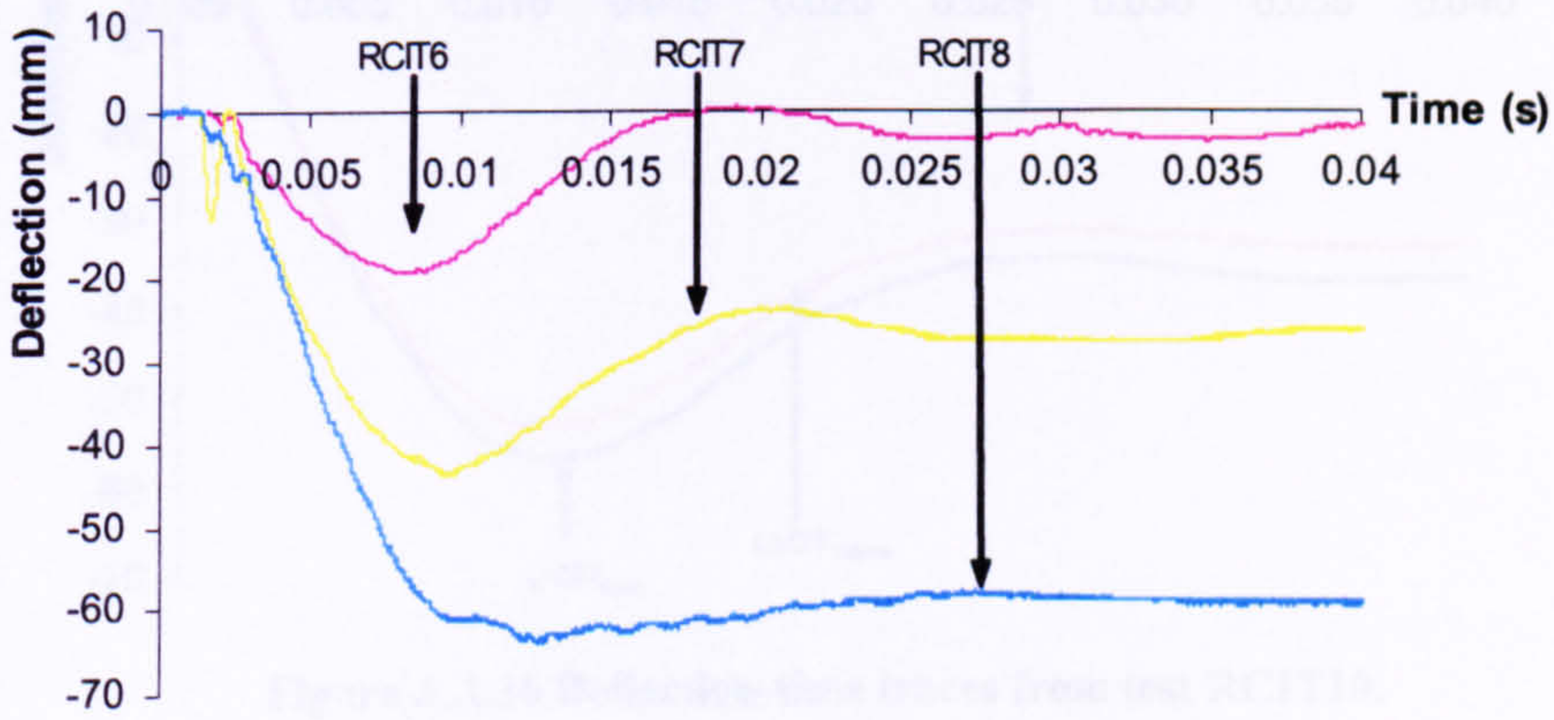

Figure A.1.13 Deflection-time traces recorded by $LVDT_{125mm}$ in tests RCIT6-8.

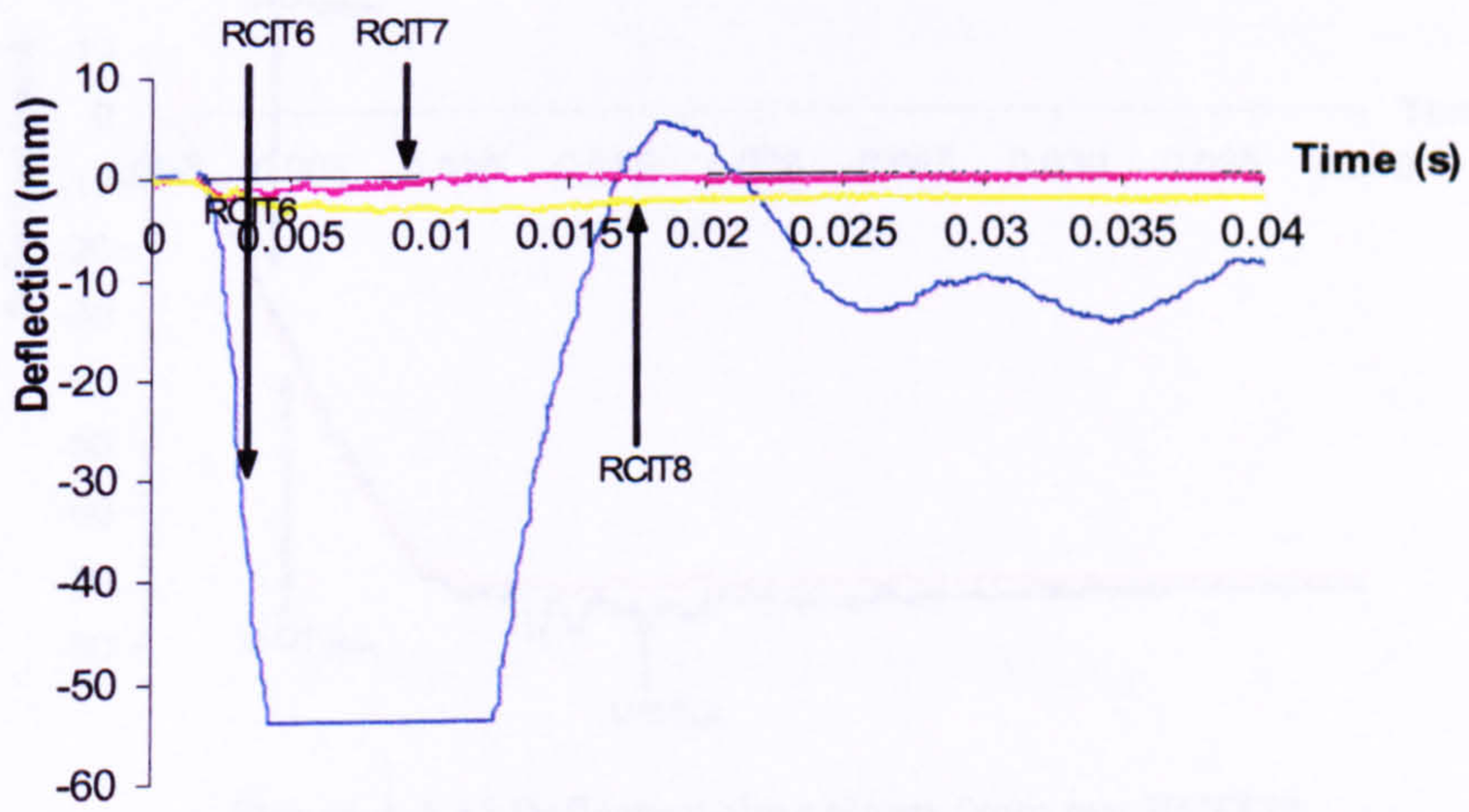

Figure A.1.14 Deflection-time traces recorded by $LVDT_{250mm}$ in tests RCIT6-8.

Group 3 results – Individual test analysis.

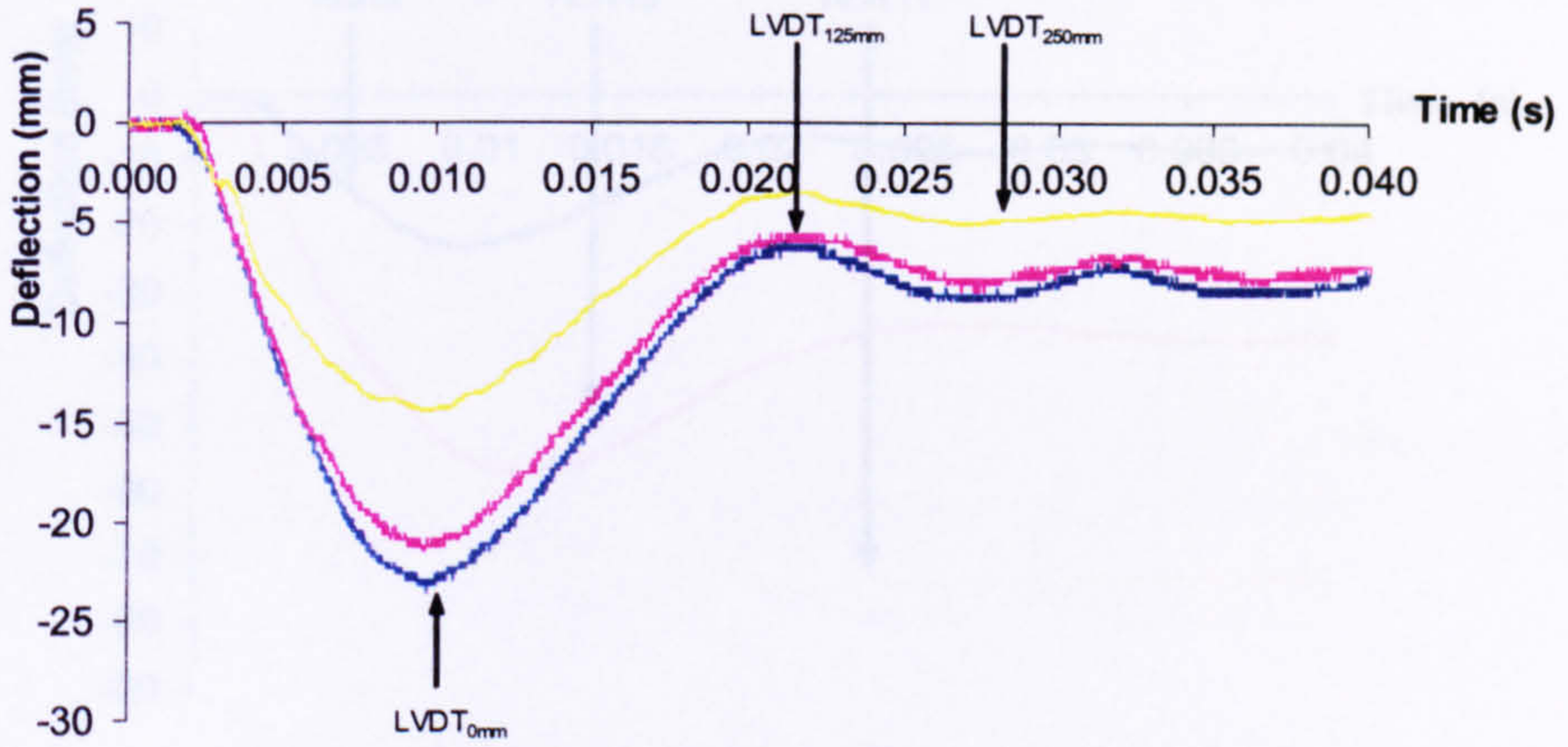

Figure A.1.15 Deflection-time traces from test RCIT9.

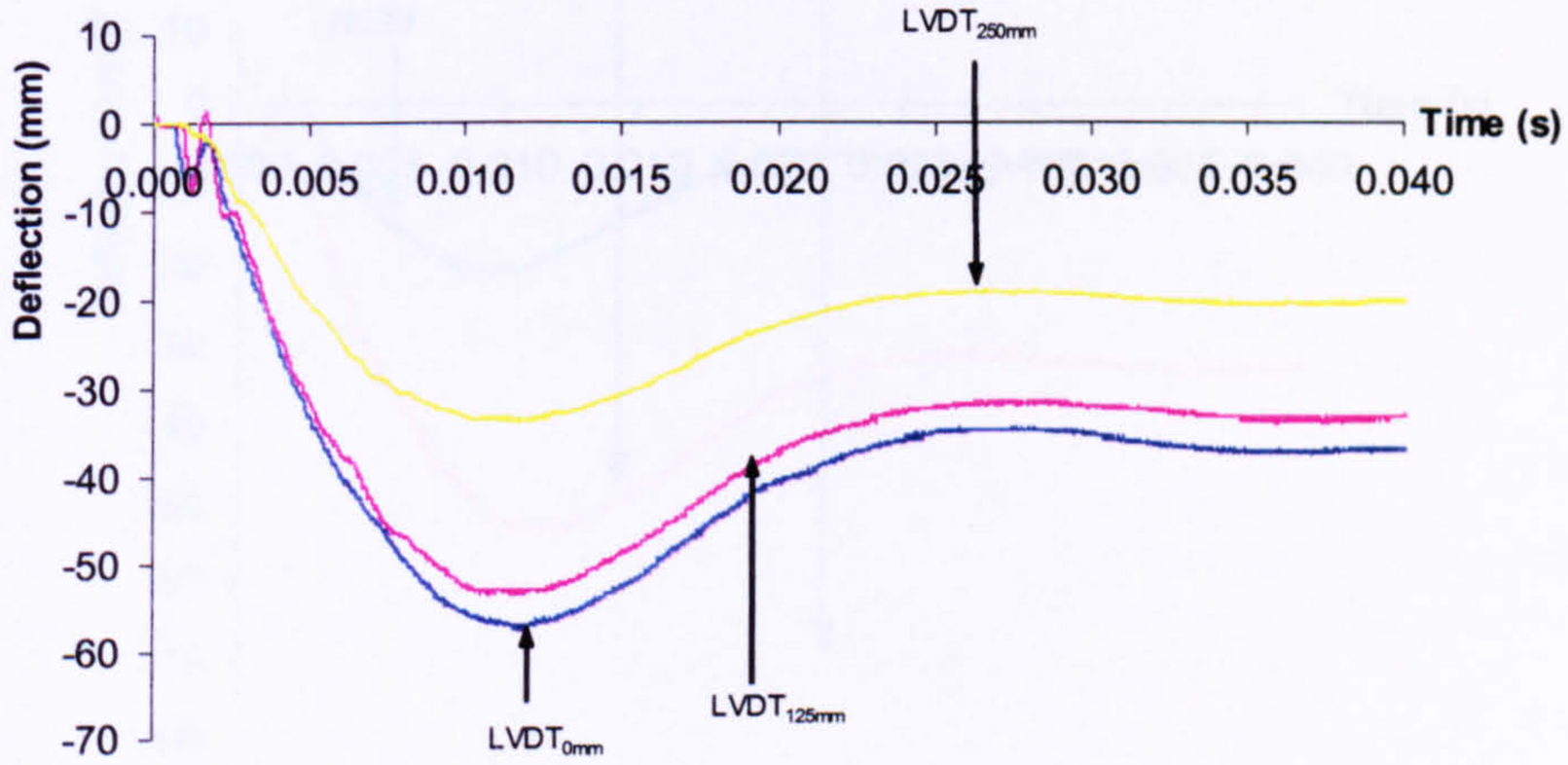

Figure A.1.16 Deflection-time traces from test RCIT10.

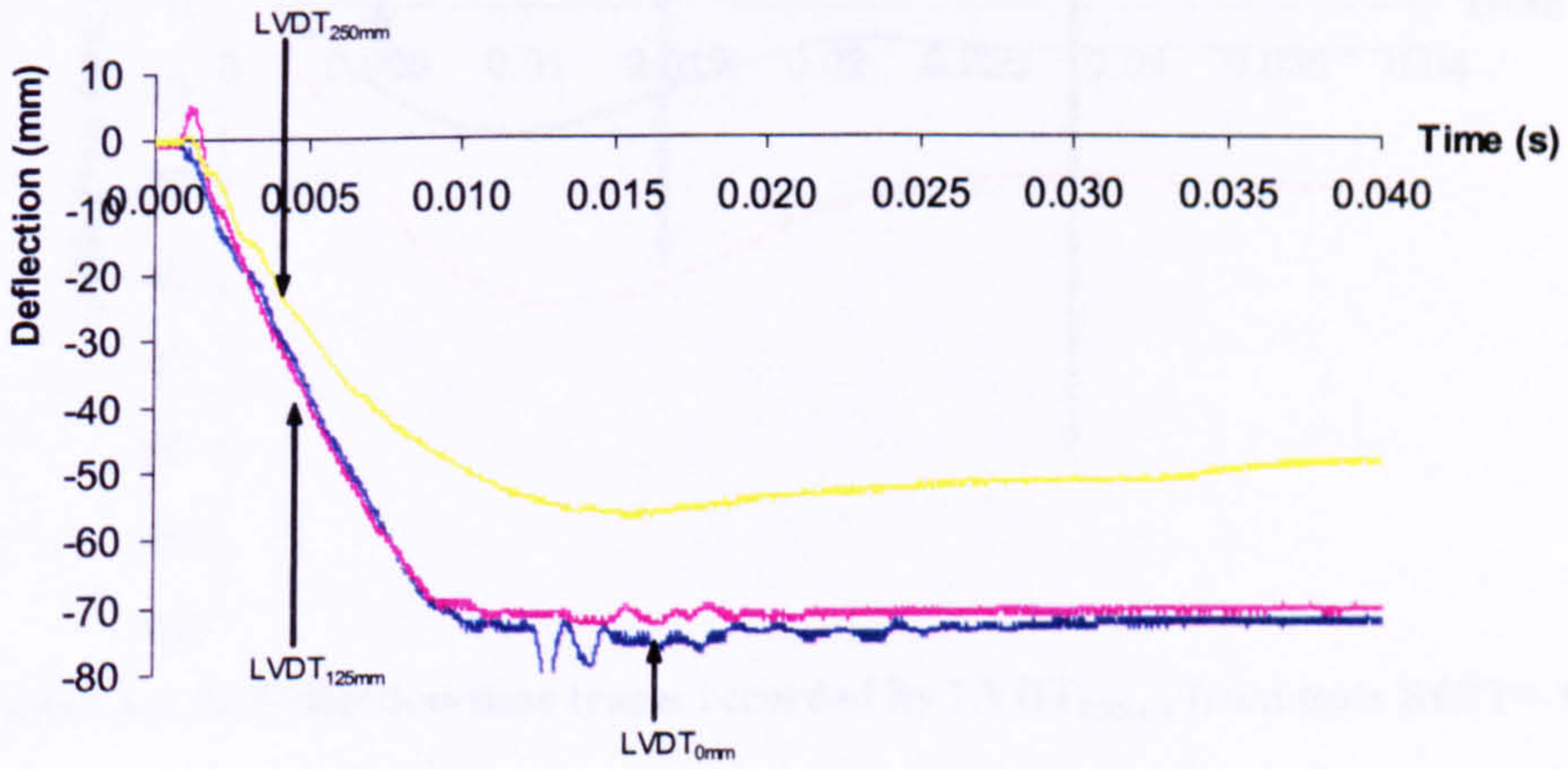

Figure A.1.17 Deflection-time traces from test RCIT11.

Group 3 results – Comparison of the tests.

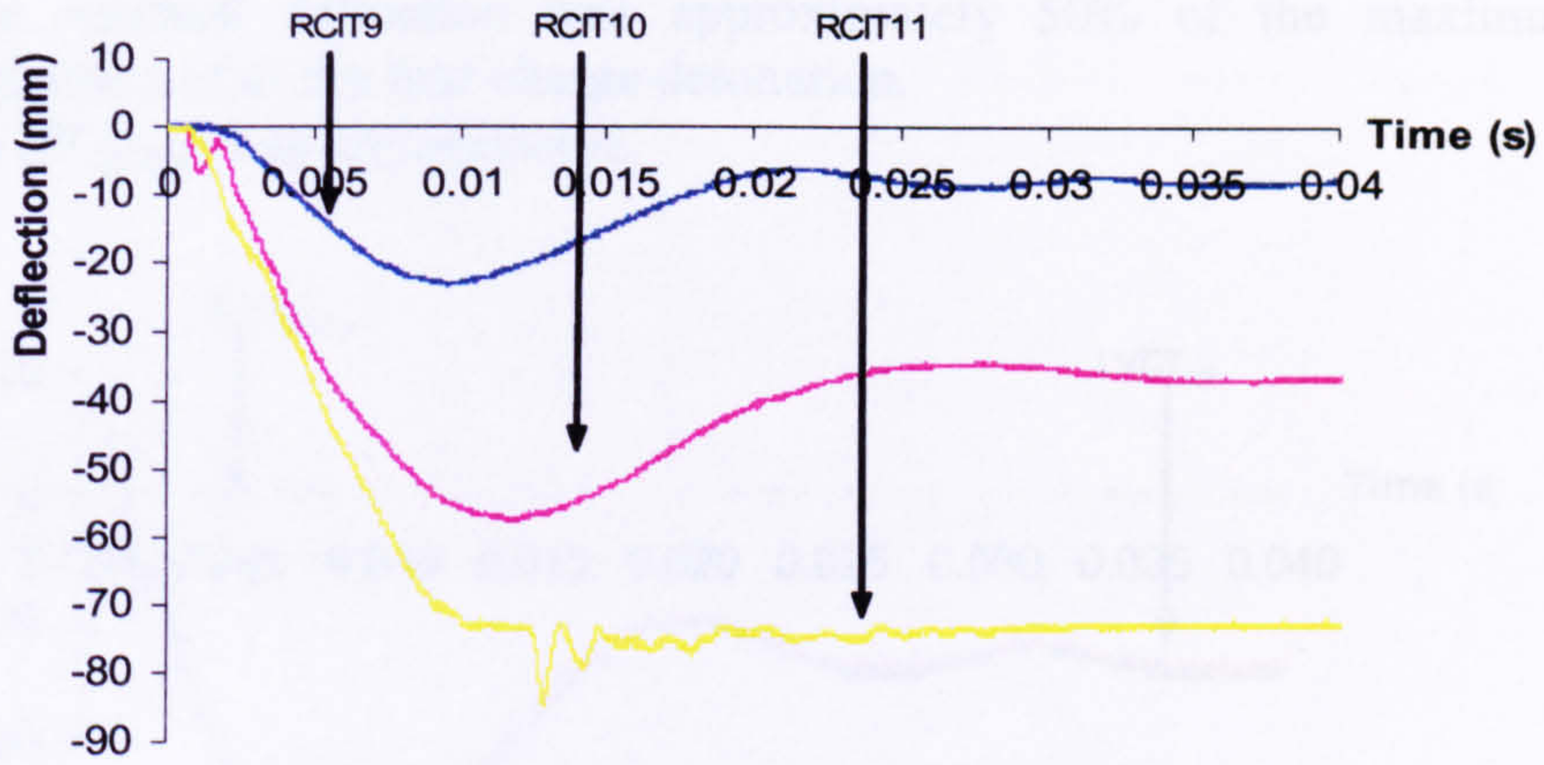

Figure A.1.18 Deflection-time traces recorded by $LVDT_{0mm}$ from tests RCIT 9-11.

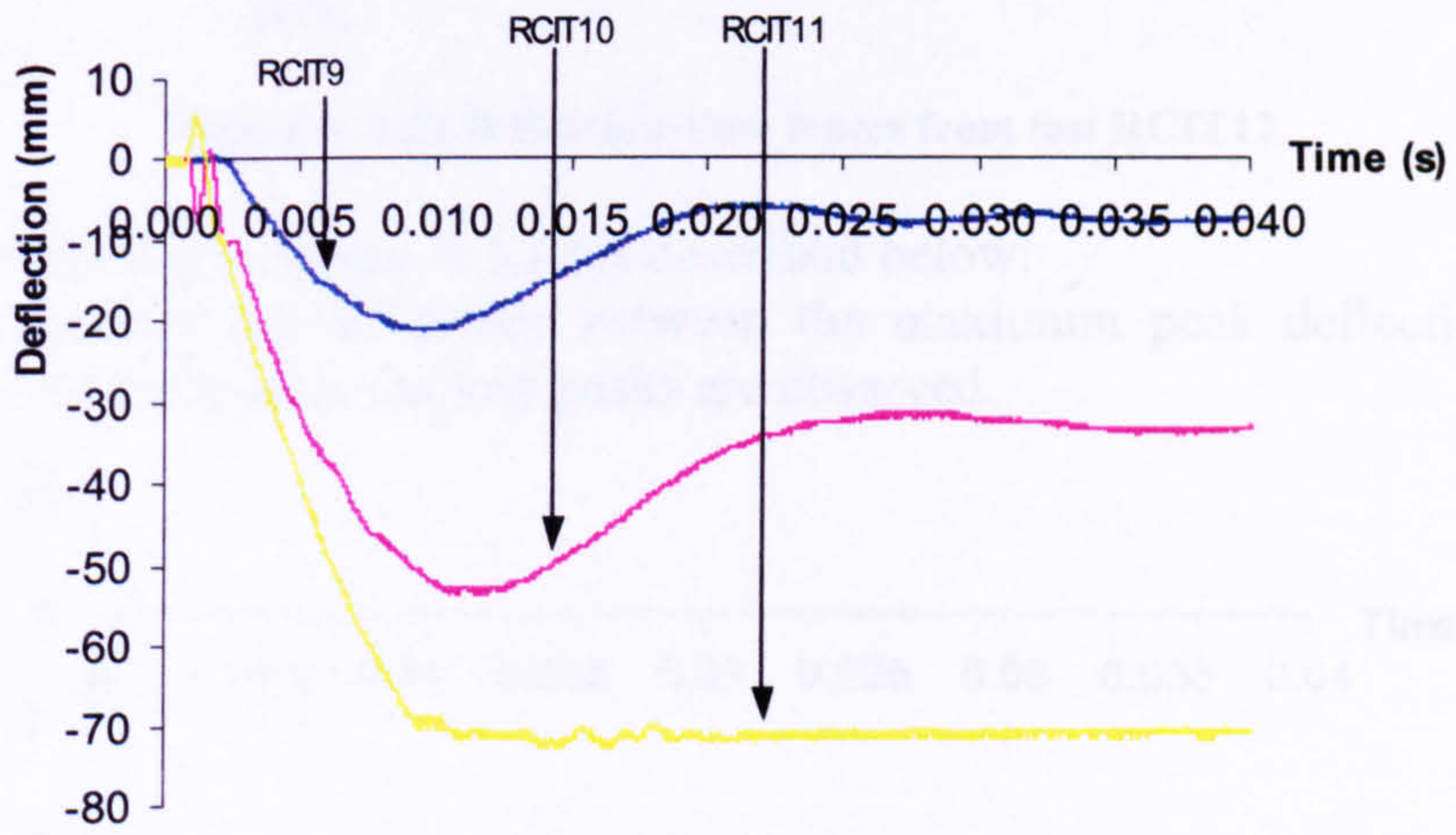

Figure A.1.19 Deflection-time traces recorded by $LVDT_{125mm}$ from tests RCIT9-11.

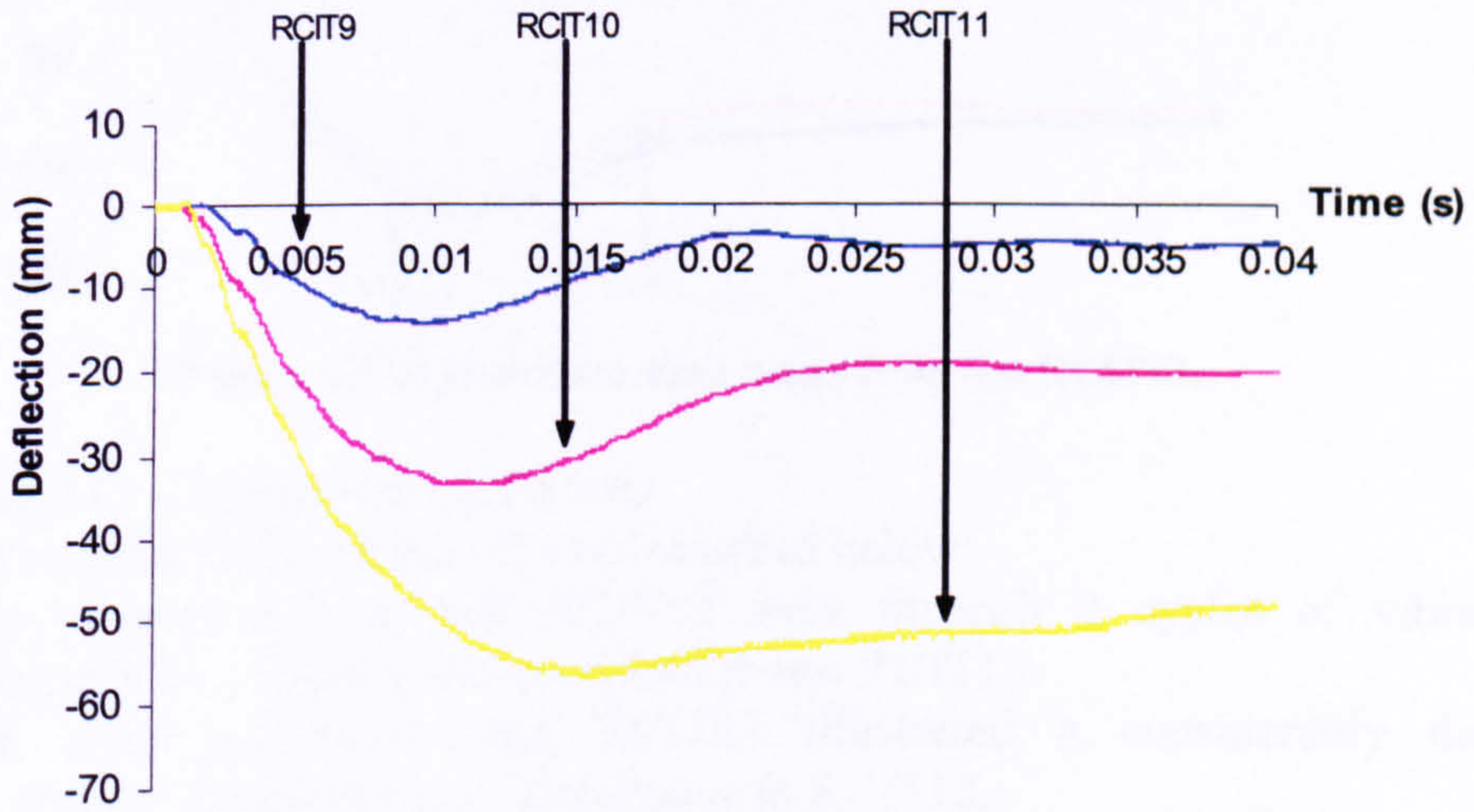

Figure A.1.20 Deflection-time traces recorded by $LVDT_{250mm}$ from tests RCIT9-11.

Group 4 results – Individual test analysis.

Comments relating to figure A.1.21 are described below:

1. The residual deflection was approximately 50% of the maximum peak deflection after the first charge detonation.
2. $LVDT_{250mm}$ was unresponsive.

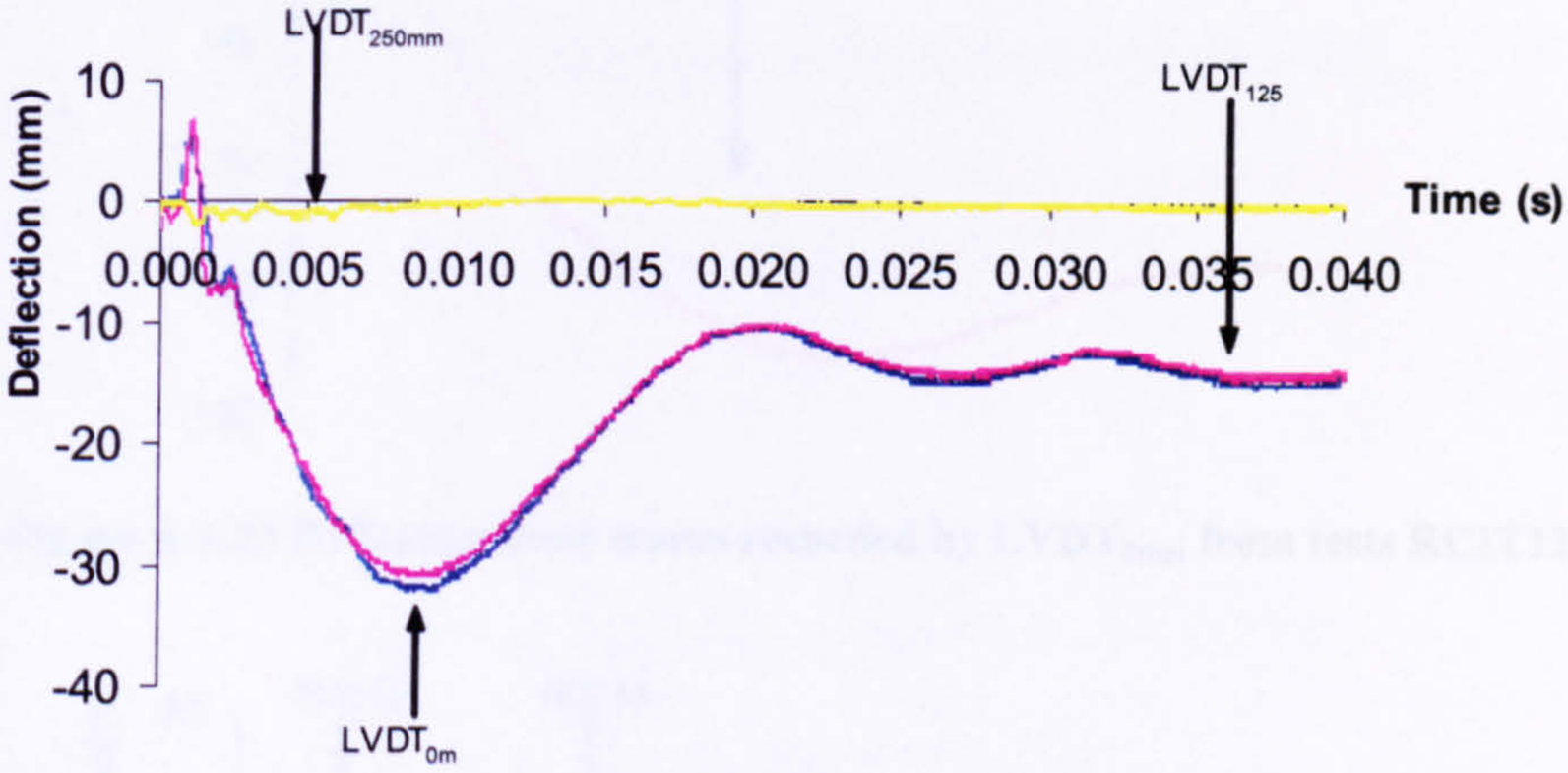

Figure A.1.21 Deflection-time traces from test RCIT12.

A comment relating to figure A.1.22 is described below:

1. The smaller the difference between the maximum peak deflection and the residual deflection, the less peaks are observed.

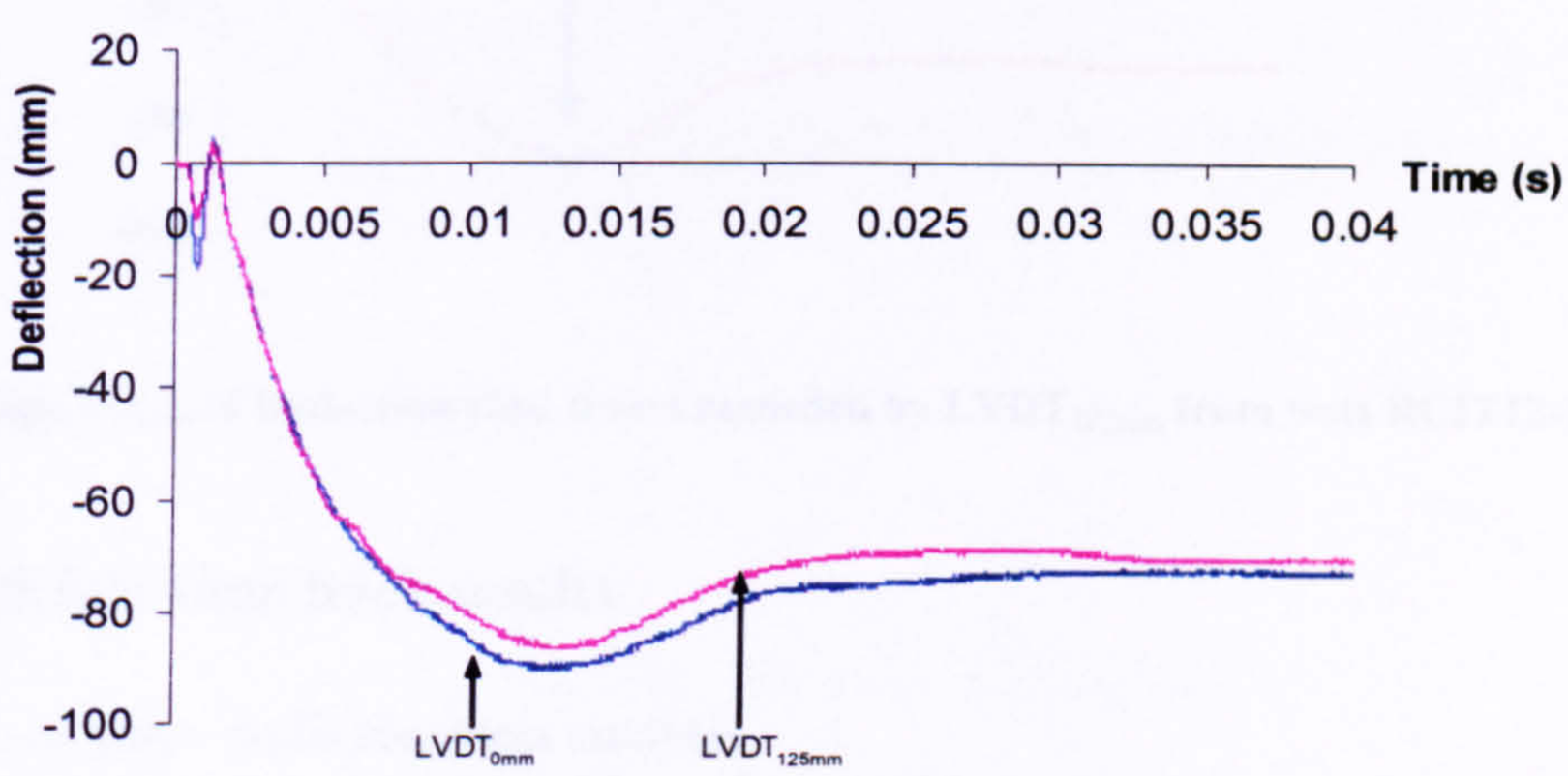

Figure A.1.22 Deflection-time traces from test RCIT13.

Group 4 results – Comparison of the tests

Comments relating to figure A.1.23 are described below:

1. The primary slab in test RCIT12 went through 2 cycles of vibrations, compared to a single cycle produced in test RCIT13.
2. The trace associated with RCIT13 illustrated a considerably damped oscillation, compared to that produced in RCIT12.

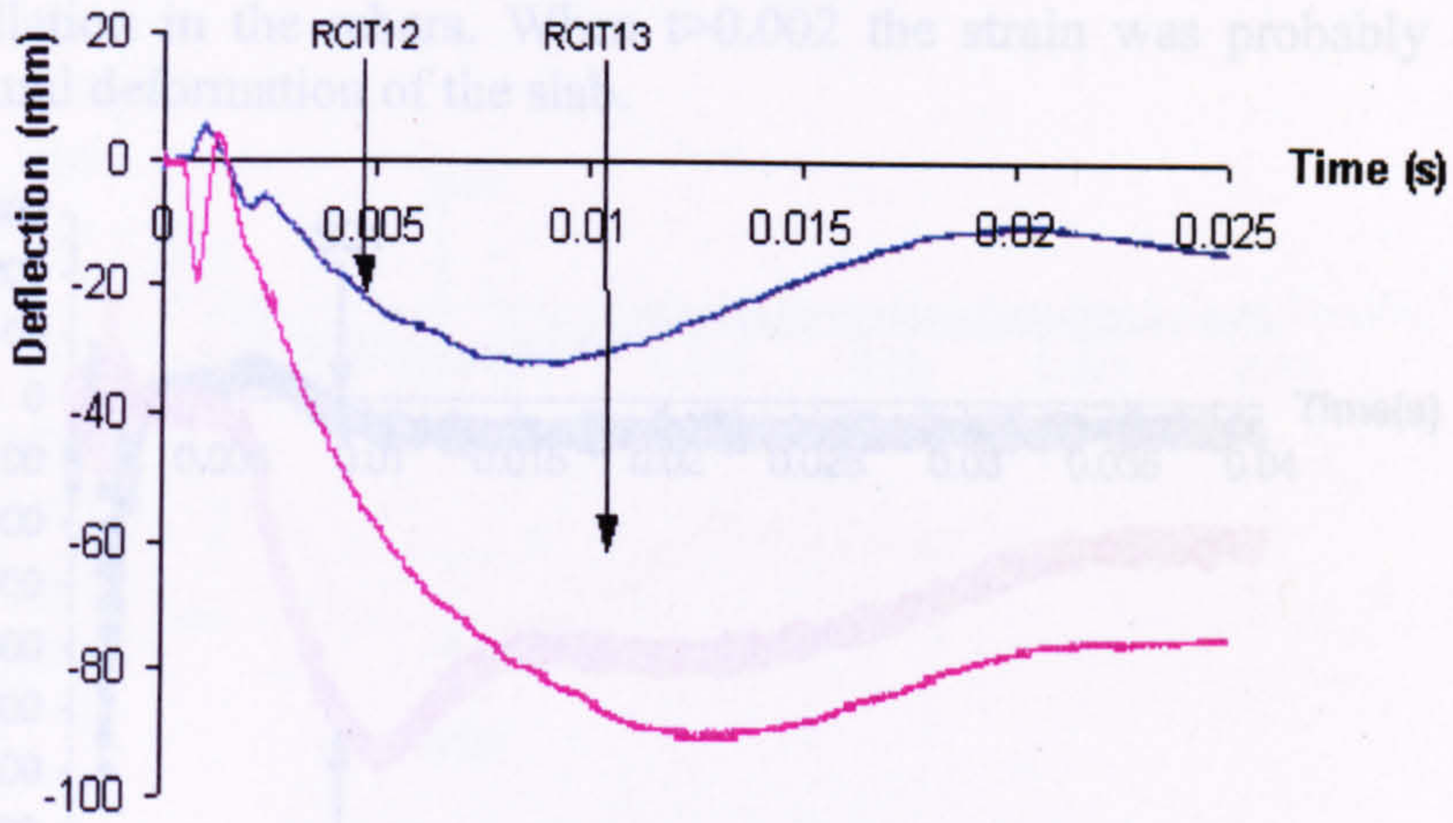

Figure A.1.23 Deflection-time traces recorded by $LVDT_{0mm}$ from tests RCIT12-13.

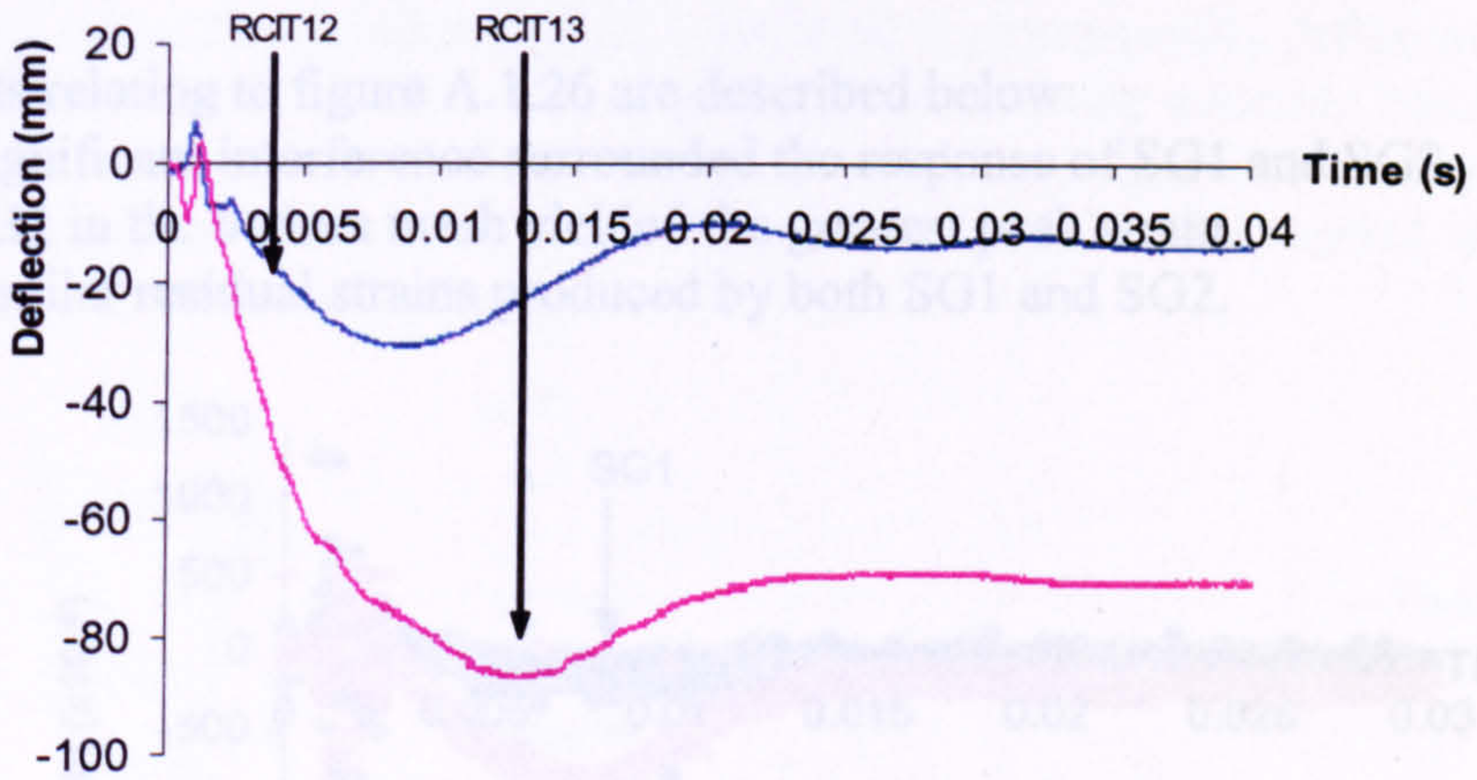

Figure A.1.24 Deflection-time traces recorded by $LVDT_{125mm}$ from tests RCIT12-13.

A.1.2 Strain-time trace results

Group 1 results – Individual test analysis.
Comments relating to figure A.1.25 are described below:

1. SG1 was positioned in the top mesh, closer to the charge and yielded a maximum peak strain in tension, before SG2 produced a maximum peak strain.
2. Both the maximum peak strains produced by SG1 and SG2 were recorded at different strain rates.
3. The residual strain produced by SG1 occurred at the time the maximum peak strain was produced by SG2.
4. The initial response of the gauges in the top and bottom meshes was difficult to establish due to interference.
5. SG2 illustrated a residual strain that was significantly greater than that produced by SG1. This indicated that perhaps the top and bottom meshes were not moving as a single unit.

6. Within the range 0<t<0.002s the interference may be axial strain wave oscillation in the rebars. When t>0.002 the strain was probably caused by flexural deformation of the slab.

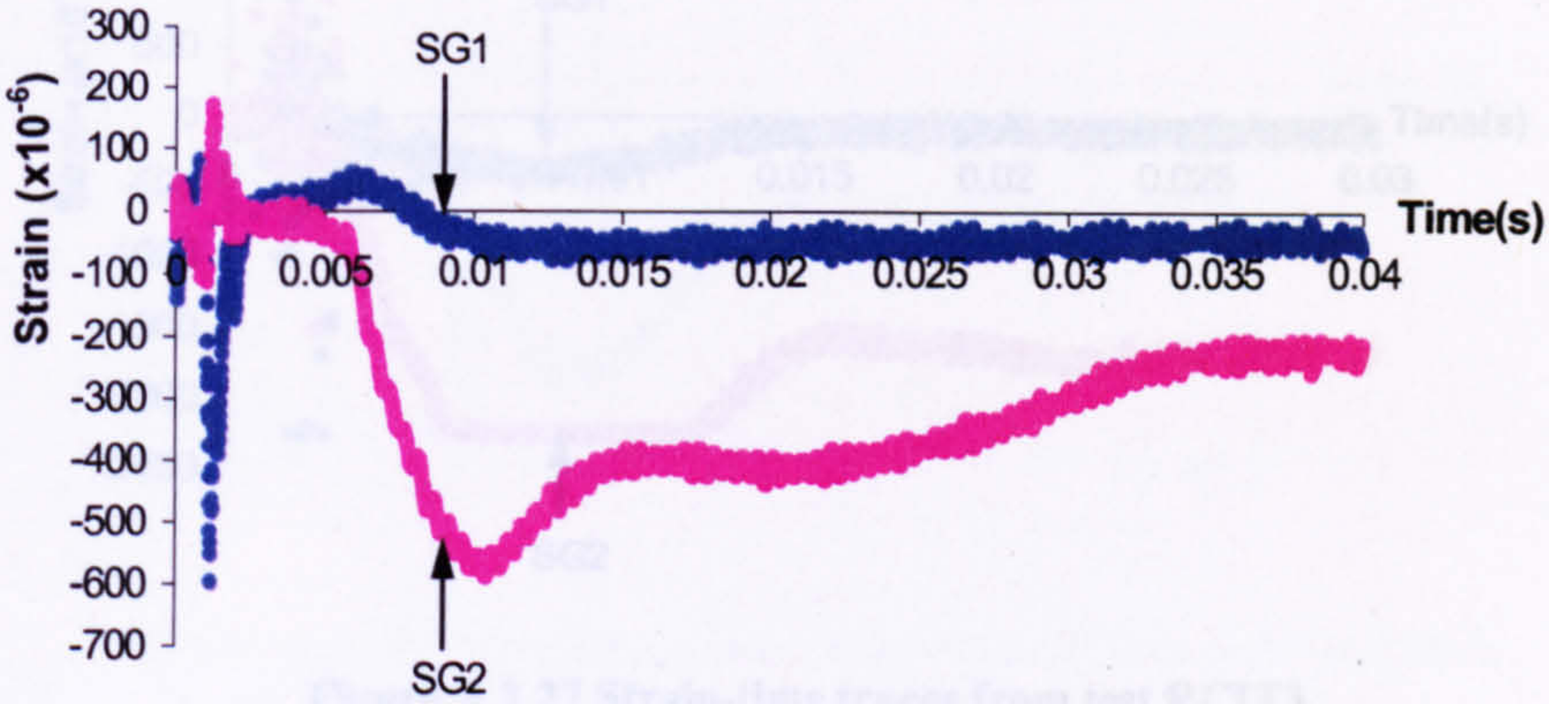

Figure A.1.25 Strain-time traces from test RCIT1.

Comments relating to figure A.1.26 are described below:

1. Significant interference surrounded the response of SG1 and SG2.
2. SG2 in the bottom mesh yielded the greatest peak strain.
3. Similar residual strains produced by both SG1 and SG2.

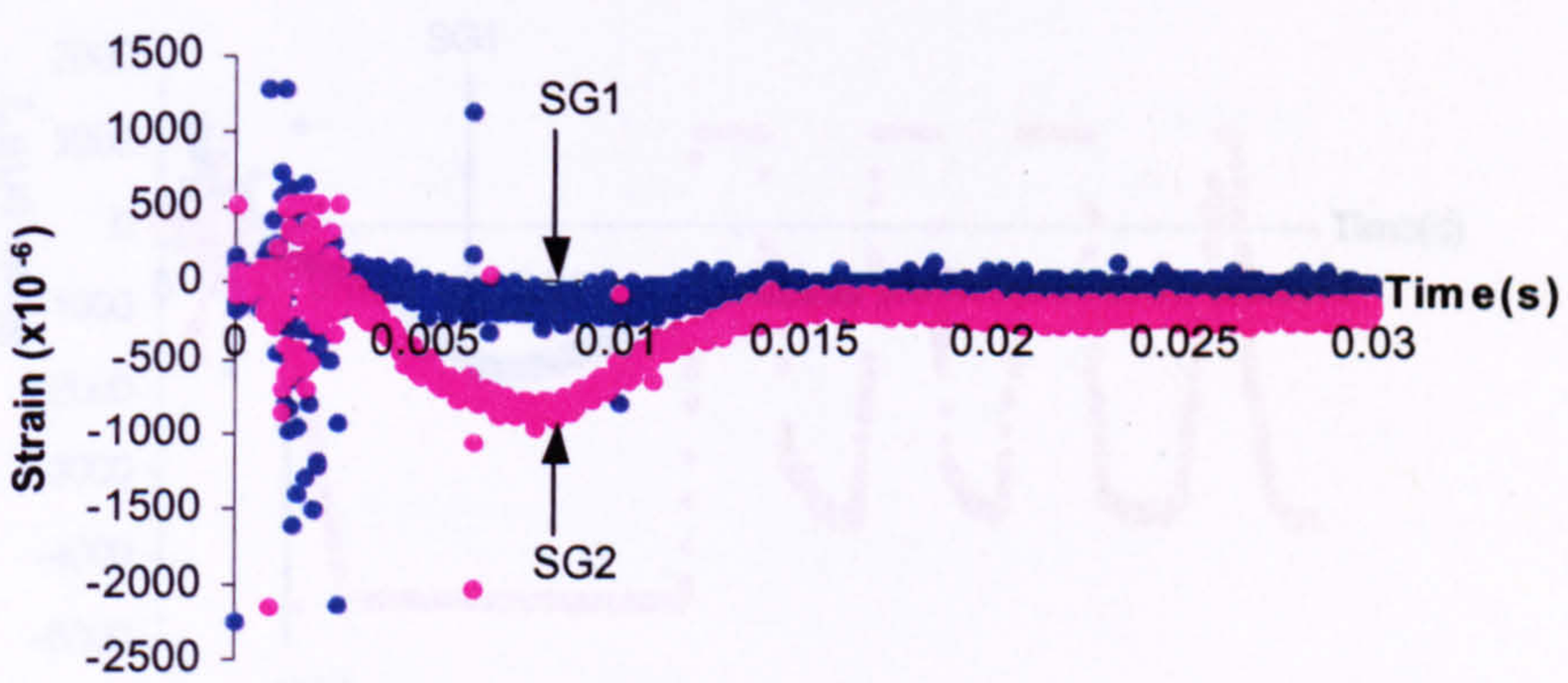

Figure A.1.26 Strain-time traces from test RCIT2.

Comments relating to figure A.1.27 are described below:

1. The sensitivity associated with captured trace of SG2 was set too high, preventing the maximum peak strain from being identified.
2. The strain rate associated with SG2 was considerable greater than that produced by SG1.
3. Large differences in the residual strain were produced by SG1 and SG2.

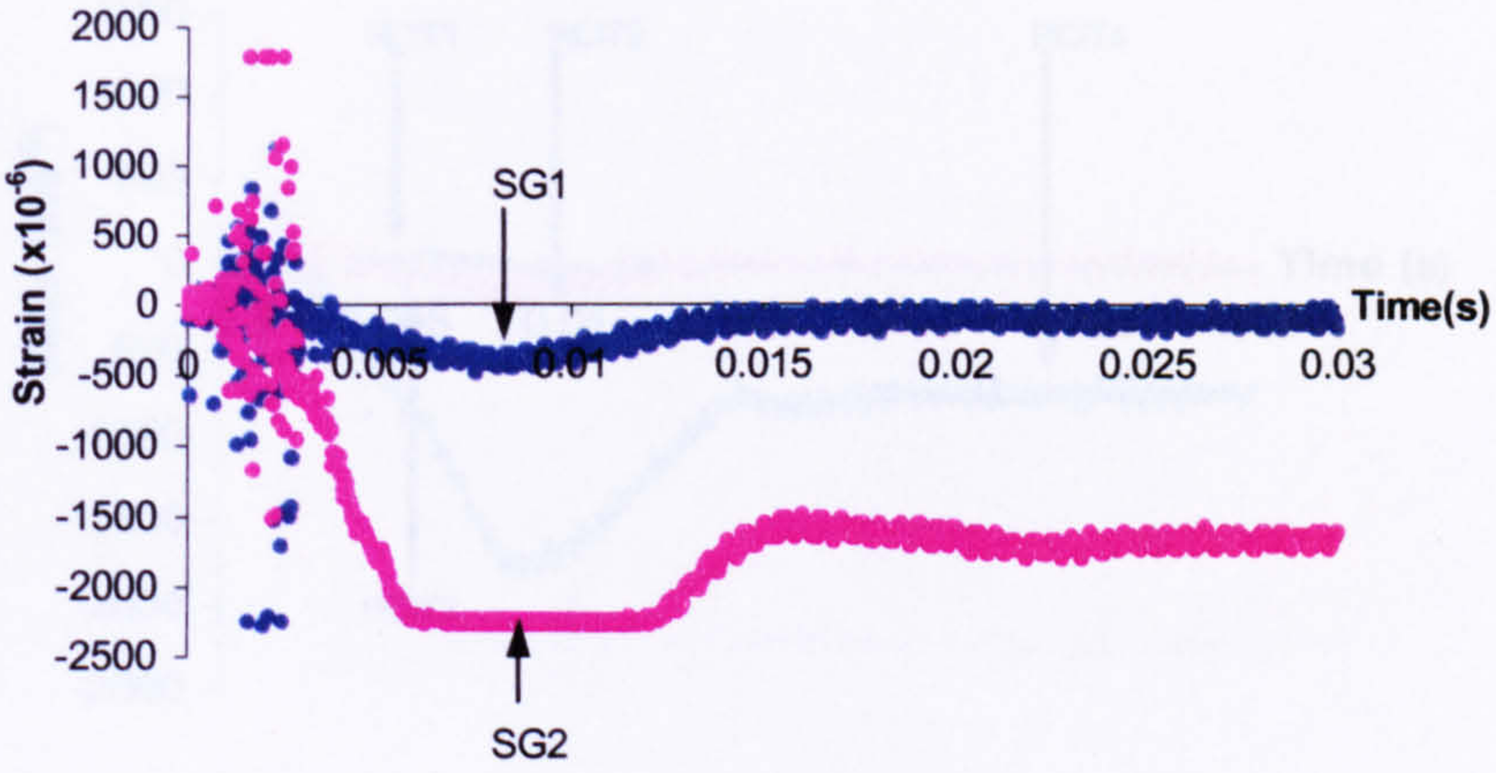

Figure A.1.27 Strain-time traces from test RCIT3.

A comment relating to figure A.1.28 is described below:

1. The trace associated with SG2 illustrated a geometrically different response to that produced by SG1. This is possibly because the concrete bond around the bottom rebar was weak from tensile reflection, identified by the severity of cracking on the bottom face. This caused the rebar to respond in a different mode to the rebar in the top mesh.

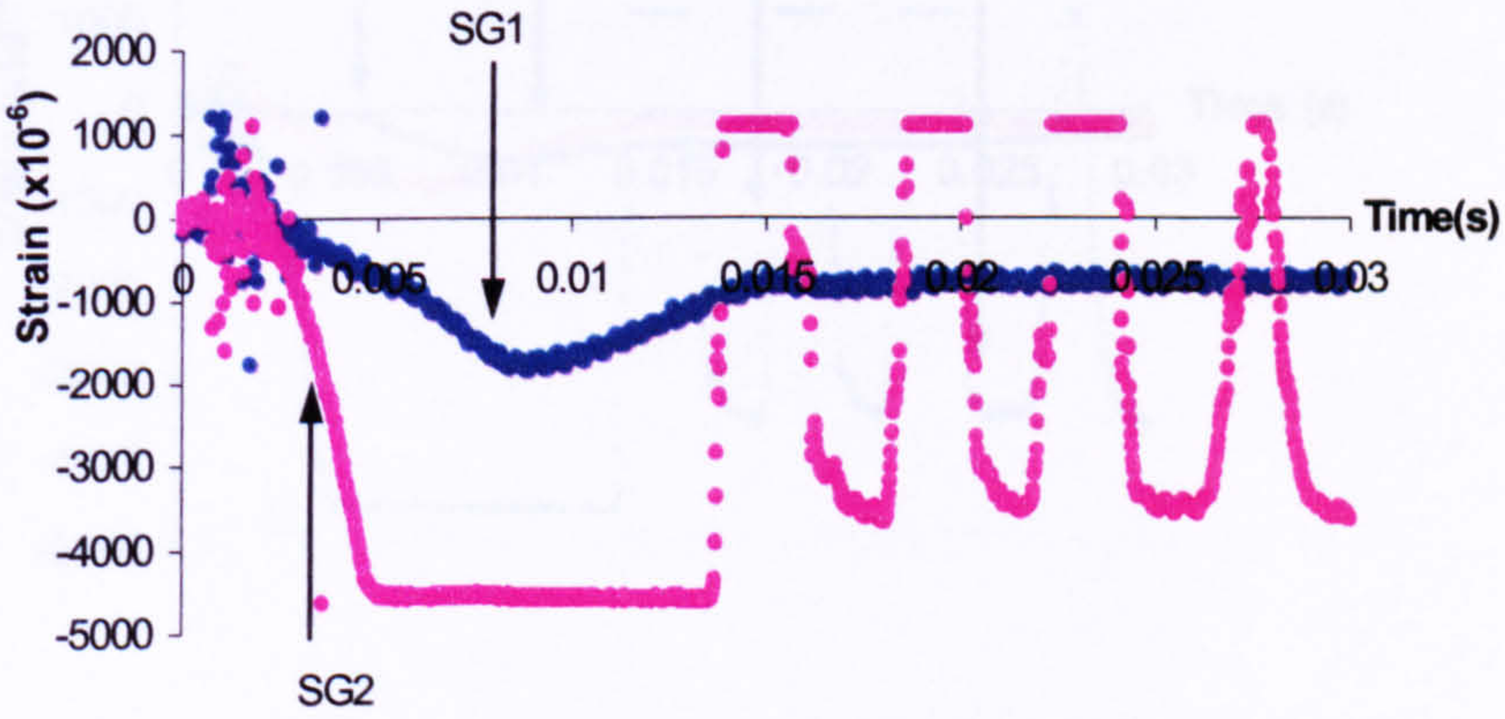

Figure A.1.28 Strain-time traces from test RCIT4.

Group 1 results – Comparison of the tests.

A comment relating to figure A.1.29 is described below:

1. RCIT4 involved positioning the charge below the bottom face of the secondary slab. This change of charge position relative to the secondary slab caused a decrease in charge standoff and a considerable increase in the maximum peak strain.

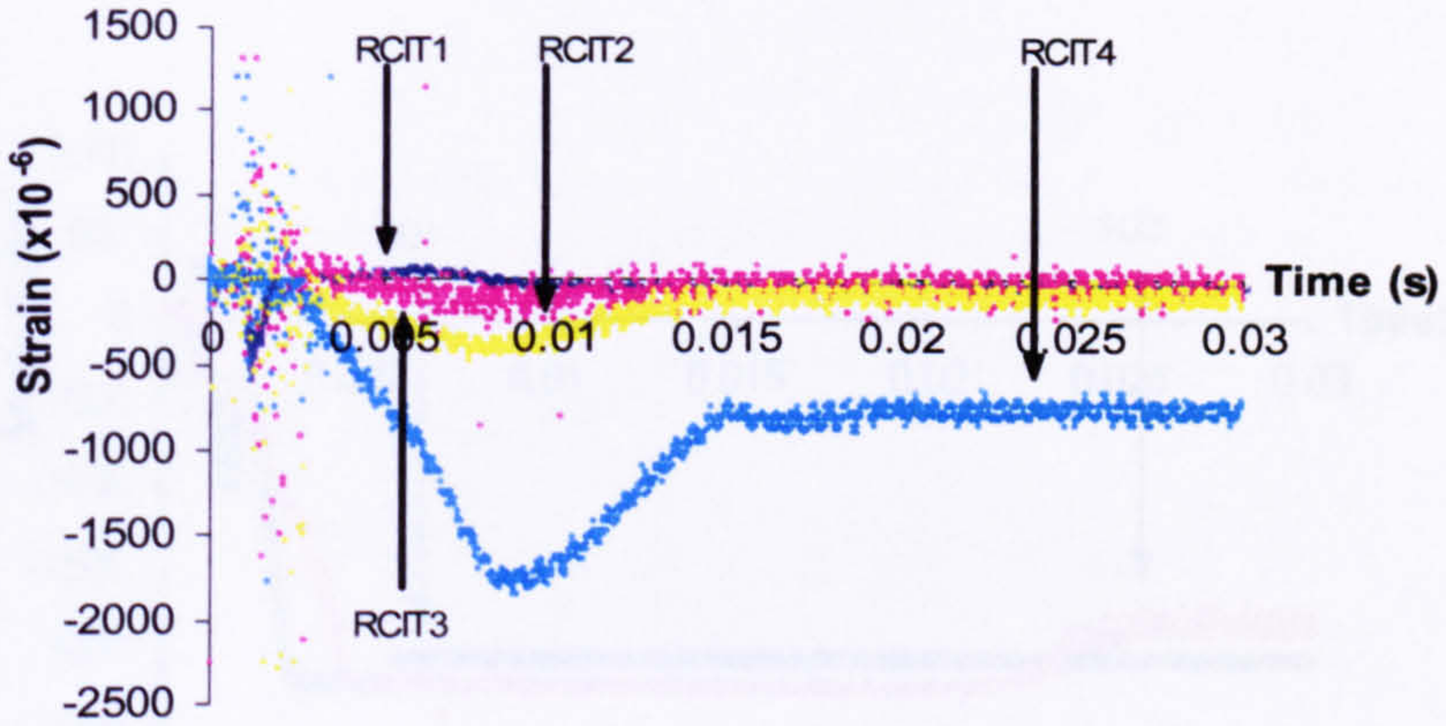

Figure A.1.29 Strain-time traces recorded by SG1 in tests RCIT1-4.

A comment relating to figure A.1.30 is described below:

1. A decrease in charge standoff and positioning of the charge caused a greater increase in maximum peak strain in SG2, compared to that in SG1.

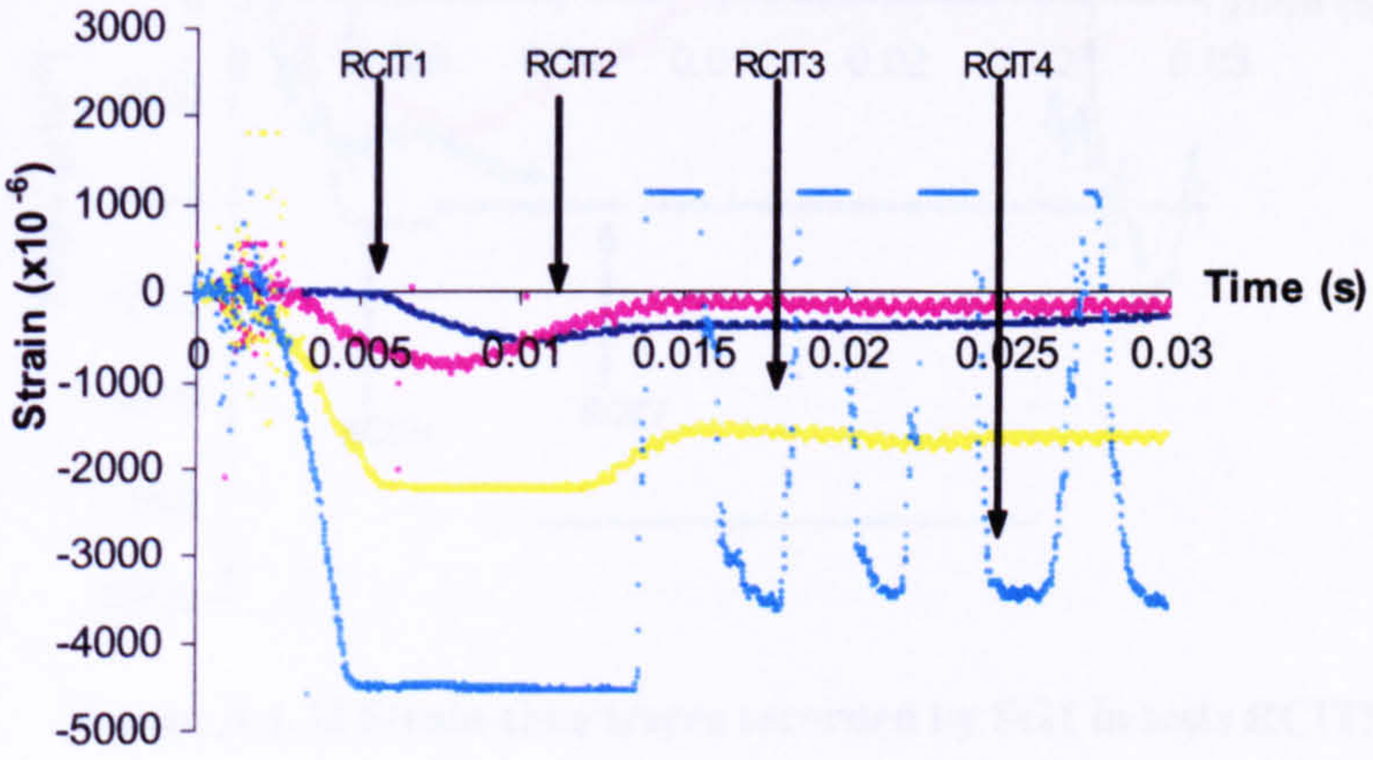

Figure A.1.30 Strain-time traces recorded by the SG2 in tests RCIT1-4.

Group 2 results – Individual test analysis.

Comments relating to figure A.1.31 are described below:

1. The sensitivity associated with the captured traces from SG1 and SG2 were set too high, preventing the maximum peak strain from being identified.
2. The strain rate associated with SG1 was greater than that produced by SG2.

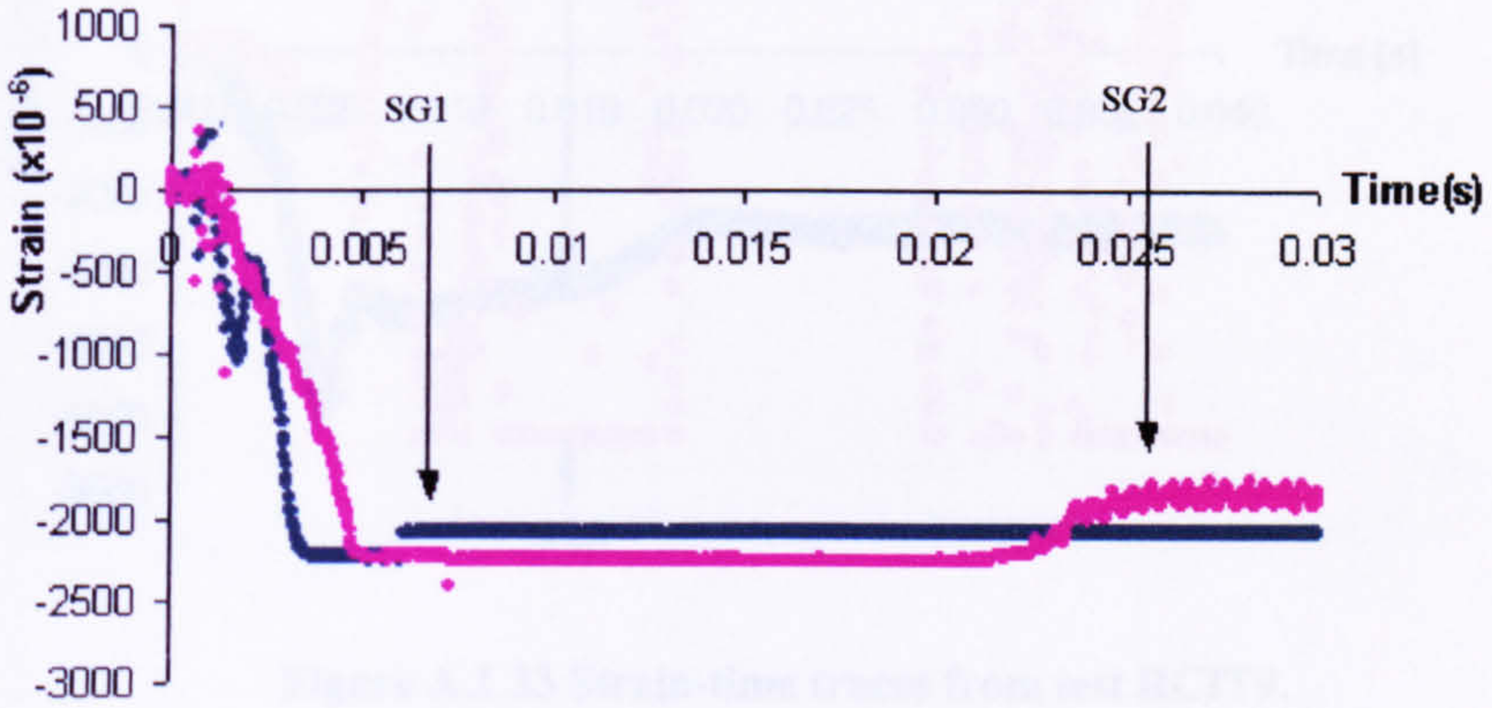

Figure A.1.31 Strain-time traces from test RCIT5.

Group 2 results – Comparison of the tests.

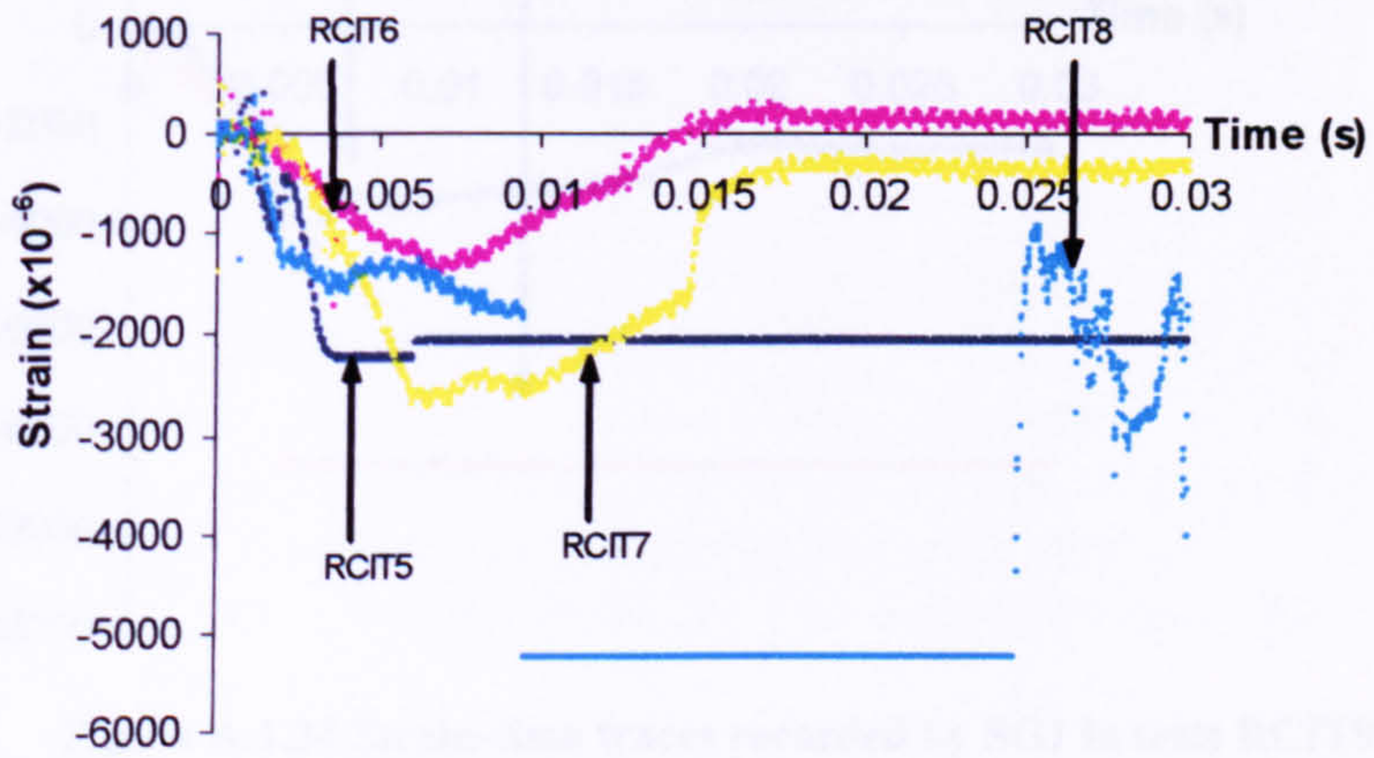

Figure A.1.32 Strain-time traces recorded by SG1 in tests RCIT5-8.

Group 3 results – Individual test analysis.
Comments relating to figure A.1.33 are described below:

1. Due to SG1 being damaged in RCIT10 and not being functional in tests RCIT11, the strain-time traces were not included in this section.
2. SG2 was damaged during RCIT9 identified by the scattered data points that were captured.

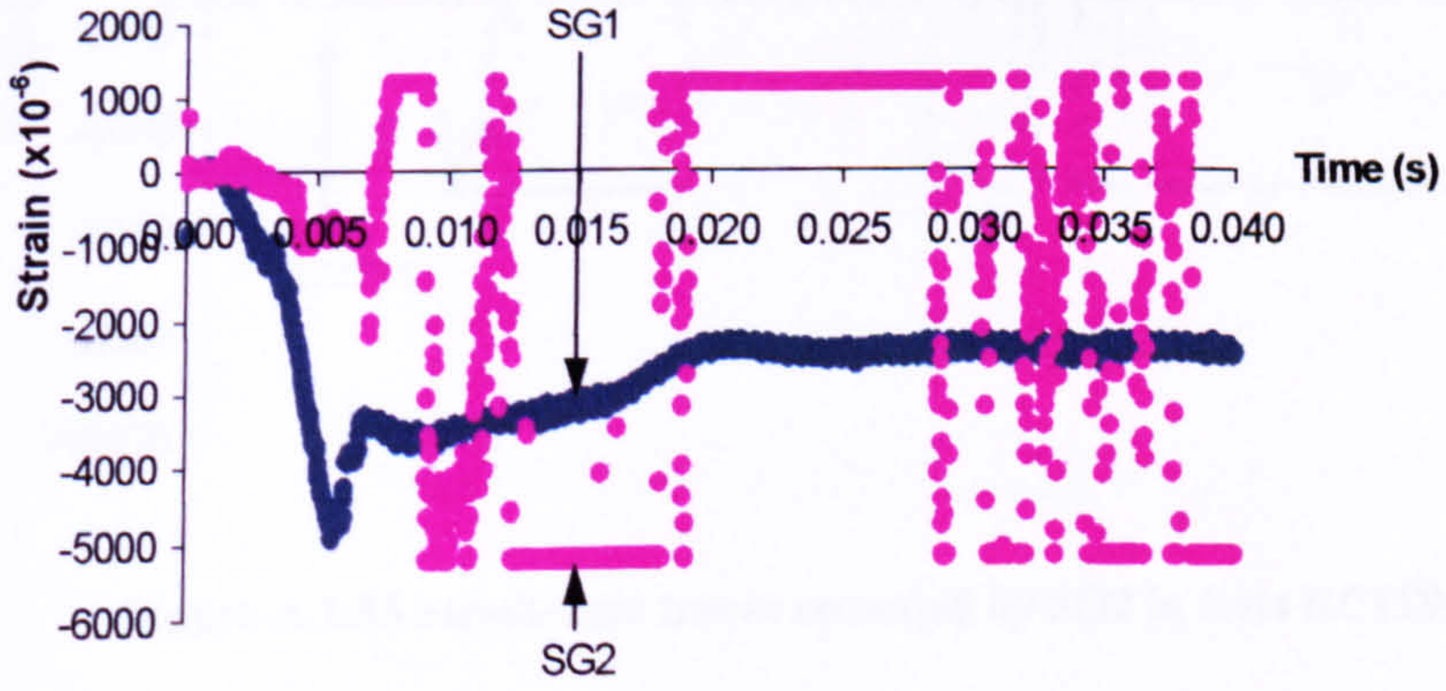

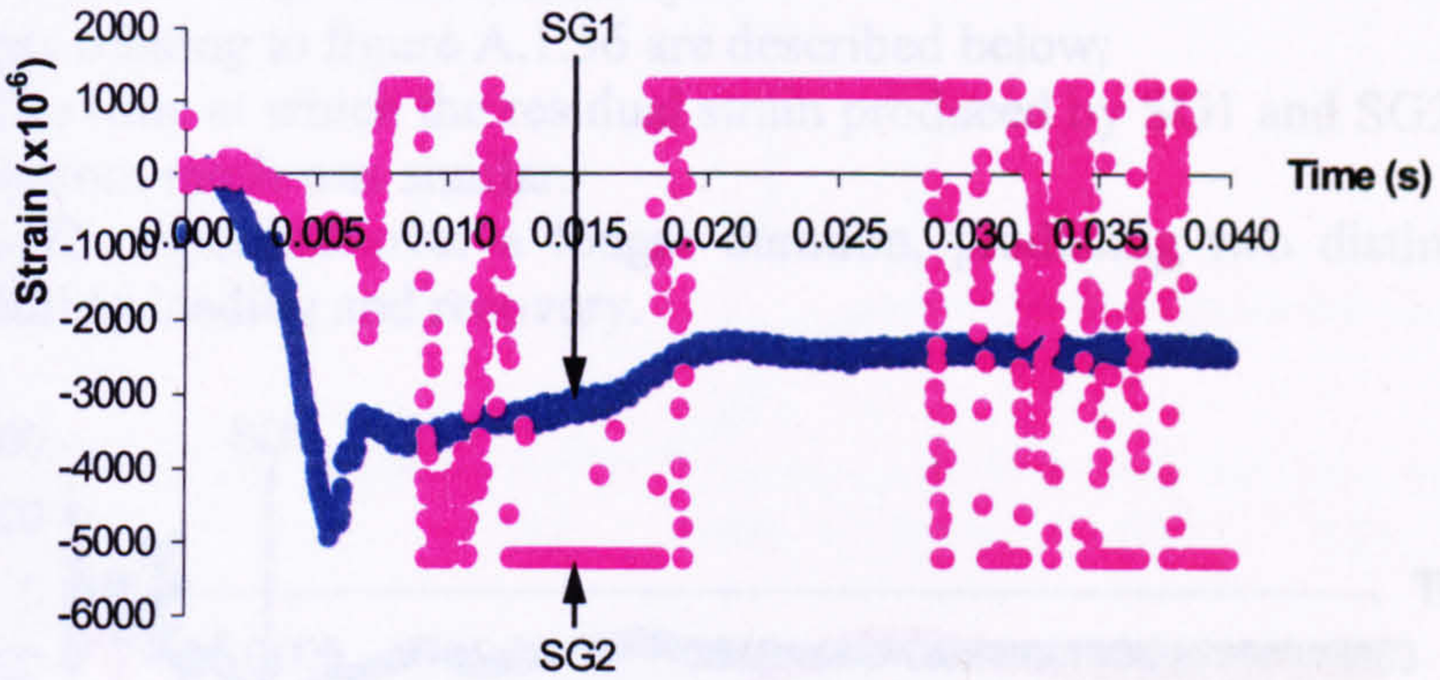

Figure A.1.33 Strain-time traces from test RCIT9.

Group 3 results – Comparison of the tests.

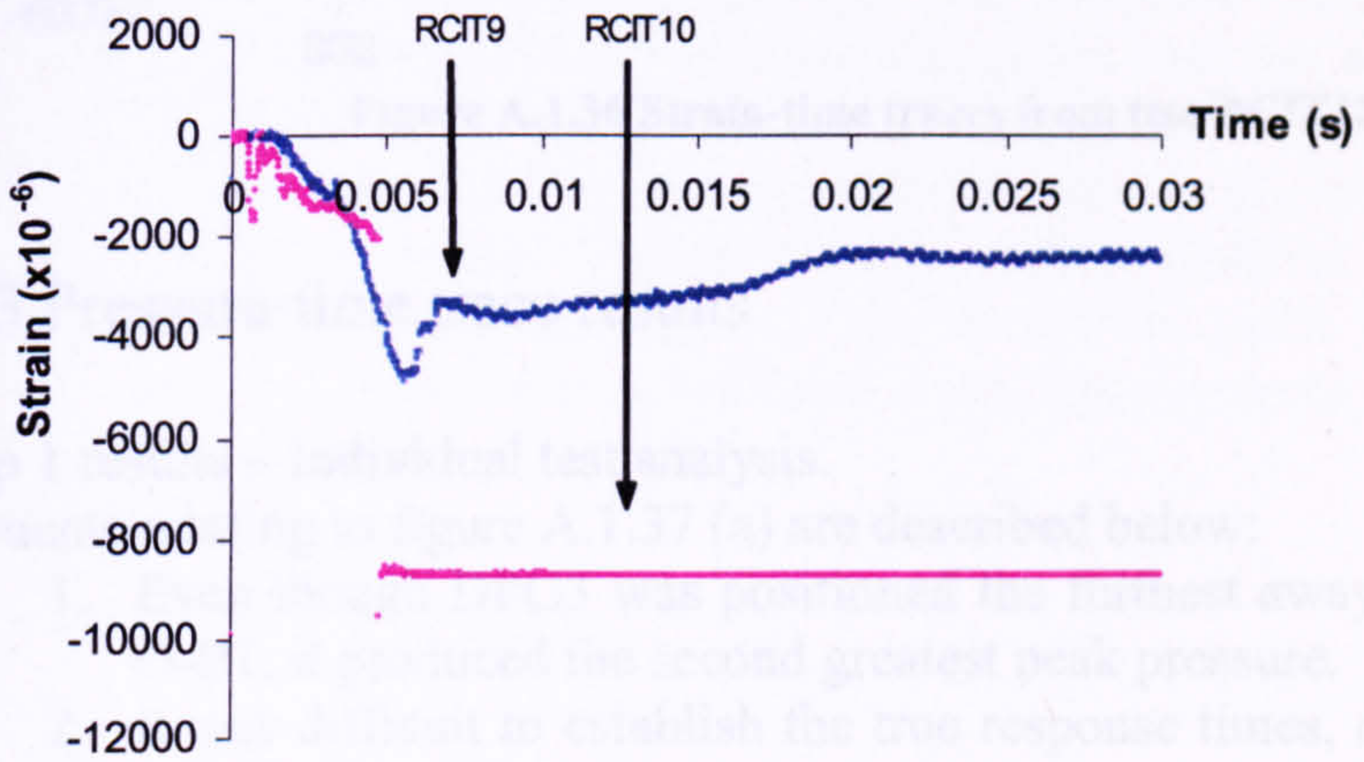

Figure A.1.34 Strain-time traces recorded by SG1 in tests RCIT9-10.

A comment relating to figure A.1.35 is described below:

1. The trace associated with SG2 from RCIT11 illustrated possible slip action occurring between the concrete and the steel. This was identified by approximate outputs of negligible strain between periods of maximum strain.

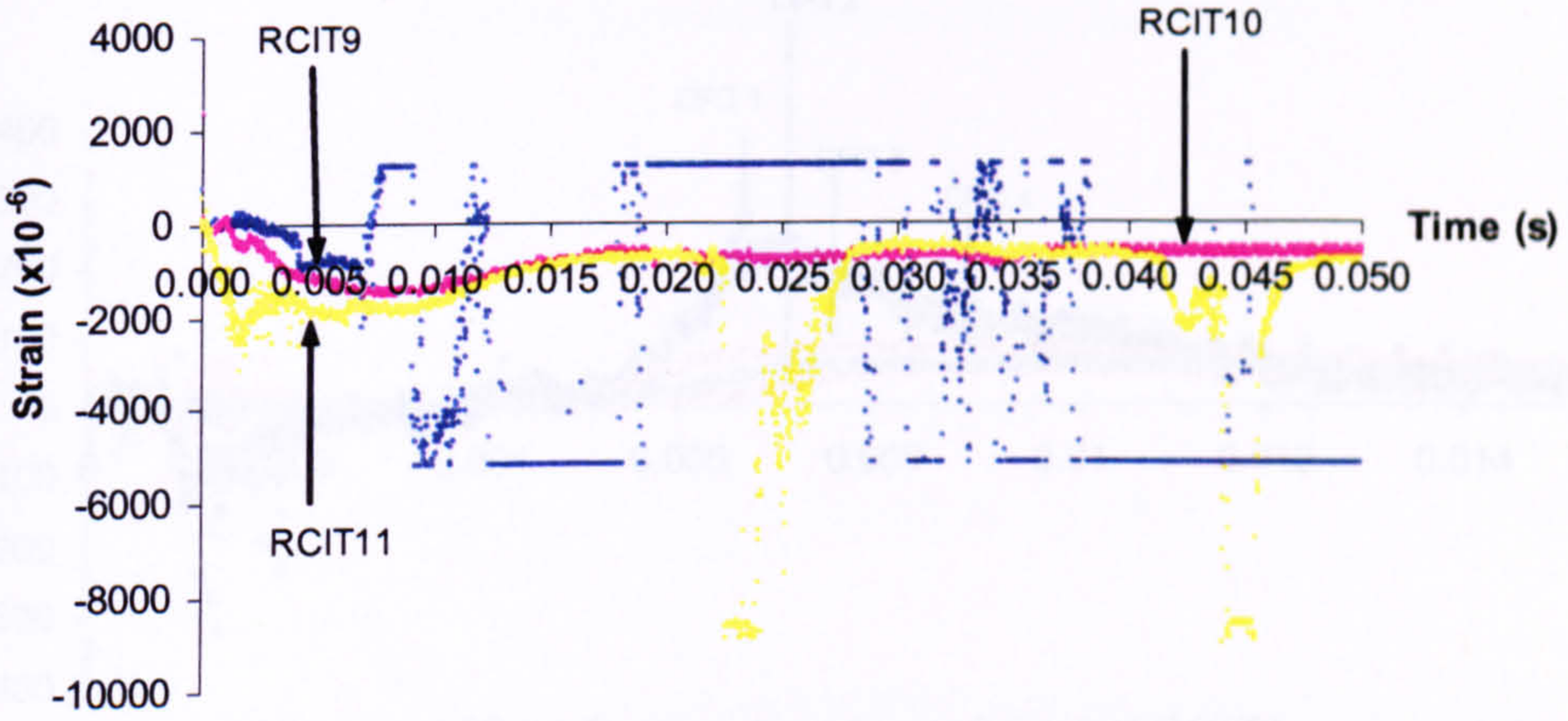

Figure A.1.35 Strain-time traces recorded by SG2 in tests RCIT9-11.

Group 4 results – Individual test analysis
Comments relating to figure A.1.36 are described below:

1. The time at which the residual strain produced by SG1 and SG2 in the top and bottom mesh was similar.
2. SG2 responded over a longer duration, producing two distinct strain rates, during loading and recovery.

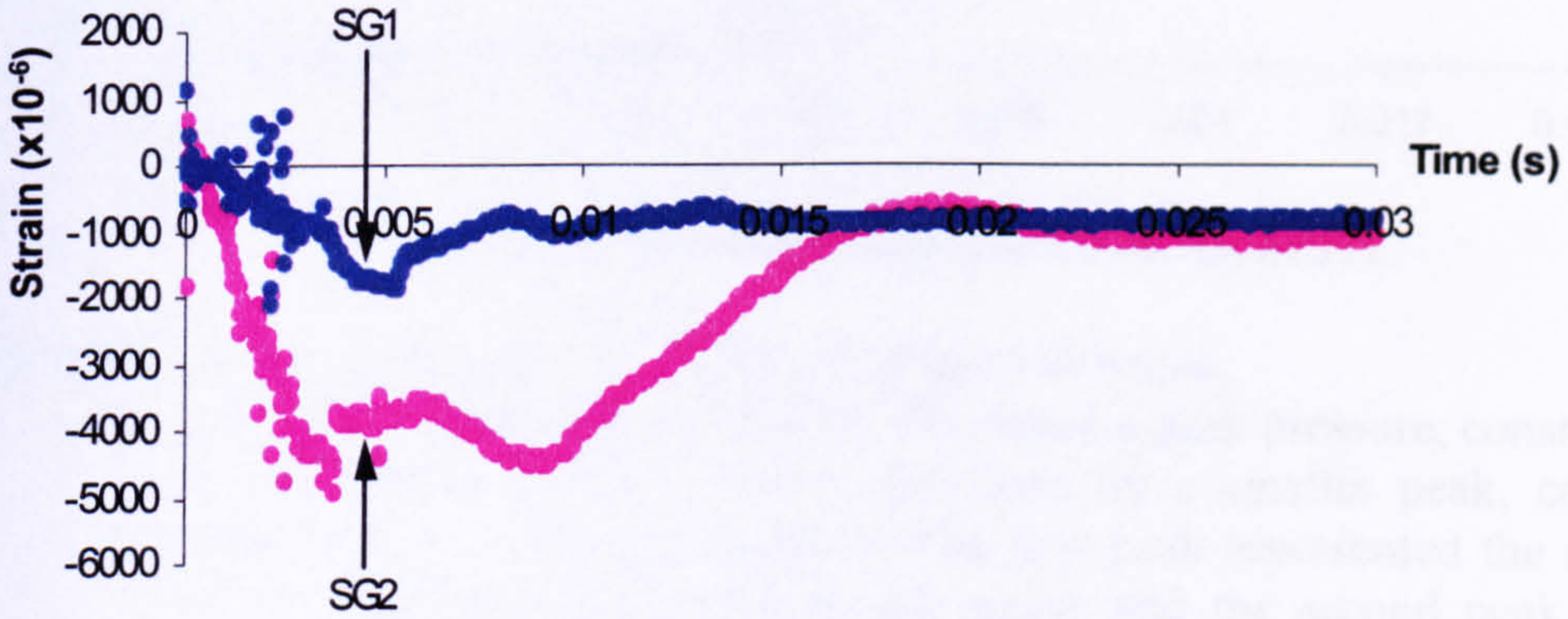

Figure A.1.36 Strain-time traces from test RCIT12.

A.1.3 Pressure-time trace results

Group 1 results – Individual test analysis.
Comments relating to figure A.1.37 (a) are described below:

1. Even though DPG3 was positioned the furthest away from O along plane O-B1, it produced the second greatest peak pressure.
2. It was difficult to establish the true response times, due to assumed noise interference.
3. All the DPGs responded elastically.
4. DPGs 2-4 all illustrated a constant maximum pressure, over a given duration, rather than peaks. This perhaps suggested that there was a greater spatial distribution of load along plane O-B1.

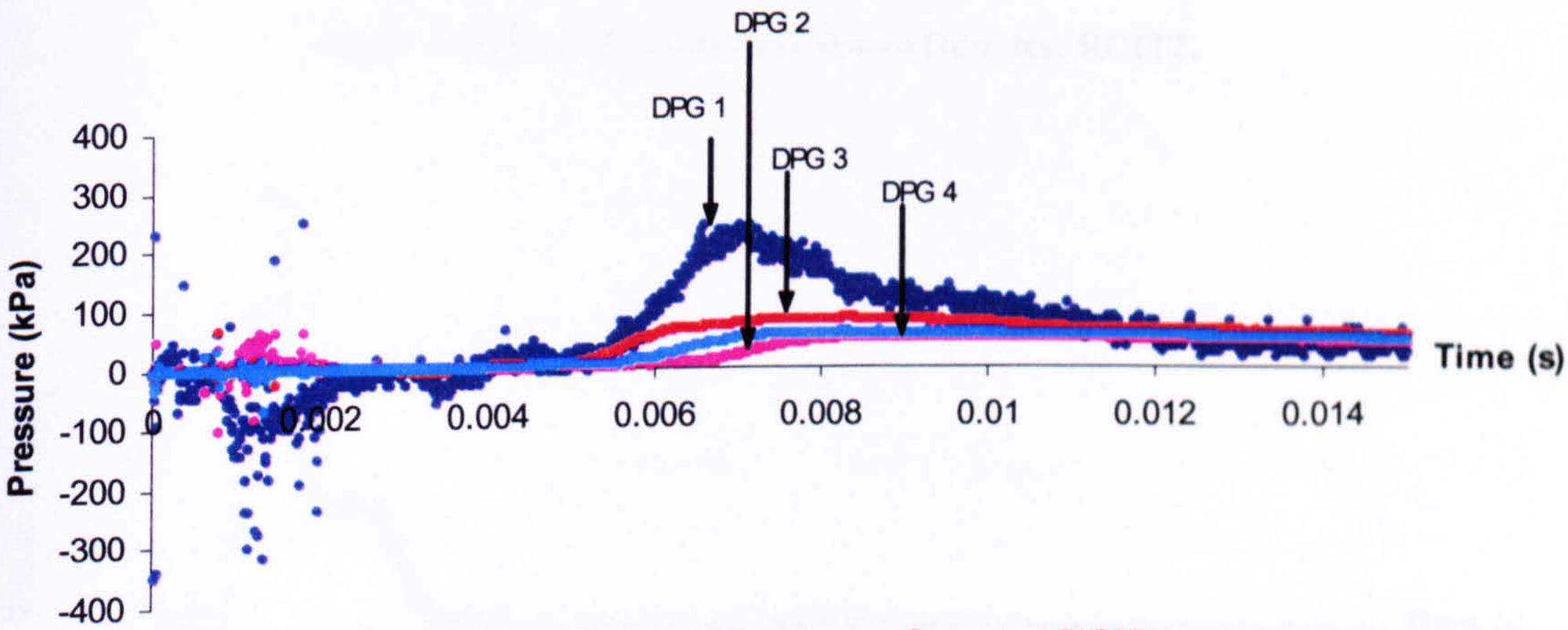

Figure A.1.37 (a) Pressure-time traces from test RCIT1.

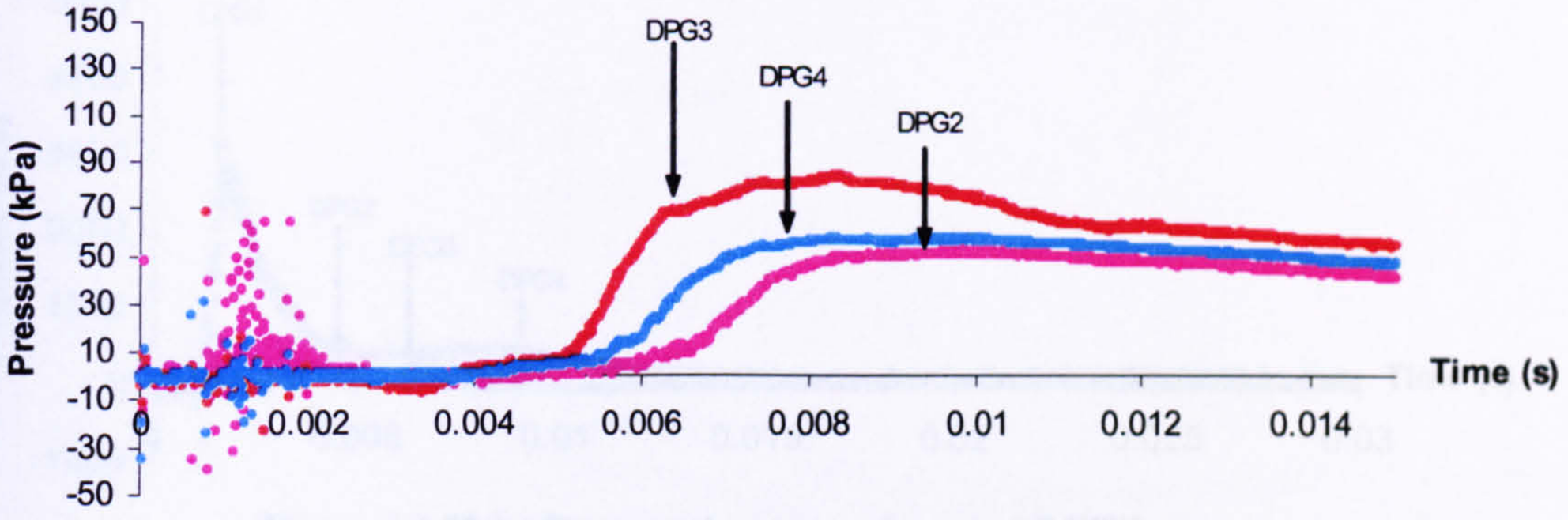

Figure A.1.37 (b) Pressure-time traces from test RCIT1.

Comments relating to figure A.1.38 (a) are described below:

1. The trace associated with DPG1 illustrated a peak pressure, constant over a small duration, then a decay, followed by a smaller peak, constant in pressure over a longer duration. The first peak represented the maximum peak pressure encountered by the gauge and the second peak could be associated with a stress wave reflecting from the sides of the test cell. Another possible explanation could be particle impact by an aggregate.
2. DPG3 illustrated a positive pressure-time gradient on the second peak, which was less than that produced on the first peak. This indicated that the second disturbance could have come from a stress wave reflecting from the polystyrene boundary.

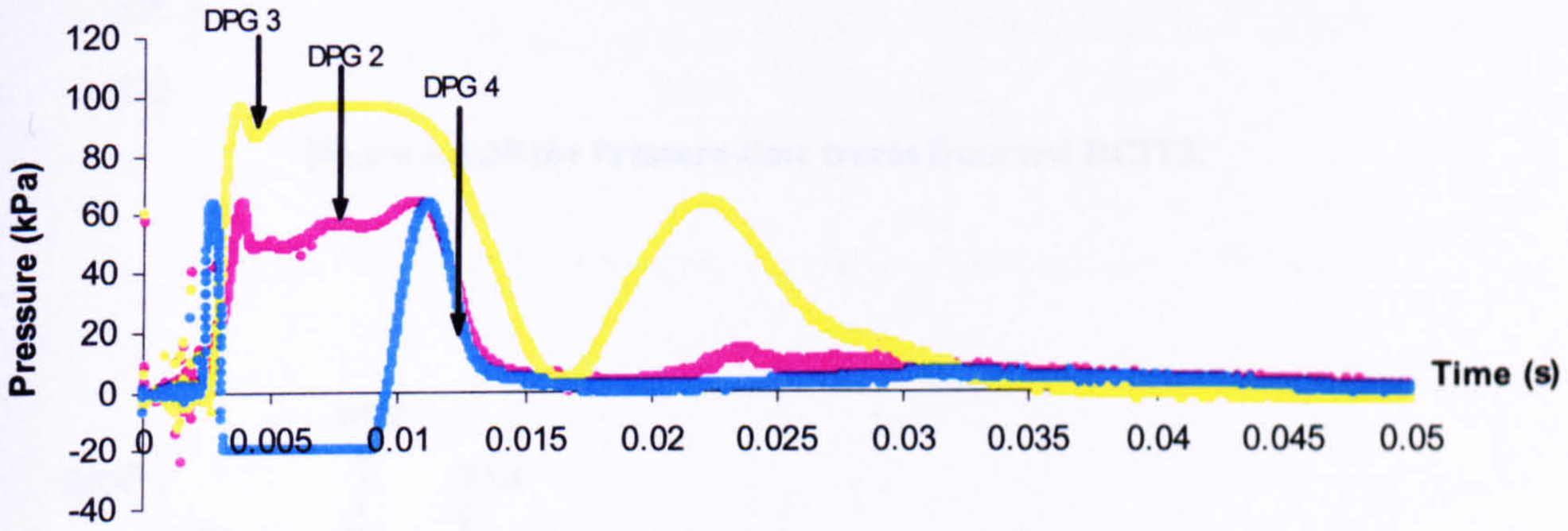

Figure A.1.38 (a) Pressure-time traces from test RCIT2.

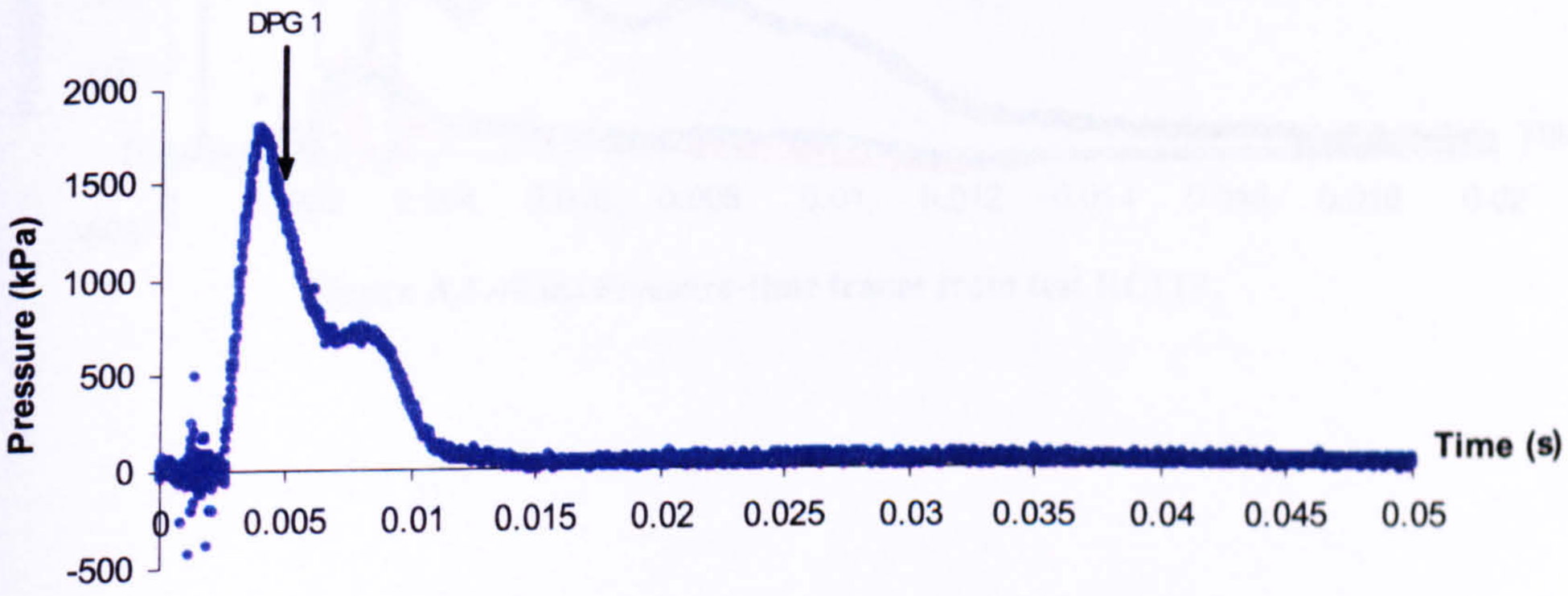

Figure A.1.38 (b) Pressure-time trace from test RCIT2.

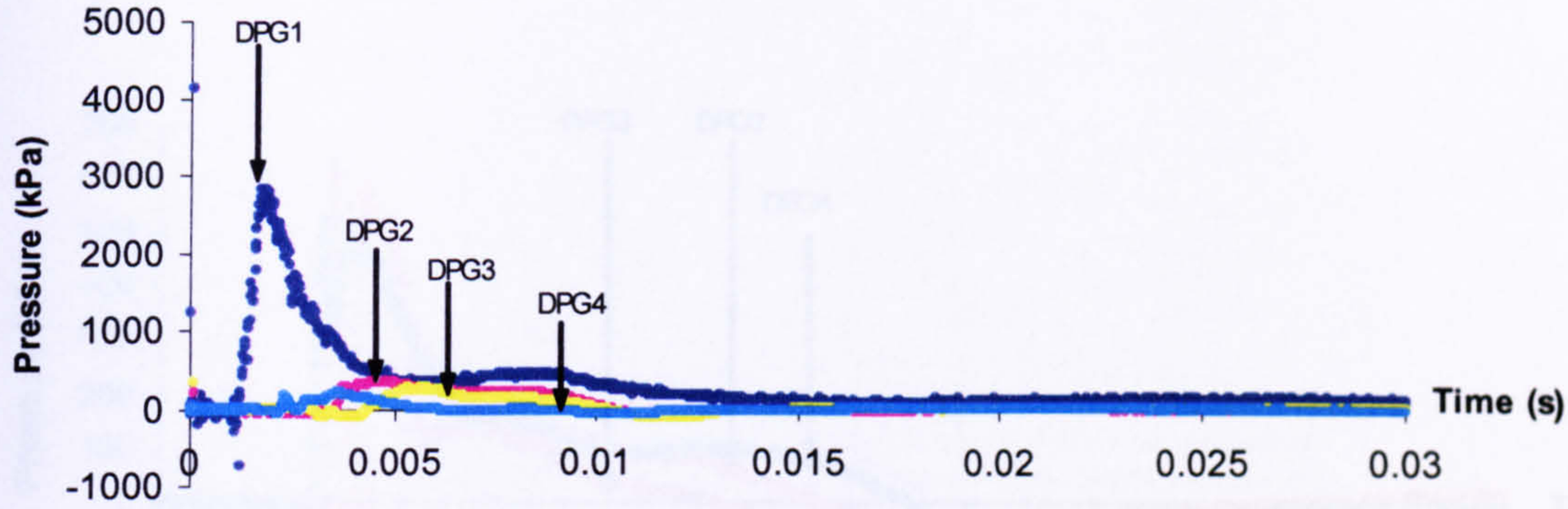

Figure A.1.39 (a) Pressure-time traces from test RCIT3.

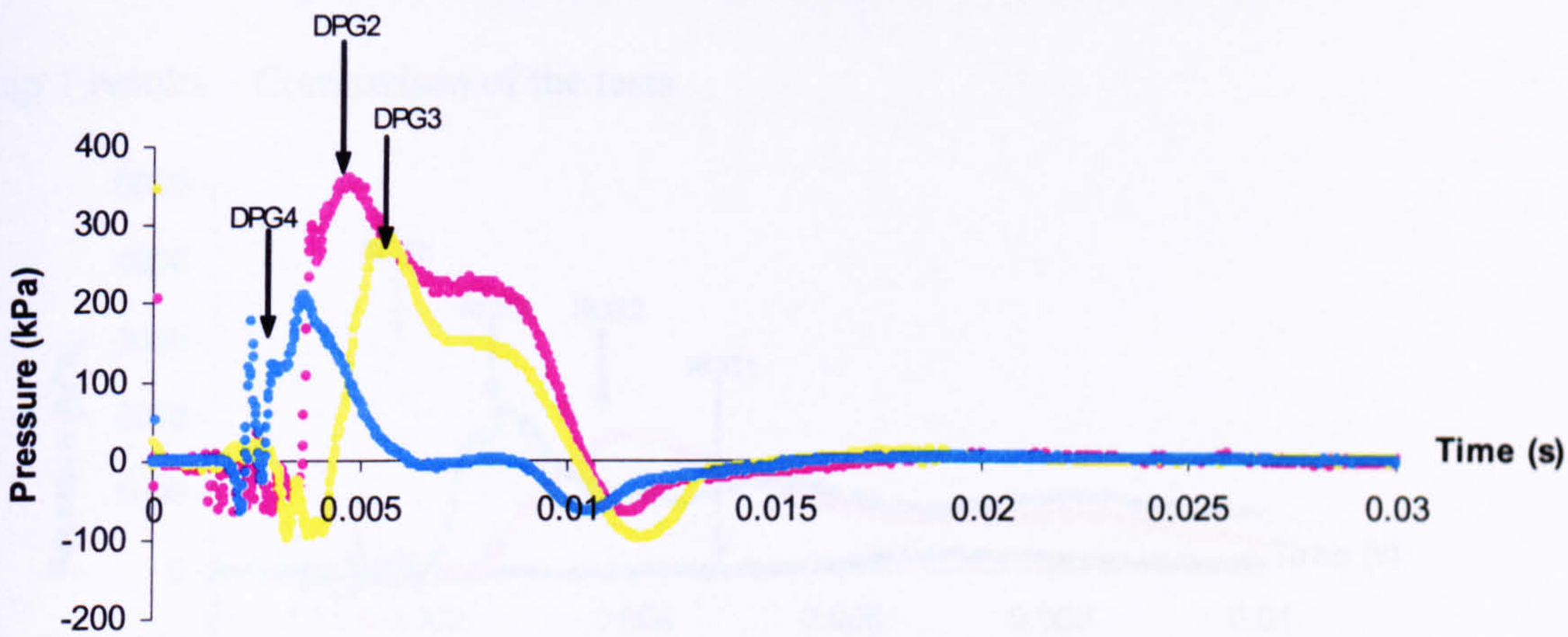

Figure A.1.39 (b) Pressure-time traces from test RCIT3.

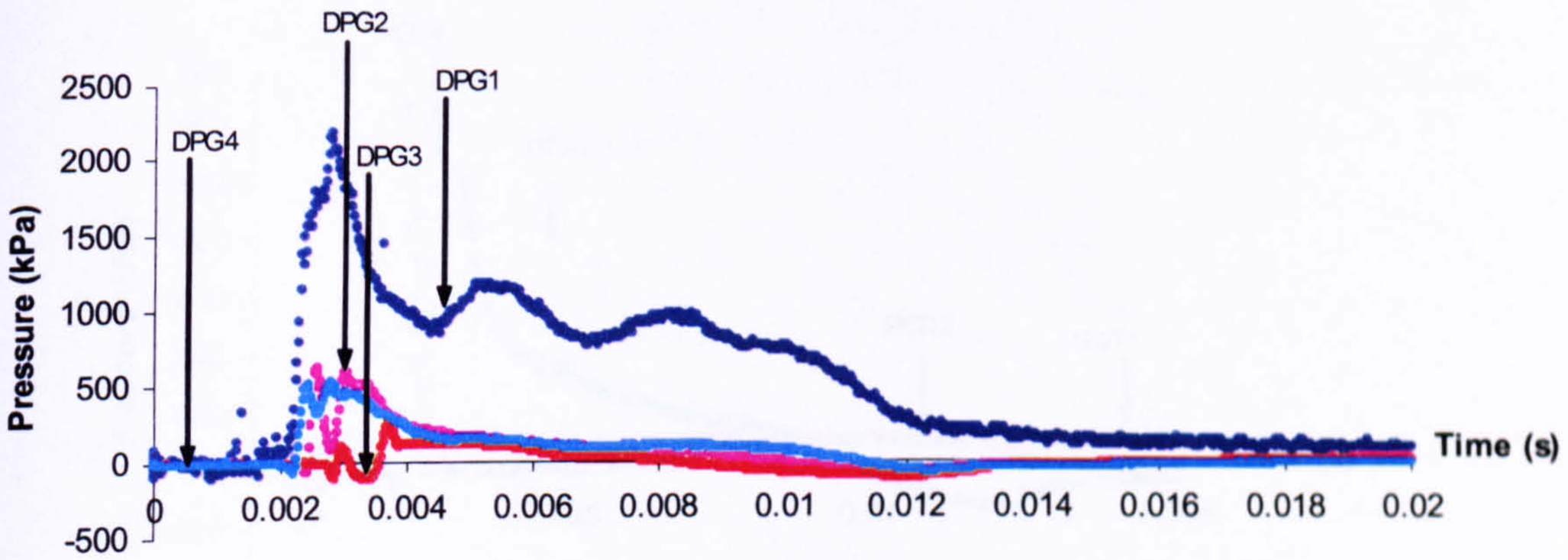

Figure A.1.40 (a) Pressure-time traces from test RCIT4.

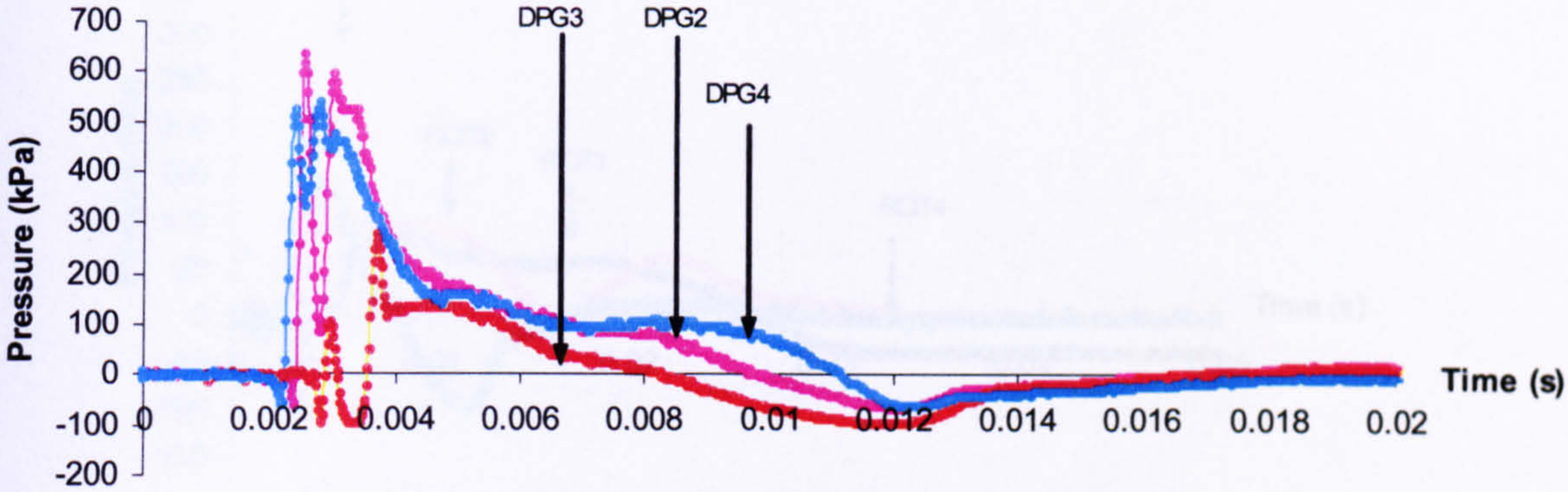

Figure A.1.40 (b) Pressure-time traces from test RCIT4.

Group 1 results – Comparison of the tests

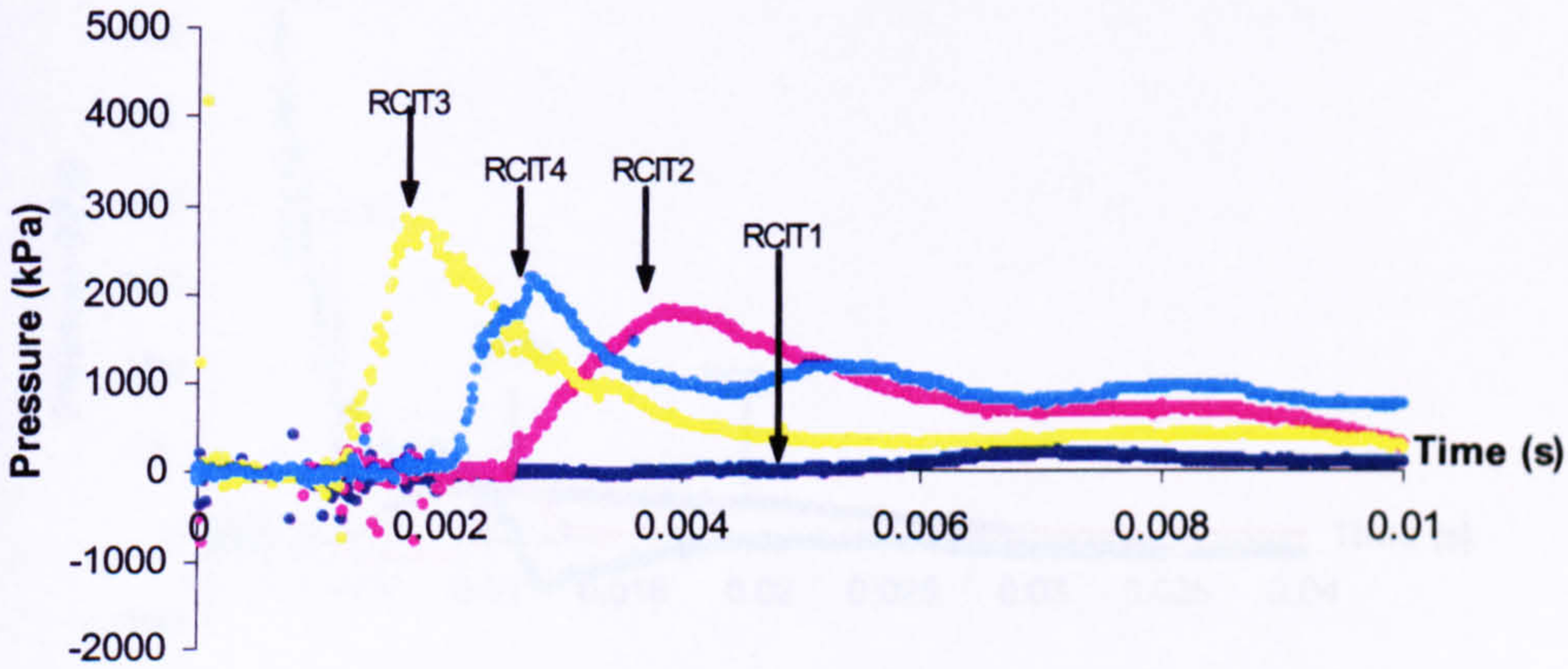

Figure A.1.41 Pressure-time traces recorded by DPG1 in tests RCIT1-4.

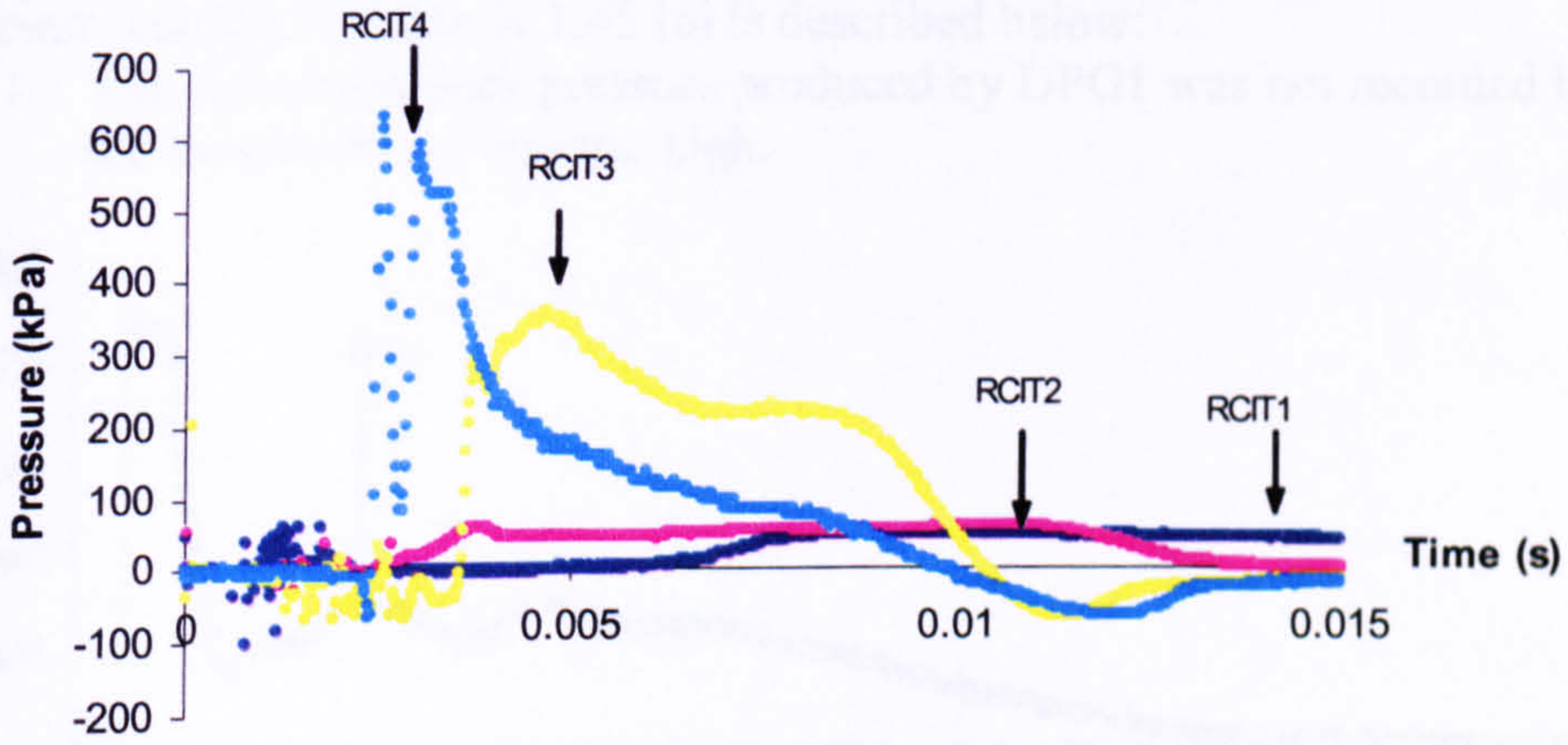

Figure A.1.42 Pressure-time traces recorded by DPG2 in tests RCIT1-4.

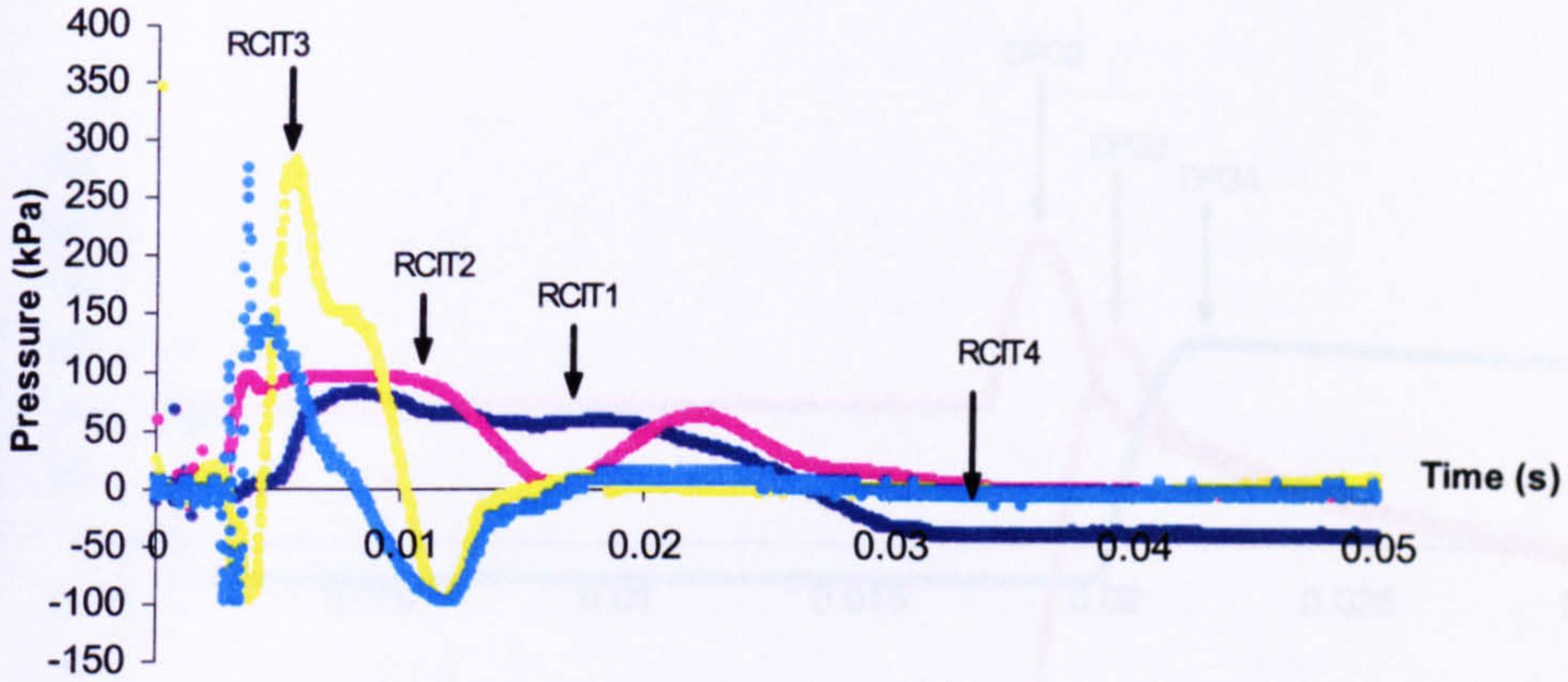

Figure A.1.43 Pressure-time traces recorded by DPG3 in tests RCIT1-4.

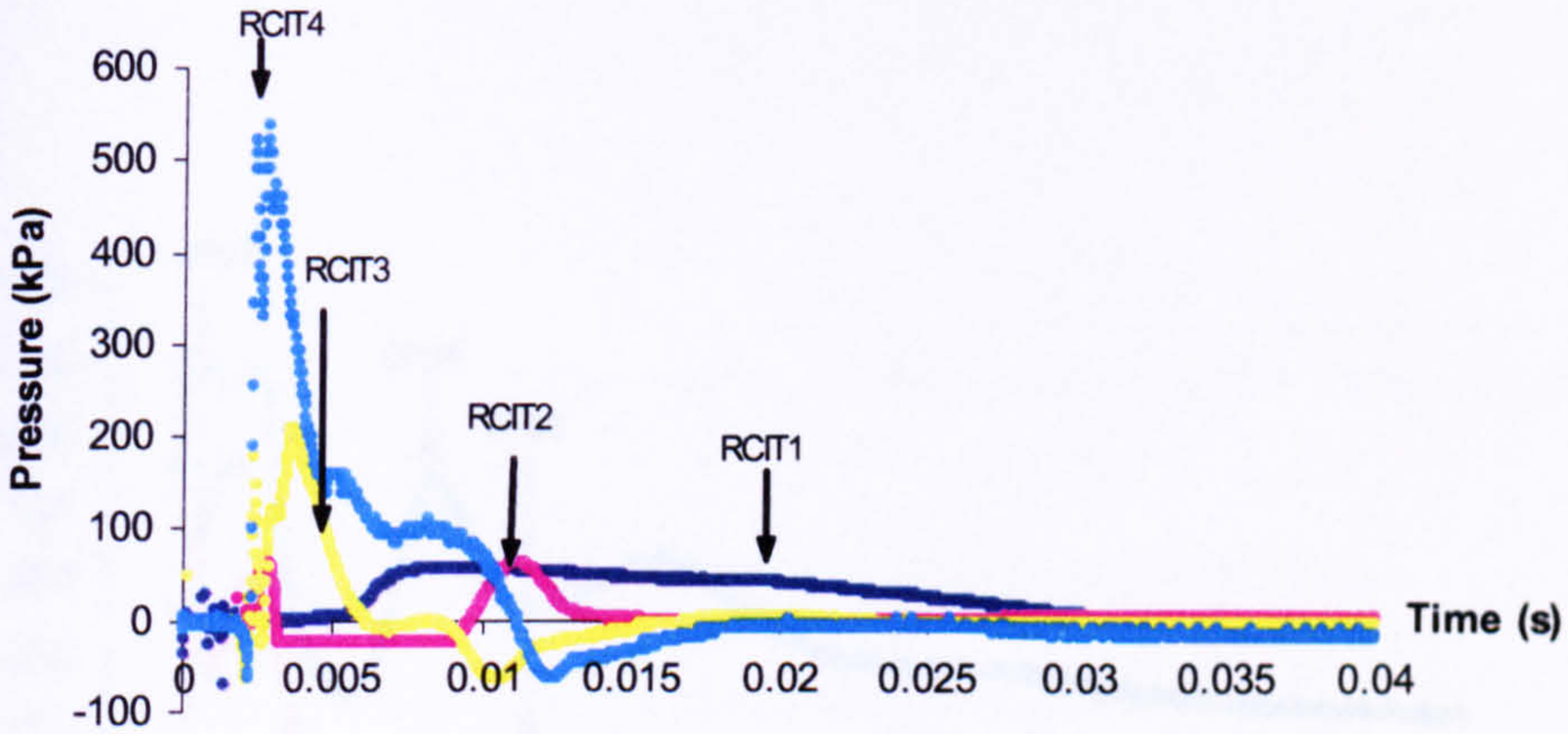

Figure A.1.44 Pressure-time traces recorded by DPG4 in tests RCIT1-4.

Group 2 results – Individual test analysis.

A comment relating to figure A.1.45 (a) is described below:

1. The maximum peak pressure produced by DPG1 was not recorded because the sensitivity set was too high.

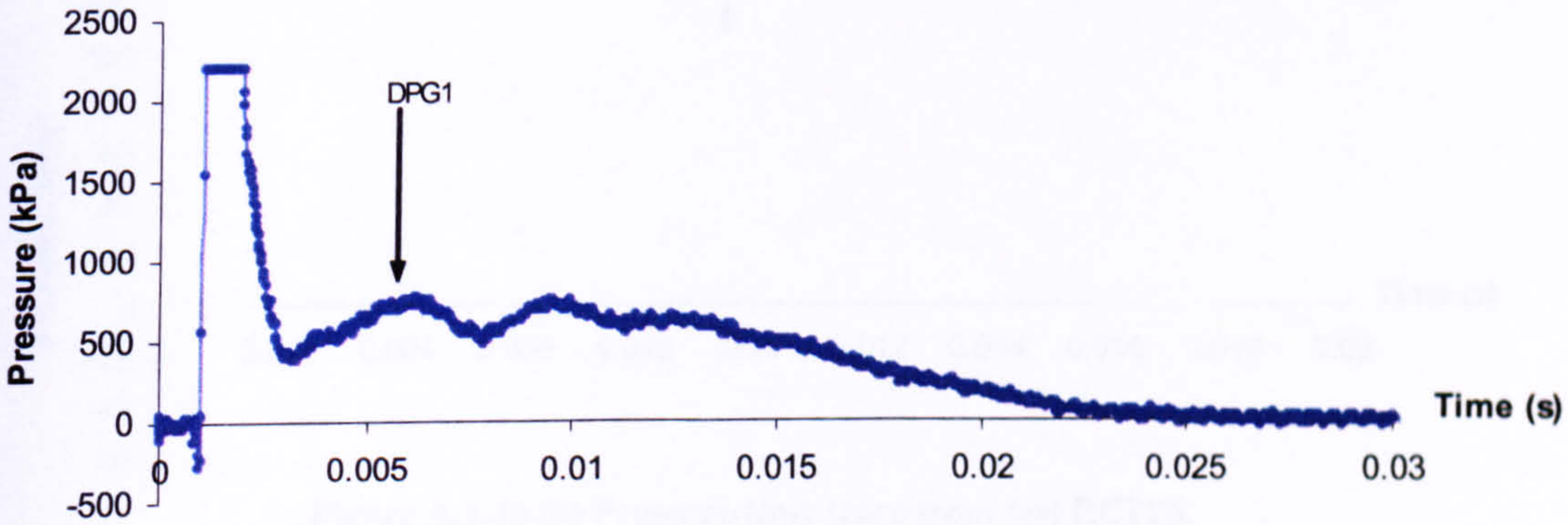

Figure A.1.45 (a) Pressure-time trace from test RCIT5.

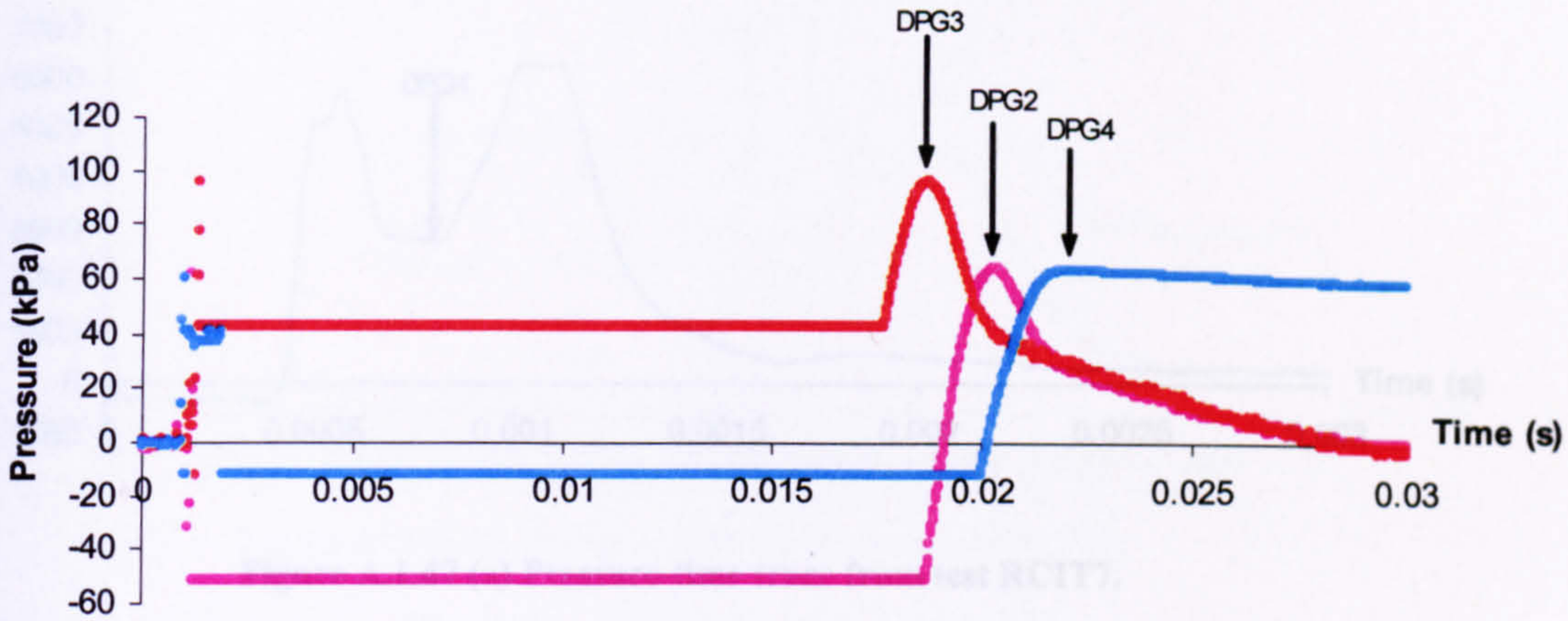

Figure A.1.45 (b) Pressure-time traces from test RCIT5.

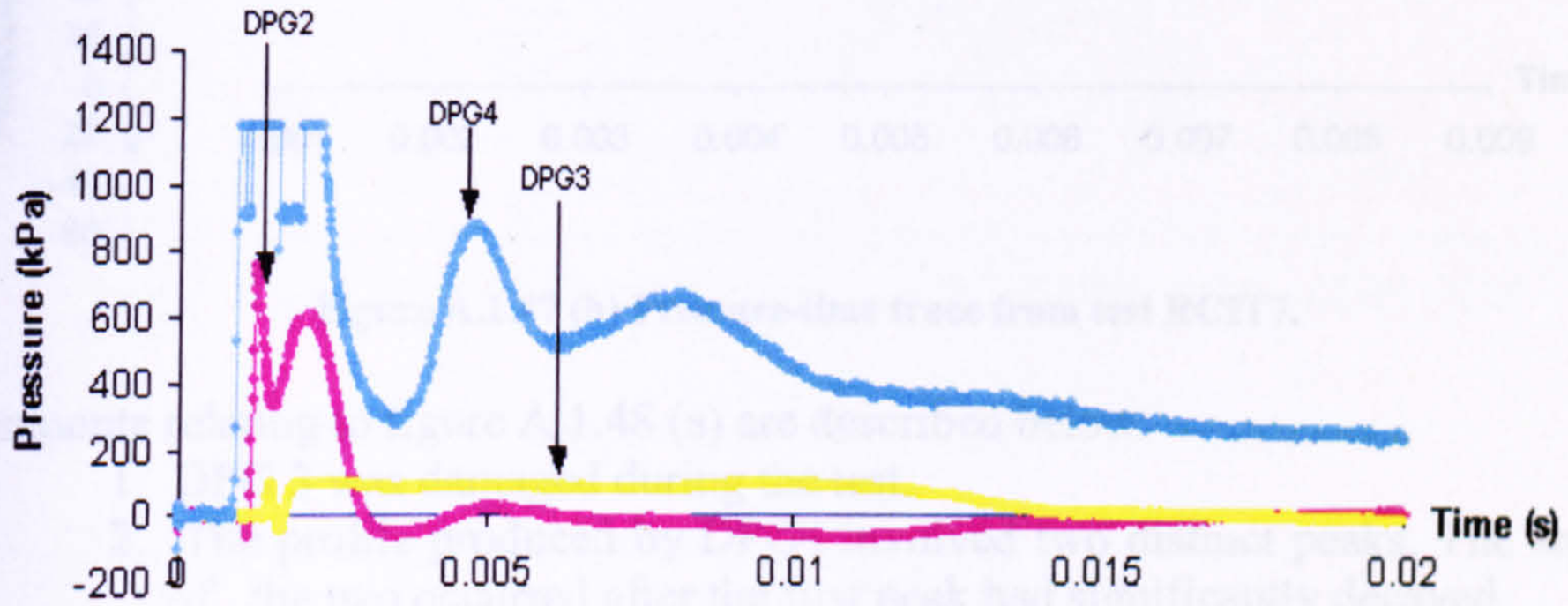

Figure A.1.46 (a) Pressure-time traces from test RCIT6.

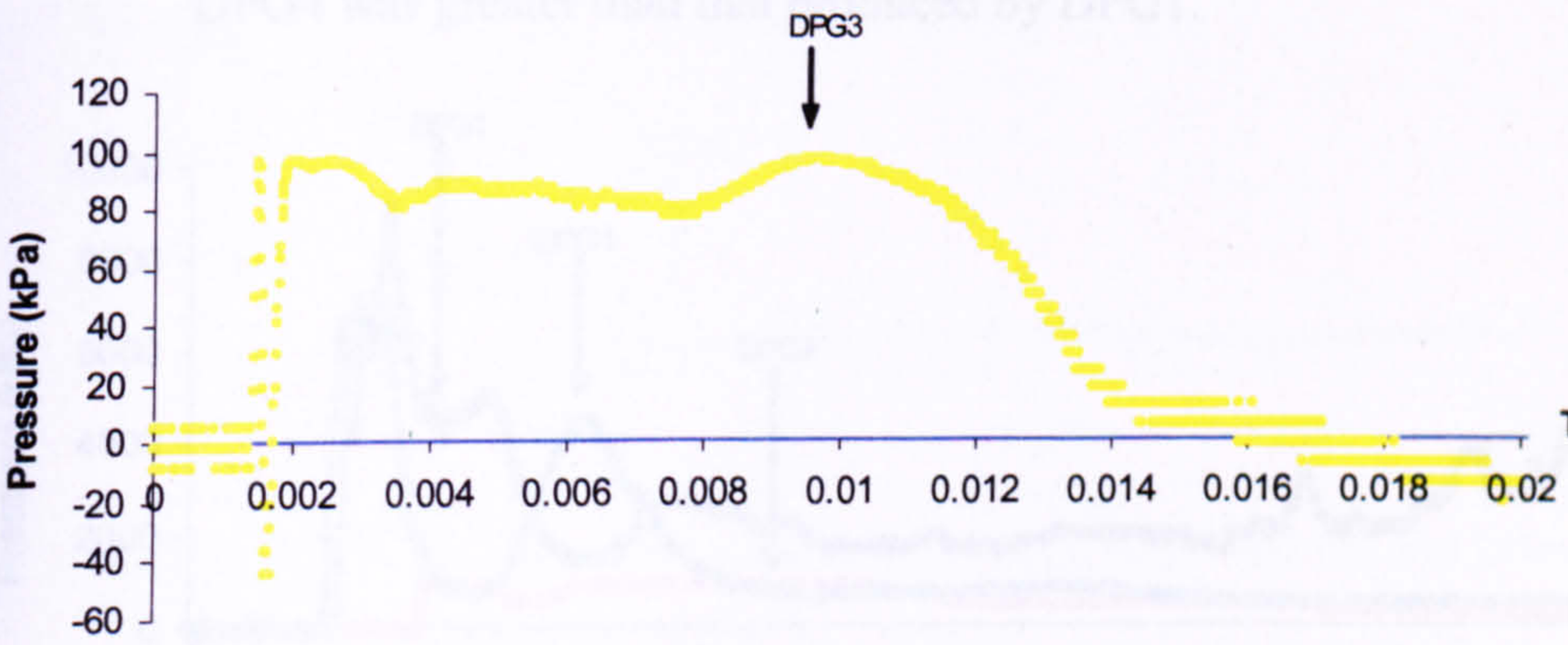

Figure A.1.46 (b) Pressure-time trace from test RCIT6.

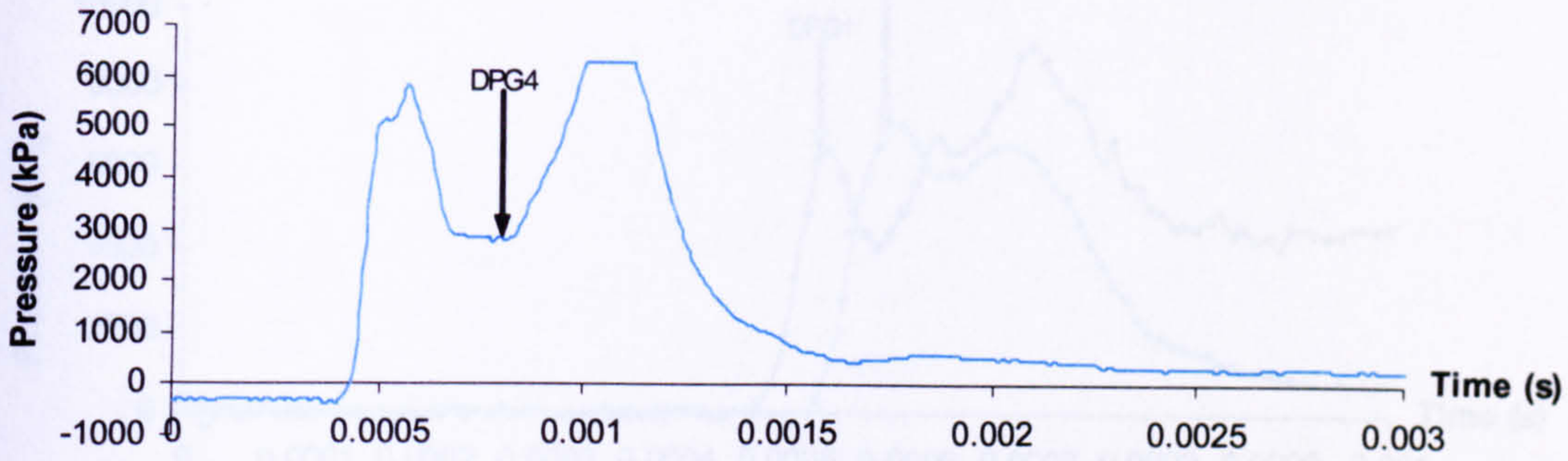

Figure A.1.47 (a) Pressure-time trace from test RCIT7.

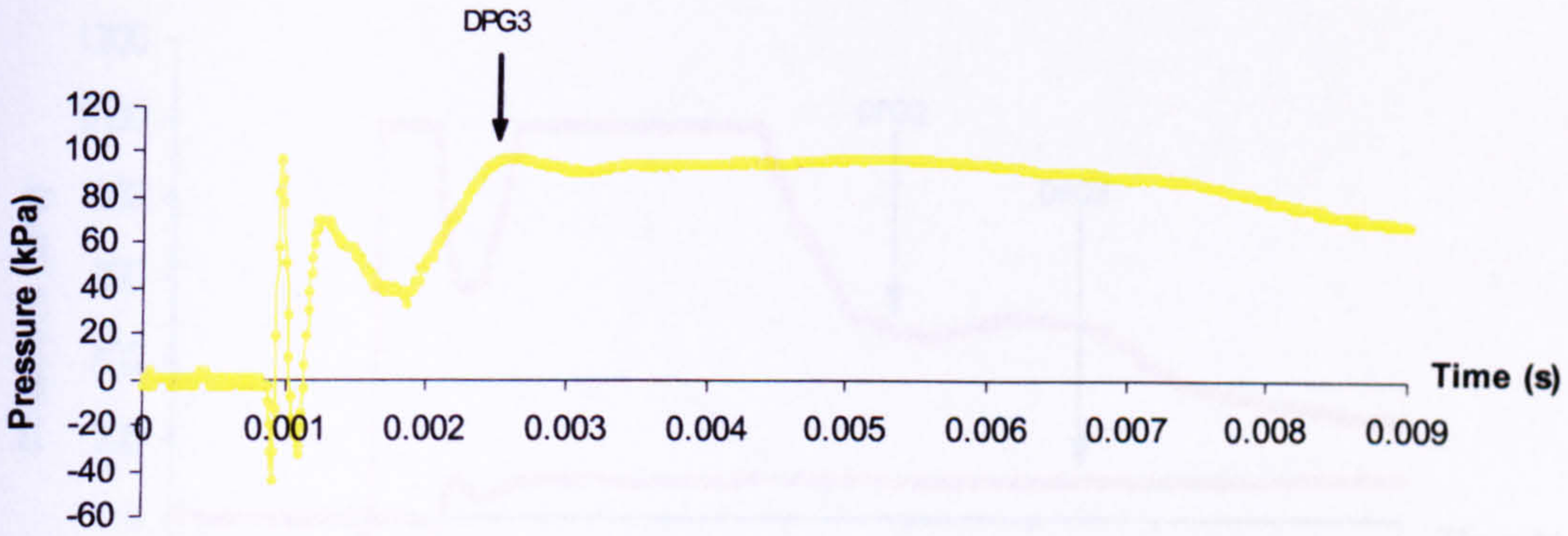

Figure A.1.47 (b) Pressure-time trace from test RCIT7.

Comments relating to figure A.1.48 (a) are described below:

1. DPG 3 was damaged during the test.
2. The profile produced by DPG4 involved two distinct peaks. The smaller of the two occurred after the first peak had significantly decayed.
3. The response of DPGs 2-4 remained elastic after the loading had been removed, compared to DPG1 that acquired a plastic deformation.
4. Although DPG1 responded before DPG4, the first peak produced by DPG4 was greater than that produced by DPG1.

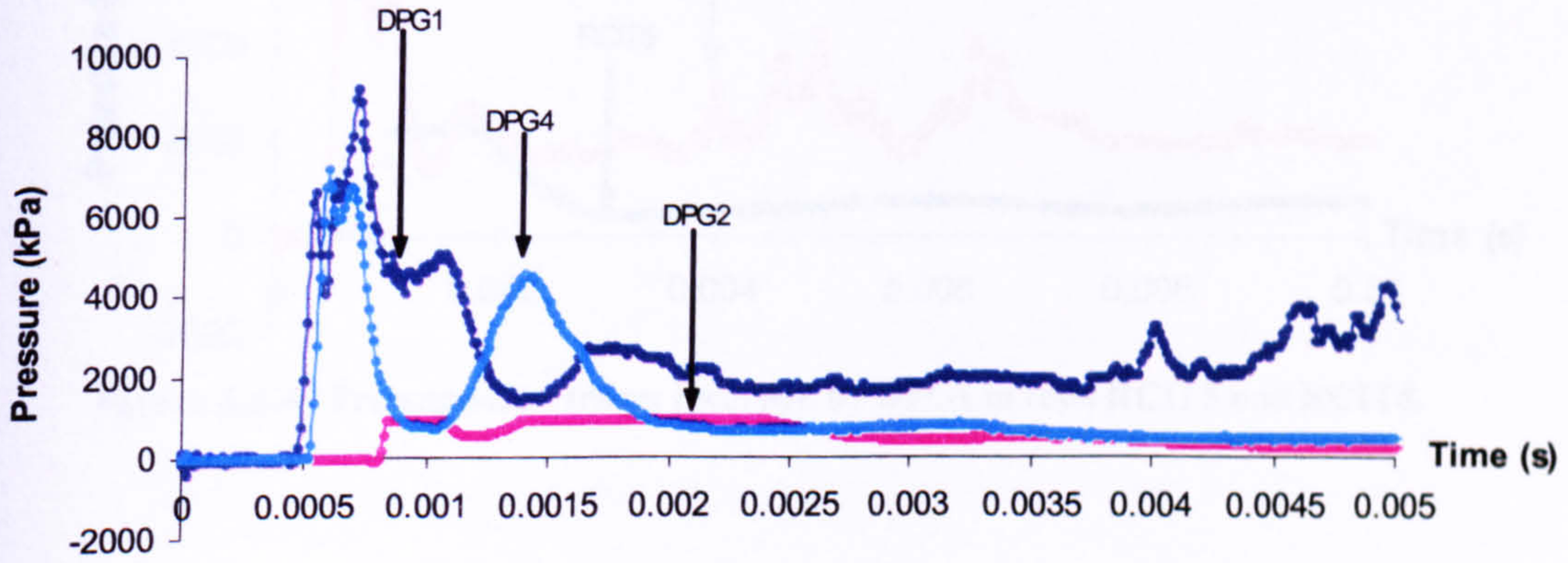

Figure A.1.48 (a) Pressure-time traces from test RCIT8.

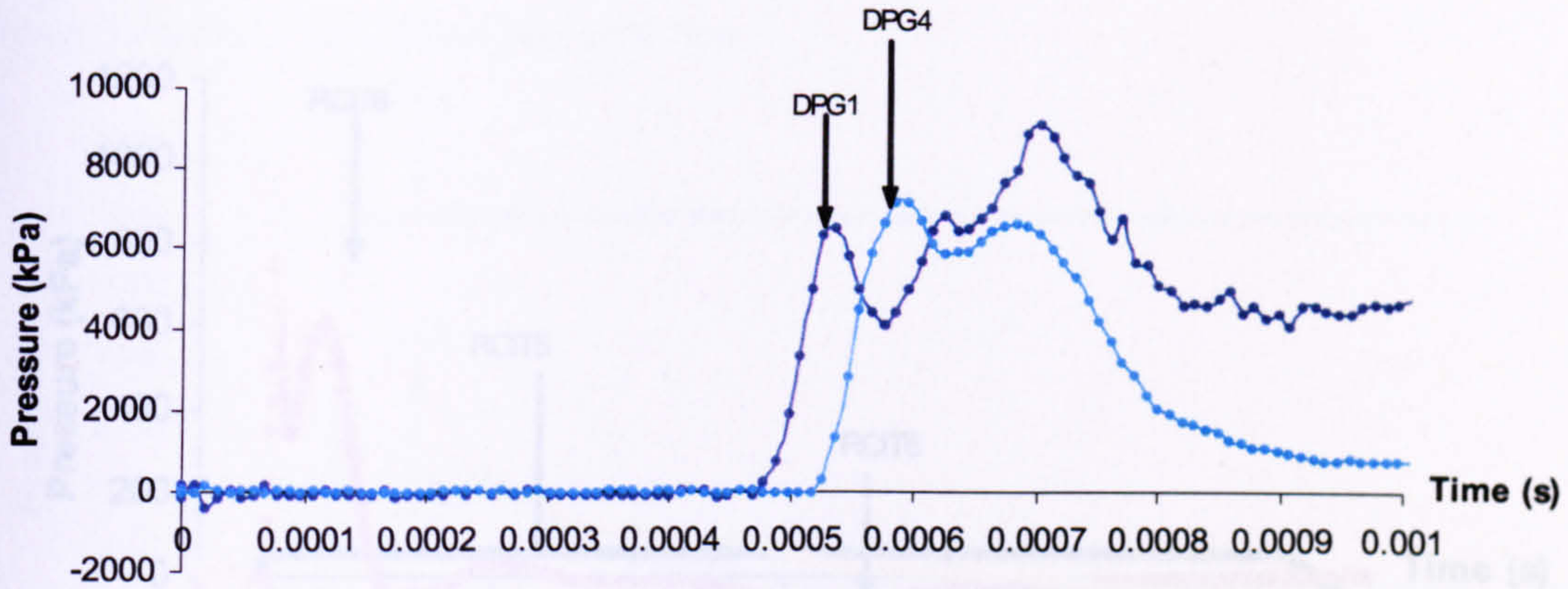

Figure A.1.48 (b) Pressure-time traces from test RCIT8.

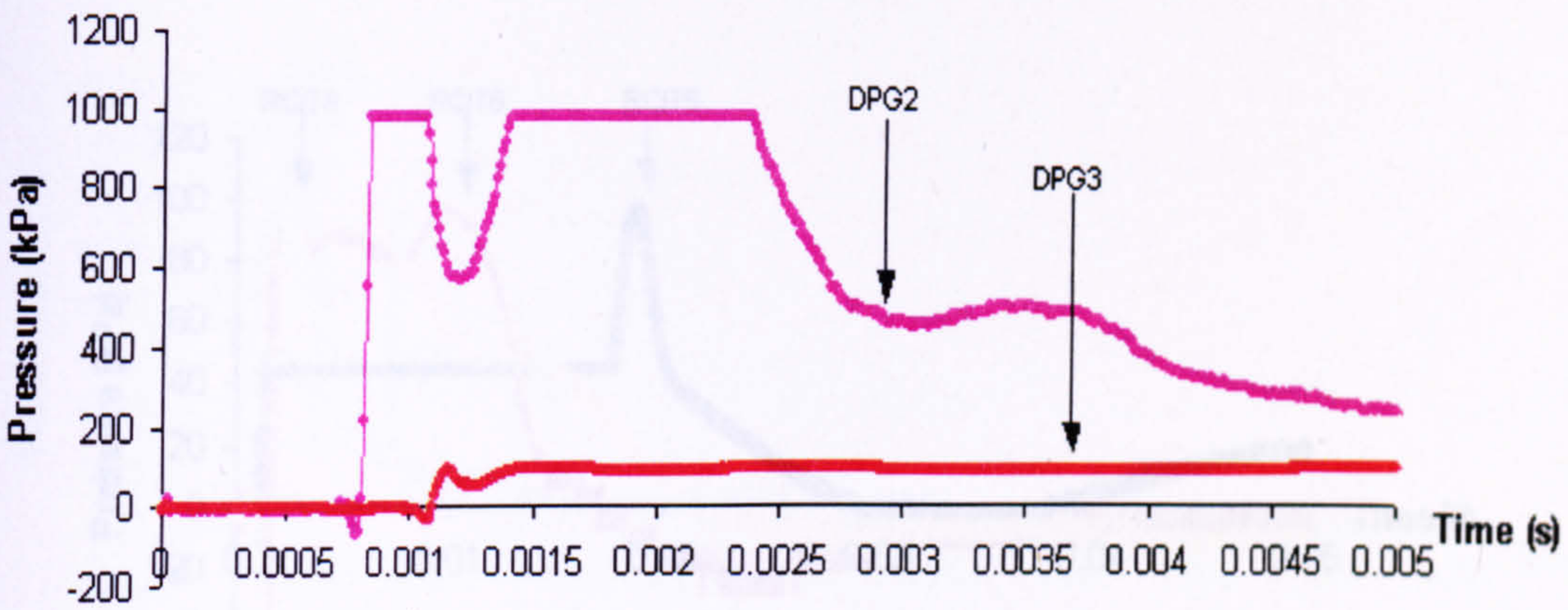

Figure A.1.48 (c) Pressure-time traces from test RCIT8.

Group 2 results – Comparison of the tests.

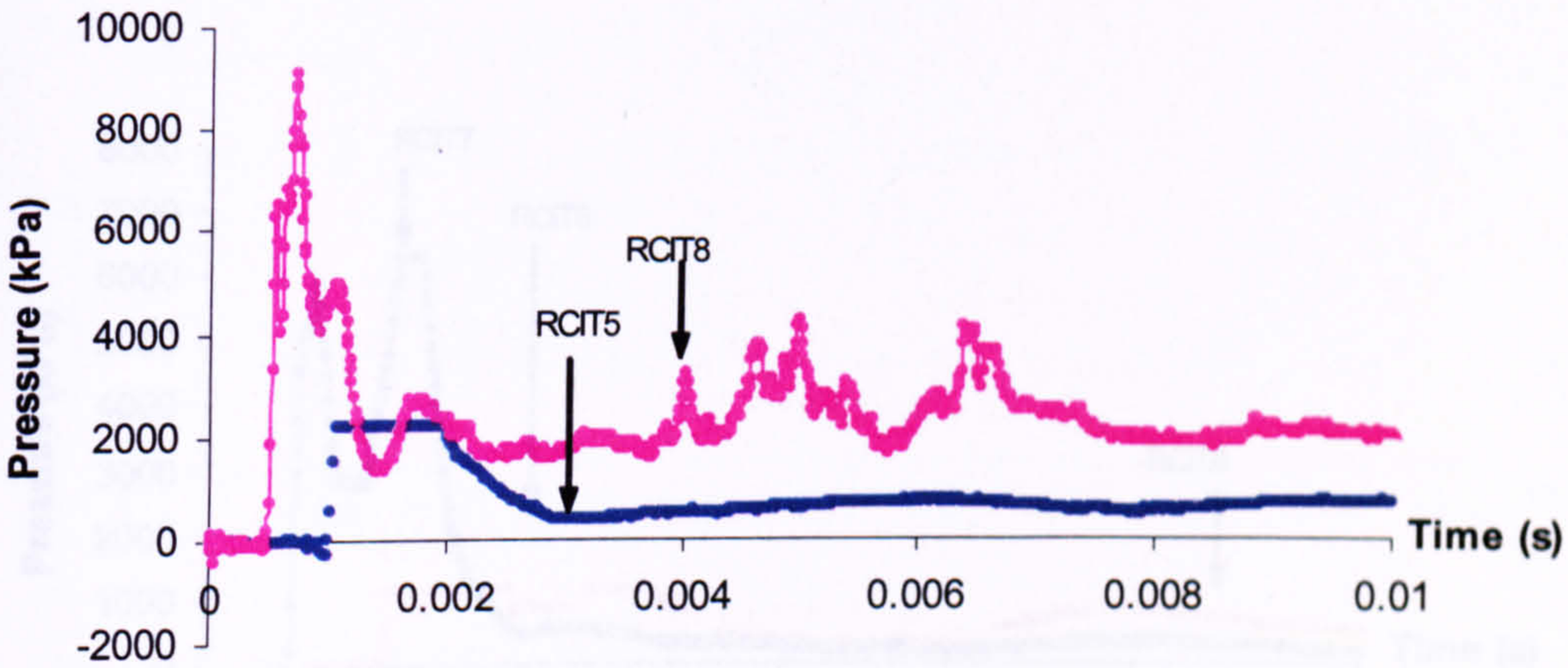

Figure A.1.49 Pressure-time traces recorded by DPG1 in tests RCIT5 and RCIT8.

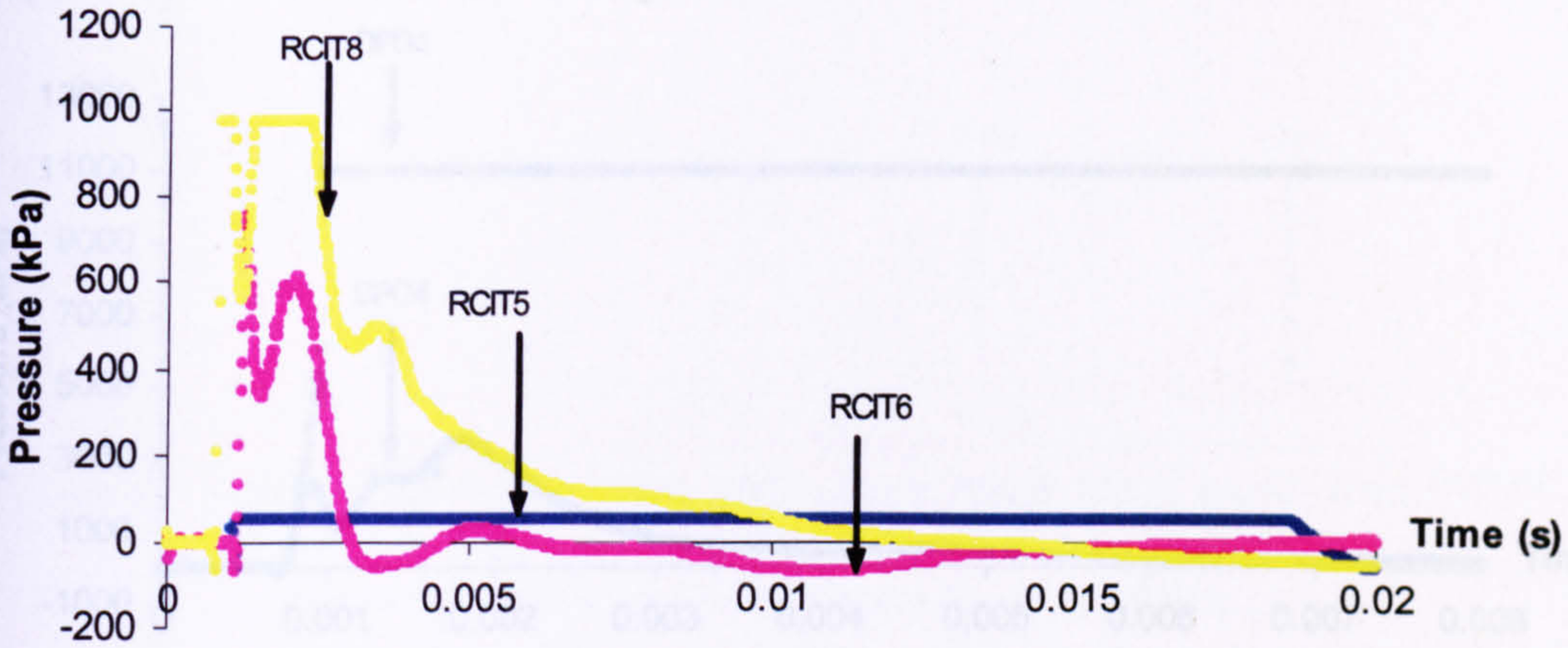

Figure A.1.50 Pressure-time traces recorded by DPG2 in tests RCIT5, RCIT 6 and RCIT 8.

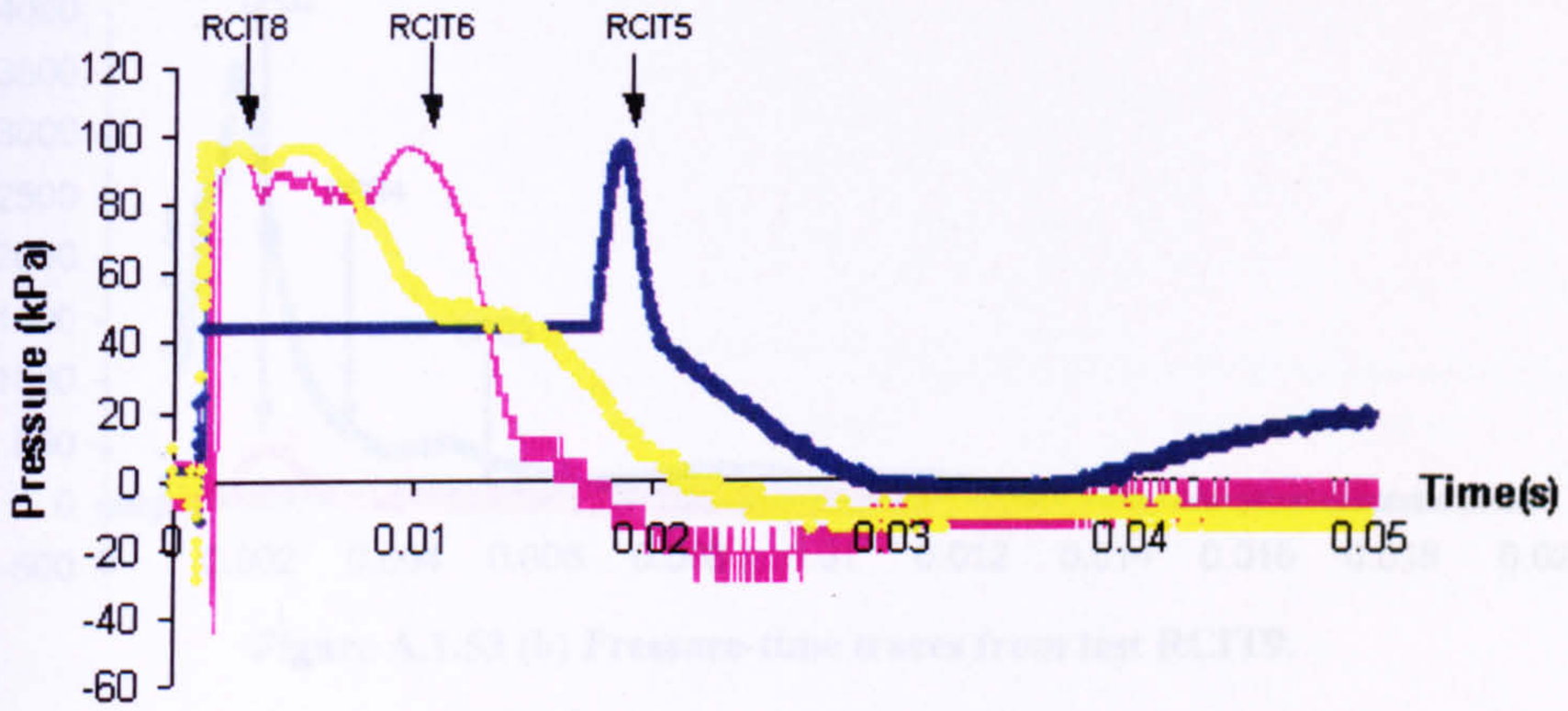

Figure A.1.51 Pressure-time traces recorded by DPG3 in tests RCIT5-8

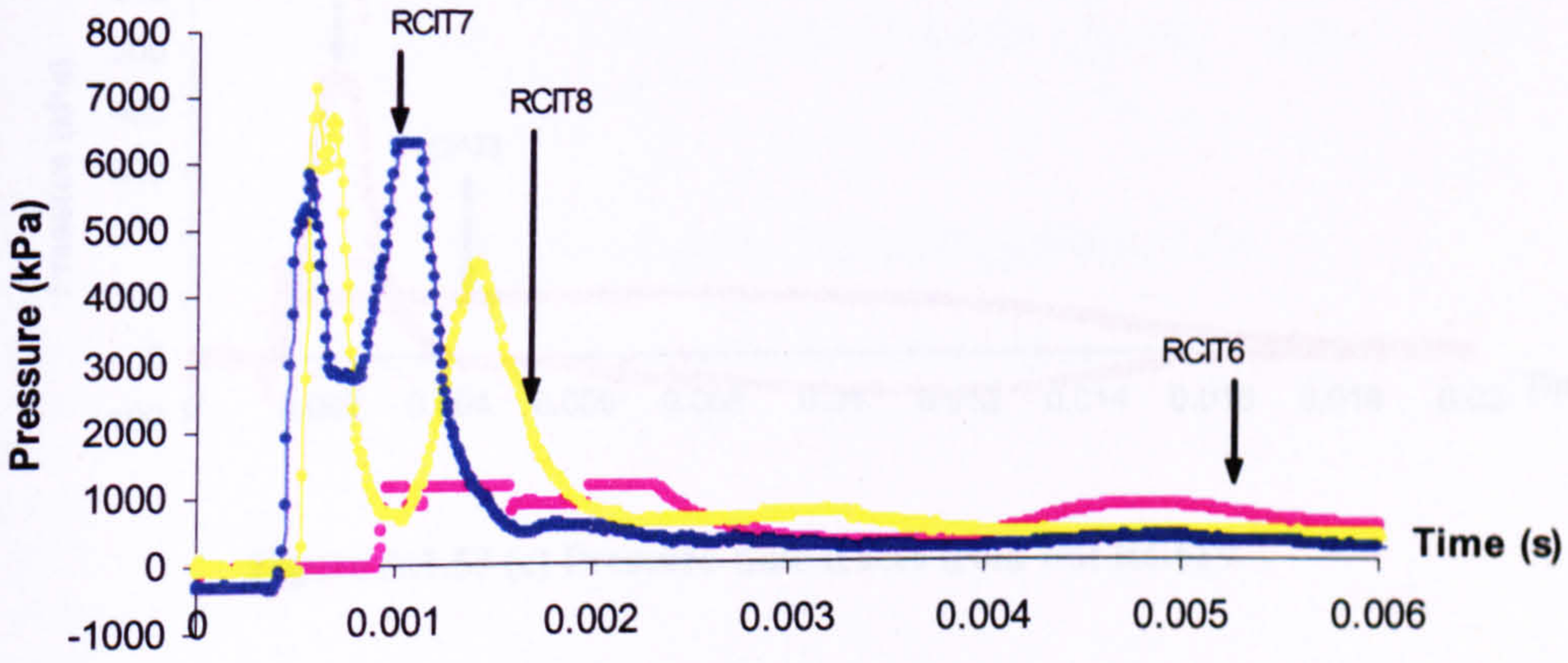

Figure A.1.52 Pressure-time traces recorded by DPG 4 in tests RCIT6-8

Group 3 results – Individual test analysis.

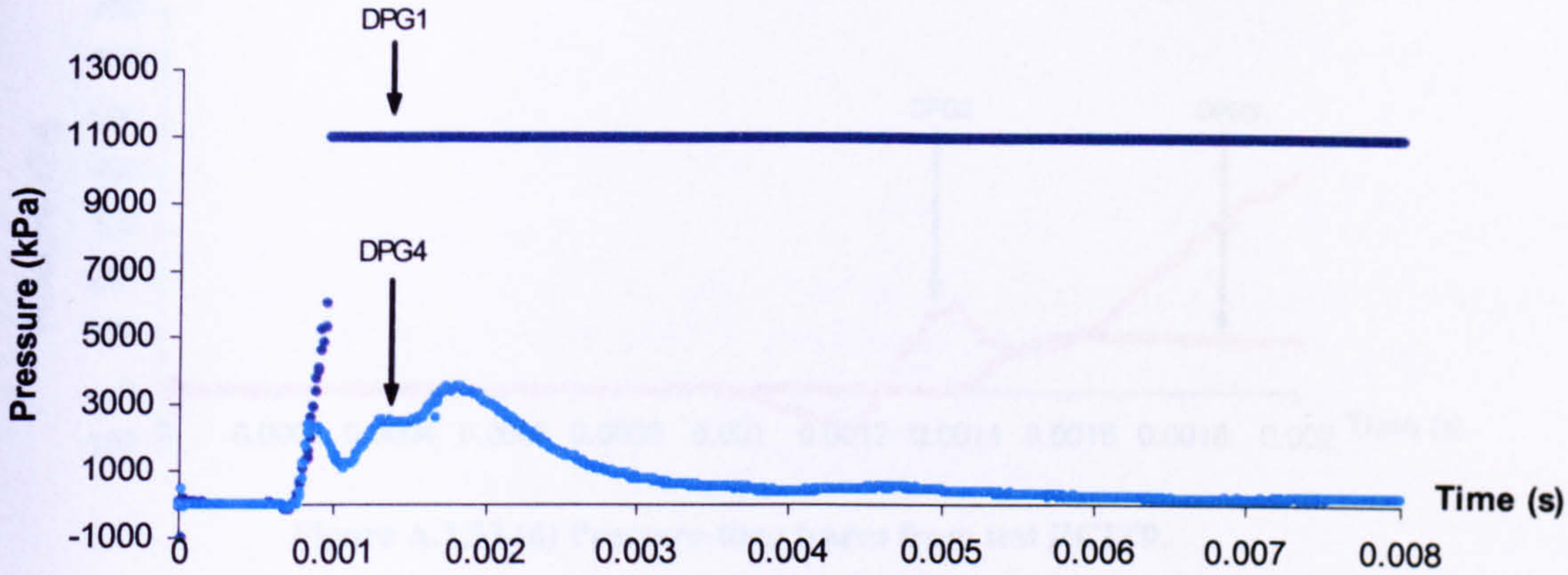

Figure A.1.53 (a) Pressure-time traces from test RCIT9.

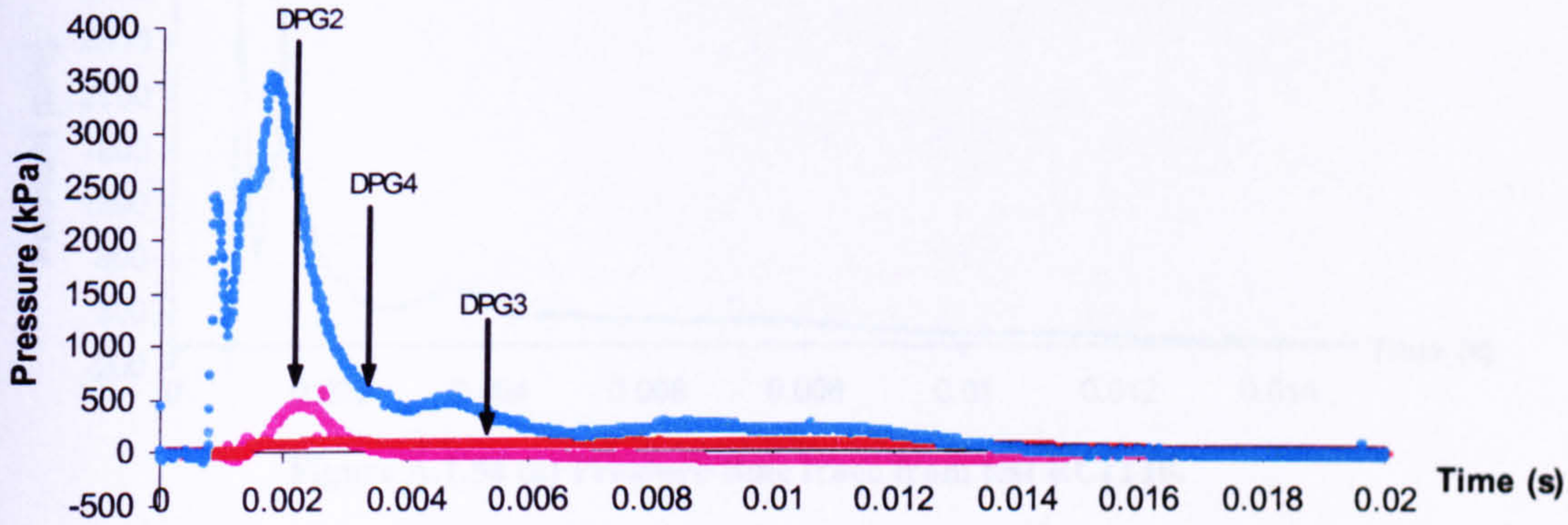

Figure A.1.53 (b) Pressure-time traces from test RCIT9.

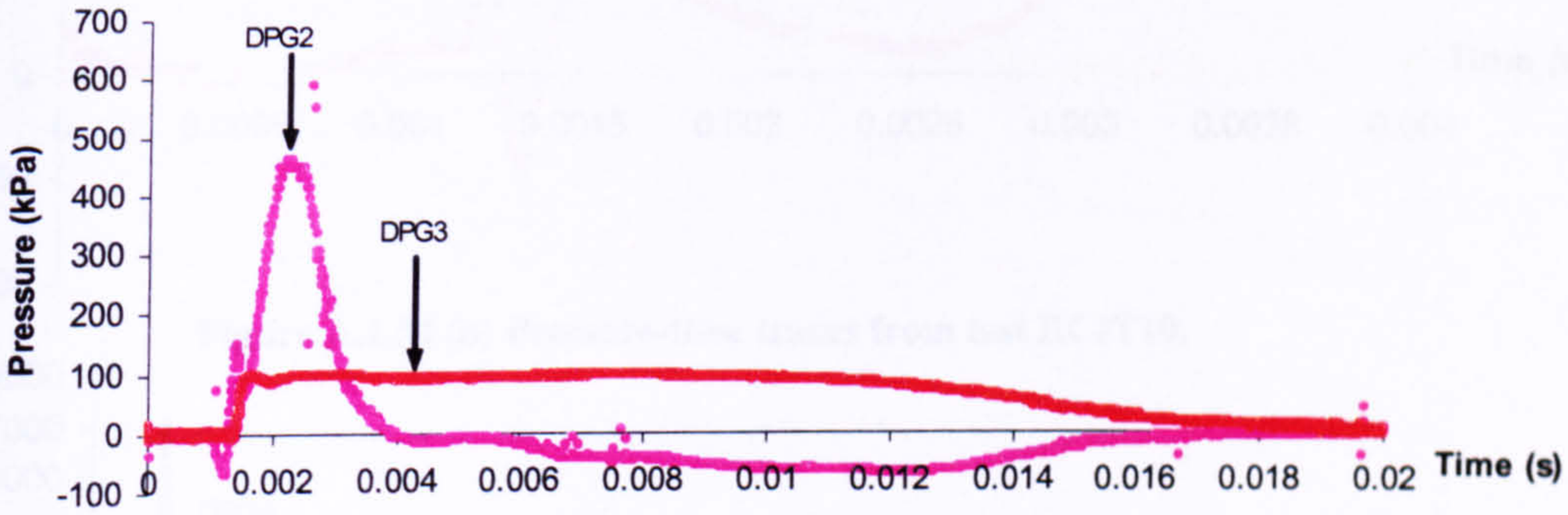

Figure A.1.53 (c) Pressure-time traces from test RCIT9.

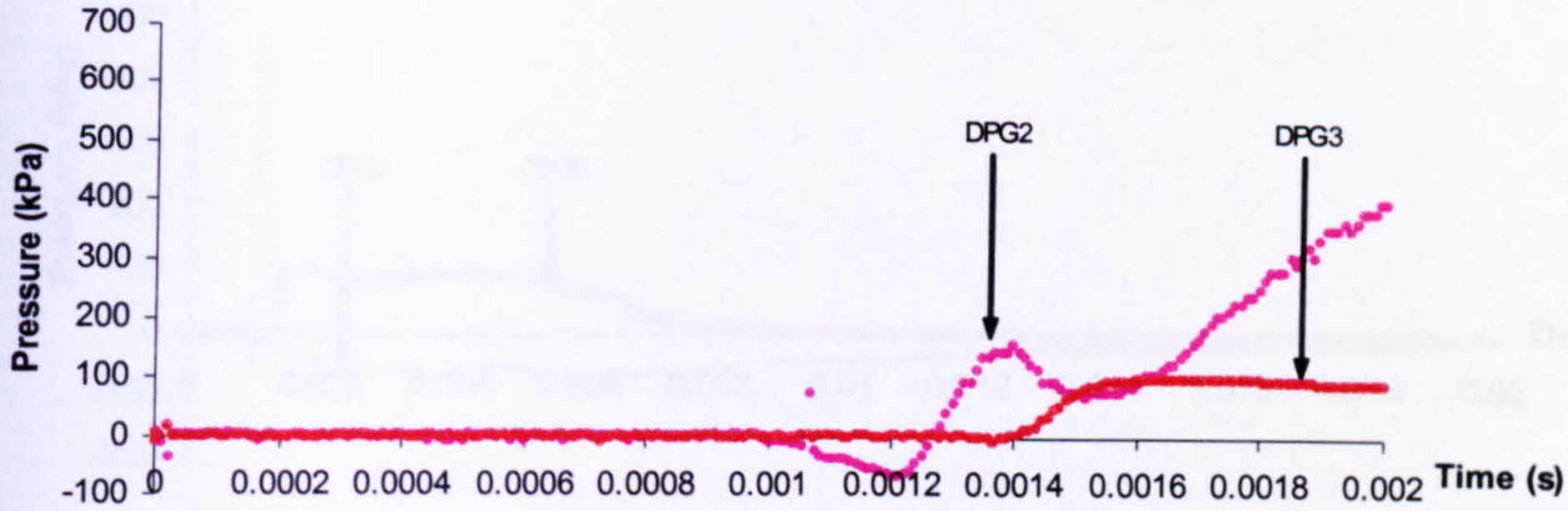

Figure A.1.53 (d) Pressure-time traces from test RCIT9.

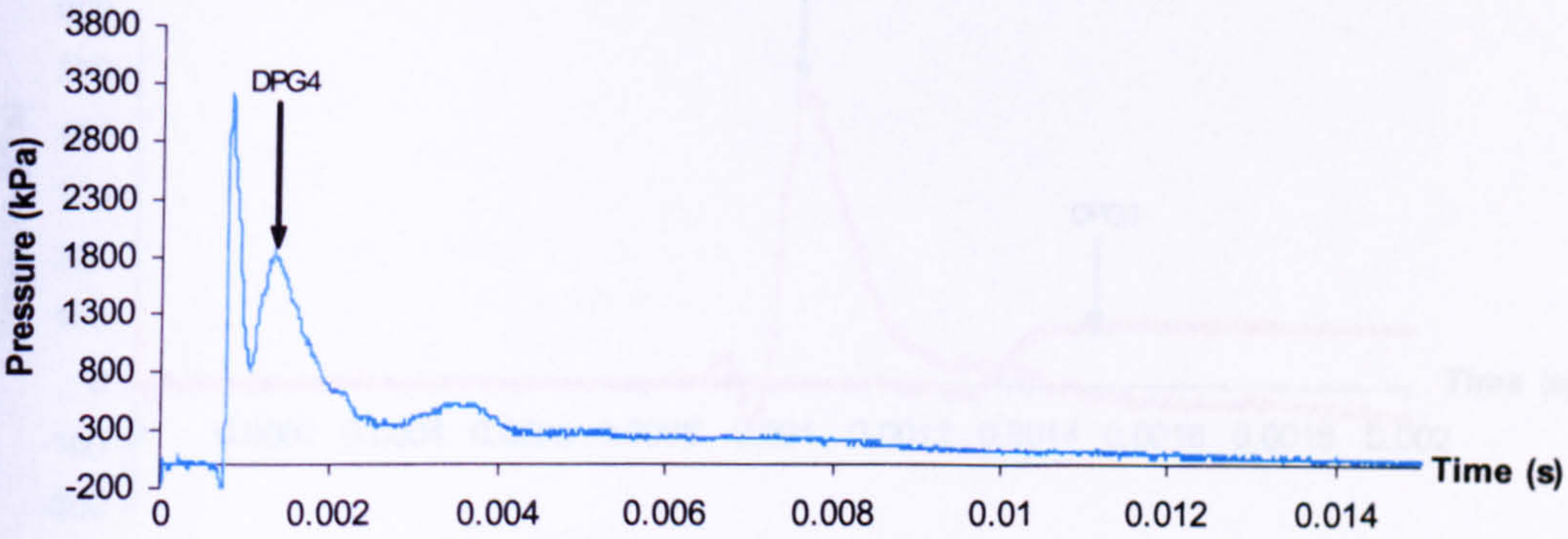

Figure A.1.54 (a) Pressure-time trace from test RCIT10.

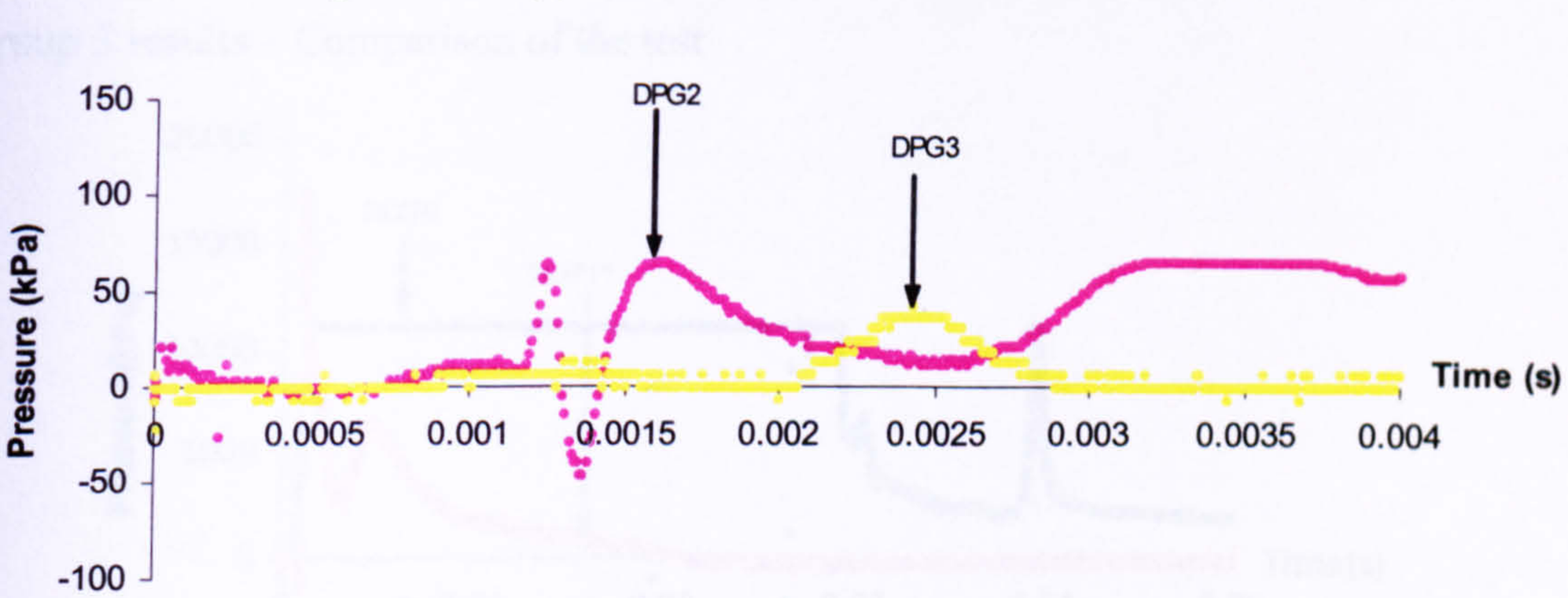

Figure A.1.54 (b) Pressure-time traces from test RCIT10.

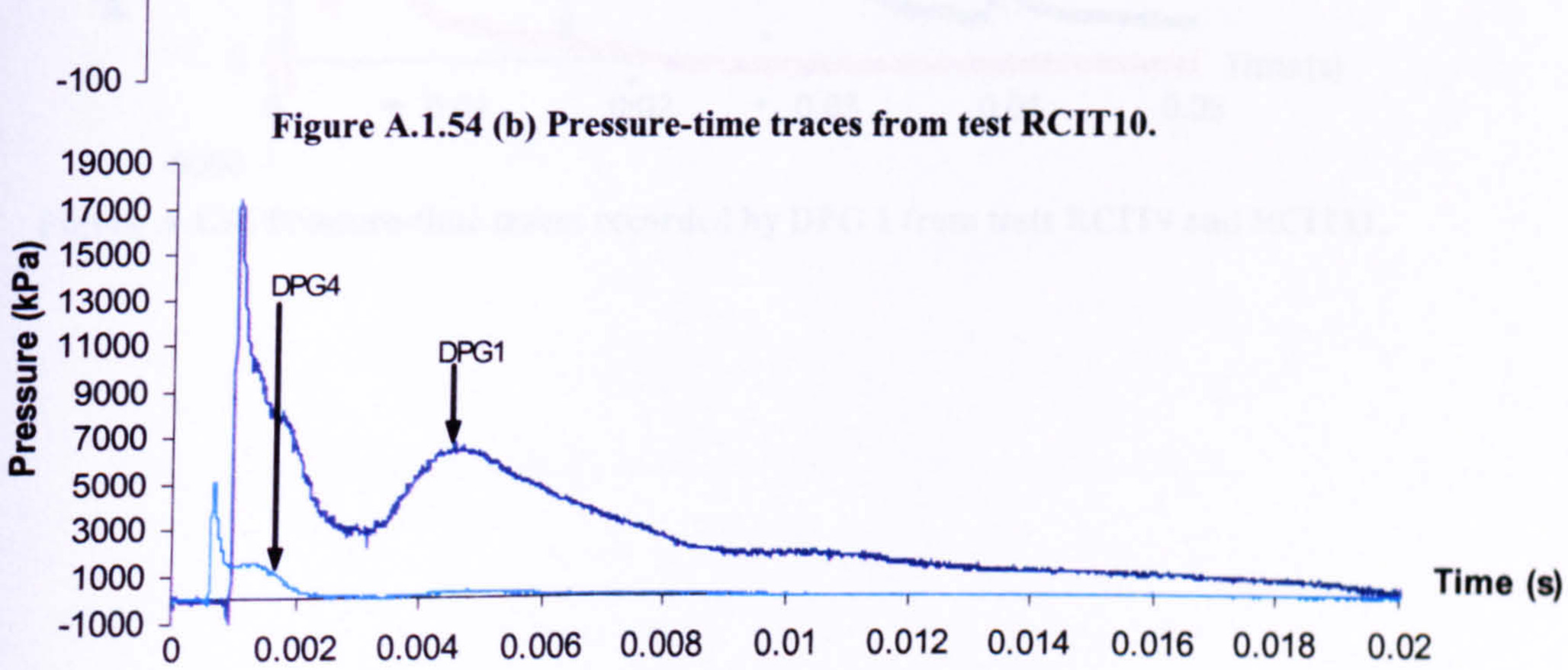

Figure A.1.55 (a) Pressure-time traces from test RCIT11.

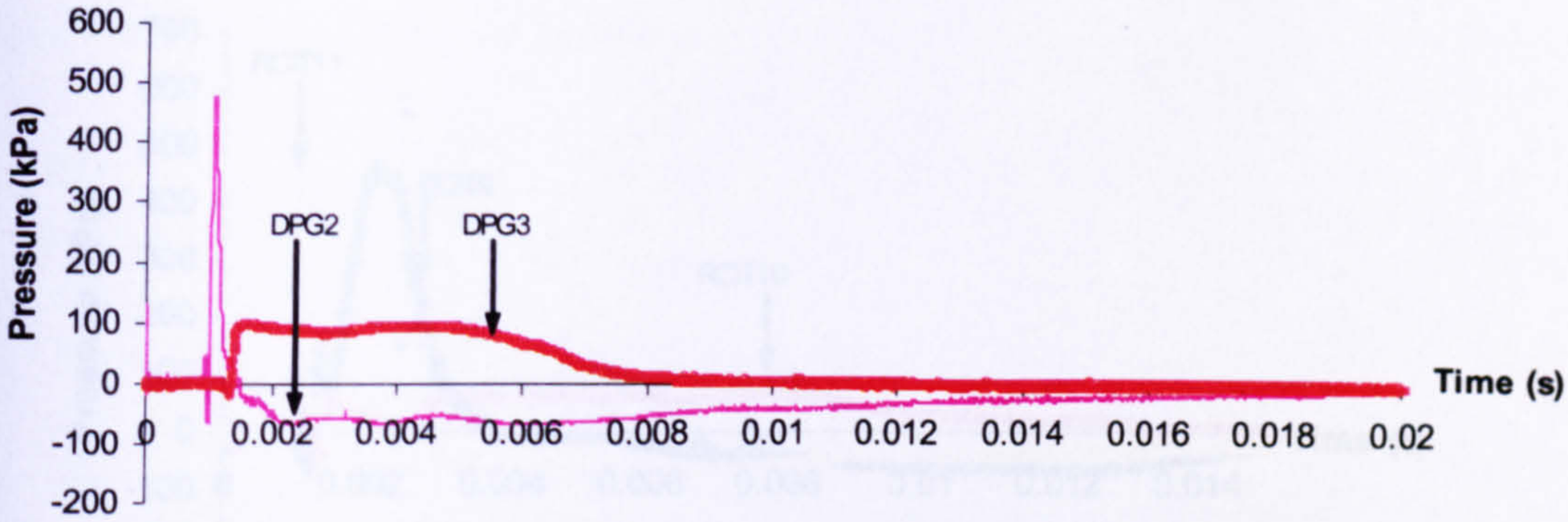

Figure A.1.55 (b) Pressure-time traces from test RCIT11.

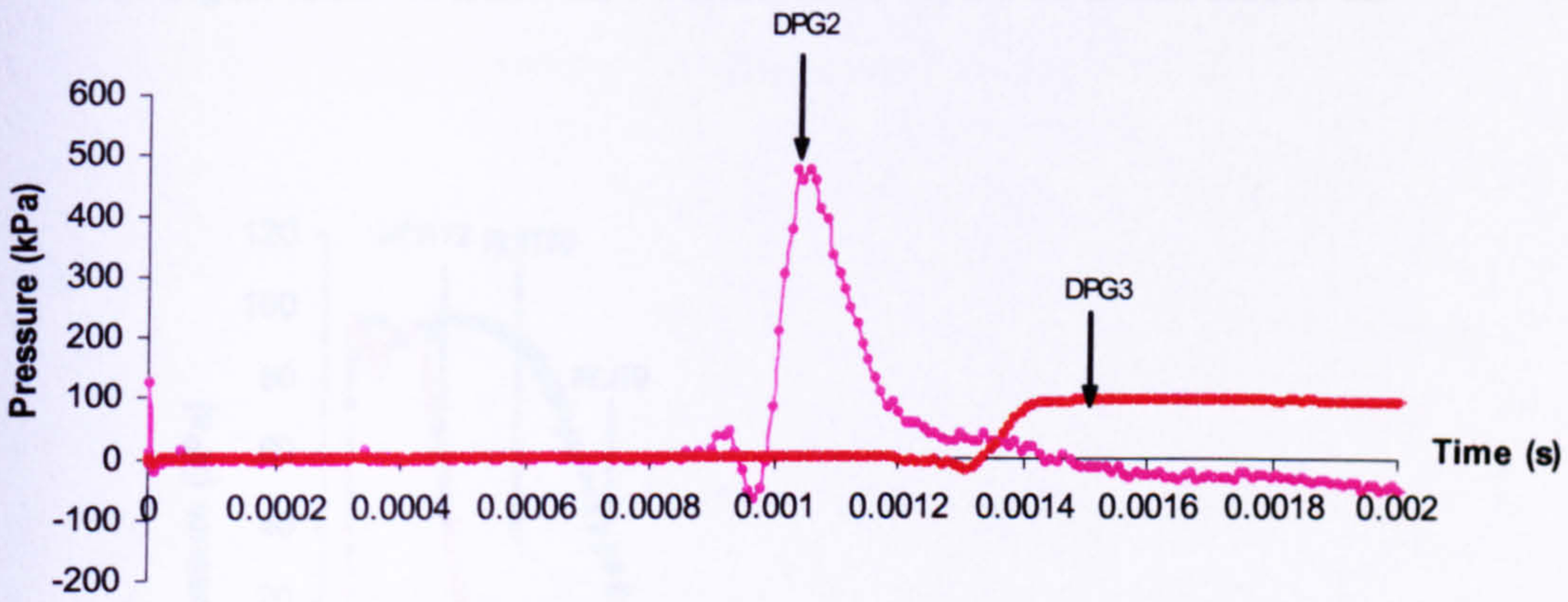

Figure A.1.55 (c) Pressure-time traces from test RCIT11.

Group 3 results – Comparison of the test

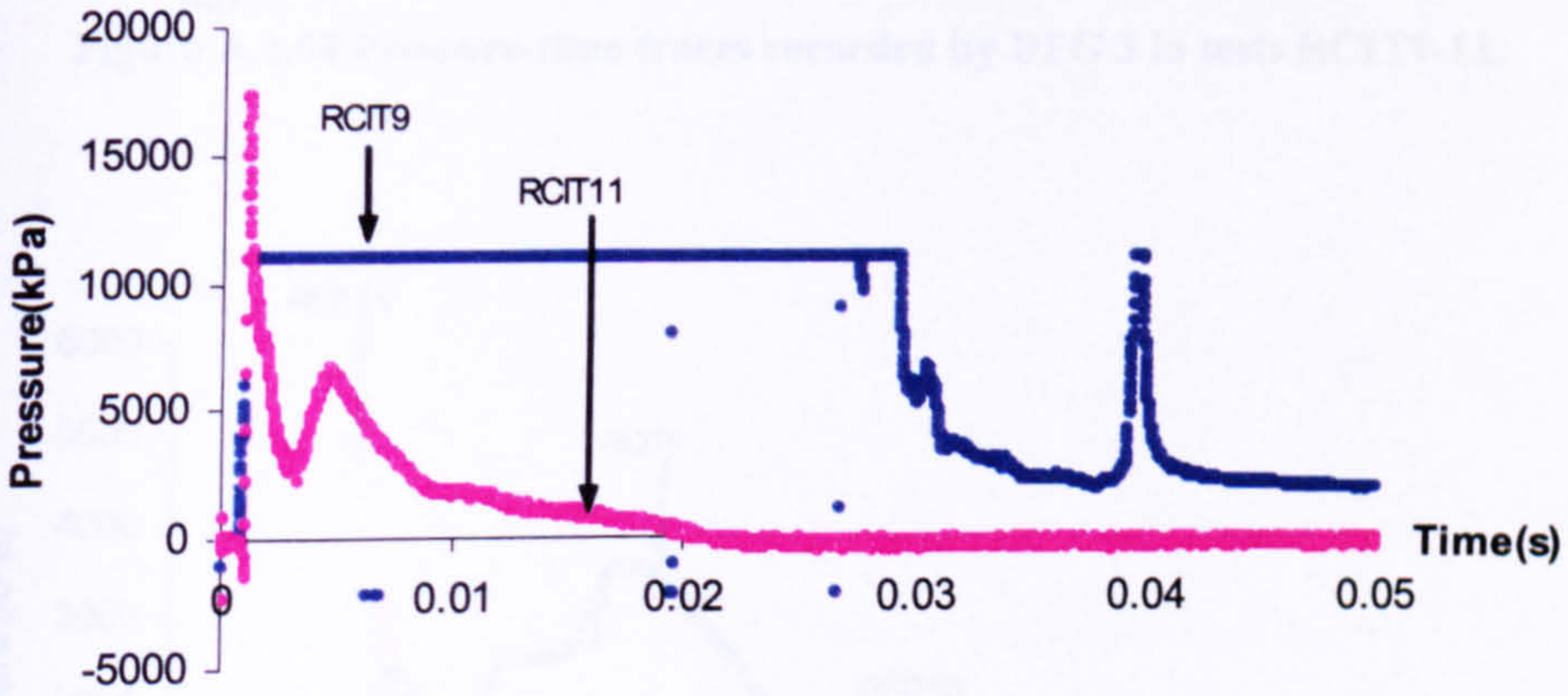

Figure A.1.56 Pressure-time traces recorded by DPG 1 from tests RCIT9 and RCIT11.

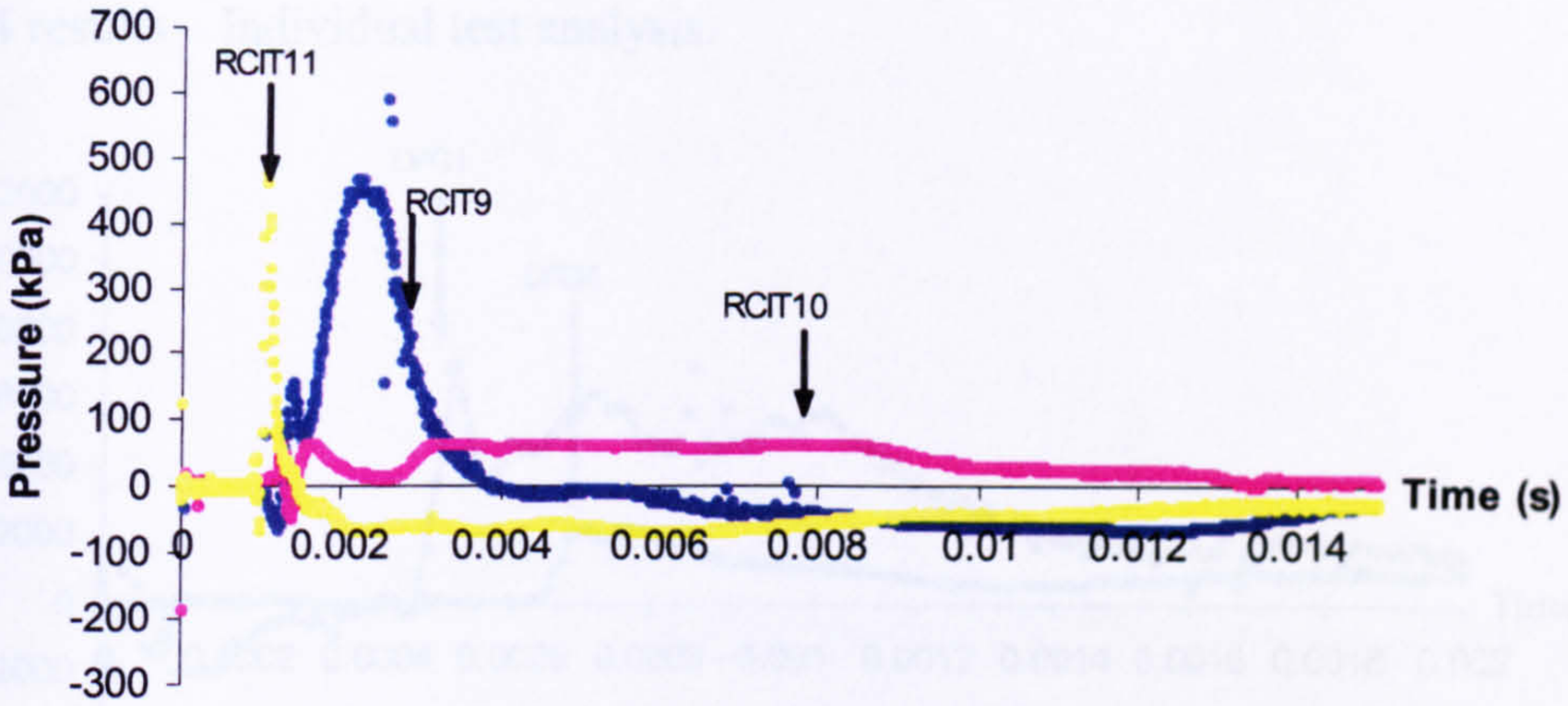

Figure A.1.57 Pressure-time traces recorded by DPG2 in tests RCIT9-11.

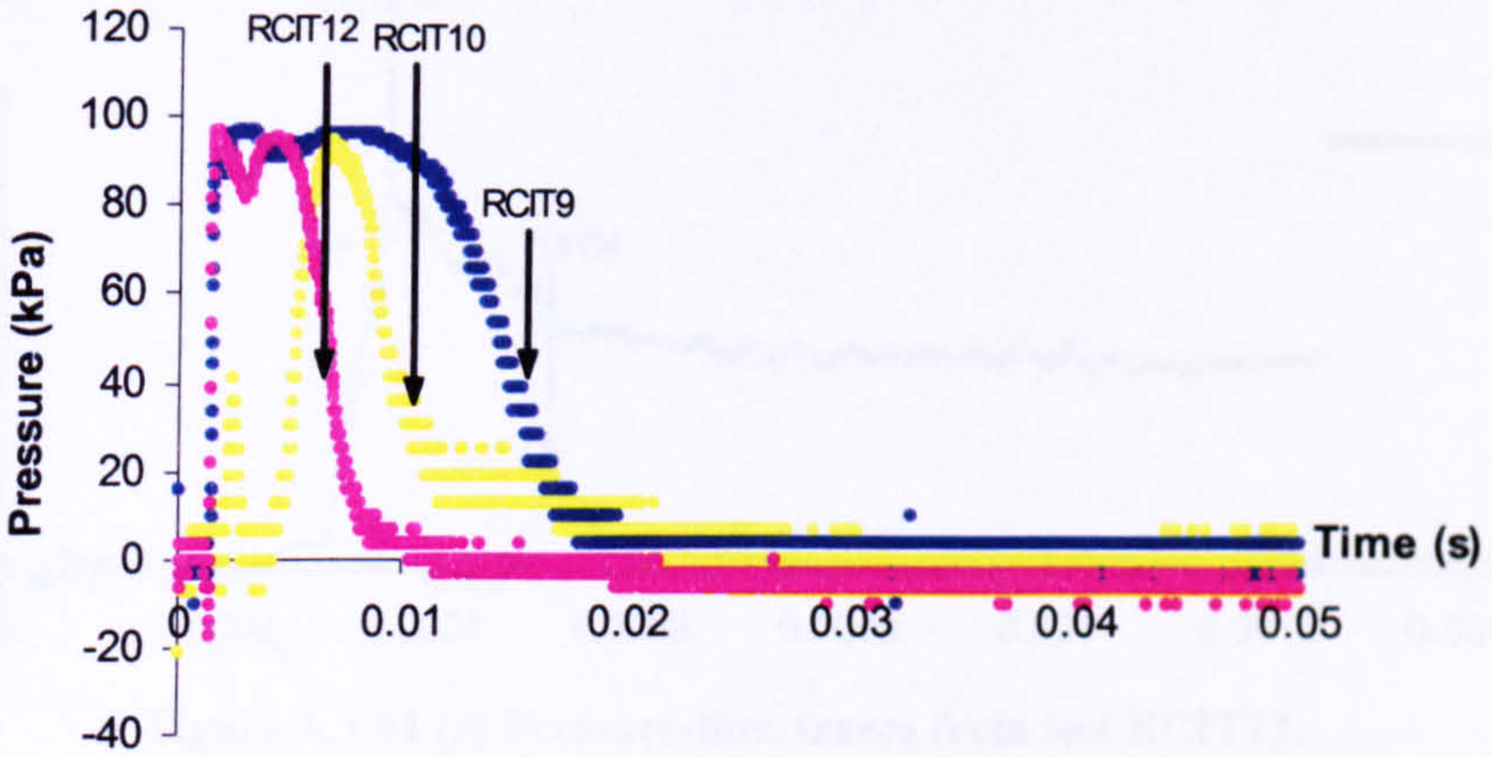

Figure A.1.58 Pressure-time traces recorded by DPG 3 in tests RCIT9-11.

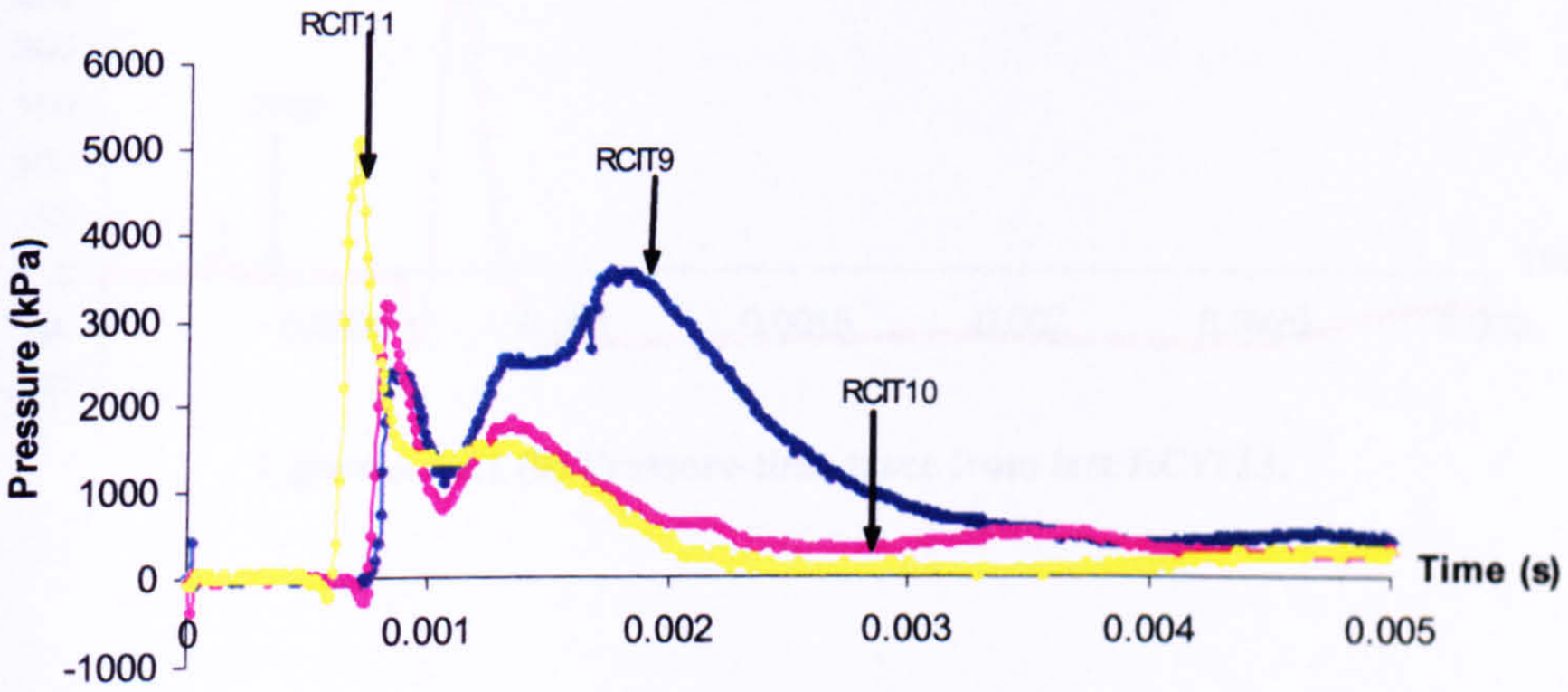

Figure A.1.59 Pressure-time traces recorded by DPG 4 in tests RCIT9-11.

Group 4 results – Individual test analysis.

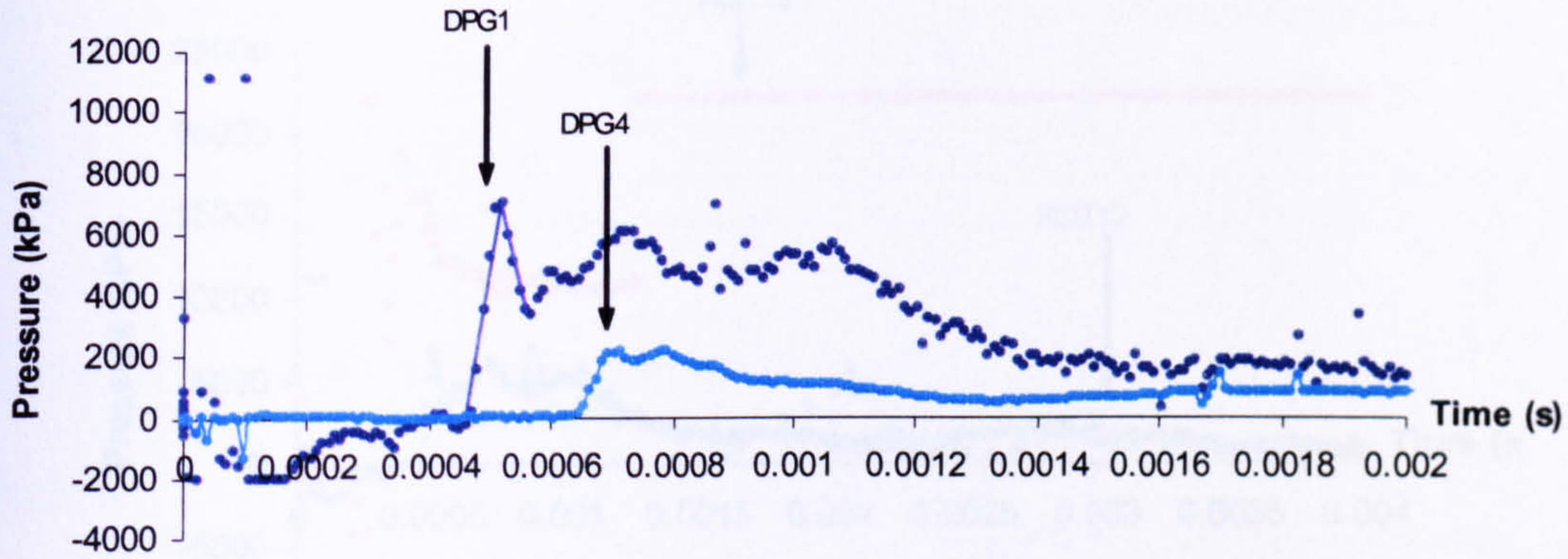

Figure A.1.60 Pressure-time traces from test RCIT12.

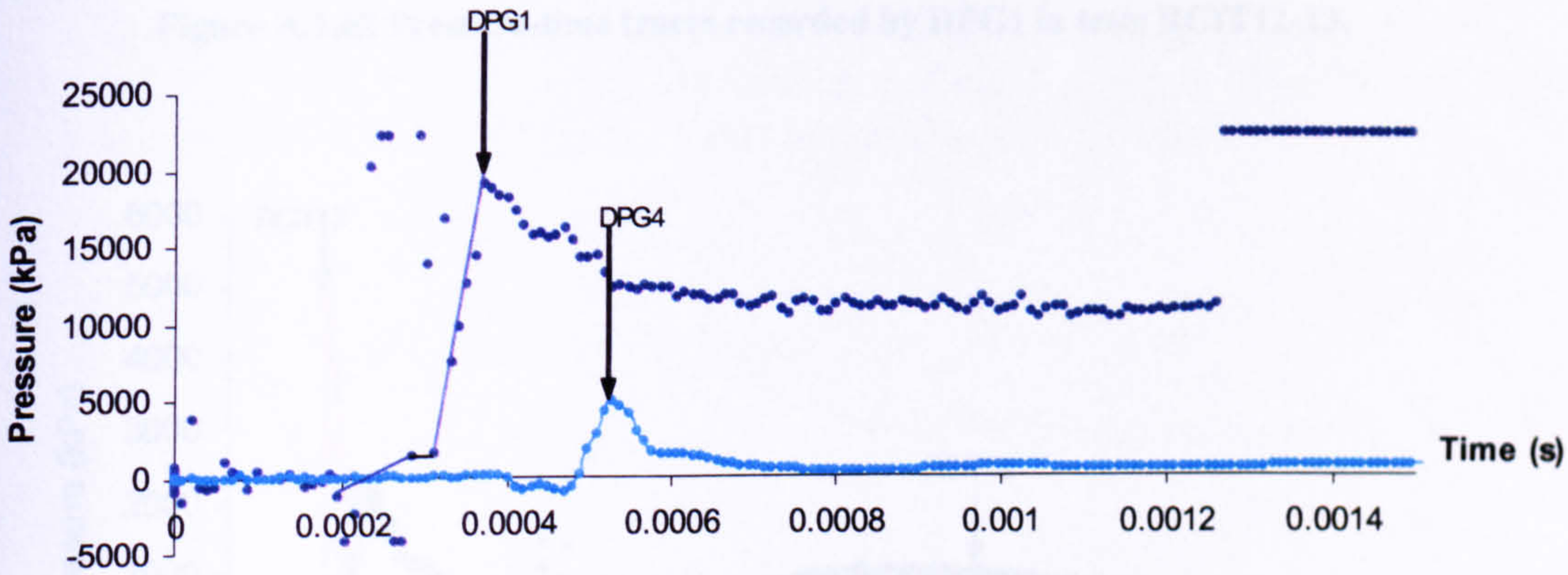

Figure A.1.61 (a) Pressure-time traces from test RCIT13.

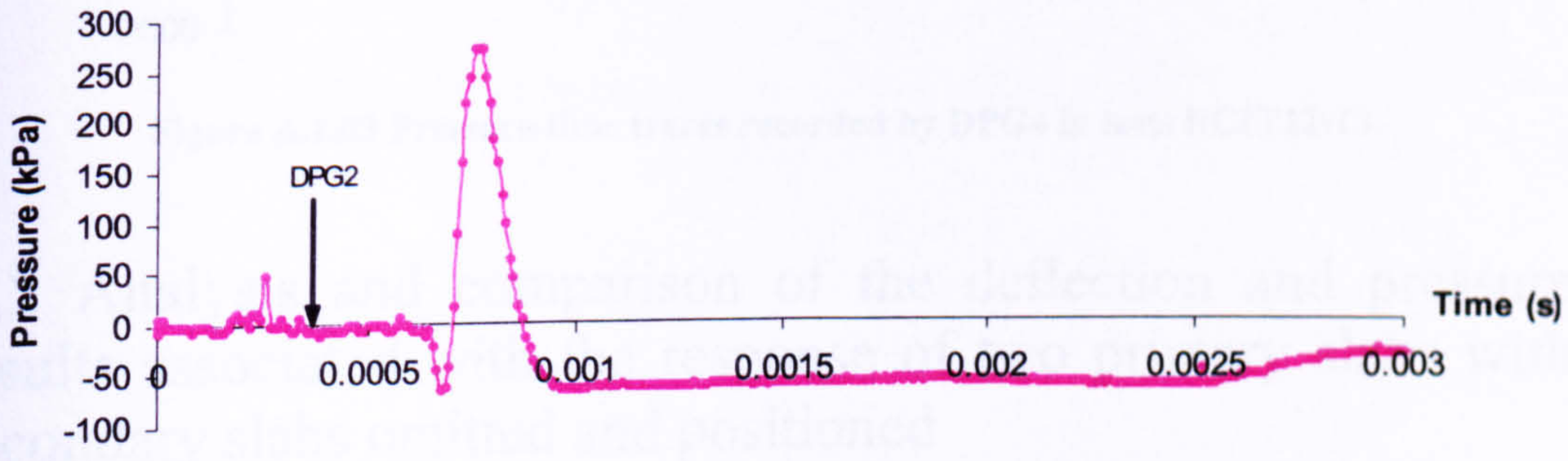

Figure A.1.61 (b) Pressure-time trace from test RCIT13.

Group 4 results – Comparison of the tests.

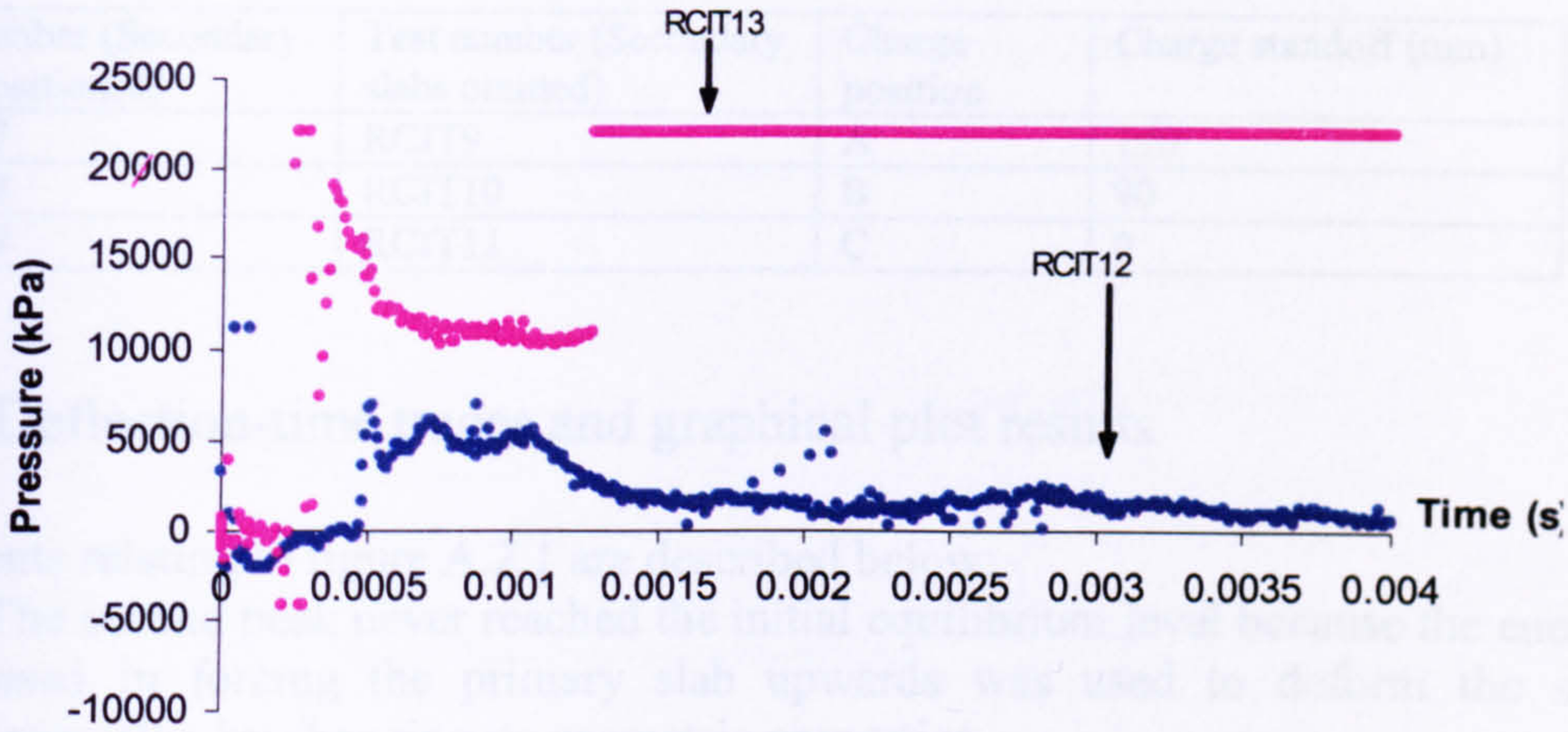

Figure A.1.62 Pressure-time traces recorded by DPG1 in tests RCIT12-13.

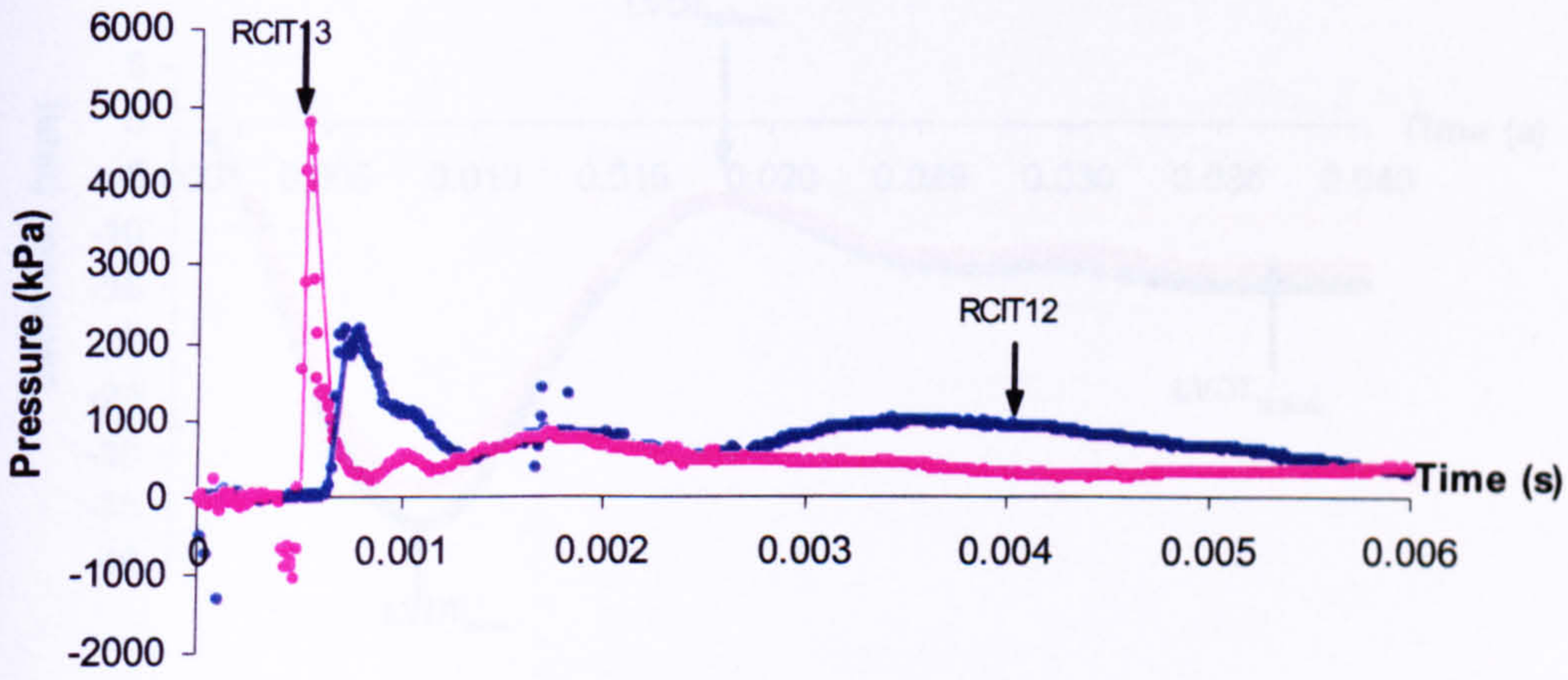

Figure A.1.63 Pressure-time traces recorded by DPG4 in tests RCIT12-13.

A.2 Analysis and comparison of the deflection and pressure results associated with the response of two primary slabs with secondary slabs omitted and positioned

The response of two primary slabs, protected and unprotected by positioned and omitted secondary slabs are illustrated in the form of deflection-time and pressure time traces, recorded at specific location on the bottom and top face of the primary slab. Results and comparisons of strain were not included because the gauges attached to the unprotected primary slab were damaged as a result. Description of tests RCIT17-19 are illustrated in table A.2.1. Within those tests, secondary slabs were omitted.

Table A.2.1 Charge standoffs associated with tests RCIT9-11 and RCIT17-19

Test number (Secondary slabs positioned)	Test number (Secondary slabs omitted)	Charge position	Charge standoff (mm)
RCIT17	RCIT9	A	190
RCIT18	RCIT10	B	90
RCIT19	RCIT11	C	0

A.2.1 Deflection-time traces and graphical plot results

Comments relating to figure A.2.1 are described below:

1. The second peak never reached the initial equilibrium level because the energy used in forcing the primary slab upwards was used to deform the slab internally, by changing its geometric properties.
2. Test RCIT19 caused severe damage to $LVDT_{0mm}$. This was as illustrated by the irregular trace during the downward movement of the slab. The other two LVDTs were not damaged, but instead recorded a residual deflection that corresponded to the maximum travel length assigned to each LVDT.

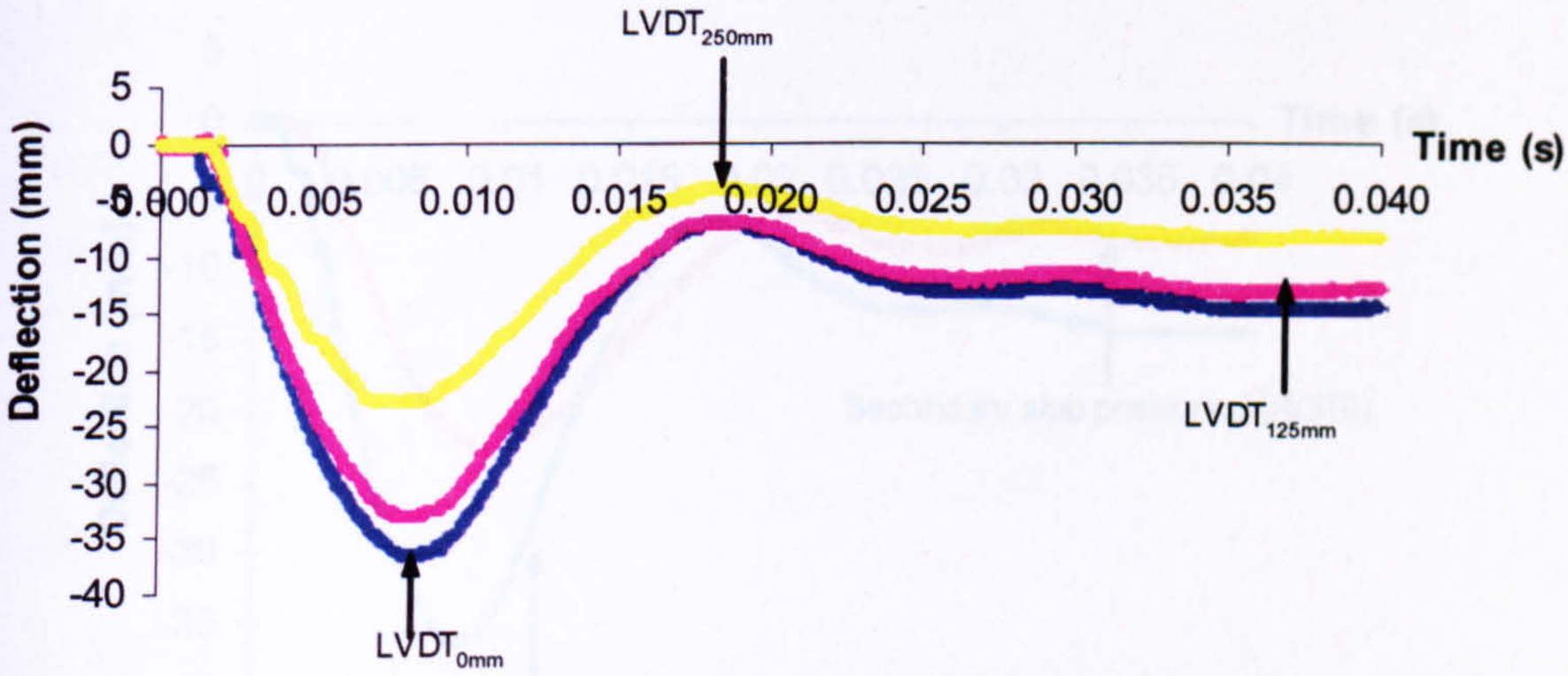

Figure A.2.1 Deflection-time traces from test RCIT17.

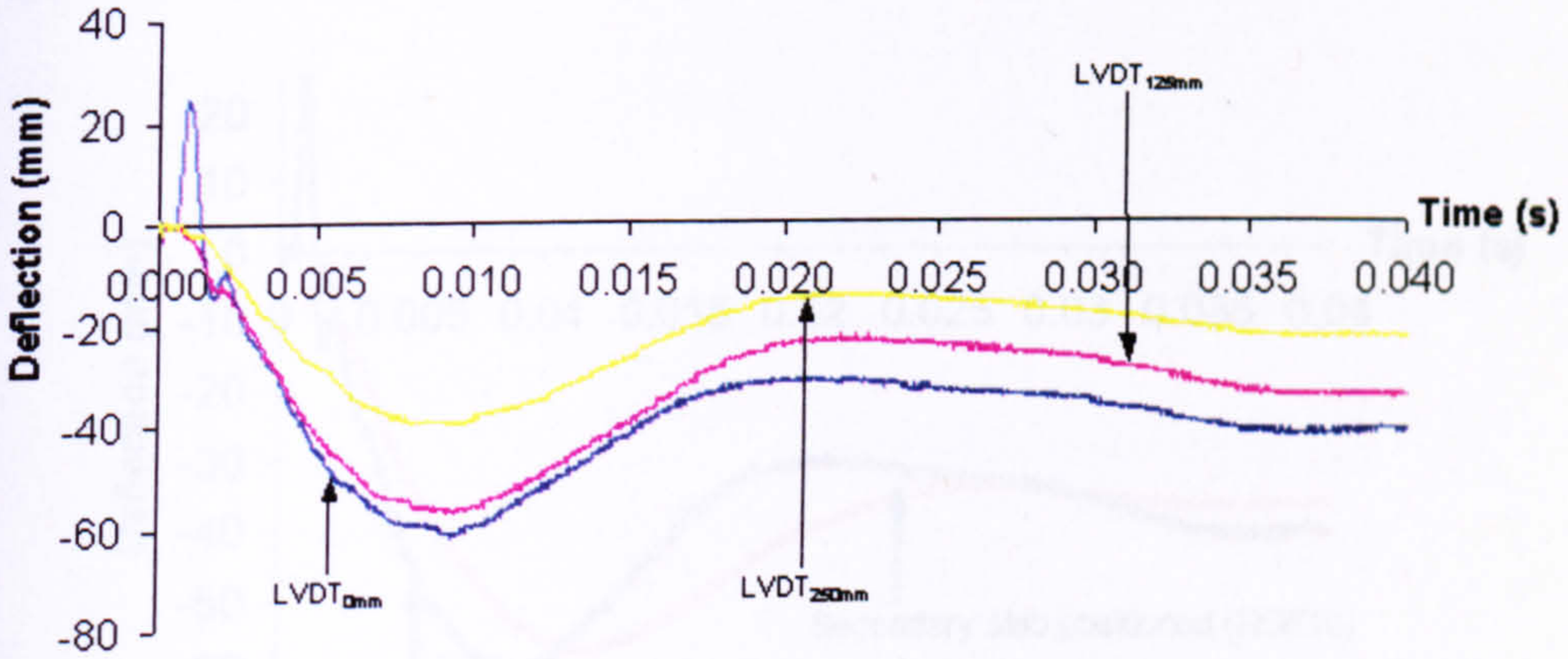

Figure A.2.2 Deflection-time traces from test RCIT18.

Comments relating to figure A.2.3 are described below:

1. $LVDT_{0mm}$ was severely damaged.
2. The trace recorded by $LVDT_{125mm}$ was captured apart from the maximum peak deflection.
3. The trace recorded by $LVDT_{250mm}$ was successfully captured.

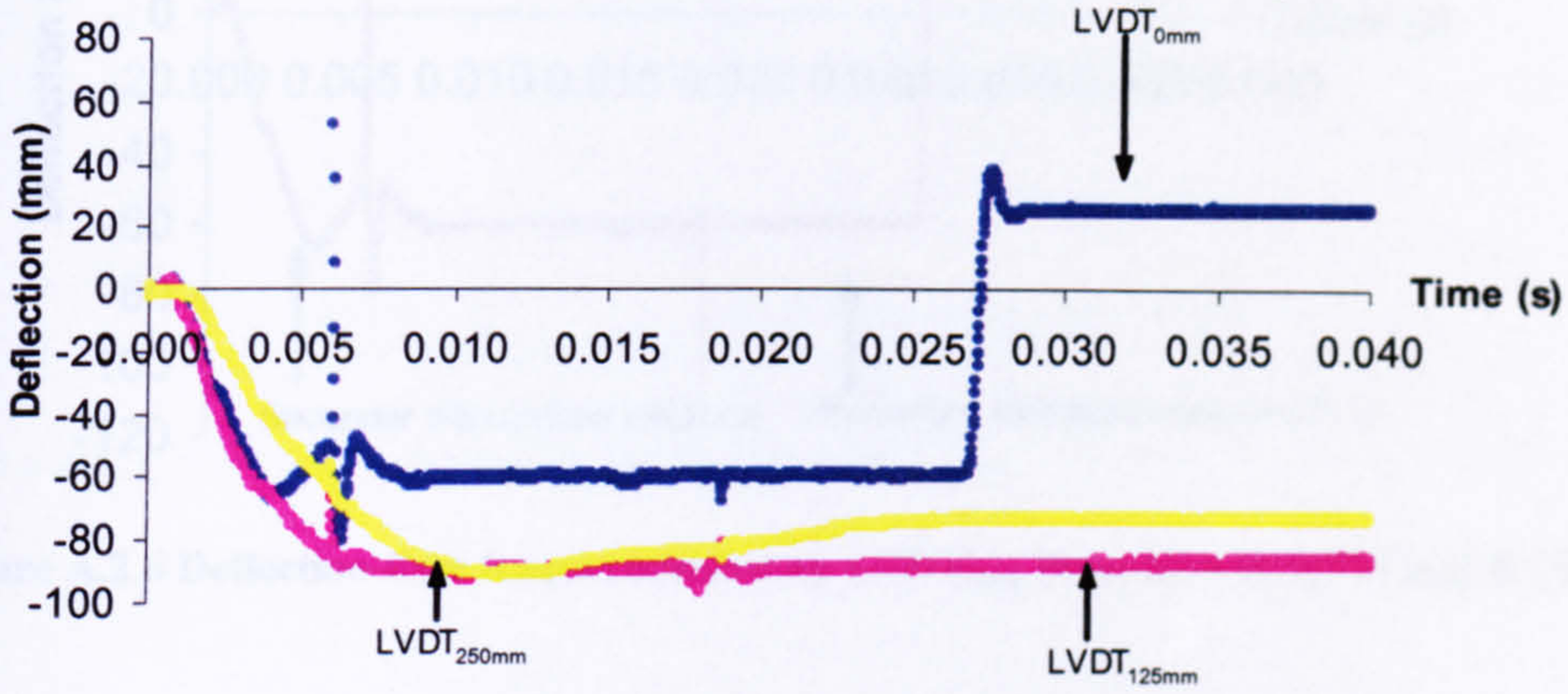

Figure A.2.3 Deflection-time traces from test RCIT19.

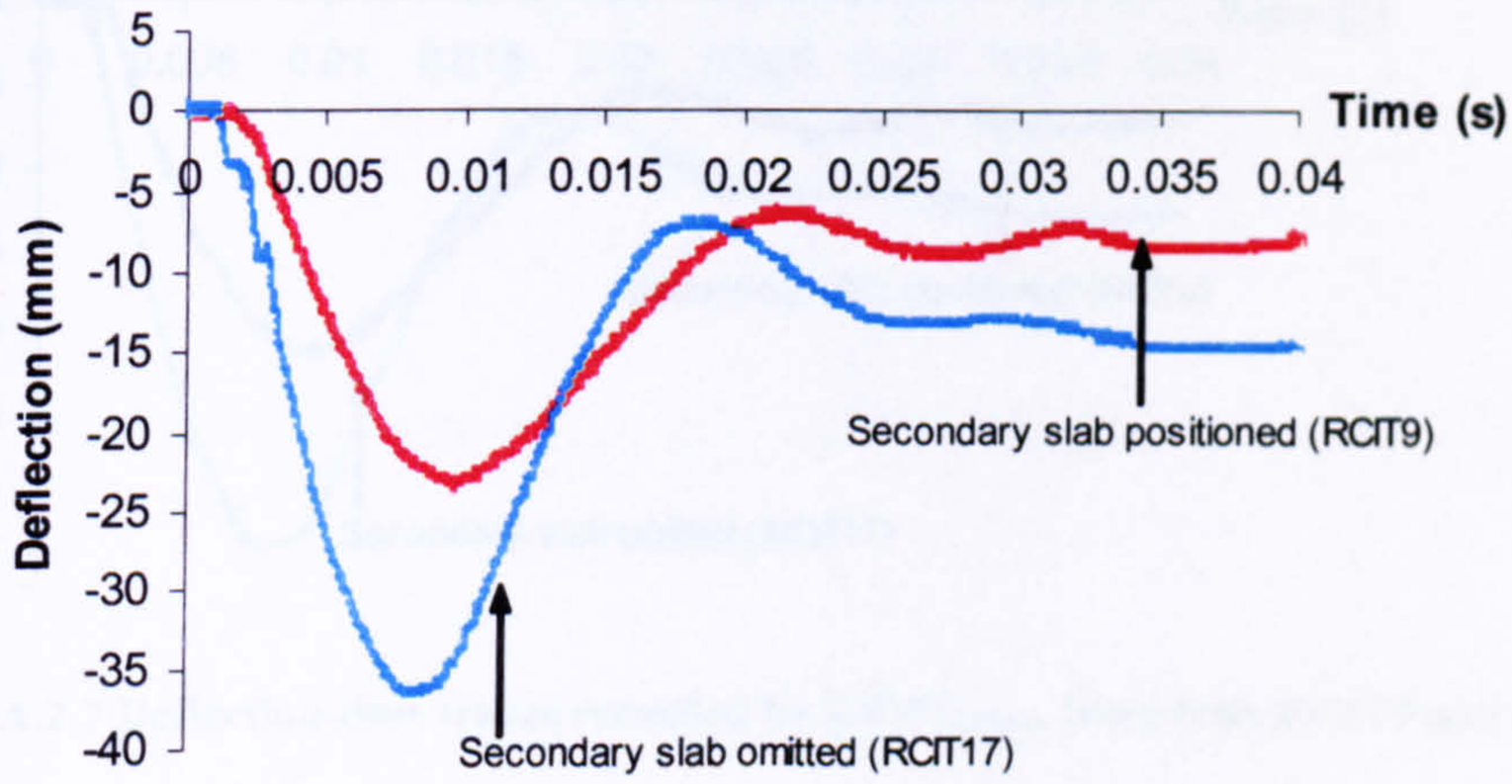

Figure A.2.4 Deflection-time traces recorded by $LVDT_{0mm}$ from tests RCIT9 and RCIT17.

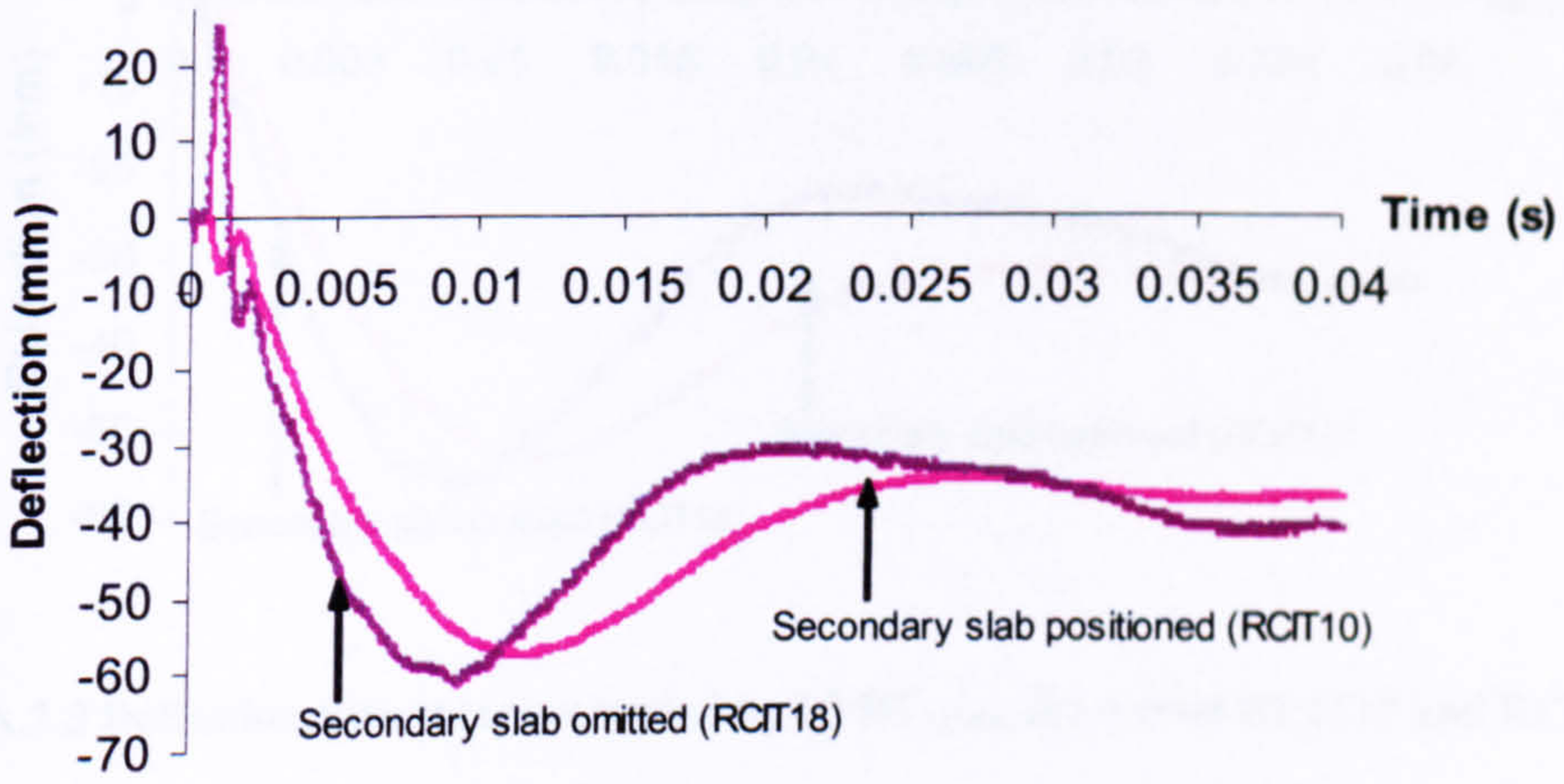

Figure A.2.5 Deflection-time traces recorded by $LVDT_{0mm}$ from tests RCIT10 and RCIT18.

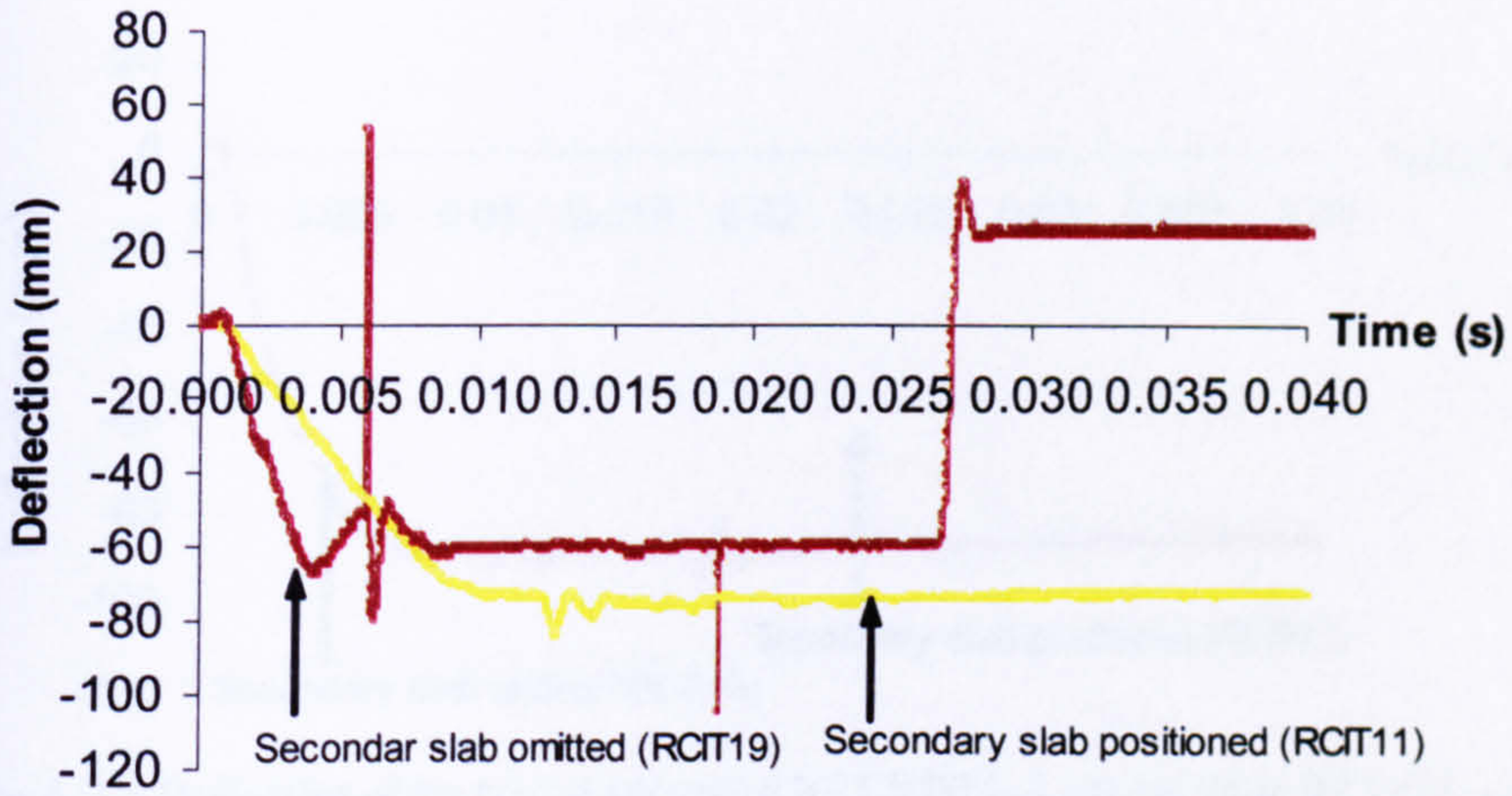

Figure A.2.6 Deflection-time traces recorded by $LVDT_{0mm}$ from tests RCIT11 and RCIT19.

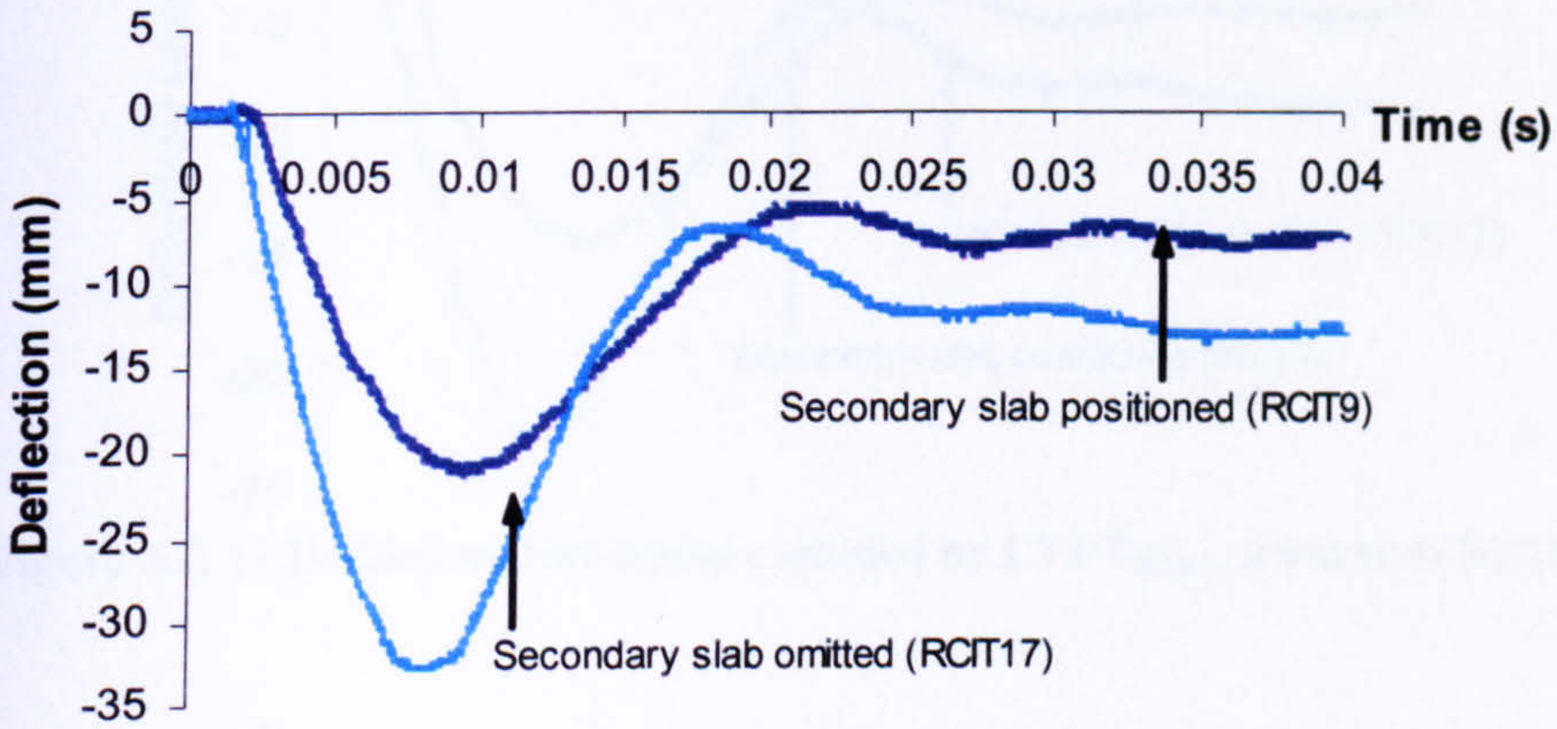

Figure A.2.7 Deflection-time traces recorded by $LVDT_{125mm}$ from tests RCIT9 and RCIT17.

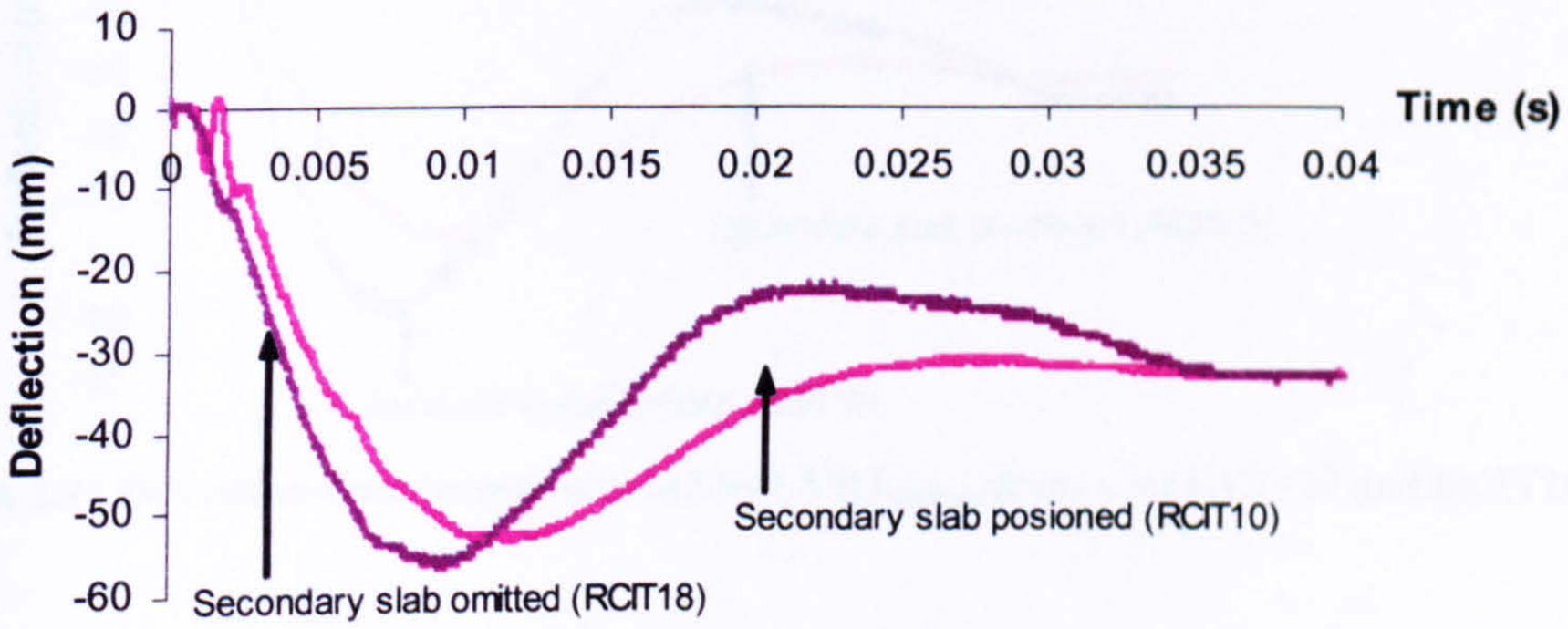

Figure A.2.8 Deflection-time traces recorded by $LVDT_{125mm}$ from tests RCIT10 and RCIT18.

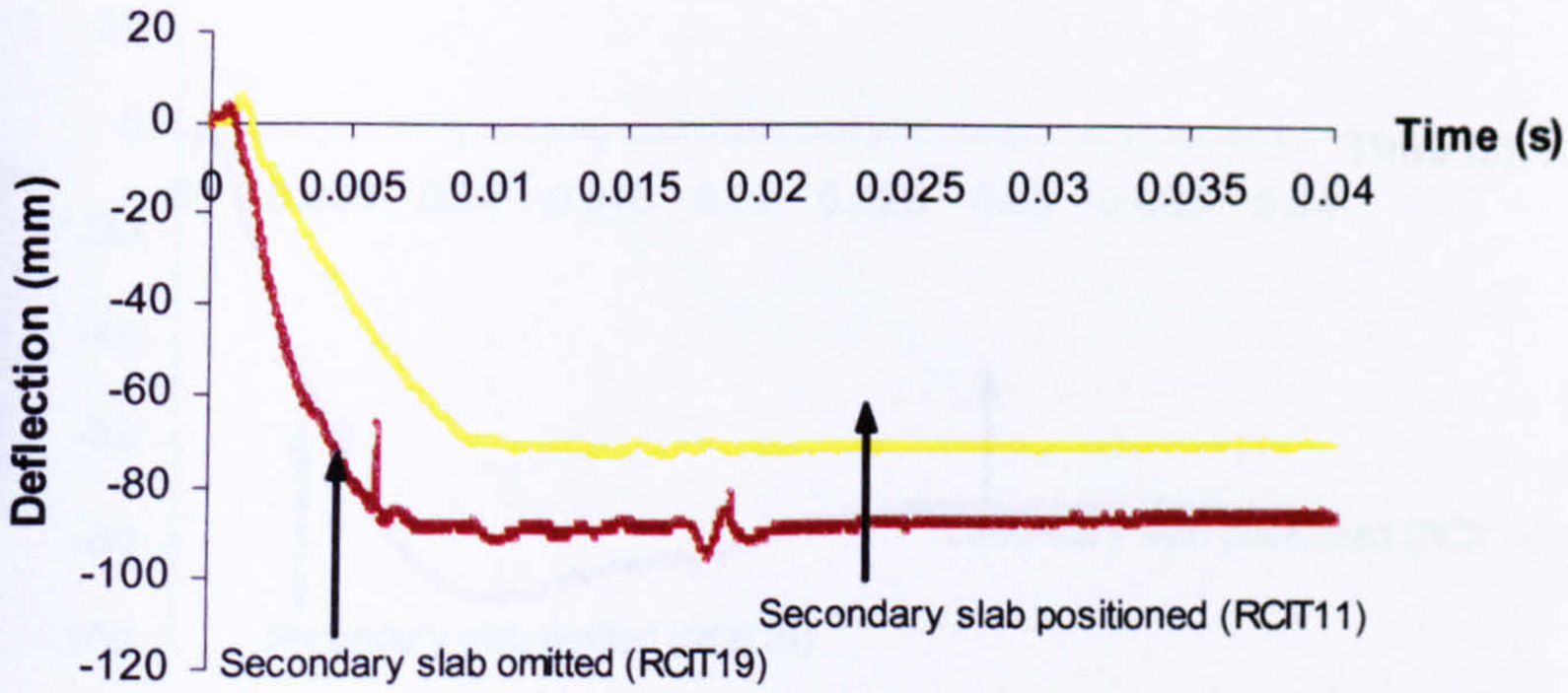

Figure A.2.9 Deflection-time traces recorded by $LVDT_{125mm}$ from tests RCIT11 and RCIT19.

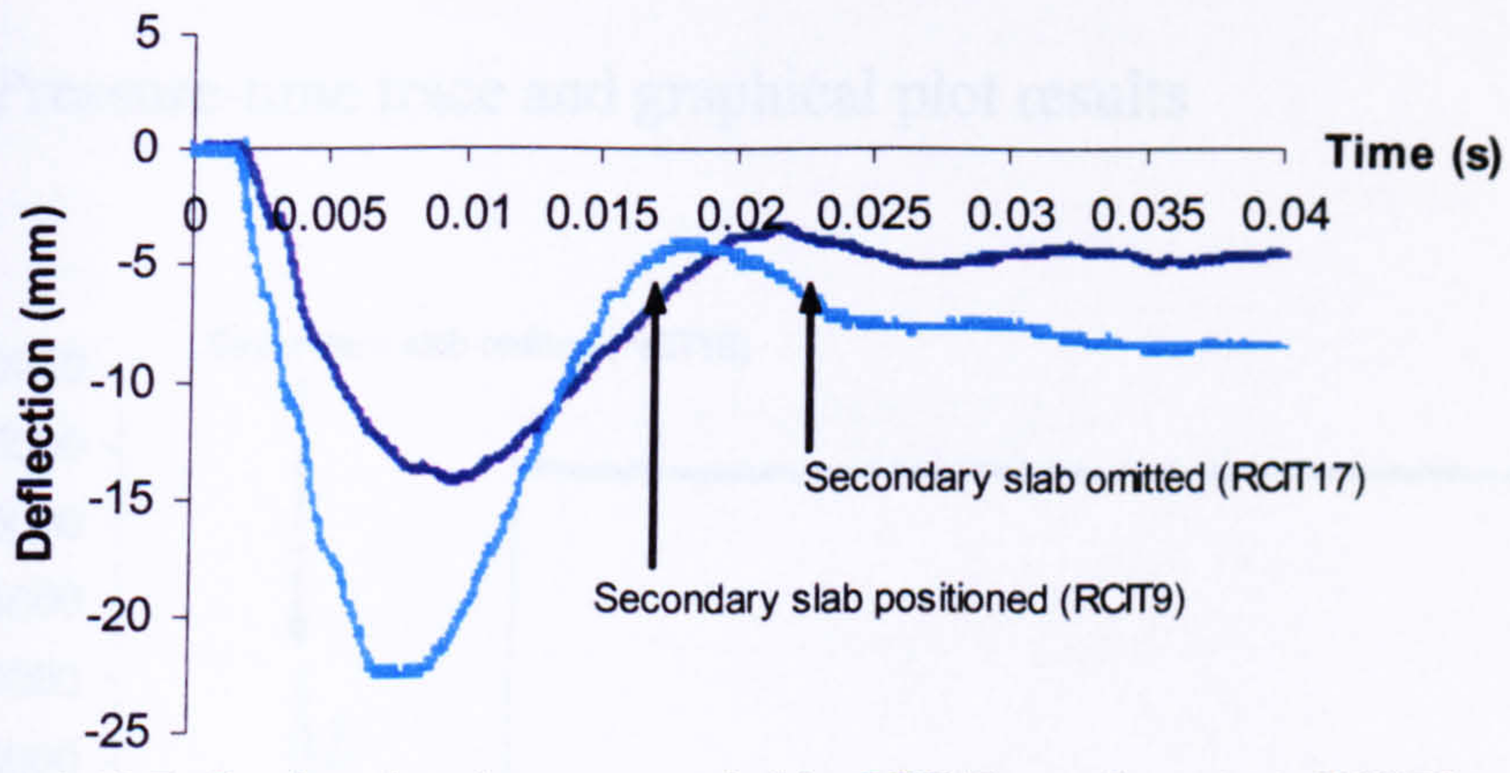

Figure A.2.10 Deflection-time traces recorded by $LVDT_{250mm}$ from tests RCIT9 and RCIT17.

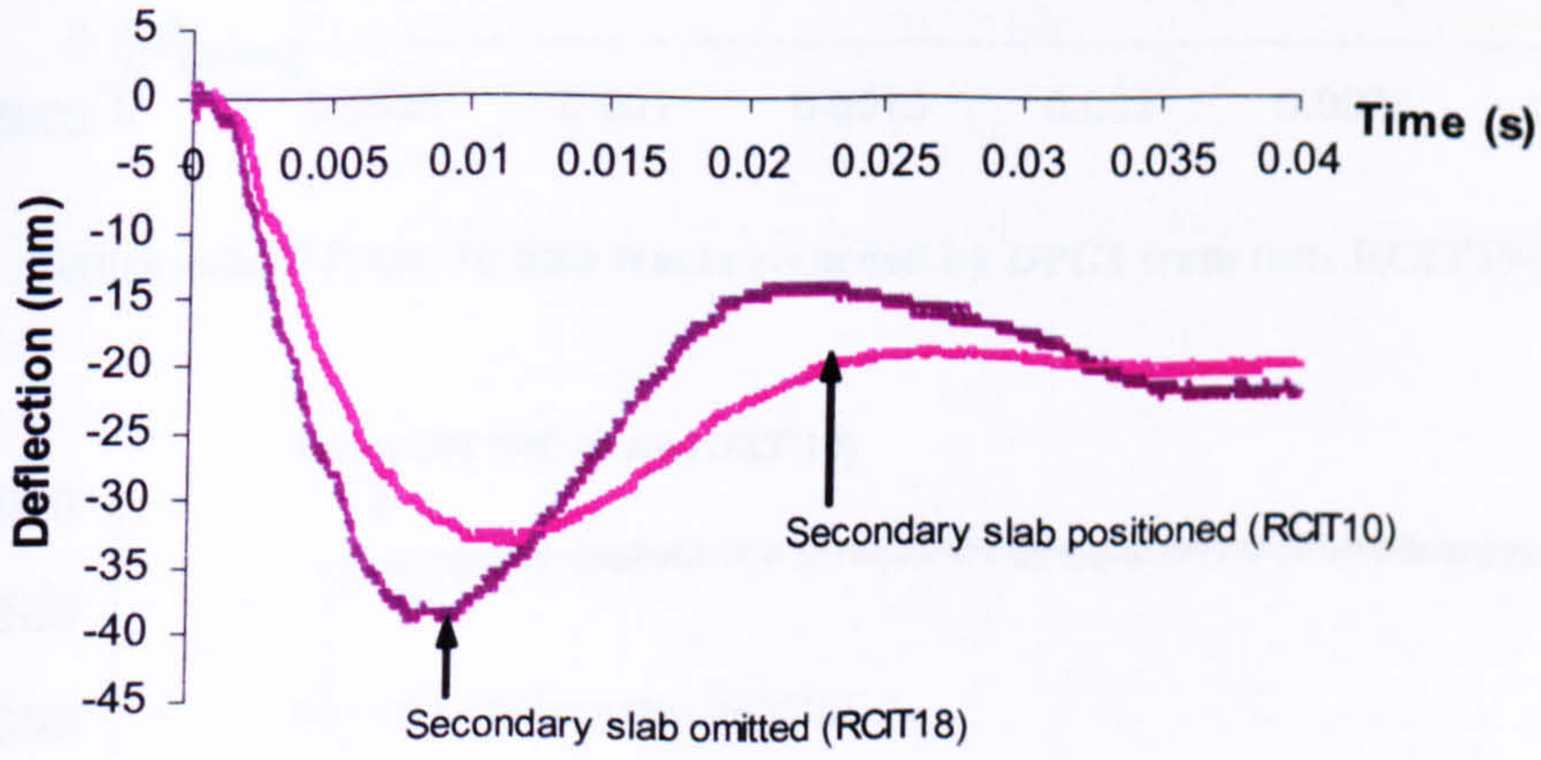

Figure A.2.11 Deflection-time traces recorded by $LVDT_{250mm}$ from tests RCIT10 and RCIT18.

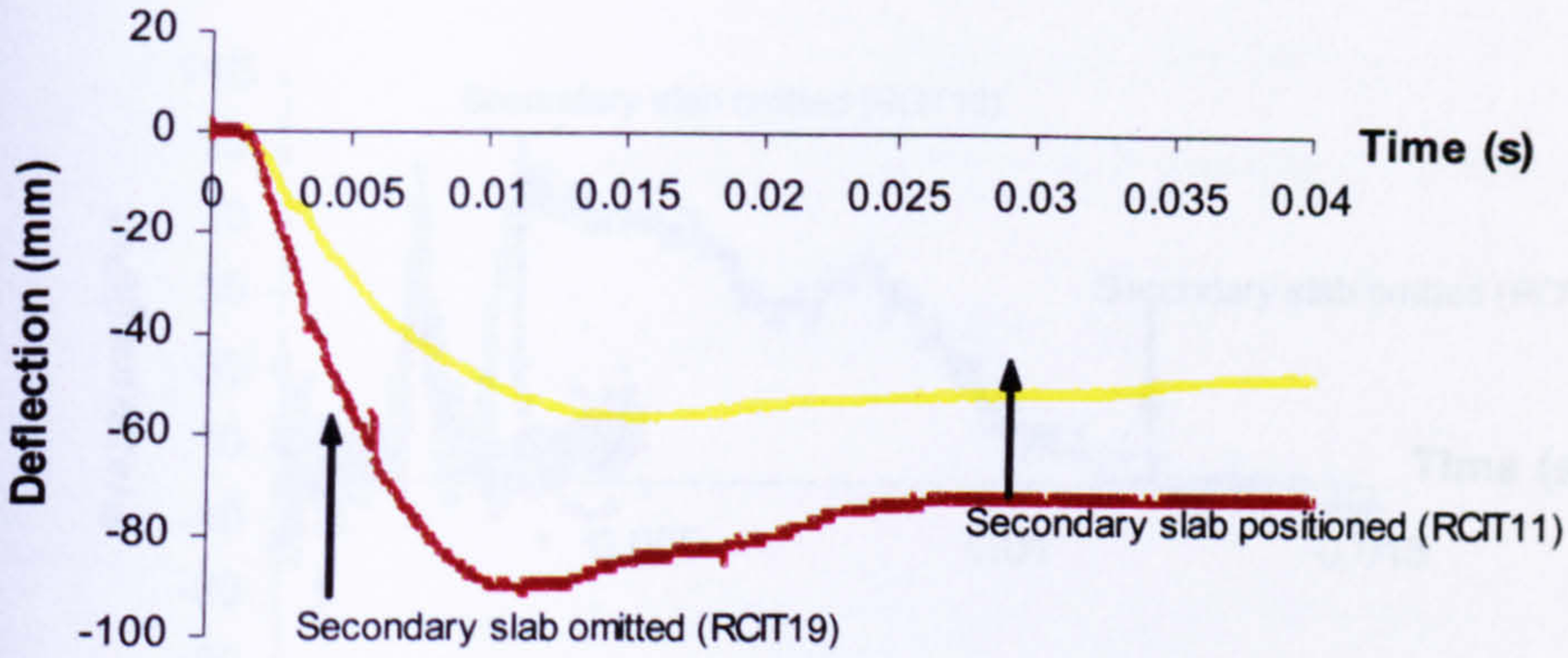

Figure A.2 12 Deflection-time traces recorded by $LVDT_{250mm}$ from tests RCIT11 and RCIT19.

A.2.2 Pressure-time trace and graphical plot results

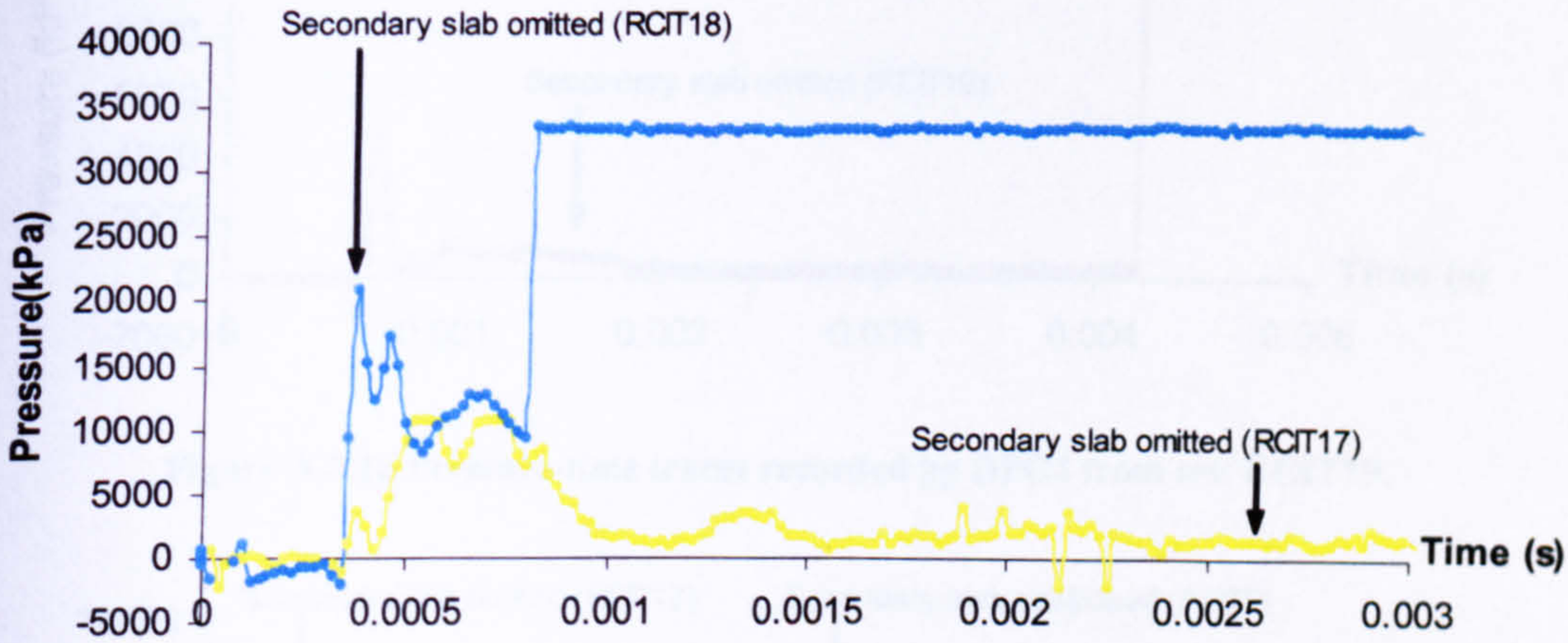

Figure A.2.13 Pressure-time traces recorded by DPG1 from tests RCIT17-18.

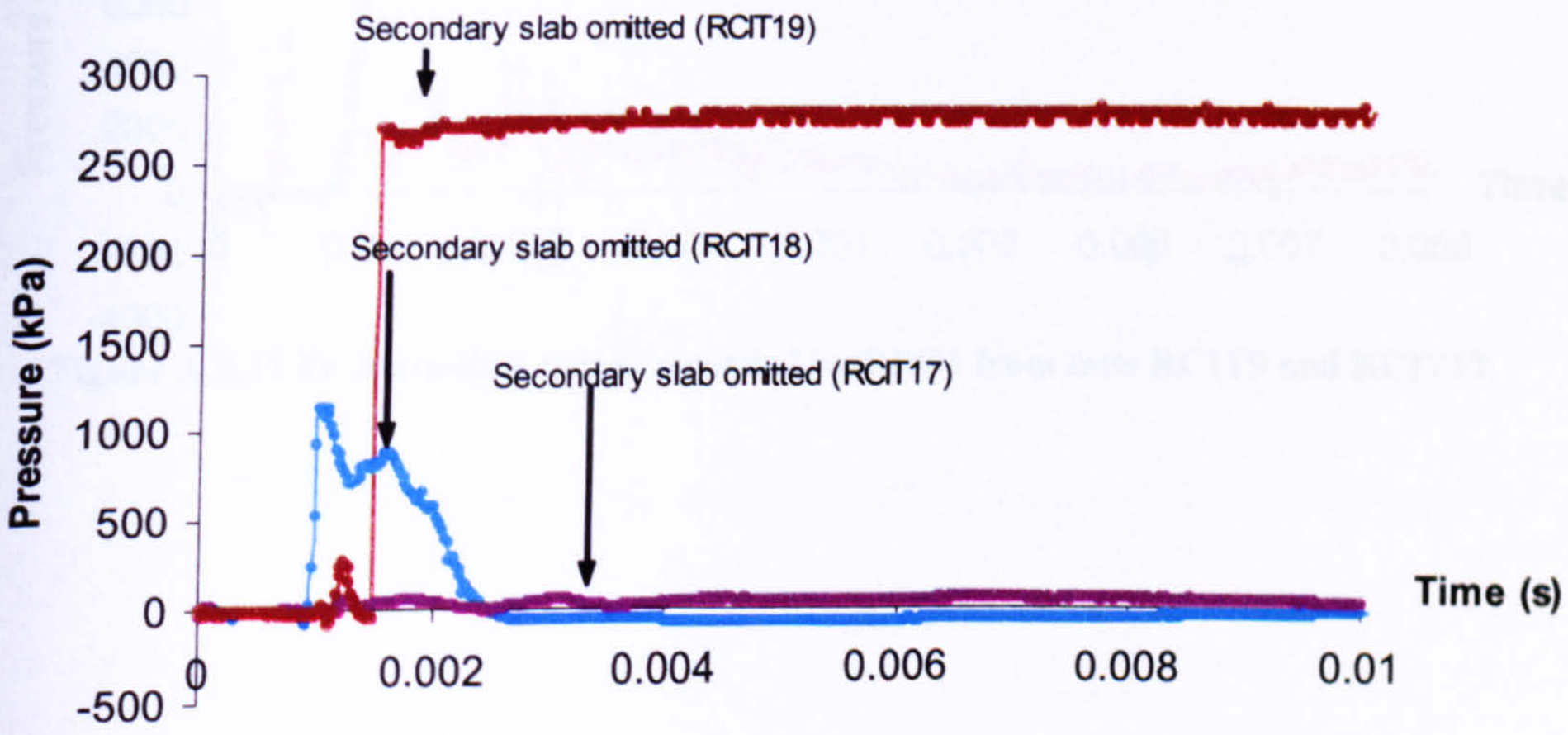

Figure A.2.14 Pressure-time traces recorded by DPG2 from tests RCIT17-19.

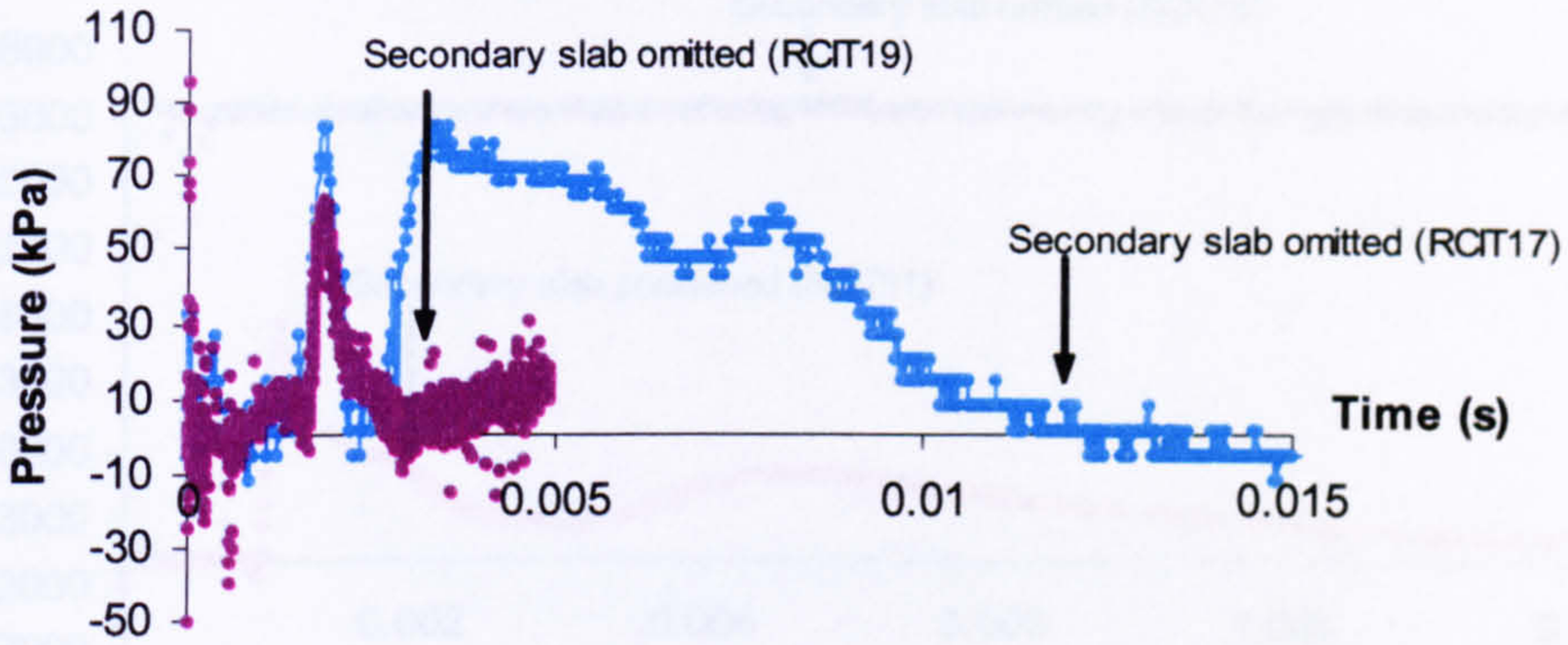

Figure A.2.15 Pressure-time traces recorded by DPG3 from tests RCIT17& RCIT19.

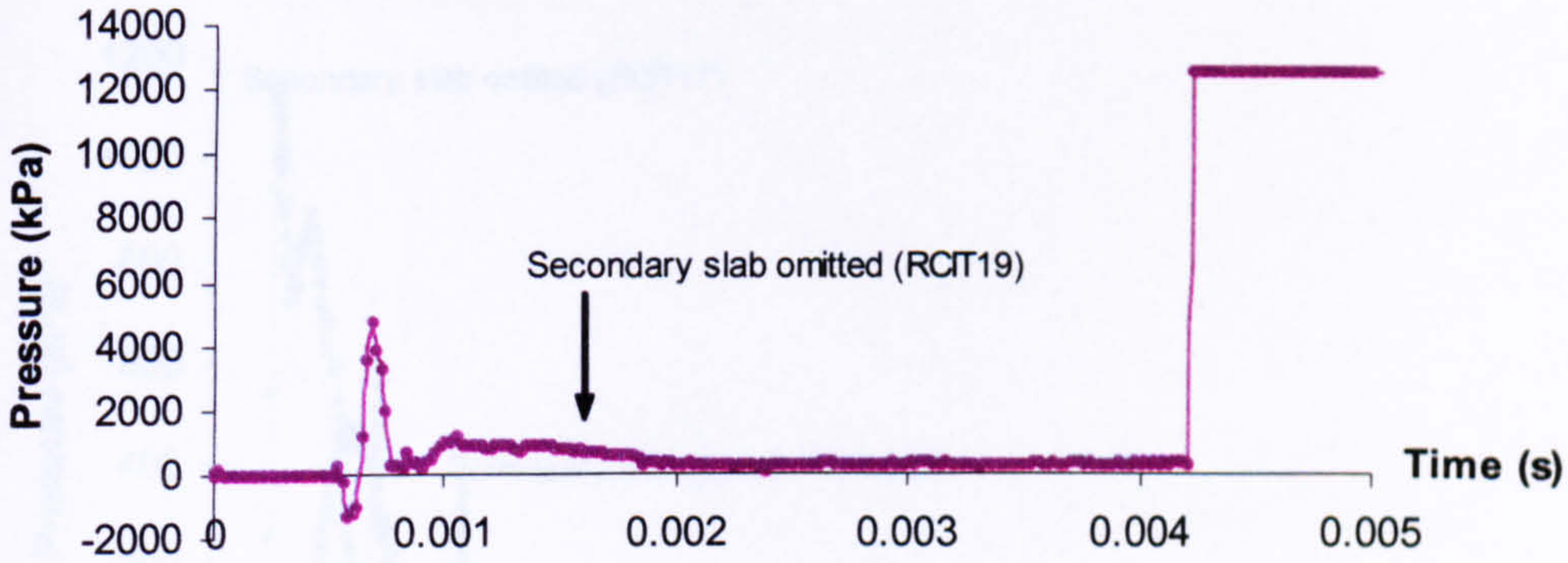

Figure A.2.16 Pressure-time traces recorded by DPG4 from test RCIT19.

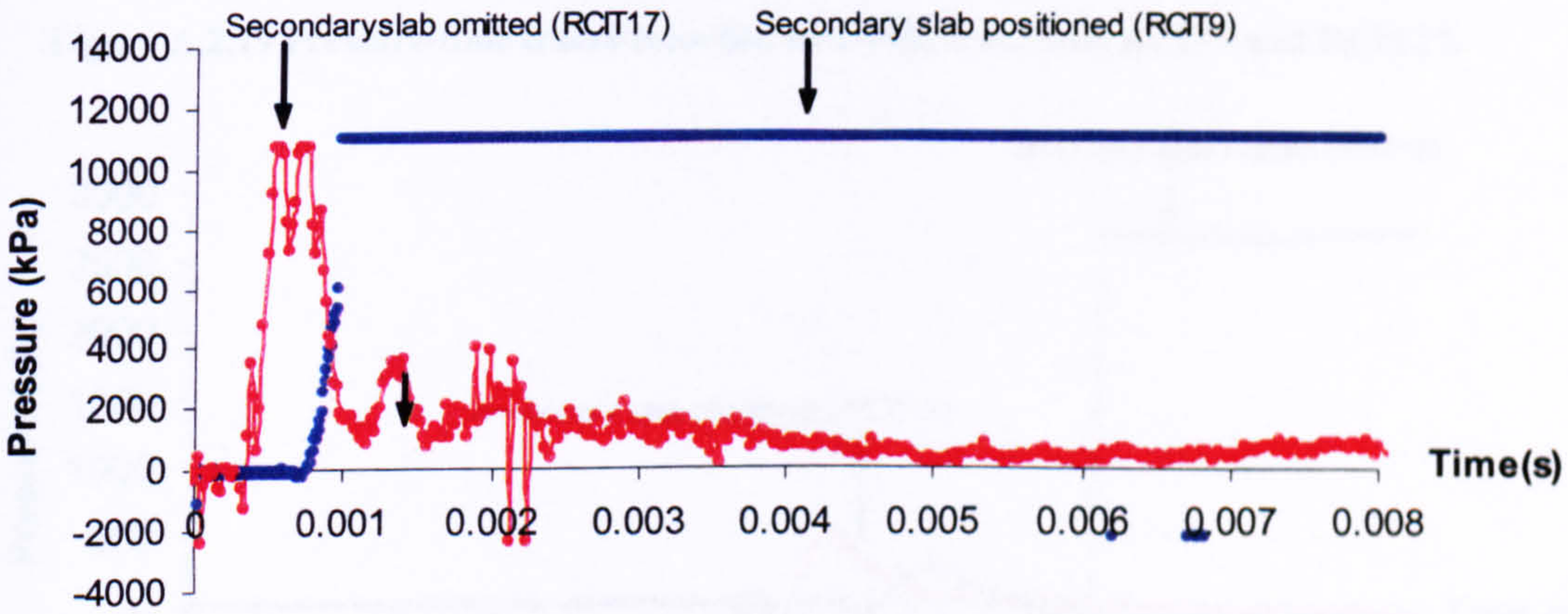

Figure A.2.17 Pressure-time traces recorded by DPG1 from tests RCIT9 and RCIT17.

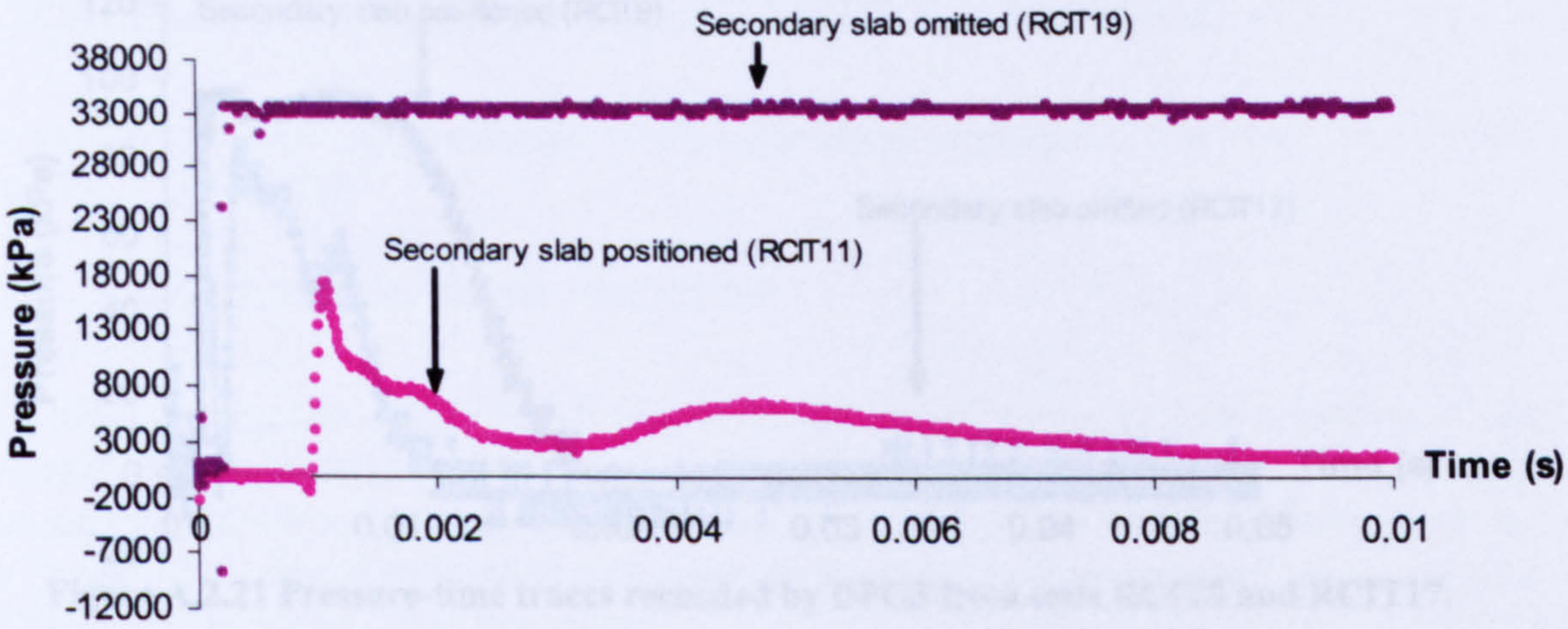

Figure A.2.18 Pressure-time traces recorded by DPG1 from tests RCT11and RCIT19.

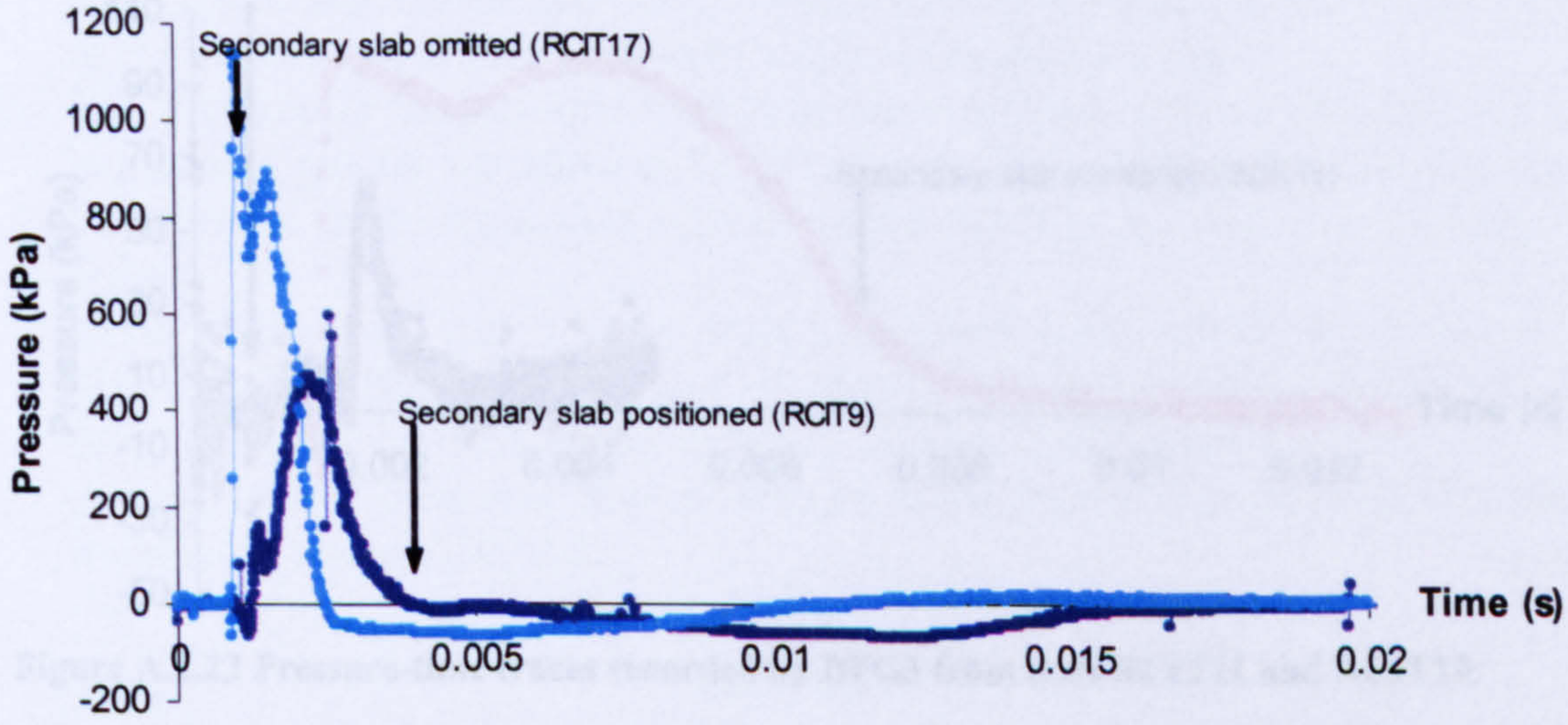

Figure A.2.19 Pressure-time traces recorded by DPG2 from tests RCIT9 and RCIT17.

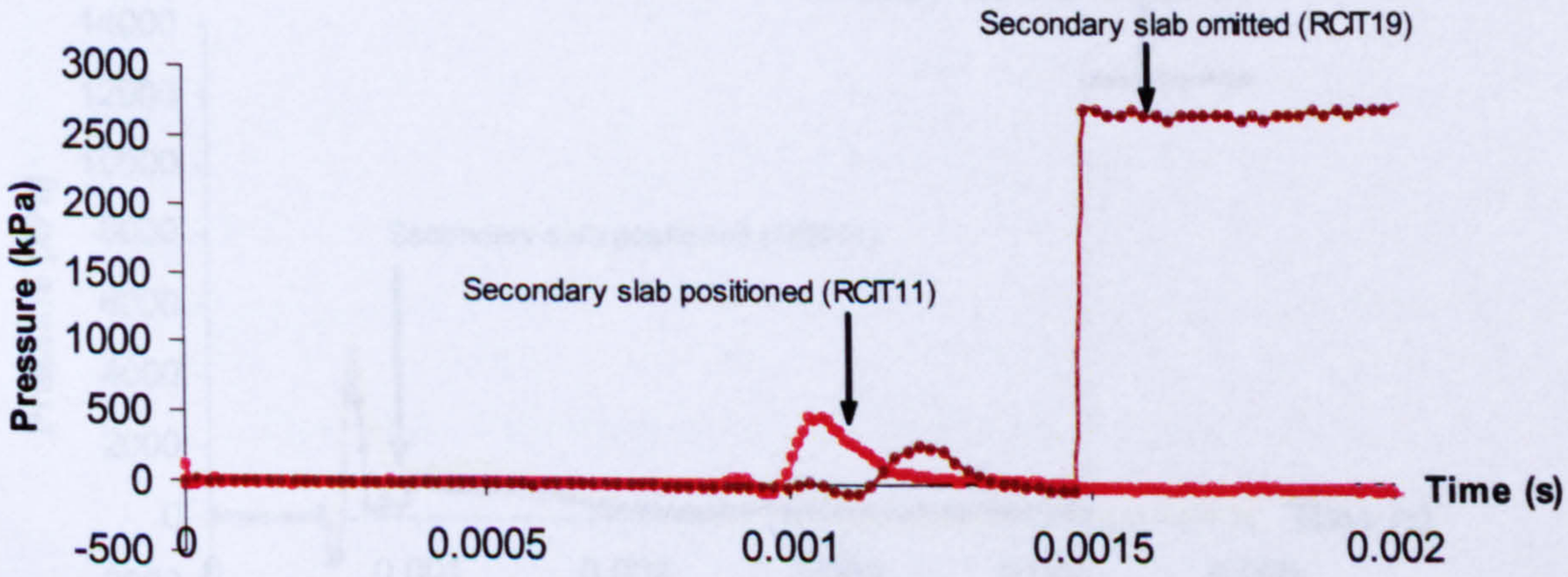

Figure A.2.20 Pressure-time traces recorded by DPG2 from tests RCIT11 and RCIT19.

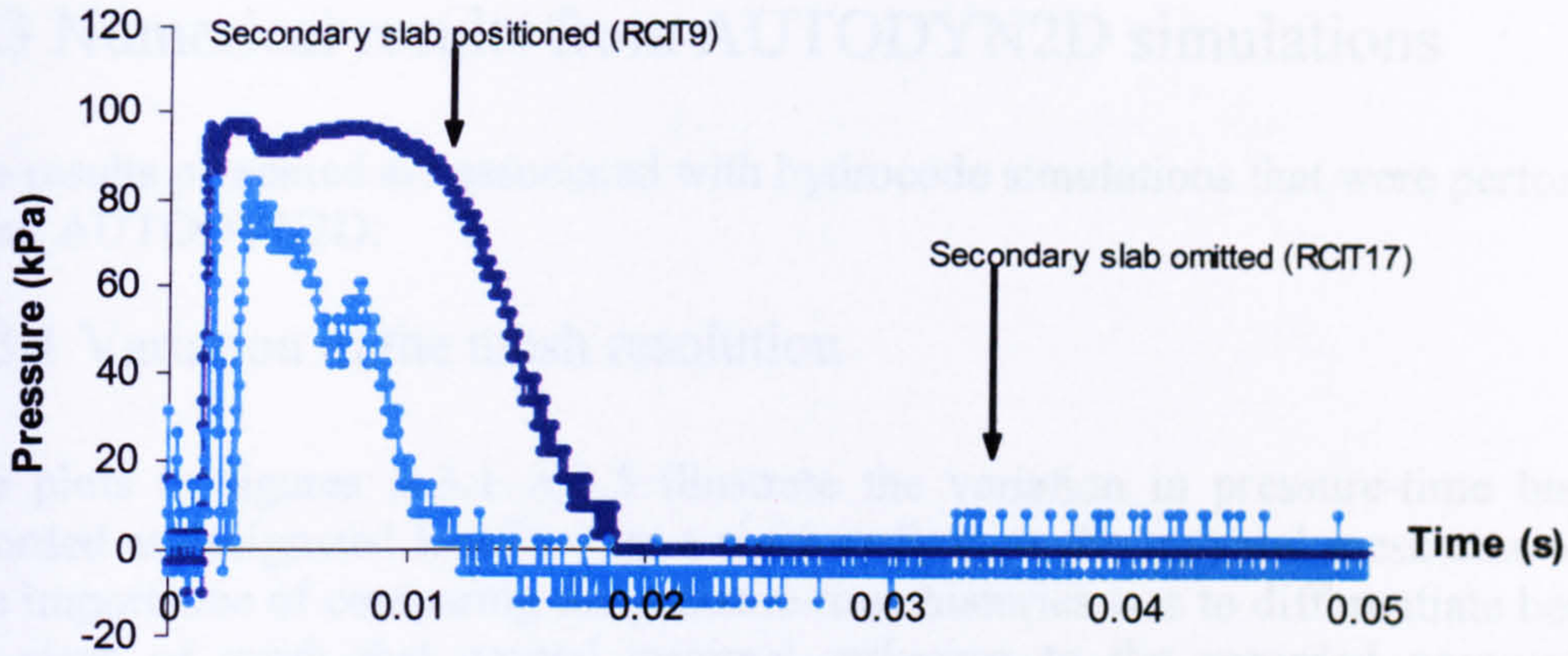

Figure A.2.21 Pressure-time traces recorded by DPG3 from tests RCIT9 and RCIT17.

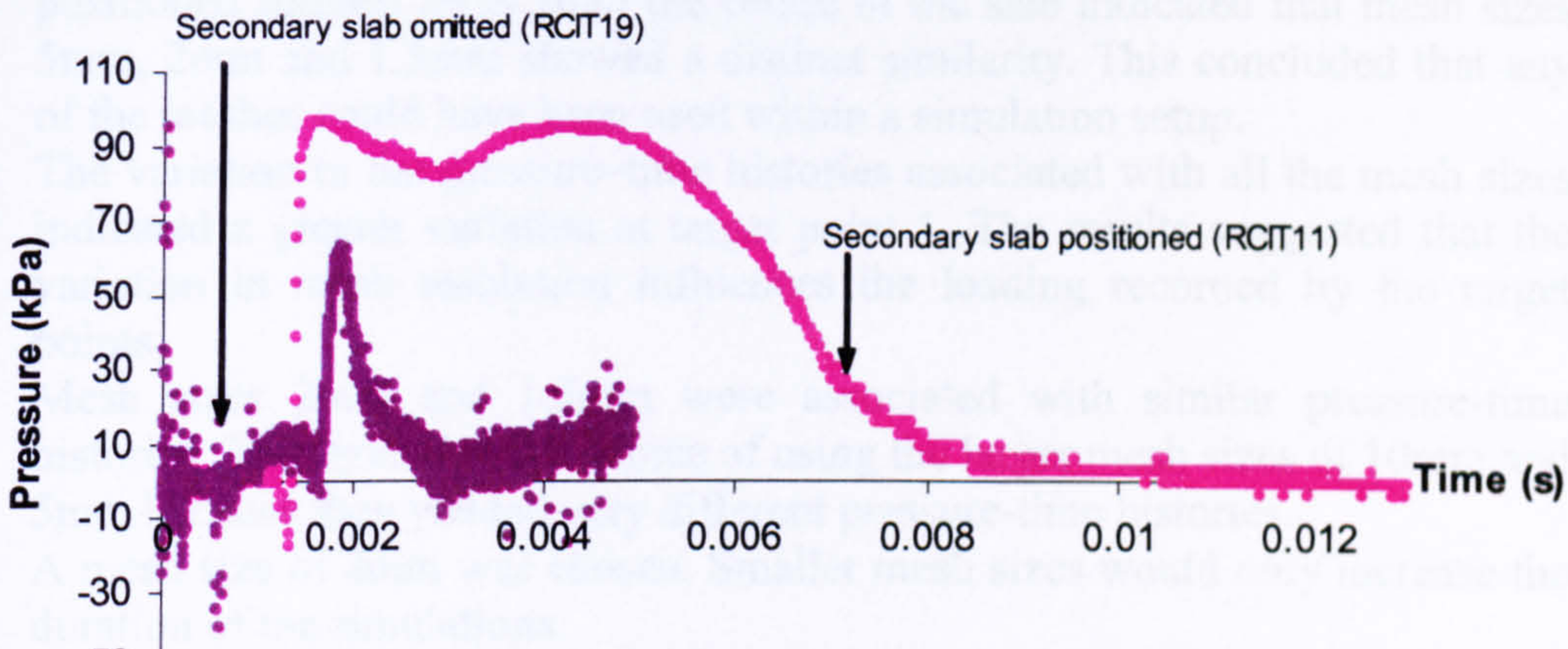

Figure A.2.22 Pressure-time traces recorded by DPG3 from tests RCIT11 and RCIT19.

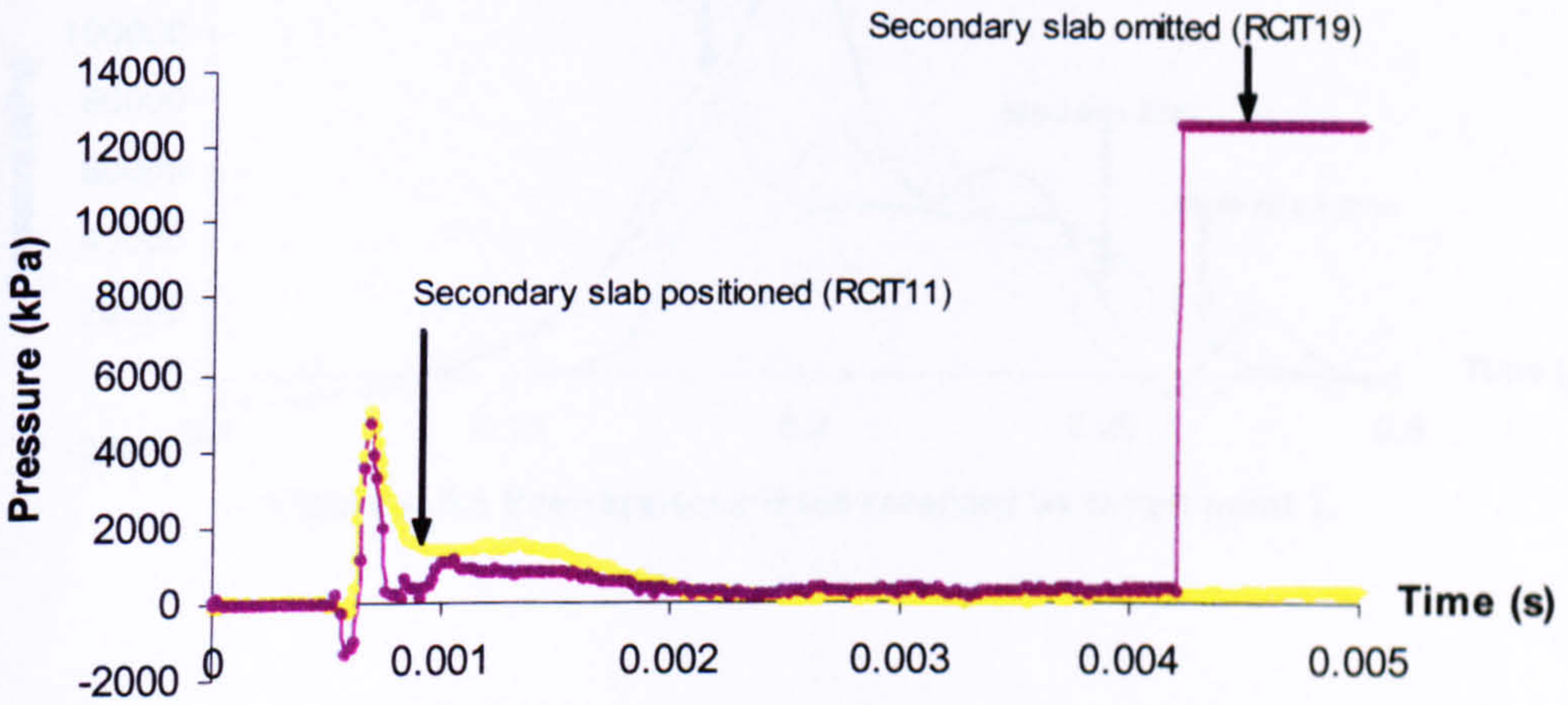

Figure A.2.23 Pressure-time traces recorded by DPG4 from tests RCIT11 and RCIT19.

A.3 Numerical results from AUTODYN2D simulations

The results presented are associated with hydrocode simulations that were performed using AUTODYN2D.

A.3.1 Variation in the mesh resolution

The plots in figures A.3.1–A.3.5 illustrate the variation in pressure-time histories recorded at designated locations on a rigid surface, as the material mesh size varied. The importance of comparing the pressure-time histories was to differentiate between the sizes of mesh that caused minimal influence to the recorded pressure-time profiles. The following was evaluated:

1. The comparison of pressure-time histories recorded by target point 5 positioned furthest away from the centre of the slab indicated that mesh sizes 5mm, 2mm and 1.5mm showed a distinct similarity. This concluded that any of the meshes could have been used within a simulation setup.
2. The variation in the pressure–time histories associated with all the mesh sizes indicated a greater variation at target point 1. The results suggested that the variation in mesh resolution influences the loading recorded by the target points.
3. Mesh sizes 2mm and 1.5mm were associated with similar pressure-time histories. This excluded the choice of using the larger mesh sizes of 10mm and 5mm because they yielded very different pressure-time histories.
4. A mesh size of 2mm was chosen. Smaller mesh sizes would only increase the duration of the simulations.

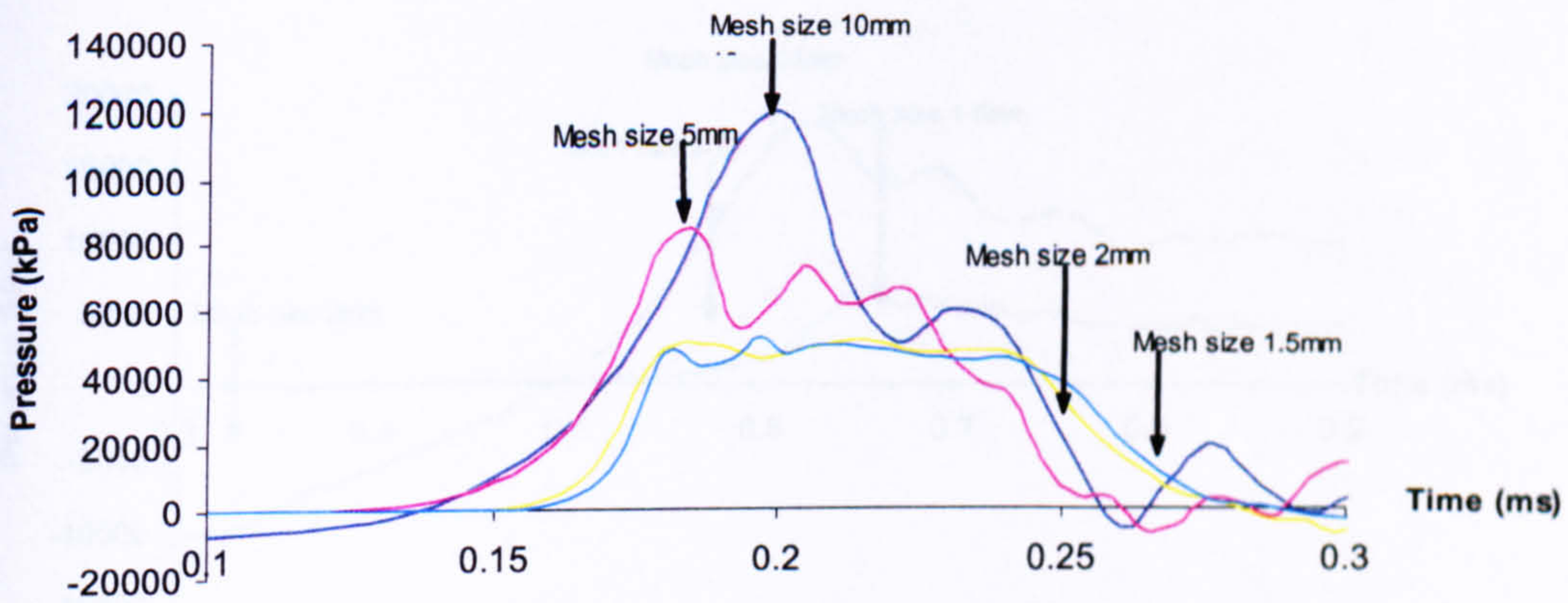

Figure A.3.1 Pressure-time trace recorded by target point 1.

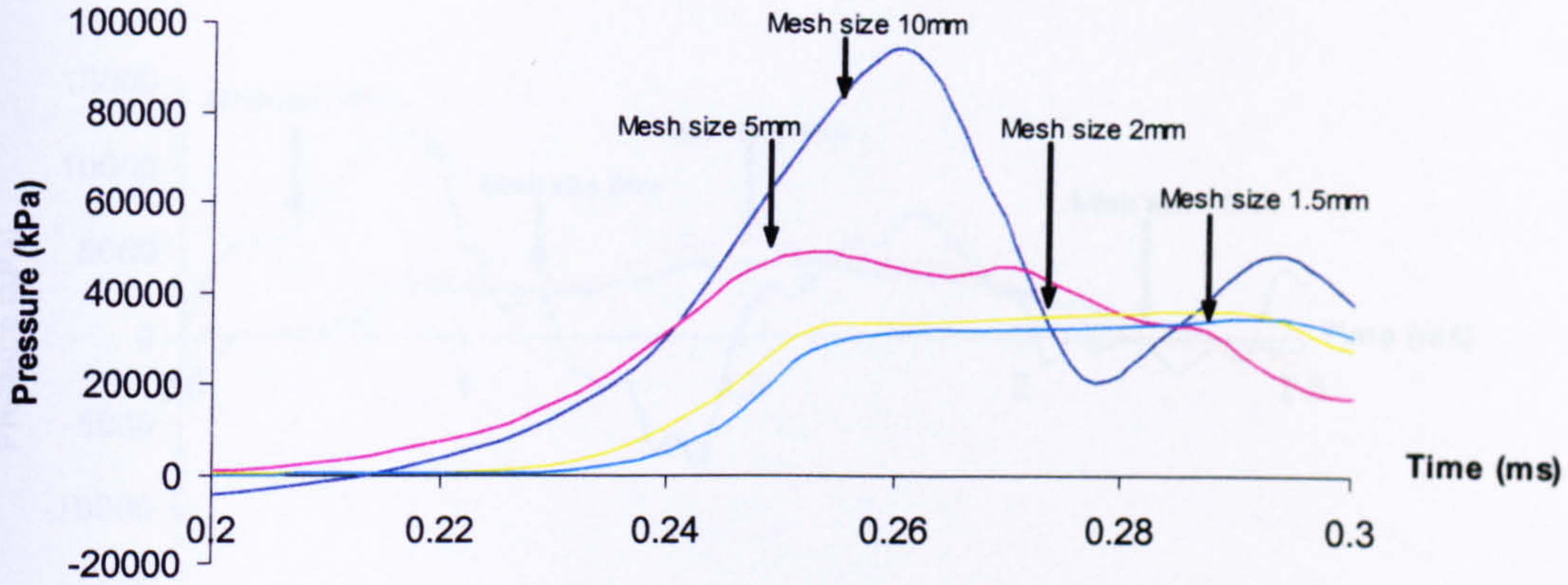

Figure A.3.2 Pressure-time trace recorded by target point 2.

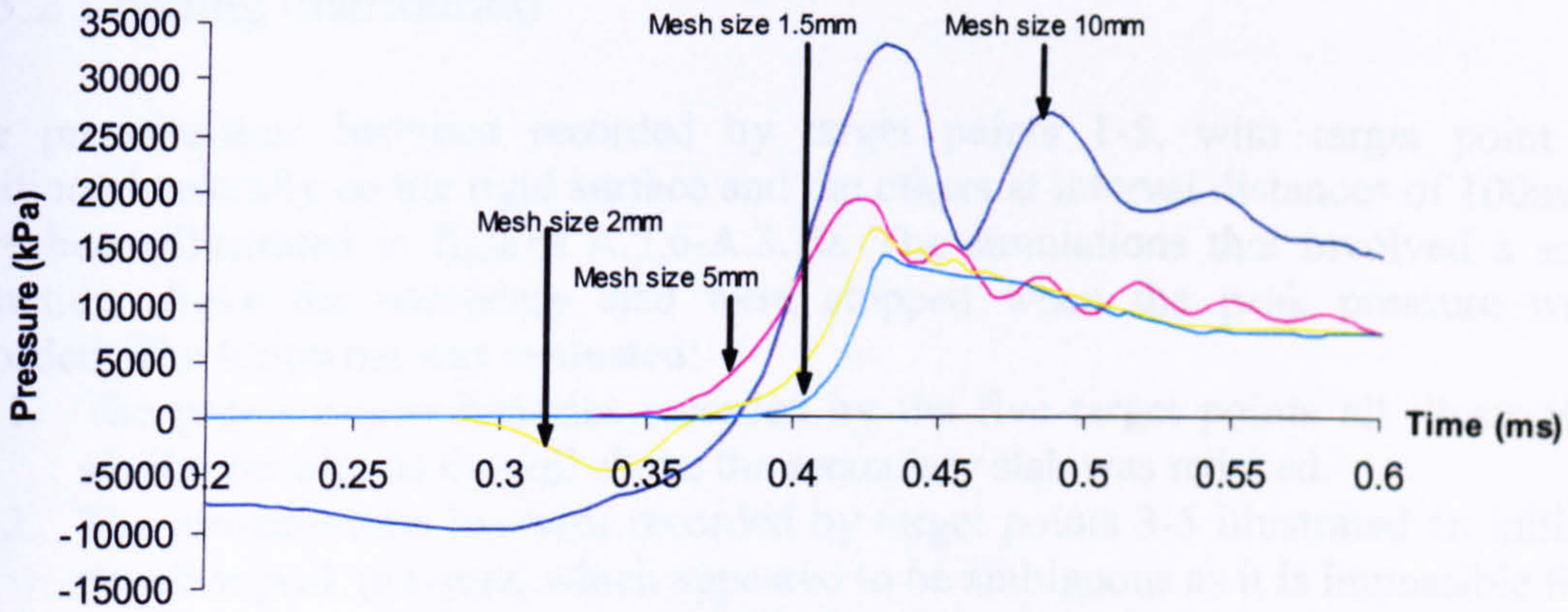

Figure A.3.3 Pressure-time trace recorded by target point 3.

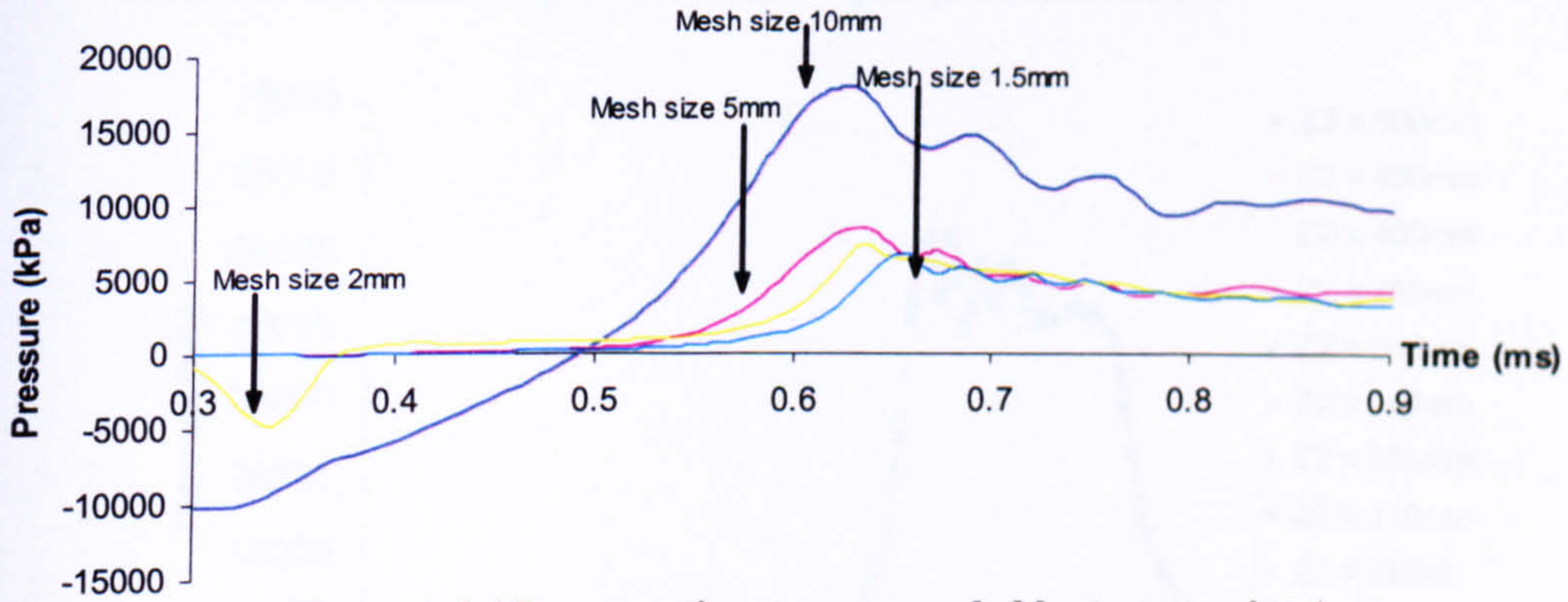

Figure A.3.4 Pressure-time trace recorded by target point 4.

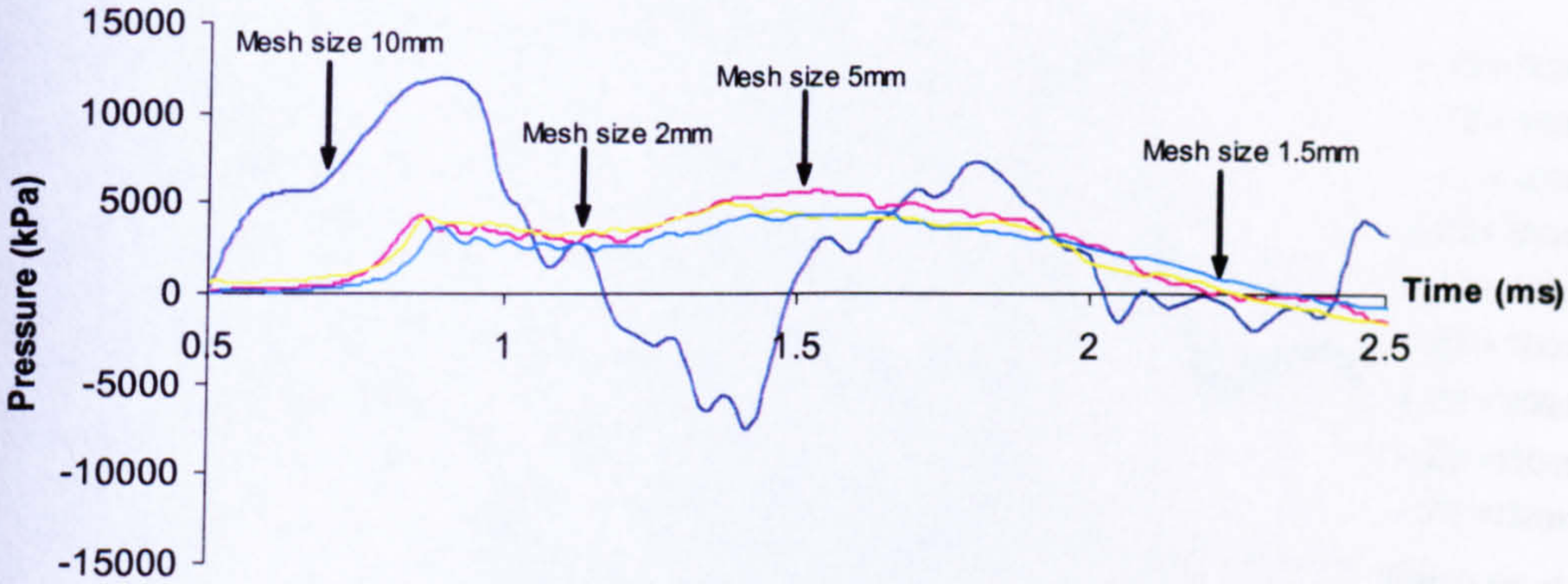

Figure A.3.5 Pressure-time trace recorded by target point 5.

A.3.2 Loading distribution

The pressure-time histories recorded by target points 1-5, with target point 1 positioned centrally on the rigid surface and the others at interval distances of 100mm have been illustrated in figures A.3.6-A.3.10. The simulations that involved a soil reduction above the secondary slab were stopped when the peak pressure was recorded. The following was evaluated:

1. The pressure-time histories recorded by the five target points all illustrated similar profiles as the soil above the secondary slab was reduced.
2. The pressure-time histories recorded by target points 3-5 illustrated an initial negative peak pressure, which appeared to be ambiguous as it is impossible for tensile stresses to be setup in sands. Therefore the only logical reason relates to inaccurate pressure calculations in AUTODYN2D. This was not the main concern, but a future problem that required rectification.

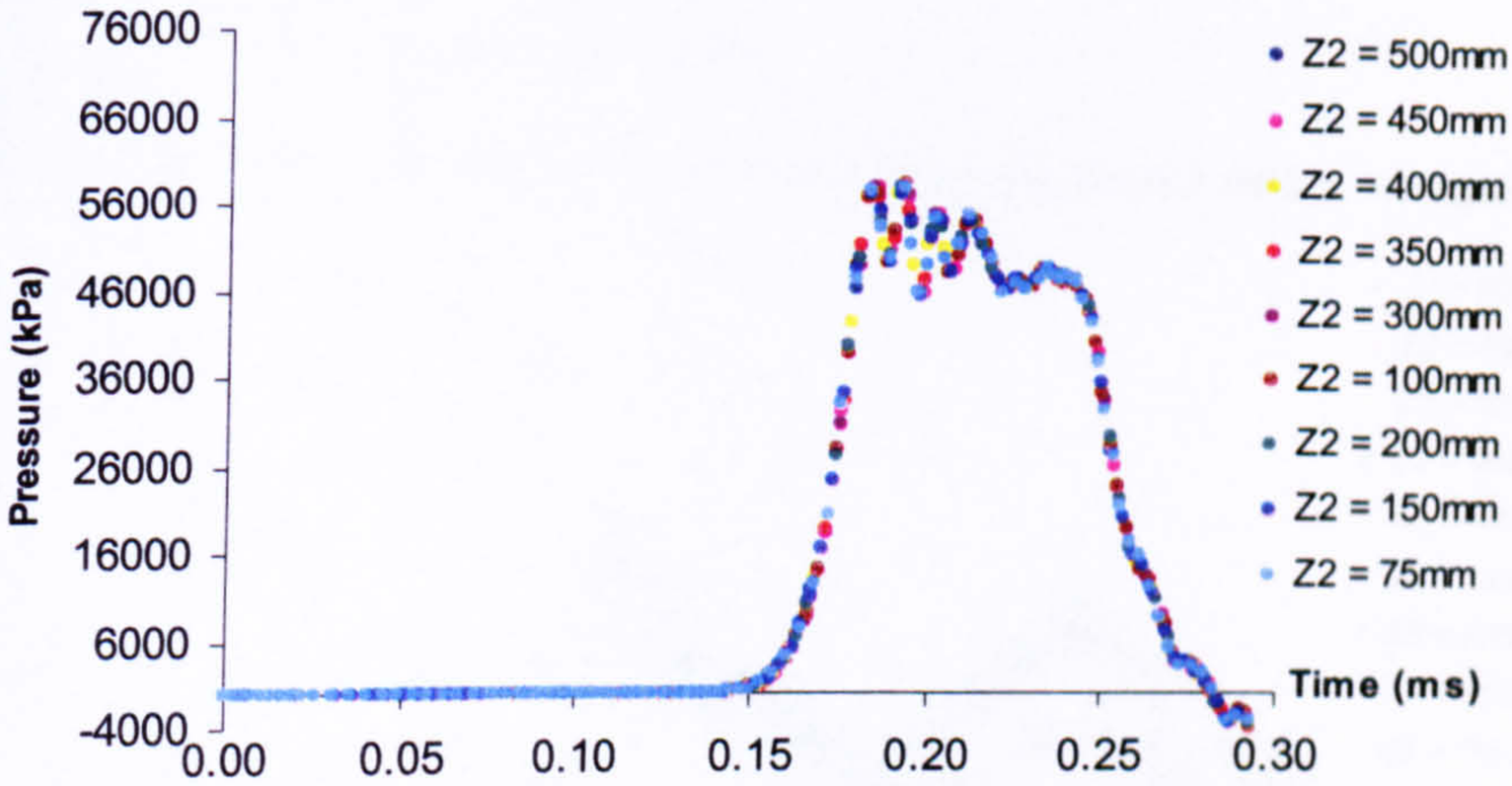

Z_2 = Soil overburden above the secondary slab

Figure A.3.6 Pressure-time traces recorded by target point 1 with a variation in Z_2.

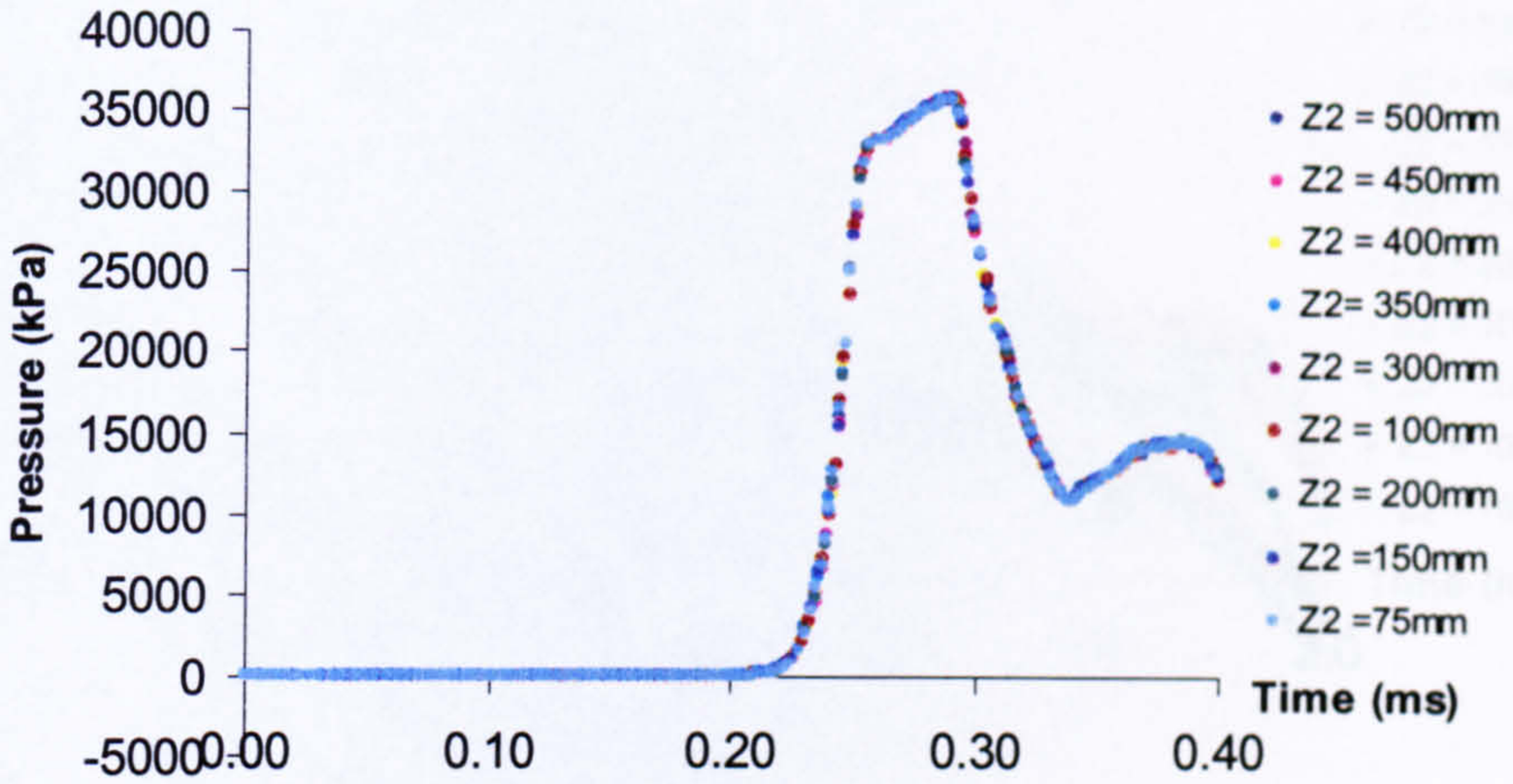

Z_2 = Soil overburden above the secondary slab

Figure A.3.7 Pressure-time traces recorded by target point 2 with a variation in Z_2.

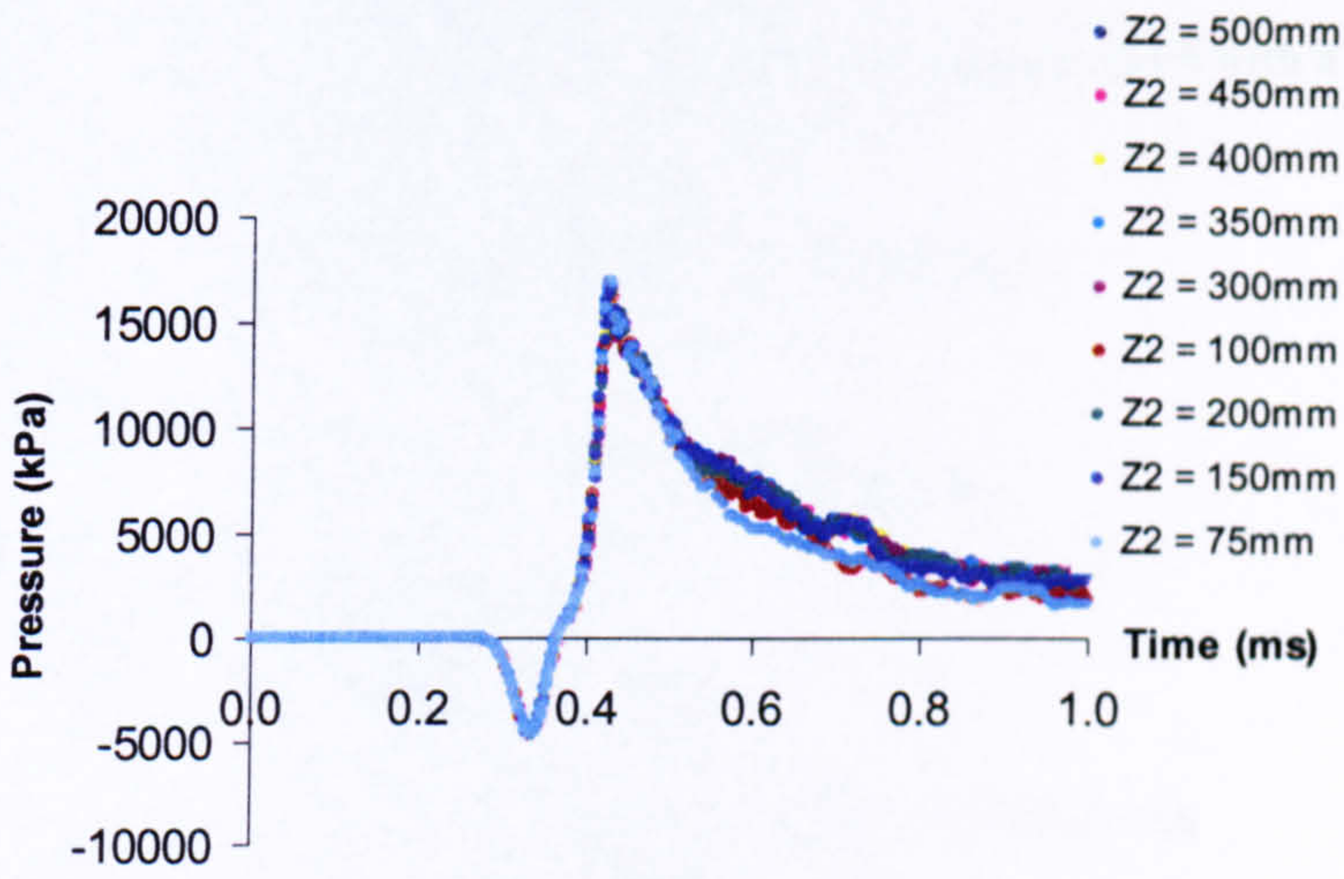

Z_2 = Soil overburden above the secondary slab

Figure A.3.8 Pressure-time traces recorded by target point 3 with a variation in Z_2.

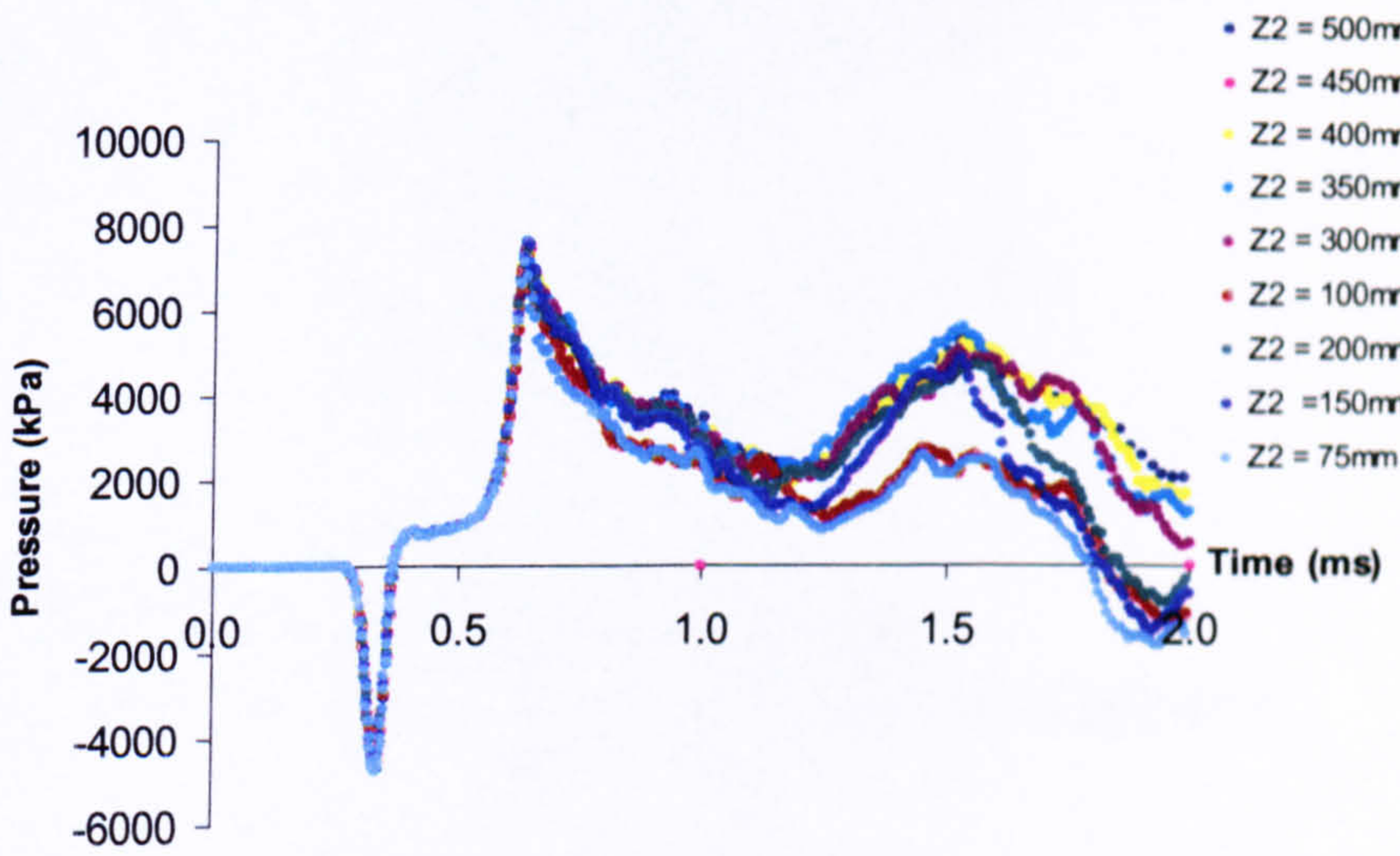

Z_2 = Soil overburden above the secondary slab

Figure A.3.9 Pressure-time traces recorded by target point 4 with a variation in Z_2.

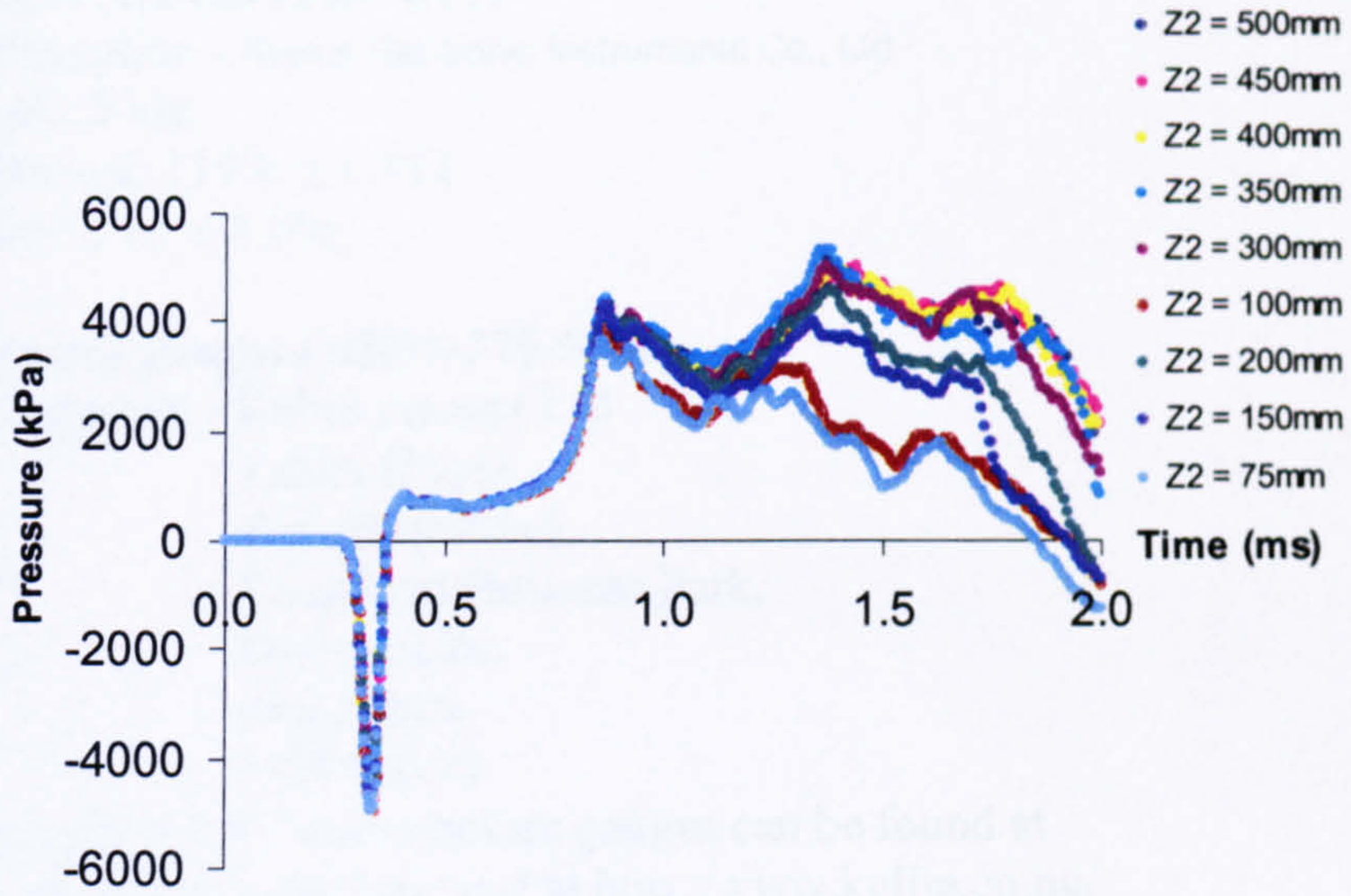

Z_2 = Soil overburden above the secondary slab

Figure A.3.10 Pressure-time traces recorded by target point 5 with a variation in Z_2.

A.4 Material and instrumental suppliers

Cement (RHPC)
Address of supplier – Markovitz Builders Supplies,
Richard Ln,
Tideswell,
Buxton.

Fine aggregate – 1271RL/Concrete sand Grade MR Lees
Address of supplier – Mercaston Quarry
Hanson Aggregate UK.

Polystyrene boards (8ft x 4ft x 50mm Jabalite polystyrene insulation boards)
Address of supplier - Markovitz builders supplies.
Tideswell Nr Buxton,
Derbyshire.

Linear variable displacement transducers (LVDT)
Address of supplier – RDP Electronics Ltd,
Grove Street,
Heath Town,
Wolverhampton,
WV10 0PY.
Information relating to LVDTs can be found at
http://www.rdpe.com/displacement/lvdt/general/act-captive.htm

Strain gauges (KFG5/120/C1/11)
Address of supplier – Kyowa Electronic Instruments Co., Ltd
Gauge length: 5mm
Gauge resistance: 119.8 $\pm 0.2\,\Omega$
Gauge factor: 2.11 $\pm 1.0\%$

Kulite pressure gauges (HKM-375-5000)
Address of supplier - Kulite sensors Ltd
Kulite House,
Stroudley Road,
Kingsland Business Park,
Basingstoke,
Hampshire,
RG24 BUG.
Information relating to these pressure gauges can be found at http://www.a-tech.ca/index.htm and at http://www.kulite.co.uk/